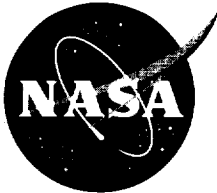


# **Annual Research Briefs – 1993**

**Center for Turbulence Research**

**December 1993**



Ames Research Center



Stanford University



# CONTENTS

<b>Preface</b>	1-7
Optimal feedback control of turbulent channel flow. T. BEWLEY, H. CHOI, R. TEMAM, and P. MOIN	3-1
Drag reduction at a plane wall. D. C. HILL	15-2
Boundary layer receptivity and control. D. C. HILL	21-5
Toward modeling wingtip vortices. O. ZEMAN	31-4
New concepts for Reynolds stress transport equation modeling of in- homogeneous flows. J. B. PEROT and P. MOIN	41-7
Turbulence modeling for non-equilibrium flows. P. A. DURBIN	67-5
Computation of turbulent flows over backward and forward-facing steps using a near-wall Reynolds stress model. S. H. KO	75-7
Large eddy simulation of a boundary layer with concave streamwise curvature. T. LUND	91-1
Large-eddy simulation of flow in a plane, asymmetric diffuser. H.-J. KALTENBACH	101-7
On the large eddy simulation of turbulent flows in complex geometry. S. GHOSAL	111-10
Dynamic localization and second-order subgrid-scale models in large eddy simulations of channel flow. W. CABOT	129-11
Toward large eddy simulation of turbulent flow over an airfoil. H. CHOI	145-12
Unstructured grid large eddy simulation of wall bounded turbulent flows. K. JANSEN	151-13
Investigation of the asymptotic state of rotating turbulence using large-eddy simulation. K. D. SQUIRES, J. R. CHASNOV, N. N. MANSOUR, and C. CAMBON	157-14
Energy transfer and constrained simulations in isotropic turbulence. J. JIMÉNEZ	171-15
A large eddy simulation scheme for turbulent reacting flows. F. GAO	187-16
The combustion program at CTR. T. POINSOT	195-17
Stretch-induced quenching in flame-vortex interactions. J.-M. SAMANIEGO	205-18
A transport equation for the scalar dissipation in reacting flows with variable density: first results. T. MANTEL	219-19

The production of premixed flame surface area in turbulent shear flow. A. TROUVÉ	229 <sup>20</sup>
On streak spacing in wall-bounded turbulent flows. J. M. HAMILTON and J. KIM	249 <sup>21</sup>
Numerical simulation of non-Newtonian free shear flows. G. M. HOMSY and J. AZAIEZ	259 <sup>22</sup>
Transition to turbulence in an elliptic vortex. T. S. LUNDGREN and N. N. MANSOUR	269 <sup>23</sup>
Vortical structure in a forced plane mixing layer. R. L. LEBOEUF	285 <sup>24</sup>
Sound radiation due to boundary layer transition. M. WANG	299 <sup>25</sup>
Direct simulation of isothermal-wall supersonic channel flow. G. N. COLEMAN	313 <sup>26</sup>
Effects of shock strength on shock turbulence interaction. S. LEE	329 <sup>27</sup>
Local isotropy in strained turbulent boundary layers at high Reynolds number. S. G. SADDUGHI	347 <sup>28</sup>
Computation of large-scale statistics in decaying isotropic turbulence. J. R. CHASNOV	365 <sup>29</sup>
On the dynamics of approximating schemes for dissipative nonlinear equations. D. JONES	373 <sup>30</sup>
Tensoral for post-processing users and simulation authors. E. DRESSELHAUS	387 <sup>31</sup>
<b>Appendix: Center for Turbulence Research 1993 Roster</b>	395 <sup>32</sup>



## Preface

This report contains the 1993 annual progress reports of the Research Fellows and students of the Center for Turbulence Research. In addition to this and the Summer Program reports, each year several CTR manuscript reports are published to expedite the dissemination of research findings by the CTR Fellows.

The Fellows of the Center for Turbulence Research are engaged in fundamental studies of turbulent flows with the objective of advancing the physical understanding of turbulence and to improve turbulence models for engineering analysis and develop techniques for turbulence control. The CTR Fellows have a broad range of interests and expertise; together with the NASA-Ames scientific staff and Stanford faculty members, they form a stimulating environment devoted to the study of turbulence.

In its seventh year of operation, CTR hosted seventeen resident Postdoctoral Fellows, four Research Associates, and four Senior Research Fellows, and it supported three doctoral students and six short term visitors. The major portion of Stanford's doctoral program in turbulence is sponsored by the United States Air Force Office of Scientific Research and the Office of Naval Research. Many students supported by these programs also conduct their research at the CTR. This report includes work only for those students who are directly supported by the CTR.

The first group of reports in this volume are directed towards the theory and application of active control in turbulent flows. A notable progress in this area was the development of a systematic mathematical procedure based on the Navier Stokes equations for flow control. The second and the largest group of reports are concerned with the prediction of turbulent flows. Last year a significant fraction of CTR's effort in large eddy simulation and Reynolds averaged turbulence modeling was focused on the *application* of models developed at the CTR to complex flows. We expect this trend to continue. The remaining articles are devoted to turbulent reacting flows, turbulence physics, experiments, and simulations. In particular, a new set of experiments addressing the question of local isotropy in high Reynolds number strained turbulence was conducted in the 80x120 tunnel at Ames. It is becoming evident that this and perhaps other similar large scale national facilities can effectively be used for fundamental flow research. In the last two years, colleagues from other universities were also able to participate in these unique experiments.

The CTR roster for 1993 is provided in the Appendix. Also listed are the members of the Advisory Committee which meets annually to review the Center's program and the Steering Committee which acts on Fellowship applications.

It is a pleasure to thank Debra Spinks, the Center's Administrative Assistant, for her skillful compilation of this report.

Parviz Moin  
William C. Reynolds



## Optimal feedback control of turbulent channel flow

By Thomas Bewley, Haechon Choi, Roger Temam<sup>1</sup>, AND Parviz Moin

Feedback control equations have been developed and tested for computing wall-normal control velocities to control turbulent flow in a channel with the objective of reducing drag. The technique used is the minimization of a "cost functional" which is constructed to represent some balance of the drag integrated over the wall and the net control effort. A distribution of wall velocities is found which minimizes this cost functional some time shortly in the future based on current observations of the flow near the wall. Preliminary direct numerical simulations of the scheme applied to turbulent channel flow indicates it provides approximately 17% drag reduction. The mechanism apparent when the scheme is applied to a simplified flow situation is also discussed.

### 1. Motivation and objectives

It is the goal of this project to study methods to counteract near-wall vortical structures in turbulent boundary layer flow using an active control system in an effort to reduce drag. From this study, we hope to better understand the physics of drag producing events and the sensitivity of boundary layer flow to control. As a more far-reaching goal, we would like to better understand how to develop control equations for general flow control problems, utilizing the equations governing fluid flow to achieve performance that is in some sense optimal for a given situation.

With a well-chosen scheme using wall control only, it has been shown that a turbulent flow may be smoothed out in a near-wall region, and the drag may be substantially reduced. This scheme applies small amounts of wall-normal blowing and suction through the computational equivalent of holes drilled in the wall. Previous *ad hoc* schemes by Choi *et al.* (1992) have reduced the drag by as much as 20% by countering the vertical velocity slightly above the wall with an equal but opposite control velocity at the wall. The objective of this work is to derive more effective schemes by applying optimal control theory, utilizing the equations of motion of the fluid to reveal the dominant physics of the control problem and the most efficient distribution of the control energy. This work is an outgrowth of the work done by Choi *et al.* (1993), where optimal control theory was applied to the stochastic Burgers equation. Here, we apply the theory to the Navier-Stokes equations, which necessitates a more involved treatment of the equations and more extensive computer resources. The scheme discussed in this report depends on measurements of flow velocities above the wall — this is not feasible in a practical implementation. The scheme will later be reduced to a more practical one involving only flow quantities which are most easily measured in an experimental rig.

<sup>1</sup> Université de Paris-Sud (FRANCE) and Indiana University (USA)

The model problem we study in this work is the turbulent flow inside a small segment of a fully developed turbulent channel (*i.e.* flow between two parallel walls, far from the inlet). This flow is governed by the same vortical structures as turbulent boundary layer flow in the near-wall region.

Thus, the problem under consideration is a turbulent channel flow with no-slip walls and wall-normal control velocities  $\phi$ . Control will be applied to this flow in order to decrease the drag integrated over the walls at the expense of some measure of the net control effort. A feedback control algorithm has been developed which minimizes a “cost functional” constructed to represent this balance of the drag and the control effort. This method is introduced in Section 2. The control equations have been coded and tested in a direct numerical simulation of turbulent channel flow. Section 3 discusses preliminary results of these calculations.

## 2. Formulation

### 2.1 State equation (Navier-Stokes equation)

As described above, the problem under consideration is a constant-flux turbulent channel flow with no-slip walls and wall-normal control velocities  $\phi$ . This problem is governed by the unsteady, incompressible Navier-Stokes equation, the continuity equation, and a constant flux integral constraint equation inside the domain  $\Omega$  and appropriate boundary conditions on the walls  $w$  (periodic conditions are implied on the remainder of the boundary of the domain  $\Gamma$ ):

$$\left. \begin{aligned} \frac{\partial u_i}{\partial t} + \frac{\partial}{\partial x_j} u_j u_i &= -\frac{\partial p}{\partial x_i} + \frac{1}{Re} \frac{\partial}{\partial x_j} \frac{\partial}{\partial x_j} u_i \end{aligned} \right\} \quad (1a)$$

$$\left. \begin{aligned} \frac{\partial u_i}{\partial x_i} &= 0 \end{aligned} \right\} \quad \text{in } \Omega \quad (1b)$$

$$\left. \begin{aligned} \iiint_{\Omega} u_1 dx_1 dx_2 dx_3 &= C \end{aligned} \right\} \quad (1c)$$

$$\left. \begin{aligned} u_1 &= 0 \\ u_2 &= \phi \\ u_3 &= 0 \end{aligned} \right\} \quad \text{on walls,} \quad (2)$$

where  $x_1$  is the streamwise direction,  $x_2$  is the wall-normal direction,  $x_3$  is the spanwise direction,  $u_i$  are the corresponding velocities, and  $p$  is the pressure. The constants in the problem are  $C$  (a measure of the flux in the channel) and  $Re$  (the Reynolds number).

### 2.2 Optimal control of state equation

The goal of controlling the channel flow is to minimize the drag on a section of wall with area  $A$  over a period of time  $T$  using the least amount of control effort possible. The relevant quantities of interest are thus the time averaged drag

$$\bar{D} = \frac{1}{AT} \int_0^T \iint_w \frac{\partial u_1}{\partial n} dx_1 dx_3 dt \quad (3)$$

(where  $n$  is a unit vector in the *inward* wall normal direction) and a term representing the expense of the control. The latter term may be taken to be the integral of the magnitude of the power input, which may be written

$$\bar{E}_1 = \frac{1}{AT} \int_0^T \iint_w |\phi(p + \rho\phi^2/2)| dx_1 dx_3 dt, \quad (4a)$$

In addition, depending on the physical mechanism used to provide the control velocities, the rate of change of the control hardware settings might be another important expense (for instance, representing the expense involve in changing the settings of control valves in the system):

$$\bar{E}_2 = \frac{1}{AT} \int_0^T \iint_w \left| \frac{\partial \phi}{\partial t} \right| dx_1 dx_3 dt. \quad (4b)$$

A physically appropriate cost functional for this problem, then, balances the expense of the input versus the drag:

$$\bar{J}(\phi) = \ell_1 \bar{E}_1 + \ell_2 \bar{E}_2 + \bar{D}, \quad (5)$$

where  $\ell_1$  and  $\ell_2$  are appropriate weighting factors. We could proceed from this point to attempt to construct a control procedure designed to minimize this cost functional. A mathematically more simple cost functional for the purpose of control theory (for reasons which will become evident as the control equations are derived) is quadratic in  $\phi$ . Physically, this represents the integral of the magnitude of the kinetic energy per unit mass input to the system, and may be written

$$\bar{J}(\phi) = \frac{\ell}{2} \frac{1}{AT} \int_0^T \iint_w \phi^2 dx_1 dx_3 dt + \frac{1}{AT} \int_0^T \iint_w \frac{\partial u_1}{\partial n} dx_1 dx_3 dt. \quad (6)$$

It will be seen later that, in most problems that we consider, the expense terms are much less significant than the drag terms (in other words, the control is relatively cheap). The use of other expense terms does not cause much additional complexity or insight into the method.

The *optimal* control procedure considered, then, involves reducing the cost functional (6) for some period of time  $T$ . This method is described in Abergel and Temam (1990) in a related situation and is also discussed in Lions (1969). However, this is a prohibitively expensive procedure for present computational resources because it involves storage and manipulation of several three-dimensional fields over the entire time period under consideration. The complexity of such an algorithm is discussed further in Choi *et al.* (1993).

We therefore resort to a *suboptimal* control procedure (Choi *et al.* 1993). In this method, the state equation is discretized in time, then a control procedure is applied to reduce an instantaneous version of the cost functional (6)

$$J(\phi) = \frac{\ell}{2A} \iint_w \phi^2 dx_1 dx_3 + \frac{1}{A} \iint_w \frac{\partial u_1}{\partial n} dx_1 dx_3 \quad (7)$$

at each time step.

By applying the control at each time step, the algorithm gives the control which minimizes the cost functional over some short time interval. Note, however, that this method does not look ahead to anticipate further development of the flow, and thus the solution by this method does not necessarily correspond to the solution by the optimal control method. Thus, posing the problem in this suboptimal form is another level of approximation to the physical problem of interest.

The differences in complexity between the optimal and suboptimal schemes described above may be realized by drawing an analogy to a computer algorithm to play chess. A suboptimal chess program looks ahead one step to determine the move that leaves as good a position on the board as possible. Similarly, a suboptimal turbulence control scheme looks ahead one time step to determine the set of control velocities that leaves as good (*i.e.* low) a value of the cost functional as possible at the next time step. An optimal chess program, on the other hand, investigates all possible developments of the game a certain number of steps into the future (knowing how the other player may respond), and then moves in the direction that leads to the best final position on the board. Similarly, an optimal turbulence control scheme investigates all possible developments of the flow a certain amount of time into the future (knowing approximately how the flow will respond), and then applies the set of control velocities that leads to the best (*i.e.* lowest) time-averaged cost functional. Such a method requires significantly more resources than the suboptimal method.

### 2.3 Time discretization of state equation

The suboptimal control procedure introduced above is now applied to the state equation (1). To do this, we discretize (1) in time, then apply a feedback control algorithm to modify the flow at the next time step. A consistent approach is to use a second order Crank-Nicolson method (implicit) on all terms. The momentum equation (1a) thus takes the form:

$$\begin{aligned} \frac{u_i^n - u_i^{n-1}}{\Delta t} + \frac{1}{2} \frac{\partial}{\partial x_j} (u_j^n u_i^n + u_j^{n-1} u_i^{n-1}) = \\ - \frac{1}{2} \left( \frac{\partial p^n}{\partial x_i} + \frac{\partial p^{n-1}}{\partial x_i} \right) + \frac{1}{2Re} \left( \frac{\partial}{\partial x_j} \frac{\partial}{\partial x_j} u_i^n + \frac{\partial}{\partial x_j} \frac{\partial}{\partial x_j} u_i^{n-1} \right), \end{aligned} \quad (8)$$

where a superscript  $n$  indicates the value at time step  $n$ .

It is now useful to put the time discretized form of the entire state equation governing the flow in the domain into the form

$$\mathcal{K}^n + \mathcal{R}^{n-1} = 0, \quad (9a)$$

where  $\mathcal{K}^n$  contains all the terms which in some way depend on the state variables

from the current time step, and  $\mathcal{R}^{n-1}$  contains the remaining terms:

$$\mathcal{K}^n = \begin{cases} u_i^n - \beta_1 \frac{\partial}{\partial x_j} \frac{\partial}{\partial x_j} u_i^n + \beta_2 \left( \frac{\partial p'^n}{\partial x_i} + \frac{dP^n}{dx_1} \delta_{i1} + \frac{\partial}{\partial x_j} u_j^n u_i^n \right) & \text{in } \Omega \\ -\beta_2 \frac{\partial u_j^n}{\partial x_j} & \text{in } \Omega \end{cases} \quad (9b)$$

$$\mathcal{R}^{n-1} = \begin{cases} \begin{cases} -u_i^{n-1} - \beta_1 \frac{\partial}{\partial x_j} \frac{\partial}{\partial x_j} u_i^{n-1} \\ + \beta_2 \left( \frac{\partial p'^{n-1}}{\partial x_i} + \frac{dP^{n-1}}{dx_1} \delta_{i1} + \frac{\partial}{\partial x_j} u_j^{n-1} u_i^{n-1} \right) \end{cases} & \text{in } \Omega \\ 0 & \text{in } \Omega \\ C' & \end{cases} \quad (9c)$$

In the above equation,  $\beta_1 = \Delta t / 2Re$ ,  $\beta_2 = \Delta t / 2$ ,  $dP/dx_1$  is the mean pressure gradient in the  $x_1$  direction (adjusted at each time step to provide constant mass flux), and  $p'$  accounts for the pressure variations within the domain (periodic in  $x_1$  and  $x_3$ ). Note that (1b) and (1c) have been multiplied by constants to obtain (9).

Associated with this problem are the boundary conditions **B**:

$$\begin{aligned} B_1 &= u_1 = 0 \\ B_2 &= u_2 = \phi \\ B_3 &= u_3 = 0. \end{aligned} \quad (10)$$

The “flow problem”, which will hereafter be denoted  $\mathcal{A}$ , is taken to refer to the differential equation (9) together with the boundary conditions (10).

#### 2.4 Suboptimal control of state equation

In this section and the next, we develop a method to solve for the gradient of the cost functional  $\mathcal{J}$  and with this a control procedure based on this gradient information to minimize  $\mathcal{J}$  at each time step.

Consider the Fréchet differential (Vainberg, 1964) of the cost functional  $\mathcal{J}$  in (7):

$$\begin{aligned} \frac{\mathcal{D}\mathcal{J}(\phi)}{\mathcal{D}\phi} \tilde{\phi} &\equiv \lim_{\epsilon \rightarrow 0} \frac{\mathcal{J}(\phi + \epsilon \tilde{\phi}) - \mathcal{J}(\phi)}{\epsilon} \\ &= \frac{\ell}{A} \iint_w \phi \tilde{\phi} dx_1 dx_3 + \frac{1}{A} \iint_w \frac{\partial}{\partial n} \left( \frac{\mathcal{D}u_1}{\mathcal{D}\phi} \tilde{\phi} \right) dx_1 dx_3. \end{aligned} \quad (11)$$

The gradient of the functional  $\mathcal{J}$  with respect to the control distribution  $\phi$  may be extracted from this equation by expressing the last term on the RHS in terms of an

inner product on  $\tilde{\phi}$ . It is for this reason that we now formulate what we shall call the "differential problem".

Define  $\Theta$  using a Fréchet differential such that

$$\Theta = \frac{\mathcal{D}U(\phi)}{\mathcal{D}\phi} \tilde{\phi} \equiv \lim_{\epsilon \rightarrow 0} \frac{U(\phi + \epsilon \tilde{\phi}) - U(\phi)}{\epsilon}, \quad (12)$$

where  $\tilde{\phi}$  is some arbitrary or "test" distribution of control velocities. Thus,  $\Theta^n$  is a differential state representing the sensitivity of the state  $U^n$  to control for a particular control distribution  $\tilde{\phi}^n$  applied over the time duration  $(t^{n-1}, t^n]$ . The differential  $\Theta$  is decomposed into components in a fashion similar to the state  $U(\phi)$ :

$$U(\phi) = \begin{pmatrix} u_i(x_1, x_2, x_3) \\ p'(x_1, x_2, x_3) \\ dP/dx_1 \end{pmatrix}, \quad \Theta = \begin{pmatrix} \theta_i(x_1, x_2, x_3) \\ \rho(x_1, x_2, x_3) \\ \lambda \end{pmatrix}.$$

The equations governing the differential state  $\Theta^n$  follow directly by taking the Fréchet differential of the state equation (9) and its boundary conditions (10). Note that the term  $\mathcal{R}^{n-1}$  in (9) does not depend on  $\tilde{\phi}^n$  and thus makes no contribution. The contribution from the term  $\mathcal{K}^n$  is linear and may be written

$$\mathbf{A}^n \Theta^n = 0, \quad (13a)$$

where

$$\mathbf{A} \Theta = \begin{cases} \theta_i - \beta_1 \frac{\partial}{\partial x_j} \frac{\partial}{\partial x_j} \theta_i + \beta_2 \left( \frac{\partial \rho}{\partial x_i} + \lambda \delta_{i1} + \theta_j \frac{\partial u_i}{\partial x_j} + u_j \frac{\partial \theta_i}{\partial x_j} \right) & \text{in } \Omega \\ -\beta_2 \frac{\partial \theta_j}{\partial x_j} & \text{in } \Omega \\ \beta_2 \iiint_{\Omega} \theta_1 dx_1 dx_2 dx_3. & \end{cases} \quad (13b)$$

The boundary conditions  $\tilde{\mathbf{B}}$ , from (10), are

$$\begin{aligned} \tilde{B}_1 &= \theta_1 = 0 \\ \tilde{B}_2 &= \theta_2 = \tilde{\phi} \\ \tilde{B}_3 &= \theta_3 = 0. \end{aligned} \quad (14)$$

The "differential problem", which will hereafter be denoted  $\mathcal{A}$ , is taken to refer to the differential equation (13) together with the boundary conditions (14).

Consider again the Fréchet differential of the cost functional  $\mathcal{J}$  in (11):

$$\frac{\mathcal{D}\mathcal{J}(\phi)}{\mathcal{D}\phi} \tilde{\phi} = \frac{\ell}{A} \iint_w \phi \tilde{\phi} dx_1 dx_3 + \frac{1}{A} \iint_w \frac{\partial \theta_1}{\partial n} dx_1 dx_3. \quad (15)$$

The gradient of the functional  $\mathcal{J}$  with respect to the control distribution  $\phi$  may be extracted from this equation by expressing the integral of  $\partial \theta_1 / \partial n$  in terms of an inner product on  $\tilde{\phi}$ . This may be done by solving the differential problem  $\mathcal{A}$ , as is done below.



### 2.5 Solution of differential problem $\tilde{\mathcal{A}}$ by adjoint method

An “adjoint problem” is now formulated which may be used to bypass direct solution of the differential problem  $\tilde{\mathcal{A}}$  itself.

Define an adjoint operator  $\mathbf{A}^*$  using the equation

$$\langle \mathbf{A} \Theta, \Psi \rangle = \langle \Theta, \mathbf{A}^* \Psi \rangle + b, \quad (16)$$

where  $\mathbf{A}$  (which depends on  $U$ ) is defined in equation (13b), the boundary conditions on  $\Theta$  are given in equation (14), and an adjoint state  $\Psi$  has been defined in a fashion similar to  $U$  and  $\Theta$ :

$$\Psi = \begin{pmatrix} \psi_i(x_1, x_2, x_3) \\ \pi(x_1, x_2, x_3) \\ \kappa \end{pmatrix}.$$

The adjoint operator is formed by moving all of the derivatives in the inner product (the integral over the volume of the product of the two terms, denoted  $\langle \cdot, \cdot \rangle$ ) from the differential  $\Theta$  to the adjoint  $\Psi$ . It is a straightforward exercise to write out the volume integrals corresponding to the LHS of (16) and then to rearrange this expression into the form of integrals corresponding to the RHS of (16) using integration by parts. From this is deduced  $\mathbf{A}^*$  and the condition at the boundary resulting from the wall terms, which are all placed into the expression for  $b$ :

$$b = \langle \mathbf{A} \Theta, \Psi \rangle - \langle \Theta, \mathbf{A}^* \Psi \rangle. \quad (17)$$

Through equation (13a), the first term on the RHS of equation (17) is zero. If we form a similar homogeneous adjoint differential equation for the adjoint  $\Psi$

$$\mathbf{A}^* \Psi = 0, \quad (18)$$

with boundary conditions as yet undetermined, then equation (17) reduces to

$$b = 0. \quad (19)$$

Using the method described above, it is easy to show that

$$\mathbf{A}^* \Psi = \begin{cases} \psi_i - \beta_1 \frac{\partial}{\partial x_j} \frac{\partial}{\partial x_j} \psi_i + \beta_2 \left( \frac{\partial \pi}{\partial x_i} + \kappa \delta_{i1} + \psi_j \frac{\partial u_j}{\partial x_i} - u_j \frac{\partial \psi_i}{\partial x_j} \right) & \text{in } \Omega \\ -\beta_2 \frac{\partial \psi_j}{\partial x_j} & \text{in } \Omega \\ \beta_2 \iiint_{\Omega} \psi_1 dx_1 dx_2 dx_3 & \end{cases} \quad (20)$$

and

$$b = \iint_w \left( \beta_1 \frac{\partial \theta_1}{\partial n} (\psi_1) - \beta_2 \rho n_2 (\psi_2) + \beta_1 \frac{\partial \theta_3}{\partial n} (\psi_3) + \tilde{\phi} \left( \beta_2 n_2 \pi - \beta_1 \frac{\partial \psi_2}{\partial n} - \beta_2 \phi n_2 \psi_2 \right) \right) dx_1 dx_3 = 0. \quad (21)$$

(Note by comparison of (20) with (13b) that the operator  $\mathbf{A}$  is not self-adjoint due to the effect of the convective terms of the momentum equation.) These adjoint equations may be exploited to solve the differential problem  $\mathcal{A}^*$ .

We now formulate an “adjoint problem”, which will hereafter be denoted  $\mathcal{A}^*$ , defining an adjoint state  $\Psi$  with the homogeneous differential equation (18) and with accompanying boundary conditions  $\mathbf{B}^*$  as yet undefined. Note by the above discussion that one of the by-products of the formulation of this problem is the relation at the boundary given by (21). We are now at liberty to choose boundary conditions for the adjoint problem such that this relation is useful — it is exactly for this reason that the formulation of an adjoint problem is considered. With this in mind, we may choose the boundary conditions  $\mathbf{B}^*$  as

$$\begin{aligned} B_1^* &= \psi_1 = 1 \\ B_2^* &= \psi_2 = 0 \\ B_3^* &= \psi_3 = 0. \end{aligned} \quad (22)$$

Using these boundary conditions and the continuity equation for the adjoint velocity, equation (21) reduces to

$$\iint_w \frac{\partial \theta_1}{\partial n} dx_1 dx_3 = -n_2 \iint_w \tilde{\phi} Re \pi dx_1 dx_3. \quad (23)$$

To compute the RHS, we must solve the adjoint problem  $\mathcal{A}^*$ . This is done numerically and must be repeated at each time step as  $\mathbf{A}^*$  changes as the flow  $U$  develops with time.

The differential of the cost functional (11) may be rewritten using (23) as

$$\frac{\mathcal{D}\mathcal{J}(\phi)}{\mathcal{D}\phi} \tilde{\phi} = \frac{\ell}{A} \iint_w \phi \tilde{\phi} dx_1 dx_3 - \frac{n_2 Re}{A} \iint_w \pi \tilde{\phi} dx_1 dx_3, \quad (24)$$

where  $\pi$  is the adjoint pressure on the wall. Finally, the desired gradient of the cost functional  $\mathcal{J}$  may be extracted (Vainberg, 1964):

$$\frac{\mathcal{D}\mathcal{J}(\phi)}{\mathcal{D}\phi} = \frac{\ell}{A} \phi - \frac{n_2 Re}{A} \pi. \quad (25)$$

A feedback control procedure using a simple gradient algorithm at each time step may now be proposed such that

$$\phi^{n,k+1} - \phi^{n,k} = -\mu \frac{\mathcal{D}\mathcal{J}(\phi^{n,k})}{\mathcal{D}\phi}, \quad (26)$$

where superscript  $n$  indicates the time step as before and superscript  $k$  indicates an iteration step at that particular time step. This algorithm attempts to update  $\phi$  in the direction opposite to the local direction of increase of  $\mathcal{J}$ . For fixed  $n$  as  $k \rightarrow \infty$  with sufficiently small  $\mu$ , this gradient algorithm should converge to some local minimum of  $\mathcal{J}$  over the control space  $\phi$  if the approximation of  $\mathcal{D}\mathcal{J}/\mathcal{D}\phi$  is sufficiently accurate. Note, however, that as the time step  $n$  advances,  $\mathcal{J}$  will not necessarily decrease (Choi *et al.* 1993).

### 3. Accomplishments and future work

#### 3.1 Elementary drag reducing mechanisms

Choi *et al.* (1992) found that by applying a control velocity equal and opposite to the vertical velocity at  $y^+ = 10$ , a drag reduction of nearly 20% could be achieved. Vertical transport of streamwise momentum in the near-wall region (primarily due to longitudinal vorticity) produces “sweep” events and thus local regions of very high drag. Applying a countering control velocity tends to reduce this effect. A related mechanism described by Lumley (1993) further explains these results; control applied to reduce the spinning of the near-wall vortices reduces their energy, stabilizing them in space and thereby reducing the “bursting” frequency, which also tends to reduce the drag.

In the transverse plane, countering the vertical velocity above the wall corresponds to a control which de-spins the near-wall vortices, as shown in Figure 1. This process leads to the removal of fluctuations in the near-wall region, which diminishes the mixing capability of the turbulence and therefore reduces drag. This type of control corresponds to blowing where the drag is high, which decreases the high velocity gradients at the wall and thus smooths out the flow in the near-wall region, as shown in Figure 2.

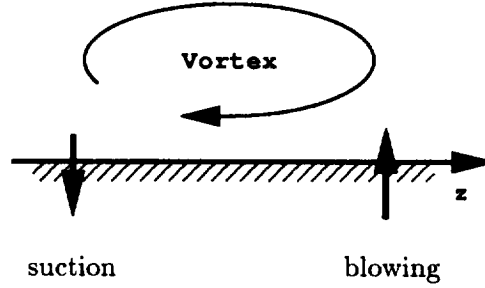


FIGURE 1. Stabilization mechanism in cross flow plane. The effect of the control velocities shown is to de-spin the near-wall vortex, reducing momentum transport near the wall.

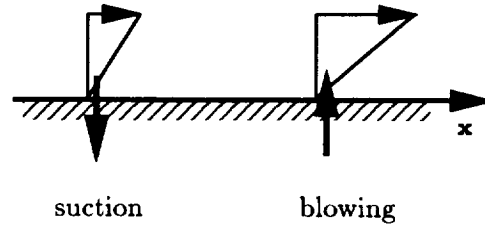


FIGURE 2. High drag is decreased by blowing at the expense of suction in the regions of low drag, resulting in a net smoothing of the near-wall velocity profiles.

Figure 3 shows the application of the suboptimal control scheme to a simple flow configuration of longitudinal vortices embedded in an initially parabolic flow. A cross flow plane is shown. In regions below downward moving fluid (sweep events) the streamwise (into the page) drag is higher and blowing is applied. In regions below upward moving fluid (ejection events), the streamwise drag is lower and suction is applied. The overall control distribution from the suboptimal scheme is in a sense that acts to de-spin the near-wall vorticity, and thus acts in accordance with mechanisms described above.

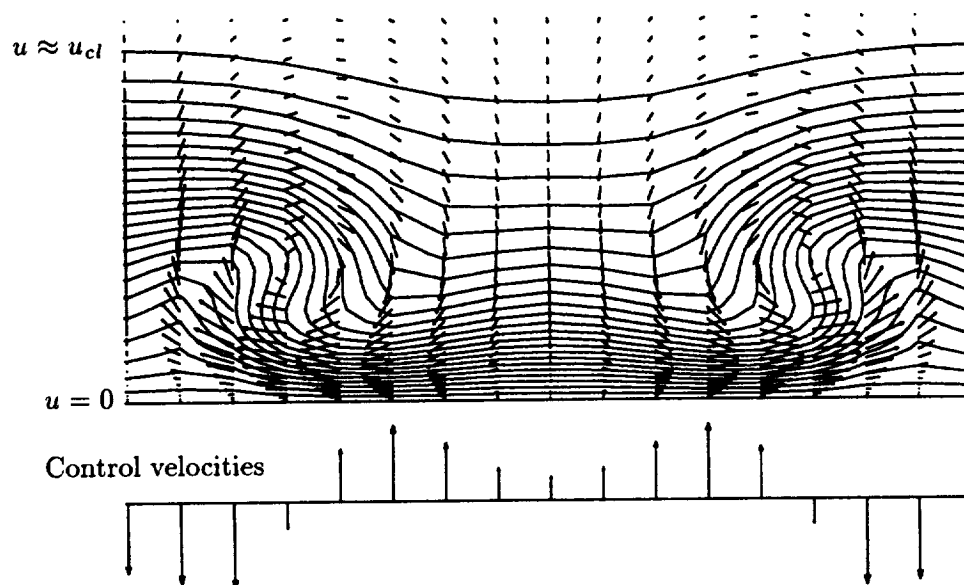


FIGURE 3. Optimal control scheme applied to longitudinal vortices. Interior vectors are cross flow velocities and contours are of streamwise velocity, indicating a sweep event between two near-wall vortices and ejection events outside of them. Control velocities shown on the wall (not to scale) indicates blowing at the sweep event and suction at the ejection events.

The adjoint analysis utilizes all the information present in the near-wall region to extract the sensitivity of the instantaneous drag to the variation of the control. This scheme may be reduced to an approximate one relying only on wall information by approximating the near-wall velocities using a Taylor's series extrapolation of the velocity gradients at the wall. The correlation between the full adjoint analysis and approximations of the adjoint problem using only information available at the wall is still being investigated; preliminary results indicate that the performance is not severely degraded by this approximation.

### 3.2 Suboptimal control of turbulent channel flow

The scheme introduced in Section 2 was tested by applying it to a direct numerical simulation of turbulent channel flow. A 17% drag reduction was seen as compared to a flow with no control. Results are plotted in Figure 4. This calculation was done in a flow with  $Re_\tau = 100$  based on the friction velocity and the channel half width using a  $32 \times 65 \times 32$  grid and the spectral method of Kim *et al.* 1987. Although these results should be considered preliminary, they are quite promising.

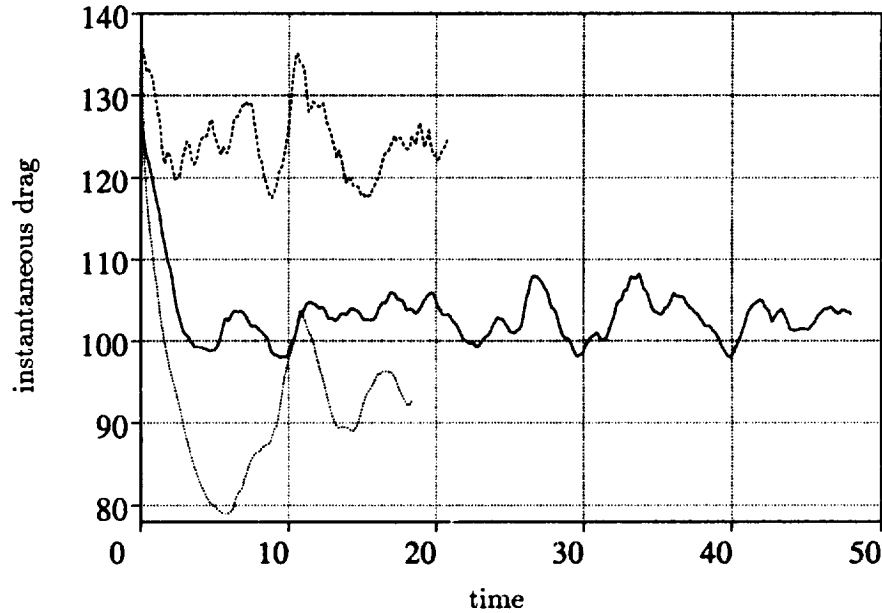


FIGURE 4. Performance of suboptimal scheme compared to no control and the scheme of Choi *et al.* (1992). Parameters for suboptimal scheme are  $\mu = 0.01$ ,  $\ell = 10$ ,  $T^+ = 1$ . Legend: — suboptimal scheme, .....  $\phi = -v|_{y^+=10}$ , ---- no control.

### 3.3 Future work

At present, the drag reduction obtained using a suboptimal control scheme is still slightly less than the drag reduction obtained using the *ad hoc* scheme of Choi *et al.* (1992), as shown in Figure 4. It is hoped that by further variation of the parameters and careful study of the numerical issues of the adjoint problem, the result using the suboptimal formulation may be significantly improved. We expect that, using the suboptimal method, a significant improvement is possible over all *ad hoc* schemes, as the suboptimal scheme uses the entire flow information in the near-wall region and is rigorously based. Also, work is currently in progress with Dr. Chris Hill to reduce the suboptimal control scheme to one which depends on wall information only. Preliminary results of this work are also quite promising — a discussion of this project is included in the next report in this volume.

### Acknowledgements

The authors gratefully acknowledge the financial support of AFOSR Grant No. F49620-93-1-0078.

### REFERENCES

- ABERGEL, F. & TEMAM, R. 1990 On some control problems in fluid mechanics. *Theor. and Comp. Fluid Dynamics*. **1**, 303.
- CHOI, H., MOIN, P., & KIM, J. 1992 Turbulent drag reduction: studies of feedback control and flow over riblets. *Report No. TF-55*, Dept. of Mech. Engr., Stanford University.
- CHOI, H., TEMAM, R., MOIN, P., & KIM, J. 1993 Feedback control for unsteady flow and its application to the stochastic Burgers equation. *J. Fluid Mech.* **253**, 509.
- HILL, D. 1993 Drag reduction at a plane wall. *Annual Research Briefs-1993*, Center for Turbulence Research, Stanford U./NASA Ames.
- KIM, J., MOIN, P., & MOSER, R. 1987 Turbulence statistics in fully developed channel flow at low Reynolds number. *J. Fluid Mech.* **177**, 133.
- LIONS, J. L. 1969 *Contrôle Optimal des Systèmes Gouvernés par des Equations aux Dérivées Partielles*. Dunod, Paris. English translation, Springer-Verlag, New York.
- LUMLEY, J. 1993 Interaction of Adjacent Bursts in the Wall Region. Presented at the *Reynolds Turbulence Symposium* in Monterey, CA, March 22-23, 1993.
- VAINBERG, M. 1964 *Variational Methods for the Study of Nonlinear Operators*. Holden-Day, p 54.

## Drag reduction at a plane wall

By D. C. Hill

### 1. Motivation and objectives

The reduction of the turbulent drag arising from flow over a wall is a major technological issue. Over the years, many schemes have been proposed to reduce turbulent drag (large eddy break-up devices, compliant walls, polymer addition, riblets etc.), with varied rates of success. The use of riblets, for example, can lead to about a 7% reduction in drag. The use of computational and theoretical methods has emerged recently as an effective tool for understanding new aspects of the physics of drag reduction.

Abergel & Temam (1990) describe how theoretical optimal control schemes can be developed for turbulent flow fields. The formulations are highly idealized and cannot be implemented even computationally due to a requirement for prohibitively large data storage and computations. The problem lies in the need to have *perfect knowledge* of the flow field and its history in order to achieve the *best* drag reduction possible.

The so-called sub-optimal scheme (Choi *et al.* 1993) has more modest objectives. A distribution of control forces is derived based on the instantaneous state of the system, thereby eliminating the need to retain and investigate the entire history. The procedure has been shown to work well for the one-dimensional Burgers equation, with both distributed and boundary control. Encouraged by the success of this approach, Bewley *et al.* have pursued the application of the sub-optimal scheme for channel flow. A detailed description of the method and their results is reported in this volume of the annual research briefs.

The objective of the present work is to determine by analytical means how drag on a plane wall may be modified favorably using a minimal amount of flow information - preferably only information at the wall. What quantities should be measured? How should that information be assimilated in order to arrive at effective control?

As a prototypical problem, we consider incompressible, viscous flow, governed by the Navier-Stokes equations, past a plane wall at which the no-slip condition has been modified. The streamwise and spanwise velocity components are required to be zero, but the normal component is to be specified according to some control law. The challenge is to choose the wall-normal velocity component based on flow conditions at the wall so that the mean drag is as small as possible. There can be no net mass flux through the wall, and the total available control energy is constrained. A turbulent flow is highly unsteady and has detailed spatial structure. The mean drag on the wall is the integral over the wall of the local shear forces exerted by the fluid, which is then averaged in time; it is a "macroscopic" property of the flow. It is not obvious how unsteady boundary control is to be applied in order to modify the mean flow most effectively, especially in view of the non- self-adjoint nature of

the governing equations. We pursue an approximate analytical solution to the sub-optimal scheme.

## 2. Accomplishments

The main accomplishment of this project has been the finding of an approximate solution to the sub-optimal problem, which requires only wall information to define a control law. In a preliminary direct simulation, this law leads to a drag reduction of the order of 15%.

The sub-optimal law is developed by first solving what will be termed a locally-optimal problem (the optimal drag reduction problem on a very short time interval) and combining that solution with a gradient algorithm.

### 2.1 The locally-optimal problem

The mean drag is found by averaging the instantaneous drag over a long time interval. In order to achieve a formally optimal reduction in the mean drag, a vast quantity of flow information must be employed. For what I will call the locally-optimal problem, the time interval,  $T$ , over which the average is made is taken to be very small ( $T \ll 1$ ). This has the highly desirable effect that only flow information near the wall is required in order to investigate how the flow can be modified efficiently. It has the further advantage that the problem can be solved analytically, at least to a good approximation (the error is  $O(T^{1/2})$ ).

Let  $\bar{D}(t)$  denote the total drag on the wall lying in the  $xz$ -plane,  $-L \leq x, z \leq L$ , averaged over the short time interval  $t$  to  $t+T$ . Let  $\Phi(x, z, T)$  be the normal velocity at the wall applied during that time interval. The first variation of  $\bar{D}$  with respect to changes in  $\Phi$  is

$$\delta \bar{D}(t) = \frac{1}{4L^2T} \int_{-L}^L dx \int_{-L}^L dz \tilde{P}(x, z, T) \delta \Phi, \quad (1)$$

where  $\tilde{P}(x, z, T)$  depends upon the instantaneous state of the flow. The field  $\tilde{P}$  can be found by solving a carefully-formulated adjoint problem. Only a cursory description of the solution procedure will be given here.

The adjoint problem requires the solution of an initial boundary value problem, in which the solution is marched backwards in time (Abergel & Temam 1990) from  $t+T$  to  $t$ . The initial stage of development is the only portion of the solution which need be found. The quantity  $\tilde{P}$  is the integral over the time interval  $[t, t+T]$  of the time-evolving adjoint wall pressure.

As a first step, a *reduced adjoint problem* is formulated and solved. In this case, only the mean flow is used in the adjoint governing equations, with the consequence that the problem reduces to a one-dimensional diffusion problem whose solution can be written as an error function. This adjoint solution defines an envelope growing away from the boundary as time evolves backwards.

To solve the adjoint problem fully, a correction must be added to this solution, and consequently a *second adjoint problem* is formulated. This second problem now involves the unsteady portion of the turbulent flow field. In order to obtain



a tractable solution, the mean flow is assumed to be uniform near the wall (the mean flow does not appear in the solution at the order of approximation used). “Higher order” convection effects are also ignored. The most important aspect of this problem, however, is that the second problem is “forced” by a combination of the solution to the reduced problem and the unsteady flow field. The reduced problem defines an envelope close to the wall beyond which events are insignificant. Thus only unsteady events *close to the wall* need be considered.

The near-wall unsteady flow field is modeled with a spanwise velocity growing linearly, and normal velocity growing quadratically, with normal distance from the wall. The streamwise component follows from continuity. The adjoint pressure at the wall is then determined for small times. The adjoint pressure represents how sensitive the drag is to changes in the wall blowing,  $\Phi$ , for a given wall blowing distribution and near-wall flow field. The solution collapses in such a way that only the control distribution,  $\Phi$ , and the local wall shear,  $(\partial u / \partial y)_{y=0}$ , are required to define  $\tilde{P}$ .

Defining the Fourier Transform of some  $f(x, z)$  by

$$\hat{f}(\alpha, \beta) = \int_{-\infty}^{\infty} dx \int_{-\infty}^{\infty} dz f(x, z) e^{-i(\alpha x + \beta z)}, \quad (2)$$

we find

$$\hat{\tilde{P}}(\alpha, \beta, T) \approx A\hat{\Phi} + B\left(\frac{\partial \hat{u}}{\partial y}\right)_{y=0} + O(T^2), \quad (3)$$

where

$$A = i\frac{\alpha T}{2\gamma} \left[1 - \frac{4\gamma}{3} \sqrt{\frac{T}{\pi R}}\right], \quad B = \frac{4T}{3} \sqrt{\frac{T}{\pi R}}, \quad \gamma = \sqrt{\alpha^2 + \beta^2}, \quad (4)$$

and  $R$  is the Reynolds number. The quantity  $(\partial \hat{u} / \partial y)_{y=0}$  is the Fourier Transform of the local shear at the wall.

## 2.2 The sub-optimal problem using wall information only

This solution (3, 4) for the adjoint pressure is employed in a direct numerical simulation to define a blowing/suction distribution based purely on wall information. If the superscript denotes the flow conditions at the  $n$ th time step, then the control distribution at the  $(n + 1)$ th time step is

$$\Phi^{n+1} = \Phi^n - \mu(\ell \Phi^n - R\tilde{P}), \quad (5)$$

(see Bewley *et al.* 1993) or in terms of transformed quantities

$$\hat{\Phi}^{n+1} = \hat{\Phi}^n [1 - \mu\ell + \mu RA] + \mu RB \left(\frac{\partial \hat{u}^n}{\partial y}\right)_{y=0}. \quad (6)$$

This law is implemented in the same code as that used by Bewley *et al.* The reader is referred to that review for details of the numerics. The parameters used are

$$R = 100, T = 0.01, \mu = 0.2, \ell = 0.5. \quad (7)$$

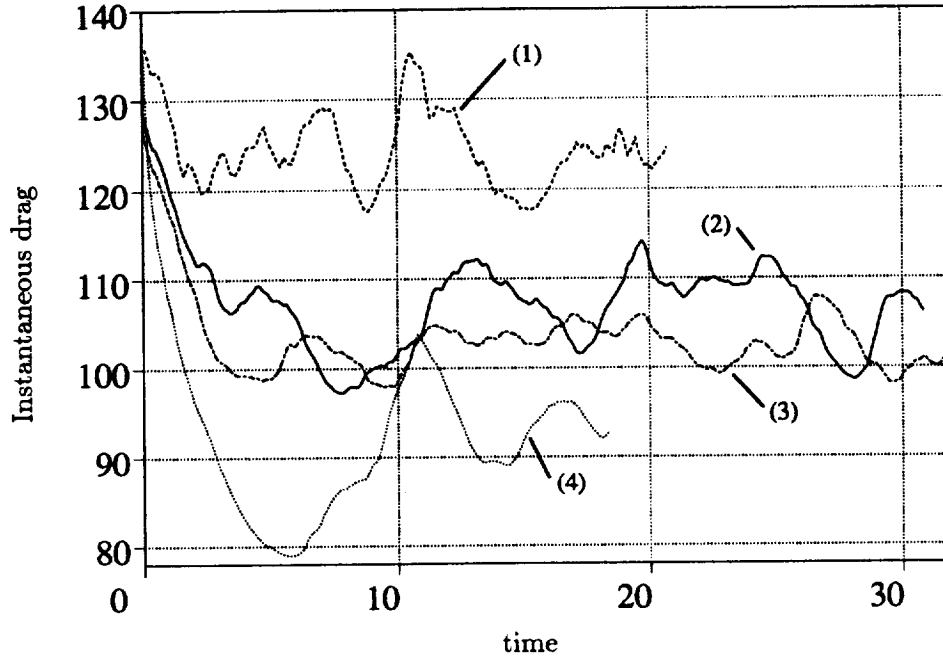


FIGURE 1. The drag on the wall as a function of time for four separate configurations. Curve 1: No control. Curve 2: Analytical scheme, Equation (6). Curve 3: Computed sub-optimal scheme. Curve 4: Scheme of Choi et al. (1993).

The history of the instantaneous drag on the wall as a function of time is shown in Figure 1 for the case of no control (curve 1), the analytical law given by equation (6) which uses only wall information (curve 2), the law based on sub-optimal computation of Bewley (curve 3), and the *ad hoc* scheme of Choi et al. (1993) (curve 4). Note that the present analytical scheme is the only one which employs only wall information.

The present rule leads to a drag reduction of the order of 15%. The performance is only slightly degraded from the direct computation of the sub-optimal law, which makes use of flow information throughout the entire domain.

### 3. Future work

It is clear that even with a relatively simple analysis of the adjoint equations, useful control laws can be derived. The effect of mean shear will be included in the adjoint problem. This will account for more complex physical processes including vortex tilting and stretching near the wall. Can such dynamics be exploited to improve drag reduction? This remains an open question.

Using the present approach, is it possible to define the dynamic properties (created by active or passive means) which a surface must have in order to reduce the drag which it experiences? What are those properties? These intriguing questions bear further investigation.

REFERENCES

- ABERGEL, F. & TEMAM, R. 1990 On some control problems in fluid mechanics. *Theoret. Comput. Fluid Dynamics*. **1**, 103.
- BEWLEY, T., CHOI, H., TEMAM, R. & MOIN, P. 1993 Optimal feedback control of turbulent channel flow. *Annual Research Briefs-1993*, Center for Turbulence Research, Stanford Univ./NASA Ames.
- CHOI, H., TEMAM, R., MOIN, P. & KIM, J. 1993 Feedback control for unsteady flow and its application to the stochastic Burgers equation. *J. Fluid Mech.* **253**, 509.



20-24  
N94-924141

## Boundary layer receptivity and control

By D. C. Hill

### 1. Motivation and objectives

Receptivity processes initiate natural instabilities in a boundary layer. The instabilities grow and eventually break down to turbulence. Consequently, receptivity questions are a critical element of the analysis of the transition process. Success in modeling the physics of receptivity processes thus has a direct bearing on technological issues of drag reduction. The means by which transitional flows can be controlled is also a major concern: questions of control are tied inevitably to those of receptivity.

Adjoint systems provide a highly effective mathematical method for approaching many of the questions associated with both receptivity and control. The reader is referred to Hill (1993) for a detailed description of their use in the receptivity context. The long term objective of this project is to develop adjoint methods to handle increasingly complex receptivity questions, and to find systematic procedures for deducing effective control strategies.

The most elementary receptivity problem is that in which a parallel boundary layer is forced by time-harmonic sources of various types. The characteristics of the response to such forcing form the building blocks for more complex receptivity mechanisms. The first objective of this year's research effort was to investigate how a parallel Blasius boundary layer responds to general direct forcing.

Acoustic disturbances in the freestream can be scattered by flow non-uniformities to produce Tollmien-Schlichting waves. For example, scattering by surface roughness is known to provide an efficient receptivity path. This problem has been investigated previously in a number of different ways. The present effort is directed towards finding a solution by a simple adjoint analysis, because adjoint methods can be extended to more complex problems.

In practice, flows are non-parallel and often three-dimensional. Compressibility may also be significant in some cases. How are receptivity characteristics to be found for such flows? Recent developments in the use of Parabolised Stability Equations (PSE) offer a promising possibility. By formulating and solving a set of adjoint parabolised equations, we have developed a method for mapping the efficiency with which external forcing excites the three-dimensional motions of a non-parallel boundary layer. The method makes use of the same computationally efficient formulation that makes the PSE currently so appealing.

In the area of flow control, adjoint systems offer a powerful insight into the effect of control forces (Hill 1992). One of the simplest control strategies for boundary layers involves the application of localized mean wall suction. Why does it work so well? The adjoint method reveals a very simple flow analogy and a concise description of the effect of mean localized suction.

## 2. Accomplishments

There are four areas where progress has been made. Firstly, the response of a two-dimensional incompressible parallel (Blasius) boundary layer to direct forcing has been investigated. This defines the elementary receptivity characteristics of a boundary layer. Secondly, a variety of natural forcing problems have been solved in which a scattering agent, such as surface roughness, couples freestream acoustic waves to Tollmien-Schlichting waves. Direct forcing of a non-parallel boundary layer is the third topic: here the adjoint to the Parabolised Stability Equations (PSE) is employed to deal in a computationally efficient manner with the non-parallel aspects of the problem. Finally, in the area of flow control, a new perspective is offered on the controlling effect of localized mean wall suction.

### 2.1 Direct forcing of the Blasius boundary layer

In last year's annual research brief, it was reported that the eigensolutions of the adjoint Orr-Sommerfeld equation, when suitably normalized, provide a detailed description of the response of a boundary layer to direct forcing. The characteristics of the adjoint to the Tollmien-Schlichting wave have been investigated, thereby developing a picture of the elementary processes by which Tollmien-Schlichting waves are produced most effectively. Software has been developed to determine the necessary normalized eigensolution of the adjoint Orr-Sommerfeld equation.

The most significant features of the adjoint eigensolution, and consequently the physical properties of the boundary layer when subjected to direct time-harmonic forcing (i.e. an external source), are summarized as follows:

1. Over a wide range of frequencies and Reynolds numbers, the adjoint stream function corresponding to the Tollmien-Schlichting eigensolution has a simple maximum, and far from the wall, it decays exponentially.
2. The boundary layer is most sensitive to *streamwise* forcing (a momentum source) in the vicinity of the critical layer — the height above the wall at which the flow speed and the phase speed of the Tollmien-Schlichting wave coincide. The most sensitive  $y$ -location is shown in Figure 1 as a function of Reynolds number  $R = \sqrt{U_\infty L}/\nu$ , and frequency  $f = 2\pi f^* \nu / U_\infty^2$ . Here,  $L$  is the distance from the leading edge of the plate,  $U_\infty$  is the flow speed at infinity,  $\nu$  is the viscosity, and  $f^*$  is the frequency in Hertz. The solid line indicates the height above the wall at which streamwise forcing is most effective (the location of the maximum of the adjoint streamwise velocity component). The dashed line defines the position of the critical layer.
3. Forcing in the wall-normal direction is much less effective than forcing in the streamwise direction.
4. At the wall, normal motions create Tollmien-Schlichting waves much more effectively than do streamwise motions.
5. The amplification of the Tollmien-Schlichting waves as they travel through the unstable region dictates that forcing at streamwise positions close to the lower branch leads to the strongest response.

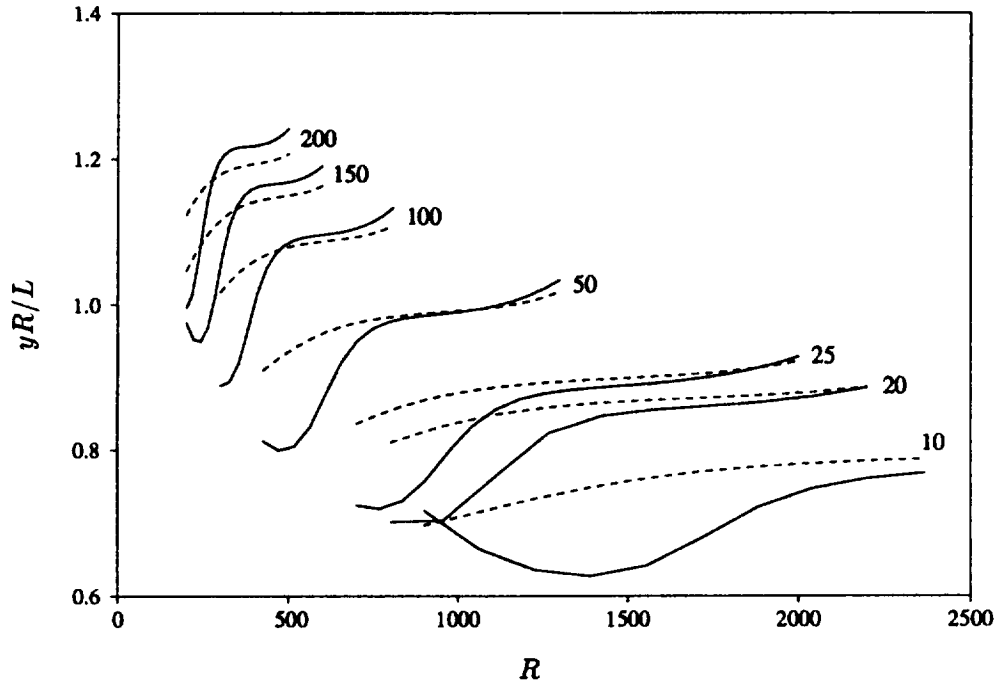


FIGURE 1. Height above wall at which a Blasius boundary layer is most sensitive to direct streamwise forcing, as a function of Reynolds number, for various frequencies  $f \times 10^6$ . Dashed lines define the location of the corresponding critical layer.

Detailed results are reported in Hill (1993).

## 2.2 Natural forcing of the Blasius boundary layer

Sound waves in the free stream can be scattered strongly into Tollmien-Schlichting waves if there is even a weak mean flow distortion containing lengthscales commensurate with those of the Tollmien-Schlichting waves. The flow distortion might be caused typically by surface roughness or by mean suction at the wall.

The 'natural response' problem in which a small surface roughness element acts as a scattering agent has been investigated by several researchers. Goldstein (1983) and Ruban (1985) used triple-deck theory to analyze the process in the infinite Reynolds number asymptotic limit. Crouch (1992) and Choudhari & Streett (1992) provide a solution of the incompressible problem at finite Reynolds number. The solutions indicate that the amplitude of the Tollmien-Schlichting wave that is produced by this mechanism is given by the product of an efficiency factor, a geometry factor, and the amplitude of the acoustic wave. The efficiency factor is a complex constant depending on the frequency and Reynolds number, and the geometry factor is the Fourier transform at the Tollmien-Schlichting wavelength of the roughness shape.

In the absence of any roughness, there is a profile  $U(y)$  on top of which is superimposed an unsteady motion

$$\underline{v}(\underline{r}, t) = u(y)e^{-i\omega t}\hat{x}, \text{ where } u(y) = 1 - e^{-(\omega R/2)^{1/2}(1-i)y}. \quad (1)$$

The planar fluctuations represent a freestream acoustic wave of unit amplitude which has a Stoke's wave signature close to the plate. The frequency  $\omega$  is defined as  $f/R$ , and  $\alpha$  is the TS waveumber at that frequency and Reynolds number.

The roughness modifies the mean flow, and the interaction of the Stoke's wave with this mean flow distortion produces a TS-wave. It is *assumed* that, far from the roughness patch, the flow field recovers sufficiently quickly that the scattering takes place in an interaction zone in the vicinity of the roughness.

The efficiency factor for the scattering process is found by examining the solution to the following inhomogeneous adjoint problem for the stream function  $\tilde{\Phi}(y)$ :

$$\begin{aligned} -i\alpha U \left( \frac{d^2}{dy^2} - \alpha^2 \right) \tilde{\Phi} - 2i\alpha \frac{dU}{dy} \frac{d\tilde{\Phi}}{dy} + \frac{1}{R} \left( \frac{d^2}{dy^2} - \alpha^2 \right)^2 \tilde{\Phi} = \alpha^2 u \tilde{v}_{\alpha\omega} - 2i\alpha \tilde{u}_{\alpha\omega} \frac{du}{dy} \\ - i\alpha u \frac{d\tilde{u}_{\alpha\omega}}{dy}, \end{aligned} \quad (2)$$

$$\tilde{\Phi} = \frac{d\tilde{\Phi}}{dy} = 0, \text{ on } y = 0, \text{ and as } y \rightarrow \infty, \quad (3)$$

where  $(\tilde{u}_{\alpha\omega}\hat{x} + \tilde{v}_{\alpha\omega}\hat{y})e^{-i(\alpha x - \omega t)}$  is the normalized adjoint eigensolution corresponding to the TS-wave.

The solution  $\tilde{\Phi}$  has some useful properties. The amplitude of the instability induced by the scattering of the freestream disturbance is

$$\Lambda \hat{h}(\alpha), \text{ where } \hat{h}(\alpha) = \int_{-\infty}^{\infty} h(x)e^{-i\alpha x} dx \quad (4)$$

and the efficiency factor

$$\Lambda = -\frac{1}{R} \left( \frac{dU}{dy} \frac{d^2\tilde{\Phi}}{dy^2} + \frac{du}{dy} \frac{d\tilde{u}_{\alpha\omega}}{dy} \right)_{y=0}. \quad (5)$$

The equations (2, 3) have been solved numerically, and  $\Lambda$  evaluated. The results are identical with those of Crouch (1992) and Cougar & Streett (1992).

The solution to (2, 3) can also be used directly in the configuration in which mean suction at the wall acts as the scattering agent. Consider a velocity distribution  $V_s(x)$  representing a suction/blowing distribution on the plate. The amplitude of the Tollmien-Schlichting wave is

$$\left( \frac{1}{i\alpha R} \frac{d^3\tilde{\Phi}}{dy^3} \hat{y} + \frac{1}{R} \frac{d^2\tilde{\Phi}}{dy^2} \hat{x} \right)_{y=0} \cdot \int_{-\infty}^{\infty} V_s(x)e^{-i\alpha x} dx. \quad (6)$$



Surface admittance is defined as the ratio at the wall of the unsteady normal velocity to the unsteady pressure, and thus can be used to represent how the surface responds dynamically to unsteady pressures. Since there is no distortion of the mean flow, in this case the solution  $\tilde{\Phi}$  is not employed. Suppose that there are spatially-uniform fluctuations  $p_0 e^{-i\omega t}$  in the pressure field. If  $\beta_w(x)$  is the surface admittance, a Tollmien-Schlichting wave of amplitude

$$|\tilde{p}_{\alpha\omega}(0)| p_0 \int_{-\infty}^{\infty} \beta_w(x) e^{-i\alpha x} dx, \quad (7)$$

will be induced. The adjoint pressure at the wall,  $\tilde{p}_{\alpha\omega}(0)$ , associated with the normalized adjoint eigensolution in this case defines the efficiency factor for the scattering of freestream pressure fluctuations into Tollmien-Schlichting waves.

### 2.3 Direct forcing of non-parallel flow

There has been considerable development in recent years in modeling transitional flows by the use of Parabolised Stability Equations (Herbert & Bertolotti 1987, Bertolotti 1991). The linear and non-linear dynamics of convectively-unstable disturbances in spatially-evolving boundary layers can be described accurately with little computational effort. The flow can be compressible, and the disturbances three dimensional.

As the name suggests, the method involves “parabolising” the governing equations for boundary layer disturbances. The solution is represented by a disturbance pattern resembling the local eigenfunction, modulated by a spatially-evolving oscillatory factor. Both the disturbance pattern and the wavelength of the oscillation are assumed to evolve slowly with streamwise position. Starting at a chosen streamwise station, the solution is marched downstream; with a single sweep the evolution of the boundary layer disturbance is described.

The formulation and solution of a set of adjoint Parabolised Stability Equations promises to provide a description of the efficiency with which a wide range of boundary layer motions are excited by direct forcing. In contrast with the regular PSE, the adjoint equations are marched *upstream*, starting at the outflow end of the computational domain. In this way, the events within the domain that give rise to a Tollmien-Schlichting disturbance at the outflow are identified. This approach is an extension to non-parallel flows of the results described in Section 2.1. The adjoint PSE can be solved within the same well-established computational framework as the regular PSE. The adjoint solutions are a natural complement to the regular solutions.

Thanks to F. Bertolotti, a copy of the PSE library of subroutines has recently been made available. The following preliminary results have been obtained:

1. The adjoint Parabolised Stability Equations have been formulated for three-dimensional disturbances in a two-dimensional spatially-evolving boundary layer.
2. Solutions for a two-dimensional Tollmien-Schlichting wave in parallel flow have been checked. Figure 2 gives a graphic illustration of the receptivity maximum that

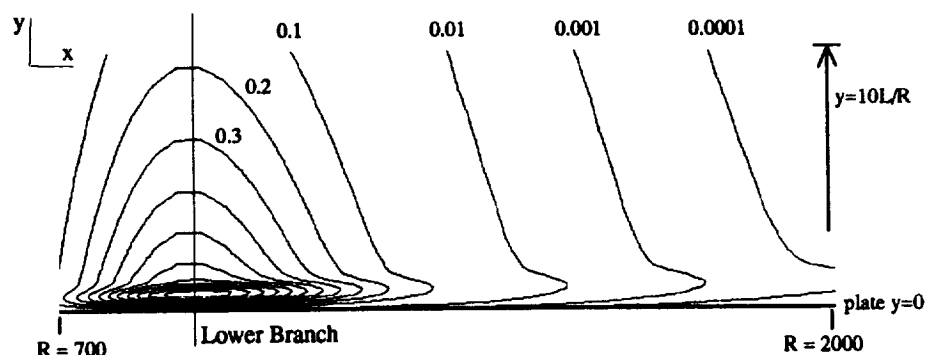


FIGURE 2. Plot of the efficiency with which Tollmien-Schlichting waves are excited by a point source of momentum of unit magnitude, oscillating at a frequency  $f = 20 \times 10^{-6}$ . Contour values are shown in order to indicate relative magnitudes only.

appears in the Blasius boundary layer (the  $y$ -scale has been expanded for purposes of visualization). It is positioned at the lower branch of the neutral stability curve and at a height of about half the displacement thickness from the wall, i.e. at the critical layer. (Figure 2 is a plot of the magnitude of the adjoint velocity and represents the magnitude of the response due to a unit amplitude harmonic momentum source.) The solution has not been normalized, so that contour values do not indicate a physical measure of the response that will arise for unit forcing. However, the relative magnitudes illustrate the zone of high sensitivity.

The effect of non-parallelism is expected to play a larger role for three-dimensional disturbances and compressible flows. This has yet to be investigated.

#### 2.4 Boundary layer control by suction

Small amounts of localized wall suction can reduce dramatically the amplitude of Tollmien-Schlichting waves travelling in a boundary layer. This significant effect has been studied in detail because of its impact on Laminar Flow Control technology (Nayfeh et al. 1986, Saric & Reed 1986, Reynolds & Saric 1986). The numerical perturbation scheme of Reed & Nayfeh (1986) provides a computational analysis of the effect of an arbitrary distribution of suction strips beneath an incompressible boundary layer. Masad & Nayfeh (1992) have developed a scheme for compressible boundary layers.

The effect of suction is to modify the mean flow both upstream and downstream of the slot. A TS-wave that enters this region of the flow grows at a rate which is different from that in the undisturbed flow. Integrating these changes over the entire flow gives the net effect of the suction on the disturbance amplitude.

We construct here an analogous flow, i.e. a flow which has an identical effect upon the TS-wave amplitude. The analogous flow involves a local modification to the boundary layer profile directly above the slot, in proportion to the amount of suction at that streamwise station.

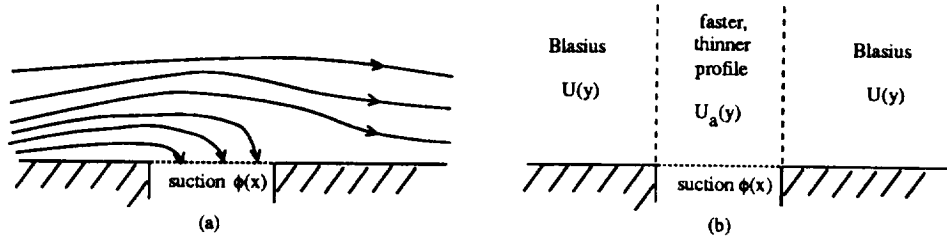


FIGURE 3. Schematic representation of the real flow (a) and analogous flow (b).

The analogous flow replaces the boundary profile by a faster, thinner profile. A simple explicit form has been found for the equivalent profile: Let  $\phi(x)$  be the strength of the wall suction velocity (scaled on  $U_\infty$ ) at streamwise location  $x$ , with local Reynolds number  $R$ . Let  $U(y)$  is the form of the profile,  $y$  being the distance from the wall. The *net* effect of the suction  $\phi(x)$  is *identical* to that of replacing  $U(y)$  locally by

$$U_a(y) = U(y) + \phi(x)R \int_0^y (1 - U(y)) dy, \quad (8)$$

together with a uniform downflow of strength  $\phi(x)$  across the entire boundary layer.

The fractional increase in the effective freestream flow speed is the product of  $\phi(x)$  with the local Reynolds number based on displacement thickness.

Figures 3(a) and 3(b) offer a schematic representation of the real flow and the analogous flow, respectively. If the effect of the modification to the local growth of a TS-wave is integrated in each case, the same net change in amplitude will be found.

To understand the effect of suction, we can thus consider the dynamics of Tollmien-Schlichting waves in thinner, faster boundary layers. For frequencies close to the lower branch of the neutral stability curve, the destabilizing influence of an increase in the flow speed is too weak to counter the stabilizing effect of the thinning of the layer. In practice, a disturbance at the frequency which is most “dangerous” from the point of view of transition is controlled by suction applied close to the lower branch. The disturbance amplitude is reduced typically by a large amount. By contrast, for frequencies close to the upper branch (much less “dangerous” from the point of view of transition), the modified profile tends to be *less* stable. Suction leads to an increase in the amplitude of disturbances at these frequencies. However, there is no reported experimental evidence of amplification of higher frequencies due to suction.

### 3. Future work

The efficiency with which acoustic waves are scattered into TS-waves by surface roughness has already been investigated in detail. The acoustic waves are taken to have infinite wavelength, which reflects the “infinitely” fast speed at which they propagate. Disturbances such as freestream turbulence convect at, or close to, the flow speed and have finite lengthscales associated with them. How efficiently do

such motions scatter into TS-waves? I intend to address this question using an extension of the adjoint method employed for the acoustic scattering problem.

Secondary instabilities play a key role in the so-called K- and H-type transition routes: three-dimensional disturbances grow upon a finite amplitude TS-wave until the flow evolves rapidly to turbulence. The following questions will be addressed: What is the most efficient means of exciting the secondary instability? Can it be controlled/suppressed?

Stationary crossflow vortices appear on swept airfoils in response to surface roughness. Secondary instabilities then lead to a breakdown to turbulence. It is important to understand the process by which the crossflow vortices arise and to identify those locations where roughness elements are most important. An investigation of this problem will be made using the adjoint PSE in combination with the classical independence principle.

### Acknowledgements

The author is grateful to P. A. Durbin for several helpful discussions, and in particular for his observation that the position of maximum sensitivity is coincident with the critical layer (Figure 1).

### REFERENCES

- BERTOLOTTI, F. P. 1991 Linear and nonlinear stability of boundary layers with streamwise varying properties. *Ph.D. Thesis*, Ohio State University.
- CHOUDHARI, M., & STRETT, C. L. 1992 A finite Reynolds number approach for the prediction of boundary-layer receptivity in localized regions. *Phys. Fluids A*, **4**, 2495-2514.
- CROUCH, J. D. 1992 Localized receptivity of boundary layers. *Phys. Fluids A*, **4**, pp.1408-1414.
- GOLDSTEIN, M. E. 1983 The evolution of Tollmien-Schlichting waves near a leading edge. *J. Fluid Mech.* **127**, 59-81.
- HILL, D. C. 1992 A theoretical approach for analyzing the restabilization of wakes. *AIAA paper No. 92-0067*.
- HILL, D. C. 1993 Adjoint systems and their role in the receptivity problem for boundary layers. *CTR Manuscript No. 146*.
- HERBERT, TH. & BERTOLOTTI, F. P. 1987 Stability analysis of non-parallel boundary layers. *Bull. Am. Phys. Soc.* **32**, 2079.
- MASAD, J. A. & NAYFEH, A. H. 1992 Laminar flow control of subsonic boundary layers by suction and heat transfer strips. *Physics of Fluids A*, **4**, pp.1259-1272.
- NAYFEH, A. H., REED, H. L. & RAGAB, S. A. 1986 Flow over bodies with suction through porous strips. *Physics of Fluids*, **29**, 2042-2053.
- REED, H. L. & NAYFEH, A. H. 1986 Numerical-perturbation technique for stability of flat-plate boundary layers with suction. *AIAA Journal*, **24**(2), 208-214.

- REYNOLDS, G. A. & SARIC, W. S. 1986 Experiments on the stability of the flat-plate boundary layer with suction. *AIAA Journal*. **24**(2), 202-207.
- RUBAN, A. I. 1985 On the generation of Tollmien-Schlichting waves by sound. *Fluid Dyn.* **19**, 709 (translation).
- SARIC, W. S. & REED, H. L. 1986 Effect of suction and weak mass injection on boundary-layer transition. *AIAA Journal*. **24**(3), 383-389.



## Toward modeling wingtip vortices

By O. Zeman

### 1. Motivations and objectives

Wingtip vortices are generated by lifting airfoils; their salient features are compactness and relatively slow rate of decay. The principal motivation for studying the far field evolution of wingtip vortices is the need to understand and predict the extent of the vortex influence during aircraft take-off or landing. On submarines a wingtip vortex ingested into a propeller can be a source of undesirable noise.

The flow field associated with a single vortex freely propagating in the environment is difficult to measure. On an aircraft, the vortices are generated in pairs, and these have a tendency to meander and interact with each other. Environmental conditions such as stratification and ambient turbulence may exert an important influence on the vortex as well. So far, the only quantitative measurements of wingtip vortex (far field) evolution in flight experiments have been reported by Rose & Dee (1963). Wind tunnel experiments of an isolated vortex have been reported by Hoffmann and Joubert (1963), Phillips and Graham (1984), and Bandyopadhyay *et al.* (1991). In these experiments, a pair of oppositely loaded airfoils have been employed to generate a turbulent vortex with a wake- or jet-like axial flow field. Measurements of trailing vortices behind a lifting hydrofoil (in water) were made by Baker *et al.* (1974) and Green & Acosta (1991). The near field turbulent structure of a single wingtip vortex has been measured by Zilliac *et al.* (1993). At present, experimental data of a far-field vortex growth are sparse, and data on turbulence quantities in the vortex are virtually nonexistent. The major difficulty in measuring vortex turbulence is the vortex meander, which results in contamination of turbulence statistics.

The main objectives of this research are i) to establish theoretical understanding of the principal mechanisms that govern the later (diffusive) stages of a turbulent vortex, ii) to develop a turbulence closure model representing the basic physical mechanisms that control the vortex diffusive stage, and further iii) to investigate coupling between the near and far field evolutions; in other words, to study the effect of initial conditions on the vortex lifetime and the ultimate state.

At this stage of the effort, I have concentrated on studying a rectilinear, or line, vortex. Thus, the actual vortex evolution in space downstream from a generating wingtip is replaced by evolution in time. The line vortex is axisymmetric in the mean and treated in cylindrical coordinates, where radial distance and time are the only independent variables. The vortex is assumed to be isolated from external influences and its evolution to be independent of the details of the initial (prescribed) conditions. The influence of different initial conditions will be investigated in future.

When compared with experiments, standard  $k-\epsilon$  models are known to overpredict the decay rate of a line vortex. This is due to the absence of the rotation effects

PAGE 30

PRECEDING PAGE BLANK NOT FRAMED

in the turbulence kinetic energy equation. Our past experience with modeling the airflow over hills indicated that a Reynolds stress closure (RSC) model is a must if one is to predict the observed distribution of Reynolds stresses and mean wind on the hilltop. Here, the (convex) streamline curvature can significantly alter the turbulence structure and stress distribution (Zeman and Jensen 1987). We have, therefore, employed a full RSC model where the curvature effects are present intrinsically and appear as explicit terms once the model equations are cast in cylindrical coordinates. As we show later, the RSC model predictions are in broad agreement with the observed line vortex growth, while the  $k - \epsilon$  version of the model yields unacceptably high turbulent intensities and vortex growth rates.

The further stages of this research effort are described in the Future Work section of this report.

## 2. Accomplishments

The main accomplishments to date have been the development of a RSC closure model and the theoretical and scaling analysis of the turbulent vortical flow. These accomplishments are described in detail in the forthcoming manuscript (Zeman 1993). The principal result reported here is the model-experiment comparison of the vortex growth rates for different vortex Reynolds numbers. It appears that the mean vortical flow generated by the wingtip very effectively suppresses the Reynolds shear stress which mediates the extraction of energy from the mean flow by turbulence. In consequence, the vortex core growth rate is controlled only by molecular viscosity and the vortex turbulence decays since the turbulence production rate is very nearly zero. This rather unexpected result appears to be supported by experiment as is evident from Figure 1. This section is subdivided in two parts: Model formulation and description and comparison with experiments.

### 2.1 Model formulation and description

The cylindrical coordinates  $(r, \theta, z)$  are the natural choice for the Reynolds-averaged description of the turbulent vortex flow. The presence of the pressure-strain and transport terms in the RSC equations requires that the equations be formulated in generalized coordinates  $x_i$ . Assigning arbitrarily the azimuthal angle  $\theta \equiv x_1$ , radius  $r \equiv x_2$ , and axial distance  $z \equiv x_3$ , we obtain the metric tensors of transformation  $g^{ij}, g_{ij}$  whose only nonzero components are  $g_{22} = g_{33} = 1$  and  $g_{11} = r^2$ ; the contravariant  $g^{\alpha\alpha} = g_{\alpha\alpha}^{-1}$ . It is then fairly straightforward but arduous to convert the equations for, say, the contravariant tensor  $u^i u^j$  to physical, Reynolds stress components in cylindrical coordinates (see e.g. Durbin 1993, also Zeman 1993). Prior to the conversion one must choose an appropriate model for the rapid part  $\Pi_{ij}^R$  of the pressure strain term  $\Pi_{ij} = p(u_{i,j} + u_{j,i})\rho^{-1}$ . Here, we employ the general (linear) version of the rapid model proposed by Zeman and Tennekes (1975); written in Cartesian tensor notation the rapid part is

$$\Pi_{ij}^R = 2q^2 \left[ \frac{1}{5} S_{ij} + \alpha_1 (S_{ik} b_{jk} + S_{jk} b_{ik} - \frac{2}{3} \mathbf{S} \cdot \mathbf{b} \delta_{ij}) + \alpha_2 (R_{ik} b_{jk} + R_{jk} b_{ik}) \right]. \quad (1)$$

Here,  $b_{ij} = \overline{u_i u_j} / q^2 - \delta_{ij} / 3$  is the turbulence anisotropy tensor and  $q^2 = \overline{u_j u_j}$  is twice the turbulent kinetic energy (hereon TKE); the mean strain ( $\mathbf{S}$ ) and rotation



(**R**) tensors are defined as  $S_{ij} = \frac{1}{2}(U_{i,j} + U_{j,i})$  and  $R_{ij} = \frac{1}{2}(U_{i,j} - U_{j,i})$ . The coefficients  $\alpha_1$  and  $\alpha_2$  can, in principle, be functions of the flow invariants and the turbulence Reynolds number. In practice,  $\alpha_1$  and  $\alpha_2$  are constant, chosen for the best agreement with experiment. The version of the above model was successfully employed in a boundary layer flow with significant streamline curvature effects (Zeman and Jensen 1987) with  $\alpha_1 = 0.375$  and  $\alpha_2 = 0.225$ .

Labeling the azimuthal, radial, and axial fluctuating velocity components as  $u$ ,  $v$ , and  $w$ , respectively, and  $U(r, t)$  as the mean azimuthal (vortical) velocity, we can write the set of turbulence model equations as follows:

$$\frac{\partial \overline{u^2}}{\partial t} = 4(1 - \alpha_2)\overline{uv}\frac{U}{r} + 2(1 - \frac{\alpha_1}{3} - \alpha_2)P_s - \Pi_{uu}^s - \frac{1}{r}\frac{\partial}{\partial r}(rT_{uuv}) - \frac{2}{r}T_{uuv} - \frac{2}{3}\epsilon, \quad (2)$$

$$\frac{\partial \overline{v^2}}{\partial t} = -4(1 - \alpha_2)\overline{uv}\frac{U}{r} + 2(\alpha_2 - \frac{\alpha_1}{3})P_s - \Pi_{vv}^s - \frac{1}{r}\frac{\partial}{\partial r}(rT_{vvv}) + \frac{2}{r}T_{uuv} - \frac{2}{3}\epsilon, \quad (3)$$

$$\frac{\partial \overline{w^2}}{\partial t} = \frac{4}{3}\alpha_1 P_s - \Pi_{ww}^s - \frac{1}{r}\frac{\partial}{\partial r}(rT_{wvv}) - \frac{2}{3}\epsilon, \quad (4)$$

$$\begin{aligned} \frac{\partial \overline{uv}}{\partial t} = & 2(1 - \alpha_2)(\overline{u^2} - \overline{v^2})\frac{U}{r} - \{0.4\overline{v^2} + (\alpha_1 - \alpha_2)\overline{u^2} - \frac{2}{3}(\alpha_1 - 0.3)q^2\}r\frac{\partial}{\partial r}\left(\frac{U}{r}\right) \\ & - \Pi_{uv}^s - \frac{1}{r^2}\frac{\partial}{\partial r}(r^2T_{uuv}) + \frac{1}{r}(T_{uuv} - T_{vvv}). \end{aligned} \quad (5)$$

In the above equations,  $\Pi_{ij}^s = 3.25(\overline{u_i u_j} - \frac{1}{3}q^2\delta_{ij})\epsilon$  stands for the so-called slow return-to-isotropy pressure term, and  $T_{ijk} = \overline{u_i u_j u_k}$  are the third moment terms ( $u_i$  stands for  $u, v, w$ ).  $P_s = -\overline{uv}(\frac{\partial}{\partial r}U - \frac{U}{r})$  is the TKE production rate (by the mean strain  $\frac{\partial}{\partial r}U - \frac{U}{r}$ ). The closure equation for the rate of dissipation used at the present time is in a standard form:

$$\frac{\partial \epsilon}{\partial t} = -3.8(f_1\epsilon - 0.75P_s)\frac{1}{\tau} - \frac{1}{r}\frac{\partial}{\partial r}(rT_{\epsilon v}), \quad (6)$$

with  $\tau = q^2/\epsilon$  is the turbulence (equilibrium) time scale and  $f_1 = 1 - 0.3\exp(-R_t^2)$  where  $R_t = q^4/(9\epsilon\nu)$  is the turbulence Reynolds number.

By summing (2), (3), and (4), the TKE rate equation is obtained

$$\frac{1}{2}\frac{\partial q^2}{\partial t} = P_s - \epsilon - \frac{1}{r}\frac{\partial}{\partial r}(rT_{qqv}). \quad (7)$$

Here  $q^2 = \overline{u^2} + \overline{v^2} + \overline{w^2}$  and  $T_{qqv} = \frac{1}{2}(T_{uuv} + T_{vvv} + T_{wvv})$  is the (total) flux of  $q^2/2$  in the outward radial direction. Note that curvature effects associated with the factor  $U/r$  in (2) to (4) are absent in (7).

### 2.1.1. Concerning the transport term model

To first approximation, the third moments  $T_{ijk}$  can be considered as radial fluxes of the second-order quantities involved. After some experimentation, we have settled on the following scalar-type, gradient transport model:

$$T_{\phi v} = -(\nu_{tr} + \nu) \frac{\partial}{\partial r} \bar{\phi}, \quad (8)$$

where  $\bar{\phi}$  is any second-order quantity in (2)-(7) including  $\epsilon$  and the (radial) eddy transport coefficient  $\nu_{tr}$  is

$$\nu_{tr} = 0.07 \tau v^2 \frac{1}{1 + d_1 \tau^2 (K_z^2)' / r^3}. \quad (9)$$

Here, the prime (') stands for radial derivative, and  $K_z = Ur = \Gamma/2\pi$  is the angular momentum (in  $z$  direction); the adjustable constant  $d_1$  is set tentatively at  $d_1 = 0.02$ . The modification of the eddy coefficient in (9) by the curved flow (stability) parameters is a novel idea, and its rationale is based on the analogous modifications in modeling buoyancy driven flows (Zeman and Lumley 1976). An analogy between streamline curvature and buoyancy has been originally suggested by Bradshaw (1969). Townsend (1976) proposed a curved flow parameter analogous to the gradient Richardson number, i.e.

$$R_{ic} = \frac{(K_z^2)' / r^3}{(U')^2}$$

The modifying factor  $(K_z^2)' / r^3$  in (9) is apparently analogous to the Brunt-Vaisala frequency squared  $N^2$  in flows with buoyancy, and the sign of  $K_z^2$  corresponds to the sign of (potential) temperature in stratified flows. Within the bulk of a turbulent vortex core,  $K_z^2 > 0$ , which means turbulence damping.

Donaldson and Sullivan (1971) employed for the modeling of the same (line vortex) flow the invariant transport model

$$\overline{u^i u^j u^k} \propto -\tau (\overline{u^i u^l} \overline{u^j u^k})_{,l} + \text{permutations in } (i, j, k).$$

The author found this type of model to give unrealistically high levels of the third moments; their effects overwhelmed the solutions. Evidently, the invariant model of Donaldson and Sullivan is incomplete because it does not include curvature (stratification) effects. Ettestad and Lumley (1985) considered the full third-moment equations with the curvature terms included. The resulting transport model was too complex to be applied in actual flow computations, but the modifying factor  $\tau^2 (K_z^2)' / r^3$  does appear repeatedly in the Ettestad and Lumley expressions for eddy coefficients. Finally, it is interesting that an eddy transport coefficient similar to (9) can also be inferred from a Lagrangian analysis (see Zeman 1993; Ettestad and Lumley 1985). The invariant form of the transport model (8) and (9) for general (non-axisymmetric) flows will be considered in future work (Zeman 1993).

### 2.1.2. Concerning boundary and initial conditions

The boundary conditions at the centerline  $r = 0$  are not readily obvious but can be inferred from the following reasoning. If the turbulence undergoes a solid body rotation, the solutions to the equations (2)-(7) must admit a homogeneous solutions independent of  $r$ . It follows that at  $r = 0$ ,

$$\frac{\partial}{\partial r} \overline{u^2} = \frac{\partial}{\partial r} \overline{v^2} = \frac{\partial}{\partial r} \overline{w^2} = 0 \text{ and } \overline{uv} = 0.$$

The last condition stems from the symmetry requirement. Symmetry also requires that near  $r = 0$  the mean flow is solid body rotation and thus  $(U/r)' = 0$ ; this, according to (5), is consistent with  $\overline{uv}(r = 0) = 0$  only if  $\overline{u^2} = \overline{v^2}$ . This centerline turbulence axisymmetry is not directly imposed on the flow, but it is satisfied in actual computations. Similar observations have been reported by Donaldson and Sullivan (1971), who used the same boundary conditions. It is noted that the above boundary conditions are consistent with a theoretical analysis of Shariff (1993) (brought to my attention by Dr. Moser of NASA Ames). Shariff's analysis is based on the requirement that the velocity components  $(u, v, w)$  be analytical near  $r = 0$ . It then follows that near  $r = 0$  the components behave as

$$\overline{u^2} = a^2 + b_u r^2 \quad \overline{v^2} = a^2 + b_v r^2, \quad \text{and} \quad \overline{w^2} = c^2 + b_w r^2.$$

Evidently, the turbulence axisymmetry is a requirement of analyticity of the fluctuating flow field at  $r = 0$ .

The centerline dissipation  $\epsilon_c$  is obtained from the integral balance of the TKE equation (7), i. e.,  $\epsilon_c$  must satisfy the integral

$$\int_0^\infty \left\{ -\frac{1}{2} \frac{\partial \overline{q^2}}{\partial t} + P_s - \epsilon \right\} r dr = 0. \quad (10)$$

Durbin (1991) showed the integral constraint to give the proper value of  $\epsilon$  at the wall in a (steady) channel flow. Here, the situation is somewhat different; the flow is unsteady and near  $r = 0$ ,  $q_{,t}^2 = (\nu_{tr} + \nu) q_{,rr}^2 - 2\epsilon_c$ .

The conditions at  $r \rightarrow \infty$  are  $\Gamma = \Gamma_o$ , (or  $U = \Gamma_o/(2\pi r)$ ), and all second-order turbulence quantities tend to zero. The turbulence time scale  $\tau = q^2/\epsilon$  is prescribed to be large (with respect to vortex core time scale) but finite as  $r \rightarrow \infty$ .

The initial profile for the azimuthal velocity conditions  $U(r, t = 0)$  is given by the prescribed circulation distribution

$$\frac{\Gamma}{\Gamma_o} = 1 - \exp -1.26(r/R_1)^2, \quad (11)$$

where  $r = R_1$  is the radius of  $\max\{U\} = U_1$ , and it delimits the size of the vortex core; for the distribution (11) the maximum velocity  $U_1$  occurs where  $\Gamma = 2\pi U_1 R_1 = 0.716\Gamma_o$ . Since the vortex evolution approximately obeys the scaling laws  $U_1 \propto (\Gamma_o/t)^{1/2}$  and  $R_1 \propto (\Gamma_o t)^{1/2}$ , the initially prescribed Reynolds number  $\Gamma_o/\nu$

remains constant in time. The Gaussian profile of  $\Gamma$  is a laminar vortex solution, or if one assumes the eddy viscosity to be constant, it is a turbulent vortex solution as well (see e.g. Govindaraju & Saffman 1971).

Initial profiles of the turbulence moments were specified as

$$\overline{u^2} = \overline{v^2} = \overline{w^2} = u_o^2 h(r/R_1), \quad \epsilon = u_o^3 r^{-1} h(r/R_1) \quad \text{and} \quad \overline{uv} = 0,$$

with  $h(\eta) = \eta^2 \exp\{1 - \eta^2\}$ . The above profiles were fairly consistent with the equation solutions but introduced transient oscillations in the  $\overline{uv}$  profiles. The initial turbulence intensity  $u_o/U_1$  is a parameter of the flow problem which also specifies the initial turbulence Reynolds number  $R_t$ . It has been found, so far, that the long-time evolution of the vortex is not very sensitive to the value of  $u_o/U_1$  or to the initial spatial distribution of turbulence. However, this aspect will be explored in more detail in future work.

### 2.1.3. Interpretation of the model equations

The equations (2) through (7) have been arranged to highlight the different effects of the mean strain  $S = \frac{1}{2}(U' - U/r)$  and rotation  $U/r$  on turbulence. According to (7), the turbulence is produced only if the mean strain  $S$  is nonzero. The circulation distribution  $\Gamma(r)$  in the bulk of a turbulent line vortex remains approximately Gaussian as described by (11), thus  $S < 0$  and the shear stress  $\overline{uv}$  is positive. Inspection of the equations reveals that for the gradient  $K'_z \propto \Gamma' > 0$ , the generation of the stress  $\overline{uv}$  is severely inhibited and so is the TKE production  $P_s = -\overline{uv}S$ . In the limit of rapid solid body rotation  $U/r = \Omega \gg 1/\tau$ , equations (2), (3) and (5) yield an oscillatory solution with (inertial wave) frequency  $4(1 - \alpha_2)^{1/2}\Omega$ . The rapid rotation theories give the frequency of oscillations to be exactly  $4\Omega$  (Mansour *et al.* 1991), suggesting that the rapid-pressure model constant  $\alpha_2$  should approach zero in the rapid limit  $\Omega\tau \gg 1$ . We found this, however, to be of little consequence for the model results and retained, for the present, the value  $\alpha_2 = \alpha_1 = 0.3$  inferred from realizability considerations (Zeman 1981). By comparing the TKE equation (7) with the RSC equations (2)-(5), one can easily see that the rotational terms (associated with  $U/r$ ) are absent in the TKE equation showing that, as alluded to earlier, standard  $k - \epsilon$  models cannot represent the stabilizing effect of the concentrated vortex flow. Results supporting this conjecture are presented in the following section.

### 2.3. Computations, comparison with experiments

The most important result of the present work is contained in Figure 1. Here, the vortex core growth parameter

$$b_1 = \frac{\Delta(R_1)}{\Delta(\Gamma_o t)^{1/2}} \quad (12)$$

is plotted against the flow Reynolds number  $\Gamma_o/\nu$ . The observation data points plotted are a mixture of flight and laboratory experiments as indicated in the figure legend. There are two set of model results; one computed with the present RSC

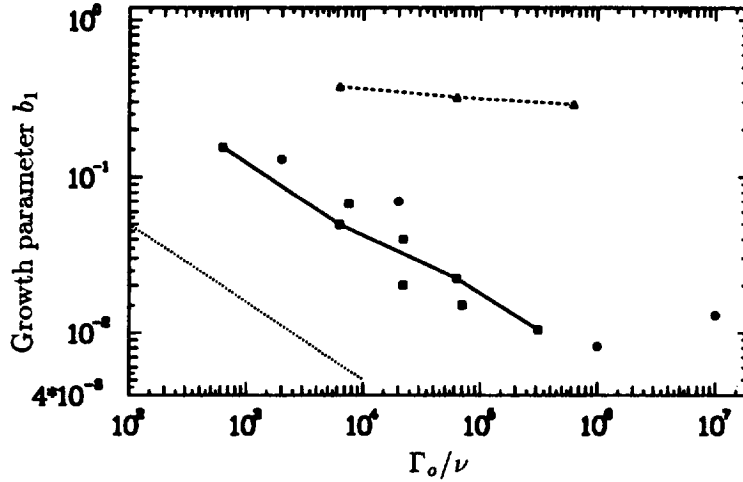


FIGURE 1. Vortex core growth rate  $b_1$  (defined in (12)) vs  $\Gamma_o/\nu$ . Data compiled in Govindraju and Saffman (1971):  $\bullet$ ; Baker *et al.* (1974):  $\blacksquare$ ; RSC model results:  $\square$  —  $\square$ ;  $k - \epsilon$  model:  $\triangle$  ----  $\triangle$ ;  $-1/2$  slope: ..... .

model, and the second with a  $k - \epsilon$  model. The  $k - \epsilon$  model consists of equations (6), (7), and the constitutive relation for the stress  $\overline{uv}$

$$\overline{uv} = -\frac{\nu_{T_o}}{1 + c_1 \tau^2 (K'_z)^2 / r^3} \left( \frac{\partial}{\partial r} U - \frac{U}{r} \right). \quad (13)$$

In (13)  $\nu_{T_o}$  is the standard eddy viscosity for curvature-free flows. The curvature effect on the eddy viscosity is included through a modification similar to (9). Without this modification, the computed turbulence levels and vortex core growth rates were hopelessly unrealistic. Even so, as shown in Figure 1, the growth rate parameter  $b_1$  computed with the modified  $k - \epsilon$  model is still an order of magnitude higher than indicated by experiments or the RSC model. This trend could not be significantly altered by increased damping through the constant  $c_1$ .

The present results, although still tentative, have some surprising implications. First, as seen in Figure 1, the experimental growth parameter  $b_1$  appears to follow a trend  $b_1 \propto (\Gamma_o/\nu)^{-1/2}$  which suggests viscous rather than turbulent diffusion of the vortices. In other words, it suggests a dependence

$$R_1 \propto (\nu t)^{1/2} \propto (\Gamma_o/\nu)^{-1/2} (\Gamma_o t)^{1/2}.$$

This trend is evidently reproduced by the RSC model results. Indeed, the inspection of computed stress profiles show that the turbulent shear stress  $\overline{uv}$  is so effectively damped by the swirl that within the vortex core the angular momentum transfer is dominated by the viscous stress. Whatever turbulence is present throughout the vortex, it is passive and does not contribute to the momentum transfer, except in the outer part of the vortex  $2R_1 < r < 3R_1$ . Hence, the RSC-computed vortex appears to be quasi-laminar. On the other hand, the same vortex predicted by the

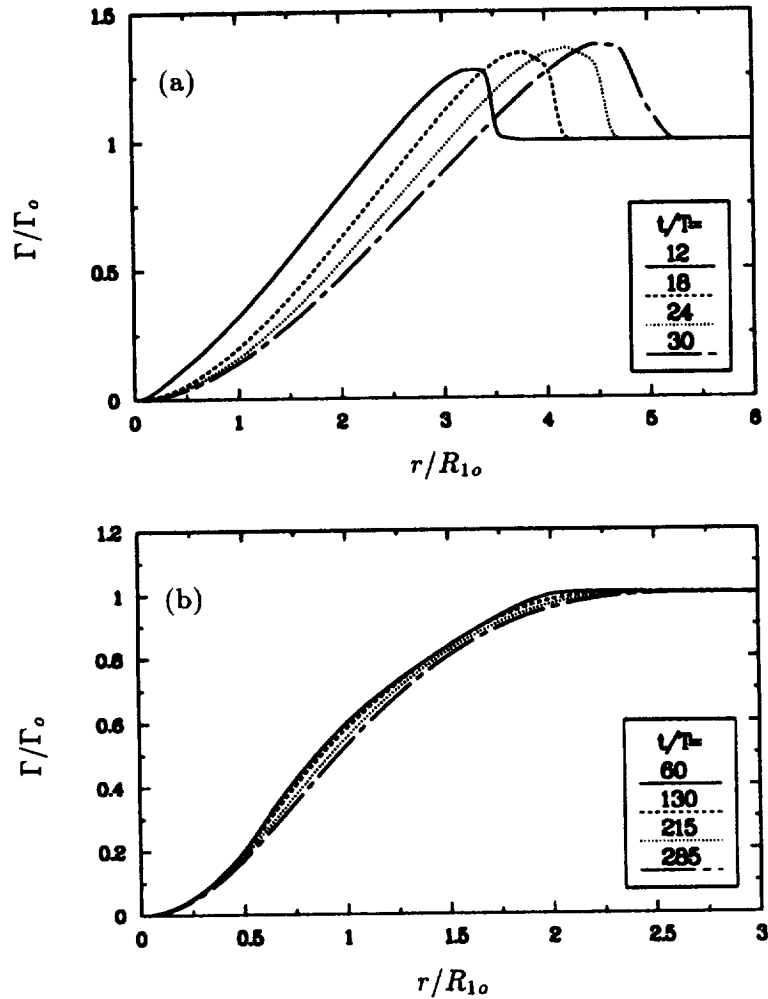


FIGURE 2. Circulation profile evolution computed by: (a)  $k - \epsilon$  model, (b) RSC model; the indicated time of evolution  $t$  is in units of  $T = (R_1/U_1)_o$ .

$k - \epsilon$  model is fully turbulent within the core and the angular momentum transfer is dominated by turbulence. Thus as indicated in Figure 1, the growth parameter  $b_1$  inferred from the  $k - \epsilon$  model results is independent of  $\Gamma_o/\nu$ .

The second result of interest is the circulation profile evolution. As seen in Figure 2, there is a striking difference between the  $\Gamma$  profile evolutions computed by the RSC and  $k - \epsilon$  models. The fully turbulent vortex computed by the  $k - \epsilon$  model develops an overshoot in circulation, while the quasi-laminar vortex computed by the RSC model evolves on the viscous time scale and changes very little within the time period shown. Both of these results are consistent with the analysis of Govindraju and Saffman (1971). They inferred from the equations of motion that

for a turbulent vortex, the nondimensional quantity

$$I_\gamma = \frac{1}{R_1^2} \int_0^\infty \frac{\Gamma_o - \Gamma}{\Gamma_o} r dr$$

should approach zero for sufficiently large times  $t \gg R_1^2/\Gamma_o$ , and thus the  $\Gamma$  distribution should develop an overshoot. Evidently this is true for the  $k - \epsilon$  model as shown in Figure 2a. On the other hand, a lack of a visible overshoot (about 1% of  $\Gamma_o$ ) in Figure 2b, indicates that  $I_\gamma$  remains approximately constant and this result is again consistent with the quasi-laminar vortex computed by the RSC model.

In conclusion, on the basis of experimental evidence presented in Figure 1, we have inferred that the vortex growth is dominated by viscous effects and not by turbulence. This view is consistent with the RSC model results, which suggest that the turbulent momentum transfer is suppressed by the stabilizing effect of the swirl and that the vortex turbulence plays only a passive role in the vortex dynamics.

### 3. Future work

The modeling results are sufficiently interesting to continue exploring the wingtip vortex modeling in the present geometry. There are many questions to be answered before proceeding to a more complex flow configuration which allows for an axial shear and pressure gradient. It has to be established whether the computed quasi-laminar vortex is a representation of physics, or whether it is an artifact of the RSC model. To this end, we shall test different model versions, investigate the effect of initial conditions, and make more detailed model-experiment comparisons.

### Acknowledgements

I wish to thank Dr. Moser of NASA Ames for many helpful discussions on the subject of this research.

### REFERENCES

- BAKER, G. R., BARKER, S. J., BOFAH, K. K., & SAFFMAN, P.G. 1974 Laser anemometer measurements of trailing vortices in water. *J. Fluid Mech.* **65**, 325-336.
- BANDYOPADHYAYA, P. R., STEAD, D. J. & ASH, R. L. 1991 Organized nature of a turbulent trailing vortex. *AIAA J.* **29**, 1627-1633.
- BRADSHAW, P. 1969 The analogy between streamline curvature and buoyancy in turbulent shear flows. *J. Fluid Mech.* **36**, 177-192.
- DONALDSON, C. DUP. & SULLIVAN, D. 1971 Decay of an isolated vortex. *Aircraft Wake Turbulence and its Detection*. Ed. J. H. Olsen and A. Goldberg, Plenum Press 1971.
- DURBIN, P. 1993 A Reynolds stress model for near-wall turbulence. *J. Fluid Mech.* **249**, 465-498.

- DURBIN, P. 1991 Near-wall turbulence closure modeling without "damping functions". *Theoret. Comput. Fluid Dyn.* **3**, 1-13.
- ETTESTAD, D. & LUMLEY, J. L. 1985 Parameterization of turbulent Transport in swirling flows. *Turbulent Shear Flows 4*. Eds: Bradbury *et al.*, Springer-Verlag.
- GOVINDARAJU & SAFFMAN, P.G. 1971 Flow in a turbulent trailing vortex. *Phys. Fluids*. **14**, 2074-80.
- GREEN, S. A., & ACOSTA, A. J. 1991 Unsteady flow in trailing vortices. *J. Fluid Mech.* **227**, 107-134.
- HOFFMANN, E. R. & JOUBERT, P. N. 1963 Turbulent line vortices. *J. Fluid Mech.* **16**, 395-411.
- PHILLIPS, W. R. C. & GRAHAM, J. A. H. 1984 Reynolds stress measurements in a turbulent trailing vortex. *J. Fluid Mech.* **147**, 353-71.
- ROSE, R. & DEE, W. F. 1965 Aircraft vortex wake and their effects on aircraft. *Aeron. Res. Council*. CP 795.
- SHARIFF, K. 1993 Comments on "Coordinate singularities" by P. R. Spalart, Unpublished note.
- TOWNSEND, A. A. 1976 *The structure of turbulent shear flows*. Cambridge University Press, pp 429.
- ZILLIAC, G. G., CHOW, J.S., DACLES-MARIANI, J., & BRADSHAW, P. 1993 Turbulent structure of a wingtip in the near field. *AIAA Paper 93-3011*. 24nd Fluid Dynamics Conference, Orlando, Florida.
- ZEMAN, O. 1981 Progress in the modeling of planetary boundary layers. *Ann. Rev. Fluid Mech.* **13**, 253-72.
- ZEMAN, O. 1993 Toward modeling wingtip vortices. In preparation.
- ZEMAN, O., & TENNEKES, H. 1975 A self-contained model for pressure terms in the turbulent stress equation. *J. Atmos. Sci.* **32**, 1808-13.
- ZEMAN, O., & LUMLEY, J. L. 1976 Modeling buoyancy driven mixed layers. *J. Atmos. Sci.* **33**, 1974-88.
- ZEMAN, O., & JENSEN, N. O. 1987 Modification of turbulence characteristics in flows over hills. *Q. J. Roy. Meteorol. Soc.* **113**, 55-80.



N94-24143

## New concepts for Reynolds stress transport equation modeling of inhomogeneous flows

By J. Blair Perot AND Parviz Moin

### 1. Motivation and objectives

The ability to model turbulence near solid walls and other types of boundaries is important in predicting complex engineering flows. Most turbulence modeling has concentrated either on flows which are nearly homogeneous or isotropic, or on turbulent boundary layers. Boundary layer models usually rely very heavily on the presence of mean shear and the production of turbulence due to that mean shear. Most other turbulence models are based on the assumption of quasi-homogeneity. However, there are many situations of engineering interest which do not involve large shear rates and which are not quasi-homogeneous or isotropic. Shear-free turbulent boundary layers are the prototypical example of such flows, with practical situations being separation and reattachment, bluff body flow, high free-stream turbulence, and free surface flows. Although these situations are not as common as the variants of the flat plate turbulent boundary layer, they tend to be critical factors in complex engineering situations.

The models developed in this work are intended to extend classical quasi-homogeneous models into regions of large inhomogeneity. These models do not rely on the presence of mean shear or production, but are still applicable when those additional effects are included. Although the focus will be on shear-free boundary layers as tests for these models, results for standard shearing boundary layers will also be shown.

Eddy viscosity models and  $k$ - $\epsilon$  type models are fundamentally incapable of representing shear-free boundary layers. They assume that there exists a proportionality between the turbulent stresses and the mean shear. This clearly can not be the case in a shear-free flow. The next level of turbulence modeling, Reynolds stress transport equation models, are the simplest type of model capable of capturing the shear-free or nearly shear-free situation.

The models developed in this work are based on our studies of the near wall behavior of turbulence in shear-free boundary layers (Perot & Moin, 1993). These studies of shear-free turbulent boundary layers have provided a physical understanding of the wall/turbulence interaction, and it is the goal of this paper to translate this physical understanding into improved near wall turbulence models. The inclusion of more physics into the models presented herein allows us to obtain better agreement with direct numerical simulation (DNS) data without resorting to additional model constants, *ad hoc* damping functions, or imposed near wall behaviors.

## 2. Dissipation model

### 2.1 Introduction

In the following section, some advances in near wall dissipation modeling are presented. What is described is not so much a new model, but a technique for extending classical (quasi-homogeneous) dissipation models into the near wall region. Unlike previous techniques which were ultimately *ad hoc* in nature, this model for the near wall dissipation is based on a simple mathematical decomposition and physical observations of the behavior of near wall turbulence.

The physical inspiration for the dissipation model is found in figure 1. This figure is from simulations of a shear-free solid wall (Perot & Moin, 1993). In these simulations, a solid wall (no-slip boundary conditions) is suddenly inserted into isotropic, homogeneous decaying turbulence. The wall interacts with the turbulence, creating a boundary layer in the turbulent statistics which grows into the turbulence as time progresses. The figure shows two planes parallel to the solid wall plotted with contours of the instantaneous tangential velocity. The top plane is far from the wall, and the min/max values of the contours correspond to *rms* intensities that are very close to their free-stream value. The bottom plane is much closer to the wall and has much smaller min/max levels (and *rms* intensities). The crucial observation from these figures is that the structure of the turbulence in the two planes is very similar (i.e., the location of the contours), while the magnitude or scale of the turbulent fluctuations (measured either by the min/max of the contours or by the *rms* intensities) differs by an order of magnitude from one plane to the other. The distance over which the turbulent intensities are damped by the wall is much smaller than the distance over which the eddy structure (as measured by the eye) changes appreciably. This implies that in very near wall turbulence, there is a separation of scales, with the turbulent intensities changing much more rapidly than variations in the actual eddy structure. These observations should also apply in the near wall region of standard flat plate boundary layers. Whether they apply in even more complicated situations is not important since this is the inspiration, not the foundation, for the dissipation tensor model.

The decomposition of turbulence into a turbulent intensity component and a turbulent structure component can be accomplished mathematically in the following way.

$$u_i = \bar{Q}_{ip} \tilde{u}_p. \quad (1)$$

Here,  $u_i$  is the fluctuating velocity,  $\bar{Q}_{ip}$  is a generalized turbulent intensity, and  $\tilde{u}_p$  is the velocity structure. This operation can also be thought of as a mapping or a transformation which scales the fluctuating velocity component, so that the resultant statistical quantity,  $\tilde{u}_p$ , is a nearly homogeneous quantity. Several appropriate choices for  $\bar{Q}_{ip}$  which accomplish this goal will be discussed in Section 2.3. However, at this point it is sufficient to observe that equation (1) is a mathematical decomposition, which is well defined as long as  $\bar{Q}_{ip}$  is an invertible matrix.

The turbulent intensity,  $\bar{Q}_{ip}$ , has an overbar to indicate that it is considered to be a statistical average of turbulence quantities and a known quantity. Mathematically,

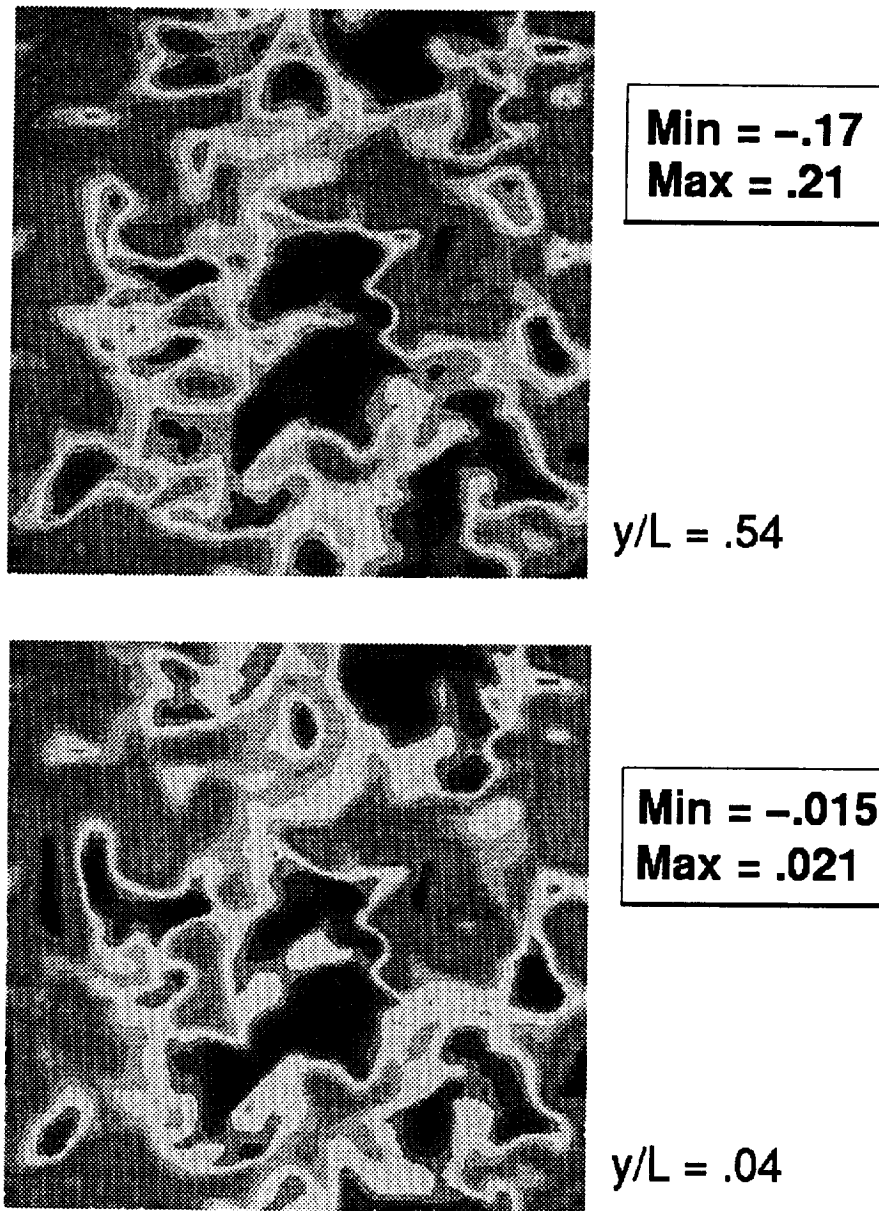


FIGURE 1. Contours of instantaneous tangential velocity in planes parallel to a shear-free solid wall. ( $Re_T = 134$ )

the definition of  $\overline{Q}_{ip}$  is arbitrary, but physically, it is important to choose a definition for  $\overline{Q}_{ip}$  which reflects its intended function as a measure of the turbulent intensity. Different definitions for  $\overline{Q}_{ip}$  produce models of varying complexity and accuracy. In the context of this work, two definitions for  $\overline{Q}_{ip}$  will be considered. One definition is based on the turbulent kinetic energy and the other definition is based on the Reynolds stress tensor. Better definitions for  $\overline{Q}_{ip}$  tend to produce better models at the price of increased complexity.

Having chosen a definition for the turbulent intensity, the properties of the velocity structure can then be derived from equation 1. The velocity structure (unlike the turbulent intensity tensor) retains the random spatial and temporal fluctuations of the original velocity field. The velocity structure can, in a sense, be thought of as a normalized fluctuating velocity scaled by the generalized turbulent intensity tensor. The result of this normalization by the turbulent intensity is that the velocity structure becomes a homogeneous, or at least a quasi-homogeneous, turbulence quantity. It now becomes possible to think of the decomposition (equation 1) as a splitting of turbulence into "homogeneous" factor (velocity structure) and "inhomogeneous" factor (turbulent intensity).

An analogy with Reynolds decomposition into mean and fluctuating velocities can be made. However, in this case, the decomposition is multiplicative rather than additive, and rather than subtracting off the mean to get to fluctuating velocity, we are dividing by some turbulent intensity to get the velocity structure. The unknown turbulent quantity of interest (the velocity structure) now has zero mean and unity (or nearly unity) variance.

## 2.2 Mathematical details

The result of substituting this mathematical decomposition (equation 1) into the definition for the homogeneous dissipation tensor,

$$\epsilon_{ij} \equiv 2\nu \overline{u_{i,p} u_{j,p}}, \quad (2)$$

is

$$\begin{aligned} \frac{\epsilon_{ij}}{2\nu} &= \overline{Q}_{im,p} (\overline{\tilde{u}_m \tilde{u}_n}) \overline{Q}_{jn,p} + \overline{Q}_{im} (\overline{\tilde{u}_{m,p} \tilde{u}_{n,p}}) \overline{Q}_{jn} \\ &+ \frac{1}{2} (\overline{Q}_{im,p} (\overline{\tilde{u}_m \tilde{u}_n})_{,p} \overline{Q}_{jn} + \overline{Q}_{im} (\overline{\tilde{u}_m \tilde{u}_n})_{,p} \overline{Q}_{jn,p}) \\ &+ \frac{1}{2} (\overline{Q}_{im,p} W_{mnp} \overline{Q}_{jn} - \overline{Q}_{im} W_{mnp} \overline{Q}_{jn,p}) \end{aligned} \quad (3)$$

where the tensor  $W_{mnp} = (\overline{\tilde{u}_m \tilde{u}_{n,p}} - \overline{\tilde{u}_{m,p} \tilde{u}_n})$  is antisymmetric in  $m$  and  $n$ .

This expression for the dissipation tensor splits the dissipation into three fundamental parts: the dissipation due to spatial variations in the turbulent intensity (first term on the right hand side), the dissipation due to spatial variations in the turbulent structure (second term on the right hand side), and coupling terms representing the interaction of the first two dissipation terms with each other (last two terms on the right hand side).

The contribution to the dissipation due to variations in the turbulent intensity (first term on the right hand side) dominates in regions of large inhomogeneity where the turbulent intensity changes rapidly. This “inhomogeneity term” depends only on the turbulent intensity tensor and the Reynolds stress tensor (by definition,  $\overline{\tilde{u}_m \tilde{u}_n} = \overline{Q_{mi}^{-1} R_{ij} Q_{jn}^{-1}}$  where  $R_{ij} = \overline{u_i u_j}$ ). The generalized turbulent intensity,  $\overline{Q}_{ij}$ , is assumed to be well defined in terms of other quantities available in the closure, so the inhomogeneity term does not need to be modeled. Because equation 3 is an exact expression, the inhomogeneity term can also be thought of as an “exact term”. In regions where the inhomogeneity term dominates (such as near walls), equation 3 will give exact results for the dissipation.

The second term on the right hand side of equation 3 involves a statistical quantity which will be called the structure dissipation tensor. This quantity is much easier to model than the dissipation tensor itself because the velocity structure is, in fact, quasi-homogeneous. Therefore, models based on the assumption of quasi-homogeneity (i.e. most classical dissipation tensor models) can be expected to work very well for this quantity.

The two coupling terms can be thought of as redistribution terms. Depending on the definition of  $\overline{Q}_{ij}$ , they either are identically zero or their trace is zero. The separation of scales between variations in the turbulent structure (with length scales on the order of the large eddy length scale) and variations in the turbulent intensity (with much smaller length scales on the order of  $\sqrt{\nu t}$ ) suggests that the coupling terms should be relatively small; typically, processes which occur at different scales tend to have little interaction. The exact nature of these terms will be further investigated when specific expressions for  $\overline{Q}_{ij}$  are examined.

### 2.3 Dissipation model

There are a number of choices that can be made for the generalized turbulent intensity tensor,  $\overline{Q}_{ij}$ . A simple choice is an isotropic scale tensor proportional to the square root of the turbulent kinetic energy,  $\overline{Q}_{ij} = k^{1/2} \delta_{ij}$ , where  $k$  is the turbulent kinetic energy. The resulting expression for the dissipation then becomes

$$\frac{\epsilon_{ij}}{2\nu} = (k^{1/2})_{,p} (k^{1/2})_{,p} \frac{R_{ij}}{k} + \frac{1}{2} (k)_{,p} \left( \frac{R_{ij}}{k} \right)_{,p} + k \overline{\tilde{u}_{i,p} \tilde{u}_{j,p}} \quad (4)$$

This equation is attractive because of its simplicity. The only term requiring modeling is the velocity structure dissipation,  $\tilde{\epsilon}_{ij} = 2\nu \overline{\tilde{u}_{i,p} \tilde{u}_{j,p}}$ . The inhomogeneity term and redistribution term (the first and second terms on the right hand side) are well defined, and in the sense described previously, they are “exact”. Despite its attractiveness, this model suffers from some basic flaws. In particular, it is only weakly realizable; the kinetic energy is guaranteed to remain positive when using this model, but the Reynolds stress tensor itself may become indefinite.

A more attractive dissipation model can be obtained by using a slightly more complicated choice for the velocity scale tensor given by  $\overline{Q_{im} Q_{mj}} = R_{ij}$ . This makes  $\overline{Q}_{ij}$  the square root of the Reynolds stress tensor. Because  $R_{ij}$  is positive definite, this square root is well defined (up to a plus or minus sign on each eigenvalue, which

can be arbitrarily chosen). Note that  $\bar{Q}_{ij}$  has the same eigenvectors as  $R_{ij}$  with eigenvalues that are the square root of the eigenvalues of  $R_{ij}$ .  $\bar{Q}_{ij}$  is, therefore, a symmetric tensor like  $R_{ij}$ . This definition is a natural generalization of the definition used to derive equation 4. The sign of the square root is not important in the model because all terms involving the generalized intensity appear in pairs, canceling out any dependence on the sign. Note that with this definition  $\bar{u}_i \bar{u}_j = \delta_{ij}$ , indicating that the velocity structure is very close to a homogeneous isotropic quantity.

With this enhanced choice for the turbulent intensity tensor, the expression for the dissipation takes the form

$$\begin{aligned} \epsilon_{ij} = & 2\nu \bar{Q}_{im,p} \bar{Q}_{jm,p} + \bar{Q}_{im} \tilde{\epsilon}_{mn} \bar{Q}_{nj} \\ & + \nu (\bar{Q}_{im,p} W_{mnp} \bar{Q}_{nj} - \bar{Q}_{im} W_{mnp} \bar{Q}_{nj,p}). \end{aligned} \quad (5)$$

where  $\tilde{\epsilon}_{mn} = 2\nu \overline{\tilde{u}_{i,p} \tilde{u}_{j,p}}$  is again the velocity structure dissipation tensor.

The first two terms of equation 5 are the now familiar inhomogeneous and homogeneous dissipation terms. The third term of equation 5 acts as a redistribution term and is particularly interesting. It is zero if the Reynolds stress tensor is either isotropic or homogeneous. In fact, it is zero if  $Q_{im,p} = s Q_{im}$  where  $s$  is a scalar quantity. This turns out to be the case in spatially decaying turbulence if there is no return to isotropy in the sense of Lumley (1978). So in some sense, this term can also be thought of as a return to isotropy term.

Further insight into the redistribution term can be gained by evaluating the Reynolds stresses in their principal coordinates. Then  $Q_{ij}$  is a diagonal tensor with  $Q_{\alpha\alpha} = R_{\alpha\alpha}^{1/2}$  (here and throughout the text, no summation is implied for Greek indices). In this arrangement, the redistribution term only contributes to the off-diagonal components of the dissipation tensor; hence, it is a coupling or redistribution term. It is partly responsible for enabling the dissipation tensor to have principal axes that differ from those of the Reynolds stress tensor. This is a useful property of the model, but one which is burdensome because the tensor  $W_{mnk}$  introduces nine new unknowns for which no model (even quasi-homogeneous) now exists. In what follows, the terms involving  $W_{mnk}$  will be neglected. In the tests that have been performed, this simplification does not appear to affect the performance of the model significantly and, therefore, appears to be warranted.

#### 2.4 Mathematical constraints

It can be shown that every component of this model has the correct leading (and often higher order) terms in a Taylor series expansion about a no-slip wall. This non-trivial result holds irrespective of the model for the structure dissipation as long as the structure dissipation approaches a constant near the wall. It is a result of the fact that inhomogeneity dominates in the near wall region, and the inhomogeneous term of equation 5 is exact.

It is important that models have the correct asymptotic behavior as they approach the wall (Launder & Reynolds, 1983). For instance, at a solid wall the transverse components of the dissipation ( $\epsilon_{11}$  and  $\epsilon_{33}$ ) must exactly balance the corresponding

diffusion components, or turbulence will spuriously be created by the wall. Some dissipation models (see Lai & So, 1990) have the asymptotic behavior for a no-slip wall imposed upon them. These models will probably fail when presented with any other type of boundary such as a free surface, a transpiring wall, etc. This is not the case for the current model, which does not impose asymptotic behavior, but which obtains correct asymptotic behavior (in numerous flow situations) by virtue of the “exact” inhomogeneous term.

This model also satisfies certain mathematical constraints. By its construction, the model is Galilean and tensorally invariant. It can be seen from equation 5 (with  $W_{mnk} = 0$ ) that if the structure dissipation tensor is positive definite, then the dissipation tensor can also be guaranteed to be positive definite. Strict realizability (Schumann, 1977) in the low Reynolds number limit can be shown by analyzing the viscous terms. In principal coordinates, the sum of the viscous diffusion term,  $D_{ij} = \nu R_{ij,kk}$ , and dissipation term becomes

$$-\epsilon_{\alpha\alpha} + D_{\alpha\alpha} = 2\nu R_{\alpha\alpha}^{1/2} R_{\alpha\alpha,pp}^{1/2} - R_{\alpha\alpha} \tilde{\epsilon}_{\alpha\alpha} \quad (6)$$

Therefore, when the Reynolds number is low, the following expression can be written,  $(R_{\alpha\alpha}^{1/2})_t = \nu(R_{\alpha\alpha}^{1/2})_{,mm} - \frac{\epsilon_{\alpha\alpha}}{2} R_{\alpha\alpha}^{1/2}$ . This indicates that the turbulent intensities diffuse and decay exponentially in time, which, along with equation 6, guarantees that the Reynolds stress tensor can not become indefinite as time advances.

### 2.5 Results

Two classical models for the homogeneous dissipation tensor assume that dissipation is isotropic, ( $\epsilon_{ij}^I = \frac{2}{3}\epsilon\delta_{ij}$ ), or that the dissipation is proportional to the Reynolds stress tensor (Rotta, 1951), ( $\epsilon_{ij}^R = \frac{\epsilon}{k}R_{ij}$ ). Figures 2a and 2b show comparisons of these two models with the direct numerical simulation (DNS) data of Perot & Moin (1993) for flow near a shear-free solid wall. It is evident that the isotropic assumption works well far from the wall and the “low Reynolds number” Rotta model works well close to the wall. An improved near wall dissipation model can, therefore, be constructed using a combination of these two classical models. A number of mixed models of this type exist, each differing in the choice of parameter which is used to blend the two models.

To demonstrate the possible improvement, a mixed model is also presented in figures 2a and 2b. The parameter  $A = 1 - \frac{9}{8}(a_{mn}a_{nm} - a_{mp}a_{pn}a_{nm})$  (Tselepidakis, 1991), where  $a_{ij} = R_{ij}/k - 2/3\delta_{ij}$  is the non-dimensional Reynolds stress anisotropy tensor, is used to blend the two models.  $A$  is 1 in isotropic turbulence and zero in the two component limit that occurs at a wall. The mixed model is then written as

$$\epsilon_{ij}^M = A\frac{2}{3}\epsilon\delta_{ij} + (1-A)\frac{\epsilon}{k}R_{ij} \quad (7)$$

An expression very similar to the mixed model will also be used to model the structure dissipation tensor in the inhomogeneity-capturing model,

$$\tilde{\epsilon}_{ij} = \frac{\tilde{\epsilon}}{k} \left( A\frac{2}{3}\delta_{ij} + (1-A)\frac{R_{ij}}{k} \right) \quad (8)$$

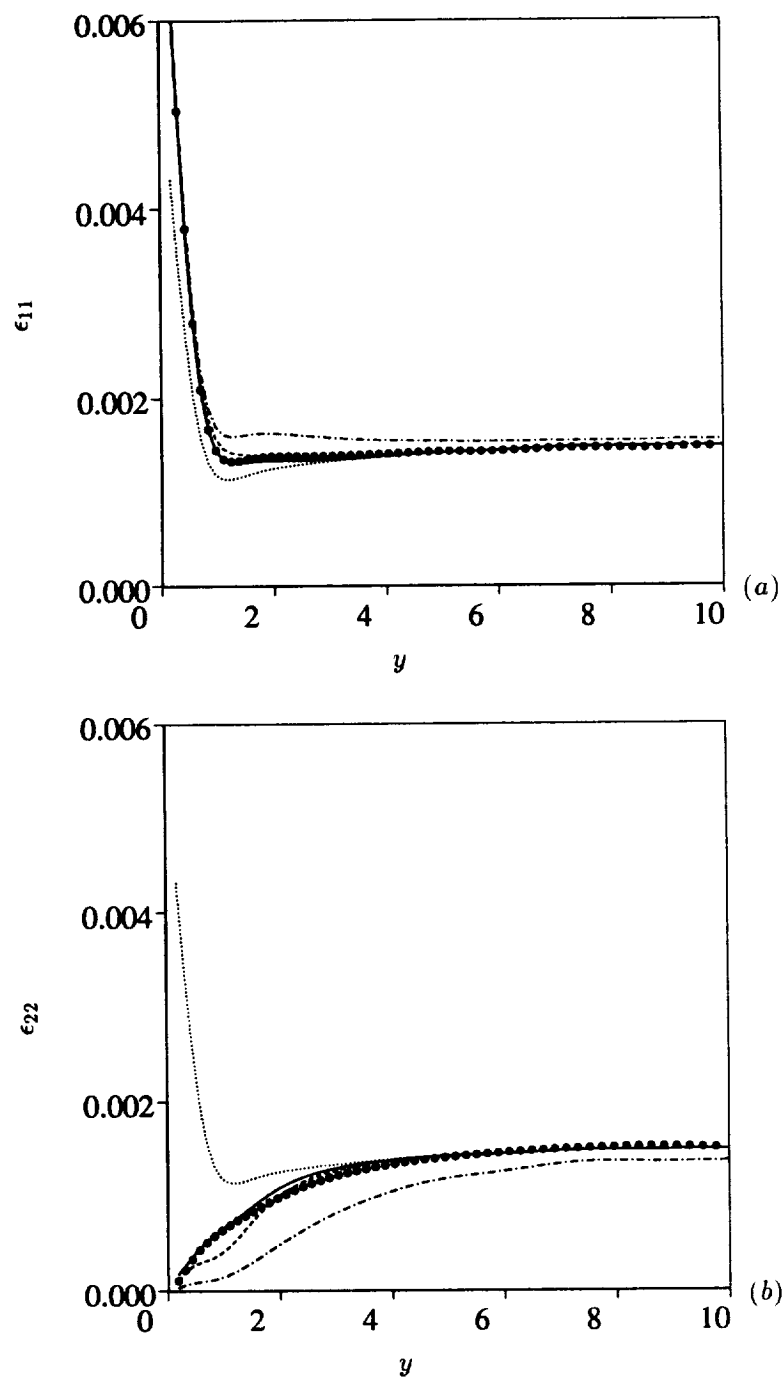


FIGURE 2. Dissipation near a shear-free solid wall. ( $Re_T = 54$ ), (a) Tangential dissipation, (b) Normal dissipation.  $\bullet$ , DNS data;  $\cdots$ , Isotropic model;  $-\cdot-$ , Rotta model;  $----$ , mixed model;  $—$ , inhomogeneity model.



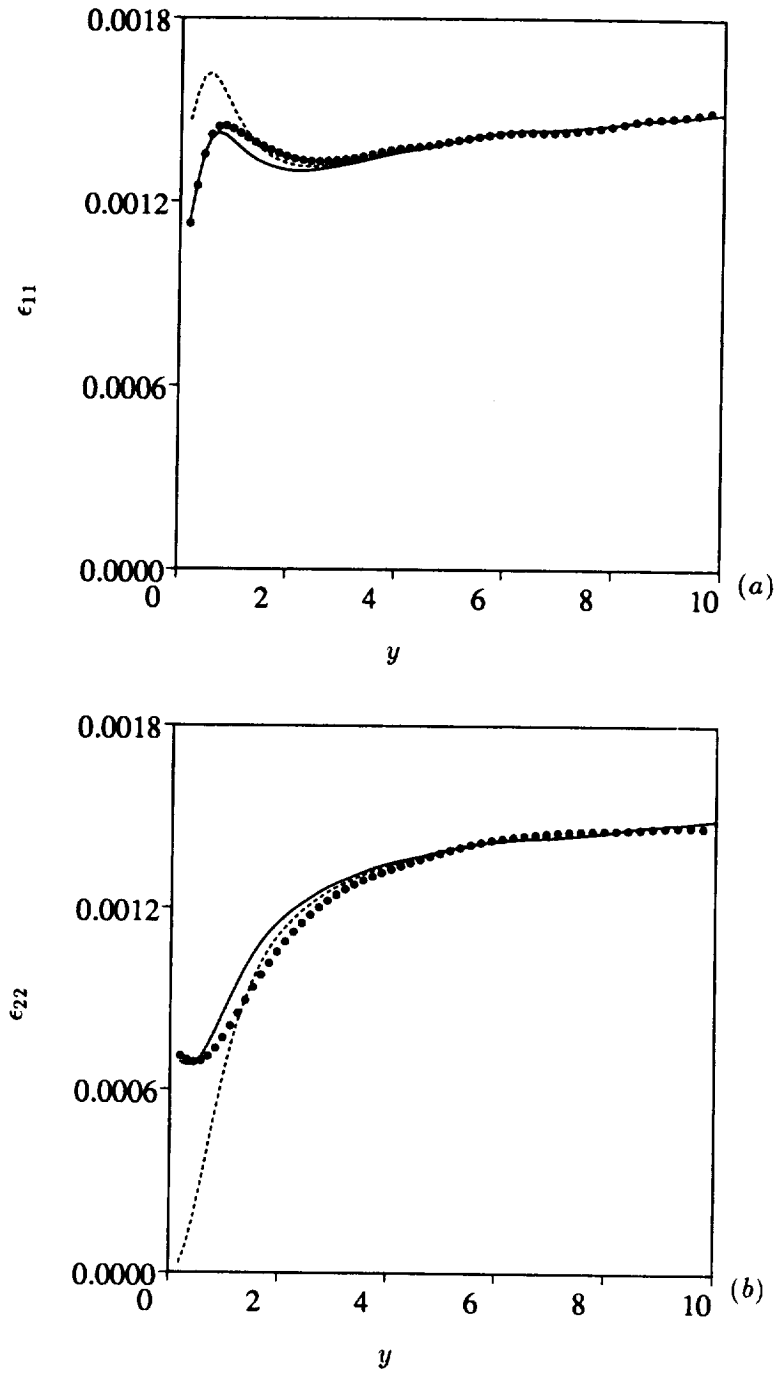


FIGURE 3. Dissipation near a free surface. ( $Re_T = 54$ ), (a) Tangential dissipation, (b) Normal dissipation.  $\bullet$ , DNS data; ----, mixed model; —, inhomogeneity model.

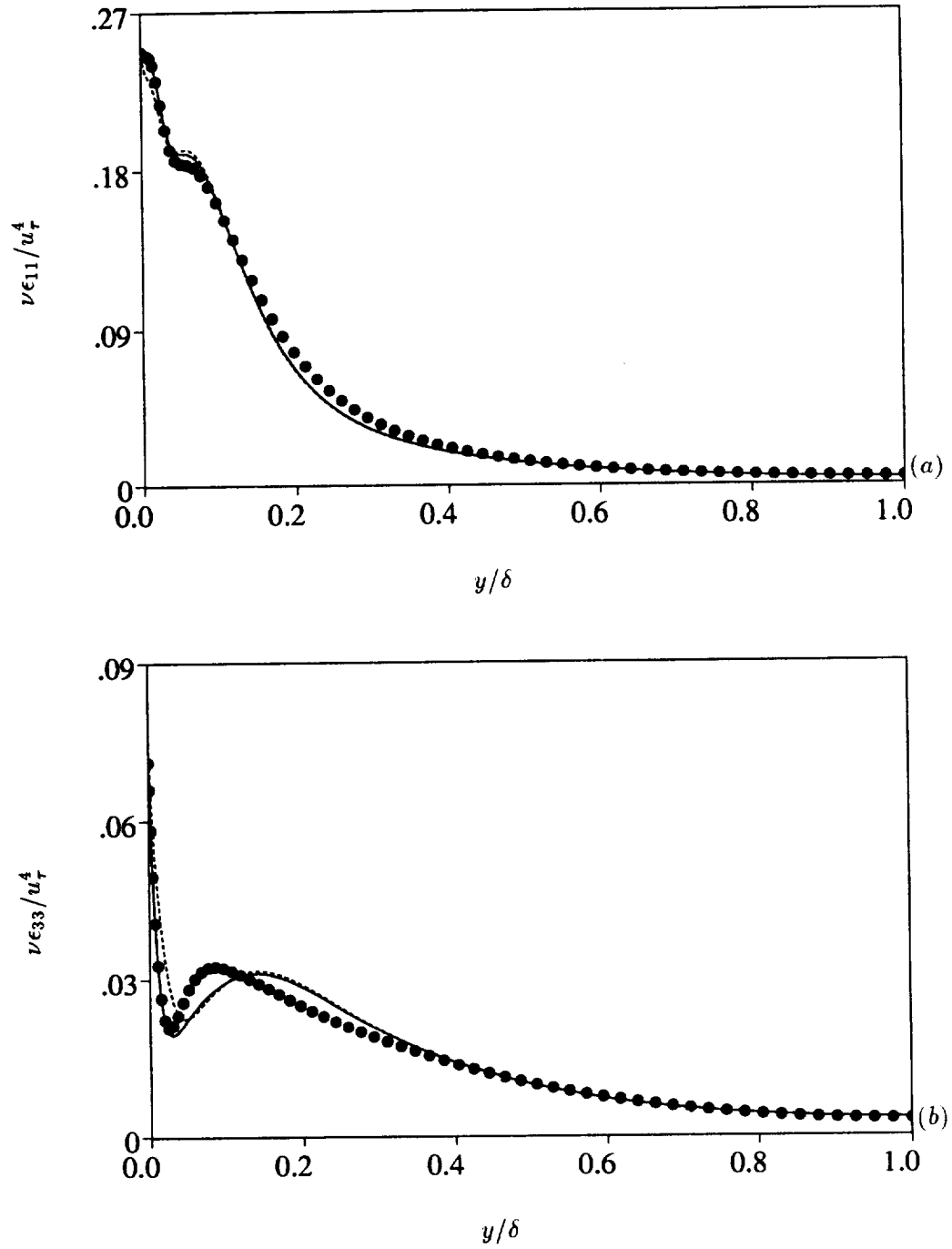


FIGURE 4. Dissipation in turbulent channel flow. (a) Streamwise dissipation, (b) Spanwise dissipation. •, DNS data of Mansour, Kim, & Moin (1988); ----, mixed model; —, inhomogeneity model.

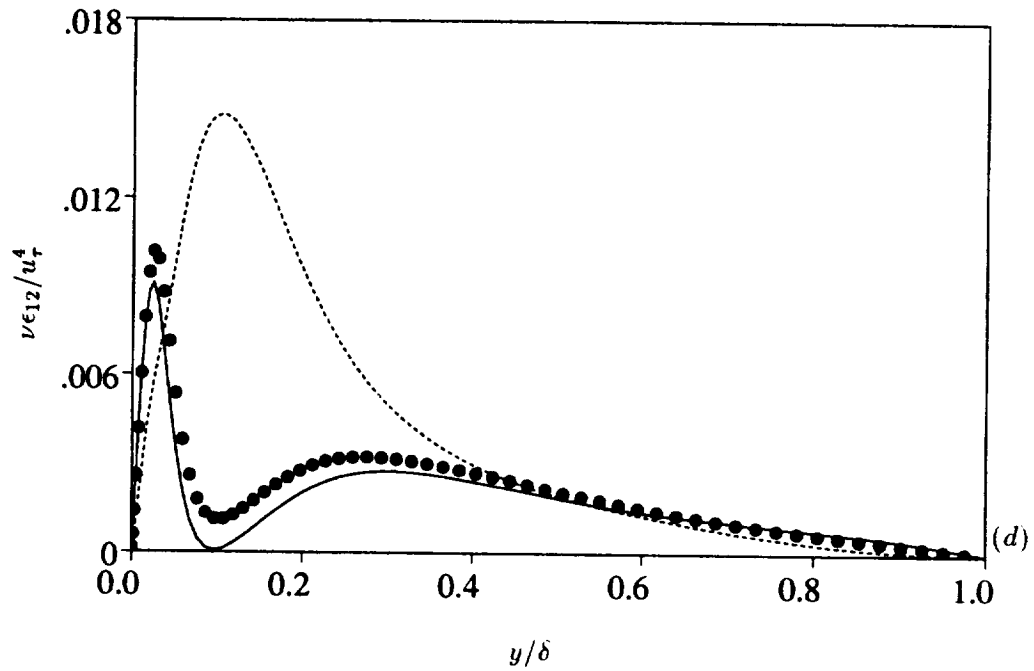
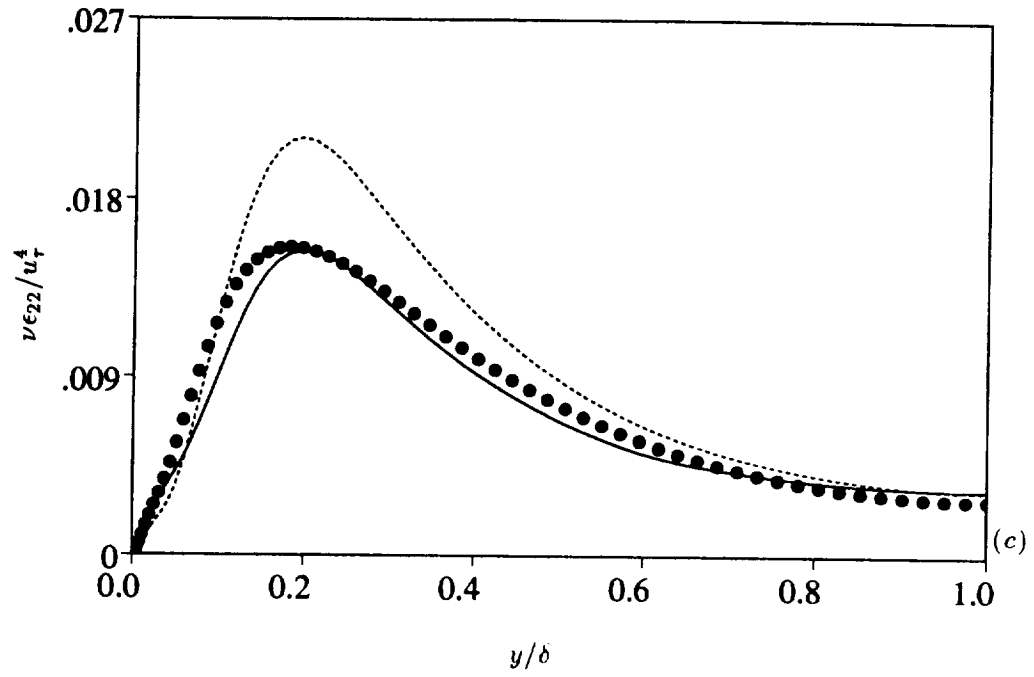


FIGURE 4. (Cont.) Dissipation in turbulent channel flow. (c) Normal dissipation, (d) Shear stress dissipation.  $\bullet$ , DNS data of Mansour, Kim, & Moin (1988); ----, mixed model; —, inhomogeneity model.

where  $\tilde{\epsilon}$  is (in analogy with the dissipation) one half of the trace of the structure dissipation tensor. Equation 5 with equation 8 and  $W_{ijk} = 0$  gives the full inhomogeneity capturing model for the dissipation tensor,

$$\epsilon_{ij}^I = 2\nu \overline{Q}_{im,p} \overline{Q}_{jm,p} + \tilde{\epsilon} \left( \frac{2}{3} A \frac{R_{ij}}{k} + (A - 1) \frac{R_{im} R_{mj}}{k^2} \right). \quad (9)$$

Note that in the mixed model  $\epsilon$  must be specified. In the inhomogeneity model,  $\tilde{\epsilon}$  must be specified. In the tests of the models, these quantities will be supplied from the direct numerical simulation (DNS) data, but in an actual modeling situation, they would have to be derived in some other manner (usually from a dissipation transport equation). The quantity  $\tilde{\epsilon}$  is probably easier to arrive at (since it is much smoother than  $\epsilon$ ). In addition,  $\tilde{\epsilon}$  has less effect on the overall model performance because the terms involving  $\tilde{\epsilon}$  are small near the wall. The inhomogeneity model is also shown in figures 2a and 2b. It falls almost exactly on the DNS data.

Both the mixed model and the inhomogeneity model work well for the case of a shear-free solid wall. A better test of the two models' ability to handle inhomogeneity is presented in figures 3a and 3b where DNS data, the mixed model, and the inhomogeneity model are shown for the case of turbulence next to a free surface. The mixed model gives an incorrect value at the surface for the tangential dissipation and completely inappropriate behavior for the normal dissipation component. The inhomogeneity model, on the other hand, closely follows the DNS data and gives particularly good far field and near surface behaviors.

The final test of the model is presented in figures 4a-d. This shows the case of fully developed channel flow. The data is from Mansour, Kim & Moin (1988). Both models work well for the streamwise component of the dissipation. The inhomogeneity model captures the function value *and* the slope exactly at the wall. The spanwise components of the models behave very similarly, with the inhomogeneity model showing an improvement in the slope at the wall. However, the mixed model severely overestimates the normal dissipation and does not have the correct qualitative behavior for  $\epsilon_{12}$ .

## 2.6 Summary

A new modeling technique for extending classical dissipation models into regions of large inhomogeneity has been developed. It is based on a hypothesis of separation of scales and derived from a simple mathematical decomposition. This decomposition uses the the square root of the Reynolds stress tensor as a generalized turbulent intensity to transform (or map) the fluctuating velocity into a quasi-homogeneous quantity (the velocity structure). The resulting inhomogeneity model, derived from this decomposition, satisfies all known mathematical constraints and is relatively simple to implement. It has been shown that the model gives superior results in both wall and surface bounded flows. The formalism developed here has also been applied to modeling of the scalar dissipation and heat flux dissipation (Malan, 1993) with equally impressive results.

### 3. Pressure-strain model

#### 3.1 Introduction

The pressure-strain term is an inter-component energy redistribution term; it causes no net change in the total kinetic energy. Experiments on homogeneous turbulence (Lumley & Newman, 1977) show that this redistribution by the pressure-strain (at least by the nonlinear (slow) part of the pressure-strain) tends to result in a return to isotropy. The logical assumption from this observation is that the pressure-strain term is driven by the non-dimensional anisotropy in the Reynolds stresses,  $a_{ij} = R_{ij}/k - 2/3\delta_{ij}$ , which by construction is a trace free tensor, like the pressure-strain.

Almost all models for the pressure-strain are based on the assumption that the pressure-strain must be a function of the anisotropy tensor. The models of Rotta (1951), Shih & Lumley (1985), and Speziale, Sarkar and Gatski (1991), are examples of models of this type. Some of these models are very complicated, but none produce truly convincing results. In fact, Reynolds (1988) has shown that any pressure-strain model based on this assumption is incapable of capturing the effects of rapid rotation. Any model of this type is also incapable of predicting a flow where the boundary condition on the tangential velocity changes suddenly, such as the sudden insertion of a permeable wall (Perot & Moin, 1993) or the sudden change from a solid wall to a free surface boundary condition. In those situations, the pressure-strain term changes instantaneously, whereas the Reynolds stress and anisotropy tensors take some time to evolve.

Furthermore, return to isotropy cannot be the driving mechanism for the pressure-strain term near a free surface or a solid wall. In such cases, the tangential stresses are larger than the normal stresses, and yet there is still a transport of energy to the tangential stresses. In many near wall flows, the pressure-strain term actually enhances anisotropy. In the face of all this evidence, it seems clear that the very assumptions upon which pressure-strain modeling are based need to be reevaluated.

#### 3.2 Modeling

The physical model for turbulent flow proposed in Perot & Moin (1994a) is a useful guide to pressure-strain modeling. In that model, it is assumed that in any turbulent flow there are opposing events. These events will tend to balance each other (resulting in zero net transfer of energy) unless one of the events is weaker than the other. In the near wall case, antisplats (blobs of fluid moving away from the boundary) are weaker due to the fact that tangential energy is removed by dissipation near the wall. This limits the antisplat's ability to convert tangential energy into normal energy. In homogeneous turbulence, the situation is somewhat different: if one component of the turbulence is less energetic than the others then it will not be able to deliver energy to the other components as effectively. This will result in a net transfer of energy into the less energetic component and a return to isotropy.

In the near wall case, dissipation and diffusion control intercomponent energy

transfer by determining the imbalance between splats and antisplats. In homogeneous turbulence, Reynolds stresses anisotropy controls energy transfer. To translate these ideas into a model, it is instructive to look at the evolution equation for the non-dimensional anisotropy. In unsheared homogeneous turbulence, the exact equation for the non-dimensional anisotropy tensor is

$$a_{ij,t} = \frac{\Pi_{ij}}{k} + \frac{\epsilon}{k} \left( \frac{r_{ij}}{k} - \frac{e_{ij}}{\epsilon} \right) \quad (10)$$

where  $r_{ij} = R_{ij} - \frac{2}{3}k\delta_{ij}$  and  $e_{ij} = \epsilon_{ij} + \frac{2}{3}\epsilon\delta_{ij}$  are the dimensional anisotropy of the Reynolds stress and dissipation tensors,  $\Pi_{ij}$  is the pressure-strain tensor, and  $a_{ij} = R_{ij}/k - 2/3\delta_{ij}$  is the nondimensional Reynolds stress anisotropy tensor. Note that typically the dissipation is more isotropic than the Reynolds stresses (due to quasi-isotropy in the smallest scales of motion), so the second term on the right hand side of the equation tends to increase anisotropy. For return to isotropy to occur, the pressure-strain must be large enough to drive the overall right hand side negative. A reasonable model for the pressure-strain is, therefore, that the pressure strain is proportional to the right hand side,

$$\Pi_{ij} = -C_\pi(-e_{ij} + \frac{\epsilon}{k}r_{ij}) \quad (11)$$

where  $C_\pi > 1$  will guarantee return to isotropy in homogeneous turbulence.

This model has the attractive property that it behaves appropriately as a function of Reynolds number. At very high Reynolds numbers, dissipation becomes isotropic, and the standard return to isotropy model (of Rotta) is recovered. At low Reynolds numbers, the approximation  $\epsilon_{ij} = \frac{\epsilon}{k}R_{ij}$  (Rotta, 1951) becomes increasingly accurate, so  $e_{ij} = \frac{\epsilon}{k}r_{ij}$  at low Reynolds numbers, and the model approaches zero in the low Reynolds number limit. Therefore, at low Reynolds numbers there is no return to isotropy, a property which was proposed by Lumley (1978) and observed in simulations performed by Hallback & Johansson (1992).

To use this model in inhomogeneous flows, it must be generalized. Instead of  $-e_{ij}$ , the quantity  $-e_{ij} + d_{ij}$  will be used;  $d_{ij} = \nu r_{ij,mm}$  is the anisotropy in the viscous diffusion term, which is zero in homogeneous turbulence. In addition, the inverse time scale  $\frac{\epsilon}{k}$ , is not correct near a wall. It is replaced by  $A\frac{\epsilon}{k}$  where  $A$  is the flatness parameter described earlier in the section on dissipation modeling.  $A$  is 1 in isotropic turbulence and 0 at a wall. This accounts for the fact that in the two component limit near a wall, classical return to isotropy is not expected. The model for the pressure-strain then becomes

$$\Pi_{ij} = -C_\pi(-e_{ij} + \nu r_{ij,mm} + A\frac{\epsilon}{k}r_{ij}) \quad (12)$$

As the next section will show, this model gives reasonable behavior in shear-free boundary layers. Since the development given here is essentially for the nonlinear (slow) pressure-strain, these shear-free flows are appropriate situations in which to test the model.

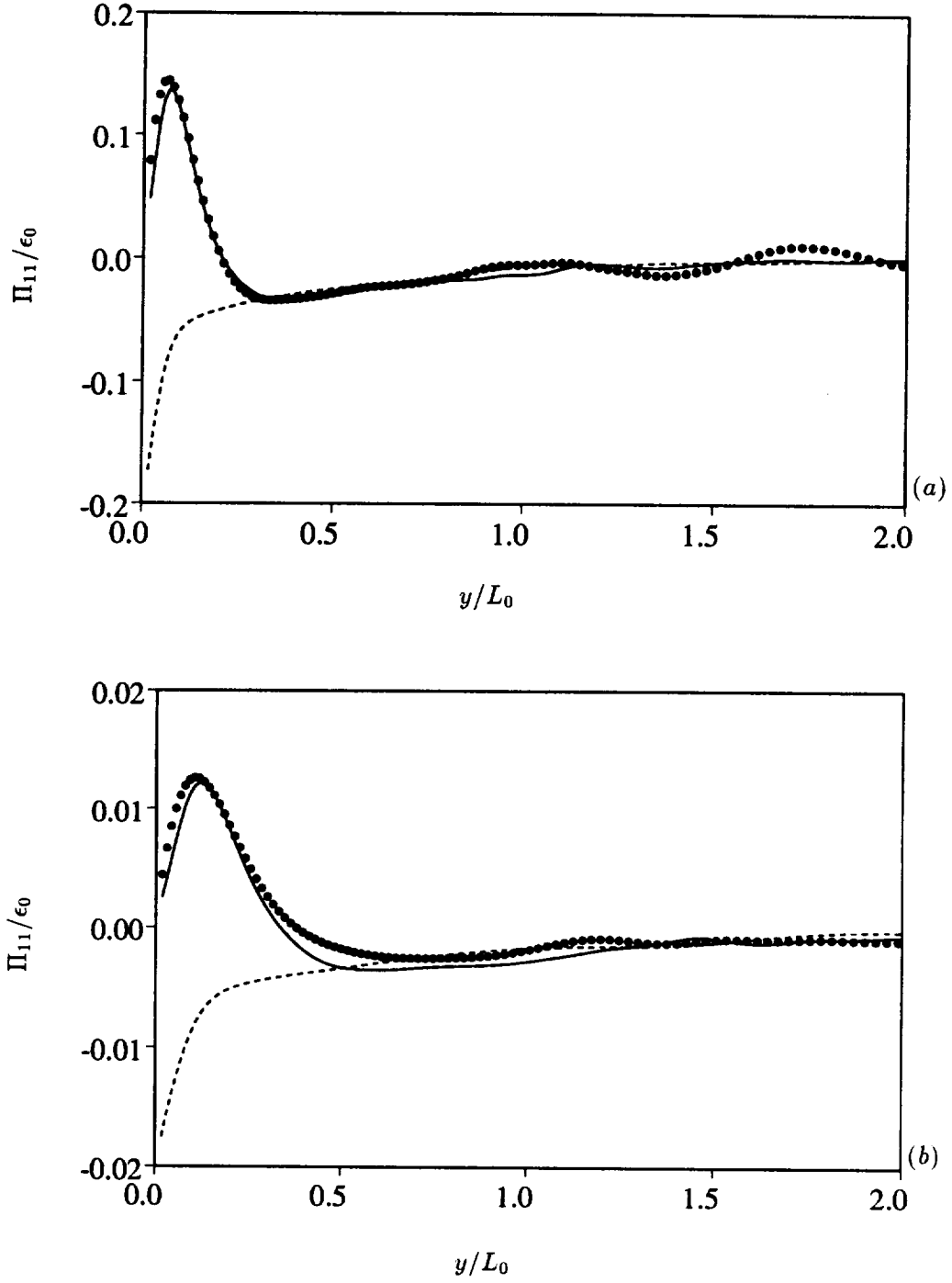


FIGURE 5. Pressure-strain near a shear-free wall. ( $Re_T = 134$ ), (a)  $t/T_0 = 1.0$ , (b)  $t/T_0 = 4.5$ .  $\bullet$ , DNS data; ----, Rotta model; —, Present model.

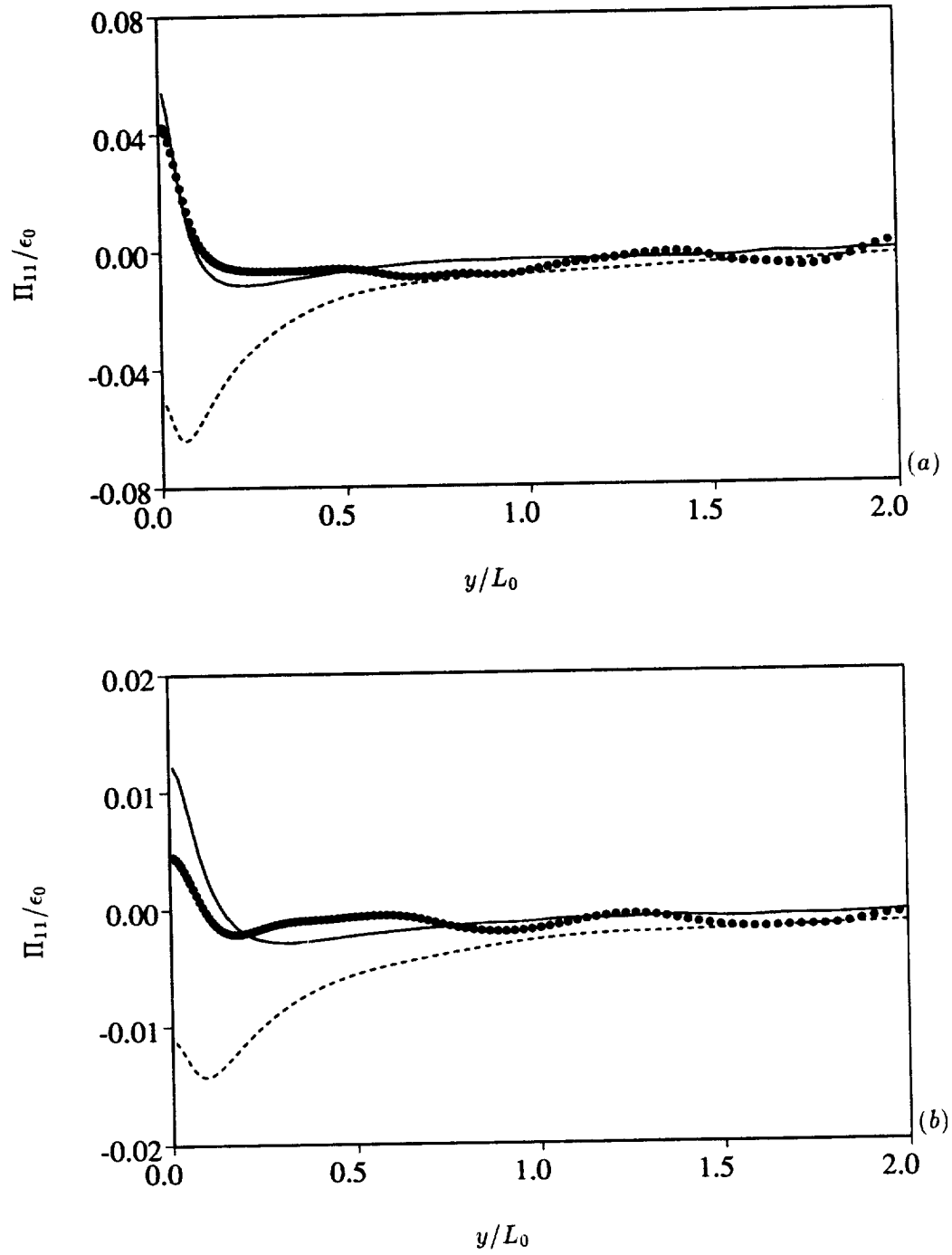


FIGURE 6. Pressure-strain near a free surface. ( $Re_T = 134$ ), (a)  $t/T_0 = 1.0$ , (b)  $t/T_0 = 4.5$ . •, DNS data; ----, Rotta model; —, Present model.



### 3.3 Results

In the following test cases, there is only one independent pressure-strain term since  $\Pi_{11} = -2\Pi_{22} = \Pi_{33}$ , and all off-diagonal terms are zero. Figure 5a shows the performance of the model (equation 12) and the Rotta model ( $\Pi_{ij} = -C_1\epsilon a_{ij}$ ) in a shear-free wall flow at a Reynolds number of 134 (Perot & Moin, 1993). The direct numerical simulation (DNS) data is for the time  $t/T_0 = 1.0$ , where  $T_0$  is the large eddy turnover time measured at the moment of boundary insertion. As previously mentioned, any model based on Reynolds stress anisotropy will have fundamentally incorrect behavior at the wall, so the more complicated variants of Rotta's model were not examined.

It can be seen that the present model, which includes the dissipation anisotropy, gives very good agreement with the DNS data. Figure 5b shows predictions for the same flow at a later time,  $t/T_0 = 4.5$ . The agreement of equation 12 ( $C_\pi = 1.5$ ) with DNS data remains very good. The Rotta model not only has the wrong shape and has asymptotic behavior near the wall, but actually predicts the wrong sign of energy transfer near the wall.

The case of a free surface (Perot & Moin, 1993) is shown in figure 6a. The Reynolds number is 134, and the time is  $t/T_0 = 1.0$ . Again, the current model (with  $C_\pi = 0.5$ ) shows good agreement with the data. Figure 6b shows the same simulation at a later time,  $t/T_0 = 4.5$ , and the model continues to be accurate. Because the pressure-strain term is smaller in the free surface case, the statistical and numerical noise is more apparent than in the shear-free solid wall case.

From these two cases and the case of homogeneous turbulence where  $C_\pi$  is typically taken in the range 1.5–1.8, it appears that the coefficient  $C_\pi$  is not universally constant. This is not entirely surprising. It is reasonable that the two terms in the anisotropy equation (equation 10) might be proportional, but overly optimistic to expect that the constant of proportionality is fixed. In fact, Lumley (1987) has shown that the constant could be a function of the turbulent Reynolds number. As mentioned previously, we believe this model explicitly accounts for those Reynolds number effects, but the possibility for dependence on additional parameters still exists.

### 3.4 Summary

The pressure-strain model presented in this section was based on the anisotropy evolution equation for unsheared homogeneous turbulence, with generalizations to include the effects of inhomogeneity and two componentality near a wall. Although adjustment of the Rotta coefficient was required, this algebraic model for the pressure-strain produces surprisingly good results in the two test cases studied. Like the model for the dissipation, it is possible to think of this pressure-strain model as a combination of two terms, a near wall term (proportional to the anisotropy of the viscous terms) and a quasi-homogeneous far field term (proportional to the Reynolds stress anisotropy). This model breaks with tradition by not *only* using the Reynolds stress anisotropy in the model. This is a simple, yet vital step.

#### 4. Turbulent transport model

##### 4.1 Introduction

There is a high degree of similarity between the role of the triple correlations in the Reynolds stress equations and the role of the Reynolds stresses in the mean momentum equations. Both enhance transport, both become increasingly important as the Reynolds number increases, and both lead to fuller profiles in the respective statistical variables. For higher Reynolds number flows, where the gradients near the wall are very steep, it is particularly important to model the turbulent transport term accurately.

The modeling history of triple correlations is rather sparse. Most often, completely different physical effects such as viscous diffusion and pressure transport are lumped with turbulent transport. Such lumping is probably an unwise practice and will not be considered further in this section; it supposes that entirely different physical phenomena can be modeled collectively. Daly & Harlow (1970) used a gradient diffusion hypothesis for the triple correlations and proposed

$$T_{ijk} = C_s \frac{k}{\epsilon} R_{kl} R_{ij,l} \quad (13)$$

where a value of  $C_s = .22$  was suggested by Launder & Morse (1979). Hanjalic & Launder (1972) noted that this model did not have the proper symmetry in its indices. They suggested

$$T_{ijk} = C_t \frac{k}{\epsilon} (R_{kl} R_{ij,l} + R_{jl} R_{ik,l} + R_{il} R_{kj,l}) \quad (14)$$

with  $C_t = .11$ . This more complicated expression can be derived from a simplification and modeling of the exact evolution equations for the triple correlations. More complicated expressions for the triple correlations also exist (Lumley 1984), but are not considered here since preliminary tests showed little difference with the Hanjalic & Launder model.

##### 4.2 Modeling

Gradient transport models of the type mentioned above give only moderate to poor agreement in shear-free boundary layers. The problem with these models is not endemic to shear-free flows; Mansour, Kim & Moin (1988) witnessed equally poor performance in the case of fully developed channel flow. The clue to better modeling of the triple correlations is contained in the very first sentence of the introductory paragraph. The triple correlations should be modeled by using generalizations of low-order Reynolds stress models.

The simplest model for the Reynolds stress uses the eddy viscosity hypothesis. The eddy viscosity hypothesis works surprisingly well in a number of different flows. We might hope that an eddy viscosity hypothesis for the triple correlations might work as well, or perhaps even better, since higher order statistics tend to be more

uniform. The standard Hanjalic & Launder model (equation 14) can, in fact, be written in an eddy viscosity formulation,

$$T_{ijk} = C_t(\nu_{kl}^T R_{ij,l} + \nu_{jl}^T R_{ik,l} + \nu_{il}^T R_{kj,l}) \quad (15)$$

where  $\nu_{ij}^T = \frac{k}{\epsilon} R_{ij}$ . The Hanjalic & Launder model is not usually viewed in this fashion; typically, it is justified as a severe simplification of the modeled triple correlation evolution equation. However, when viewed as an eddy viscosity model, there seems to be little justification for this choice of eddy viscosity. Instead, it is proposed that the eddy viscosity be a velocity scale times a length scale, as originally proposed by Prandtl in 1926. The previous section on dissipation modeling indicated that the generalized square root of the Reynolds stress tensor is an appropriate tensor velocity scale. So the following eddy viscosity is proposed,  $\nu_{ij}^T = \bar{Q}_{ij} L_M$ , where  $\bar{Q}_{ik} \bar{Q}_{kj} = R_{ij}$  and  $L_M$  is a mixing length.

The wealth of literature on mixing length theory, originally developed for Reynolds stress modeling, can now be adopted at this higher level for the triple correlations. In this work, the mixing length will be assumed to be proportional to the large eddy length scale,  $L_\infty = \frac{k^{3/2}}{\epsilon} |_\infty$ , except close to walls or surfaces, in which case the mixing length is proportional to the distance from the wall. This choice of a mixing length, essentially due to Von Karman (1931), is simplistic. In complicated geometries, the distance to the wall is ill defined. It is not the goal of this section to evaluate mixing length models in detail, but to evaluate the modeling of the triple correlations and the turbulent transport term. It will be shown that this new method for defining the eddy viscosity improves turbulent transport models and is a promising direction to be moving in terms of triple correlation modeling.

The full eddy viscosity model for the turbulent transport terms then becomes

$$T_{ijk} = C_u L_M (\bar{Q}_{kl} R_{ij,l} + \bar{Q}_{jl} R_{ik,l} + \bar{Q}_{il} R_{kj,l}) \quad (16)$$

where the constant  $C_u$  has been adjusted to a value of .18 and the mixing length is given by  $L_M = (L^{-1} + y^{-1})^{-1}$ , which gives a smooth transition between the near wall and far field limits.

#### 4.3 Results

Figures 7a and 7b show comparisons of the models with direct numerical simulation (DNS) data from Perot & Moin (1994b). Figure 7a shows the tangential turbulent transport term for the case of a shear-free wall at a Reynolds number of 134 and time  $t/T_0 = 1.0$ . Figure 7b shows the normal turbulent transport term under identical conditions. The triple correlations take longer to converge than double correlations so there is some noise in the data, particularly far from the wall where turbulence length scales are largest. There is also some noise in the models from numerical differentiation.

The Daly & Harlow model captures the normal component well but overestimates the magnitude and position of the peak in the tangential component (it is, of course, also tensorally incorrect). The Hanjalic & Launder model captures the tangential

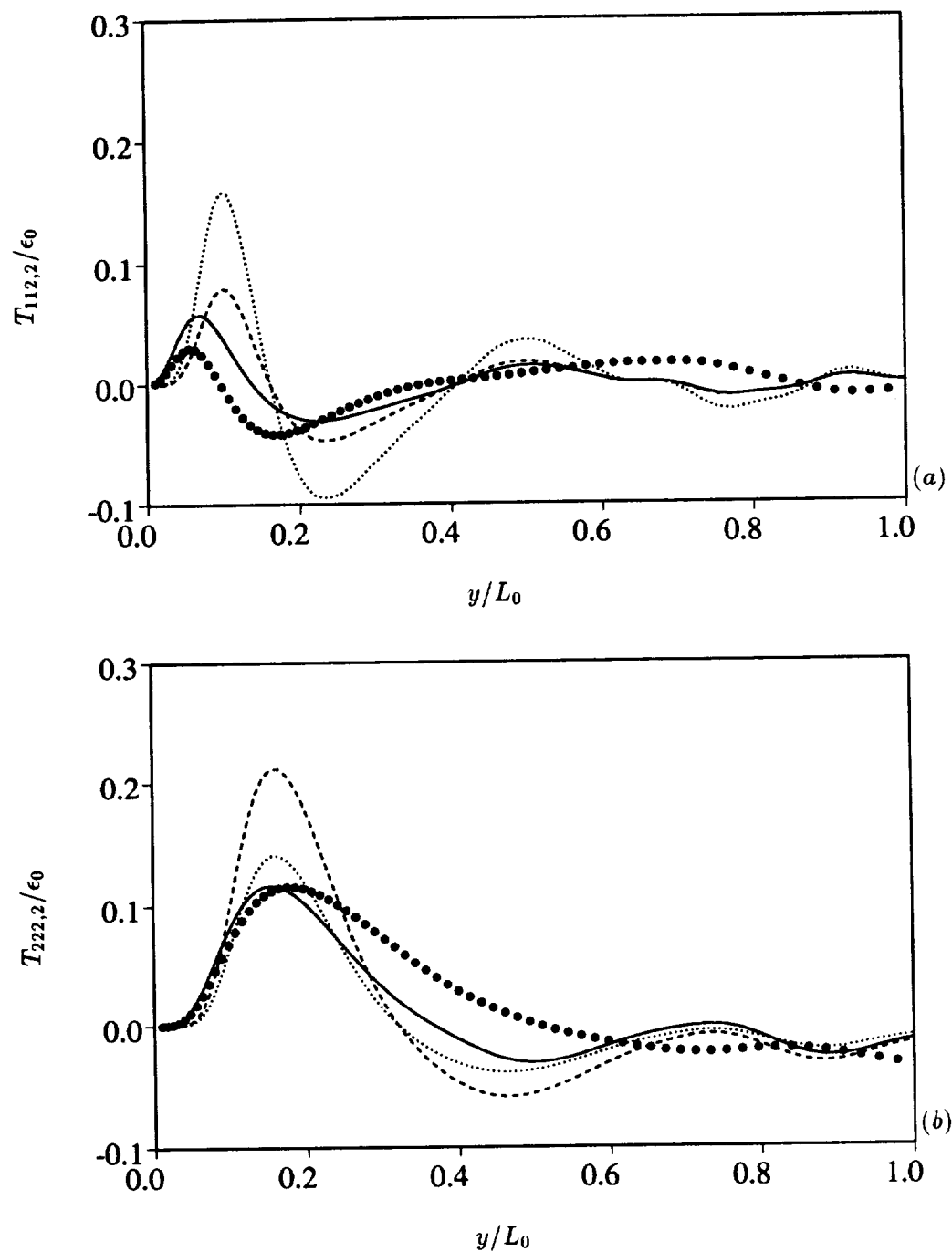


FIGURE 7. Turbulent transport near a shear-free wall. ( $Re_T = 134$ ) ( $t/T_0 = 1.0$ )  
 (a) Tangential turbulent transport, (b) Normal turbulent transport.  $\bullet$ , DNS data;  $\cdots$ , Daly & Harlow model;  $---$ , Hanjalic & Launder model;  $—$ , Eddy viscosity model.

component better, but at the expense of overestimating the normal component. The eddy viscosity model gives better overall results than either of the previous two models. Similar results are shown for the shear-free wall case at a later time ( $t/T_0 = 3.0$ ) in figures 8a and 8b. The conclusions remain the same.

The case of a free surface at a Reynolds number of 134 and time  $t/T_0 = 1.0$  is shown in figures 9a and 9b. In this case, both the Daly & Harlow and the Hanjalic & Launder models overestimate the turbulent transport terms. The Daly & Harlow model is worse for the tangential component, and the Hanjalic & Launder model is worse for the normal component. Again, the eddy viscosity model gives better overall agreement with the DNS data. The eddy viscosity model tends to decay too quickly as one moves away from the wall, but this could easily be remedied by letting the  $O(y)$  behavior in the mixing length persist farther into the flow.

It should also be mentioned that the eddy viscosity model has the right asymptotic behavior at the wall, whereas the standard models do not. Considering the simplicity of the eddy viscosity model and its relationship with an already well understood branch of turbulence modeling, and considering the fact that the eddy viscosity model gives similar or improved performance for these shear-free flows, it seems reasonable to recommend this approach in the future for triple correlation modeling.

#### 4.4 Summary

One of the most obvious physical effects of turbulent flows is their increased ability to mix and transport flow quantities; eddy viscosity mimics this physical process. In this section, the Hanjalic & Launder model for turbulent transport was rewritten in an eddy viscosity formulation. An improved model for the triple correlations was developed, and good agreement with DNS data was achieved. Even better agreement with the DNS data could be achieved with improved and expanded definitions of the mixing length.

### 5. Conclusions

Near wall models for terms in the Reynolds stress evolution equations have been developed. These improved models perform well in the cases studies. The improvement shown by the models is based upon the inclusion of more physics into the modeling procedure. None of the models require additional constants over their quasi-homogeneous counterparts, and no *ad hoc* functions or *a priori* limiting behaviors have been imposed on the models.

Three fundamentally new concepts have been proposed in the context of this paper. The idea of decomposing the fluctuating velocity using a multiplicative decomposition into an intensity and a structure term led to an enhanced dissipation model. In terms of pressure-strain modeling, we have shown the efficacy of using the dissipation and diffusion anisotropy in conjunction with Reynolds stress anisotropy. Finally, we have suggested that the concept of eddy viscosity is useful at any modeling level when used to represent the effects of higher order correlations (in this case, triple correlations).

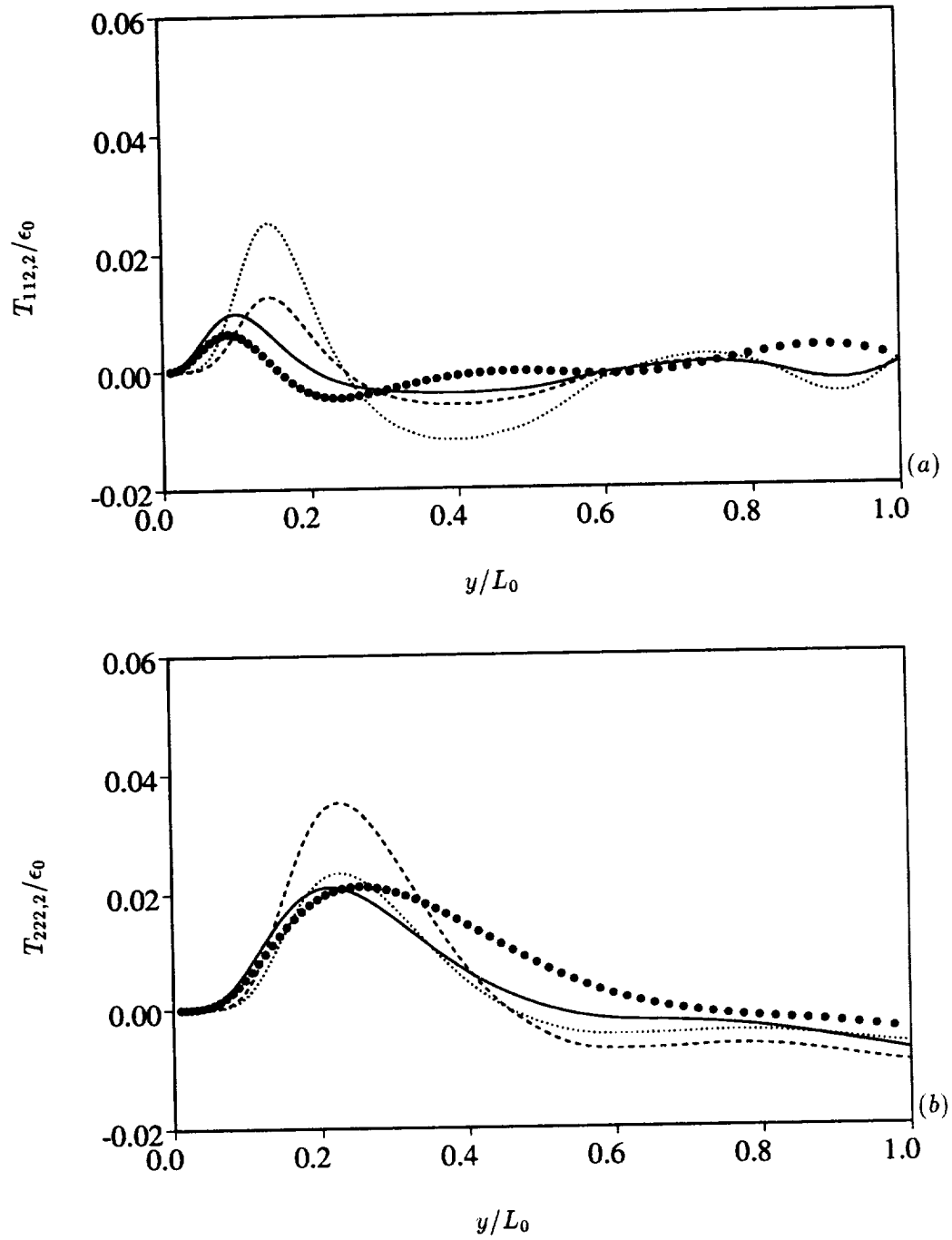


FIGURE 8. Turbulent transport near a shear-free wall. ( $Re_T = 134$ ) ( $t/T_0 = 3.0$ )  
 (a) Tangential turbulent transport, (b) Normal turbulent transport.  $\bullet$ , DNS data;  $\cdots$ , Daly & Harlow model;  $----$ , Hanjalic & Launder model;  $—$ , Eddy viscosity model.

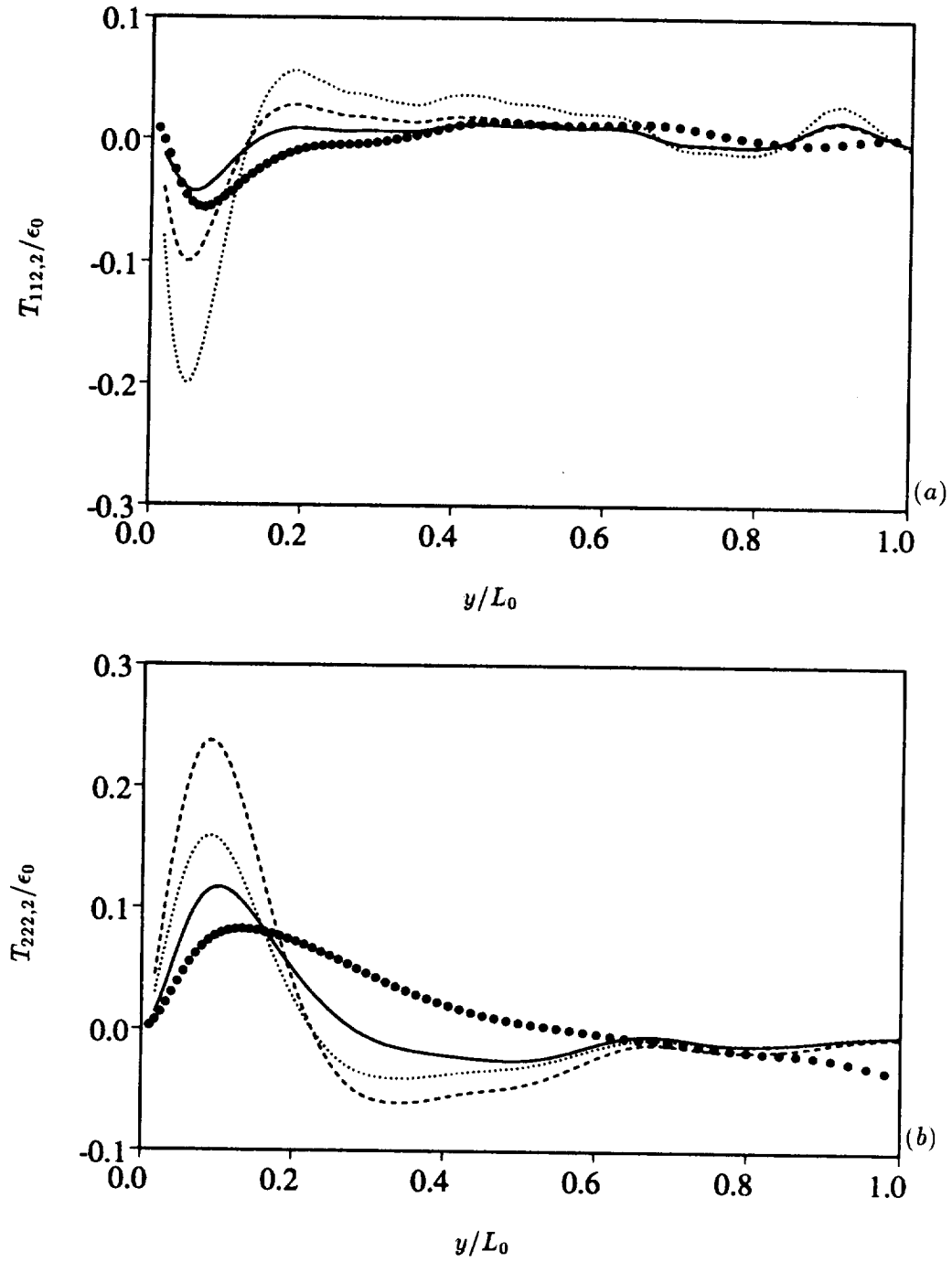


FIGURE 9. Turbulent transport near a free surface. ( $Re_T = 134$ ) ( $t/T_0 = 1.0$ ) (a) Tangential turbulent transport, (b) Normal turbulent transport. •, DNS data; ..... , Daly & Harlow model; ---- , Hanjalic & Launder model; — , Eddy viscosity model.

Financial support for this work was provided by the National Science Foundation and the Center for Turbulence Research. Supercomputer time on the Connection Machine 200 and the Connection Machine 5 was provided by the NAS Division of NASA-Ames Research Center.

## REFERENCES

- DALY B. J. & HARLOW F. H. 197 Transport equations in turbulence. *Phys. Fluids*. **13**, 2634-2649.
- DURBIN, P. A. 1993 A Reynolds stress model for near-wall turbulence. *J. Fluid Mech.* **249**, 465-498.
- HALLBACK, M. 1993 Development of Reynolds stress closures of homogeneous turbulence through physical and numerical experiments. *Ph.D. Thesis*, Dept. of Mechanics, Royal Institute of Technology, Stockholm.
- HALLBACK, M. & JOHANSSON, A. V. 1992 Modeling of pressure-strain in homogeneous turbulence. *Advances in Turbulence 4*, TU Delft, Holland.
- HANJALIC, K. & LAUNDER, B. E. 1975 Contribution towards a Reynolds-stress closure for low-Reynolds-number turbulence. *J. Fluid Mech.* **74**, 593-610.
- KARMAN, T. VON 1931 *Proc. 3d Int. Congr. Appl. Mech.*, Stockholm pp. 85.
- LAI, Y. G. & SO, R. M. C 1990 On near-wall turbulent flow modelling. *J. Fluid Mech.* **221**, 641-673.
- LAUNDER, B. E., & MORSE, A. P. 1979 Numerical prediction of axisymmetric free shear flows with a Reynolds stress closure. *Turbulent Shear Flows I* (eds. Durst *et al.*), Springer Verlag, New York.
- LAUNDER, B. E., REECE, G. J. & RODI, W. 1974 Progress in the development of a Reynolds-stress turbulent closure. *J. Fluid Mech.* **68**, 537-566.
- LAUNDER, B. & REYNOLDS W. C. 1983 Asymptotic near-wall stress dissipation rates in a turbulent flow. *Phys. Fluids*. **26**, 1157-1158.
- LUMLEY, J. L. 1978 Computational Modeling of Turbulent Flows. *Advances in applied mechanics*, C-S Yih, ed., Academic Press, New York, 123-176.
- LUMLEY, J. L. & NEWMAN, G. R. 1977 The return to isotropy of homogeneous turbulence. *J. Fluid Mech.* **82**, 161-178.
- MALAN, P. 1993 Heat transfer in shear-free turbulent boundary layers. *Report No. MD-64*, Department of Mechanical Engineering, Stanford University.
- MANSOUR, N., KIM, J. & MOIN, P. 1988 Reynolds-stress and dissipation budgets in a turbulent channel flow. *J. Fluid Mech.* **194**, 15-44.
- PEROT, J. B. & MOIN, P. 1993 Shear-free turbulent boundary layers: Physics and Modeling. *Report No. TF-60*, Department of Mechanical Engineering, Stanford University.
- PRANDTL, L. 1926 *Proc 2d Int. Cong. Appl. Mech.*, Zurich, 62-75.



- REYNOLDS, W. C. 1989 Effects of rotation on homogeneous turbulence. *Proceedings of the 10th Australasian Fluid Mechanics Conference*, University of Melbourne, Australia.
- ROTTA, J. 1951 Statistical Theory of inhomogeneous turbulence. Part I. *Zeitschrift für Physik*. **129**, 257-572.
- SCHUMANN, U. 1977 Realizability of Reynolds stress turbulence models. *Phys. Fluids*. **20**, 721-725.
- SHIH, T. H. & LUMLEY, J. L. 1986 Second-order modeling of near-wall turbulence. *Phys. Fluids*. **29**, 971-975.
- SPEZIALE, C. G., SARKAR, S. & GATSKI, T. B. 1991 Modeling the pressure-strain correlation of turbulence: an invariant dynamical systems approach. *J. Fluid Mech.* **227**, 245-272.
- TSELEPIDAKIS, D. P. 1991 Development and application of a new second-moment closure for turbulent flows near walls. *Ph.D. Thesis*, Dept. of Mechanical Engineering, University of Manchester.



N 9 4 - 2 4 1 4 2

## Turbulence modeling for non-equilibrium flows

By P. A. Durbin

### 1. Motivation

Two projects are reported herein. The first is the development and testing of an eddy viscosity transport model. This project also is a starting point for our work on developing computational tools for solving turbulence models in complex geometries—the computational aspect is collaborative with Nagi Mansour. The second project is a stochastic analysis of the realizability of Reynolds stress transport models. This work was motivated by private discussions with Charles Speziale (Boston University) and related collaborative work with him, and also by Steve Pope's presentation at the (Bill) Reynolds Turbulence Symposium in Monterey this year (Pope 1993).

#### 1.1 Eddy viscosity transport

Momentum mixing-length, eddy viscosity models have been popular since the idea was introduced by Prandtl. They invoke a quasi-equilibrium assumption, essentially requiring that the mixing of lumps of fluid takes place in a time short compared to that of the mean flow evolution. In many situations of fluid dynamical interest, mixing cannot be assumed instantaneous and a dynamical equation for the turbulence is required. A rather important example is that of boundary layers subjected to strong pressure gradients: on a practical level, it has been found that mixing length models are unable to predict this type of strongly non-equilibrium flow. A reasonable step is to formulate an analytical eddy viscosity transport model that extends the mixing-length idea by admitting non-equilibrium effects; this is what I have done.

This research has a strong practical incentive. Engineering fluid dynamicists are recognizing a need for more elaborate turbulence models as the complexity of the flows they calculate increases. This has led to a willingness, even a desire, to introduce turbulent transport models into prediction codes. Currently most aerodynamics codes (that solve the Reynolds averaged Navier-Stokes equations) use algebraic eddy viscosity models. It has been found that algebraic models are unable to predict the region of reversed flow near the trailing edge of an airfoil at angle of attack. The failure in this particular case indicates a general inadequacy for calculating complicated mean flows. This shortcoming of simple algebraic models motivated recent research into dynamical equations for eddy viscosity, including that reported herein (Durbin *et al.* 1994). Baldwin and Barth (1990) first proposed that an eddy-viscosity transport equation might be effective in complex aerodynamic flows. The Baldwin-Barth study led to further development of their formulation by Spalart and Almaras (1992) and was a primary impetus for the present work.

Notable features of the present model are that it uses an elliptic relaxation equation to avoid damping functions, that it is formulated solely in terms of local variables, and that it is tensorially and Galilean invariant. In these respects, the model was formulated with complex flows in mind.

### 1.2 Realizability

The exact, unclosed Reynolds-stress transport equations are usually the starting point for formulations of second-moment closure models. Modeling consists of replacing unclosed terms by semi-empirical formulae that express these terms as functions of the dependent variables. After introducing models, quantities with names like ' $\overline{u^2}$ ' no longer represent non-negative functions obtained by squaring and averaging a random variable; rather, they are simply the dependent variables of the model; they are obtained as the solution to a differential equation. However, it is desirable to formulate the equations of the model so that variables like  $\overline{u^2}$  do maintain their non-negativity. In essence, this is the issue of realizability in second-order turbulence closure modeling.

The present report demonstrates how realizability can be addressed by a constructive method. This involves formulating a stochastic process for which the Reynolds-stress model is the exact evolution equation of second moments. The model then is guaranteed to be realizable because it is exact for a well defined stochastic process. In the present analysis, second-moment closure models of the type currently in use are shown to be exact for the statistics of a particular form of Langevin equation. When that Langevin equation is well-defined, the Reynolds-stress model is guaranteed to be realizable.

It is assumed that the appropriate physics are accommodated by the moment closure; the stochastic analysis is purely a mathematical method for analyzing such models. The realizability criteria that are derived are *sufficient*, but not necessary, conditions; also, the analysis is only of homogeneous turbulence.

## 2. Accomplishments

### 2.1 The eddy viscosity transport model

The model is described at length in Durbin *et al.* (1994). It consists of a parabolic transport equation for the eddy viscosity:

$$\frac{D}{Dt}\nu_T = \nabla(\nu + \nu_T)\nabla\nu_T + P_\nu - c_2|S|\nu_T - c_4\frac{\nu_T^2}{L_\nu^2}; \quad (1)$$

and an elliptic relaxation equation for  $P_\nu$ :

$$L_p^2\nabla^2 P_\nu - P_\nu = c_3|\nabla\nu_T|^2 - |S|\nu_T. \quad (2)$$

The dependent variable  $P_\nu$  contains the turbulence production. The elliptic relaxation in (2) introduces a wall effect that suppresses the production of eddy viscosity near a surface. In (1) and (2) the  $c$ 's are model constants, the  $L$ 's are length scales, and  $|S|^2 = 1/2(\partial_i U_j + \partial_j U_i)(\partial_j U_i + \partial_i U_j)$  is a measure of the mean rate of strain.

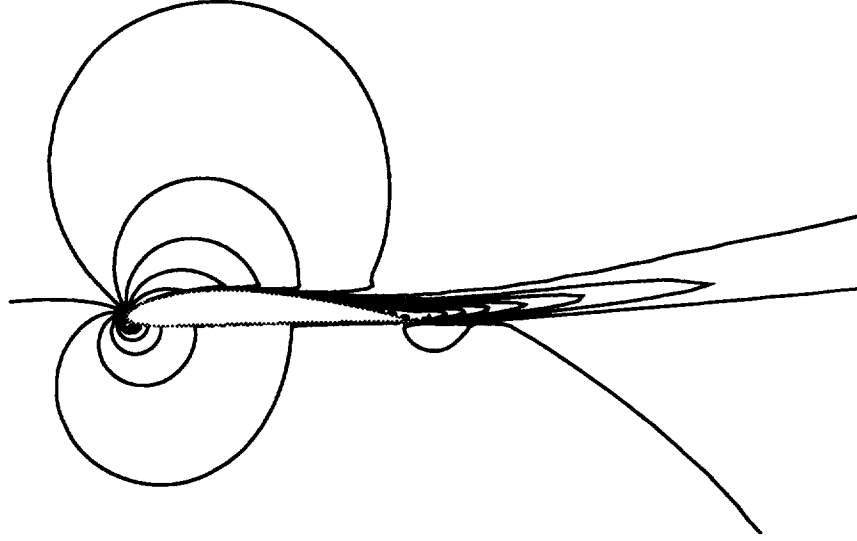


FIGURE 1. Contours of constant  $U$ , showing trailing edge separation and flow geometry.

The ellipticity in (2) is important near surfaces; away from surfaces, or regions of strong inhomogeneity, the model relaxes to a parabolic transport equation. The first term on the right side of (1) describes turbulent and molecular transport; the third and fourth terms model dissipation of  $\nu_T$ , as does the first term on the right side of (2); the second term on the right side of (2) allows for production of turbulence from mean flow gradients.

To complete the model, the length scales must be prescribed and then the constant coefficients chosen. A difficulty of a model with only one primary dependent variable—or, more precisely, only one non-negative dependent variable—is that local turbulent length and time scales cannot be formed from turbulence quantities alone. For this reason  $L_p$  and  $L_\nu$  have been prescribed as functions of the local mean rate of strain, as well as of  $\nu_T$ :

$$L_\nu^2 = \frac{|S|^2}{|\nabla S|^2} + c_m \frac{|\nabla \nu_T|^2}{|S|^2} \quad (3)$$

$$L_p^2 = c_p^2 \min(L_\nu^2, \max(\nu_T, c_l^2 \nu)/|S|). \quad (4)$$

The boundary conditions to the model are

$$\nu_T = \hat{n} \cdot \nabla \nu_T = 0 \quad (5)$$

at a no-slip surface with unit normal  $\hat{n}$ ,

$$\hat{n} \cdot \nabla \nu_T = P_\nu = 0 \quad (6)$$

at the edge of a boundary-layer, or prescribed free-stream values far from an airfoil. No surface boundary condition needs to be imposed on  $P_\nu$  to satisfy (5).

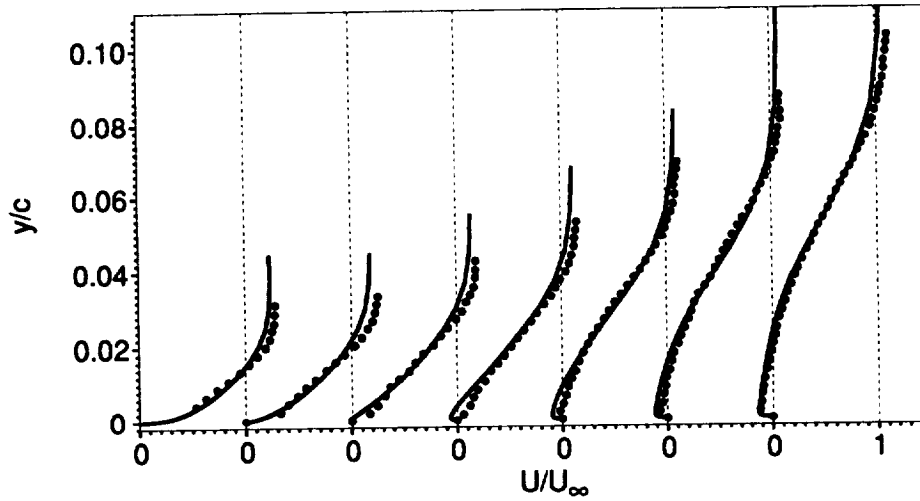


FIGURE 2. Mean velocity profiles at locations along the suction surface of an airfoil at angle of attack, showing trailing edge separation. The profiles are at  $x/c = 0.62, 0.675, 0.731, 0.786, 0.842, 0.897$  and  $0.953$ . The circles are experimental data.

The selection of model constants is described in Durbin *et al.* (1994). To summarize, the present values are  $c_2 = 0.85$ ,  $c_4 = 0.2$ ,  $c_l = 3.3$ ,  $c_p = 1.2$ ,  $c_m = 2$  and  $c_3 = (1 - c_2)/\kappa^2 + 1 - c_4/(1 + \kappa^4 c_m)$  where  $\kappa$  is the von Karman constant.

Figures 1 and 2 illustrate the model solutions. They are from a computation of flow around a NACA4412 airfoil at  $14^\circ$  angle of attack. Contours of constant  $U$ -component of mean velocity are plotted in figure 1. These illustrate that the flow separates just upstream of the trailing edge. The whole computational domain is not shown: the inflow is 14 chords upstream and is angled upward by  $14^\circ$ .

Figure 2 contains mean velocity profiles on the suction surface near the trailing edge. The last two profiles show that the model predicts the correct degree of separation. The Baldwin-Lomax, equilibrium eddy-viscosity model fails to predict separation in this flow; the rapid evolution of the flow as it undergoes separation violates the assumption of near equilibrium. The operation of the non-equilibrium model would seem to be as follows: the eddy viscosity transports mean momentum from the free-stream to the surface, counter balancing deceleration by the adverse pressure gradient. As the boundary layer thickens, eddy viscosity will be produced in the outer region of the boundary layer. However, this process is not instantaneous. If the pressure gradient decelerates the near-wall flow before the eddy viscosity can increase, the flow will separate. The transport equation describes the temporal evolution and spatial redistribution of the eddy viscosity as the flow passes through separation. Equilibrium, or algebraic, models assume that the eddy viscosity adjusts instantaneously to the level of shear and hence they overpredict the turbulent transport in this trailing edge flow.

### 2.2 Stochastic analysis of realizability

The stochastic method will be presented by describing how it is used to derive a sufficient condition for realizability of the most general, linear, second-order closure model for Reynolds stresses. However, this method is far more widely useful and can be applied to all existing Reynolds stress transport models, including those that are non-linear in the Reynolds stress tensor. The method is presented at greater length in Durbin and Speziale (1993). It involves showing the Reynolds-stress model to be the exact second-moment equation of a Langevin stochastic differential equation. The exact moment equation of a well defined stochastic process is realizable, by definition—for instance, quantities like  $\overline{u^2}$  have non-negative values that could be obtained by squaring and averaging a random variable.

In homogeneous turbulence, the General Linear Model consists of the following ordinary differential equation for the evolution of the Reynolds stress tensor

$$\begin{aligned} \frac{d\overline{u_i u_j}}{dt} = & -\frac{c_1}{T}(\overline{u_i u_j} - \frac{2}{3}k\delta_{ij}) - c_2(P_{ij} - \frac{2}{3}P\delta_{ij}) \\ & - c_3(D_{ij} - \frac{2}{3}P\delta_{ij}) - c_s k S_{ij} + P_{ij} - \frac{2}{3}\varepsilon\delta_{ij}. \end{aligned} \quad (7)$$

In this equation,  $P_{ij} = -\overline{u_i u_k} \partial_k U_j - \overline{u_j u_k} \partial_k U_i$  is the production tensor,  $D_{ij} = -\overline{u_i u_k} \partial_j U_k - \overline{u_j u_k} \partial_i U_k$  is a tensor introduced by Launder *et al.* (1975),  $P = 1/2 P_{ii}$  is the rate of turbulent energy production, and  $\varepsilon$  is its rate of dissipation. All the  $c_i$ 's are empirical, numerical constants and  $T$  is a time-scale.

We will show (7) to be the second moment of the stochastic differential equation

$$\begin{aligned} du_i = & -\frac{c_1}{2T}u_i dt + (c_2 - 1)u_k \partial_k U_i dt + c_3 u_k \partial_i U_k dt \\ & + \sqrt{c_0 \varepsilon} dW_i(t) + \sqrt{c_s \varepsilon} M_{ik} dW'_k(t) \end{aligned} \quad (8)$$

with

$$c_0 = \frac{2}{3} \left[ c_1 \frac{k}{\varepsilon T} - 1 + (c_2 + c_3) \frac{P}{\varepsilon} \right] - \frac{c_s}{3} M^2. \quad (9)$$

In (8),  $W$  and  $W'$  are independent Weiner processes ( $dW'_i dW_j = 0$ ).  $M$  is a symmetric matrix that is required to satisfy

$$M_{ij}^2 - \frac{1}{3}M^2\delta_{ij} = -\frac{k}{\varepsilon}S_{ij} \quad (10)$$

where  $M_{ij}^2 = M_{ik}M_{kj}$ ,  $M^2 = M_{kk}^2$ , and  $S_{ij}$  is the rate of strain tensor, defined as  $[\partial_i U_j + \partial_j U_i]/2$ . The matrix  $M$  can be constructed as follows: in incompressible flow,  $S$  is a sym metric matrix with eigenvalues that sum to zero; it can be diagonalized by the unitary matrix  $U$  of eigenvectors:

$$S = U \cdot \text{diag}[\lambda_1, \lambda_2, \lambda_3] \cdot U^t \quad (11)$$

where  $\lambda_1 \geq \lambda_2 \geq \lambda_3$  are the eigenvalues in decreasing order. They satisfy

$$\lambda_1 + \lambda_2 + \lambda_3 = 0. \quad (12)$$

In terms of these eigenvalues

$$\mathbf{M} = \mathbf{U} \cdot \text{diag} \left[ 0, \sqrt{\lambda_1 - \lambda_2}, \sqrt{\lambda_1 - \lambda_3} \right] \cdot {}^t\mathbf{U}. \quad (13)$$

By virtue of (12) and (13),  $M^2 = 3\lambda_1$ .

The second moment equation for (8) is derived by applying the rules

$$\begin{aligned} \overline{d\mathcal{W}_i} &= 0 \\ \overline{d\mathcal{W}_i d\mathcal{W}_j} &= dt \delta_{ij} \\ \overline{u_j d\mathcal{W}_i} &= 0. \end{aligned} \quad (14)$$

Using these to compute  $d\overline{u_i u_j}/dt$  for (8) shows that (7) is formally the exact second moment equation of the stochastic process (8) (Durbin and Speziale 1993). The only issue is whether the Langevin equation (8) is well-defined.

If the coefficients are all bounded, then (8) will be well-defined if the square roots are real valued. This requires  $c_s$  and  $c_0$  to be non-negative.  $c_s$  is an empirical constant of the model (7) that can be chosen to be positive.  $c_0$  is a function given by (9). The condition that  $c_0 \geq 0$  translates to

$$c_1 \geq 1 - (c_2 + c_3) \frac{P}{\varepsilon} + \frac{3}{2} c_s \lambda_1 \quad (15)$$

where  $M^2 = 3\lambda_1$  has been used and the time-scale has been set to  $T = k/\varepsilon$ . The right side of this inequality depends on the flow. As long as (15) is met, solutions to the general linear model are certain to be realizable; however, (15) is not guaranteed to be met, so the general linear model need not always have realizable solutions. Our experience with models that are special cases of (7) is that (15) is usually satisfied.

In extreme cases, far from equilibrium, unrealizable solutions to the general linear model can be generated. However, the present analysis shows that one easily can modify the model to guarantee realizable solutions: just alter  $c_1$  so that (15) is always satisfied. For instance, if  $c_1 = 1.8$  is usually a satisfactory value, then replacing this constant by the function

$$c_1 = \max \left[ 1.8, 1 - (c_2 + c_3) \frac{P}{\varepsilon} + \frac{3}{2} c_s \lambda_1 \right] \quad (16)$$

will enforce the inequality (15). This ensures realizability in extreme cases without altering the model in usual cases.



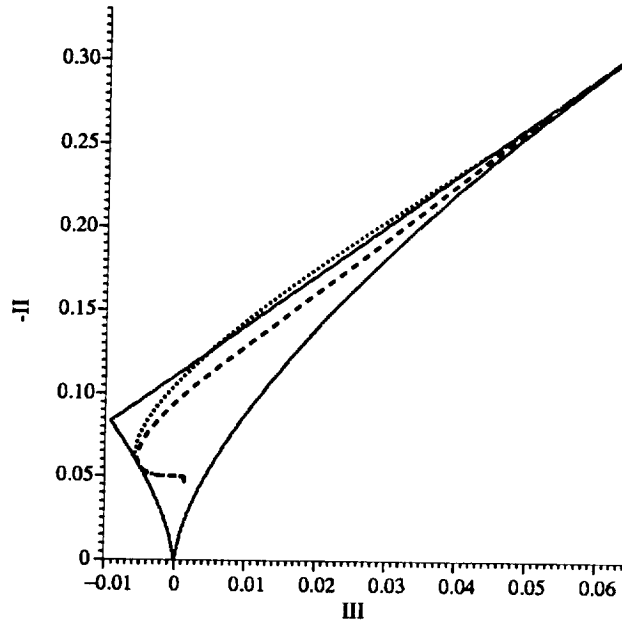


FIGURE 3. Solution trajectories of the LRR model projected onto the second-invariant-third-invariant plane.  $\cdots$ , original LRR model;  $---$ , modified, realizable LRR model.

Launder *et al.* (1975) imposed certain symmetry and normalization constraints that led them to specialize (7) by setting

$$c_2 = \frac{c+8}{11}; \quad c_3 = \frac{8c-2}{11}; \quad c_s = \frac{60c-4}{55} \quad (17)$$

where  $c$  is a constant they set to 0.4—this is the LRR model. With (17), the condition (16) becomes

$$c_1 = \max \left[ 1.8, 1 - 0.873 \frac{P}{\varepsilon} + 0.545 \lambda_1 \right]. \quad (18)$$

Figure 3 shows trajectories of the LRR model for homogeneously sheared turbulence, with the initial condition

$$Sq^2/\varepsilon = 20; \quad b_{11} = -0.27; \quad b_{22} = -0.33; \quad b_{33} = 0.6; \quad b_{12} = b_{13} = b_{23} = 0.$$

These values give  $P/\varepsilon = 0$ ,  $-II = 0.27$  and  $III = 0.053$ , where  $II$  and  $III$  are the invariants of the Reynolds stress tensor. The trajectories in figure 3 are solutions to the LRR model projected into the second-third invariant plane. They start in the upper right corner of the triangle and ultimately are attracted to the equilibrium point in the lower center of the triangle. The initial value of  $1 - 0.873P/\varepsilon + 0.545\lambda_1$  is 3.73 (note that  $\lambda_1 = Sq^2/4\varepsilon$ ) so that (15) is violated if  $c_1 = 1.8$ . Realizable

solutions must remain inside the curvilinear triangle of figure 3. The dotted curve shows that the LRR model exits the realizable region for this initial condition. Thus, although (15) is a sufficient but not necessary condition, it provides an insight into the existence of unrealizable trajectories. The solution trajectory remains inside the realizable region when the modification (18) is applied, as shown by the dashed curve in figure 3.

### 3. Future plans

Development of numerical tools for solving Reynolds-stress models in complex geometries is under way. These are needed so that we can test and further develop models. The computer program being developed is based on the incompressible Navier-Stokes solver (INS-2D) written by Stuart Rogers at NASA Ames. This is a general geometry code and the Reynolds stress solver is being written so that models can be implemented readily. The program under development is an extension of that used to calculate figure 1.

The greatest potential utility of Reynolds stress transport models is in strongly non-equilibrium flows. However, certain difficulties remain. For instance, all existing models predict incorrect rates of relaxation toward equilibrium in highly perturbed flows. Future work will include this area.

The analysis of realizability raises some intriguing questions. The realizability of models for non-homogeneous flows is largely unexplored. Although I have considered this issue for the type of near-wall models that I have developed, I have no mathematical understanding of why they seem to produce realizable solutions. The ellipticity of non-local wall effects suggests using maximum principles.

Stochastic differential equations are popular models for Lagrangian dispersion calculations. The present use of stochastic equations was solely to analyze statistical moment models. This work can be made the basis of self-consistent Reynolds-stress and Lagrangian dispersion models.

### REFERENCES

- BALDWIN, B. S. & BARTH, T. J. 1990 A one-equation turbulence transport model for high Reynolds number wall-bounded flows. *NASA TM 102847*.
- DURBIN, P. A., MANSOUR, N. & YANG, Z. 1994 Eddy Viscosity Transport Model for Turbulent Flow. *Phys. Fluids* (to appear.)
- DURBIN, P. A. & SPEZIALE, C. G. 1993 Realizability of second moment closure via stochastic analysis. *CTR Manuscript 148*.
- LAUNDER, B. E., REECE, G. J. & RODI, W. 1975 Progress in the development of Reynolds stress turbulence closure. *J. Fluid Mech.* **68**, 537.
- POPE, S. B. 1993 On the relationship between stochastic Lagrangian models of turbulence and second-moment closures. Presented at Reynolds Symposium, Monterey, CA; to appear in *Phys. Fluids A* (February 1994).
- SPALART, P. R. & ALLMARAS, S. R. 1992 A one-equation turbulence model for aerodynamic flows. *AIAA-92-0439*.

N94-24145

## Computation of turbulent flows over backward and forward-facing steps using a near-wall Reynolds stress model

By S. H. Ko

### 1. Motivation and objectives

Separation and reattachment of turbulent shear layers is observed in many important engineering applications, yet it is poorly understood. This has motivated many studies on understanding and predicting the processes of separation and reattachment of turbulent shear layers. Both of the situations in which separation is induced by adverse pressure gradient, or by discontinuities of geometry, have attracted attention of turbulence model developers. Formulation of turbulence closure models to describe the essential features of separated turbulent flows accurately is still a formidable task.

The present report describes computations of separated flows associated with sharp-edged bluff bodies. For the past two decades, the backward-facing step flow, the simplest separated flow, has been a popular test case for turbulence models. Detailed studies on the performance of many turbulence models, including two-equation turbulence models and Reynolds stress models, for flows over steps can be found in the papers by Thangam & Speziale (1992) and Lasher & Taulbee (1992). These studies indicate that almost all the existing turbulence models fail to accurately predict many important features of backstep flow such as reattachment length, recovery rate of the redeveloping boundary layers downstream of the reattachment point, streamlines near the reattachment point, and the skin friction coefficient.

An elliptic relaxation model was proposed by Durbin (1991) to represent inhomogeneous effects near the surface of wall-bounded shear flows. This model obviated the need for *ad hoc* eddy viscosity damping functions in the near wall region. After showing that the elliptic relaxation approach was successful in simple flows such as channel flow and flat plate, attached boundary layers, the model was extended to a full near-wall Reynolds stress model (Durbin, 1993) (hereinafter NRSM).

Using the NRSM, Ko & Durbin (1993) computed the massively separated boundary layer experiment of Simpson *et al.* (1981) and found that the new model was able to produce a reasonable separated flow. However, due to ambiguities in the experimented flow condition, it was difficult to draw any conclusion on the model performance. Therefore, it is necessary to have a well-defined test case with clear-cut boundary conditions in order to isolate phenomena which are directly related to the turbulence model. In addition, Direct Numerical Simulation (hereinafter DNS) data (Le & Moin, 1993) has recently become available for a low Reynolds number backward-facing step flow.

The main objectives of the present study are to calculate flows over backward- and forward-facing steps using the NRSM and to make use of the newest DNS data for detailed comparison. This will give insights for possible improvement of the turbulence model.

## 2. Accomplishments

As stated previously, the NRSM is capable of describing near-wall effects without using *ad hoc* damping functions. The model utilizes elliptic differential equations to account for non-local wall blocking effects. The model equations will not be listed here. Detailed discussion of the model and its boundary conditions can be found in Durbin (1991, 1993); our computational methods are described in Ko (1993).

### 2.1. Turbulent flows over backward-facing steps

Turbulent backward-facing step flows were computed for the experimental conditions reported by three different groups: Kim *et al.* (1980, KKJ), Driver & Seegmiller (1985, DS), and Jovic & Driver (1993, JD). DNS data of Le & Moin (1993, LM) is used for detailed comparison of the Reynolds-stress budgets. Table 1 summarizes flow conditions of the test cases. It is desirable to have a small expansion ratio  $E_r$  to minimize freestream pressure gradient effects (Narayanan *et al.*, 1974): the KKJ case is subjected to a significant freestream pressure gradient due to the large expansion ratio; the other two cases are not. Notice also that JD's experiment and LM's DNS have identical flow conditions; in fact, JD's experiment was performed in order to verify the accuracy of the DNS. The predicted reattachment lengths  $X_r$  for all cases are in very good agreement with the measured  $X_r$ , although slightly underestimated.

Group	$E_r$ $= H_1/H_2$	$Re_h$ $= U_o H/\nu$	$\delta^*/h$	Meas. $X_r$	Pred. $X_r$
Kim <i>et al.</i>	1.5	45,000	0.03867	7	6.8
Driver and Seegmiller	1.125	37,500	0.2	6.3	6.1
Jovic and Driver	1.2	5,100	0.19	6	5.4
Le and Moin	1.2	5,100	0.19	6	-

Table 1. Test cases for backward-facing step flows

For all the turbulent backward-facing flow problems, the computational domain extended from the step ( $x = 0$ ) to  $40H$ , where  $H$  is the step height. This long domain ensures that the zero-normal gradient boundary condition,  $\partial/\partial x = 0$ , is appropriate for all flow variables at the outlet of the domain. It is often observed that a shorter computational domain results in unstable and/or unsteady solutions for separated flow problems.

Along the inlet of the domain, profiles of all the flow variables were specified. Since the inlet is at the step, which is the onset of sudden changes, the whole computation procedure and the resulting flowfield are sensitive to the specified inlet conditions. Therefore, it is very important to use reasonable inlet profiles in order to simulate a given backstep flow experiment. In the present study, the

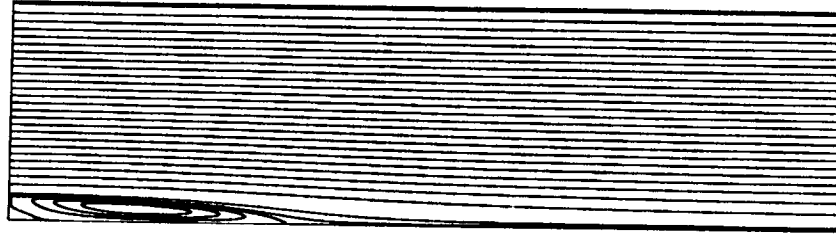


FIGURE 1. Computed streamlines for DS experiment.

inlet profiles were obtained by the following procedure: (1) obtain the displacement thickness  $\delta^*$  and the Reynolds number  $Re$ , based on the reference velocity  $U_o$  and the step height  $H$ , at the step from experimental data; (2) calculate the mean  $U$ -velocity,  $U_m$ , for the channel upstream of the step using the relation  $U_m = U_o(1 - 2\delta_{in}^*/H_1)$ , where  $H_1$  is the channel height at the inlet of the domain; (3) run a channel calculation starting with a plug flow having mean velocity  $U_m$  at the inlet; (4) find the downstream location where the calculated displacement thickness  $\delta^*$  matches  $\delta_{in}^*$ ; and (5) use the channel solution at that location for the inlet boundary conditions for the backward-facing step flow problems. This amounts to computing the inlet section independently of the backstep region.

After grid independence testing, the selected grids consisted of 140 uniformly expanding grid lines in the streamwise direction and 140 (107 for JD's case) highly non-uniform grid lines in the transverse direction. The maximum expansion (or contraction) rates of the grid lines ranged from 8 to 10% depending on the case. This high non-uniformity of the grid is due to the high density of the grid lines in the near-wall regions and in the mixing layer at the top of the step in order to resolve the viscous layer: the first grid point off the wall is at  $y^+ \leq 0.5$ , where the wall unit  $y^+$  is defined as  $y^+ \equiv yu_\tau/\nu$ ,  $u_\tau = \sqrt{\tau_w/\rho}$  and  $\tau_w$  is the wall shear stress.

Figure 1 shows calculated streamlines for the DS case (with zero deflection angle of the top wall). The sharp discontinuity of the backward-facing step geometry produces a strong shear layer near the step. A large recirculation region is formed underneath the shear layer, which, in turn, creates a small corner eddy. As the shear layer spreads, it impinges on the bottom wall near the reattachment point  $X_r$ . Some of the impinging shear layer goes downstream and starts to develop into a boundary layer (the redeveloping boundary layer). Notice that the present streamline plot does not show an unrealistic behavior of the separation streamline near the reattachment point: Lasher and Taulbee<sup>2</sup> observed that the separation streamline was pulled back underneath the recirculating region when a fine grid was used in the near-wall region. We used a fine grid and did not observe that spurious behavior.

Figures 2(a), 2(b) and 2(c) show calculated skin friction coefficients  $C_f$  for JD, DS and KKJ cases, compared with corresponding experimental and DNS data. In all three cases, the model calculations underpredict the negative peak values of  $C_f$

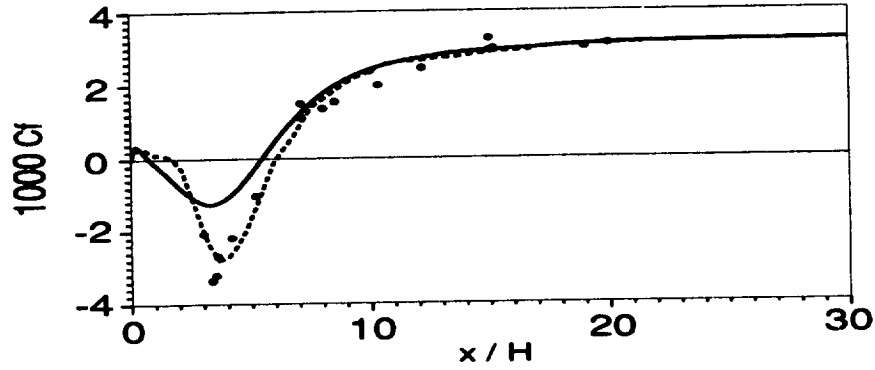


FIGURE 2A. Skin friction coefficients: • : JD experiment; —: NRSR; - - -: DNS.

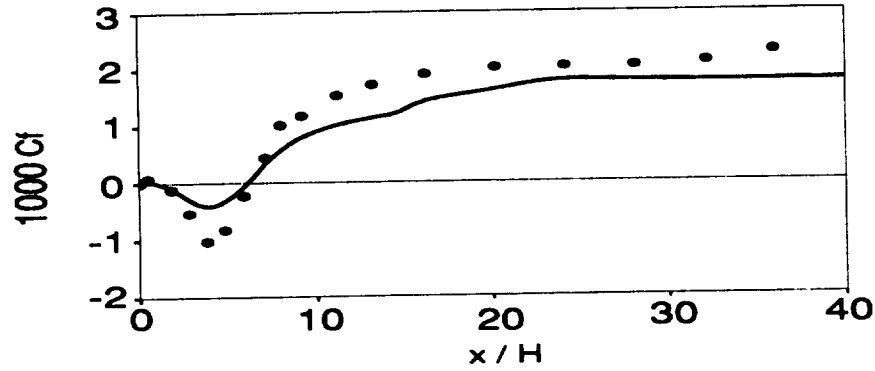


FIGURE 2B. Skin friction coefficients: • : DS experiment; —: NRSR.

in the recirculation zones. Also, for DS and KKJ cases (Figs. 2(b) and 2(c)), the calculated  $C_f$  is significantly below the experimental data in the regions downstream of  $X_r$ , which means slow and weak recovery of the redeveloping boundary layer.

In all three cases, the model underpredicts the negative peak values of  $C_f$  in the recirculation zones. In the DS and KKJ cases (Figs. 2(b) and 2(c)), the calculated  $C_f$  is significantly below the experimental data in the regions downstream of  $X_r$ , which means slow and weak recovery of the redeveloping boundary layer. It is interesting to note that, for JD's low Reynolds number case (Fig. 2(a)), the negative peak of the measured  $C_f$  in the recirculation region is comparable in magnitude to that in the redeveloping boundary layer region downstream of the reattachment point.

Surface pressure coefficients  $C_p$  ( $\equiv 2(P - P_o)/(\rho U_o^2)$ ) are shown in Figs. 3(a), 3(b) and 3(c) for the three cases. With minor deviation, the calculations show fairly

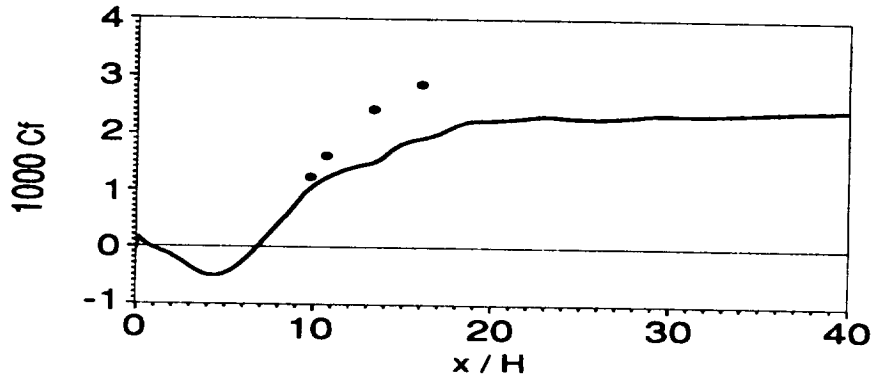


FIGURE 2C. Skin friction coefficients: • : KKJ experiment; — : NRSM.

good agreement with the measurements for the JD and DS cases. The agreement for the KKJ case (Fig. 3(c)) is the worst.

Figures 4(a), 4(b) and 4(c) show mean  $U$ -velocity profiles at various positions upstream and downstream of the reattachment point, compared with experimental data of JD, DS and KKJ, correspondingly. Overall, the agreement of the computation with the experimental data is very good. For the JD case (Fig. 4(a)), the computed  $U$ -velocity profile at  $x/H = 4$  shows insufficient backflow in the recirculation region, but otherwise the model predicts the redeveloping boundary layer almost perfectly. For the higher  $Re$  cases, the computations predict not only weak separated regions but also slow recovery of the redeveloping boundary layers downstream of  $X_r$ . This finding suggests that low  $Re$  DNS data might not be suitable for developing turbulence models that are mainly used for high  $Re$  flows.

Figures 5(a), 5(b) and 5(c) show computed profiles of the Reynolds stress components  $\overline{u^2}$ ,  $\overline{v^2}$ ,  $-\overline{uv}$ , at various positions upstream and downstream of the reattachment point, compared with JD's experimental data and LM's DNS data. It is quite encouraging to see that all three Reynolds stress profiles at the step, obtained from the channel flow solution with  $Re$  and  $\delta^*$  matched to the experiment, show excellent agreement with the experimental data. Thus the inlet conditions computed with the model are in accord with experiment. In Fig. 5(a), the  $\overline{u^2}$  profiles at  $x/H = 4$  and 6 represent the dominance of the shear layer. At  $x/H = 10$ , JD's experimental data already show double peaks of the  $\overline{u^2}$  profile, one peak being very near the wall. In the DNS and the model computations, the wall peak emerges further downstream, as shown in the profiles at  $x/H = 19$ . In addition, the  $\overline{u^2}$  profiles at  $x/H = 19$  indicate that the redeveloping boundary layer is not fully recovered from the free shear layer. The agreement between the calculated and the measured  $\overline{v^2}$  profiles in Fig. 5(b) is as good as that between the DNS data and the measurements. In Fig. 5(c), the model calculations overpredict the peak values of  $-\overline{uv}$  in the region near the reattachment point, while the DNS underpredicts them.

The calculated Reynolds shear stress,  $\overline{uv}$ , is compared with DS's experimental

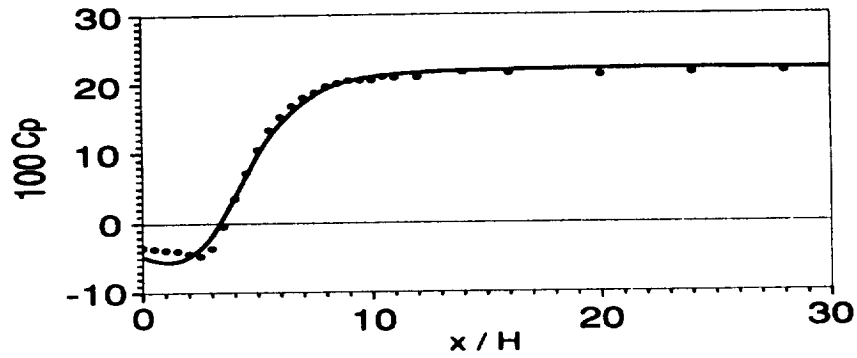


FIGURE 3A. Surface pressure coefficients for JD case: —, NRSM; •, experimental data.

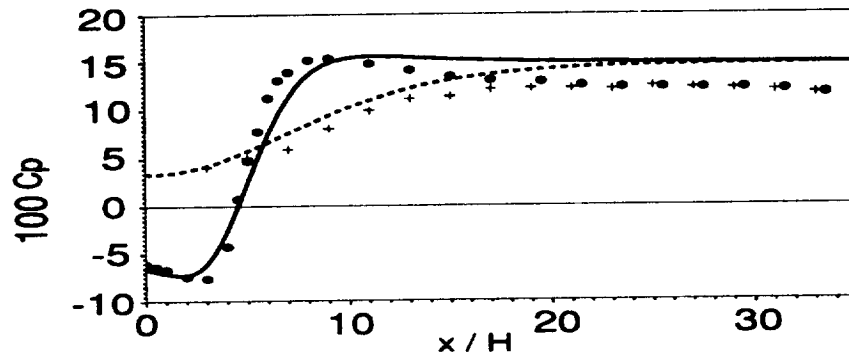


FIGURE 3B. Surface pressure coefficients for DS case: —, •, step-wall; ---, +, opposite-wall. Symbols: experiment; lines: NRSM.

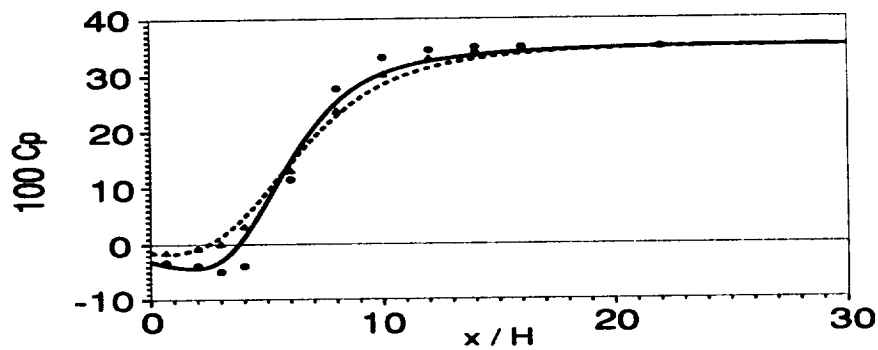


FIGURE 3C. Surface pressure coefficients for KKJ case: —, •, step-wall; ---, +, opposite-wall. Symbols: experiment; lines: NRSM.



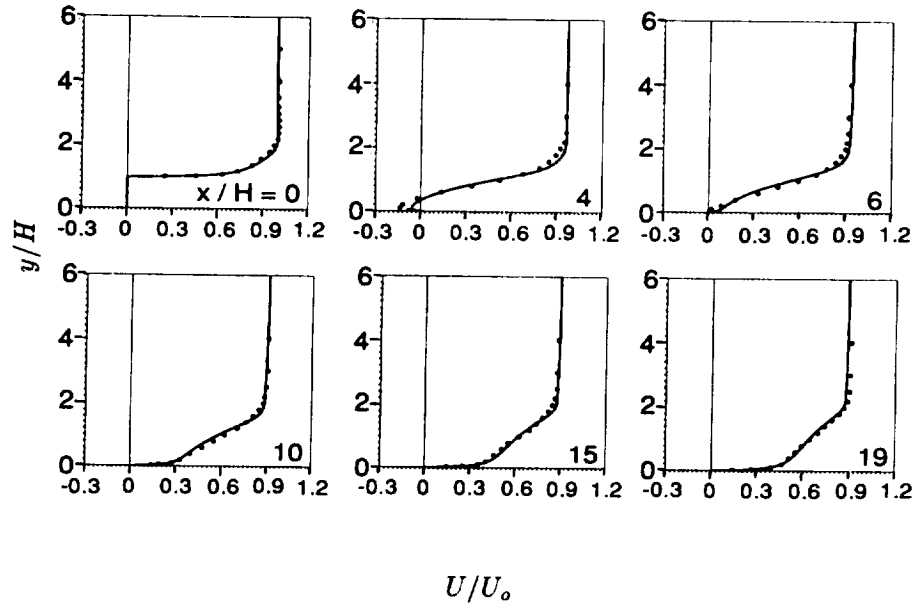


FIGURE 4A. Mean  $U$ -velocity profiles for JD case. • : experiment; — : NRSM.

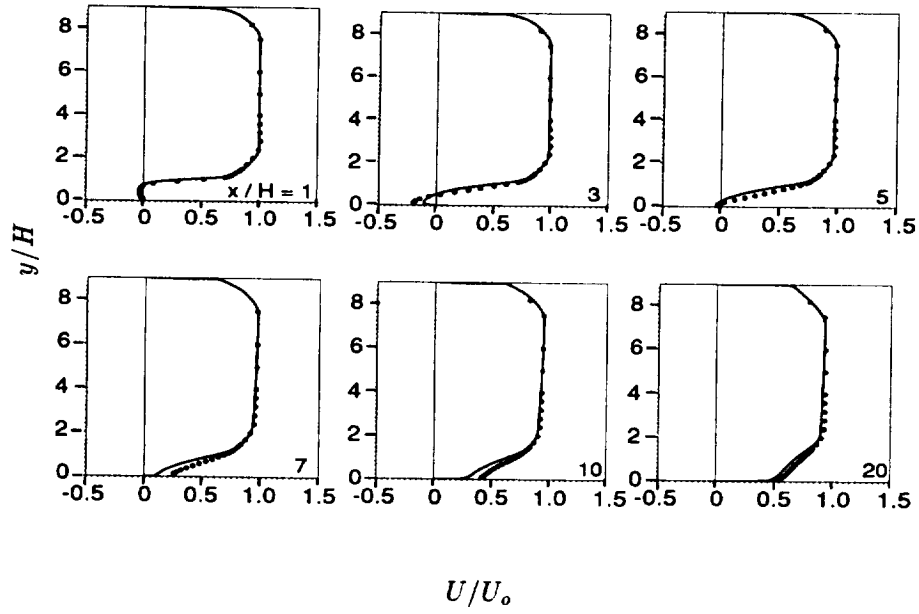


FIGURE 4B. Mean  $U$ -velocity profiles for DS case. • : experiment; — : NRSM.

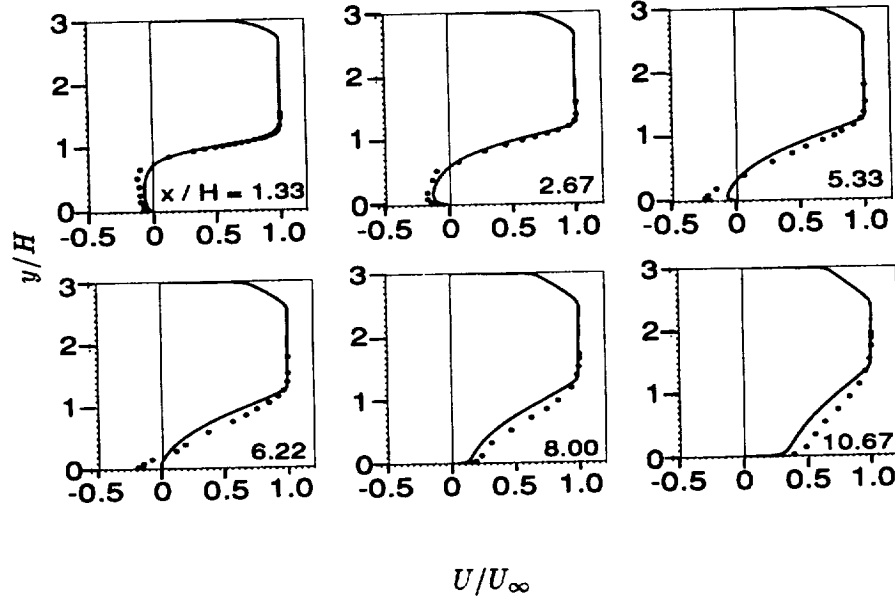


FIGURE 4C. Mean  $U$ -velocity profiles for KKJ case.  $\bullet$ : experiment; —: NRSM.

data in Fig. 6. The calculated  $\bar{u}\bar{v}$  profiles at  $x/H = 7$  and 10 show the peaks overpredicted by nearly 50%. In the recirculation region, the calculations show the peaks located higher than the experimental data.

Figures 7(a), 7(b), and 7(c) show the calculated budgets of the transport equations of  $U$ -velocity,  $k$ , and  $\bar{u}\bar{v}$  at four different positions upstream and downstream of the reattachment point, compared with LM's DNS data. Lines represent the model calculation and the symbols are the DNS data. Note that all the terms in the equations were normalized by the reference velocity  $U_o$  and the step height  $H$ , and then multiplied by 100.

In Figure 7(a), the convection term  $-U_k \partial U / \partial x_k$  is balanced by the sum of the Reynolds stress gradient  $\partial(-\bar{u}\bar{u}_k) / \partial x_k$  and the pressure gradient  $-\partial P / \partial x$ . Since the Reynolds stress gradient is the only term through which the turbulence acts on the mean momentum, it is quite important to understand the meaning of the profiles of  $\partial(-\bar{u}\bar{u}_k) / \partial x_k$ . The fact that at  $x/H = 2$  the  $\partial(-\bar{u}\bar{u}_k) / \partial x_k$  profiles change from being negative to being positive around  $y/H = 1$  shows that momentum is being transferred by the turbulence from the shear layer to the flow in the wall region. As figure 7(a) reveals, the major deviation in the  $\partial(-\bar{u}\bar{u}_k) / \partial x_k$  profiles is found in the negative peak levels. The viscous diffusion terms  $\nu \nabla^2 k$  is negligible everywhere except in the region very near the wall. Notice that at  $x/H = 2$  the calculation shows negative  $-\partial P / \partial x$  while the DNS data shows positive  $-\partial P / \partial x$ . This deviation in  $-\partial P / \partial x$  seems to be responsible for the deviation in the convection terms. As the flow goes downstream, the agreement between the model computation and the

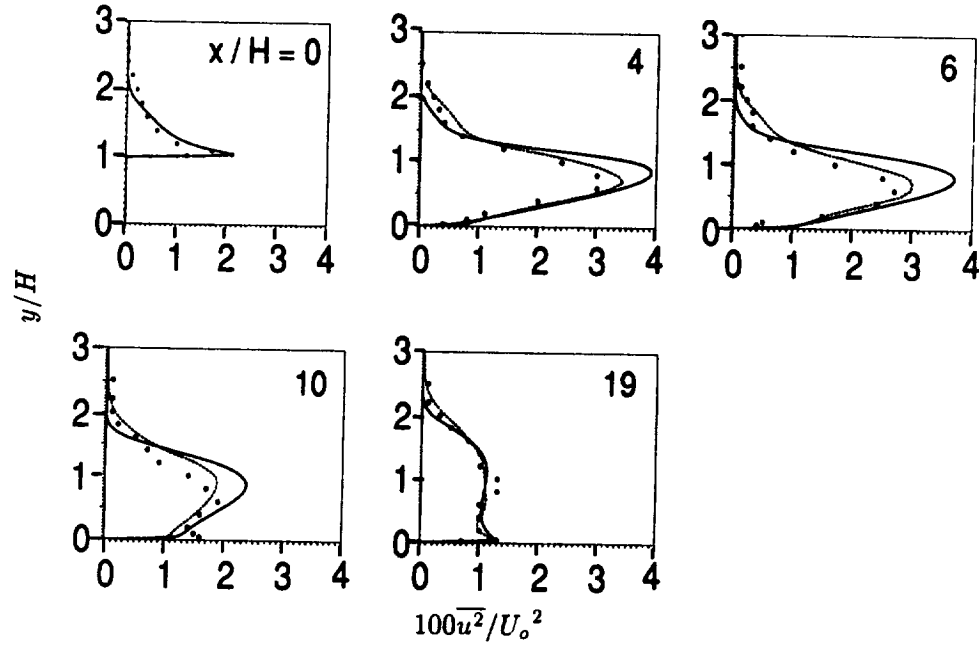


FIGURE 5A. Reynolds stress  $\overline{u^2}$  profiles for JD case: —, NRSM; ---, DNS; •, experimental data.

DNS data gets better. In fact, the agreement is very good at  $x/H = 10$  where the  $-\partial P/\partial x$  term is negligible.

As shown in Fig. 7(b), the production rate  $\mathcal{P}$  in the transport equation of the turbulence kinetic energy is balanced mainly by the sum of the dissipation rate  $\epsilon$ , the convection  $-U_m \partial k / \partial x_m$  and the turbulent diffusion  $\partial / \partial x_m \{ \nu_{mI} / \sigma_k (\partial k / \partial x_I) \}$ . The viscous diffusion  $\partial / \partial x_m \{ \nu (\partial k / \partial x_I) \}$  is negligible everywhere. Notice from the profiles of the turbulent diffusion that the turbulence kinetic energy is extracted from the middle of the shear layer and then transferred to the outer regions of the shear layer. Overall, the model calculation shows very good agreement with the DNS data.

In the budget of the  $\overline{uv}$  transport equation, shown in Fig. 7(c), the production rate  $\mathcal{P}_{12}$  is balanced by the sum of the redistribution  $F_{12}$  and the turbulent diffusion, according to the DNS data. However, the model calculation shows that the contribution from the turbulent diffusion is somewhat smaller than that from the anisotropic dissipation. In fact, the underprediction of turbulent diffusion seems to be the major deficiency of the present computation. The NRSM employs the simple gradient-diffusion hypothesis of Daly & Harlow (Durbin, 1993) for the triple velocity correlations. A more sophisticated formula for the triple velocity correlations may improve the model predictions.

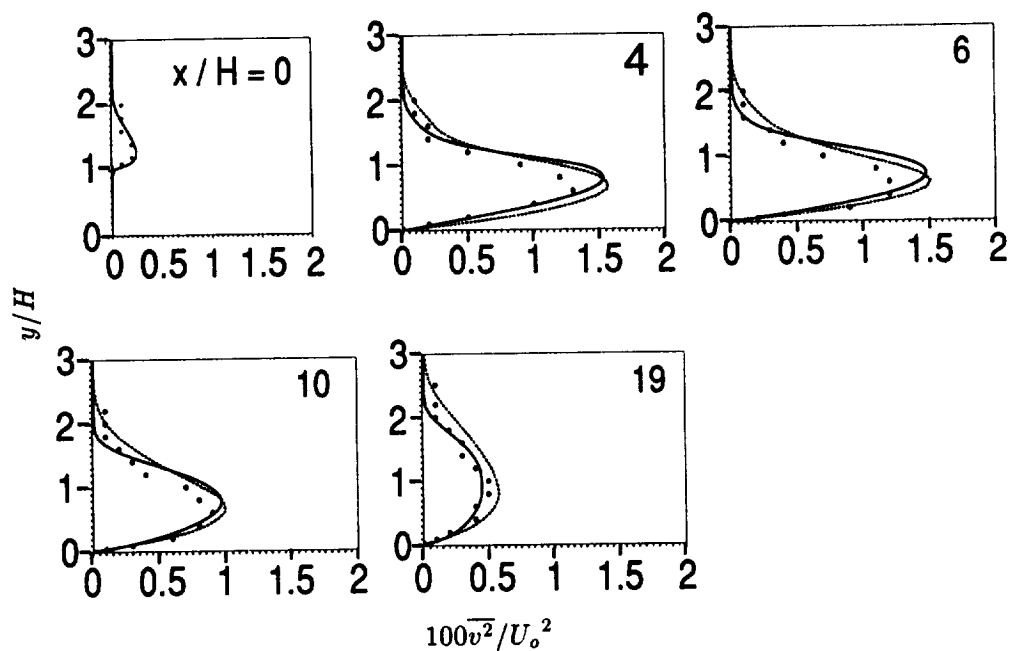


FIGURE 5B. Reynolds stress  $\overline{v^2}$  profiles for JD case: —, NRSM; ---, DNS; •, experimental data.

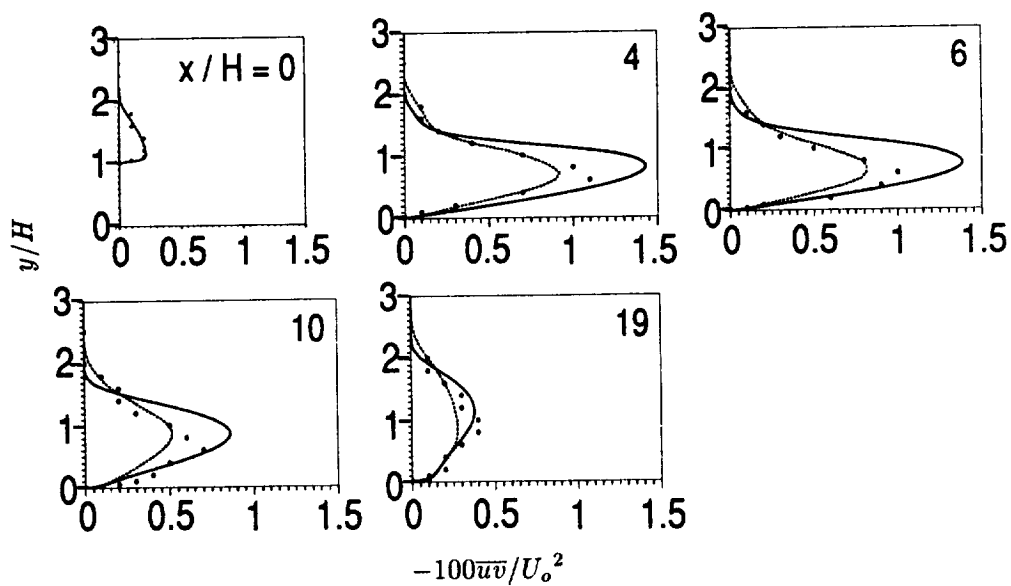


FIGURE 5C. Reynolds stress  $-\overline{uv}$  profiles for JD case: —, NRSM; ---, DNS; •, experimental data.

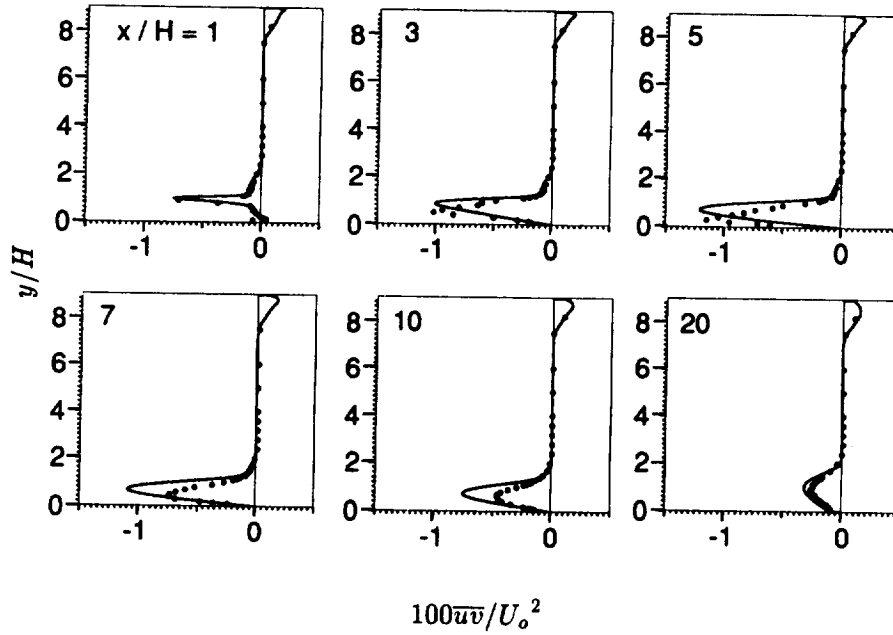


FIGURE 6. Reynolds stress  $\overline{uv}$  profiles for DS case:  $\bullet$ : experiment; —: NRSM.

## 2.2. Turbulent flow over forward-facing step

Turbulent flows over block-like structures are observed in a number of important engineering applications such as vehicles, buildings, and electronic chips. Understanding the flowfields over the forward-facing step will enhance the design of such applications. In addition, the forward-facing step flow provides an example of pressure-driven separation in a well characterized geometry.

Experimental data reported by Moss & Baker (1980) will be used for comparison. The contraction ratio  $H_1/H_2$  is 10/11 and the Reynolds number, based on the step height  $H$  and the reference velocity  $U_o$ , is 46,000. The inlet of the computational domain is  $10H$  upstream of the step ( $x/H = 0$ ) and the exit is located  $40H$  downstream of the step.

A computed streamline plot near the step is shown in Figure 8. As the boundary layer approaches to the step, it undergoes an adverse pressure gradient due to the presence of the step. The boundary layer separates at some distance upstream of the step, forming a corner separation bubble. Due to the sharp edge of the step, a secondary separation bubble occurs on the top surface of the lower wall downstream of the step. The length and height of the corner separation bubble predicted by the model computation are  $1.0 H$  and  $0.45 H$  whereas those given by the experimental data are  $1.1 H$  and  $0.6 H$ , correspondingly. Also, the predicted length of the secondary bubble is  $5.5 H$  while the measured one is  $4.8 H$ .

Figure 9 shows the calculated and measured profiles of the surface pressure coefficient  $C_p$  ( $\equiv 2(P - P_o)/\rho U_o^2$ ) for the stepped wall. For the reference pressure  $P_o$ , the

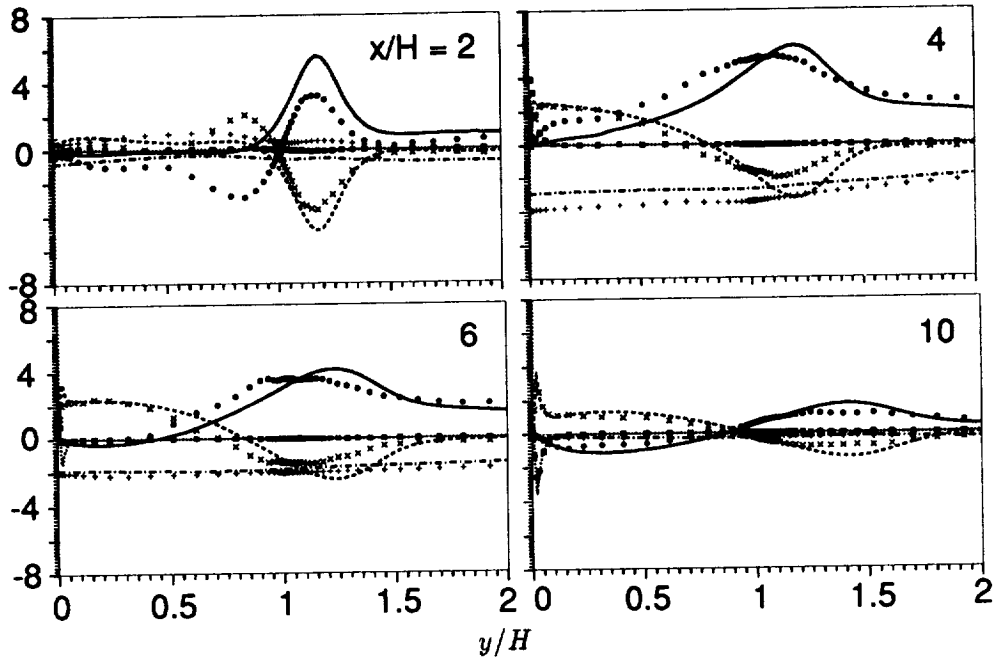


FIGURE 7A. Budgets of the mean  $U$ -momentum equation for JD case: —, •,  $-U_k \partial U / \partial x_k$ ; ---, +,  $-\partial P / \partial x$ ; ···, ×,  $\partial(-\bar{u}u_k) / \partial x_k$ ; - · -, ■,  $\nu \partial / \partial x_k (\partial U / \partial x_k)$ . Symbols: DNS; lines: NRSM

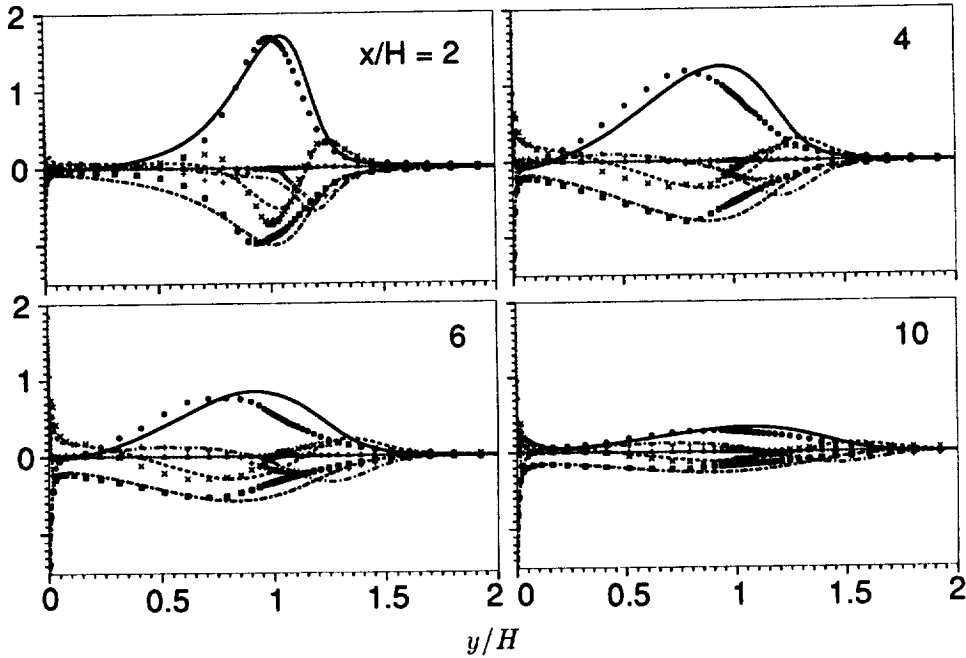


FIGURE 7B. Budgets of the  $k$ -equation for JD case: - · -, +,  $-U_m \partial k / \partial x_m$ ; —, •,  $P$ ; ---, ■,  $\epsilon$ ; ···, △,  $\nu \nabla^2 k$ ; ···, ×,  $\partial / \partial x_m \{ \nu_{ml} / \sigma_k (\partial k / \partial x_l) \}$ . Symbols: DNS; lines: NRSM

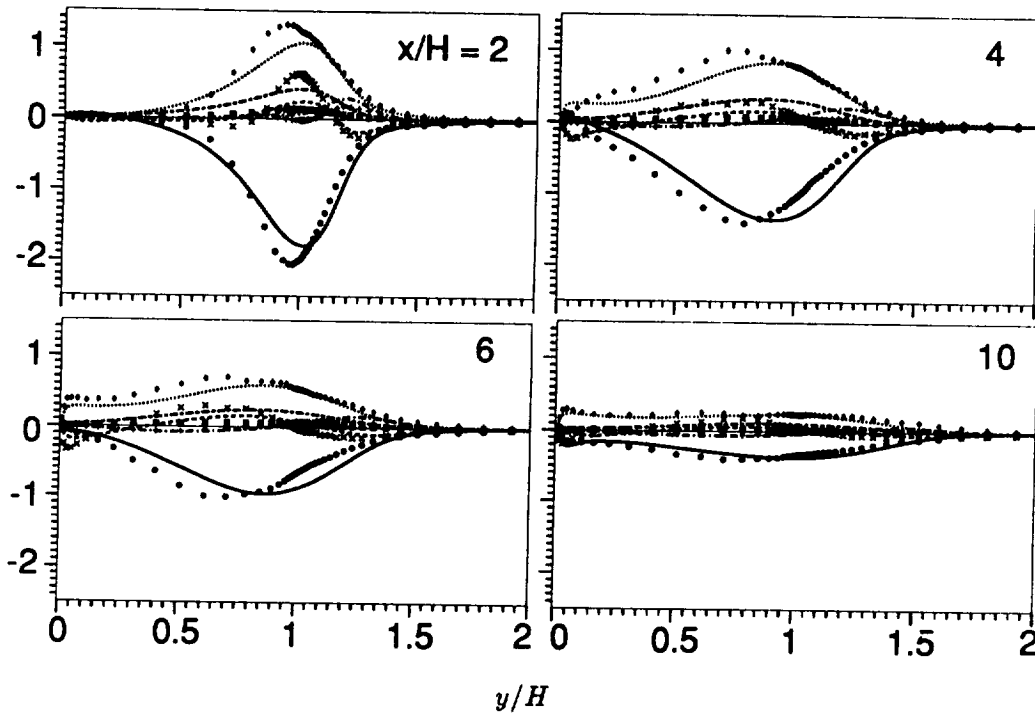


FIGURE 7C. Budgets of the  $\bar{u}\bar{v}$ -equation for JD case: — - —, +,  $-U_m \partial \bar{u}\bar{v} / \partial x_m$ ; —, •,  $P_{12}$ ; - - -,  $\diamond$ ,  $F_{12}$ ; - - -,  $\times$ ,  $\partial / \partial x_m \{ \nu_{m1} / \sigma_k (\partial \bar{u}\bar{v} / \partial x_l) \}$ ; - - -,  $\blacksquare$ ,  $(\bar{u}\bar{v} / k) \epsilon$ . Symbols: DNS; lines: NRSM

freestream pressure at  $x/H = -8$  was used. The calculation agrees very well with the measurement in the region upstream of the step. As the approaching boundary layer decelerates in the corner separation region,  $C_p$  reaches its peak value of 0.52. Then  $C_p$  drops suddenly to  $-1.0$  at the step, slowly recovering downstream of the step. Notice that the experimental data show a slight decrease in  $C_p$  in the region extending from the step to a couple of step heights downstream of the step where the computation shows a monotonic increase in  $C_p$ .

In Figure 10, the calculated profiles of the  $U$ -velocity at various measuring stations upstream and downstream of the step ( $x = 0$ ) are compared with the experimental data. Notice that the boundary layer thickness of the approaching flow is comparable to the step height. As indicated in the profiles downstream of the step, the model calculation predicts a weak secondary separation bubble and slow recovery of the boundary layer after the bubble. These findings are consistent with those for the backstep flow cases. Other than these deficiencies, the calculation is able to predict the separation of the forward-facing step flows reasonably well.

Finally, the profiles of the Reynolds stress  $\bar{u}^2$  are plotted in Fig. 11 along with the measurements. The calculation agrees excellently with the measurements, quantitatively as well as qualitatively. The calculated and the measured  $y$  locations of the



FIGURE 8. Computed streamlines for a forward-facing step flow.

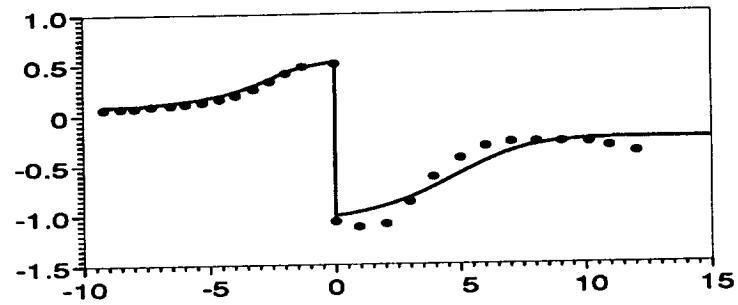


FIGURE 9. Surface pressure coefficients for a forward-facing step flow. • : experiment (Moss & Baker); —: NRSM.

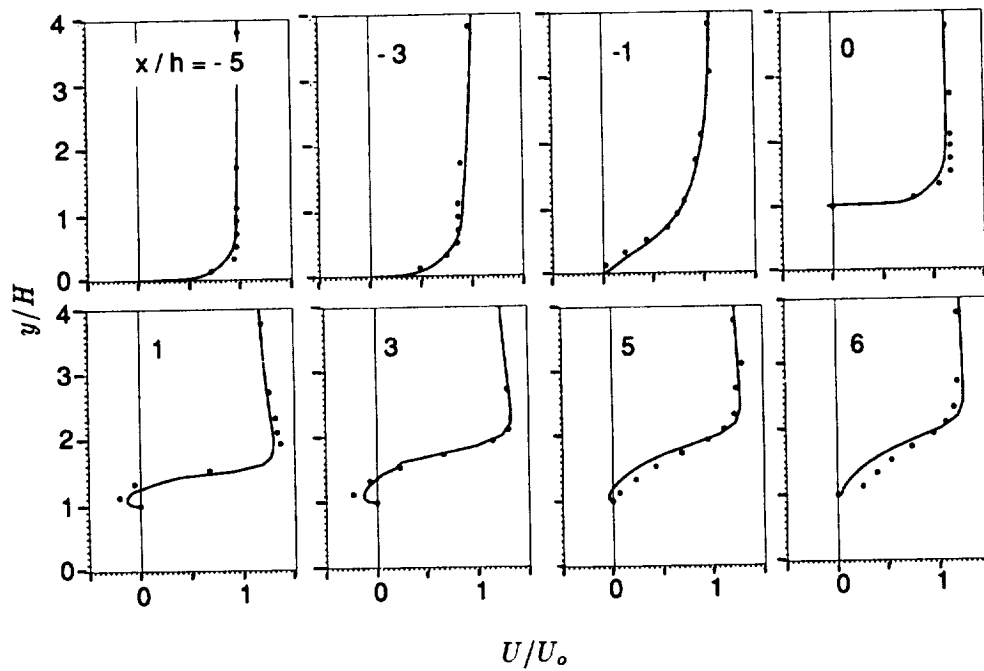


FIGURE 10. Mean  $U$ -velocity profiles for a forward-facing step flow. • : experiment (Moss & Baker); —: NRSM.



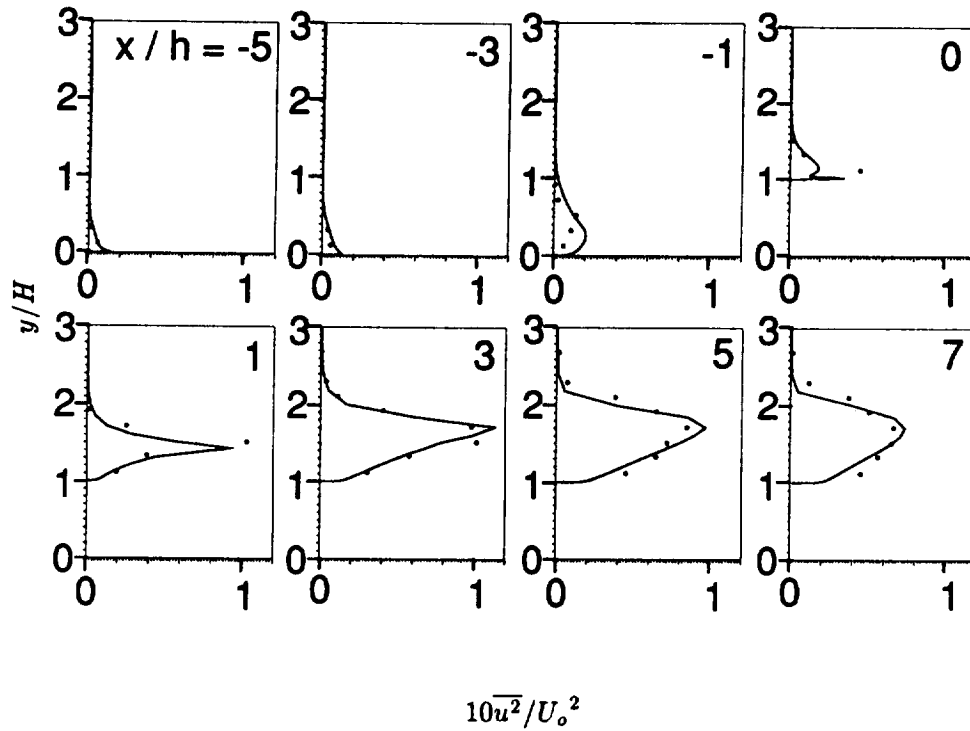


FIGURE 11. Reynolds stress  $\overline{u^2}$  profiles for a forward-facing step flow. • : experiment (Moss & Baker); —: NRSM.

$\overline{u^2}$  peaks in the region downstream of the step are in good agreement, which implies that the calculation predicts the  $y$  location of the shear layer and the separation bubble correctly.

### 3. Summary

A near-wall Reynolds stress model (NRSM) has been used in numerical computations for two-dimensional, incompressible turbulent flows over backward and forward-facing steps. Numerical results were compared with Direct Numerical Simulation (DNS) data as well as experimental data for various flow quantities. The comparison reveals that the NRSM predicts the reattachment length fairly accurately. The NRSM also predicts the development of the boundary layer downstream of the reattachment point correctly when the Reynolds number is low. However, the model generally predicts a weak separation bubble and a slowly developing boundary layer when the Reynolds number is high. For more detailed comparison, budgets of the transport equations for the  $U$ -velocity, turbulence kinetic energy  $k$ , and the Reynolds shear stress  $-\overline{uv}$  were calculated and compared with DNS data.

## REFERENCES

- BADRI NARAYANAN, M. A., KHADGI, Y. N. & VISWANATH, P. R. 1974 Similarities in pressure distribution in separated flow behind backward-facing steps. *The Aeronautical Quarterly*. **25**, 305-312.
- BRADSHAW, P. & WONG, F. Y. F. 1972 The reattachment and relaxation of a turbulent shear layer. *J. Fluid Mech.* **52**, 113-135.
- DRIVER, D. M. & SEEGLER, H. L. 1985 Features of a reattaching turbulent shear layer in divergent channel flow. *AIAA J.* **23**, 163-171.
- DURBIN, P. A. 1991 Near-wall turbulence closure modeling without "damping functions". *Theoretical and Computational Fluid Dynamics*. **3**, 1-13.
- DURBIN, P. A. 1993 A Reynolds stress model for near-wall turbulence. *J. Fluid Mech.* **249**, 465-498.
- JOVIC, S. & DRIVER, D. M. 1993 Backward-facing step measurements at low Reynolds number.  $Re_h = 5,000$ . NASA TM to be published.
- JOVIC, S. & DRIVER, D. M. 1993 Reynolds number effects on the skin-friction in separated flows behind a backward-facing step submitted for publication.
- KIM, J., KLINE, S. J. & JOHNSTON, J. P. 1980 Investigation of a reattaching turbulent shear layer: flow over a backward-facing step. *J. Fluids Engr.* **102**, 302-308.
- KO, S. 1993 Application of a Reynolds stress model to separating boundary layers. Annual Research Briefs-1992, Center for Turbulence Research, Stanford Univ./NASA Ames, 199-211.
- KO, S. & DURBIN, P. A. 1993 Application of a near-Wall turbulence model to adverse pressure gradient and separating boundary layers. *Near-Wall Turbulent Flows*, edited by So *et al.*, Elsevier, 145-153.
- LASHER, W. C. & TAULBEE, D. B. 1992 On the computation of turbulent back-step flow. *Int. J. Heat and Fluid Flow*. **13**, 30-40.
- LE, H. AND MOIN, P. 1993 Direct numerical simulation of turbulent flow over a backward-facing step. Report TF-58, Thermosciences Division, Department of Mechanical Engr., Stanford University.
- MOSS, W. D. & BAKER, S. 1980 Re-circulating flows associated with two-dimensional steps. *The Aeronautical Quarterly*. **31**, 151-172.
- SIMPSON, R. L., CHEW, Y.-T., & SHIVAPRASAD, B. G. 1981 The structure of a separating turbulent boundary layer. Part 1. Mean flow and Reynolds stresses. *J. Fluid Mech.* **113**, 23-51.
- THANGAM, S. & SPEZIALE, C. G. 1992 Turbulent flow past a backward-facing step: A critical evaluation of two-equation models. *AIAA J.* **30**, 1314-1320.

N94-24146

## Large eddy simulation of a boundary layer with concave streamwise curvature

By T. S. Lund

### 1. Motivation and objectives

One of the most exciting recent developments in the field of large eddy simulation (LES) is the dynamic subgrid-scale model (Germano *et al.* 1991). The dynamic model concept is a general procedure for evaluating model constants by sampling a band of the smallest scales actually resolved in the simulation. To date, the procedure has been used primarily in conjunction with the Smagorinsky (1963) model. The dynamic procedure has the advantage that the value of the model constant need not be specified *a priori*, but rather is calculated as a function of space and time as the simulation progresses. This feature makes the dynamic model especially attractive for flows in complex geometries where it is difficult or impossible to calibrate model constants.

The dynamic model has been highly successful in benchmark tests involving homogeneous and channel flows (*c.f.* Germano *et al.* 1991, Moin *et al.* 1991, Cabot and Moin 1991). Having demonstrated the potential of the dynamic model in these simple flows, the overall direction of the LES effort at CTR has shifted toward an evaluation of the model in more complex situations. The current test cases are basic engineering-type flows for which Reynolds averaged approaches have been unable to model the turbulence to within engineering accuracy. Flows currently under investigation include a backward-facing step, wake behind a circular cylinder, airfoil at high angles of attack, separated flow in a diffuser, and boundary layer over a concave surface. Preliminary results from the backward-facing step (Akselvoll and Moin 1993) and cylinder wake simulations are encouraging. Progress toward the airfoil simulations are discussed by Choi and by Jansen, while preliminary diffuser simulations are discussed by Kaltenbach (all in this volume). The present paper discusses progress on the LES of a boundary layer on a concave surface.

Although the geometry of a concave wall is not very complex, the boundary layer that develops on its surface is difficult to model due to the presence of streamwise Taylor-Görtler vortices. These vortices arise as a result of a centrifugal instability associated with the convex curvature. The vortices are roughly  $1/3$  of a boundary layer thickness in diameter, alternate in sense of rotation, and are strong enough to induce significant changes in the boundary layer statistics. Owing to their streamwise orientation and alternate sign, the Taylor-Görtler vortices induce alternating bands of flow toward and away from the wall. The induced upwash and downwash motions serve as effective agents to transport streamwise momentum normal to the wall, thereby increasing the skin friction. As evidenced by the 1980 AFOSR-Stanford conference on complex turbulent flows, Reynolds averaged models perform poorly for concave curvature since the Taylor-Görtler vortices are not resolved in

these calculations. Historically the *ad hoc* corrections for the effects of curvature have been unsatisfactory. The objective of this work is to investigate the effectiveness of large eddy simulation and the dynamic subgrid-scale model for this flow.

The simulation targets the experimental data of Barlow and Johnston (1988). This experiment is an ideal test case since a rather complete set of velocity statistics are available for several streamwise stations.

## 2. Accomplishments

A preliminary large eddy simulation of a boundary layer along a concave surface has been performed. The geometry and flow conditions were close to those studied in the laboratory by Barlow and Johnston (1988). A limited comparison with the experimental data has been undertaken. These items are discussed in more detail below.

### 2.1 Numerical procedure

The computer code for this work is an adaptation of the code written by Choi and Moin (1993). Boundary conditions have been generalized and the dynamic subgrid-scale model has been added (see Kaltenbach, this volume). The incompressible Navier-Stokes equations are solved in a coordinate space where two directions are curvilinear and the third (spanwise) direction is Cartesian. Spatial derivatives are approximated with second-order finite differences on a staggered mesh. A fully-implicit fractional step algorithm is used for the time advancement.

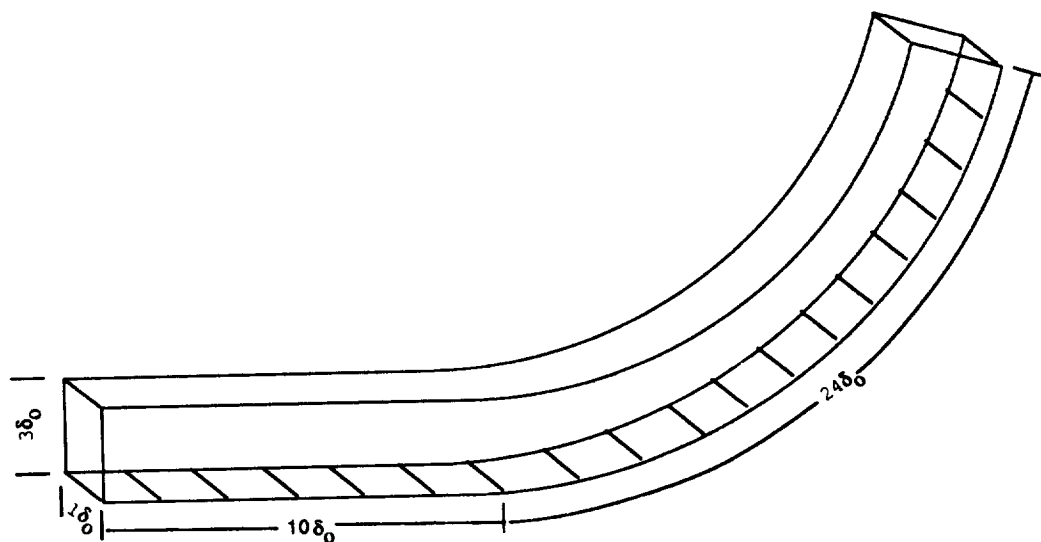


FIGURE 1. Computational domain. All dimensions are referred to the boundary layer thickness measured at the location where the curvature begins ( $\delta_0$ ). The radius of curvature is  $R = 18.1\delta_0$ .

Figure 1 shows the geometry for the present simulation. This geometry is similar to that used by Barlow and Johnston (1988) in their experimental study. The boundary layer is allowed to develop along a flat entry section approximately  $10\delta_0$  in length, where  $\delta_0$  is the boundary layer thickness measured at the location where the curvature begins. At this point the boundary layer encounters a constant radius of curvature bend that turns the flow through  $75^\circ$ . The ratio of the boundary layer thickness to the radius of curvature,  $\delta_0/R$ , is 0.055. The domain extends  $\delta_0$  in the spanwise direction and  $3\delta_0$  in the wall-normal direction. According to the measurements of Barlow and Johnston (1988), the computational domain is just wide enough to enclose one pair of streamwise Taylor-Görtler vortices. Periodic boundary conditions are applied in the spanwise direction while a no-stress condition is applied at the upper boundary. No-slip conditions are applied at the wall. Turbulent boundary layer data from an independent simulation is supplied at the inflow boundary (see Section 2.2 below). A convective boundary condition is applied at the outflow. The computational grid contains  $178 \times 40 \times 32$  points in the streamwise, normal, and spanwise directions respectively. The mesh is stretched in the wall-normal direction and uniform in the other two. The grid spacings, based on wall units at the location where the curve begins, are  $\Delta x^+ = 98$ ,  $\Delta y_{\min}^+ = 1$ , and  $\Delta z^+ = 16$ .

The flow conditions match those in the experiment. The momentum thickness Reynolds number at the start of curvature is 1300. The experiment was conducted in water and is therefore incompressible.

## 2.2 Inflow boundary data

A spatially-evolving simulation such as this one requires the specification of instantaneous turbulent data at the inflow boundary. Although some level of approximation must be made, accurate inflow data is desired to insure minimal transients and realistic turbulence within a short distance downstream of the inlet. Fairly realistic instantaneous inflow data is generated via an auxiliary large eddy simulation of a parallel flow boundary layer. The grid used for the inflow simulation is a truncated version of that used in the main simulation. It extends only one boundary layer thickness in the wall-normal direction and  $5\delta_0$  in the streamwise direction. Periodic boundary conditions are applied in the streamwise and spanwise directions, while a no-stress boundary condition is applied at the upper boundary. The inflow simulation is run in parallel with the main simulation in a time-synchronous fashion. At each time step, the velocity field is extracted from the central  $y-z$  plane in the inflow simulation. This data is used as the inflow boundary conditions. In practice, the inflow simulation can be either run at the same time as the main simulation or run ahead of time and the inflow data stored on disk. The inflow simulation increases the overall cost of the main simulation by less than 4%.

## 2.3 Preliminary results

Although the simulation was patterned after the experiment of Barlow and Johnston, there is one important difference in geometry between the two. The experiment

of Barlow and Johnston was conducted in a duct where the boundary layer thickness,  $\delta_0$  was about  $1/3$  of the duct width. The duct was of variable cross-section with the width tailored to minimize the streamwise pressure gradient on the concave wall. The simulation can be viewed as taking place in a constant-width duct where the boundary layer on the convex wall is not present.

Since the simulation was performed in a constant width duct, the boundary layer will experience a streamwise pressure gradient in the vicinity of the onset of curvature. The reason for this is that a normal pressure gradient is required in the curved section to balance the centrifugal force associated with the streamline curvature. The normal pressure gradient requires the pressure to be higher at the concave wall and lower at the convex wall. The development of the normal pressure gradient in the region where the curvature begins induces an adverse pressure gradient along the concave wall. This effect is shown in Figure 2. The pressure is seen to increase abruptly along the concave wall in the vicinity of the onset of curvature. The gradual drop in pressure over the entire length is due to acceleration of the free-stream by the thickening of the boundary layer. Also shown in Figure 2 is the concave wall pressure estimated from the experimentally measured velocity profiles. By virtue of contouring the convex wall, Barlow and Johnston were able to achieve a nearly constant pressure distribution.

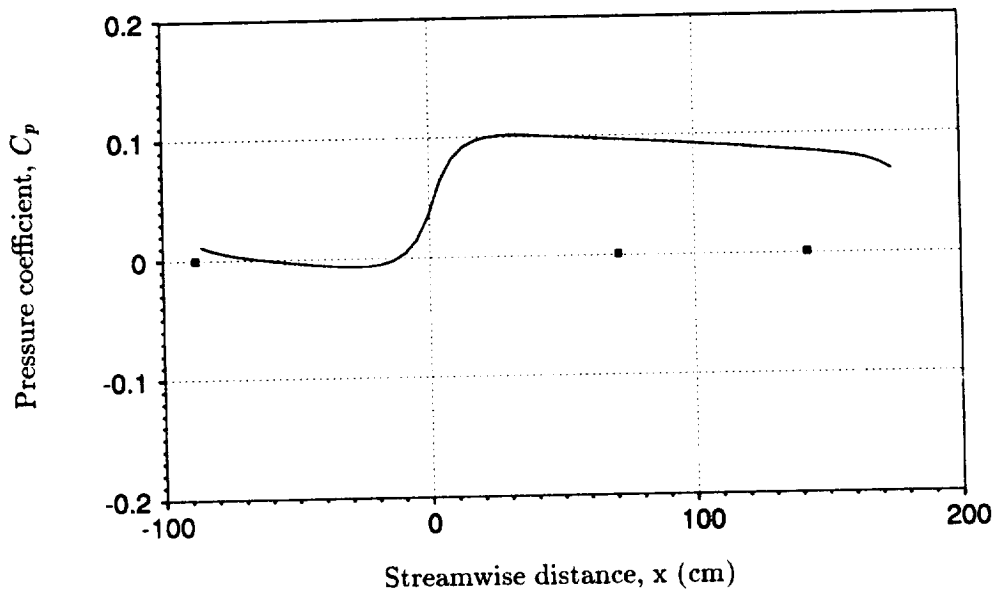


FIGURE 2. Pressure distribution along the concave wall. — : simulation; ■ : experiment. The curve begins at  $x = 0$ .

As discussed below, an inviscid analysis has been performed to determine the location of the streamline in the Barlow and Johnston experiment that lies near the center of the duct. In future simulations this streamline will be used as the upper

boundary where no normal velocity and no stress conditions will be applied. For the present, a rough comparison with the data of Barlow and Johnston can still be made provided that the region affected by the pressure gradient is excluded.

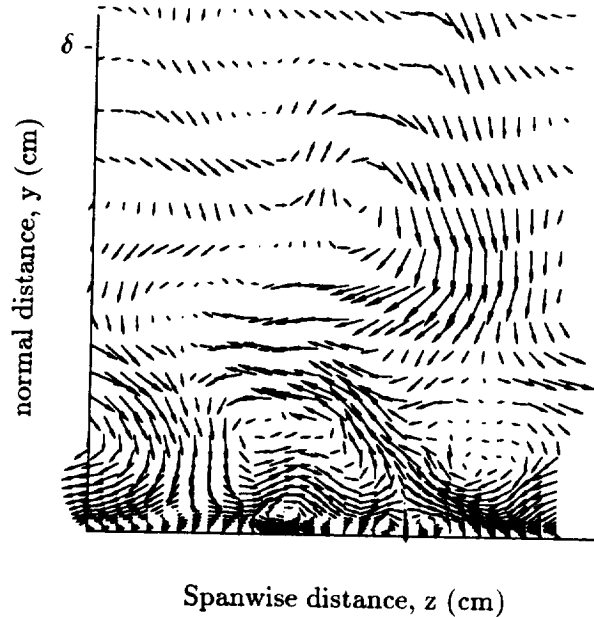


FIGURE 3. Instantaneous velocity vectors in the cross-flow plane at the  $60^\circ$  ( $x = 142$  cm) station. The label  $\delta$  indicates the boundary layer thickness.

Instantaneous velocity vectors in the cross-flow plane at the  $60^\circ$  ( $x = 142$  cm) station are shown in Figure 3. A pair of Taylor-Görtler vortices is evident in the lower  $1/3$  of the boundary layer. As in the experiment of Barlow and Johnston, the vortices develop a few boundary layer thicknesses downstream of the onset of curvature and are coherent from that point to the  $60^\circ$  station. The vortex diameter is about  $1/3$  of the boundary layer thickness at the  $60^\circ$  station. The vortices enhance turbulent mixing near the wall and increase the skin friction as a consequence. This effect is shown in Figure 4 where the skin friction (presented as friction velocity) is plotted as a function of distance along the wall. The curvature begins at  $x = 0$ . The skin friction initially drops sharply as the boundary layer enters the curve, but this effect is due to the adverse pressure gradient in that region. Following a quick recovery, the skin friction undergoes a monotonic growth with streamwise distance. After the flow has been turned through  $30^\circ$  ( $x = 71$  cm), the pressure gradient is minimal and the simulation results are expected to differ from the experiment only through history effects. Indeed the simulation results are in reasonable agreement with the experimental data between  $30^\circ$  and  $60^\circ$ . It is also important to note that the skin friction is well behaved near the inflow boundary and does not exhibit a visible transient arising from the approximate turbulent inflow data.

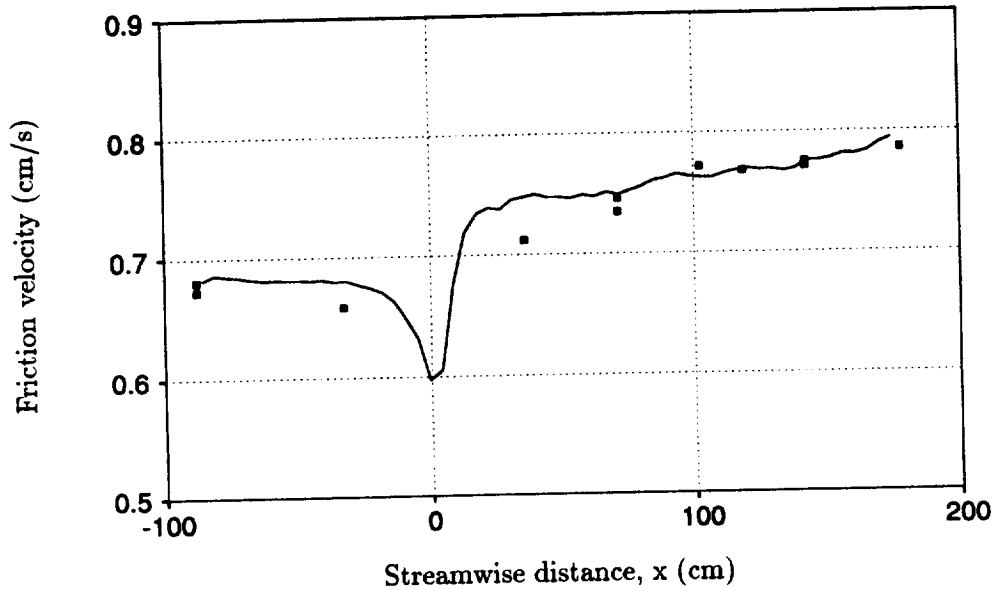


FIGURE 4. Computed skin friction. — : simulation; ■ : experiment. The curvature starts at  $x = 0$ .

#### 2.4 Streamline for zero pressure gradient

The streamwise pressure gradient discussed above must be removed before a detailed comparison can be made with the experimental data. An obvious way to do this would be to simulate the exact geometry used in the experiment. The drawback of this approach is that the boundary layer on the convex wall would have to be resolved and consequently nearly twice as many grid points would be required. A more economical approach is adopted here where the location of the streamline that lies approximately midway between the two walls of the experimental geometry is determined. This streamline forms the upper boundary in the simulation and results in a pressure distribution very close to that found in the experiment.

The location of the streamline is found using a procedure analogous to that used in designing the experimental facility. An inviscid analysis is used to determine the pressure distribution along the concave wall of a constant-width duct. The shape of the streamline that forms the duct convex wall is then iteratively adjusted in an attempt to minimize the pressure gradient on the concave wall. Once the optimal geometry is determined, the displacement thickness of the boundary layer is estimated and the streamline position adjusted to allow for the thickening of the boundary layer.

Figure 5 shows the streamline determined by the inviscid analysis. The corresponding pressure distribution along the convex wall is shown in Figure 6. For reference, the pressure distribution for a constant-width duct is also shown in Figure 6. It can be seen that the pressure gradient is greatly reduced, but not completely



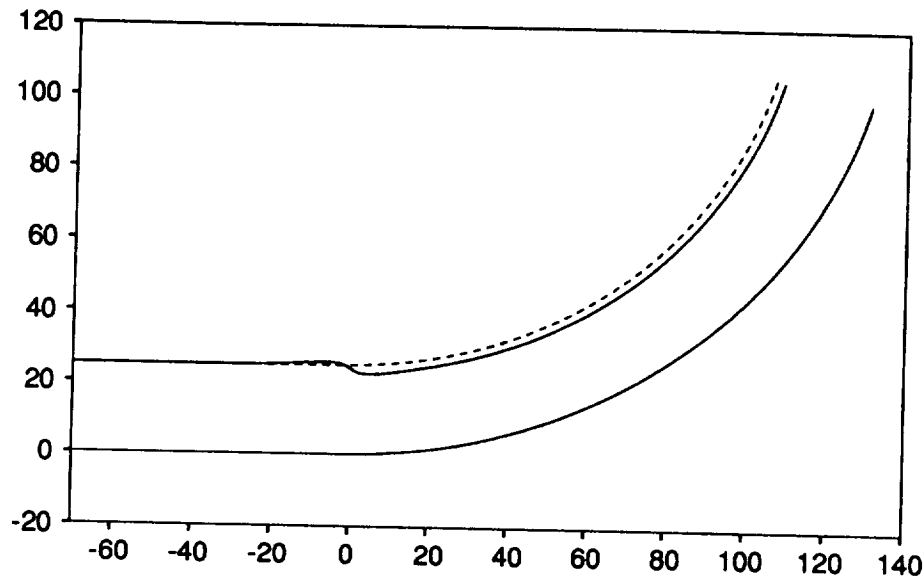


FIGURE 5. Streamline location for minimization of the pressure gradient at the wall. — : streamline; ---- : constant-width reference. Dimensions are in cm.

eliminated. The residual excursions could not be eliminated with a simple algorithm that adjusts the streamline locally in response to the pressure deviation on the opposite side of the duct. Nearly identical pressure excursions are also present in the inviscid analysis used to design the experimental facility. For this reason no attempts were made to further refine the streamline. The boundary layer displacement thickness distribution was estimated from the experimental measurements and the streamline was displaced away from the concave wall accordingly. The final streamline will be used as the upper computational boundary in all future simulations.

### 3. Future plans

Future work will focus on refining the simulations and in making detailed comparisons with experimental data. The upper boundary location will be changed as described above in order to minimize the streamwise pressure gradient. The mesh spacings will be varied in order to determine the minimal resolution for which acceptable results are obtained. The spanwise extent of the domain will be enlarged so that the spacing of the Taylor-Görtler vortices are not imposed directly. Ideally the spanwise extent should be large enough to support several pairs of vortices. The spanwise length will be made as large as practical given the computer resource constraints. Detailed comparisons will be made between the LES, experimental data, and a simulation run with no subgrid-scale model. The latter will be used to determine the influence of the subgrid-scale model in the overall accuracy of the simulation.

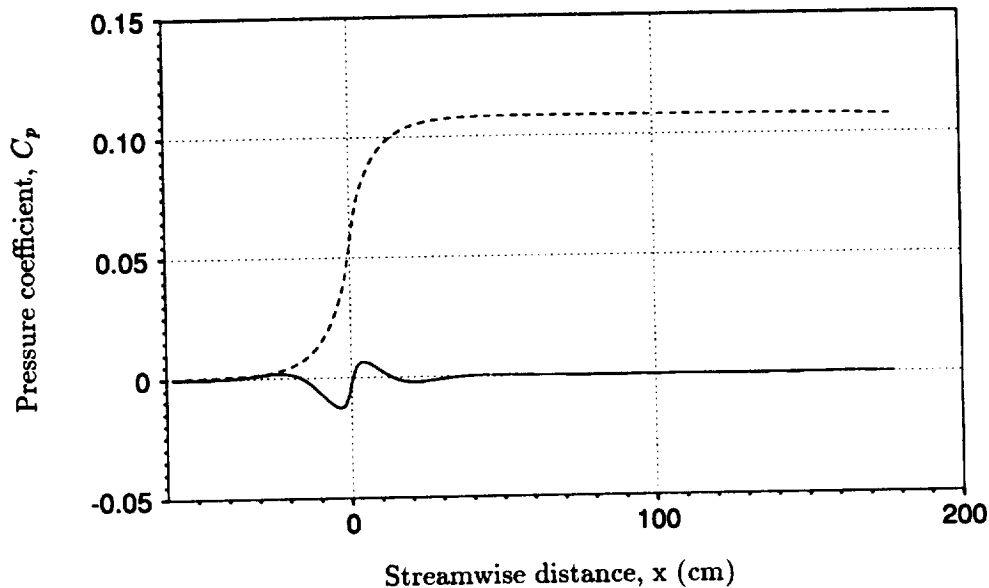


FIGURE 6. Wall pressure distribution for the streamline shown in Figure 5. — : using the streamline boundary; ---- using a constant-width boundary.

#### REFERENCES

- AKSELVOLL, K. & MOIN, P. 1993 Application of the dynamic localization model to large-eddy simulation of turbulent flow over a backward-facing step. In *Engineering applications of large eddy simulations*, ed. by S. A. Ragab and U. Piomelli. Presented at the ASME fluid engineering conference, Washington D. C. June 20-24, 1993.
- BARLOW, R. S. & JOHNSTON, J. P. 1988 Structure of a turbulent boundary layer on a concave surface. *J. Fluid Mech.* **191**, 137-176.
- CABOT, W. & MOIN, P. 1993 Large eddy simulation of scalar transport with the dynamic subgrid-scale model. In *Large Eddy Simulation of Complex Engineering and Geophysical Flows*, ed. by B. Galperin. Cambridge University Press.
- CHOI, H., & MOIN, P. 1993 The effect of computational timestep on numerical simulation of turbulent flow. to appear in *J. Comp. Phys.* Also published as *Rep. TF-55, Dept. of Mech. Eng.*, Stanford University, 1992.
- GERMANO, M., PIOMELLI, U., MOIN, P., & CABOT, W. H. 1991 A dynamic subgrid-scale eddy viscosity model. *Phys. Fluids A*, **3**, 1760-1765.
- MOIN, P., SQUIRES, K., CABOT, W., & LEE, S. 1991 A dynamic subgrid-scale model for compressible turbulence and scalar transport. *Phys. Fluids A*, **3**, 2746-2757.

SMAGORINSKY, J. 1963 General circulation experiments with the primitive equations. *Mon. Weather Rev.* **91**, 99-164.



59-34  
20649  
101  
N94-24147

## Large-eddy simulation of flow in a plane, asymmetric diffuser

By Hans-Jakob Kaltenbach

Recent improvements in subgrid-scale modeling as well as increases in computer power make it feasible to investigate flows using large-eddy simulation (LES) which have been traditionally studied with techniques based on Reynolds averaging. However, LES has not yet been applied to many flows of immediate technical interest. This report describes *preliminary* results from LES of a plane diffuser flow. The long term goal of this work is to investigate flow separation as well as separation control in ducts and ramp-like geometries.

### 1. Motivation and objectives

Flow separation is a fundamental phenomenon which occurs in many engineering flow configurations such as airfoils, diffusers, and cascades. Prevention of separation usually improves the performance of such devices by increasing pressure recovery, enhancing lift, and decreasing total drag. Methods which delay or prevent separation include passive devices like vortex generators and active systems which use auxiliary power to modify the flow. Recent experiments (Katz *et al.* 1989, Seifert *et al.* 1992, 1993, Obi *et al.* 1993) have shown that flow control strategies which rely on adding small amounts of periodic disturbances (e.g. suction and blowing at specific locations) can delay separation efficiently without consuming large amounts of auxiliary power.

Investigation of unsteady control concepts using numerical simulation requires a method which computes the spatial as well as the temporal evolution of the turbulent fluctuations. Methods based on the Reynolds averaged Navier Stokes equations have difficulty dealing with the unsteadiness which is essential for the control concept. LES seems to be an ideal tool for studying unsteady control because experimental work has shown that the delay of separation is mostly due to the creation of large-scale vortical structures which improve the entrainment of high-speed fluid into separated zones (Katz *et al.* 1989). LES is very likely to adequately describe this physical mechanism at a reasonable cost. Conversely, direct numerical simulation (DNS) would be rather expensive at the Reynolds numbers under consideration.

The use of generalized coordinates largely enhances the range of possible flow configurations accessible for LES. Finite differences are more convenient to use than highly accurate spectral methods for approximation of derivatives. Little is known about the mutual dependency of use of the SGS-model in combination with a numerical scheme with considerable dispersive properties like second order central differences. One way of exploring this dependency consists of studying the sensitivity of the solution with respect to grid resolution.

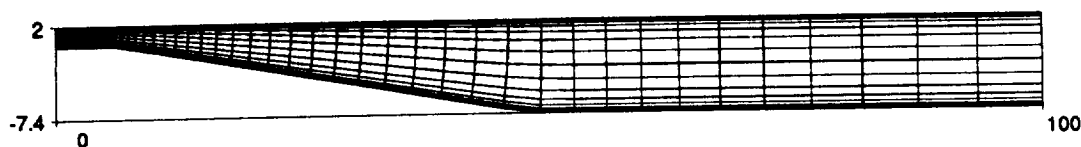


FIGURE 1. Computational domain for the plane diffuser in units of  $\delta$ . Only each 4th of the wall-normal and each third of the streamwise grid lines are plotted.

The objective of this study is to perform large-eddy simulation of turbulent flow in a one-sided diffuser. The results will be validated by comparison with the experiment of Obi *et al.* (1993). Once the minimum resolution requirements for accurately simulating this flow have been determined, periodic disturbances with various frequencies and amplitudes will be added to the flow as was done in the experiment. The final goal of this study is to understand the physics of flow control through periodic forcing and to determine the parameters (location, frequency, amplitude) that are most efficient in delaying flow separation.

## 2. Accomplishments

The DNS code of Choi & Moin (1993) has been modified to allow for simulation of inflow/outflow configurations with either no-slip or no-stress conditions at the upper boundary. A detailed description of the coordinate transformation and the numerical scheme is given in Choi *et al.* (1992). The code solves the unsteady, incompressible Navier-Stokes equations in generalized coordinates in two dimensions and a Cartesian equidistant grid in the third (spanwise) direction. The fully-implicit time integration scheme (Crank-Nicholson) uses Newton linearization along with approximate factorization. The time advancement allows rather large time-steps and CFL-numbers. The Poisson solver makes use of the spanwise periodicity of the domain which allows a Fourier transformation in this direction. The remaining 2D problems are solved by using LU decomposition for the first spanwise wavenumber and an iterative solver for higher wavenumbers. The major part of CPU-time needed for advancing the fractional step scheme by one timestep is spent on performing 3-4 Newton iterations per timestep. Depending on the spanwise resolution, the Poisson solver consumes between 10 and 30% of the computational effort.

Unsteady data are specified at the inflow, and a convective boundary condition is applied at the outflow. The upper and lower boundaries are no-slip walls. The data to be specified at the inflow plane of the domain are created in an independent LES of a fully developed channel flow. At each timestep, a cross-section of the velocity field is stored on disk using data reduction to 4 Byte words in order to minimize data storage and input/output time. These channel flow data are subsequently fed into the code which simulates flow through a non-periodic duct configuration.

A simple version of the dynamic SGS model (Germano *et al.* 1991) has been implemented and tested for a periodic channel flow. It makes use of least-square contraction (Lilly 1992) in combination with spanwise averaging. The total viscosity is constrained to be positive through a clipping operation. The test filter is applied

in the spanwise direction and along horizontal lines in the transformed space. No filtering takes place in the wall-normal direction. The SGS-model increases the CPU-time by less than 10% and has no significant effect on memory requirements. A formulation of the SGS-model in generalized coordinates is given in the appendix.

The code has been used for simulation of turbulent flow through a plane, one-sided diffuser. The dimensions of the computational domain are shown in figure 1. The diffuser geometry and the Reynolds number  $Re_b = U_b \delta / \nu = 9000$  match the experimental configuration of Obi *et al.* (1993). Here,  $U_b$  denotes the bulk velocity of the incoming fully developed turbulent channel flow of height  $2\delta$ . The flow from the inlet channel of length  $6\delta$  enters an asymmetric diffuser with an expansion ratio of  $a = 4.7$ . The diffuser and the outlet channel extend over  $42\delta$  and  $52\delta$ , respectively. The upper wall remains parallel to the inlet channel whereas the lower wall is deflected by approximately  $10^\circ$ . Both corners formed by the inlet and outlet channels with the lower wall are slightly rounded. With a width of  $12\delta$ , the aspect ratios of inlet and outlet channel are  $1 : 6$  and  $1 : 1.28$ , respectively. The experiment had much higher aspect ratios of  $1 : 35$  and  $1 : 7.45$  in order to guarantee a two-dimensional core flow free from sidewall effects.

The grid spacing is based on an estimate for the skin friction coefficient as a function of bulk Reynolds number as given by Dean;  $c_{f,b} = 0.061 Re_b^{-0.25}$ . For  $Re_b = 9000$ , this relation gives a value  $c_{f,b} = 0.0063$ , which corresponds to  $Re_\tau = u_\tau \delta / \nu = 500$ . Therefore, a wall-unit in the inlet section of the diffuser is  $0.002\delta$ . Assuming that the flow in the outlet channel will finally evolve into a fully developed channel flow, the wall-unit in the outflow section increases by the expansion ratio,  $a$ , to  $0.0094\delta$ . Linear stretching of the mesh sizes in the streamwise and wall-normal directions accounts for this increase. The grid with  $\Delta x = 0.375\delta$  ( $\Delta x^+ = 190$ ) in the inflow and  $\Delta x = 1.25\delta$  ( $\Delta x^+ = 133$ ) in the outflow section has 124 streamwise points. In the wall-normal direction, 64 points are distributed by using hyperbolic tangent stretching. It should be noted, however, that estimates for grid spacing in the outflow section based on wall-units are probably not very relevant because the flow is partially separated. The proper spacing must be verified from sensitivity studies.

For the present flow it would be highly desirable to use "zonal grids" for the spanwise direction. This would allow accurate simulation of the inlet with a fine spanwise grid and with increasingly coarser grids towards the diffuser outlet. However, the spanwise spacing  $\Delta z$  has to remain constant throughout the domain in the present code. The spanwise spacing must be chosen as a compromise between the different requirements in the inflow and the outflow section. Distribution of 64 points over a spanwise extent of  $12\delta$  results in  $\Delta z^+ = 94$  in the inflow and  $\Delta z^+ = 20$  in the outflow section. These estimates are based on  $Re_\tau = 500$ , which might not be reached everywhere in the actual simulation. The grid is fine enough to resolve near wall streaks with a characteristic spacing of approximately 100 wall-units in the diffuser outlet but certainly too coarse to realistically simulate the flow in the diffuser inlet section. For the purpose of studying the effect of unsteady blowing and suction on the pressure recovery in the rear part of the diffuser, the features

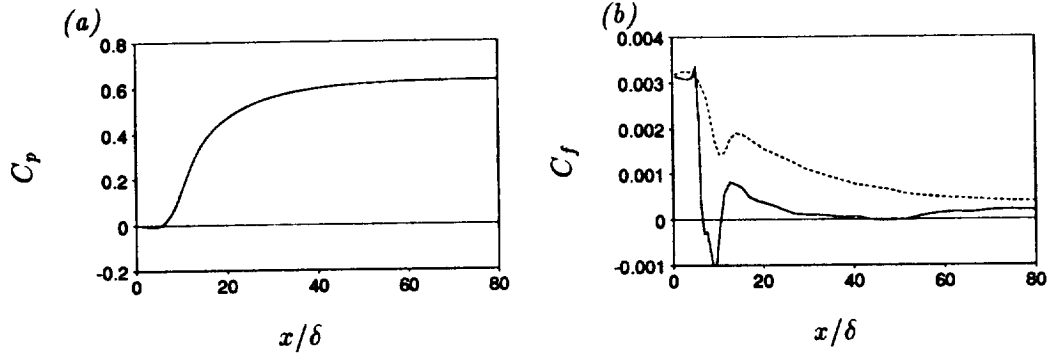


FIGURE 2. (a) Pressure coefficient  $c_p$  along the upper wall and (b) skin friction  $c_f$  based on centerline velocity at the inflow plane along lower (—) and upper (.....) walls as function of streamwise distance from the inflow plane.

of the flow in the inlet channel might be of minor importance. However, this issue must be tested by means of grid refinement studies.

An estimate of the quality of the simulated inlet flow can be obtained by comparison with Dean's empirical relations for skin friction and ratio of the centerline to the bulk velocity. Dean's correlation  $U_c/U_b = 1.27Re_b^{-0.0116}$  gives 1.14 for the Reynolds number considered. Three channel flow LES have been carried out for  $Re_b = 9000$  with spanwise spacings  $\Delta z^+ = 12, 29$  and  $73$  based on the *actual* wall shear which changes significantly with the grid resolution. Only the finest case reaches a  $c_{f,b} = 0.0064$  ( $Re_\tau = 510$ ), which is close to the value derived from Dean's relation. The other cases reach  $c_{f,b} = 0.0054$  ( $Re_\tau = 465$ ) and  $0.0038$  ( $Re_\tau = 393$ ). This means that the coarsest simulation which is used as database for unsteady inflow underpredicts the skin friction by 40%. However, the values of  $U_c/U_b = 1.12, 1.09$  and  $1.10$  do not differ much between the three cases, indicating that the interior of the flow is well captured by all three simulations. The case with the finest spacing is actually not too far from a DNS because the SGS-eddy viscosity contributes less than 20% to the total viscosity. The plane averaged SGS-eddy viscosity is larger than the molecular viscosity in 60% of the domain in the coarsest case.

The inertial time scale  $\tau = 0.5h(x)/U_b(x)$  increases with the square of the expansion ratio from the inlet to the outlet section, i.e.  $\tau_{out} = a^2\tau_{in}$ . Here,  $h(x)$  is the diffuser height at location  $x$ . The same holds for the viscous time scale  $\tau_{visc} = \nu/u_\tau^2$  which mainly determines the choice of the maximum timestep. Again - as for the spanwise spacing - the choice of the timestep is a compromise between the very different requirements of inlet and outlet section. Running the code with 10 time steps per  $\tau_{in}$  corresponds to a timestep which is three times bigger than the viscous timescale of the inflow but only one seventh of the viscous timescale of the outflow. In order to obtain converged statistics, data have to be sampled over a period of 100 inertial time scales. Because the inertial timescale of the flow increases by a factor of 22 from inlet to outlet rather long simulation times - of the order of 10000 timesteps - are required.



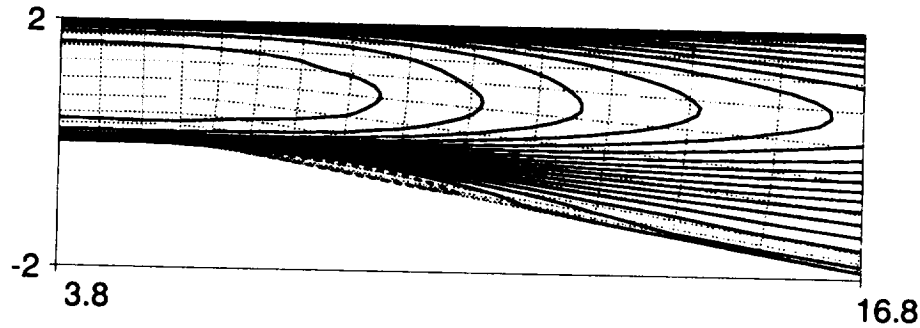


FIGURE 3. Region with reversed flow. Shown are isolines of the contravariant velocity component which is aligned with the horizontal grid lines. The grid lines shown are a subset of the actual grid.

*Preliminary* results from a coarse grid simulation are shown in figures 2 to 5. Data have been sampled over 300 inlet inertial timescales after running the code for 1000 inlet timescales. Statistics are not fully converged, but the main features of the flow seem to be established.

Figure 2 depicts pressure recovery along the upper wall and skin friction along both walls. Negative values of  $c_f$  behind the inlet corner mark the streamwise extent of a first separation bubble. This separated zone, which is shown in more detail in figure 3, was not reported by Obi *et al.* (1993). The flow separation close to the inlet might be an artifact of the coarse spanwise resolution in the diffuser inlet. This can be understood in the following way: the low value of skin friction in the inlet channel indicates that the velocity profile is less full than expected for the given Reynolds number based on centerline velocity. A less full mean velocity profile arises because the turbulent shear stress is underpredicted. Less high speed fluid from the channel core is transported towards the wall which makes separation more likely to occur. Grid refinement studies will be carried out to clarify this point. The skin friction approaches zero in the vicinity of the diffuser outlet. In this region the flow seems to be close to separation. However, we do not find a zone of reversed flow as for the first bubble. In accordance with this finding, mean profiles in the experiment do not show significant backflow at the diffuser outlet.

Profiles of mean velocity and turbulence intensities change drastically inside the diffuser. As described by Simpson (1985), relative high turbulence levels might be found in regions with backflow. Figure 4 shows a strong increase of the streamwise velocity fluctuation in the vicinity of the first separation bubble ( $x/\delta \approx 9$ ). Throughout the rear part of the diffuser, the turbulence intensities remain high compared to the value of the mean velocity (figure 5). The scatter in these profiles is higher than in figure 4 because much longer sampling times are required in the outflow section to obtain converged statistics. There is little evidence from the mean flow profiles that the flow is separated at the diffuser exit.

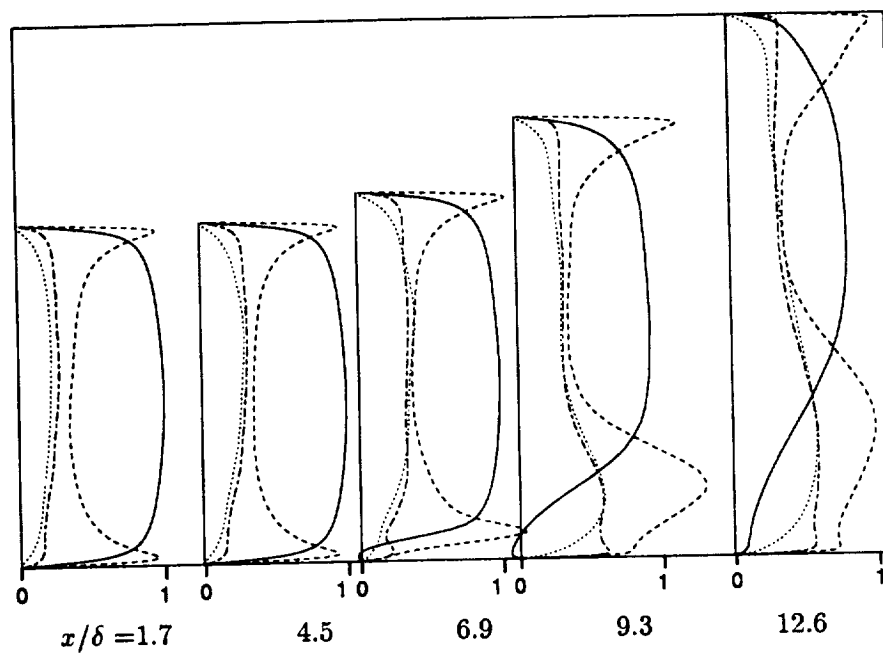


FIGURE 4. Profiles of mean velocity  $U/U_c$  (—) and contravariant fluctuations  $u'/U_c$  (---),  $v'/U_c$  (.....) and  $w'/U_c$  (-.-) close to the diffuser inlet. Rms-values are enhanced by a factor of five compared to the mean velocity.

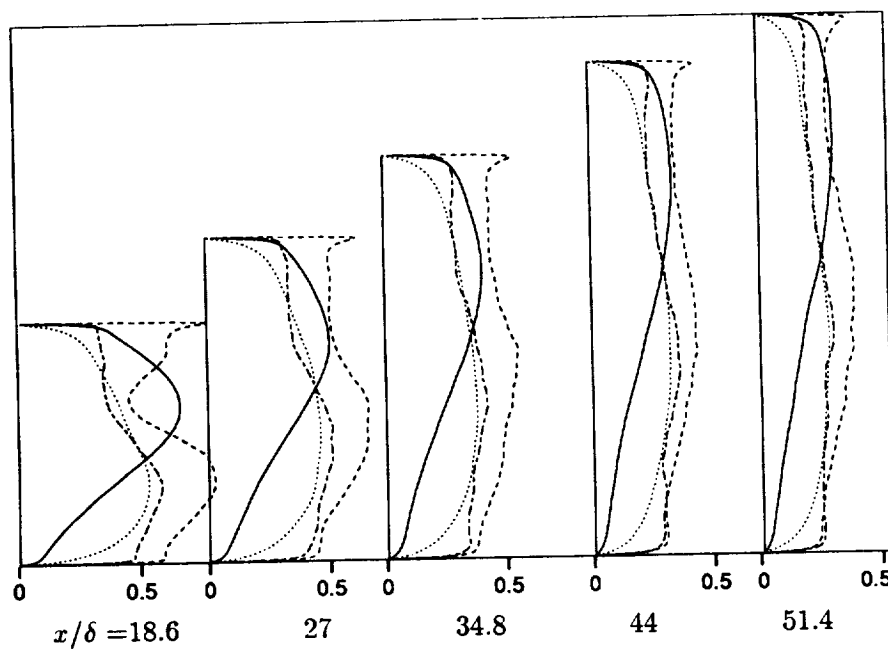


FIGURE 5. Same as figure 4 for the rear part of the diffuser. Note the scale change between this figure and figure 4.

### 3. Future plans

Grid refinement studies will be carried out in order to see whether underprediction of skin friction in the inlet channel has a significant effect on the flow inside the diffuser. A detailed comparison with available experimental data as well as results from simulations based on statistical turbulence models will be carried out. Once the undisturbed flow is predicted well, oscillatory control of the diffuser will be studied in order to see whether the same gains in pressure recovery are reached in the simulation as in the experiment.

In addition to flow through a diffuser, flow separation at a corner formed by a wall with a hinged rearward facing ramp will be investigated. This configuration resembles the generic flap which is the subject of an ongoing experimental investigation (Seifert *et al.* 1993). The computational domain will be designed such that it matches the experimental configuration of Katz *et al.* (1989). The long term goal of these studies, which are carried out in collaboration with Dr. I. Wygnanski and Dr. A. Seifert, Tel Aviv University, is the improvement of high-lift devices such as highly deflected flaps.

### Appendix: The dynamic SGS-model in generalized coordinates

The dynamic model for residual stresses (Germano *et al.*, 1991) requires computation of the Leonard term  $L^{ij}$  and the deformation rate tensor  $S^{ij}$ . One obtains the scalar model coefficient through contractions of these tensors (and their filtered counterparts). Several possibilities exist to formulate the model in generalized coordinates. If the model formulation is based on a Cartesian system, the Cartesian tensors  $L^{ij}$  and  $S^{ij}$  have to be computed from the contravariant velocity components. This procedure leads to moderately complex expressions for the components of  $L^{ij}$ .

On the other hand, the model can be formulated in generalized coordinates. In this case, contravariant as well as covariant components of strain-rate and Leonard term  $\Sigma^{ij}$ ,  $\Sigma_{ij}$ ,  $\Lambda^{ij}$ ,  $\Lambda_{ij}$  have to be evaluated. It turns out that this formulation with certain assumptions leads to rather simple expressions for the Leonard term. This will be shown in the following sections where the definitions

$y^i$	Cartesian coordinate
$x^i$	generalized coordinate
$v^i$	Cartesian velocity component
$u^i$	contravariant velocity component
$q^i \equiv Ju^i$	velocity component weighted with Jacobian (mesh volume)
$c_i^j \equiv \frac{\partial y^j}{\partial x^i}$	derivative of Cartesian with respect to generalized coordinates
$(c_i^j)^{-1} \equiv \frac{\partial x^i}{\partial y^j}$	derivative of generalized with respect to Cartesian coordinates
$\alpha^{ij} \equiv g^{ij}J$	contravariant metric coefficient weighted with Jacobian

are used.

Starting from the Cartesian formulation for the Leonard term  $L^{ij} = \widehat{v^i v^j} - \widehat{v^i} \widehat{v^j}$ , where  $\widehat{\phantom{x}}$  stands for filtering, the contravariant tensor can be written as

$$\begin{aligned}\Lambda^{ij} &= (c_i^m)^{-1} (c_j^n)^{-1} L^{mn} = (c_i^m)^{-1} (c_j^n)^{-1} (\widehat{v^m v^n} - \widehat{v^m} \widehat{v^n}) \\ &= (c_i^m)^{-1} (c_j^n)^{-1} (\widehat{c_p^m u^p c_q^n u^q} - \widehat{c_p^m u^p} \widehat{c_q^n u^q})\end{aligned}$$

Under the assumption that  $c_i^j$  changes only weakly over the distance corresponding to the test filter width, it might be extracted from beneath the filter operator. This leads to

$$\begin{aligned}\Lambda^{ij} &\approx (c_i^m)^{-1} (c_j^n)^{-1} c_p^m c_q^n (\widehat{u^p u^q} - \widehat{u^p} \widehat{u^q}) \\ &= \delta_p^i \delta_q^j (\widehat{u^p u^q} - \widehat{u^p} \widehat{u^q}) = (\widehat{u^i u^j} - \widehat{u^i} \widehat{u^j}) \quad .\end{aligned}$$

Thus, the Leonard term is computed in generalized coordinates from the contravariant velocity components in the same way as  $L^{ij}$  from the Cartesian velocity components.

For computation of the strain-rate, the use of non-conservative expressions for derivatives leads to compact expressions. For the purpose of computing the SGS-eddy viscosity, it is probably of little importance whether or not the derivatives are formulated strictly conservative. The code conserves momentum as long as the momentum fluxes over cell surfaces are formulated with a “telescoping” scheme. One obtains the contravariant components  $\Sigma^{ij}$  of the strain rate tensor from

$$\begin{aligned}\Sigma^{ij} &= (c_i^m)^{-1} (c_j^n)^{-1} \frac{1}{2} \left( \frac{\partial v^m}{\partial y^n} + \frac{\partial v^n}{\partial y^m} \right) \\ &= (c_i^m)^{-1} (c_j^n)^{-1} \frac{1}{2} \left[ (c_p^n)^{-1} \frac{\partial v^m}{\partial x^p} + (c_q^m)^{-1} \frac{\partial v^n}{\partial x^q} \right] \\ &= \frac{1}{2} \left[ (c_i^m)^{-1} (c_j^n)^{-1} (c_p^n)^{-1} \frac{\partial v^m}{\partial x^p} + (c_i^m)^{-1} (c_j^n)^{-1} (c_q^m)^{-1} \frac{\partial v^n}{\partial x^q} \right] \\ &= \frac{1}{2J} \left[ (c_i^m)^{-1} \alpha^{pj} \frac{\partial v^m}{\partial x^p} + (c_j^n)^{-1} \alpha^{qi} \frac{\partial v^n}{\partial x^q} \right],\end{aligned}$$

where

$$v^m = \frac{1}{J} c_i^m q^i \quad \text{and} \quad v^n = \frac{1}{J} c_s^n q^s$$

has to be inserted because the code is actually formulated in terms of the weighted velocities  $q^i$ .

## REFERENCES

- CHOI, H. & MOIN, P. 1993 The effect of computational timestep on numerical simulation of turbulent flow, to appear in *J. Comp. Phys.*

- CHOI, H., MOIN, P. & KIM, J. 1992 Turbulent drag reduction: studies of feedback control and flow over riblets. *Rep. No. TF-55*, Thermosc. Div., Dept. Mech. Engr., Stanford University.
- GERMANO, M., PIOMELLI, U., MOIN, P. & CABOT, W. H. 1991 A dynamic subgrid-scale eddy viscosity model. *Phys. Fluids A*. **3**, 1760-1765.
- KATZ, Y., NISHRI, B. & WYGNANSKI, I. 1989 The delay of turbulent boundary layer separation by oscillatory active control. *Phys. Fluids A*. **1**, 179-181. Extended version: AIAA paper 89-1027.
- LILLY, D. K. 1992 A proposed modification of the Germano subgrid scale closure method. *Phys. Fluids A*. **3**, 2746-2757.
- OBI, S., OHIMUZI, H., AOKI, K. & MASUDA, S. 1993 Turbulent separation control in a plane asymmetric diffuser by periodic perturbation; in: *Engineering Turbulence Modelling and Experiments 2*, W. Rodi and F. Martelli (Eds.), Elsevier Science Publ.
- SEIFERT, A., BACHAR, T., KOSS, D., SHEPSHELOVICH, M. & WYGNANSKI, I. 1992 Oscillatory blowing, a tool to delay boundary layer separation. *AIAA paper 93-0440*, to be published in AIAA J.
- SEIFERT, A., DARABY, A., NISHRI, B. & WYGNANSKI, I. 1993 The effects of forced oscillations on the performance of airfoils. *AIAA paper 93-3264*.
- SIMPSON, R.L. 1985 Two-dimensional turbulent separated flow. *AGARDograph* **287**.



510-34  
201050  
P. 18 111  
N94-24148

## On the large eddy simulation of turbulent flows in complex geometry

By S. Ghosal

### 1. Motivation and objectives

Application of the method of LES to a turbulent flow consists of three separate steps. First, a filtering operation is performed on the Navier-Stokes equations to remove the small spatial scales. The resulting equations that describe the space-time evolution of the 'large eddies' contain the subgrid-scale (sgs) stress tensor that describes the effect of the unresolved small scales on the resolved scales. The second step is the replacement of the sgs stress tensor by some expression involving the large scales — this is the problem of 'subgrid-scale modeling'. The final step is the numerical simulation of the resulting 'closed' equations for the large scale fields on a grid small enough to resolve the smallest of the large eddies, but still much larger than the fine scale structures at the Kolmogorov length. In dividing a turbulent flow field into 'large' and 'small' eddies, one presumes that a cut-off length  $\delta$  can be sensibly chosen such that all fluctuations on a scale larger than  $\delta$  are 'large eddies' and the remainder constitute the 'small scale' fluctuations. Typically,  $\delta$  would be a length scale characterizing the smallest structures of interest in the flow. In an inhomogeneous flow, the 'sensible choice' for  $\delta$  may vary significantly over the flow domain. For example, in a wall bounded turbulent flow, most statistical averages of interest vary much more rapidly with position near the wall than far away from it. Further, there are dynamically important organized structures near the wall on a scale much smaller than the boundary layer thickness. Therefore, the minimum size of eddies that need to be resolved is smaller near the wall. In general, for the LES of inhomogeneous flows, we must consider the width of the filtering kernel  $\delta$  to be a function of position. If a filtering operation with a nonuniform filter width is performed on the Navier-Stokes equations, one does not in general get the standard large eddy equations. The complication is caused by the fact that a filtering operation with a nonuniform filter width in general does not commute with the operation of differentiation. This is one of the issues that we have looked at in detail as it is basic to any attempt at applying LES to complex geometry flows. Our principal findings are summarized in this report. For details the reader is referred to Ghosal and Moin, 1993.

In the field of subgrid-scale modeling, a large effort was invested in research on the dynamic localization model. The theoretical fundamentals have been set out in detail in our last report (Ghosal, Lund & Moin, 1993). In this report, we present some further results of tests performed on the model. These tests are on homogeneous turbulence, but tests on wall bounded flows have also been conducted by other members of the LES group and will be presented elsewhere (see the report by Cabot in this volume).

## 2. Accomplishments

This section is divided into two parts. In §2.1, we summarize the theoretical work on the derivation of the basic LES equations for flows requiring nonuniform grids. In §2.2, some results from the ongoing tests of the dynamic localization model are presented.

### 2.1 The basic equations for the LES of turbulent flows in complex geometry

#### 2.1.1 Nonuniform filtering in one space dimension (definition)

Consider a field  $\phi(\xi)$  defined in the domain  $(-\infty, +\infty)$ . A filtering operation with a constant filter width  $\Delta$  is defined by (Leonard, 1974)

$$\bar{\phi}(\xi) = \frac{1}{\Delta} \int_{-\infty}^{+\infty} G\left(\frac{\xi - \eta}{\Delta}\right) \phi(\eta) d\eta \quad (1)$$

where  $G$  is any function with domain  $(-\infty, +\infty)$  and endowed with the following properties:

- (i)  $G(-\xi) = G(\xi)$
- (ii)  $\int_{-\infty}^{+\infty} G(\xi) d\xi = 1$
- (iii)  $G(\xi) \rightarrow 0$  as  $|\xi| \rightarrow \infty$  sufficiently fast so that all moments

$$\int_{-\infty}^{+\infty} G(\xi) \xi^n d\xi$$

( $n \geq 0$ ) exist.

- (iv)  $G(\xi)$  is very small (in some suitably defined sense) outside  $(-\frac{1}{2}, +\frac{1}{2})$ .

Some examples of possible filter functions are the 'top-hat' filter

$$G(\xi) = \begin{cases} 1, & \text{if } |\xi| \leq \frac{1}{2}; \\ 0, & \text{otherwise} \end{cases} \quad (2)$$

and the 'Gaussian' filter

$$G(\xi) = \sqrt{\frac{2}{\pi}} \exp(-2\xi^2). \quad (3)$$

(For a discussion of the various types of filters used in LES, see Aldama, 1990.)

In situations where the domain might be finite or semi-infinite and a variable filter width is desirable, the definition (1) can have many possible generalizations. For example, a generalization of (1) when  $G$  is the top-hat filter might be

$$\bar{\phi}(\xi) = \frac{1}{(\Delta_+(\xi) + \Delta_-(\xi))} \int_{\xi - \Delta_-(\xi)}^{\xi + \Delta_+(\xi)} \phi(\eta) d\eta \quad (4)$$

where  $\Delta_+(\xi)$  and  $\Delta_-(\xi)$  are positive functions and  $\Delta_+(\xi) + \Delta_-(\xi)$  is the effective filter width at location ' $\xi$ '. For a finite or semi-infinite domain,  $\Delta_+(\xi)$  and  $\Delta_-(\xi)$



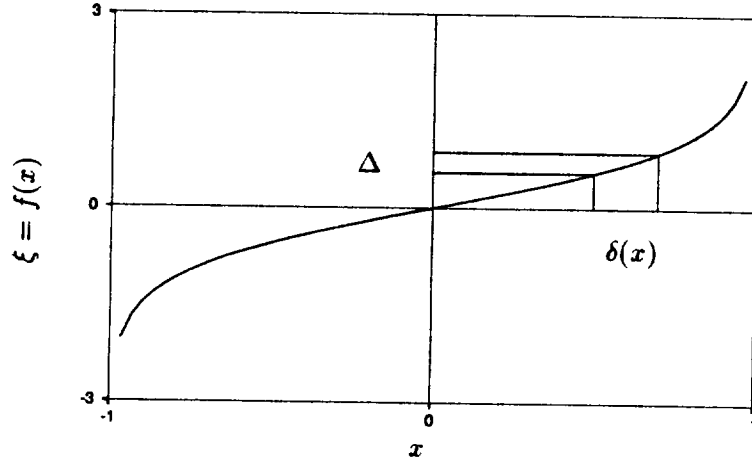


FIGURE 1. The space  $x$ , with variable filter width  $\delta(x)$ , is shown mapped into a space  $\xi$ , with constant filter width  $\Delta$ , by the 'tan-hyperbolic map'  $f(x) = \tanh^{-1} x$ .

must go to zero at the boundaries sufficiently rapidly so that  $(\xi - \Delta_-(\xi), \xi + \Delta_+(\xi))$  is always in the domain of  $\phi$ .

A filtering operation with a nonuniform filter width (such as the one defined in (4)) does not in general commute with the operation of differentiation. It may be shown (Moin *et al.*, 1978), for example, that with the definition (4),

$$\frac{\overline{d\phi}}{d\xi} - \frac{d\bar{\phi}}{d\xi} = \frac{\frac{d}{d\xi}(\Delta_+(\xi) + \Delta_-(\xi))}{\Delta_+(\xi) + \Delta_-(\xi)} \bar{\phi} - \frac{1}{(\Delta_+ + \Delta_-)} \left[ \phi(\xi + \Delta_+) \frac{d\Delta_+}{d\xi} + \phi(\xi - \Delta_-) \frac{d\Delta_-}{d\xi} \right]. \quad (5)$$

Thus,

$$\left( \frac{d\phi}{d\xi} \right) \neq \frac{d\bar{\phi}}{d\xi}. \quad (6)$$

One would like to believe that the right-hand side of (5) would be small for some reasonable class of nonuniform filters, but this has never been conclusively demonstrated. This lack of commutativity between filtering and differentiation causes every spatial derivative operator in the Navier-Stokes equations to generate terms that cannot be expressed solely in terms of the filtered fields. Therefore, a 'closure problem' is introduced not only for the nonlinear terms, but for the linear terms as well. To remedy this situation we first propose an alternate definition for the filtering operation that is more general than (4).

Let  $\phi$  be some field defined in a finite or infinite domain  $[a, b]$ . Any nonuniform grid in the domain  $a \leq x \leq b$  can be mapped to a uniform grid of spacing  $\Delta$  in the domain  $[-\infty, +\infty]$  by means of some mapping function

$$\xi = f(x). \quad (7)$$

Here  $f(x)$  is a monotonic differentiable function such that

$$f(a) = -\infty, \quad (8)$$

$$f(b) = +\infty. \quad (9)$$

The nonuniform grid spacing  $\delta(x)$  is clearly given by

$$\delta(x) = \frac{\Delta}{f'(x)} \quad (10)$$

(see figure 1). Clearly, if  $a$  (or  $b$ ) is finite, (8)-(9) requires  $f'(a)$  (or  $f'(b)$ ) to be infinite so that  $\delta(a)$  (or  $\delta(b)$ ) = 0. Since  $\delta(x)$  can be regarded as a 'local' filter width (see equation (16)), the filtering kernel becomes a Dirac delta function at finite boundaries. This, of course, is an ideal limit that in a practical numerical computation can be achieved only approximately. Thus, our stipulation that the grid spacing be approximately equal to the filter width must break down when we are sufficiently close to a wall because in practice one cannot have an infinitely dense clustering of grid points at the boundary.

The filtering operation is defined as follows. Given an arbitrary function  $\psi(x)$ , we first make a change of variables to  $\xi$  to obtain the new function  $\phi(\xi) = \psi(f^{-1}(\xi))$ . The function  $\phi(\xi)$  is then filtered using the usual definition (1) appropriate for filtering on a uniform grid. Finally, we transform back to the variable  $x$ . Thus,

$$\bar{\psi}(x) \equiv \bar{\phi}(\xi) = \frac{1}{\Delta} \int_{-\infty}^{+\infty} G\left(\frac{f(x) - \eta}{\Delta}\right) \phi(\eta) d\eta, \quad (11)$$

or, on using (7), we have

$$\bar{\psi}(x) = \frac{1}{\Delta} \int_a^b G\left(\frac{f(x) - f(y)}{\Delta}\right) \psi(y) f'(y) dy. \quad (12)$$

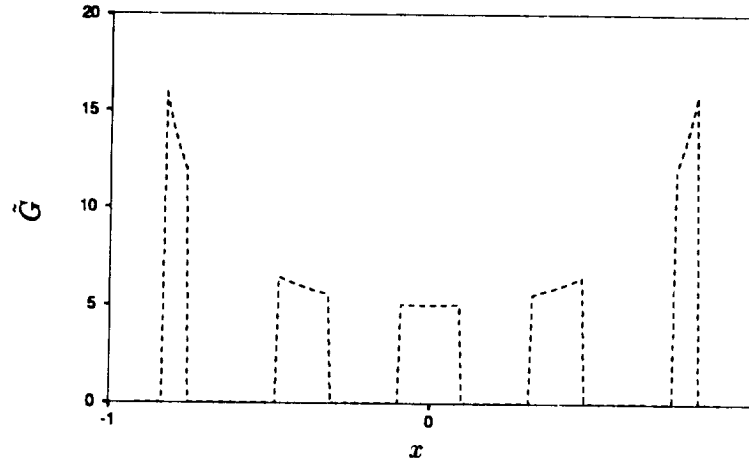
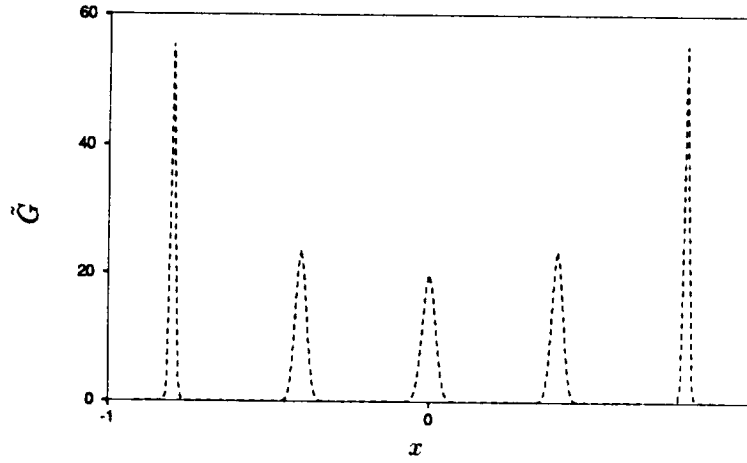
Equation (11) or, equivalently, (12) is the definition we shall adopt for the filtering operation with a nonuniform filter width. For reasons that will become apparent in the next section, we will call this the Second Order Commuting Filter (SOCF). It should be noted that the definition (4) used by Moin *et al.* is quite different from what one would get on substituting the expression (2) for the top-hat filter into (12).

**Example:** In channel flow, one often uses the 'tanhhyperbolic grid' (see for example Moin & Kim, 1982. The mapping function discussed below is slightly different from the version actually used in numerical computations since there one uses only a finite number of grid points whereas our filters become infinitely sharp at the walls).

$$f(x) = \tanh^{-1} x \quad (13)$$

where  $+1 \geq x \geq -1$ . ( $x = \pm 1$  correspond to the channel walls.) From equation (12), the filtering operation is defined as

$$\bar{\psi}(x) = \int_{-1}^{+1} \tilde{G}(x, y) \psi(y) dy \quad (14)$$

FIGURE 2A. The shape of the filter function  $\tilde{G}$  when  $G$  is a top-hat filter.FIGURE 2B. The shape of the filter function  $\tilde{G}$  when  $G$  is a Gaussian filter.

where

$$\tilde{G}(x, y) = \frac{1}{\Delta} G\left(\frac{f(x) - f(y)}{\Delta}\right) f'(y) \quad (15)$$

with  $f(x) = \tanh^{-1} x$ . The function  $\tilde{G}(x, y)$  is plotted in figure 2A when  $G$  is a top-hat filter and in figure 2B when  $G$  is a Gaussian filter. If the approximations  $f(x) - f(y) \approx f'(x)(x - y)$  and  $f'(y) \approx f'(x)$  for  $y$  near  $x$  are used in (15), we have on using (10)

$$\tilde{G}(x, y) \approx \frac{1}{\delta(x)} G\left(\frac{x - y}{\delta(x)}\right). \quad (16)$$

Thus, as a first approximation, the filtering kernel  $\tilde{G}$  contracts in a self-similar manner on approaching a finite boundary (see figures 2 A and B). However, the exact

formula (15) has an additional higher order effect that causes the filter function  $\tilde{G}$  to become asymmetric near the wall giving more weight to points nearer the wall than further from it. The effect is most clearly seen in figure 2A.

### 2.1.2 Calculation of the commutation error

Let us define the commutation error as

$$C[\psi] \equiv \left( \overline{\frac{d\psi}{dx}} \right) - \frac{d\bar{\psi}}{dx} \quad (17)$$

Then it is easily shown that

$$C[\psi] = \frac{1}{\Delta} \int_a^b G \left( \frac{f(x) - f(y)}{\Delta} \right) \psi'(y) f'(y) \left[ 1 - \frac{f'(x)}{f'(y)} \right] dy. \quad (18)$$

(The boundary terms are strictly zero due to the conditions (8) and (9).)

It is convenient to introduce the new variable  $\zeta$  such that  $y$  is expressed implicitly in terms of  $\zeta$  through the equation

$$f(y) = f(x) + \Delta\zeta \quad (19)$$

Equation (19) can be inverted by expressing  $y$  in a power series

$$y = y_0(\zeta) + \Delta y_1(\zeta) + \Delta^2 y_2(\zeta) + \dots \quad (20)$$

where  $y_0(\zeta)$ ,  $y_1(\zeta)$ ,  $\dots$  are functions to be determined. On substituting (20) in (19) and equating like powers of  $\Delta$ , one obtains the expansion

$$y = x + \frac{\Delta\zeta}{f'} - \frac{\Delta^2 f''}{2f'^3} \zeta^2 + \dots \quad (21)$$

(Note: When the argument of any function is omitted, we imply that the function is evaluated at 'x'.) In terms of  $\zeta$ , equation (18) may be written as

$$C[\psi] = \int_{-\infty}^{+\infty} G(\zeta) \psi'(y) \left[ 1 - \frac{f'(x)}{f'(y)} \right] d\zeta \quad (22)$$

where  $y$  is given by (21) (the limits of integration are obtained on using (8) and (9) in (19)). On expanding each of the factors in the integrand of (22) in Taylor series in  $\Delta$  and collecting terms of the same order, we have,

$$C[\psi] = c_1 \Delta + c_2 \Delta^2 + \dots = c'_1 \delta + c'_2 \delta^2 + \dots \quad (23)$$

where

$$c_1 = \frac{f'' \psi'}{f'^2} \int_{-\infty}^{+\infty} \zeta G(\zeta) d\zeta, \quad (24)$$

$$c_2 = \frac{2f'f''\psi'' + f'f'''\psi' - 3f''^2\psi'}{2f'^4} \int_{-\infty}^{+\infty} \zeta^2 G(\zeta) d\zeta, \quad (25)$$

$c_1' = c_1 f'$  and  $c_2' = c_2 (f')^2$ . Since  $G(\zeta)$  is symmetric,  $c_1 = c_1' = 0$ . Thus, the commutation error  $\mathcal{C}[\psi] \sim O(\delta^2)$ .

In an LES, the grid spacing is approximately equal to the 'filter-width',  $\delta$ . If a second order numerical scheme is used to represent the derivatives, the finite differencing error is then of the same order as the error due to the lack of commutativity of the differentiation and the filtering operations. Therefore, in an LES of an inhomogeneous turbulent flow using a second order finite differencing scheme, the filtering operation can be considered to commute with the differentiation operation to within the accuracy of the numerical approximation. This is our most important result from the point of view of practical application.

### 2.1.3 Spectral distribution of the commutation error

Let us substitute

$$\psi = \hat{\psi}_k \exp(ikx) \quad (26)$$

and (21) in (22). Then,

$$\mathcal{C}[\psi] = ik\psi \int_{-\infty}^{+\infty} G(\zeta) \left[ 1 - \frac{f'(x)}{f'(x + \frac{\Delta\zeta}{f'} + \dots)} \right] \exp\left(ik \frac{\Delta\zeta}{f'} + \dots\right) d\zeta. \quad (27)$$

On expanding the integrand of (27) in a power series in  $\Delta$ , we have

$$\frac{\mathcal{C}[\psi]}{\psi} = \mathcal{F}_0(k\Delta) + \Delta \mathcal{F}_1(k\Delta) + \dots \quad (28)$$

where  $\mathcal{F}_0, \mathcal{F}_1, \dots$  contain  $\Delta$  only in the combination  $k\Delta$ .

Now  $\Delta \ll 1$ , but  $k\Delta$  may be as large as order one. Thus, we may neglect the successive terms in (28) in comparison to the first term to obtain

$$\frac{\mathcal{C}[\psi]}{\psi} \simeq \mathcal{F}_0(k\Delta). \quad (29)$$

On evaluating  $\mathcal{F}_0(k\Delta)$  from (27), we have

$$\frac{\mathcal{C}[\psi]}{\psi} = ik\Delta \frac{f''}{(f')^2} \mathcal{F}\left(\frac{k\Delta}{f'}\right) \quad (30)$$

where  $\mathcal{F}$  is defined by

$$\mathcal{F}(x) = \int_{-\infty}^{+\infty} \zeta G(\zeta) \exp(ix\zeta) d\zeta. \quad (31)$$

Equation (30) can also be written as

$$\frac{C[\psi]}{\psi} = -ik\delta \left( \frac{\delta'}{\delta} \right) \mathcal{F}(k\delta) \quad (32)$$

where  $\delta$  is the local filter width as defined in (10). On expanding the exponential in (31) in a Taylor series, we see by virtue of  $G(\zeta)$  being symmetric that  $\mathcal{F}(k\delta) \sim k\delta$  so that  $|C[\psi]/\psi| \sim (k\delta)^2$  as shown in the last section.

Comparison with finite differencing errors is facilitated if the commutation error is expressed as a 'modified wave-number'. If  $C[\psi]$  were zero, we will have for the function (26)

$$\frac{d\bar{\psi}}{dx} = \frac{d\bar{\psi}}{dx} = ik\bar{\psi} = ik\bar{\psi}. \quad (33)$$

Therefore, if we define a 'modified wave-number'  $k'$  by

$$\frac{d\bar{\psi}}{dx} = ik'\bar{\psi}, \quad (34)$$

then the departure of  $k'$  from  $k$  is a measure of the commutation error. On making the change of variable (19) in (12), we obtain

$$\bar{\psi}(x) = \int_{-\infty}^{+\infty} G(\zeta)\psi(y)d\zeta. \quad (35)$$

On substituting (26) in (35) and on using the definition (34), we obtain

$$\frac{k'}{k} = \frac{\int_{-\infty}^{+\infty} G(\zeta) \exp(iky(x, \zeta)) \frac{\partial y(x, \zeta)}{\partial x} d\zeta}{\int_{-\infty}^{+\infty} G(\zeta) \exp(iky(x, \zeta)) d\zeta} \quad (36)$$

where  $y$  has been expressed as a function of  $\zeta$  by inverting (19) for each fixed value of  $x$ . Equation (36) is an exact result. A simplified asymptotic form is obtained on substituting the expansion (21) in (36) and dropping all terms such as  $\Delta(k\Delta)$ ,  $\Delta^2(k\Delta) \dots$  which are negligible compared to  $k\Delta$ . Thus,

$$\frac{k'}{k} = 1 - \Delta \frac{f''}{f'^2} \frac{\int_{-\infty}^{+\infty} \zeta G(\zeta) \exp\left(\frac{ik\Delta\zeta}{f'}\right) d\zeta}{\int_{-\infty}^{+\infty} G(\zeta) \exp\left(\frac{ik\Delta\zeta}{f'}\right) d\zeta}. \quad (37)$$

Since  $G(\zeta)$  is a symmetric function, (37) simplifies to

$$\frac{k'}{k} = 1 - i\Delta \frac{f''}{f'^2} \frac{\int_{-\infty}^{+\infty} \zeta G(\zeta) \sin\left(\frac{k\Delta\zeta}{f'}\right) d\zeta}{\int_{-\infty}^{+\infty} G(\zeta) \cos\left(\frac{k\Delta\zeta}{f'}\right) d\zeta}. \quad (38)$$

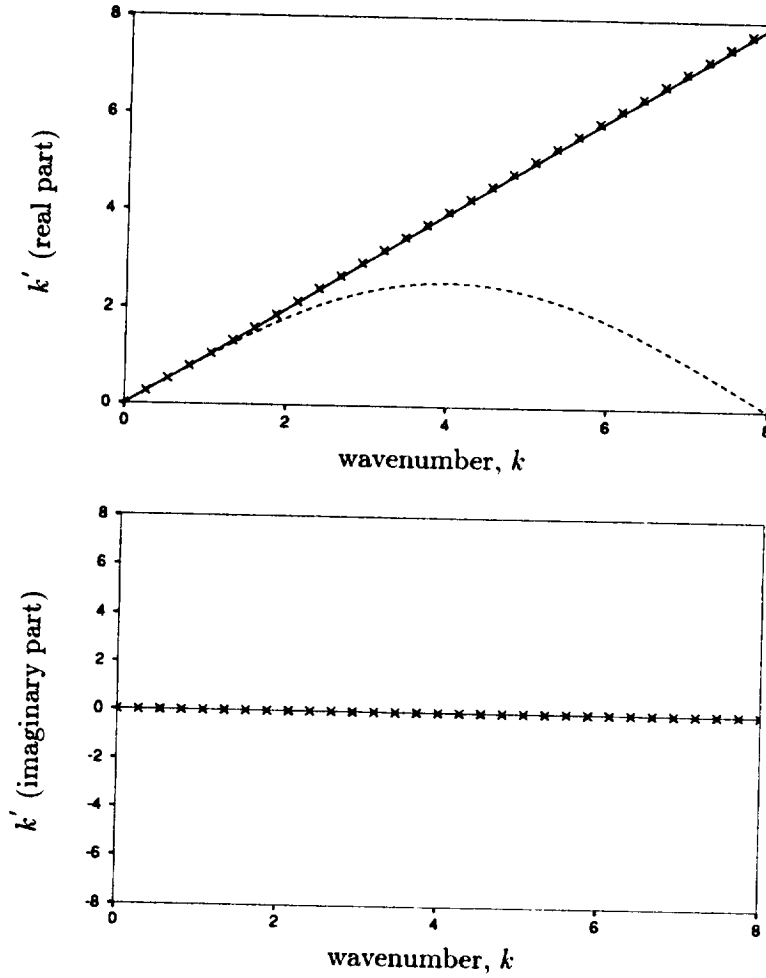


FIGURE 3A. The modified wavenumber ( $k'$ ) for the commutation error (—) compared to that of the central differencing error (---). The symbols 'x' are the result of using the approximate formula (42). Here  $\Delta = 2\pi/16$ ,  $x = 0$  (channel center), and the maximum wavenumber is  $\pi/\delta$  where  $\delta$  is the local filter width.

Example : Let us consider the top-hat filter defined by (2) together with the tan-hyperbolic map  $f(x) = \tanh^{-1} x$ . For this map, equation (19) can be inverted to give

$$y = \frac{x + \tanh \Delta \zeta}{1 + x \tanh \Delta \zeta}. \quad (39)$$

On substituting (39) in (36), we obtain

$$\frac{k'}{k} = \frac{\int_{-\infty}^{+\infty} \exp(iky) G(\zeta) \left[ \frac{1 - \tanh^2 \Delta \zeta}{(1 + x \tanh \Delta \zeta)^2} \right]}{\int_{-\infty}^{+\infty} \exp(iky) G(\zeta) d\zeta}, \quad (40)$$

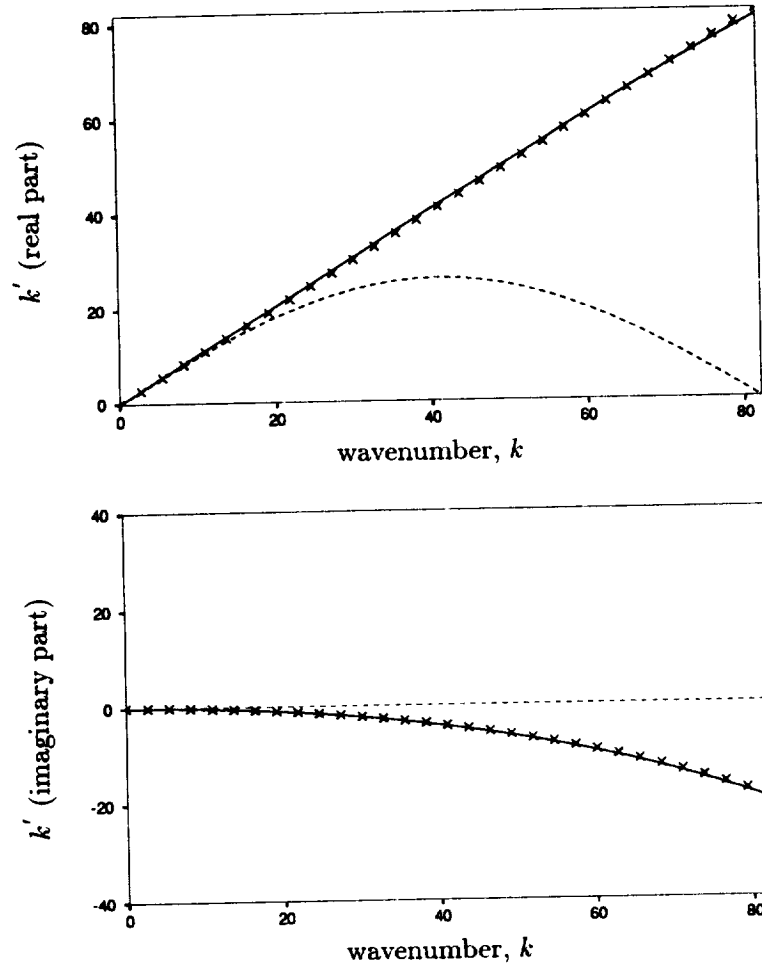


FIGURE 3B. Same as figure 3A for  $x = 0.95$  (close to channel wall).

with  $y$  given by (39). As a typical example, we consider a channel whose walls are at  $x = 0$  and  $x = 2\pi$  with 16 grid points in the spanwise direction. Thus,  $\Delta = 2\pi/16$ . The integral (40) can be evaluated numerically. The result is shown in figure 3. The modified wavenumber for the second order central difference scheme is given by

$$\frac{k'}{k} = \frac{\sin(k\delta)}{k\delta}. \quad (41)$$

Equation (41) is also plotted in figure 3 for comparison. The asymptotic formula (38) can be evaluated analytically in the case of the tan-hyperbolic map and top-hat filter. A straightforward computation gives

$$k' = k + \frac{2ix}{(1-x^2)} \left[ \frac{k\delta}{2} \cot\left(\frac{k\delta}{2}\right) - 1 \right]. \quad (42)$$



Equation (42) is also shown in figure 3. The agreement of the asymptotic result (42) with the exact result (40) is seen to be very good.

The asymptotic formula (38) can be written in the following convenient form:

$$k'_R = k, \quad (43)$$

$$k'_I = \left( \frac{\delta'}{\delta} \right) F(k\delta) \quad (44)$$

where  $\delta$  is the local filter width given by (10),

$$F(x) = x \left[ \frac{\int_{-\infty}^{+\infty} \zeta G(\zeta) \sin(x\zeta) d\zeta}{\int_{-\infty}^{+\infty} G(\zeta) \cos(x\zeta) d\zeta} \right] \quad (45)$$

and the suffixes  $R$  and  $I$  denote real and imaginary parts respectively. Thus, to a very good approximation, the commutation error is seen to be purely dissipative in nature in contrast to the central differencing error, which is dispersive. The commutation error vanishes in regions where  $\delta' = 0$  (such as at the center of a channel). From the example above, it is clear that for the top-hat filter,

$$F(k\delta) = 1 - \frac{k\delta}{2} \cot \left( \frac{k\delta}{2} \right) = \frac{(k\delta)^2}{12} + \frac{(k\delta)^4}{720} + \dots \quad (46)$$

A simple calculation shows that for the Gaussian filter (3),

$$F(k\delta) = \frac{(k\delta)^2}{4}. \quad (47)$$

#### 2.1.4 Higher order corrections to the commutation error

We have shown in the previous section that  $\mathcal{C}[\psi] \approx \psi \mathcal{F}_0(k\Delta)$  and  $\mathcal{F}_0(k\Delta) \sim (k\Delta)^2$  at leading order in  $k\Delta$ . In this section, we shall attempt to approximate the commutation error  $\mathcal{C}[\psi]$  by an expression involving  $\bar{\psi}$  and its derivatives such that the residual is of order  $(k\Delta)^4$ . The procedure can be readily generalized to represent  $\bar{\psi}'(x)$  in terms of  $\bar{\psi}'(x)$  and higher derivatives of  $\bar{\psi}(x)$  such that the error in the approximation is at most of order  $(k\Delta)^{2m}$  where  $m$  is any positive integer.

We have, on expanding the exponential in (31) and noting that  $G(\zeta)$  is a symmetric function,

$$\mathcal{F}(x) = ix \int_{-\infty}^{+\infty} \zeta^2 G(\zeta) d\zeta - \frac{ix^3}{3!} \int_{-\infty}^{+\infty} \zeta^4 G(\zeta) d\zeta + \dots \quad (48)$$

Substitution of (48) in (30) gives

$$\mathcal{C}[\psi] = -(k\Delta)^2 \frac{f''}{(f')^3} \psi \int_{-\infty}^{+\infty} \zeta^2 G(\zeta) d\zeta + O(k\Delta)^4. \quad (49)$$

From (35),

$$\bar{\psi}(x) = \int_{-\infty}^{+\infty} G(\zeta) \psi \left( x + \frac{\Delta \zeta}{f'} + \dots \right) d\zeta. \quad (50)$$

On substituting  $\psi = \hat{\psi}_k \exp(ikx)$  in (50) and differentiating twice with respect to  $x$ , we have

$$\bar{\psi}''(x) = -k^2 \psi \left[ 1 - \alpha \frac{(k\Delta)^2}{2f'^2} + O(k\Delta)^4 \right] \quad (51)$$

where

$$\alpha = \int_{-\infty}^{+\infty} \zeta^2 G(\zeta) d\zeta \quad (52)$$

and  $\Delta \ll 1$  has been assumed. Equation (51) implies that

$$-k^2 \psi = \bar{\psi}''(x) + O(k\Delta)^2. \quad (53)$$

On substituting (53) in (49) we get

$$\mathcal{C}[\psi] = \alpha \frac{f''}{f'^3} \Delta^2 \bar{\psi}''(x) + O(k\Delta)^4. \quad (54)$$

Thus,

$$\frac{d\bar{\psi}}{dx} = \frac{d\psi}{dx} + \alpha \frac{f''}{f'^3} \Delta^2 \frac{d^2 \bar{\psi}}{dx^2} + O(k\Delta)^4. \quad (55)$$

The procedure can be continued to extend the accuracy of the representation to any order in  $k\Delta$ . Equation (55) can also be written in terms of the local grid spacing  $\delta(x)$  as follows:

$$\frac{d\bar{\psi}}{dx} = \frac{d\psi}{dx} - \alpha \delta^2 \left( \frac{\delta'}{\delta} \right) \frac{d^2 \bar{\psi}}{dx^2} + O(k\delta)^4. \quad (56)$$

Equation (56) was established only for the function (26). However, it is clearly valid for any linear superposition of functions of the type (26), that is, any function that admits a Fourier representation.

#### 2.1.4 Generalization to three space dimensions

These results can be generalized to three space dimensions (see Ghosal and Moin, 1993 for details). Let us consider curvilinear grids defined by the co-ordinate surfaces

$$\mathbf{H}(\mathbf{x}) = \text{constant} \quad (57)$$

where  $\mathbf{x}$  are rectilinear co-ordinates in physical space. Let us also introduce a new 'computational space'  $\mathbf{X}$  through the map

$$\mathbf{X} = \mathbf{H}(\mathbf{x}) \quad (58)$$

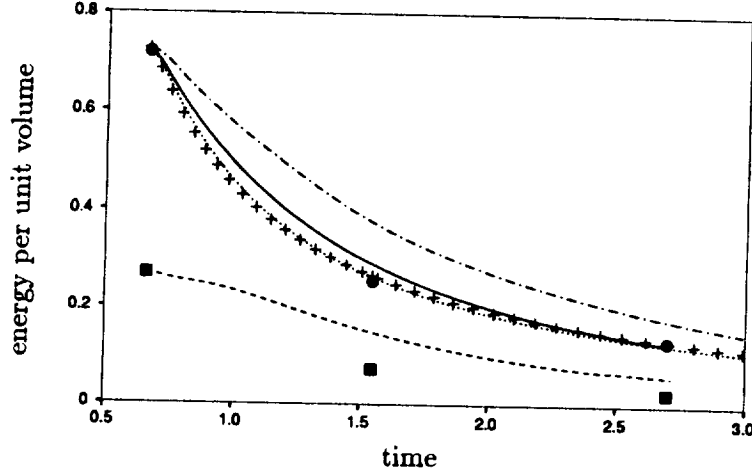


FIGURE 4A. Decay of energy in a simulation of the Comte-Bellot and Corrsin experiment with  $48^3$  grid points. Large scale energy (—); sgs energy ( $k$ ) (---), as predicted by DLM(G). This is compared with an identical computation with the DLM(C) (+), the DM (· · · · ·), and with the model turned off (— — —). Experimental: resolved energies (•); subgrid energies (■)

which maps the physical space domain into  $\mathbf{R}^3$  meshed with a uniform grid of spacing  $\Delta$ . The filtering operation is now defined as

$$\bar{\psi}(\mathbf{x}) = \frac{1}{\Delta^3} \int \prod_{i=1}^3 G\left(\frac{H_i(\mathbf{x}) - H_i(\mathbf{x}')}{\Delta}\right) \psi(\mathbf{x}') J(\mathbf{x}') d^3 \mathbf{x}' \quad (59)$$

where  $J(\mathbf{x})$  is the Jacobian of the transformation (58).

It can be shown that for the general three dimensional filter (59), equation (54) takes the form

$$C_k[\psi] = -\alpha \Delta^2 \Gamma_{kmp} \frac{\partial^2 \bar{\psi}}{\partial x_m \partial x_p} + O(|\mathbf{k}| \Delta)^4 \quad (60)$$

where

$$\Gamma_{kmp} = h_{m,jq}(\mathbf{H}(\mathbf{x})) h_{p,q}(\mathbf{H}(\mathbf{x})) H_{j,k}(\mathbf{x}) \quad (61)$$

and  $\mathbf{h}$  is the inverse of  $\mathbf{H}$ . Further, an expression for  $C_k[\psi]$  in terms of  $\bar{\psi}$  can be written down to any order in  $\Delta$ . Thus,

$$\overline{\partial_k \psi} = (\partial_k - \alpha \Delta^2 \Gamma_{kmn} \partial_{mn}^2 + \dots) \bar{\psi}. \quad (62)$$

## 2.2 Tests of the dynamic localization model

Two versions of the dynamic localization model (DLM) were introduced in last year's Annual Research Briefs (Ghosal, Lund & Moin, 1993). The first of these

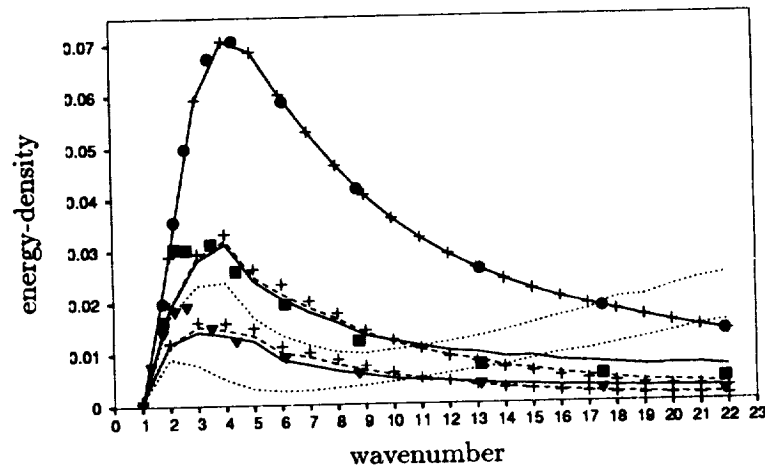


FIGURE 4B. The spectra at three times for the same computation as in figure 4A. DLM(G) (—); DM (— — —); DLM(C) (+); no model (.....). The solid circles, squares, and triangles are the experimental values at the three experimental points in figure 4A. The initial conditions are chosen so that the spectra at the earliest time matches the experiment.

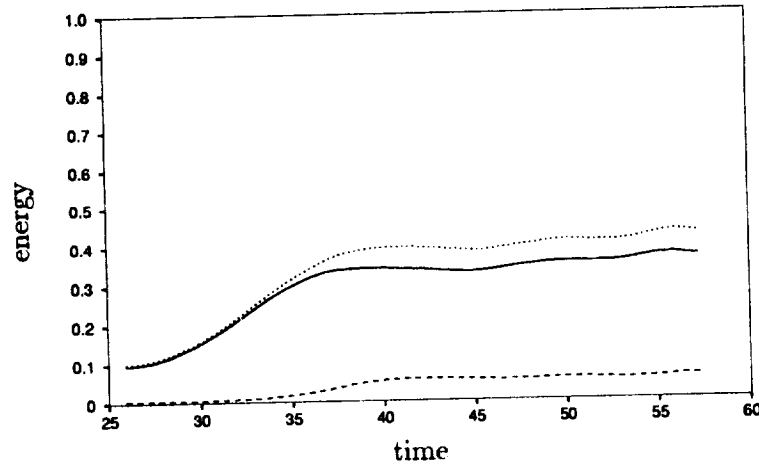


FIGURE 5A. Time dependence of energy in a forced simulation of homogeneous isotropic turbulence at infinite Reynolds number on a  $32^3$  grid using the DLM(G). Energy per unit volume in the resolved scales (—); subgrid-scale energy (— — —); Total energy (.....).

(which we will call the ‘constrained’ dynamic localization model or DLM(C)) constrains the Smagorinsky coefficient to be nonnegative and therefore does not exhibit the phenomenon of backscatter – the (locally) reverse transfer of energy from the subgrid to supergrid scales. The second formulation (which we will call the ‘general’ dynamic localization model or DLM(G)) removes this restriction. However,

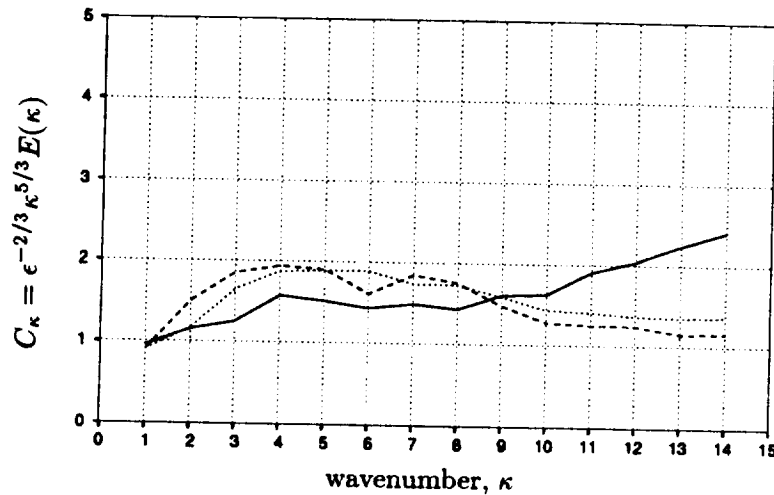


FIGURE 5B. Equilibrium spectrum in a forced simulation of homogeneous isotropic turbulence at infinite Reynolds number on a  $32^3$  grid. Kolmogorov's five-thirds law would correspond to a horizontal straight line with an ordinate equal to the Kolmogorov constant  $C_\kappa \approx 1.5$ . DLM(G) (—); DLM(C) (---); DM (.....).

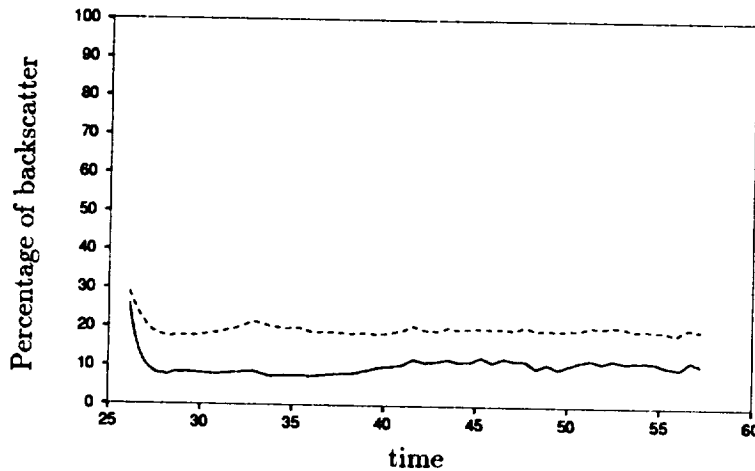


FIGURE 5C. Fraction of backscatter in a forced simulation of homogeneous isotropic turbulence at infinite Reynolds number on a  $32^3$  grid using DLM(G). Volume averaged rate of energy transfer from subgrid to supergrid scales as a fraction of the net transfer (—); Fraction of points experiencing backscatter at a given instant of time (---).

the generality is gained at the cost of added computational expense. The so called 'volume-averaged' version of the dynamic model which can be rigorously derived as a special case of the variational formulation (Ghosal, Lund & Moin, 1993) will be simply referred to as the dynamic model (DM). It is useful only for flows with

homogeneous directions.

Previous tests had shown (Ghosal, Lund & Moin, 1993) that while DLM(C) and DM used in a  $32^3$  LES simulation of the Comte-Bellot and Corrsin experiment (Comte-Bellot and Corrsin, 1971) gave excellent predictions, the results obtained with DLM(G) were not as satisfactory. This discrepancy was more thoroughly investigated. It was found that at a resolution of  $32^3$ , the subgrid-scale energy ( $k$ ) was almost equal to the total energy in the LES field. As such a situation is not fully consistent with the basic assumption of LES that the resolved scales carry most of the energy, the simulation was repeated on a more refined ( $48^3$ ) mesh.

At this resolution the total resolved energy is about thrice the subgrid-scale energy, and the performance of the DLM(G) is greatly improved. The performance of DLM(C), DLM(G) and DM are compared in figure 4 starting with identical initial conditions consistent with the experimental data at the initial time. All three models are seen to give comparable results in good agreement with the experiment. The result of running the simulation with the model turned off is also shown in the same figure. The crucial role played by the model in these simulations is apparent.

This was followed up with a simulation of forced homogeneous isotropic turbulence at infinite Reynolds number using a  $32^3$  grid. The forcing was provided by the simple artifice of resetting the six modes corresponding to  $\mathbf{k} = (\pm 1, \pm 1, \pm 1)$  ( $\mathbf{k}$  is the wavenumber vector) to fixed values at the end of each time-step. The achievement of steady state was monitored by plotting the energy as a function of time and also by looking for time independence in the shape of the spectra. Figure 5A illustrates the extent to which a 'steady-state' was achieved during a run using the DLM(G). Though a plateau was reached in the total energy, some oscillations remained. These could probably be reduced by running the simulation for a longer time, but part of it might be an artefact of the forcing scheme. If a strict Kolmogorov spectrum was achieved, the sgs energy would be

$$k = \int_{\kappa_m}^{\infty} C_{\kappa} \epsilon^{2/3} \kappa^{-5/3} d\kappa = \frac{3}{2} C_{\kappa} \epsilon^{2/3} \kappa_m^{-2/3} \quad (63)$$

where  $\epsilon$  is the dissipation rate,  $\kappa_m$  is the wavenumber magnitude at cutoff, and  $C_{\kappa} \approx 1.5$  is the Kolmogorov constant. In our simulation,  $\kappa_m = 14$  (the number of full energy shells) and  $\epsilon \approx 0.07$ . If these numbers are substituted in (63,) we find  $k \approx 0.03$ . It is reassuring to note that the computed sgs energy (see figure 5A) is within a factor of two of this figure. (Of course, an accurate quantitative prediction of subgrid-scale energy cannot be expected from a large eddy simulation.)

The quantity  $\epsilon^{-2/3} \kappa^{5/3} E(\kappa)$ , where  $E(\kappa)$  is the energy spectrum and  $\epsilon$  is the sgs dissipation, is plotted in figure 5B for runs using each of the three models. No time averaging has been performed, so there is some sampling fluctuations especially at the low wavenumbers. All three models show good agreement with Kolmogorov's law with a Kolmogorov constant close to 1.5. The rising 'tail' in the DLM(G) simulation at high wavenumber appears to be real since the high wavenumber part shows negligible fluctuations among different samples. On the other hand, the DLM(G) appears to give a better plateau at intermediate wavenumbers at a value

very close to  $C_\kappa \approx 1.5$ . Again, this behavior was seen when the simulation was repeated with a different initial spectrum, so the effect is probably real and not just an accidental sampling fluctuation.

The percentage of ‘backscatter’ is shown in figure 5C using two different measures. The solid line is the rate of transfer of energy from the subgrid to supergrid scales (integrated over the volume of the box) as a fraction of the total transfer. The dashed line is the fraction of points engaged in this ‘backscatter’ of energy at a given time. The results on backscatter can be tested using a DNS database of a high Reynolds number simulation of homogeneous turbulence, but this has not been done yet. However, Piomelli *et al.* (1991) found, using a DNS of channel flow at  $Re = 3300$ , that the fraction of backscattered energy is about 10-20 percent while the fraction of backscattering points is about 20-30 percent. These numbers depend on the type of filter used. The figures quoted here are for the ‘box filter’ (see figure 9 in the paper of Piomelli *et al.*) which is what we are using as our ‘test-filter’. Figure 5C is roughly consistent with Piomelli *et al.*’s results. These simulations were repeated using a more refined ( $48^3$ ) mesh. None of the above results were changed in any significant way.

If one has to choose a model for an LES of a complex flow, then, based solely on these tests, the DLM(C) will perhaps be the model of choice since it is the simpler of the two available local models and gives results that are just as good as the more elaborate DLM(G). The extra effort invested in modeling backscatter does not seem to significantly improve predictions of quantities of practical interest. However, in more complex flow situations where backscatter is known to play an important role, the DLM(G) might turn out to be the preferred model. This issue will be settled in the near future as the results of applying these theories to complex flows become available.

### 3. Future plans

It is expected that these ideas will be useful in the near future in the context of the application of the dynamic localization model to LES of complex flows.

An explicit knowledge of the nature of the filtering operation was not needed in the past in sgs modeling. However, all models in the ‘dynamic model’ category rely on an explicit ‘test’ filtering operation (which is supposed to be self-similar to the grid-level filter) to extract useful information about the subgrid scales. Thus, the issue of the commutativity of the filtering and differentiation operations is important not only for providing a firm theoretical basis for LES in complex geometry, but also for practical calculations which make use of the dynamic model.

The DLM should be applied to progressively more challenging flows to evaluate its performance. Faster and more efficient algorithms for solving the relevant integral equations need to be examined.

I would like to thank Dr. Nagi Mansour for providing the basic code that was modified to do some of these tests and for his patient help in teaching the author to use it. I would also like to thank Dr. T. S. Lund for reviewing the manuscript and offering valuable suggestions.

## REFERENCES

- ALDAMA, A. A. 1990 Filtering techniques for turbulent flow simulation. *Lecture notes in engineering, Springer-Verlag*. 56.
- COMTE-BELLOT, G. & CORRSIN, S. 1971 Simple Eulerian time correlation of full and narrow-band velocity signals in grid-generated 'isotropic' turbulence. *J. Fluid Mech.* 48, 273-337.
- GHOSAL, S., LUND, T. S. & MOIN, P. 1993 A local dynamic model for large eddy simulation. *Annual Research Briefs-1992* Center for Turbulence Research, Stanford Univ./NASA Ames, 3-25.
- GHOSAL, S. & MOIN, P. 1993 The basic equations for the large eddy simulation of turbulent flows in complex geometry. *CTR Manuscript 143*.
- LEONARD, A. 1974 Energy cascade in large-eddy simulations of turbulent fluid flows. *Ad. Geophys.* 18 A, 237-248.
- MOIN, P. & KIM, J. 1982 Numerical investigation of turbulent channel flow. *J. Fluid Mech.* 118, 341-377.
- MOIN, P. & KIM, J. 1980 On the numerical solution of time-dependent viscous incompressible fluid flows involving solid boundaries. *J. Comput. Phys.* 35, 381-392.
- MOIN P., REYNOLDS, W. C. & FERZIGER, J. H. 1978 Large eddy simulation of incompressible turbulent channel flow. *Rept. no. TF12*, Dept. of Mech. Engr., Stanford University.
- PIOMELLI, U., CABOT, W. H., MOIN, P. & LEE, S. 1991 Subgrid-scale backscatter in turbulent and transitional flows. *Phys. of Fluids.* 3, 1766-1771.



## Dynamic localization and second-order subgrid-scale models in large eddy simulations of channel flow

By W. Cabot

### 1. Motivation & objectives

The dynamic subgrid-scale (SGS) model (Germano *et al.*, 1991; Lilly, 1992) has been applied successfully in the large eddy simulation (LES) of flows with relatively simple geometry and physics, e.g., in homogeneous flow (Moin, *et al.*, 1991) and in channel flow (Germano *et al.*, 1991; Cabot & Moin, 1993). In these flows a global dynamic coefficient is determined from averages over one or more homogeneous directions, which generally gives well behaved results (i.e., positive eddy viscosities, or, at least, positive net eddy plus molecular viscosities). But for arbitrary, complex geometries, no global homogeneity may exist, precluding this averaging procedure. The dynamic localization (DL) model of Ghosal, Lund & Moin (1993) addresses this problem by fitting *local* dynamic coefficients with a global minimization procedure. However, this model, like all local dynamic SGS models, results in persistent points or regions of negative eddy viscosity that become numerically unstable. Ghosal *et al.* (1993) have proposed to alleviate this problem either (1) by constraining the dynamic coefficient (and eddy viscosity) to be non-negative or (2) by limiting the time that a point can have negative eddy viscosity by evolving an auxiliary equation for the residual SGS kinetic energy  $k$ . When  $k$  is forced to zero by a persistently negative eddy viscosity, the eddy viscosity also vanishes. Both of these procedures with the DL model were found in homogeneous flow to give stable numerics and to give results in good agreement to those using global averaging and to experiments (Ghosal *et al.*, 1993; Ghosal, this volume). The objective here is to test the DL model in a wall-bounded channel flow for numerical stability and accuracy of results.

Algebraic stress models (cf. Gatski & Speziale, 1993) suggest that the model for the residual SGS Reynolds stress and scalar flux should generally have terms comprising most of the unique products of the resolved strain ( $\mathbf{S}$ ) and rotation ( $\mathbf{R}$ ) tensors with  $\mathbf{S}$  and the resolved scalar gradient. The standard dynamic SGS model uses a simple (Smagorinsky) base model for the residual Reynolds stress, which is made proportional to  $\mathbf{S}$ , and down-gradient base models for residual scalar fluxes; these correspond to the lowest, "first-order" terms in algebraic stress models. Temporal scaling terms in these base models are formed from the magnitude of the resolved strain rate. While this is appropriate for simple shear flows, it may not be appropriate for more complicated flows (relevant to geophysical and astrophysical problems) that include any combination of shear, rotation, buoyancy, etc. On the other hand, the coefficient in the dynamic SGS model readily adjusts itself to different flow conditions and may adequately take account of these effects without the need for more complicated base models. Cabot (1993) has begun to test the

dynamic SGS model in buoyant flows (Rayleigh-Bénard and internally heated convection) with and without buoyancy terms explicitly included in the scaling terms of the base model; no great differences were found in LES results for the different base model scalings. The second objective in this work is to test base models with additional, “second-order” terms (e.g.,  $\mathbf{S}^2$  and  $\mathbf{RS}$  for the residual Reynolds stress). These terms have been found to improve large-scale flow predictions by  $k$ - $\epsilon$  models in the presence of rotation and shear (Gatski & Speziale, 1993). Second-order base models will be tested here in the LES of channel flow with and without solid-body rotation and compared with results from the standard first-order base models to determine if there are significant differences or improvements in results that would warrant the added complexity of the second-order base models.

## 2. Accomplishments

### 2.1 Dynamic localization subgrid-scale models in channel flow

#### 2.1.1 The constrained model

The dynamic localization (DL) model was implemented in a pseudospectral channel flow code (cf. Kim, Moin & Moser, 1987). The procedure was tested using a Smagorinsky base model for the trace-free (\*) part of the residual SGS Reynolds stress at the resolved scale (denoted by  $-$ ),

$$\tau_{ij}^* \equiv (\overline{u_i u_j} - \bar{u}_i \bar{u}_j)^* \simeq -2\nu_t \bar{S}_{ij} = -2C\Delta^2 |\bar{S}| \bar{S}_{ij}, \quad (1a)$$

and at a coarser test scale (denoted by  $\hat{\phantom{x}}$ ),

$$T_{ij}^* \equiv (\widehat{\overline{u_i u_j}} - \hat{u}_i \hat{u}_j)^* \simeq -2\hat{\nu}_t \hat{S}_{ij} = -2C\hat{\Delta}^2 |\hat{S}| \hat{S}_{ij}, \quad (1b)$$

where the *local* coefficient  $C(\mathbf{x})$  is constrained to be  $\geq 0$  to ensure numerical stability (model “DL+”). The strain rate tensor  $S_{ij} \equiv (u_{i,j} + u_{j,i})/2$ , and its magnitude  $|S| \equiv (2S_{ij}S_{ij})^{1/2}$ ;  $\Delta$ ,  $\hat{\Delta}$  are the effective filter widths of the resolved and test fields, defined as some average of the grid spacings in each direction. The coefficient  $C$  is solved by the iterative global minimization procedure described by Ghosal *et al.* (1993). By using the coefficient field from the previous time step, only two or three iterations were needed per time step to converge the minimization to acceptable accuracy ( $< 1\%$  error in the  $L^1$  norm); most of the computational expense of the procedure results from the many additional filtering operations that are needed.

Also, because the code is pseudospectral, terms involving the spatially varying eddy viscosity must be computed explicitly, unlike the terms with uniform molecular viscosity, which are computed implicitly. For a plane in the channel, the locally computed dynamic coefficient has extrema about 10 times the plane average. Even in low Reynolds number simulations, this causes the time step to be limited to several times lower than the limit from the convective CFL number.

A low Reynolds number simulation (with friction Reynolds number  $Re_\tau \equiv u_\tau \delta / \nu = 180$ , where  $\delta$  is the channel half-width and the friction velocity  $u_\tau = |\nu dU/dy|^{1/2}$

at the walls for mean streamwise velocity  $U$  and wall-normal direction  $y$ ) was performed for a channel with streamwise, wall-normal, and spanwise dimensions of  $4\pi \times 2 \times 4\pi/3$  (in units of  $\delta$ ) on a  $32 \times 65 \times 32$  grid. Filtering and dynamic minimization was performed only in homogeneous horizontal planes. A localized real-space ("tophat") filter was used that employed a trapezoidal integration over adjacent points. The effective ratio of test to resolved field filter width  $\hat{\Delta}/\Delta$  was taken to be 2 in these simulations, although T. Lund (private communication) later showed that the correct (unidirectional) filter width ratio should be  $\sqrt{6}$  for trapezoidal integration (but 2 for integration with Simpson's rule). The issue of how one properly combines the unidirectional filter width ratios into the effective filter width ratios for non-uniform grids (e.g., Scotti, Meneveau & Lilly, 1993) or for two-dimensional filtering is still not settled.

As found in simulations of homogeneous flow, constraining the dynamic coefficient to be non-negative, while stabilizing the numerics, causes the mean eddy viscosity  $\langle \nu_t \rangle$  from the DL+ model to be about twice that found from the same base model (Eq. [1]) with plane averaging (model "DA1"). (In the interior,  $\langle \nu_t \rangle$  is found to be about half the molecular viscosity  $\nu$  in the DA1 model.) However, the final large-scale statistics (mean streamwise velocity  $U$ , and resolved Reynolds stress  $\langle -\bar{u}\bar{v} \rangle$  and velocity fluctuation intensities  $u_{rms}$ ) are almost indistinguishable between the two cases (see Fig. 1) and are in good agreement with the well resolved direct numerical simulation (DNS) of Kim *et al.* (1987) computed on a  $128 \times 129 \times 128$  grid. The insensitivity in this flow to the SGS model is also a consequence of the small contribution to the total  $\langle uv \rangle$  by the residual SGS component (about 20% very near the wall to  $< 10\%$  in the interior). But note in Figure 1 that a "coarse DNS" (computed at the LES resolution with *no* SGS model) gives quite poor results for  $U$ , which is seen to be about 15% lower than in the well resolved DNS, and equally poor results for resolved turbulence intensities and Reynolds stress are obtained when compared with filtered DNS results. Note that, in general, when  $\nu_t$  is increased in plane-averaged models,  $U$  increases and  $u_{rms}$  decreases.

### 2.1.2 Auxiliary one-equation models

Retaining negative local values of the dynamic coefficient  $C$  requires that their persistence be limited by use of an auxiliary equation for the residual SGS kinetic energy  $k \equiv \tau_{ii}/2$ . When persistent negative eddy viscosities use up all the local SGS kinetic energy, one wants the eddy viscosity to turn off. The base model for the residual SGS Reynolds stress is now given in terms of  $k$  as

$$\tau_{ij}^* \simeq -2\nu_t \bar{S}_{ij} = -2C \Delta k^{1/2} \bar{S}_{ij}, \quad (2a)$$

$$T_{ij}^* \simeq -2\hat{\nu}_t \hat{S}_{ij} = -2C \hat{\Delta} K^{1/2} \hat{S}_{ij}, \quad (2b)$$

where  $K \equiv T_{ii}/2$ . The governing equations for the  $k$  and  $K$  are

$$k_{,t} + (k\bar{u}_i)_{,i} = -\bar{S}_{ij}\tau_{ij}^* - d_{i,i} - \varepsilon + \nu k_{,ii}, \quad (3a)$$

$$K_{,t} + (K\hat{u}_i)_{,i} = -\hat{S}_{ij}T_{ij}^* - D_{i,i} - E + \nu K_{,ii}, \quad (3b)$$

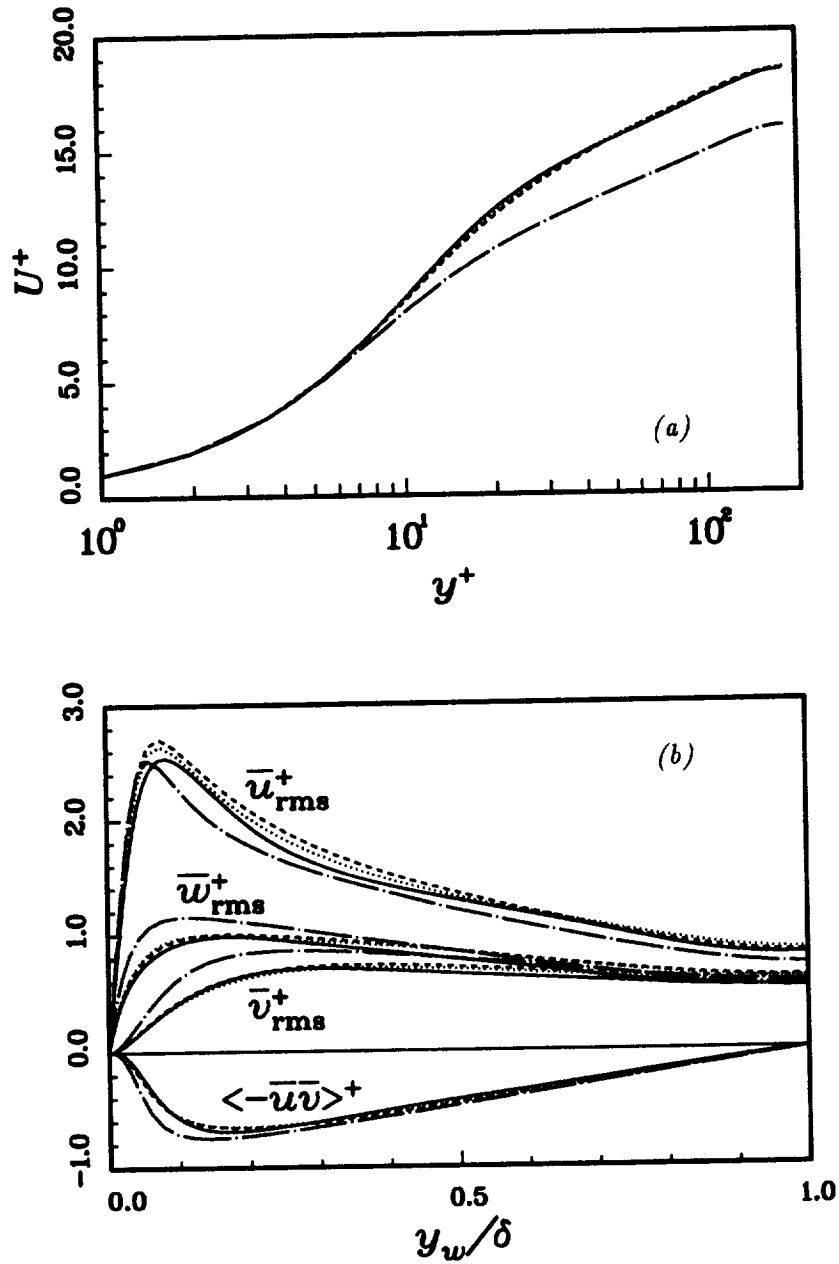


FIGURE 1. (a) Mean streamwise velocity as a function of distance from the wall  $y_w$  (in wall units:  $U^+ = U/u_\tau$ ,  $y^+ = y_w u_\tau / \nu$ ), and (b) resolved rms velocity intensities and Reynolds stress for (—) DNS (Kim *et al.*, 1987), (----) LES with the DA1 model, (-.-.-) coarse DNS, and (.....) LES with the DL+ model. The DNS data are filtered in (b). The first three curves are nearly indistinguishable except for  $u_{rms}$  in (b).

where the residual SGS dissipations,

$$\varepsilon = \nu(\overline{u_{i,j}u_{i,j}} - \bar{u}_{i,j}\bar{u}_{i,j}) \simeq C_\varepsilon k^{3/2}/\Delta, \quad (4a)$$

$$E = \nu(\widehat{u_{i,j}u_{i,j}} - \widehat{u}_{i,j}\widehat{u}_{i,j}) \simeq C_\varepsilon K^{3/2}/\widehat{\Delta}, \quad (4b)$$

and the residual SGS diffusive fluxes,

$$d_i = -(\overline{(p + u_j u_j / 2)u_i} + (\bar{p} + \bar{u}_j \bar{u}_j / 2 + 5k/3)\bar{u}_i + \bar{u}_j \tau_{ji}^*) \simeq C_d \Delta k^{1/2} k_{,i}, \quad (5a)$$

$$D_i = -(\widehat{(p + u_j u_j / 2)u_i} + (\widehat{p} + \widehat{u}_j \widehat{u}_j / 2 + 5K/3)\widehat{u}_i + \widehat{u}_j T_{ji}^*) \simeq C_d \widehat{\Delta} K^{1/2} K_{,i}, \quad (5b)$$

are modeled by analogy with standard  $k$ - $\varepsilon$  models for large scales. In general, the DL procedure is used to determine the local values of  $C$ ,  $C_d$ , and  $C_\varepsilon$  by globally minimizing the residuals of the computable quantities  $\mathcal{L}_{ij} \equiv T_{ij} - \widehat{\tau}_{ij}$ ,  $D_i - \widehat{d}_i$ , and  $E - \widehat{\varepsilon}$  with their model expressions in equations (3–5) above. In this formulation, the pressure field  $\bar{p}$  must be computed and saved at each time step.

An alternative formulation is given by Ghosal *et al.* (1993), who write from equations (3) and (5)

$$(D_j - \widehat{d}_j)_{,j} = [(\mathcal{L}_{ii,i} + \widehat{u}_j \mathcal{L}_{ii,j} - \nu \mathcal{L}_{ii,jj})/2 + \widehat{S}_{ij} T_{ij}^* - \widehat{S}_{ij} \tau_{ij}^*] + (K \widehat{u}_j - \widehat{k} \widehat{u}_j)_{,j}. \quad (6)$$

The non-diffusive terms in the square brackets are incorporated in the expression for  $E - \widehat{\varepsilon}$ , and only the last, remaining terms are used for  $D_j - \widehat{d}_j$ . In this formulation, the terms in (6) with  $\mathcal{L}_{ii} = 2(K - \widehat{k})$  must be computed and saved at each time step. Note that the dynamic coefficients from either formulation are Galilean invariant. At this time it is not known how this rearrangement of terms affects the model coefficients in channel flow applications. However, S. Ghosal (private communication) has pointed out that the formulation of the residual dissipation used here, unlike that of Ghosal *et al.* (1993), has the unphysical property of vanishing in the high Reynolds number limit ( $\nu \rightarrow 0$ ).

A low Reynolds number LES (with the same setup and parameters as described in the previous subsection) was initiated using this (“DLk”) model. All terms in (3a), except the molecular viscosity term, are integrated explicitly in the numerical code. For real space filters,  $k$  and  $\varepsilon$  are positive semi-definite by definition. In the DL procedure,  $C_\varepsilon$  is therefore constrained to be non-negative. For points where diffusion occasionally causes  $k$  to become negative, an artificial source term is substituted for the right-hand side of (3a) to drive the point to zero at the next time step, and the eddy viscosity is taken to be zero. Although there is no direct constraint on the sign of  $C_d$ , in most cases it is also constrained to be non-negative in order to ensure the realizability of  $k$ . However, its unconstrained interior values were found to be almost 50% negative with no preferred sign in the mean, so that the mean constrained diffusive eddy viscosity  $\langle C_d \Delta k^{1/2} \rangle \sim 20\nu$  is probably greatly overestimated. Near the wall, the unconstrained values of  $C_d$  are finite, but small,

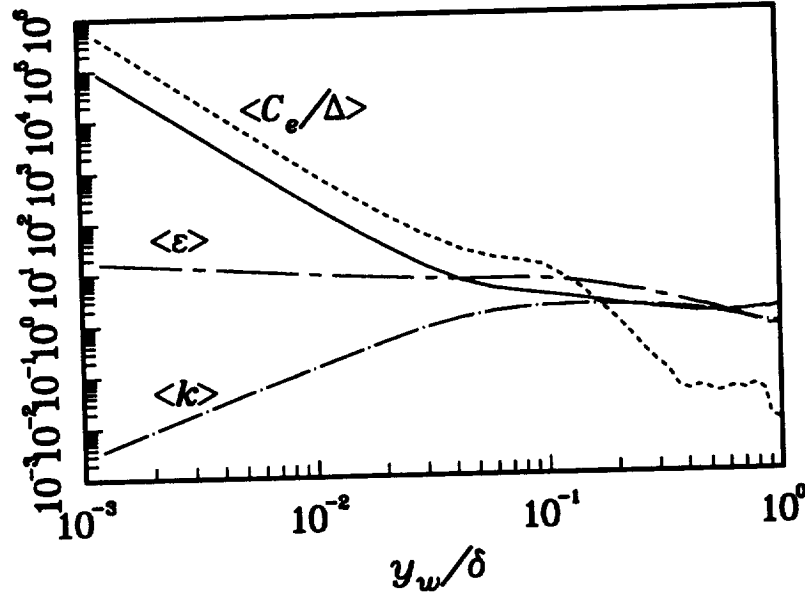


FIGURE 2. Near-wall behavior of the mean dynamic dissipation coefficient for the  $k$ -equation in channel flow using ( — )  $\Delta_e$  and ( ---- )  $\Delta$  as the effective filter width. Also the mean residual SGS dissipation rate,  $\langle \varepsilon \rangle = \langle C_e k^{3/2} / \Delta_e \rangle$ , and  $\langle k \rangle$ .

and almost entirely positive. It will be interesting to compare the results using Ghosal *et al.*'s (1993) alternative expression for  $C_d$ .

At first, the filter width ratios  $\hat{\Delta}/\Delta$  for equations (2), (4), and (5) were assumed to be all the same. It was found, however, that constrained  $C_e$  from the DLk model became largely (90%) zero near centerline in the flow, giving very small values of  $\langle \varepsilon \rangle$  there. An alternative definition for effective filter width was tried for  $C_e$  (by analogy with wavenumbers) as the harmonic mean of the unidirectional filter widths,  $\Delta_e^{-2} = \sum_i \Delta_i^{-2}$ ; this causes the effective filter width ratio  $\hat{\Delta}_e/\Delta_e$  to be nearly unity (due to the small grid spacing in the wall-normal direction, for which no explicit filtering occurs) instead of 2. This results in very few zero points and a mean value of  $C_e$  that varies smoothly throughout the channel. A comparison of  $C_e/\Delta$  and  $C_e/\Delta_e$  is shown in Figure 2. In both cases,  $C_e/\Delta_{(e)}$  approaches the wall as nearly  $y_w^{-3}$ , where  $y_w$  is the normal distance from the wall. This nearly balances the approximate (but slightly sub-)  $y_w^3$  behavior of  $k^{3/2}$  near the wall so that  $\langle \varepsilon \rangle$  rises relatively slowly near the wall. Note that the near- $y_w^2$  behavior of  $k$  found at the wall is not guaranteed by the differential equations, which only require that  $k$  vanish linearly at the walls.

The extremely rapid rise of  $C_e/\Delta_e$  at the wall leads to severe time step constraints since the dissipation term is integrated explicitly and the CFL number  $(C_e k^{1/2} / \Delta_e)_{\max} \delta t$  goes as  $y_w^{-2}$  near the wall. The time step  $\delta t$  must be reduced by more than 100 times that used for the standard DA1 model. This makes the use

of the DLk model prohibitively expensive unless one can perform the integration of the  $\varepsilon$ -term in (3a) implicitly. This can be accomplished with a finite-difference channel code, which is presently being developed.

In fact, statistics have not been generated for this LES due to its great computational expense. However, instantaneous large-scale statistics look quite good (see Fig. 3) for this model. The mean eddy viscosity was found to be about twice that from the plane-averaged dynamic SGS model. Nevertheless, its prediction of the near-wall streamwise velocity fluctuation intensity (Fig. 3b) appears to be somewhat better than from the plane-averaged SGS model. The value of the residual SGS kinetic energy  $k$  can be compared with that computed from the residual of a well resolved DNS field (Kim *et al.*, 1987) when filtered to the LES scale. This is shown in Figure 4, where it is seen that  $k$  from the DLk model is generally about twice the actual value in the interior, but dips inappropriately near the wall below DNS values. Note, however, that neither is the SGS model expected to give an accurate prediction of  $k$ , nor should the incompressible LES be particularly sensitive to the exact value of  $k$ , since it acts only as a scaling term in the eddy viscosity.

Another version of the one-equation DL model has been considered in which  $q = (\tau_{ii})^{1/2} = (2k)^{1/2}$  is used in the auxiliary equation. This ("DLq") model was originally proposed by Cabot (1993) to ensure the exact  $k \propto y_w^2$  behavior near the wall. (It has been found, meanwhile, that this behavior is approximated reasonably well using the DLk model.) Equation (3a) governing  $k$  becomes

$$q[q, t + (q\bar{u}_i), i] = 2c\Delta q|\bar{S}|^2 - q[(c_d\Delta q + \nu)q, i], i + (c_d\Delta q + \nu)(q, i q, i) - \varepsilon, \quad (7)$$

where factors of  $2^{1/2}$  have been absorbed in the new dynamic coefficients,  $c$  and  $c_d$ . One cannot divide through by  $q$  in (7) because of the term  $\nu(q, i q, i)$ . However, the combination  $\varepsilon' = \varepsilon - \nu(q, i q, i)$  vanishes as  $y_w^2$  at the wall, so that  $\varepsilon'/q$  vanished linearly there and can be modeled by  $c_e q^2/\Delta_e$ . Dividing (7) through by  $q$  now gives

$$q, t + (q\bar{u}_i), i = 2c\Delta|\bar{S}|^2 - [(c_d\Delta q + \nu)q, i], i + c_d\Delta(q, i q, i) - c_e q^2/\Delta_e. \quad (8)$$

While this equation is good in exhibiting no extreme near-wall behavior in any of its terms and guaranteeing the right wall behavior of  $k$ , it also presents some problems, mathematically and in implementation. When  $q \rightarrow 0^+$ , the first term on the right-hand side of (8) can remain finite (positive or negative) whereas it vanishes in (3a). This mathematical point still needs to be resolved.

Determining the coefficient  $c_e$  from  $\varepsilon' = \varepsilon - \nu(q, i q, i)$  with the DL procedure has proved unsuccessful because  $\varepsilon$  (depending on  $\bar{u}_i$ ) and the term in  $q$  (an independent variable) do not precisely balance near the wall, causing  $c_e/\Delta_e \rightarrow y_w^{-3}$  again, instead of  $y_w^{-1}$ . A suitable proxy to  $\varepsilon'$  for computing  $c_e$  with both the right wall and interior behavior has not been found. A low Reynolds number LES was performed with completely *ad hoc* models of  $c_d\Delta = \max(0.032\Delta_d, 0.4\nu/u_\tau)$  and  $c_e/\Delta_e = 0.4/\Delta_d$ , where  $\Delta_d^{-1} = \Delta^{-1} + 0.4y_w^{-1}$ . The choice of numerical coefficients can be chosen to give fair agreement with  $k = q^2/2$  computed from the DNS; in Figure 4, it is seen that this particular guess gave values of  $k$  about half those from DNS. The

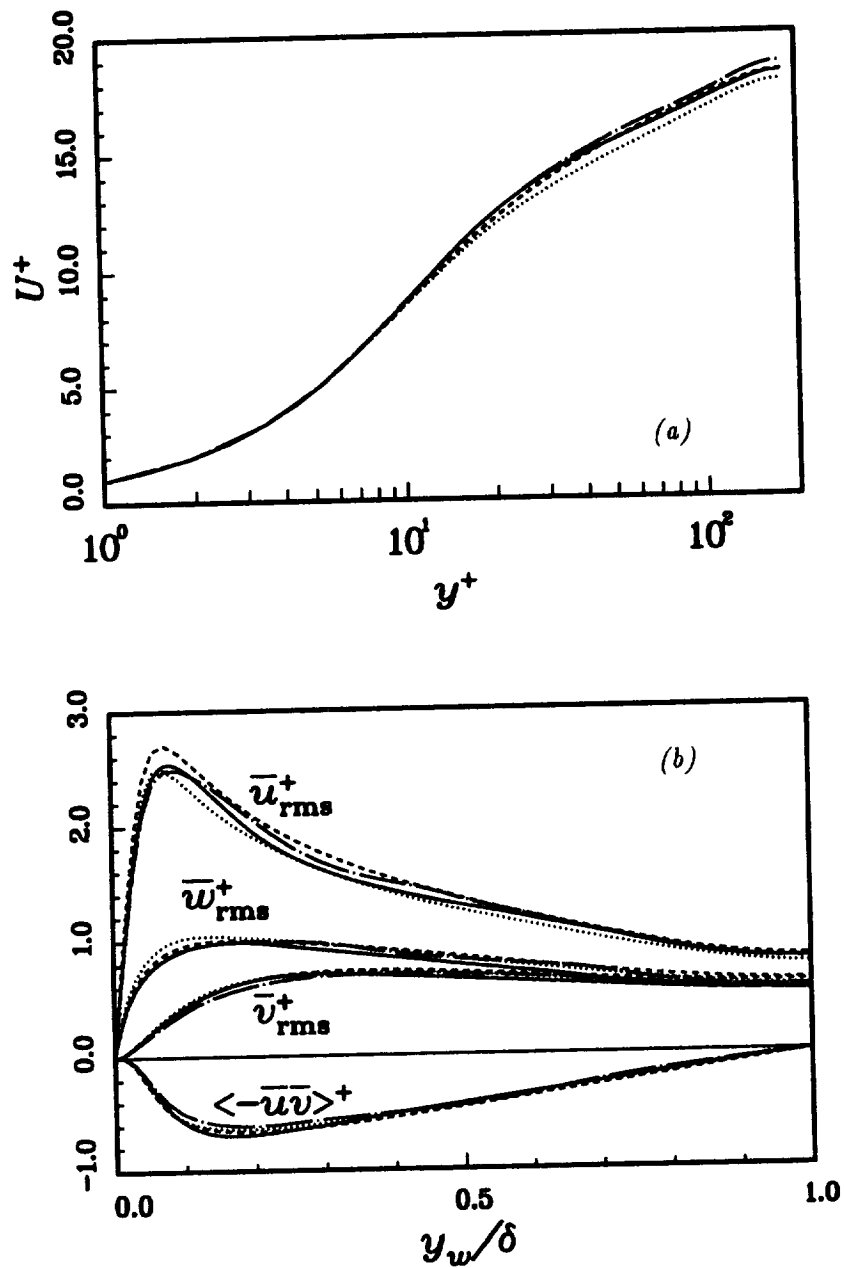


FIGURE 3. (a) Mean streamwise velocity as a function of distance from the wall (in wall units), and (b) resolved rms velocity intensities and Reynolds stress for (—) DNS (Kim *et al.*, 1987), (----) LES with the DA1 model, (-.-) LES with the DLk model (from an instantaneous field), and (.....) LES with the (*ad hoc*) DLq model. The DNS data are filtered in (b).



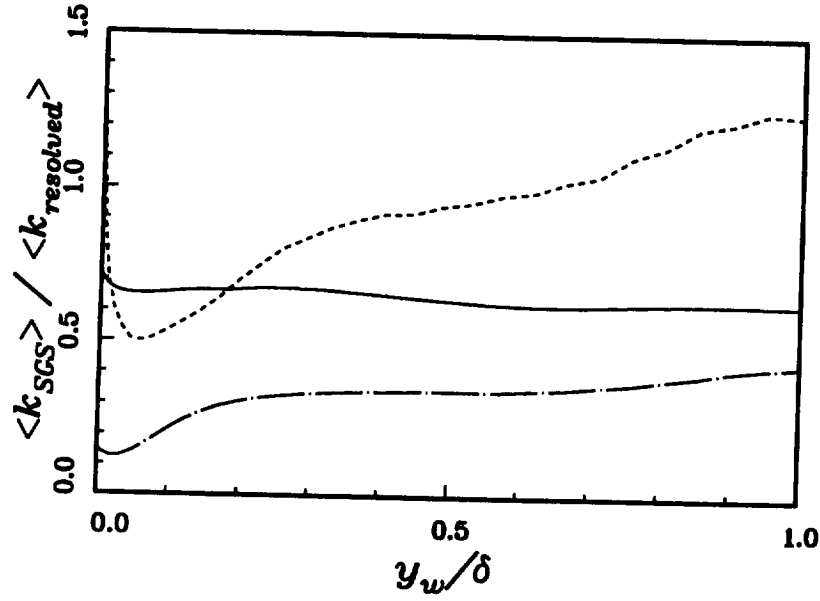


FIGURE 4. The ratio of mean residual SGS kinetic energy to mean resolved kinetic energy computed from ( — ) DNS, and predicted by ( ---- ) the DLk model and ( - · - ) the *ad hoc* DLq model.

inappropriate dip near the wall also generally occurs for  $q$  as it did for  $k$  from the DLk model. The simulation was found to be numerically stable and to give about as good agreement with the DNS results as with other SGS models (see Fig. 3). The mean eddy viscosity is found to be slightly lower than from the DLk model, about 80% larger than from the plane-averaged DA1 model.

## 2.2 Second-order dynamic subgrid-scale models in channel flow

In LES of channel flow with the plane-averaged dynamic SGS model, a second-order base model ("DA2") has been used instead of equation (1) (model "DA1"), having the form

$$\tau_{ij} \simeq -2C_1\Delta^2|\bar{S}|\bar{S}_{ij} + 2C_2\Delta^2[\bar{A}_{ik}\bar{S}_{kj} + \bar{A}_{jk}\bar{S}_{ki} - 2\bar{S}_{ij}\text{Tr}(\bar{S}^3)/\text{Tr}(\bar{S}^2)], \quad (9)$$

and for the residual SGS flux  $h_i$  for a passive scalar  $\theta$ ,

$$h_i = \bar{\theta}u_i - \bar{\theta}\bar{u}_i \simeq -C_{\theta 1}\Delta^2|\bar{S}|\bar{\theta}_{,i} + 2C_{\theta 2}\Delta^2[\bar{A}_{ik}\bar{\theta}_{,k} - \bar{\theta}_{,i}(\nabla\bar{\theta} \cdot \bar{S} \cdot \nabla\bar{\theta})/(\nabla\bar{\theta} \cdot \nabla\bar{\theta})], \quad (10)$$

The tensor  $A_{ij}$  is defined

$$A_{ij} \equiv S_{ij} + a_1 R_{ij}, \quad R_{ij} \equiv (u_{i,j} - u_{j,i})/2 - 2\Omega_k a_2 \epsilon_{ijk}, \quad (11)$$

where  $\Omega_k$  is the system rotation. The lattermost terms in the square brackets in (9) and (10) are included to make the second terms in the model orthogonal to the

first and hence dissipation-free. In practice, the trace is also generally subtracted from (9). This general form is suggested by lowest-order solutions of algebraic stress models (cf. Gatski & Speziale, 1993). The prescribed constants,  $a_1$  and  $a_2$ , depend on one's favorite model coefficients; e.g., for the second-order model derived by Gatski & Speziale,  $a_1 \approx 1-3$  and  $a_2 \approx 1-2$  for commonly used  $k-\epsilon$  model constants. This type of large-scale Reynolds stress model has been shown to perform well in flows with rapid solid-body rotation and shear (Speziale, Sarkar & Gatski, 1991).

In initial tests, the more general second-order model was used for (9), in which strain-strain terms ( $\mathbf{S}^2$ ) and rotation-strain terms ( $\mathbf{RS}$ ) are kept separate in the dynamic procedure,

$$\begin{aligned} \tau_{ij} \simeq & -2C_1\Delta^2|\bar{\mathbf{S}}|\bar{S}_{ij} + 2C_2\Delta^2(\bar{R}_{ik}\bar{S}_{kj} - \bar{S}_{ik}\bar{R}_{kj}) \\ & + 2C_3\Delta^2[2\bar{S}_{ik}\bar{S}_{kj} - 2\bar{S}_{ij}\text{Tr}(\bar{\mathbf{S}}^3)/\text{Tr}(\bar{\mathbf{S}}^2)]. \end{aligned} \quad (12)$$

It is found that  $C_3$  predicted by the dynamic procedure in channel flow (with  $\Omega_k = 0$ ) is typically about half  $C_2$  and comparable to  $C_1$  (see Fig. 5a), suggesting that the  $\mathbf{RS}$  term may be more important than the  $\mathbf{S}^2$  term. Meneveau, Lund & Moin (1992) and Lund & Novikov (1993) also found that, of all the unique products of  $\mathbf{S}$  and  $\mathbf{R}$  (including  $\mathbf{S}$  by itself), the  $\mathbf{RS}$  term was the most highly correlated with  $\tau_{ij}$  computed from DNS channel flow fields. Another interesting note is that these second-order base models for  $\tau_{ij}$  in either (9) or (12) *with the trace retained* and for  $h_i$  in (10) give the correct (no-slip, fixed scalar) near-wall behavior for *all* of their components (since  $C_1\Delta^2, C_{\theta 1}\Delta^2 \propto y_w^3$  but  $C_{2,3}\Delta^2, C_{\theta 2}\Delta^2 \propto y_w^2$ ), which was not the case using only the first terms. The trace of either (9) or (12) also returns the model for the residual SGS kinetic energy used by Moin *et al.* (1991) for LES of compressible flow.

The simultaneous solution of three coefficients in (12) is much more expensive than the two in (9) because many more filtering operations need to be performed, so it was decided to use (9) and (10) in the actual LES of low Reynolds number channel flow (with the same setup and parameters described in the previous subsection). The constants  $a_1$  and  $a_2$  were simply taken as unity (even though  $a_1 \approx 2$  is suggested by Fig. 5a). The values of the coefficients returned by the dynamic procedure are shown in Figure 5b: in the interior of the channel we see that  $C_2 \approx 2C_1$  and that  $C_{\theta 2} \approx C_{\theta 1} \approx C_2$  for  $Pr = 0.71$ . Large-scale statistics from the LES of channel flow using the DA2 model are compared in Figure 6 with those from LES using the DA1 model and from DNS. The mean eddy viscosity from the DA2 model ( $\langle C_1\Delta^2|\bar{\mathbf{S}}| \rangle$ ) is found to be nearly the same as that from the DA1 model (about half that of molecular in the interior). And there is not a great deal of difference between the LES results using first- or second-order SGS base models, except that the agreement of resolved  $u_{rms}$  (and thus the resolved kinetic energy) with that from the DNS is somewhat better for the second-order base model, while the mean streamwise velocity is slightly lower like the results using the DLq model (cf. Fig. 3).

The DA2 model was then tested in LES of channel flow rotating about its spanwise axis, which stabilizes the upper wall and destabilizes the lower wall (cf. review by

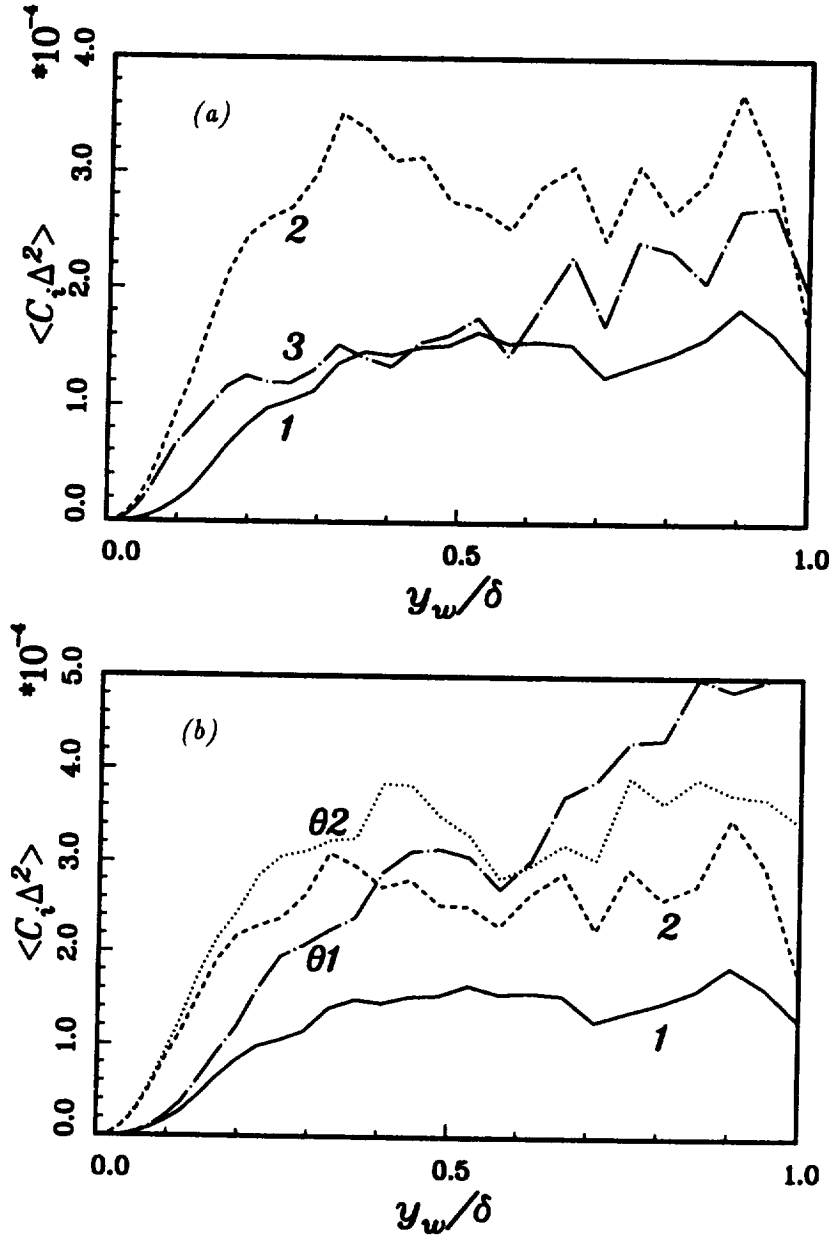


FIGURE 5. Mean dynamic coefficients in channel flow for the second-order base model (a) in Eq. (12), and (b) in Eqs. (9) and (10).

Moin & Jimenez, 1993). Again, the standard low Reynolds number case was used (corresponding to a mass-flux Reynolds number  $Re_m \equiv 2U_m\delta/\nu \equiv \int_{-\delta}^{\delta} U dy/\nu \approx 5,400$ ) and for a higher Reynolds number ( $Re_m \approx 12,000$ ) in a  $3\pi \times 2 \times \pi$  box (in units of  $\delta$ ). The rotation rates in mass-flux units were  $Ro_m \equiv 2\Omega\delta/U_m \approx 0.21$ . A

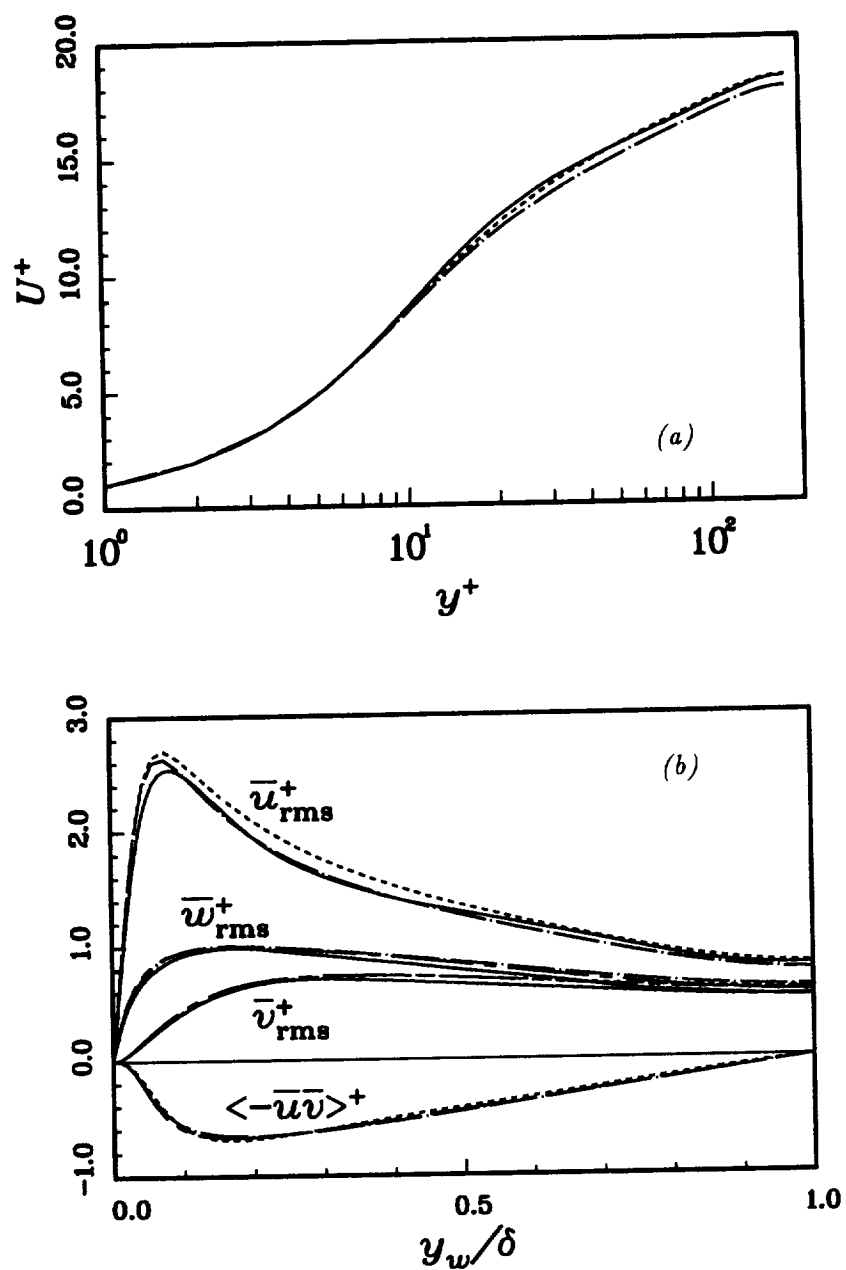


FIGURE 6. (a) Mean streamwise velocity as a function of distance from the wall (in wall units), and (b) resolved rms velocity intensities and Reynolds stress for ( — ) DNS (Kim *et al.*, 1987), and for LES with ( ---- ) the DA1 model and ( -.- ) the DA2 model. The DNS data are filtered in (b).

Case	SGS model	$\hat{\Delta}/\Delta$	$Re_m$	$Ro_m$	$u_{\tau 1}/u_{\tau}$	$u_{\tau 2}/u_{\tau}$
1	1st order (DA1)	2	5,443	0.217	1.19	0.76
2	2nd order (DA2)	2	5,432	0.218	1.19	0.76
3	1st order (DA1)	2	12,150	0.202	1.16	0.81
4	2nd order (DA2)	2	12,035	0.204	1.15	0.82
5	2nd order (DA2)	$\sqrt{6}$	11,685	0.210	1.14	0.83

TABLE 1. LES of rotating channel flow for different SGS base models:  $u_{\tau 1}$  and  $u_{\tau 2}$  are the friction speeds at the upper and lower walls, and  $u_{\tau}^2 = (u_{\tau 1}^2 + u_{\tau 2}^2)/2$ .

better resolved LES at the higher  $Re_m$  was performed in a  $4\pi \times 2 \times \pi$  box on a  $48 \times 65 \times 32$  grid. This LES also used the correct effective filter width ratio of  $\sqrt{6}$  for physical space filtering with integration by trapezoidal rule, instead of the value of 2 used in the rest of LES reported here. It did not give appreciably different results. The parameters and resulting asymmetry of the friction speeds measured at the two walls are summarized in Table 1. The results agree quite well with LES results of Squires & Piomelli (1994), who used the standard DA1 model. The asymmetry in the friction speeds induced by the rotation is seen to be almost independent of  $Re_m$ , although the overall asymmetry in the mean streamwise velocity profiles (Fig. 7a) is a little more pronounced. There is again virtually no differences in large-scale statistics using the DA1 as opposed to the DA2 models. About the only noticeable difference is in the shape of the mean residual SGS Reynolds stress  $\langle \tau_{12} \rangle$  (Fig. 7b): for the DA2 models it is larger in the interior of the flow and less concentrated at the lower, rotationally unstable wall than for the DA1 models. However,  $\langle \tau_{12} \rangle$  is still an order of magnitude less than the resolved Reynolds stress here, which is in part why the large-scale flow is rather insensitive to these differences.

### 3. Future plans

The dynamic localization model will be implemented in a finite-difference channel code. Terms in the auxiliary governing equation for the residual SGS kinetic energy that are large in near-wall region will be integrated implicitly with much larger time steps than possible with the explicit integration required in the pseudospectral code. This will allow us to generate steady-state statistics in channel flow LES and perform more extensive tests for this local dynamic SGS model.

Second-order base models for the plane-averaged dynamic SGS model will be tested in the LES of uniformly and differentially rotating thermal convection including additional buoyancy terms as suggested by algebraic stress models (cf. Schumann, 1991), and the results will be compared with previous DNS results (Cabot *et al.*, 1990; Cabot & Pollack, 1992) and those from LES performed with the first-order (Smagorinsky) base model. We will again attempt to determine whether the added complexity and computational expense of higher-order, more sophisticated base models is needed in more physically complicated flows or, as it appears so far, that the self-adjusting nature of the dynamic procedure allows one to obtain the same result with simple, relatively inexpensive base models.

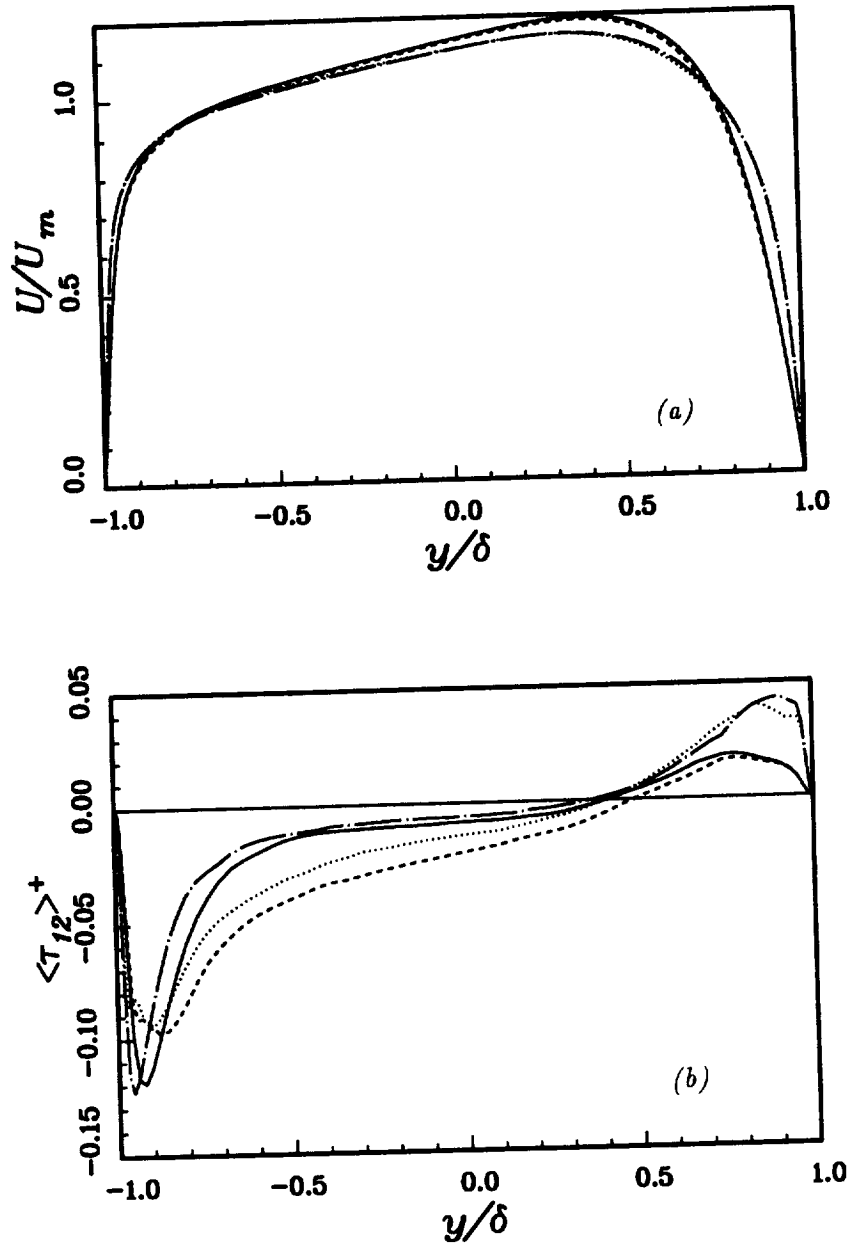


FIGURE 7. The asymmetric vertical distribution of (a) mean streamwise velocity and (b) mean residual SGS Reynolds stress in the LES of rotating channel flow with  $Re_m \approx 5,400$  and  $12,000$  and using the DA1 model ( — , case 1; — — , case 3) and, hardly distinguishable in (a), the DA2 model ( - - - - , case 2; ····· , case 4) (see Table 1).

## REFERENCES

- CABOT, W. 1993 Large eddy simulations of time-dependent and buoyancy-driven channel flows. In *CTR Annual Research Briefs 1992*, Center for Turbulence Research, Stanford Univ./NASA Ames Research Center, 45–60.
- CABOT, W., HUBICKYJ, O., POLLACK, J. B., CASSEN, P., & CANUTO, V. M. 1990 Direct numerical simulations of turbulent convection: I. Variable gravity and uniform rotation. *Geophys. Astrophys. Fluid Dyn.* **53**, 1–42.
- CABOT, W., & MOIN, P. 1993 Large eddy simulation of scalar transport with the dynamic subgrid-scale model. In *Large Eddy Simulation of Complex Engineering and Geophysical Flows*, ed. B. Galperin & S. A. Orszag (Cambridge Univ. Press), ch. 7.
- CABOT, W., & POLLACK, J. B. 1992 Direct numerical simulations of turbulent convection: II. Variable gravity and differential rotation. *Geophys. Astrophys. Fluid Dyn.* **64**, 97–133.
- GATSKI, T. B., & SPEZIALE, C. G. 1993 On explicit algebraic stress models for complex turbulent flows. *J. Fluid Mech.* **254**, 59–78.
- GERMANO, M., PIOMELLI, U., MOIN, P., & CABOT, W. H. 1991 A dynamic subgrid-scale eddy viscosity model. *Phys. Fluids A*, **3**, 1760–1765.
- GHOSAL, S., LUND, T. S., & MOIN, P. 1993 A local dynamic model for large eddy simulation. In *CTR Annual Research Briefs 1992*, Center for Turbulence Research, Stanford Univ./NASA Ames Research Center, 3–25.
- KIM, J., MOIN, P., & MOSER, R. 1987 Turbulence statistics in fully developed channel flow at low Reynolds number. *J. Fluid Mech.* **177**, 133–166.
- LILLY, D. 1992 A proposed modification of the Germano subgrid-scale closure method. *Phys. Fluids A*, **4**, 633–635.
- LUND, T. S., & NOVIKOV, E. A. 1993 Parameterization of subgrid-scale stress by the velocity gradient tensor. In *CTR Annual Research Briefs 1992*, Center for Turbulence Research, Stanford Univ./NASA Ames Research Center, 27–43.
- MENEVEAU, C., LUND, T. S., & MOIN, P. 1992 Search for subgrid scale parameterization by projection pursuit regression. In *CTR Proceedings of the Summer Program 1992*, Center for Turbulence Research, Stanford Univ./NASA Ames Research Center, 61–81.
- MOIN, P., & JIMENÉZ, J. 1993 Large eddy simulation of complex turbulent flows, *AIAA-93-3099*, 24th Fluid Dyn. Conf., Orlando, Florida.
- MOIN, P., SQUIRES, K., CABOT, W., & LEE, S. 1991 A dynamic subgrid-scale model for compressible turbulence and scalar transport. *Phys. Fluids A*, **3**, 2746–2757.
- SCHUMANN, U. 1991 Subgrid length-scales for large-eddy simulation of stratified turbulence. *Theoret. Comput. Fluid Dyn.* **2**, 279–290.

- SCOTTI, A., MENEVEAU, C., & LILLY, D. K. 1993 Generalized Smagorinsky model for anisotropic grids. *Phys. Fluids A*. **5**, 2306–2308.
- SPEZIALE, C. G., SARKAR, S., & GATSKI, T. B. 1991 Modelling the pressure-strain correlation of turbulence: an invariant dynamical systems approach. *J. Fluid Mech.* **227**, 245–272.
- SQUIRES, K. D., & PIOMELLI, U. 1994 Dynamic modeling of rotating turbulence. In *Turbulent Shear Flows 9*, ed. F. Durst, N. Kasagi, B. E. Launder, F. W. Schmidt & J. H. Whitelaw (Springer-Verlag, Heidelberg), in press.



70-02  
20/02  
p. 5 145  
N94-24150

## Toward large eddy simulation of turbulent flow over an airfoil

By Haechon Choi<sup>1</sup>

### 1. Motivation and objectives

The flow field over an airfoil contains several distinct flow characteristics, e.g. laminar, transitional, turbulent boundary layer flow, flow separation, unstable free-shear layers, and a wake. This diversity of flow regimes taxes the presently available Reynolds averaged turbulence models. Such models are generally tuned to predict a particular flow regime, and adjustments are necessary for the prediction of a different flow regime. Similar difficulties are likely to emerge when the large eddy simulation technique is applied with the widely used Smagorinsky model. This model has not been successful in correctly representing different turbulent flow fields with a single universal constant and has an incorrect near-wall behavior.

Germano *et al.* (1991) and Ghosal, Lund & Moin (1992) have developed a new subgrid-scale model, the *dynamic* model, which is very promising in alleviating many of the persistent inadequacies of the Smagorinsky model: the model coefficient is computed dynamically as the calculation progresses rather than input *a priori*. The model has been remarkably successful in prediction of several turbulent and transitional flows.

We plan to simulate turbulent flow over a "2D" airfoil using the large eddy simulation technique. Our primary objective is to assess the performance of the newly developed dynamic subgrid-scale model for computation of complex flows about aircraft components and to compare the results with those obtained using the Reynolds average approach and experiments. The present computation represents the first application of large eddy simulation to a flow of aeronautical interest and a key demonstration of the capabilities of the large eddy simulation technique.

### 2. Accomplishments

#### 2.1 Code modification

For the simulation of the flow over an airfoil, we have modified the direct numerical simulation code of Choi, Moin & Kim (1993), which was successfully applied to simulation of turbulent flow over longitudinal riblets. The code uses generalized coordinates in two dimensions and a Cartesian coordinate in the third direction. The code is based on the unsteady, three-dimensional, incompressible Navier-Stokes equations along with the equation of continuity. The fully implicit time integration scheme, which uses an approximate factorization method in conjunction with Newton-iterative scheme, allows rather large time-steps and, therefore, reduces the

<sup>1</sup> Present address: Seoul National University, Korea

computational effort for solving the Poisson equation. The code makes use of a multi-grid method in order to accelerate the convergence rate of the Poisson solver.

The convective outflow boundary condition is used at the flow exit, and the unsteady "turbulent" inflow condition is similar to that developed by Lee *et al.* (1992). No-stress or uniform velocity boundary conditions are applied at far-field boundaries far from the airfoil surface. Periodic boundary condition is used in the spanwise direction. Arbitrary velocity boundary condition on the surface of the airfoil is also incorporated in the code for future flow control applications.

The *C*-type mesh configuration is used in this study (Thompson *et al.* 1985). This grid is better than the *O*-type grid for flows with massive separation because the wake region after bluff bodies can be more adequately resolved with the *C*-type grid. The boundary condition along the branch-cut in the *C*-type grid is treated *implicitly*, i.e. periodic boundary conditions are applied along the branch cut, which makes the code significantly more complicated. The commonly used *explicit* interpolation technique using adjacent grids near the branch cut deteriorates the time accuracy due to the time-lagging nature of the explicit method. However, the implicit boundary condition along the branch cut used in this study maintains the overall time accuracy. The use of explicit interpolation method along the branch cut does not accurately predict the Strouhal number for the flow over a cylinder, while the implicit boundary condition predicts the Strouhal number very well compared with the experimental results (see section 2.2).

The development of the dynamic subgrid-scale model (Germano *et al.* 1991; Ghosal, Lund & Moin 1992) is the key inducement for the undertaking of the present computation. The dynamic subgrid-scale model is incorporated in the code (in generalized coordinates).

## 2.2 Code verification

In order to verify the code, we first applied it to the laminar flow over a circular cylinder at the Reynolds number,  $Re = u_\infty d / \nu = 100$ , where  $u_\infty$  is the upstream velocity,  $d$  is the cylinder diameter, and  $\nu$  is the kinematic viscosity. At this Reynolds number, the flow is periodic, and experimental data are available for comparison.

The flow domain and grid system are shown in figure 1. The flow domain covers about 25 and 20 cylinder diameters in the streamwise and normal directions, respectively. A uniform velocity field,  $u = u_\infty$  and  $v = 0$ , is prescribed at  $t = 0$ . Here,  $u$  and  $v$  are the velocity components in the streamwise ( $x$ ) and normal ( $y$ ) directions, respectively. An initial random disturbance with magnitude of  $0.01u_\infty$  is imposed at the flow field in order to induce vortex shedding behind the cylinder.

Figure 2 shows the time history of the streamwise velocity at several points behind the cylinder. After a transient period ( $tu_\infty/d \approx 0 \sim 100$ ), the flow behind the cylinder shows a periodic behavior. The Strouhal number is calculated from figure 2,  $S = d/(Tu_\infty) = 0.163$ , where  $T$  denotes the period of the flow oscillation. This result is in a very close agreement with the experimental result by Williamson (1989), where  $S = 0.164$  (see figure 3).

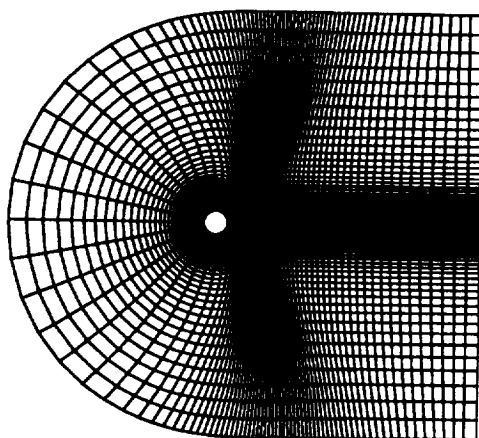


FIGURE 1. Computational domain and grid system. The *C*-type mesh configuration is used for flow over a cylinder. The branch cut is located along the centerline of the cylinder wake.

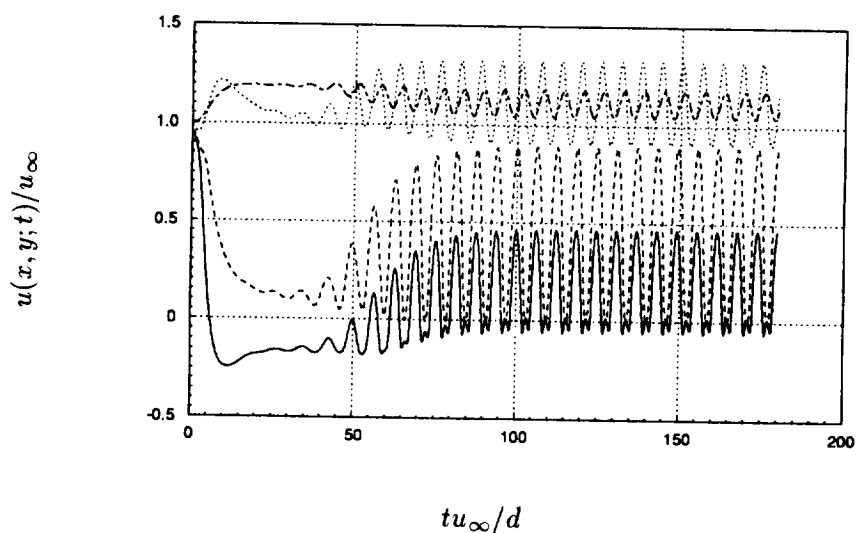


FIGURE 2. Time history of the streamwise velocity at several points ( $x = 2.4d$ ) behind the cylinder: —,  $y = -0.21d$ ; ----,  $y = -0.52d$ ; ·····,  $y = -1.1d$ ; — · —,  $y = -2.1d$ . Here, the position  $x = y = 0$  corresponds to the center of the cylinder.

It is interesting to note that the periodic behavior behind the cylinder was not found when an explicit interpolation method using adjacent points was used as

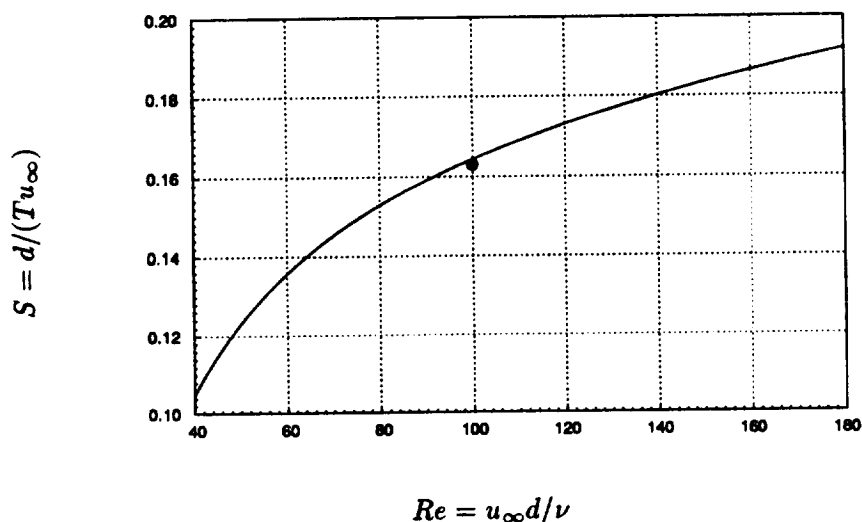


FIGURE 3. Variation of  $S$  with  $Re$ : —, the least square curve fit from Williamson (1989),  $S = A/Re + B + CRe$ , where  $A = -3.3265$ ,  $B = 0.1816$ ,  $C = 1.6 \times 10^{-4}$ ; •, the present calculation.

the branch-cut boundary condition. It turns out that the use of the explicit interpolation method along the branch cut indirectly prescribes zero pressure-gradient across the branch cut. Apparently, the absence of oscillating pressure force across the branch cut precludes vortex generation behind the cylinder.

### 3. Future plans

Future research plan includes two phases.

*Phase 1:* Laminar test cases will be computed and compared with experimental results. We will also compare laminar flow solutions of the NACA 0012 airfoil with those of a flat-plate airfoil for non-zero angles of attack in order to investigate the effect of the finite thickness of the airfoil on laminar separation characteristics.

*Phase 2:* We will first simulate turbulent flow over an airfoil with zero angle of attack using the dynamic subgrid-scale model and compare the solution with experimental results and with those by Reynolds averaged turbulence closure models. The angle of attack for maximum lift (or for maximum lift-drag ratio) will be considered subsequently.

### REFERENCES

- CHOI, H., MOIN, P. & KIM, J. 1993 Direct numerical simulation of turbulent flow over riblets. *J. Fluid Mech.* **255**, 503.

- GERMANO, M., PIOMELLI, U., MOIN, P. & CABOT, W. H. 1991 A dynamic subgrid-scale eddy viscosity model. *Phys. Fluids A* **3**, 1760.
- GHOSAL, S., LUND, T. S. & MOIN, P. 1992 A dynamical localization model for large eddy simulation of turbulent flows. *CTR Manuscript 199*. Center for Turbulence Research, Stanford U./NASA Ames.
- LEE, S., LELE, S. & MOIN, P. 1992 Simulation of spatially evolving turbulence and the application of Taylor's hypothesis in compressible flows. *Phys. Fluids A* **4**, 1512.
- THOMPSON, J. F., WARSI, Z. U. A. & MASTIN, C. W. 1985 *Numerical Grid Generation - Foundations and Applications*. Elsevier Science Publishing Co., New York.
- WILLIAMSON, C. H. K. 1989 Oblique and parallel modes of vortex shedding in the wake of a circular cylinder at low Reynolds number. *J. Fluid Mech.* **206**, 579.



913-34  
201653  
6 151  
N94-24151

## Unstructured grid large eddy simulation of wall bounded turbulent flows

By Kenneth Jansen

### 1. Motivation and objectives

Historically, large eddy simulations (LES) have been restricted to simple geometries where spectral or finite difference methods have dominated due to their efficient use of structured grids. Structured grids, however, not only have difficulty representing complex domains and adapting to complicated flow features, but also are rather inefficient for simulating flows at high Reynolds numbers. The lack of efficiency stems from the need to resolve the viscous sublayer which requires very fine resolution in all three directions near the wall. Structured grids make use of a stretching to reduce the normal grid spacing but must carry the fine resolution in the streamwise and spanwise directions throughout the domain. The unnecessarily fine grid for much of the domain leads to disturbingly high grid estimates. Chapman (1979), and later Moin & Jiménez (1993), pointed out that, in order to advance the technology to airfoils at flight Reynolds numbers, structured grids must be abandoned in lieu of what are known as nested or unstructured grids. Figure 1 illustrates the ability of an unstructured mesh to refine only the near wall region. Note the large number of points near the wall (where the fine vortical features need better resolution) and the coarseness in all directions away from the wall (where the scales are much larger). The important difference between this approach and the usual structured grid stretching is that the number of elements used to discretize the spanwise and streamwise features of the flow is reduced in each successive layer coming off the wall. This is due to the fact that the elements not only grow in the normal direction, but in the other directions as well. This greatly reduces the total number of points or elements required for a given Reynolds number flow.

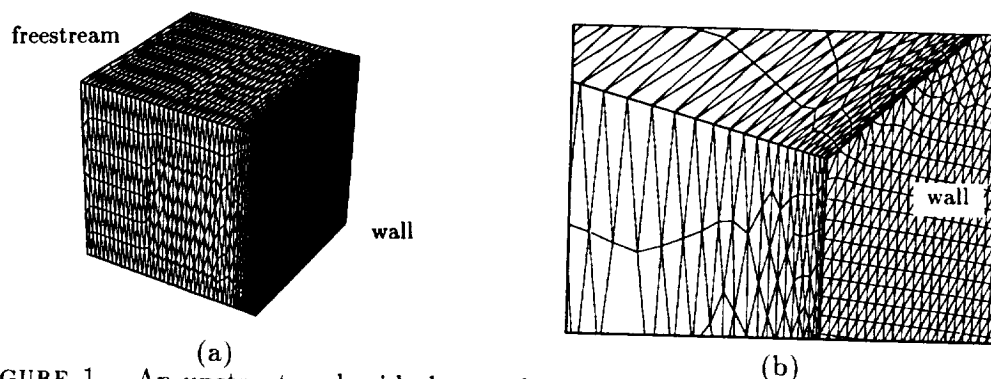


FIGURE 1. An unstructured grid places a large number of points at the wall but remains coarse in the freestream. The full mesh is shown in part (a) while a zoom of near wall corner is shown in part (b) to illustrate the refinement.

PRECEDING PAGE BLANK NOT FILMED

To estimate the number of unstructured grid elements required to simulate an airfoil, Chapman used flat plate skin friction analogies and a computational domain extending one-fifth chord in the spanwise direction to obtain

$$N = 0.2 \frac{Re_c^{1.8}}{\Delta_x^+ \Delta_z^+} \quad (1)$$

where  $\Delta_x^+$  and  $\Delta_z^+$  are the grid resolutions in the streamwise and spanwise directions on the body surface and  $Re_c$  is the Reynolds number based on the chord,  $c$  and the freestream velocity,  $u_{inf}$ . This estimate assumes that the fine resolution near the wall is carried out for 10 layers to accurately resolve the viscous sublayer. Then, outside of the viscous sublayer, the elements grow rapidly in all three dimensions with increasing distance from the wall as described above. Moin & Jimenéz suggest that current subgrid-scale models should allow  $\Delta_x^+ = 200$  and  $\Delta_z^+ = 50$ . When these values are substituted into (1), we observe that approximately  $1.2 \times 10^6$  elements will be required for airfoils with a chord Reynolds number of  $Re_c = 10^6$  and  $80 \times 10^6$  elements for the more practical flight Reynolds number of  $Re_c = 10^7$ . Simulations of this scale are possible on today's supercomputers.

The use of unstructured grids, coupled with the advances in dynamic subgrid-scale modeling such as those made by Germano *et al.* (1991) and Ghosal *et al.* (1992), make LES of an airfoil tractable. The finite element method can efficiently solve the Navier-Stokes equations on unstructured grids. Although the CPU cost per time step per element is somewhat higher than structured grid methods, this effect is more than offset by the reduction in the number of elements.

## 2. Accomplishments

### 2.1 Computer code

The proposed finite element formulation is based on the work of Jansen *et al.* (1993), who used the method to model the compressible Reynolds-averaged Navier-Stokes equations. These simulations were performed by time marching a transient simulation to a steady solution. The code was optimized for rapid convergence without regard for time accuracy. For the current work, greater attention has been given to the efficient time accuracy before application to LES. Both explicit and implicit time integration methods have been developed and tested. Currently, the formulation has two implicit methods (first-order for acceleration towards a steady state and third-order for time accurate integration) and a higher order accurate family of explicit time integration methods.

### 2.2 Time step estimates

There is, in general, a tradeoff between explicit methods, which are cheaper per time step, and implicit methods, which require fewer time steps due to the avoidance of the stability limits. It can be shown through methods similar to Chapman's spatial estimate that the viscous stability limit leads to the following time step limit

$$\Delta_t^v = \frac{\Delta_y^+}{C_{fmax} Re_c} T \quad (2)$$



where  $T$  is the time it takes the mean flow to cross the chord of the airfoil ( $T = c/u_{\text{inf}}$ ) and  $C_{f_{\text{max}}}$  is the maximum of the coefficient of friction.

There is also a stability limit associated with advection. The time step associated with this stability limit is a little more difficult to estimate since it depends on both the mean flow advection,  $u$ , and the length of the element in the flow direction,  $\Delta_x$ . These quantities vary throughout the flow. Assuming a logarithmic velocity profile and geometric stretching of the elements coming off the wall, it can be shown that the critical point occurs in the buffer layer near  $y^+ = 10$ . Respecting this advective stability limit leads to the following advective time step limit

$$\Delta_t^u = \alpha \Delta_t^v \quad (3)$$

where

$$\alpha \approx \frac{0.6 \Delta_x^+}{\Delta_y^{+2}} \quad (4)$$

For the problem proposed above,  $\Delta_x^+ = 200$  and  $\Delta_y^+$  is expected to be near 1.0, which makes  $\alpha \approx 120$ . This time step corresponds to a  $\Delta_t^+ \approx 120$ , which will not yield sufficient accuracy. Therefore, this stability limit is not likely to have any bearing on the size of the time step.

Since we are solving the compressible Navier-Stokes equations, a third time step restriction must be considered. The acoustic stability limit can be estimated as follows

$$\Delta_t^c = \beta \Delta_t^v \quad (5)$$

where

$$\beta = \frac{2.0M\sqrt{C_{f_{\text{max}}}}}{\Delta_y^+} \quad (6)$$

where  $a$  is the acoustic speed and  $M = u_{\text{inf}}/a$  is the freestream Mach number. Clearly,  $\beta$  is less than one, making this the most restrictive stability limit.

If  $\Delta_y^+$  is equal to one, it can be shown that  $\Delta_t^v$  corresponds to a  $\Delta_t^+ = 1.0$ . Current channel flow LES simulations have had success with  $\Delta_t^+ = 10.0$ . Assuming that this temporal resolution is adequate for the airfoil, the acoustic time step stability limit will be far too restrictive. The implication of this result is that compressible formulations must provide an implicit treatment of the advective term. Furthermore, special care must be taken to show that the method is not adversely affected by simulating the flow at very high acoustic CFL numbers. For the conditions described above, typical flows lead to the following acoustic CFL estimate

$$\frac{a\Delta_t}{\Delta_x} = \frac{10.0}{\beta} \approx \frac{70.7}{M} \quad (7)$$

which exceeds 350 for a Mach number of 0.2.

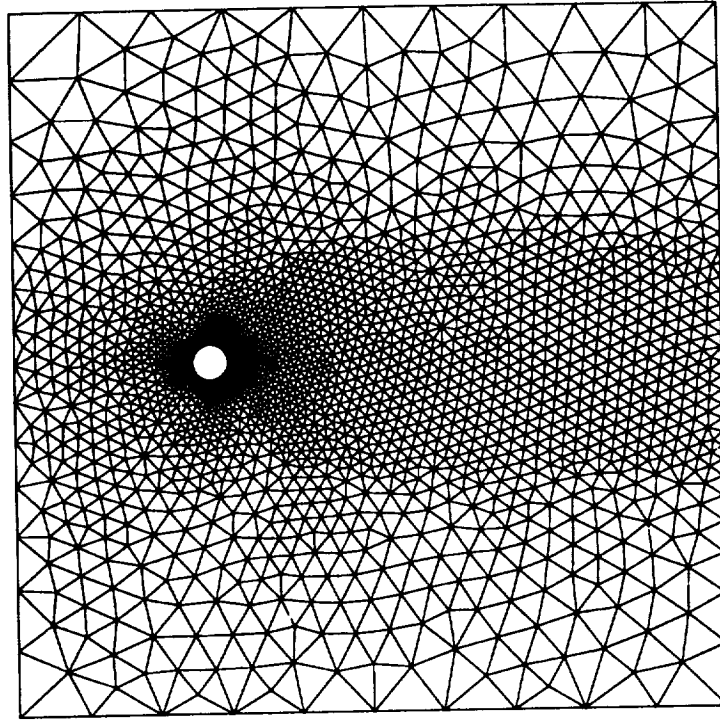


FIGURE 2. Unstructured grid for flow around a cylinder at  $Re_d = 100$ ,  $M = 0.2$ . This mesh contains 4004 elements which corresponds to 2056 nodes for a linear space.

### 2.3 Preliminary simulations

To verify that the modifications to the code achieve time accuracy, the method was applied to laminar flow over a cylinder at  $Re_d = 100$ ,  $M = 0.2$ . This flow leads to periodic vortex shedding and, therefore, gives some measure of a method's temporal-accuracy. The unstructured triangular mesh is shown in Figure 2. Note the local refinement near the cylinder and in the wake. The lift coefficient obtained by using piecewise linear shape functions in space and time can be seen in Figure 3. The Strouhal number for this discretization is 0.167. The acoustic CFL for this problem is 20.0.

## 3. Future plans

### 3.1 Time integration

The cylinder problem is not an adequate test of the formulation's ability to run at very high acoustic CFL numbers. A channel flow at a higher Reynolds will be run to determine the upper limit for the acoustic CFL number. Should problems arise, a change to an incompressible formulation may be appropriate. Such finite element formulations are currently being used by Hauke & Hughes (1993) and Simo

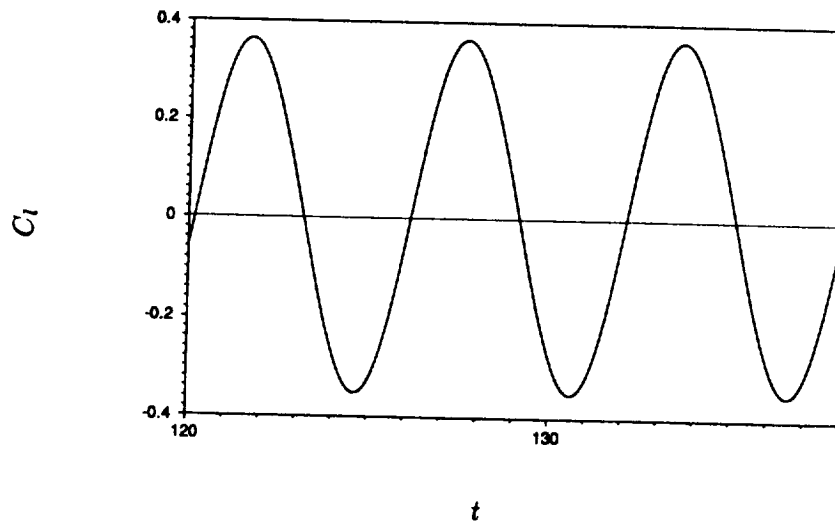


FIGURE 3. Periodic vortex shedding illustrated through the lift coefficient.

& Armero (1993) for laminar flows. The drawback to an incompressible formulation is that many interesting airfoil problems require the consideration of compressibility effects.

### 3.2 Mesh generation

The mesh requirements of the airfoil problem exceed existing mesh generation capability. In order to stretch the elements to the level described above and to reduce the number of elements with distance from the wall, new mesh generation techniques must be developed. It is crucial that elements do not have angles which approach  $180^\circ$ . An algorithm to accomplish this goal for airfoils is under development in collaboration with Tim Barth of NASA Ames. This algorithm also should provide smoother element shape changes than those observed in Figure 1, resulting in higher quality solutions.

### 3.3 Subgrid-scale modeling

The dynamic models developed at CTR need to be implemented into the unstructured grid code. This is not expected to be too difficult, especially for higher order elements which have a built-in test grid (the corner nodes).

### 3.4 Further speeding up of the code

The code has been largely optimized for marching to steady state solutions. It may be possible to further optimize the code for time accurate calculations. The code currently runs at 440 MFLOPS on the Cray C90 and 25 MFLOPS per processor on the Thinking Machines CM5. These execution rates are quite fast, but some savings in the number of FLOPS per time step per element may be attainable.

### 3.5 Airfoil simulation

Upon the successful completion of these tasks, the code will be applied to airfoil problems with the ultimate target being airfoils at or near maximum lift; see Coles and Wadcock (1979). These flows commonly have separation bubbles that are difficult to predict with Reynolds-averaged Navier-Stokes equation models and, therefore, present an opportunity to demonstrate the utility of LES approaches.

### REFERENCES

- CHAPMAN, D. R. 1979 Computational aerodynamics development and outlook. *AIAA J.* **17**, 1293.
- COLES, D., & WADCOCK, A. J. 1979 A flying-hot-wire study of two-dimensional mean flow past an NACA 4412 airfoil at maximum lift. *AIAA J.* **17**, 321.
- GERMANO, M., PIOMELLI, U., MOIN, P. & CABOT, W. H. 1991 A dynamic subgrid-scale eddy viscosity model. *Phys Fluids A.* **3**, 1760.
- GHOSAL, S., LUND, T. S. & MOIN, P. 1992 A dynamical localization model for large eddy simulation of turbulent flows. *CTR Manuscript 139*.
- HAUKE, G., & HUGHES, T. J. R. 1993 A unified approach to compressible and incompressible flows. *Comp. Meth. Appl. Mech. Eng.* To appear.
- JANSEN, K., JOHAN, Z., & HUGHES, T. J. R. 1993 Implementation of a one-equation turbulence model within a stabilized finite element formulation of a symmetric advective-diffusive system. *Comp. Meth. Appl. Mech. Eng.* **105**, 405.
- MOIN, P. & JIMENÉZ, J. 1993 Large eddy simulation of complex turbulent flows. *AIAA-03-3099*, AIAA 24th Fluid Dynamics Conference.
- SIMO, J. C., & ARMERO F. 1993 Unconditional stability and long term behavior of transient algorithms for the incompressible Navier-Stokes and Euler equations. *Comp. Meth. Appl. Mech. Eng.* To appear.

157  
P. 14  
N94-24152

## Investigation of the asymptotic state of rotating turbulence using large-eddy simulation

By Kyle D. Squires<sup>1</sup>, Jeffrey R. Chasnov,  
Nagi N. Mansour<sup>2</sup> AND Claude Cambon<sup>3</sup>

### 1. Motivation and objectives

Study of turbulent flows in rotating reference frames has long been an area of considerable scientific and engineering interest. Because of its importance, the subject of turbulence in rotating reference frames has motivated over the years a large number of theoretical, experimental, and computational studies (e.g., Greenspan 1968, Bardina *et al.* 1985, Jacquin *et al.* 1990, Mansour *et al.* 1991). The bulk of these previous works has served to demonstrate that the effect of system rotation on turbulence is subtle and remains exceedingly difficult to predict.

A rotating flow of particular interest in many studies, including the present work, is examination of the effect of solid-body rotation on an initially isotropic turbulent flow. One of the principal reasons for the interest in this flow is that it represents the most basic turbulent flow whose structure is altered by system rotation but without the complicating effects introduced by mean strains or flow inhomogeneities. The assumption of statistical homogeneity considerably simplifies analysis and computation.

For an initially isotropic turbulence, it is well known that system rotation inhibits the non-linear cascade of energy from large to small scales. This effect is manifest in a reduction of the turbulence dissipation rate and associated decrease in the decay rate of turbulence kinetic energy (e.g., see Traugott 1958, Veeravalli 1991, Mansour *et al.* 1992). An issue considerably less resolved, however, is the development of a two-dimensional state in rotating homogeneous turbulence. Both computations and experiments have noted an increase in integral length scales along the rotation axis relative to those in non-rotating turbulence (Bardina *et al.* 1985, Jacquin *et al.* 1990). Increase in the integral length scales has been thought to be a prelude to a Taylor-Proudman reorganization to two-dimensional turbulence. However, it has also been shown using direct numerical simulation (DNS) of rotating isotropic turbulence (Speziale *et al.* 1987, Mansour *et al.* 1992) that in the limit of very rapid rotation, turbulence remains isotropic and three-dimensional. In fact, Mansour *et al.* (1992) showed that the evolution of rapidly rotating turbulence was accurately predicted using rapid distortion theory (RDT). Furthermore, Mansour *et al.* also

<sup>1</sup> University of Vermont

<sup>2</sup> NASA Ames Research Center

<sup>3</sup> Ecole Centrale de Lyon

showed that the RDT solution violates a necessary condition for occurrence of a Taylor-Proudman reorganization.

It is worth noting that as is typically the case with DNS, the computations performed by Speziale *et al.* (1987) and Mansour *et al.* (1991,1992) were performed at low Reynolds numbers. In rotating turbulence at low Reynolds number, the effects of viscous decay progressively reduce the Rossby number and drive the flow to the RDT limit. Thus, other mechanisms for obtaining two-dimensional turbulence, e.g., through non-linear interactions which occur on a turbulence time scale, are precluded using DNS, and evolution of a two-dimensional state, therefore, requires significantly higher Reynolds numbers than can be attained using DNS.

An issue closely connected to development of two-dimensional turbulence in rotating flows is the existence of asymptotic self-similar states. The issue of self-similarity is a topic central to studies of turbulent flows (e.g., see Chasnov 1993). A similarity state is characterized by the predictability of future flow statistics from current values by a simple rescaling of the statistics; the rescaling is typically based on a dimensional invariant of the flow. Knowledge of the existence of an asymptotic similarity state allows a prediction of the ultimate statistical evolution of the flow without detailed knowledge of the complex, and not well understood, non-linear transfer processes.

Large-eddy simulation (LES) is ideally suited for examination of the long-time evolution of rotating turbulence since it circumvents the Reynolds number restriction of DNS. The drawback is, of course, that it requires use of a model to parameterize subgrid-scale stresses. However, large-scale statistics are relatively insensitive to the exact form of the model, and alternative approaches, i.e., laboratory experiments or direct simulations, are simply not feasible for examination of the long-time evolution of rotating flows.

The principal objective of the present study has thus been to examine the asymptotic state of solid-body rotation applied to an initially isotropic, high Reynolds number turbulent flow. Of particular interest has been to determine (1) the degree of two-dimensionalization and (2) the existence of asymptotic self-similar states in homogeneous rotating turbulence. As shown in §2, development of a two-dimensional state is very pronounced; much more so than observed in previous studies using DNS. It is also shown that long-time evolution of quantities such as turbulence kinetic energy and integral length scales are accurately predicted using simple scaling arguments.

## 2. Accomplishments

### 2.1 Simulation overview

In the present study, the filtered Navier-Stokes equations for an incompressible fluid were solved in a rotating reference frame:

$$\nabla \cdot \mathbf{u} = 0 \quad (1)$$

$$\frac{\partial \mathbf{u}}{\partial t} + \mathbf{u} \cdot \nabla \mathbf{u} = -\frac{1}{\rho} \nabla p + \nu_e \nabla^2 \mathbf{u} - 2\boldsymbol{\Omega} \times \mathbf{u}. \quad (2)$$

In (1) and (2),  $\mathbf{u}$  is the velocity vector,  $p$  and  $\rho$  the fluid pressure and density, respectively, and  $\boldsymbol{\Omega}$  is the rotation vector. For purposes of discussion, the rotation vector is considered to act along the  $z$  or “vertical” axis,  $\boldsymbol{\Omega} = (0, 0, \Omega)$ . An eddy viscosity hypothesis was used to parameterize the subgrid-scale stresses. In this work, the spectral eddy viscosity of Chollet & Lesieur (1981) was modified for rotating turbulence

$$\nu_e = \nu_{e0} f(\alpha) \quad (3)$$

where  $\nu_{e0}$  is the “baseline” viscosity and  $f(\alpha)$  a function accounting for the reduction of  $\nu_e$  by system rotation. The baseline viscosity,  $\nu_{e0}$ , from Chollet & Lesieur, is

$$\nu_{e0}(k|k_m, t) = \left[ 0.145 + 5.01 \exp \left( \frac{-3.03 k_m}{k} \right) \right] \left[ \frac{E(k_m, t)}{k_m} \right]^{1/2} \quad (4)$$

where  $k_m$  is the maximum wavenumber magnitude of the simulation and  $E(k, t)$  is the spherically integrated three-dimensional Fourier transform of the co-variance  $\frac{1}{2} \langle u_i(\mathbf{x}, t) u_i(\mathbf{x} + \mathbf{r}, t) \rangle$  ( $\langle \cdot \rangle$  denotes an ensemble or volume average). The reduction in  $\nu_e$  is expressed using  $f(\alpha)$

$$f(\alpha) = \frac{2 \left[ (1 + \alpha^2)^{3/2} - \alpha^3 - 1 \right]}{3\alpha^2} \quad (5)$$

where

$$\alpha = \frac{8\Omega^2}{3E(k_m)k_m^3} \quad (6)$$

(Cambon, private communication).

The initial energy spectrum of the simulations was of the form

$$E(k, 0) = \frac{1}{2} C_s \frac{u_0^2}{k_p} \left( \frac{k}{k_p} \right)^s \exp \left[ -\frac{1}{2} s \left( \frac{k}{k_p} \right)^2 \right] \quad (7)$$

where  $s$  is equal to 2 or 4,  $C_s$  is given by

$$C_s = \sqrt{\frac{2}{\pi}} \frac{s^{\frac{1}{2}(s+1)}}{1 \cdot 3 \cdot \dots \cdot (s-1)} \quad (8)$$

and  $k_p$  is the wavenumber at which the initial energy spectrum is maximum. In this study, simulations with  $s = 2$  and  $s = 4$  were performed, corresponding to the initial energy spectra with a low wavenumber form proportional to either  $k^2$  or  $k^4$ .

Because the principal interest of this work was examination of the long-time evolution of rotating turbulence, it was necessary to use as large a value of  $k_p$  as possible in order that flow evolution not be adversely affected by the periodic boundary conditions used in the simulations; adverse affects occurring when the integral length scales of the flow become comparable to the box size. Another important consideration in these simulations was the aspect ratio of the computational domain.

Because of the rapid growth of turbulence length scales along the direction of the rotation axis, it was necessary to use a computational box which was longer along the rotation axis than in the other directions. Preliminary calculations of rotating turbulence on cubic domains had shown an adverse affect of periodicity because of the rapid integral scale growth along the rotation axis. Numerical experiments showed that it was necessary to use a computational box which was four times larger along the rotation axis than in the directions orthogonal to the rotation vector. Four times as many collocation points were used in the vertical direction in order to avoid any effects of grid anisotropy at the smallest resolved scales.

Simulations were performed using resolutions of  $96 \times 96 \times 384$  and  $128 \times 128 \times 512$  collocation points. The governing equations (1) and (2) were solved using the pseudo-spectral method developed by Rogallo (1981). The statistical evolution of the flow using either resolution was essentially the same, and, therefore, only the results from the higher resolution computation are reported in this brief. The maximum physical wavenumber of the  $128 \times 128 \times 512$  computations was 95 (for a computational domain having total volume of  $8\pi^3$ ). The initial root-mean-square velocity fluctuation  $u_0$  in (7) was equal to unity and  $k_p = 75$ . Following Chasnov (1993), the initial energy spectrum was set to zero for wavenumbers greater than 93 to allow the subgrid-scale eddy viscosity to build up from zero values. For each spectrum type, i.e., low wavenumber part proportional to  $k^2$  or  $k^4$ , simulations were performed with  $\Omega = 0, 0.5$ , and  $1.0$ .

## 2.2 Results

The instantaneous power-law exponent (i.e., the logarithmic time derivative) of the mean-square velocity fluctuation,  $\langle \mathbf{u}^2 \rangle$ , is shown in Figure 1 for each rotation rate and spectrum type used in the simulations. The time axis in Figure 1 and following figures has been made dimensionless using the eddy turnover time in the initial field

$$\tau(0) = L_u(0)/\langle \mathbf{u}^2 \rangle^{1/2} \quad (9)$$

where  $L_u(t)$  is the velocity integral scale defined at time  $t$  as

$$L_u(t) = \frac{\pi}{2} \frac{\int_0^\infty k^{-1} E(k, t) dk}{\int_0^\infty E(k, t) dk}. \quad (10)$$

In isotropic turbulence,  $L_u$  is two-thirds the usual longitudinal integral scale measured in experiments (see also Chasnov 1993). Throughout this work, “ $k^2$  spectrum” refers to an initial energy spectrum  $E(k)$  with low wavenumber part proportional to  $k^2$  while “ $k^4$  spectrum” refers to an initial  $E(k)$  with low wavenumbers proportional to  $k^4$ . For both spectrum types, the characteristic effect of system rotation in reducing the decay rate of  $\langle \mathbf{u}^2 \rangle$  is evident in Figure 1. Furthermore, it is also clear from the Figure that the value of the decay exponent for non-zero rotation rates at long times is independent of  $\Omega$ , depending only on the form of the initial energy spectrum.

It is possible to predict the exponents in Figure 1 if one assumes that the asymptotic scaling of  $\langle \mathbf{u}^2 \rangle$  is dependent on the form of  $E(k)$  at low wavenumbers and



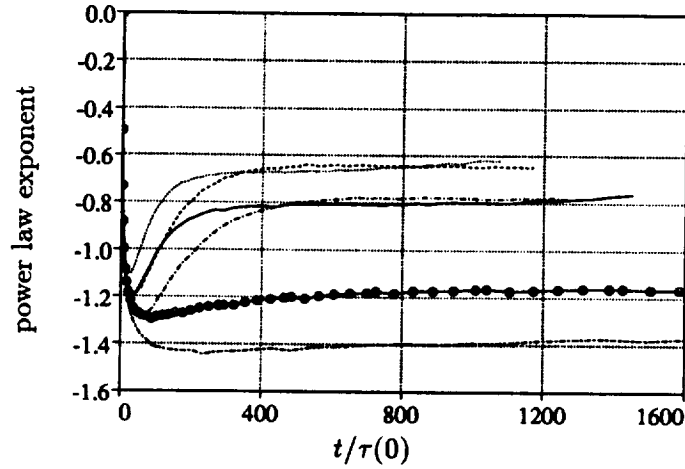


FIGURE 1. Time development of the power law exponent of  $\langle \mathbf{u}^2 \rangle$  in rotating turbulence.  $\circ$ — $\circ$ ,  $\Omega = 0$ ,  $k^2$  spectrum; ----,  $\Omega = 0.5$ ,  $k^2$  spectrum; ..... ,  $\Omega = 1.0$ ,  $k^2$  spectrum; ---,  $\Omega = 0$ ,  $k^4$  spectrum; —·—,  $\Omega = 0.5$ ,  $k^4$  spectrum; —,  $\Omega = 1.0$ ,  $k^4$  spectrum.

independent of viscosity. For high Reynolds number turbulence, this is a reasonable assumption since the direct effect of viscosity occurs at much larger wavenumber magnitudes than those scales which contain most of the energy. Thus, it is possible to derive expressions for the asymptotic scaling of  $\langle \mathbf{u}^2 \rangle$  using an expansion of the energy spectra near  $k = 0$ :

$$E(k) = 2\pi k^2(A_0 + A_2 k^2 + \dots) \quad (11)$$

where  $A_0, A_2, \dots$  are the Taylor series coefficients of the expansion. As shown by Batchelor & Proudman (1956), assuming that the velocity correlation tensor  $\langle u_i(\mathbf{x})u_j(\mathbf{x} + \mathbf{r}) \rangle$  is analytic at  $k = 0$  results in  $A_0 = 0$  and a time-dependent value of  $A_2$ . On the other hand, Saffman (1967) showed that it is also physically possible to create an isotropic turbulence with a non-zero value of  $A_0$ , which is also invariant in time. As also shown by Chasnov (1993) the asymptotic scalings of  $\langle \mathbf{u}^2 \rangle$  for these two cases are

$$\langle \mathbf{u}^2 \rangle \propto A_0^{2/5} t^{-6/5} \quad (k^2 \text{ spectrum}) \quad (12)$$

and

$$\langle \mathbf{u}^2 \rangle \propto A_2^{2/7} t^{-10/7} \quad (k^4 \text{ spectrum}). \quad (13)$$

It may be observed from Figure 1 that the agreement between the LES results and (12) and (13) is excellent for both spectrum types. An analysis similar to that leading to (12) and (13) may also be performed for flows having non-zero rotation rates. For non-zero  $\Omega$ , the asymptotic scalings of  $\langle \mathbf{u}^2 \rangle$  are predicted to be

$$\langle \mathbf{u}^2 \rangle \propto A_0^{2/5} t^{-3/5} \Omega^{3/5} \quad (k^2 \text{ spectrum}) \quad (14)$$

and

$$\langle \mathbf{u}^2 \rangle \propto A_2^{2/7} t^{-5/7} \Omega^{5/7} \quad (k^4 \text{ spectrum}). \quad (15)$$

For the  $k^2$  spectrum, the value of the decay exponent from the rotating flows in the asymptotic region, approximately -0.64, is in very good agreement with (14). Similar agreement between the predicted value of the decay exponent, -5/7, and the measured values for the  $k^4$  spectrum is also observed.

Evolution of the integral length scales are shown in Figures 2a and 2b. The vertical integral scale is defined as

$$L_v = \frac{1}{\langle \mathbf{u}^2 \rangle} \int \langle u_i(x, y, z) u_i(x, y, z + r) \rangle dr \quad (16)$$

while the horizontal integral scale is given by

$$L_h = \frac{1}{\langle \mathbf{u}^2 \rangle} \int \frac{\langle u_i(\mathbf{x}) u_i(\mathbf{x} + \mathbf{r}) \rangle}{2\pi r} d\mathbf{r}. \quad (17)$$

Figure 2 clearly shows the significantly greater growth in time of the vertical integral scales relative to their horizontal counterparts in rotating turbulence. Also shown in the Figure is the velocity integral scale,  $L_u$ , for  $\Omega = 0$ . It is evident from Figure 2 that the horizontal integral scales in the simulations with non-zero  $\Omega$  are essentially independent of rotation rate and evolve similarly to the length scale from the non-rotating case.

The results in Figure 2 may be used to deduce *a posteriori* the asymptotic scaling laws of the integral scales. For the  $k^2$  spectrum, dimensional arguments and the LES results in Figure 2a give the following dependence of the length scales on the invariant  $A_0$ ,  $t$ , and  $\Omega$

$$L_h \propto A_0^{1/5} t^{2/5} \quad (k^2 \text{ spectrum}), \quad (18)$$

i.e., no dependence of  $L_h$  on  $\Omega$ . The appropriate scaling of the vertical length scales for the  $k^2$  spectrum is

$$L_v \propto A_0^{1/5} t \Omega^{3/5} \quad (k^2 \text{ spectrum}) \quad (19)$$

since the long-time growth of  $L_v$  is observed from the LES results to be directly proportional to time. Similarly, dimensional arguments together with the results in Figure 2b can be used to deduce the length scale dependence on  $A_2$ ,  $t$ , and  $\Omega$  for the  $k^4$  spectrum:

$$L_h \propto A_2^{1/7} t^{2/7} \quad (k^4 \text{ spectrum}), \quad (20)$$

similar to the non-rotating case. For the vertical length scales

$$L_v \propto A_2^{1/7} t \Omega^{5/7} \quad (k^4 \text{ spectrum}). \quad (21)$$

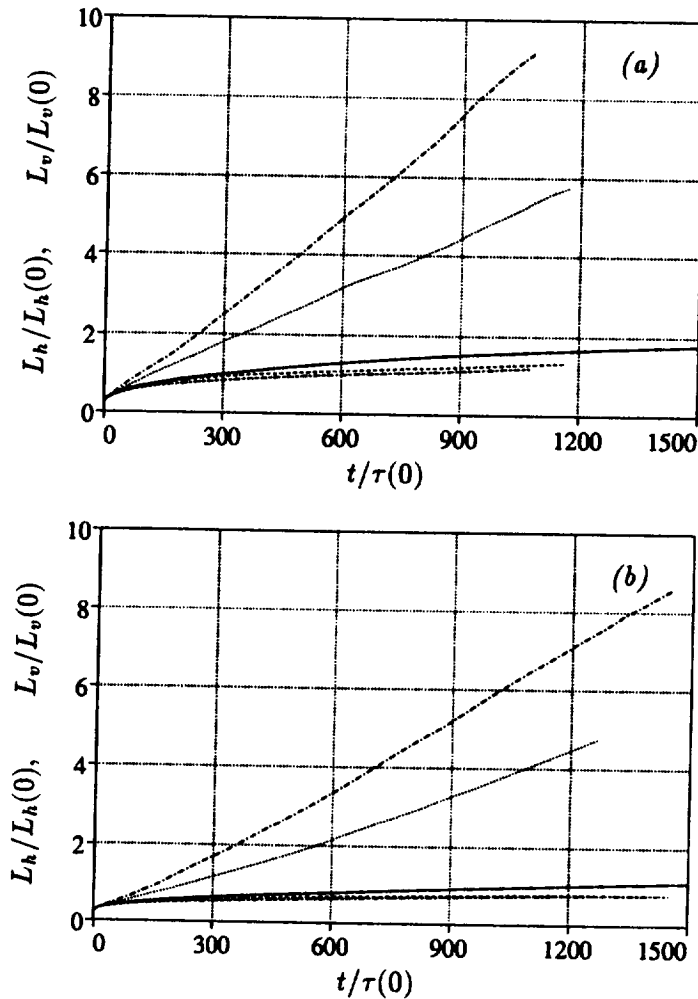


FIGURE 2. Time development of the integral length scales in rotating turbulence. (a)  $k^2$  spectrum, (b)  $k^4$  spectrum. —,  $L_u$ ,  $\Omega = 0$ ; ----,  $L_h$ ,  $\Omega = 0.5$ ; ..... ,  $L_v$ ,  $\Omega = 0.5$ ; -.-,  $L_h$ ,  $\Omega = 1.0$ ; —·—,  $L_v$ ,  $\Omega = 1.0$ .

As was the case for the simulations possessing a  $k^2$  spectrum, long-time evolution of  $L_v$  in the simulations having a  $k^4$  spectrum was also observed to be directly proportional to time.

As shown in Figures 2a and 2b, the evolution of the flow in the direction along the vertical axis is strongly enhanced relative to the horizontal directions. Rapid growth of the vertical length scales provides an indication of evolution towards a two-dimensional state. This can be more clearly seen through examination of the energy spectrum as a function of spatial wavenumber  $k$  as well as the cosine of the polar angle in wave space (schematically illustrated in Figure 3).

Shown in Figure 4a is the energy spectrum as a function of both  $k$  and  $\cos \theta$  from a simulation with  $\Omega = 0$  and possessing an initial spectrum with low wavenumber part

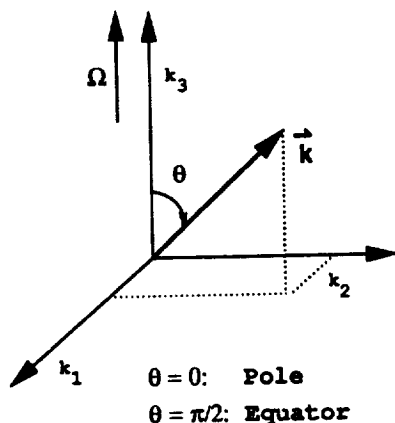


FIGURE 3. Wavenumber space showing rotation vector and polar angle  $\theta$ . For simulations of rotating turbulence, the pole is defined as  $\theta = 0$  ( $\cos\theta = 1$ ); the equator as  $\theta = \pi/2$  ( $\cos\theta = 0$ ). Energy and transfer spectra are considered to be functions of both  $k$  and  $\cos\theta$ .

proportional to  $k^4$ . It may be observed from the Figure that, as expected, the energy is essentially equi-partitioned with respect to  $\cos\theta$ . Plotted in Figure 4b is the energy spectrum from a simulation with  $\Omega = 1$  (and  $k^4$  spectrum). It is clear there is a marked concentration of energy in the equatorial plane,  $\theta = \pi/2$ ; the Figure provides very strong evidence of the development of two-dimensional turbulence. This result is also in sharp contrast to the previous examinations of  $E(k, \cos\theta)$  by Mansour *et al.* (1992) using direct numerical simulation. Mansour *et al.* found only a slight tendency for a concentration of energy near the equator. Because of viscous dissipation in their simulations, it was not possible for Mansour *et al.* to integrate the flow fields for long enough times in order to observe development of two-dimensional turbulence. It is important to emphasize that development of a two-dimensional state as demonstrated by Figure 4b cannot be captured by DNS because of viscous decay. LES circumvents this restriction and permits long enough integrations such that the non-linear interactions responsible for two-dimensionalization can occur.

Further evidence of the profound effect of rotation is contained in Figures 5a and 5b. Figure 5a is the transfer function,  $T(k, \cos\theta)$ , from a simulation with  $k^2$  spectrum and  $\Omega = 0$ . The Figure shows the expected behavior, i.e., negative transfer at low wavenumbers and positive transfer at higher wavenumbers. It is also reasonably clear from Figure 5a that, as was the case with the energy spectrum, the transfer term is independent of  $\theta$ . The transfer term from the simulation with a  $k^2$  spectrum and  $\Omega = 1.0$  is shown in Figure 5b. As is clear from the Figure, rotation has substantially altered the transfer spectrum. For values of  $\cos\theta$  near 1 (the pole in  $k$ -space), the energy transfer is small for the low wavenumbers and zero at the higher wavenumbers. For  $\cos\theta$  near 0 (the equator in  $k$ -space), the transfer term is actually *positive* at low wavenumbers, indicating a transfer of energy *into* these modes.

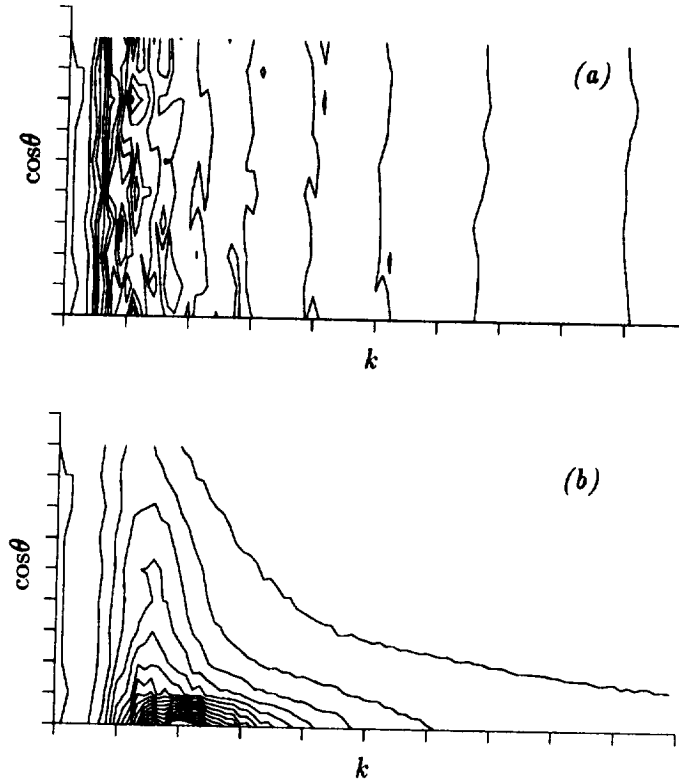


FIGURE 4. Energy spectrum as a function of wavenumber  $k$  and cosine of the polar angle  $\theta$ ; spectrum obtained from LES with  $k^4$  spectrum. (a)  $\Omega = 0$  at  $t/\tau(0) = 427$ , (b)  $\Omega = 1.0$  at  $t/\tau(0) = 575$ .

Time development of the two- and three-dimensional components of the kinetic energy are shown in Figures 6a and 6b for both spectrum types and each rotation rate. The two-dimensional component of the energy is obtained from Fourier modes in the plane  $k_z = 0$  while the three-dimensional component is from Fourier modes with  $k_z \neq 0$ . The behavior is similar in both Figures and corroborates many of the aspects of the flows observed in the previous Figures. As expected, it may be observed that the decay of the energy is reduced with increasing rotation rates. More importantly, the Figures also show that for non-zero  $\Omega$  the two-dimensional energy actually *increases* at later times in the flow evolution, consistent with Figure 5b showing a transfer of energy into the low wavenumber modes in the equatorial plane.

Figures 7a and 7b show the temporal evolution of the diagonal components of the anisotropy tensor of the Reynolds stress

$$b_{ij} = \frac{\langle u_i u_j \rangle}{\langle \mathbf{u}^2 \rangle} - \frac{\delta_{ij}}{3} \quad (22)$$

for each spectrum type and  $\Omega = 0$  and 1.0. It is interesting to note that, while

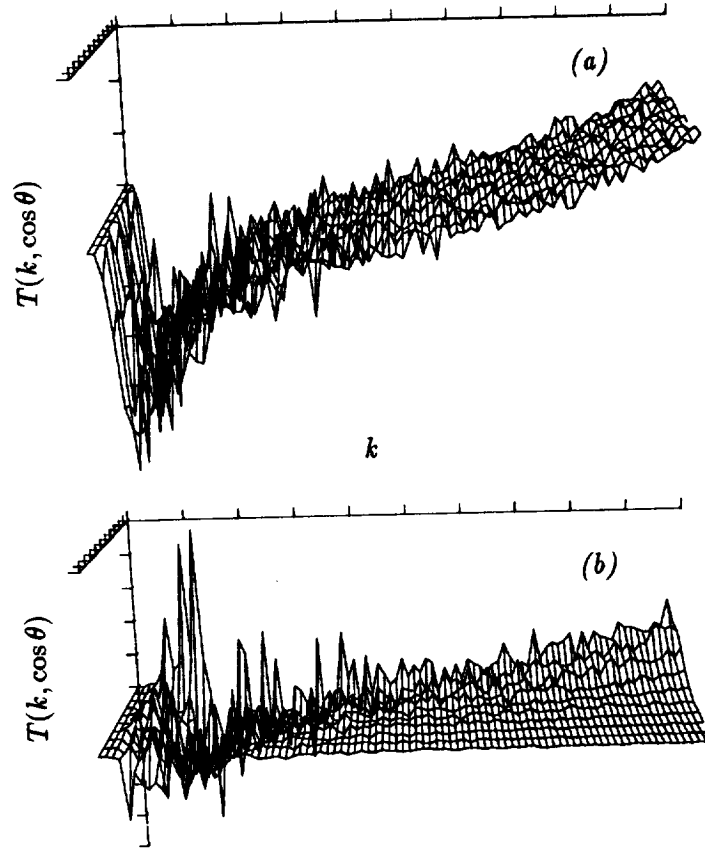


FIGURE 5. Transfer spectrum as a function of wavenumber  $k$  and cosine of the polar angle  $\theta$ ; spectrum obtained from LES with  $k^2$  spectrum. (a)  $\Omega = 0$  at  $t/\tau(0) = 725$ , (b)  $\Omega = 1.0$  at  $t/\tau(0) = 552$ .

the flow is becoming two-dimensional under the influence of system rotation, the distribution of kinetic energy amongst the three components shows little departure from isotropic values. As shown in the Figures, the vertical fluctuations are slightly enhanced by rotation relative to the fluctuations in the horizontal plane. The development of the diagonal components of the anisotropy tensor of the vorticity

$$v_{ij} = \frac{\langle \omega_i \omega_j \rangle}{\langle \omega^2 \rangle} - \frac{\delta_{ij}}{3} \quad (23)$$

is shown in Figure 8. In contrast to the Reynolds stress anisotropy, this Figure shows an enhancement of vertical vorticity relative to the horizontal components.

It is worthwhile to point out that recent work by Bartello *et al.* (1993) showed a much stronger departure from isotropy of the component energies in rotating turbulence. Bartello *et al.* used cubic domains to examine the long-time evolution of the flow and consequently the evolution of the component energies was adversely impacted. Based on their findings, Bartello *et al.* concluded that the long-time

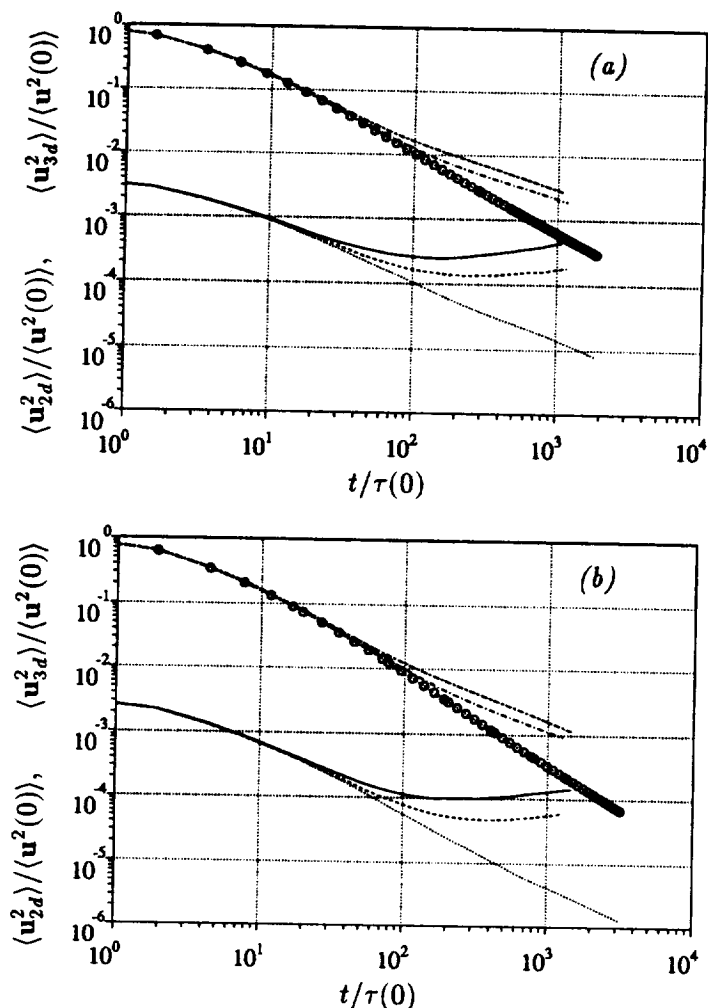


FIGURE 6. Evolution of two-dimensional and three-dimensional energy in LES. (a)  $k^2$  spectrum, (b)  $k^4$  spectrum. ...., 2D energy,  $\Omega = 0$ ;  $\circ \cdots \circ$ , 3D energy,  $\Omega = 0$ ; ----, 2D energy,  $\Omega = 0.5$ ; —, 3D energy,  $\Omega = 0.5$ ; ———, 2D energy,  $\Omega = 1.0$ ; ———, 3D energy,  $\Omega = 1.0$ .

state of homogeneous rotating turbulence was two-dimensional and two-component. However, it is clear from Figures 7 and 8 that the asymptotic state of homogeneous rotating turbulence is two-dimensional but *three*-component.

### 3. Future plans

LES results presented in this work demonstrated the existence of asymptotically self-similar states in rotating homogeneous turbulence. Additional investigations are planned to further corroborate this finding, e.g., examining the collapse of the spatial spectra under the appropriate scalings. Related to this issue are the particular scalings found in the present work. For example, the scaling laws for  $\langle u^2 \rangle$

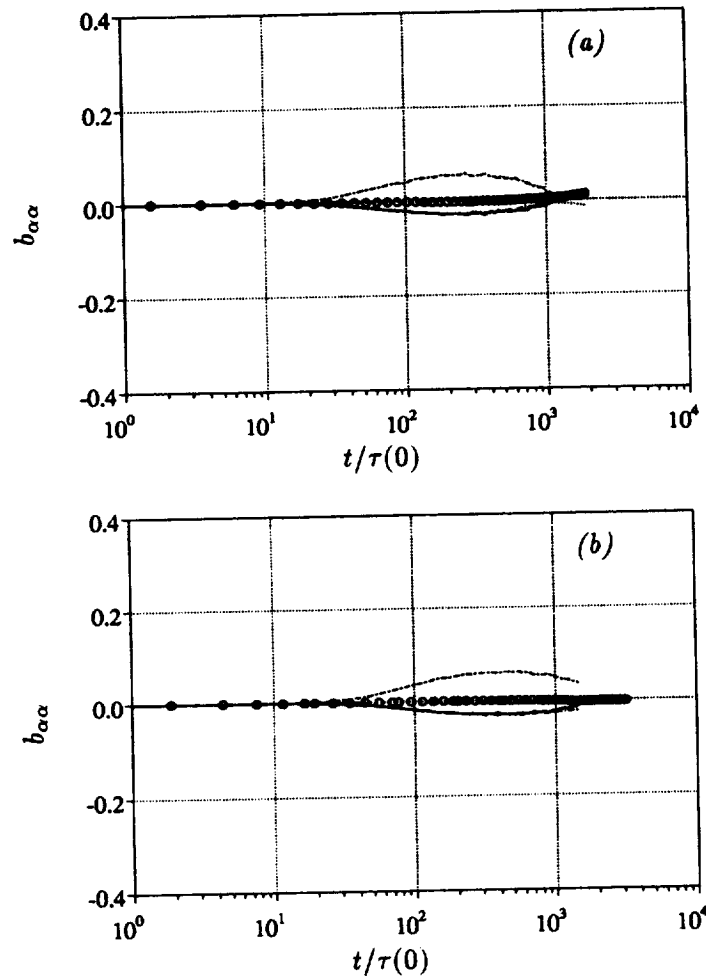


FIGURE 7. Evolution of Reynolds stress anisotropy tensor. (a)  $k^2$  spectrum, (b)  $k^4$  spectrum. Note that the curves for  $\Omega = 0$  are essentially coincident and lie along the axis  $b_{\alpha\alpha} = 0$ . ..... ,  $b_{11}$ ,  $\Omega = 0$ ;  $\circ \cdots \circ$  ,  $b_{22}$ ,  $\Omega = 0$ ; ---- ,  $b_{33}$ ,  $\Omega = 0$ ; — — — ,  $b_{11}$ ,  $\Omega = 1.0$ ; ——— ,  $b_{22}$ ,  $\Omega = 1.0$ ; — · — · ,  $b_{33}$ ,  $\Omega = 1.0$ .

in rotating turbulence (Equations 14 and 15) can be obtained using the transport equation for  $\langle u^2 \rangle$  together with dimensional analysis. The scaling laws for the length scales, however, (Equations 18–21) rely on only dimensional analysis and *a posteriori* examination of LES results. Development of a more rigorous approach for predicting the length scale evolution observed in the present work would be desirable.

This study also showed the utility of large-eddy simulation. As shown in this work, development of an asymptotic state which is two-dimensional (but three-component) is very significant, much more so than in previous examinations of rotating turbulence using DNS. Given the encouraging results obtained to date, a



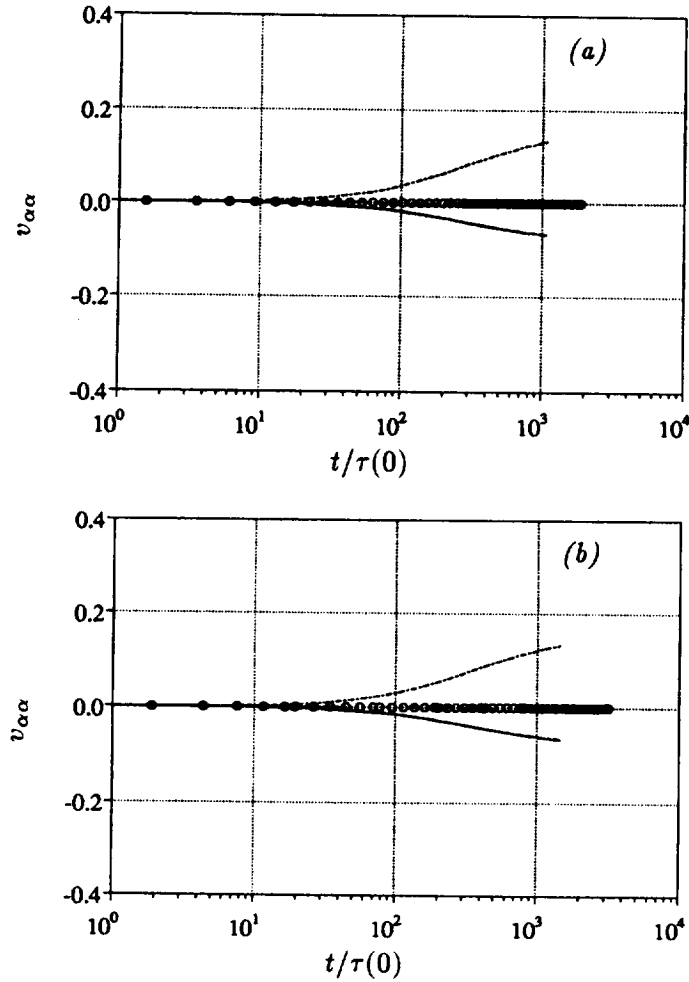


FIGURE 8. Evolution of vorticity anisotropy tensor. (a)  $k^2$  spectrum, (b)  $k^4$  spectrum. Note that the curves for  $\Omega = 0$  are essentially coincident and lie along the axis  $v_{\alpha\alpha} = 0$ . ..... ,  $v_{11}$ ,  $\Omega = 0$ ;  $\circ \cdots \circ$ ,  $v_{22}$ ,  $\Omega = 0$ ; ----,  $v_{33}$ ,  $\Omega = 0$ ; — — —,  $v_{11}$ ,  $\Omega = 1.0$ ; ———,  $v_{22}$ ,  $\Omega = 1.0$ ; — — —,  $v_{33}$ ,  $\Omega = 1.0$ .

likely extension of this work will be use of the LES database for developing a high Reynolds number extension of the  $k$ - $\varepsilon$  model for rotating flows.

### Acknowledgements

Financial support of the first author provided by a NASA-ASEE Summer Faculty Fellowship is gratefully acknowledged. The authors are also grateful to Dr. Robert Rogallo for the use of his code and the support of Dr. Alan Wray for his assistance with the Vectoral language. The simulations were performed on the Cray C90 at the NASA Ames Research Center.

## REFERENCES

- BARDINA, J., FERZIGER, J. H. & ROGALLO, R. S. 1985 Effect of rotation on isotropic turbulence: computation and modeling. *J. Fluid Mech.* **154**, 321-336.
- BARTELLO, P., METAIS, O. & LESIEUR, M. 1993 Coherent structures in rotating three-dimensional turbulence. *J. Fluid Mech.* In press.
- BATCHELOR, G. K. & PROUDMAN, I. 1956 The large-scale structure of homogeneous turbulence. *Phil. Trans. Roy. Soc.* **248**, 369.
- CHASNOV, J. R. 1993 Similarity states of passive scalar transport in isotropic turbulence. *Phys. Fluids A* in press.
- CHOLLET, J. P. & LESIEUR, M. 1981 Parameterization of small scales of three-dimensional isotropic turbulence utilizing spectral closures. *J. Atmos. Sci.* **38**, 2747.
- JACQUIN, L., LEUCHTER, O., CAMBON, C. & MATHIEU, J. 1990 Homogeneous turbulence in the presence of rotation. *J. Fluid Mech.* **220**, 1-52.
- GREENSPAN, H. P. 1968 *The Theory of Rotating Fluids*. Cambridge University Press.
- MANSOUR, N. N., CAMBON, C. & SPEZIALE, C. G. 1991 Single point modeling of initially isotropic turbulence under uniform rotation. *Annual Research Briefs - 1991*, NASA-Stanford Center for Turbulence Research.
- MANSOUR, N. N., CAMBON, C. & SPEZIALE, C. G. 1992 Theoretical and computational study of rotating isotropic turbulence. *Studies in Turbulence*, edited by T. B. Gatski, S. Sarkar & C. G. Speziale, (Springer-Verlag).
- ROGALLO, R. S. 1981 Numerical experiments in homogeneous turbulence. *NASA TM 81315*.
- SAFFMAN, P. G. 1967 The large-scale structure of homogeneous turbulence. *J. Fluid Mech.* **27**, 581.
- SPEZIALE, C. G., MANSOUR, N. N. & ROGALLO, R. S. 1987 The decay of isotropic turbulence in a rapidly rotating frame. *Proc. of the 1987 Summer Program, Report CTR-S87*, NASA-Stanford Center for Turbulence Research.
- TRAUGOTT, S. C. 1958 Influence of solid-body rotation on screen-produced turbulence. *NACA Tech. Note 4135*.
- VEERAVALLI, S. V. 1991 An experimental study of the effects of rapid rotation on turbulence. *Annual Research Briefs - 1991*, NASA-Stanford Center for Turbulence Research.

15-24  
20/6/95  
171

P-16  
N94-24153

## Energy transfer and constrained simulations in isotropic turbulence

By J. Jiménez<sup>1</sup>

### 1. Motivation

The defining characteristic of turbulent flows is their ability to dissipate energy, even in the limit of zero viscosity. The Euler equations, if constrained in such a way that the velocity derivatives remain bounded, conserve energy. But when they arise as the limit of the Navier-Stokes (NS) equations, when the Reynolds number goes to infinity, there is persuasive empirical evidence that the gradients become singular as just the right function of  $Re$  for the dissipation to remain non-zero and to approach a well defined limit (Sreenivasan 1984). It is generally believed that this limiting value of the dissipation is a property of the Euler equations themselves, independent of the particular dissipative mechanism involved, and that it can be normalized with the large scale properties of the turbulent flow (e.g. the kinetic energy per unit volume  $u'^2/2$ , and the integral scale  $L$ ) without reference to the Reynolds number or to other dissipative quantities (Batchelor 1953, §6). This is usually taken to imply that the low wave number end of the energy spectrum, far from the dissipative range, is also independent of the particular mechanism chosen to dispose of the energy transfer.

While these considerations have proved adequate in analyzing the solutions of the NS equations at different Reynolds numbers, they are recently being used in a more general context to predict the effect of different subgrid models in Large Eddy Simulations (LES) of turbulent flows. The LES equations are neither the Euler nor the NS equations. Because of the intrinsically finite capacity of computers, the Euler equations are first truncated to a relatively low number of degrees of freedom, generally much lower than that needed to represent the dissipative scales, and the missing dissipation is provided by the addition of a "subgrid" model whose goal is to mimic the effect on the large scales of the degrees of freedom that have been filtered in the original truncation. In most cases, the resulting model is very different from the quadratic viscosity characteristic of the NS equations, and the hope that it will approximate the behavior of the original high Reynolds number flow hinges on the belief that the dissipation independence observed empirically for the energy transfer mechanism of the NS equations will persist in the new systems.

This is, therefore, a good time to re-evaluate the original assumptions and the limits of their applicability. This will also give us a new tool to investigate the mechanism of the energy cascade itself and its relation to normal viscosity. It has always been an open question how much of NS turbulence is unique to the solutions

<sup>1</sup> Also with the School of Aeronautics, Madrid.

of the NS equations, and what parts of it would be shared by other nonlinear systems of partial differential equations. The arguments outlined above suggest that the quadratic nonlinearity might be essential but that the dissipative model is not. While physical experiments with non-Newtonian fluids are difficult and relatively rare, numerical experiment with different viscosity models are commonplace and have been used for a long time to achieve higher Reynolds numbers than those obtainable with Direct Numerical Simulation, especially in two dimensional flows. As argued above, most LES computations also fall into this category. Although many of these simulations have been quite successful in approximating the results of experiments, relatively few detailed comparisons are available, and the presence in most cases of adjustable parameters makes the agreement less compelling.

Moreover, there is some experimental evidence that this dissipation independence is not complete in all cases. The addition of small concentrations of polymers in wall bounded flows is known to produce a dramatic decrease of skin friction (Berman 1978). Since skin friction for a given flow rate is directly proportional to energy dissipation, and since polymers are thought to act only on the small structures, that evidence is troubling. The same is true of riblets (Walsh 1990), which also modify friction even if they are small scale features. Finally, the friction coefficient of smooth-walled channels does not asymptote to a fixed value, even at the highest Reynolds numbers observed (Dean 1978). While wall bounded flows may be different from isotropic or free shear flows, most conspicuously because in the wall region the "local" Reynolds number can always be argued to be low, these observations should be taken into account when extending the results of the latter into the behavior of the former. In this work, we will only concern ourselves with the behavior of isotropic periodic numerical simulations of the Euler or LES equations and with their relation to NS turbulence.

Even in this case, we have to qualify our support for the hypothesis of complete independence of the large scale motions from the details of the small scales. It is well known that a consequence of an inviscid energy cascade is the famous Kolmogorov (1941)  $E(k) \sim k^{-5/3}$  spectral law. Since this result is independent of viscosity, the arguments above would make it a property of the Euler equations. But it has been known for a long time that those equations have at least another power law equilibrium spectrum  $E(k) \sim k^2$ , corresponding to energy equipartition among the spectral modes (Lee 1952). In physical systems, flow fields with such a spectrum are highly singular and are not expected to be observable since any residual viscosity, however small, would damp the high wave numbers and force a decreasing spectral tail. These solutions are, however, consistent with the inviscid equations, and they reappear as soon as the possibility of a singularity is removed. In fact, as soon as the Euler equations are truncated to a finite number of degrees of freedom, they tend spontaneously to the equipartition solution (Fig. 1). This is relevant to our discussion because it shows that the effect of dissipation in the NS equations is not only to fix the length scale of the viscous limit (the Kolmogorov scale  $\eta$ ), but to select the "desired"  $k^{-5/3}$  spectrum away from the "contamination" of the equipartition component  $k^2$ . It is not immediately clear whether other dissipation mechanisms

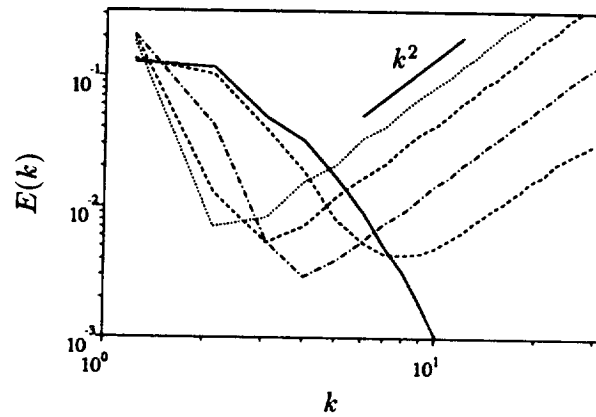


FIGURE 1. Evolution of the three-dimensional energy spectrum of the Euler equations in a  $64^3$  numerical box. Time increases with energy at high wave numbers. The initial flow field is fully developed turbulence from a NS simulation (solid line).

are able to do the same.

In the following sections, we present some numerical experiments on the effect of substituting different dissipation models into the truncated Euler equations. We will see that the effect is mainly felt in the “near dissipation” range of the energy spectrum, but that this range can be quite wide in some cases, contaminating a substantial range of wave numbers. In the process, we will develop a “practical” approximation to the subgrid energy transfer in isotropic turbulence, and we will gain insight into the structure of the nonlinear interactions among turbulent scales of comparable size, and into the nature of energy backscatter. Some considerations on future research directions are offered at the end.

## 2. Inertial simulations

### 2.1 The truncated Euler equations

This section of the paper will deal with attempts to model the inertial spectral range of isotropic turbulence at infinite Reynolds number.

Our first numerical experiment simulates spatially periodic turbulence with no viscosity. The numerical method is fully spectral, using primitive variables  $\mathbf{u}$ ,  $p$ , with dealiasing achieved by spherical masking in Fourier space and phase shifting (Rogallo, 1981, see description in Canuto *et al.*, 1987). The resolutions quoted for the different simulations reflect the number of real Fourier modes in each direction before dealiasing; the number of actual useful modes in the power spectra,  $k_{\max}$ , is slightly less than half that number. The Fourier expansion functions are  $\exp(ik_j x_j)$ ,  $|k_j| = 0, 1, \dots, N/2$ , so that the length of the box side is always  $2\pi$ . The time stepping procedure is second-order Runge-Kutta for the nonlinear terms and an analytic integrating factor for the viscous ones, when present. The time step is automatically controlled to satisfy the numerical stability condition. Unless stated otherwise, all experiments are forced to achieve a statistically stationary flow, and

the results presented are long term averages, usually taken over periods of the order of one or two large scale turnover times after stationarity is achieved. Forcing is achieved by multiplying all the modes in a spherical spectral shell by an appropriate real factor at every time step until the total kinetic energy contained in the shell matches a predetermined value. The energy dissipation is measured by monitoring the multiplying factor.

The first inviscid simulation was carried out at  $64^3$  resolution, and forcing was used to fix the energy in the low wavenumber shell  $k = |\mathbf{k}| \leq 2.5$ . The simulation was initiated from a fully resolved NS forced field at the same resolution and with  $k_{\max}\eta \approx 2$ , where  $\eta$  is the Kolmogorov scale, with a microscale Reynolds number  $Re_\lambda \approx 36$  (Jiménez *et al.* 1993). It was not carried to a stationary state due to time limitations. As expected, energy accumulated immediately at the high wavenumber end of the spectrum, which took a characteristic  $k^2$  shape. Several stages of its evolution are shown in Fig. 1. The absence of an appreciable numerical viscosity was checked by monitoring the skewness of the velocity derivatives, which rose from an initial value of approximately -0.5, characteristic of NS turbulence, to a final one of  $\pm 10^{-3}$ .

The inability to obtain a dissipative spectrum from the truncated Euler equations themselves shows that an extra condition is needed in the simulation. Since *two* possible similarity solutions exist, *two* conditions have to be used to decide the proportion in which they enter in the final solution. A useful model in which to explore what practical conditions might be most appropriate is the “diffusion” approximation to turbulent energy transfer proposed by Leith (1967). He obtains a differential equation for  $E(k)$  as a function of time and wave number

$$\partial E / \partial t + \partial \epsilon / \partial k = -2\nu k^2 E. \quad (1a)$$

where the dissipation  $\epsilon$  appears as an energy flux in spectral space, and is given by

$$\epsilon = -k^{13/2} \frac{\partial}{\partial k} k^{-3} E^{3/2}. \quad (1b)$$

Equation (1b) was constructed to have the solutions  $k^2$  and  $k^{-5/3}$  in the inviscid steady state limit and can be derived from an energy shell model with both forward and backward scatter, in the limit of infinitely thin spectral shells (Bell and Nelkin, 1978). The two similarity solutions are

$$\epsilon = \text{const.}, \quad E = (2\epsilon/13)^{2/3} k^{-5/3}, \quad (2)$$

and

$$\epsilon = 0, \quad E \sim k^2. \quad (3)$$

Since eq. (1) is nonlinear, the final stationary inviscid spectrum is not simply a linear combination of both solutions, but

$$E = (2\epsilon/13)^{2/3} \left( k^{-5/2} + ak^3 \right)^{2/3}. \quad (4)$$

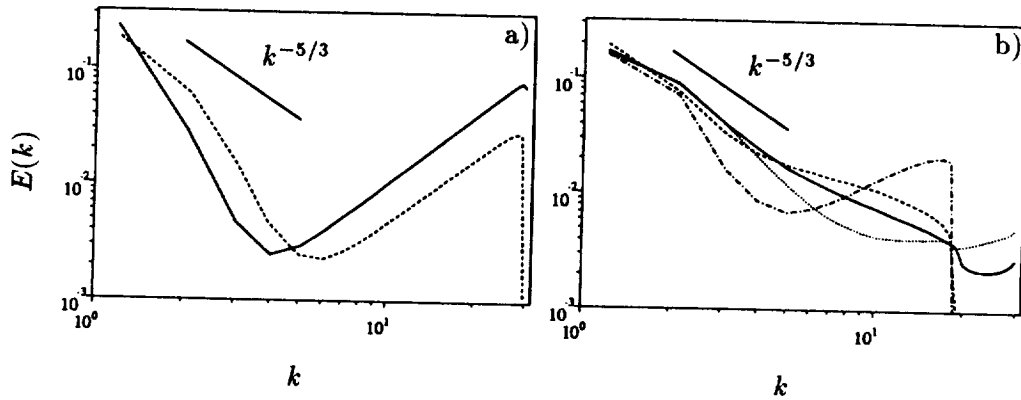


FIGURE 2. Three dimensional energy spectra for Euler simulations in which the total energy at high wavenumbers,  $k > k_c$ , is kept fixed, in addition to the forcing at low wave numbers. (a)  $k_c = k_{\max} - 1$ . — : energy in damped shell,  $E_c = 7.5 \times 10^{-2}$ ; ---- :  $10^{-3}$ . (b)  $k_c = 2k_{\max}/3$ . ..... line:  $E_c = 0.05$ ; — : approx. 0.027, see text; ---- :  $5 \times 10^{-3}$ ; — :  $5 \times 10^{-4}$ .

This solution has the right Kolmogorov form up to an (arbitrary) constant but contains an extra term coming from the equipartition component. Two conditions are needed to adjust the dissipation,  $\epsilon$ , and the constant  $a$ . Note that in the model as well as in the actual flow, the equipartition spectrum is conservative. Because the behaviors of the two spectra are very different, one of them increasing and the other decreasing with  $k$ , the two constants are determined almost independently by disjoint wave number ranges. Fixing the energy in a low wave number shell essentially fixes the dissipation because  $k^2$  is small in that range, while fixing the energy in a high wave number shell does the same for the equipartition component. This is consistent with the common statement that the large scales of the flow fix the dissipation, but it is true only if the equipartition component,  $a$ , can be guaranteed to be  $O(1)$ . The previous inviscid example shows that this only happens if the energy at high wave numbers has been forced to be small. The role of viscosity, from the point of view of the large scales, can be seen as that of avoiding the accumulation of energy at high wavenumbers and thus of controlling the  $k^2$  component of the spectrum. In general, spectra with an insufficient dissipation mechanism look “almost right” at low wave numbers but have a large “hook” at high wave numbers, where the  $k^2$  component takes over. Small spectral hooks of this kind are common in the last few wave numbers of direct numerical simulations.

## 2.2 Constrained simulations

Figure 2a shows the results of two attempts at fixing the energy both in the high and in the low spectral shells for a direct Euler simulation. The numerical parameters and the forcing scheme in the low wave numbers are exactly the same as for Fig. 1, but the code also adjusts independently the last spectral shell (of width

$\Delta k = 1$ ) by multiplying all the modes in it by a new damping factor, computed every time step, that brings the total energy in the shell to the desired level. This proves to be effective only when the energy chosen is high enough but fails if it is too small, in which case the rest of the spectrum decouples from the damped shell. A little thought shows that too small an energy in the high wave numbers inhibits the energy transfer and that the next lower shell cannot dump energy into it fast enough. This is no more than saying that the Reynolds stresses, and the turbulent energy transfer, can only work if there are small scales to generate them, and that the dissipation of a laminar flow is much smaller. The result is an accumulation of energy similar to the one in the inviscid case. In fact, the limit in which the energy in the last shell is set exactly to zero is numerically equivalent to de-aliasing, and it would produce the same result as the unconstrained simulations in Fig. 1.

Controlling the energy over a thicker shell is more efficient since the lower modes have more spectral triads into which the energy can be transferred (or more active small scales). The result of fixing, in the same way as before, the total energy contained in all the modes with wave numbers  $k > k_c = 2k_{\max}/3$  is shown in Fig. 2b. It is now possible to control the energy of the high modes almost well enough to obtain a  $k^{-5/3}$  extrapolation from the modes that are completely resolved by the simulation. The solid line in Fig. 2b is defined in that way; the energy above  $k_c$  is controlled at each step to coincide with the value it would have if its spectrum was a smooth inertial extrapolation of  $E(k_c)$ . That choice seems to be close to optimal from the point of view of obtaining a  $k^{-5/3}$  over most of the inviscid scales. However, in this case also, an attempt to make the energy too small in the damped shell gross contamination of the spectrum with the equipartition component.

In all these simulations, the resolved scales are inviscid. In Fig. 1, all the spectral modes, except those in the lower forced shell, satisfy the Euler equations, and since there is no energy dissipation, the solution tends to equipartition. In the simulations in Fig. 2, only those modes with  $k \leq k_c$  satisfy the inviscid equations. They receive energy from the lower forced shell and lose it to those modes above  $k_c$ , where it is removed every time step by the damping factor. This factor acts as an effective viscosity which is zero for all modes below  $k_c$ , but which is active above that threshold and which can be considered as an extreme case of wavenumber dependent hyperviscosity.

Fornberg (1977) used a similar simulation scheme to compute two dimensional turbulence. He let the enstrophy in a high shell grow for some time under the effect of the cascade and zeroed it periodically. The present scheme is probably a better representation of the true cascade dynamics in that it gives the flow a stationary energy reservoir with which to interact

In both schemes, the effect of the damped high-wavenumber shell is to provide a spectral bucket into which energy can be dumped naturally by the nonlinear interactions. It appears from the results of the simulations that a simple uniform damping factor, which adjusts the amplitudes of the small scale modes but does not modify their phase relationships, provides an approximation to the small scale flow that is good enough to produce a reasonably accurate level of energy transfer



into the damped shell. The key seems to be having the right amount of energy in that shell to produce the correct cascade rate. This suggests that an ideal transfer could be obtained if the energy spectrum in the damped shell was adjusted to follow exactly the  $k^{-5/3}$  law.

A similar experiment was performed by (She & Jackson 1993, Zhou 1993). Both investigators constrained the entire spectrum to follow exactly the  $k^{-5/3}$  law and studied different aspects of the energy transfer. In both cases, the correct scaling behaviors were observed and the Kolmogorov constant fell in the range of the experimental values. Shtilman and Chasnov (1992) also studied a constrained Euler system in which the spectrum was forced to remain exactly equal to that of a direct simulation of the same flow, run in parallel at higher resolution. Their goal was to determine whether the statistics of the constrained flow would be similar to those of the DNS field at the same time when filtered down to the same resolution. The correspondence was shown to be only approximate, especially for the higher statistical moments, but the low order statistics, those involved in the energy transfer mechanism, agreed well.

Our goal is different. We are not only trying to understand the degree to which the constrained system approximates locally the energy transfer, but also to determine whether an unconstrained system can be made to simulate the inviscid inertial spectrum by providing it with a downstream spectral “boundary condition” which absorbs energy in the right way. If this turns out to be possible, the unconstrained system might better approximate the statistics of the large scales, even though those of the small scales are only accurate to the extent of providing a correct energy sink. Such a scheme also offers a better chance of being adaptable to the study of inhomogeneous turbulent flows. We are therefore interested in constraining only a partial spectral shell at high wave numbers to a spectrum that is the  $k^{-5/3}$  extrapolation of the energy in the last fully resolved shell  $k_c$ .

This was done for the dotted line in Fig. 3. The modes in  $k > k_c = k_{\max}/2$  were divided into sub-shells of thickness  $\Delta k = 1$ , and an independent damping factor was computed for each sub-shell at each time step to bring the spectrum to the form  $E(k, t) = E(k_c, t)(k_c/k)^{5/3}$ . As expected from the previous discussion, the behavior of the whole spectrum and not just that of the forced part was much closer to inertial than before. When the compensated spectrum is plotted in linear coordinates, however, it is seen that the result is still not perfect (Fig. 3b). A perfect inertial spectrum in this representation would be strictly equal to the Kolmogorov constant.

### 2.3 Turbulent viscosity

What are still missing are the nonlinear interactions involving scales smaller than those at the high end of the damped shell, which are not resolved in the simulation. Those interactions, linking the unconstrained modes with those in the sub-grid scales, act across a spectral gap imposed by the damped shell, and it is generally accepted (Kraichnan 1976, Yoshizawa 1982) that under those circumstances the effect of the small scales is equivalent to that of a constant eddy viscosity. The presence in filtered DNS fields of an eddy viscosity plateau at wave numbers one or

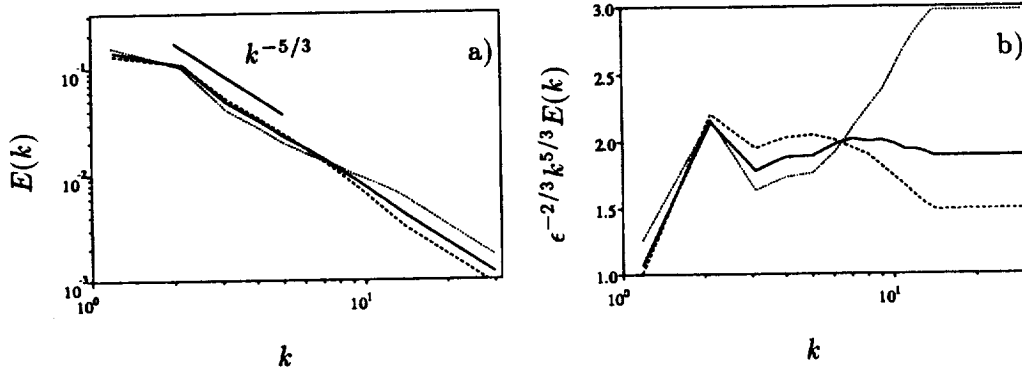


FIGURE 3. Three dimensional energy spectra for Euler simulations in which the energy spectrum in the high wavenumber shell,  $k > k_{\max}/2$  is adjusted continuously to  $k^{-5/3}$ , in addition to a constant eddy viscosity and to the forcing at low wave numbers. (a) Uncompensated, (b) Normalized. .... : normalized eddy viscosity,  $\alpha/\alpha_0 = 0$ ; — : 0.8; ---- : 1.4.

more octaves lower than the filter width has been confirmed experimentally (Lesieur and Rogallo 1989). From dimensional considerations (Kraichnan 1976), the viscosity coefficient can be written as

$$\nu_e = \alpha [E(k_{\max})/k_{\max}]^{1/2}. \quad (5)$$

The normalized eddy viscosity  $\alpha$  can be evaluated within the EDQNM approximation for infinite Reynolds number as  $\alpha_0 \approx 0.267$  (Lesieur, 1990, pg. 324). This value assumes that the energy spectrum is strictly inertial beyond  $k_{\max}$ , with a Kolmogorov constant of 1.4. The effect of adding this viscosity to the previous simulation is shown in Fig. 3. All modes are first marched according to the NS equations, with the viscosity given by rescaled to  $k^{-5/3}$ . Different values of  $\alpha$  produce slightly different results, but the spectrum seems to fit best a single  $k^{-5/3}$  law for a value slightly smaller than the EDQNM result,  $\alpha \approx 0.214 = 0.8\alpha_0$ . The corresponding Kolmogorov constant is in the range 1.8-1.9 (see Fig. 3b), in excellent agreement with that obtained in (She & Jackson 1993). This value is somewhat larger than the usually accepted one of 1.5, and the reason for the discrepancy is not clear. Zhou (1993) obtains a value of approximately 1.5 using a method which is conceptually similar to the one in (She & Jackson 1993). It has been suggested (Rogallo, private communication) that the discrepancy between the numerical and experimental values may result from the relatively small number of numerical modes in the simulation ( $64^3$ ) which robs the cascade of the interactions with the low wavenumber modes at scales larger than the size of the computational box. If that were so, the correct value would be approached for larger simulations. A single experiment in a  $128^3$  box, using the same subgrid mode, gave a slightly lower constant in the range 1.75-1.85, but the difference was too small for a definite conclusion.

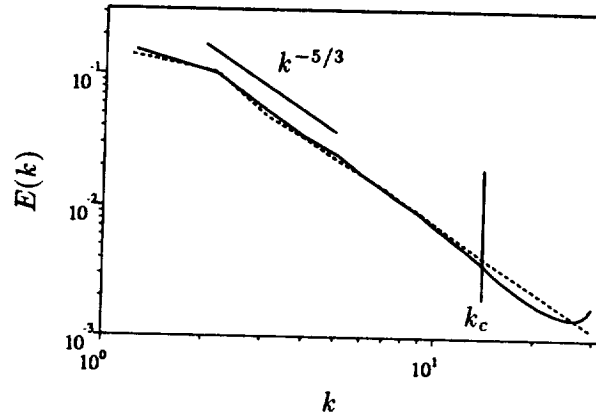


FIGURE 4. Equilibrium three-dimensional energy spectrum for  $64^3$  numerical boxes in which energy is forced both at the low wavenumber shell, and for modes above  $k_c = k_{\max}/2$ . — : Total energy in the high shell extrapolated to  $k^{-5/3}$ . ---- : Energy spectrum in high shell extrapolated. Vertical line is limit of damped shell. Turbulent viscosity in both cases:  $\alpha/\alpha_0 = 0.8$ .

In any case, these experiments suggest that, besides the constant eddy viscosity introduced to model the interaction with the very small scales, all that is needed to correctly model the dissipation at high Reynolds numbers is to have a “sacrificial” spectral shell with the right amount of energy, just beyond the scales of interest. The nonlinear interactions with the modes in that shell mimic those with scales just below the fully resolved ones in the real flow. It is important to realize that there is little reason to expect the modes in the damped shell to be correctly computed and that they should be filtered out when flow statistics higher than the energy are calculated.

For the infinite Reynolds number case studied here, the optimum damping strategy seems to be to constrain the spectrum in the sacrificial shell to the extrapolated  $k^{-5/3}$  law. Other similar strategies can probably be developed for flows at lower Reynolds numbers. While this is trivial to implement in the present isotropic spectral code, it is interesting to inquire whether the energy transfer outside the damped shell is sensitive to the detailed form of the constrained spectrum, or whether a simpler strategy might be used.

Figure 4 shows the results of an experiment in which the total energy in the last shell ( $k > k_c = k_{\max}/2$ ), rather than its spectrum, was used as a constraint, with the extra addition of the eddy viscosity of Fig. 3. The total energy is adjusted to the one that would be contained in the damped layer if its spectrum were extrapolated from  $E(k_c)$  according to the  $k^{-5/3}$  law. The optimum simulation from Fig. 3 is also included for comparison, and the results are seen to differ little outside the damped layer.

From a practical point of view, this scheme is much simpler than the full  $k^{-5/3}$  one since it involves only the calculation of a single global energy and of a single

damping factor. It could, in principle, be implemented in a finite difference code by the use of appropriate filters.

### 3. Backscatter

The results in the previous section are consistent with the classical idea that the interaction of a given range of turbulent scales with features of much smaller size can be approximately modeled by an eddy viscosity, even though the interaction between similar scales can not. A common scheme for the modeling of these near interactions is to separate them into an enhanced wave-number dependent eddy viscosity and a backscatter component which moves energy from the small to the large scales (Kraichnan 1976, Leslie & Quarini 1979). The backscatter component is sometimes represented as a random stirring force (Chasnov 1991) because it can be shown that the effect of such a force is always to feed energy into the flow. The separation into forward and backward cascade has been re-encountered recently in a different context. When a direct simulation of turbulence is divided into large and small scale components by filtering the velocity field, the flow of energy between the two components is found to be randomly positive and negative at different *spatial* locations in the flow, so that the global energy drain to the small scales is only the small residue from two large terms of opposite sign (Piomelli *et al.* 1991). It has also been shown that most of this random energy exchange is dominated by interactions among structures separated at most by a factor of two in wavenumber magnitude (Domaradzki, Liu & Brachet 1993).

There is no clear correspondence between the two different definitions of backscatter, and in fact, it can be argued that the existence of regions of positive and negative energy transfer has little to do with the presence of a cascade. It is easy to find examples of steady laminar flows in which there is no net transfer of energy, but which contain regions of localized forward and backward “cascade”. An examination of such flows might be useful in understanding more complicated situations. We will discuss a simple example which admits an analytical solution.

Consider a velocity field  $u$  which is decomposed into large and small scale components by means of a circular box filter

$$G(x) = 1/\pi a^2 \quad \text{if } |x| < a, \quad G(x) = 0 \quad \text{otherwise.} \quad (6)$$

Denote filtered, large scale, variables by an overbar. The subgrid Reynolds stress is defined as

$$\tau_{ij} = \overline{u_i u_j} - \bar{u}_i \bar{u}_j. \quad (7)$$

It is also possible to define a large scale rate of strain tensor

$$\bar{S}_{ij} = (\bar{u}_{i,j} + \bar{u}_{j,i})/2, \quad (8)$$

and a local subgrid “Reynolds” energy transfer rate

$$Q = \tau_{ij} \bar{S}_{ij}. \quad (9)$$

This term appears on the right hand side of the energy equation for the large scales and, with the opposite sign, on that for the small scales. Consider now a simple steady two dimensional flow formed by a point vortex, of circulation  $\gamma$ , located at the origin in the pure straining field

$$u_1 = -\sigma x_2, \quad u_2 = -\sigma x_1. \quad (10)$$

It is easy to see that the effect of the filter on the point vortex is to spread it into a circular patch of uniform vorticity  $\omega_a = \gamma/4\pi a^2$  with radius  $2a$ , while the straining flow (10) is left invariant. The full Reynolds stress and rate of strain tensors can be computed explicitly (see Appendix) and the dominant terms near the origin are

$$\tau_{ij} = \frac{\gamma^2 \log(a/r)}{2\pi^2 a^2} \begin{pmatrix} \sin^2 \phi & -\sin \phi \cos \phi \\ -\sin \phi \cos \phi & \cos^2 \phi \end{pmatrix}, \quad (11)$$

which is due to the vortex, and

$$\bar{S}_{ij} = \begin{pmatrix} 0 & -\sigma \\ -\sigma & 0 \end{pmatrix}, \quad (12)$$

which is due to the stagnation flow, where  $(r, \phi)$  are polar coordinates based on  $(x_1, x_2)$ . When  $r \ll a$ , the transfer term behaves as

$$Q = \frac{\gamma^2 \sigma}{2\pi^2 a^2} \log(a/r) \sin 2\phi, \quad (13)$$

which is not zero pointwise even though its integral vanishes identically when taken over the whole plane, as it must for any stationary flow.

The interpretation is easy. The small scales of the flow lie near the vortex, where gradients are large. The vortex alone produces no transfer since fluid particles follow circular trajectories at a constant distance from the center and, therefore, remain at the same "scale". When the stagnation flow is added, the particles move towards the vortex when they pass near  $\phi = \pi/4$  or  $5\pi/4$ , and away from it when they pass near  $\phi = 3\pi/4$  or  $7\pi/4$ . In the first case, the particle moves from a large scale to a small scale environment, and the energy appears to cascade to higher wave numbers. In the second case, the opposite is true, and the cascade is reversed. Note that in reality there is only a reversible deformation of fluid particles as they are carried by the flow into regions in which the dominant local gradients are larger or smaller. It can be shown that in situations less symmetric than the one discussed here, the energy exchange is most active when the scales of the advecting flow are roughly similar to those of the flow generating the gradients. The "true" cascade, resulting in an irreversible transfer of energy from one scale to another, comes from those interactions in which the two scales are very different and in which the deformations are not reversible. The idea that most of the interaction between neighboring scales is not a simple energy diffusion process was put forward forcibly by Kraichnan (1976), Rose (1977), and many others afterwards.

The situation is complicated further because the quantity  $Q$  is only part of the real subgrid energy flux  $\epsilon(x, t) = -D(\bar{u}^2/2)/Dt$ , although it is often used to represent the entire flux because the volume integrals of the two are the same. The local difference, which contains the divergence of pressure-velocity and stress-velocity products, can be of the same order of magnitude as the flux itself, and in fact, it is easily seen that the sign of (13) is not even necessarily the same as that of the real transfer because it is compensated by the divergence terms. A consequence is that while it makes sense to speak of energy transfer over large volumes of the fluid or of transfer between widely separated scales in which the surface terms tend to cancel statistically, the *local* energy transfer due to the type of eddy advection displayed by the previous example is a poorly defined quantity that may be difficult to model in any locally deterministic way. The procedure outlined in the previous section avoids this by providing a model for the subgrid scales rather than trying to model the stresses that they produce.

#### 4. Discussion and future work

We have shown that, at least for the calculation of the energy spectrum, isotropic turbulence at high Reynolds numbers can be modeled rather simply by damping a high wavenumber spectral shell in such a way that the energy it contains is the same as that which would be contained in a corresponding shell within an inertial range. The simulations are improved somewhat by the addition of a constant eddy viscosity to account for the nonlinear interactions with scales smaller than those contained in the constrained shell. The magnitude of the viscosity coefficient is a function of the energy in the last spectral shell and agrees approximately with the predictions of EDQNM calculations. The interactions with the flow scales in the constrained shell are approximately accounted for by providing that shell with the right energy, and they include all the backscatter from small to large scales since the effect of the eddy viscosity is purely dissipative.

The effect on the resolved scales of varying the normalized eddy viscosity, the only adjustable parameter in the model, is slight (Fig. 3) although it has a large effect on the behavior of the damped shell. This is best explained by the fact that most of the energy transferred from the resolved scales goes into the spectral octave immediately below it, but that the scales themselves are insensitive to the eventual fate of the energy once it has been transferred. For example, in both of the simulations in Fig. 4, approximately 72% of the energy is lost to the damped shell while only the remaining 28% is withdrawn directly from the resolved scales by the eddy viscosity. These values are broadly comparable to those predicted by the simplified analysis of Tennekes & Lumley (1972), who on the basis of qualitative arguments about the physical mechanism of the cascade, conclude that the energy transfer between shells with wave numbers  $k$  and  $k' > k$  should vary as  $(k/k')^{7/3}$ . This behavior has been verified in (Zhou 1993) for shells with large wave number disparities. An integration of that law results in a prediction that 61% of the transfer should go to the next wave number octave.

The insensitivity of the resolved scales to the details of the energy dissipation in the damped shell can be seen from the comparatively small differences between their

spectra in the  $\alpha = 0$  and  $\alpha/\alpha_0 = 0.8$  simulations in Fig. 3. The energy budgets of the damped shell in both cases are very different. For  $\alpha = 0$ , energy is removed only from the damped shell by the damping factor, while for  $\alpha/\alpha_0 = 0.8$ , 28% is removed from the resolved scales by viscosity, 52% is removed by viscosity from the damped shell, and only the remaining 20% is removed by the damping factor. It is this locality of the energy transfer, coupled with insensitivity to the details of the unresolved energy shells, that makes modeling practical.

The present set of experiments belongs to the recently developed class in which part of the flow field is computed as auxiliary to the calculation of the largest scales and eventually discarded. The best known of them is the Dynamic model in (Germano *et al.* 1991). In that model, the subgrid dissipation is modeled by an eddy viscosity whose magnitude is computed by enforcing similarity of two different scales of the flow. Because the similarity is applied locally, the presence of pointwise backscatter results in locally negative viscosity coefficients that cause numerical problems. It follows from the arguments in §3 that such diffusive models for the backscatter are unlikely to be successful.

We have followed a different route in that we have simulated the near interactions by providing an actual energy shell of roughly the right amplitude with which the flow can interchange energy naturally. There is no guarantee that the flow structures whose scales are in this shell are correctly computed, and they should be filtered before the results are used. This is true of the smallest scales in most LES calculations. On the other hand, the present scheme is intrinsically dissipative and unlikely to develop numerical instabilities. As in the Dynamic model, most of the dissipation is computed from the flow parameters themselves, and the residual eddy viscosity can be computed from analytic arguments. Furthermore, since the eddy viscosity scales with the turbulent energy, the laminar limit is contained in the model. Although the discussion in this paper is framed in terms of a spectral approach, it is indicated at the end of §2 how the model could be adapted to finite difference codes.

The experience gained in this work provides some insight into the reasons for the success of the Dynamic model in many situations. The similarity assumption in the Dynamic model essentially provides the right eddy viscosity for a smooth extrapolation of the spectrum of the resolved scales (the “test” filter) into the smaller scales and, therefore, provides a high wavenumber component with the right extrapolated energy. We have shown here that this seems to be enough to provide the field with the right dissipation.

The present model has been developed as a research tool for the study of energy transfer in isotropic turbulence and has only been tested on low order statistics. Since most high order statistical moments are known to be dominated by the small scales of the flow, they are unlikely to be captured correctly by this, or by any, LES model. More important, we have only dealt with homogeneous turbulence, and as outlined in the introduction, there are reasons to believe that some of the conclusions might not be directly applicable to inhomogeneous situations. In particular, the crucial independence of the large scale flow from the small scale details may not be

true in any local sense for those cases. Clearly, much more work is needed in all those directions.

### Acknowledgements

I have benefitted from many fruitful discussions with P. Moin, S. Ghosal and T. Lund on LES. The input of A. Wray and R. Rogallo is reflected in much of the discussion on the dynamics of the turbulent cascade. In addition, the simulations were carried out on the NAS 128-node Intel hypercube using a code developed by both of them. I am grateful to Rogallo and Ghosal for their reviewing of an early draft of this manuscript.

### REFERENCES

- BATCHELOR, G. K. 1953 *The theory of homogeneous turbulence*. Cambridge Univ. Press.
- BELL, T. L. & NELKIN, M. 1978 Time dependent scaling relations and a cascade model of turbulence. *J. Fluid Mech.* **88**, 369-391.
- BERMAN, N. S. 1978 Drag reduction by polymers. *Ann. Rev. Fluid Mech.* **10**, 47-64.
- CANUTO, C., HUSSAINI, M. Y., QUARTERONI, A. & ZANG, T. A. 1987 *Spectral methods in fluid dynamics*. Springer, pp. 85-86.
- CHASNOV, J. R. 1991 Simulation of the Kolmogorov inertial subrange using an improved subgrid model. *Phys. Fluids*. **A 3**, 188-200.
- DEAN, R. B. 1978 Reynolds number dependence of skin friction and other bulk flow variables in two-dimensional rectangular ducts. *J. Fluid Eng.* **100**, 215-223.
- DOMARADZKI, J. A., LIU, W. & BRACHET, M. E. 1993 An analysis of subgrid-scale interactions in numerically simulated isotropic turbulence. *Phys. Fluids*. **A 5**, 1747-1759.
- FORNBERG, B. 1977 A numerical study of two-dimensional turbulence. *J. Comput. Phys.* **25**, 1-31.
- GERMANO, M., PIOMELLI, U., MOIN, P. & CABOT, W. H. 1991 A dynamic subgrid scale eddy viscosity model. *Phys. Fluids*. **A 3**, 1760-1765. Erratum, *Phys. Fluids* **A 3**, 3128.
- JIMÉNEZ, J., WRAY, A., SAFFMAN, P. G. & ROGALLO, R. S. 1993 The structure of intense vorticity in isotropic turbulence. *J. Fluid Mech.* **255**, 65-90.
- KRAICHNAN, R. H. 1976 Eddy viscosity in two and three dimensions. *J. Atmos. Sci.* **33**, 1521-1536.
- KOLMOGOROV, A. N. 1941 The local structure of turbulence in incompressible viscous fluids at very large Reynolds numbers. *Dokl. Nauk. SSSR*. **30**, 301-305 (see e.g. L. D. Landau & E. M. Lifshitz, 1959, *Fluid mechanics*, Pergamon, 116-123).



- LEE, T. D. 1952 On the statistical properties of hydrodynamics and magneto-hydrodynamical fields. *Quart. App. Math.* **10**, 69-74.
- LEITH, C. E. 1967 Diffusion approximation to inertial energy transfer in isotropic turbulence. *Phys. Fluids*. **10**, 1409-1416.
- LESIEUR, M. 1990 *Turbulence in fluids*. Kluwer.
- LESIEUR, M. & ROGALLO, R. S. 1989 Large eddy simulation of passive scalar diffusion in isotropic turbulence. *Phys. Fluids. A* **4**, 718-722.
- LESLIE, D. C. & QUARINI, G. L. 1979 The application of turbulence theory to the formulation of subgrid scale procedures. *J. Fluid Mech.* **91**, 65-91.
- PIOMELLI, U., CABOT, W. H., MOIN, P. & LEE, S. 1991 Subgrid-scale backscatter in turbulent and transitional flows. *Phys. Fluids. A* **3**, 1766-1771.
- ROGALLO, R. S. 1981 Numerical experiments in homogeneous turbulence. *NASA Tech. Mem.* **81315**.
- ROSE, H. A. 1977 Eddy diffusivity, eddy noise and subgrid scale modeling. *J. Fluid Mech.* **81**, 719-734.
- SHE, Z-S., JACKSON, E. 1993 A constrained Euler system for Navier Stokes turbulence. *Phys. Rev. Lett.* **70**, 1255-1258.
- SREENIVASAN, K. R. 1984 On the scaling of the turbulence energy dissipation rate. *Phys. Fluids*. **27**, 1048-1051.
- SHTILMAN, L. & CHASNOV, J. R. 1992 LES vs. DNS: a comparative study, *Summer Program Proceedings-1992*, Center for Turbulence Research, Stanford Univ./NASA Ames, 137-143.
- TENNEKES, H. & LUMLEY, J. L. 1972 *A first course in turbulence*, MIT Press, pp. 260-261.
- WALSH, M. J. 1990 Riblets, in *Viscous drag reduction in boundary layers*, edited by D. M. Bushnell and J. N. Hefner. AIAA, pp. 203-261.
- YOSHIZAWA, A. 1982 A statistically derived subgrid model for the large-eddy simulation of turbulence. *Phys. Fluids*. **25**, 1532-1538.
- ZHOU, Y. 1993 Interacting scales and energy transfer in isotropic turbulence. *Phys. Fluids. A* **5**, 2511-2524.

### Appendix: Energy transfer in a simple stationary flow

We present here the detailed analysis of the flow discussed in §3, formed by a point vortex at the stagnation point of a straining flow in eq. (10). We define polar coordinates  $(r, \phi)$ , but express all vectors and tensors as components on the Cartesian axes  $(x_1, x_2)$ . The velocity field due to the vortex is given by

$$u_v = \frac{\gamma}{2\pi r} (\sin \phi, -\cos \phi), \quad (\text{A} - 1)$$

and that due to the straining flow is

$$u_s = -\sigma r (\sin \phi, \cos \phi). \quad (\text{A} - 2)$$

After filtering, the vortex becomes a uniform circular vortex patch. We will only be interested in the behavior of the energy inside the patch, where  $r \leq 2a$ . The filtered velocity is

$$\bar{u}_v = \frac{\gamma r}{8\pi a^2} (\sin \phi, -\cos \phi), \quad (\text{A} - 3)$$

while the filtered straining flow is equal to itself because of linearity. The Reynolds stresses are computed according to equation (7) and contain terms coming from the interaction of the vortex with itself, from the interaction of the straining flow with itself, and from the mutual interaction,

$$\tau_{vv} = \frac{\gamma^2}{4\pi^2 a^2} \left[ \log \left( \frac{a^2}{r^2} - 1 \right) - \frac{r^2}{16a^2} \right] \begin{pmatrix} \sin^2 \phi & -\sin \phi \cos \phi \\ -\sin \phi \cos \phi & \cos^2 \phi \end{pmatrix}, \quad (\text{A} - 4)$$

$$\tau_{vs} = \frac{\gamma\sigma}{\pi} \left[ 1 - \frac{r^2}{4a^2} \right] \begin{pmatrix} -\sin^2 \phi & 0 \\ 0 & \cos^2 \phi \end{pmatrix}, \quad (\text{A} - 5)$$

$$\tau_{ss} = \frac{\sigma^2 a^2}{2} \begin{pmatrix} \sin^2 \phi & -\sin \phi \cos \phi \\ -\sin \phi \cos \phi & \cos^2 \phi \end{pmatrix}. \quad (\text{A} - 6)$$

The dominant term when  $r \ll a$  is the logarithmic term in (A-4), which is reflected in eq. (11) in the body of the paper. In the same way, the filtered rate of strain tensor has a term coming from the vortex and another coming from the straining field,

$$\bar{S}_v = \frac{-\gamma}{16\pi a^2} \begin{pmatrix} -\sin 2\phi & \cos 2\phi \\ \cos 2\phi & \sin 2\phi \end{pmatrix}, \quad (\text{A} - 7)$$

$$\bar{S}_s = -\sigma \begin{pmatrix} 0 & 1 \\ 1 & 0 \end{pmatrix}. \quad (\text{A} - 8)$$

Both are of the same order near the origin, but (A-7) is orthogonal to the dominant stress, and the vortex does not generate energy transfer when interacting with itself. The "Reynolds" transfer,  $Q$ , near the origin is given by eq. (13).

Most of this transfer, however, is spurious and cancels with various divergence terms in the energy equation. The real transfer of kinetic energy from the subgrid scales into the filtered flow field is

$$-\epsilon = \frac{D\bar{u}^2/2}{Dt} = \bar{u} \cdot \nabla \bar{u}, \quad (\text{A} - 9)$$

and can be computed exactly as

$$-\epsilon = \sigma \left( \frac{\gamma^2}{64\pi^2 a^4} - \sigma^2 \right) r^2 \sin 2\phi. \quad (\text{A} - 10)$$

Its angular structure is the same as that of  $Q$ , but its sign depends on the balance between the increase of the azimuthal velocity as a particle approaches the vortex and the decrease of its radial velocity as it approaches the stagnation point.

## A large eddy simulation scheme for turbulent reacting flows

By Feng Gao

### 1. Motivation and objectives

Turbulent reacting flow has been an important problem and has attracted much attention from researchers in a variety of science and engineering disciplines. Despite intense research activity, however, much remains to be done in this field (O'Brien 1980; Pope 1985, 1990). One of the key issues in engineering application is to employ the existing models and techniques to develop a relatively simple numerical scheme for simulating complicated reacting flow systems.

Several approaches have been introduced to overcome the closure problems encountered in turbulent reacting flow simulations. Among them, the probability density function (PDF) method provides a closed form representation for the chemical source terms (O'Brien 1980; Pope 1985); for this reason it has become a preferred choice. However, the scalar PDF does not contain information concerning the transporting velocity field and the interactions between the scalar and velocity fields that has to be provided by supplementary turbulent transport and mixing models in reacting flow simulations.

The recent development of the dynamic subgrid-scale (SGS) model (Germano 1992; Germano *et al* 1991; Ghosal *et al* 1992) has provided a consistent method for generating localized turbulent mixing models and has opened up great possibilities for applying the large eddy simulation (LES) technique to real world problems. Given the fact that the direct numerical simulation (DNS) can not solve for engineering flow problems in the foreseeable future (Reynolds 1989), the LES is certainly an attractive alternative. It seems only natural to bring this new development in SGS modeling to bear on the reacting flows.

The major stumbling block for introducing LES to reacting flow problems has been the proper modeling of the reaction source terms. Various models have been proposed, but none of them has a wide range of applicability. For example, some of the models in combustion have been based on the flamelet assumption (Kerstein *et al* 1988; Trouvé & Poinso 1992), which is only valid for relatively fast reactions. Some other models have neglected the effects of chemical reactions on the turbulent mixing time scale (Valiño & Gao 1992), which is certainly not valid for fast and non-isothermal reactions (Vervisch 1993).

The PDF method can be usefully employed to deal with the modeling of the reaction source terms. In order to fit into the framework of LES, a new PDF, the large eddy PDF (LEPDF), is introduced. This PDF provides an accurate representation for the filtered chemical source terms and can be readily calculated in the simulations. The details of this scheme are described below.

## 2. Accomplishments

### Large eddy PDF

The large eddy fields, which are explicitly simulated in the LES, can be obtained by filtering the true fields with certain filters  $G$  (Germano 1992; Rogallo & Moin 1984); namely,

$$\bar{A}(\mathbf{x}, t) = \int_{-\infty}^{\infty} A(\mathbf{x}', t) G(\mathbf{x}' - \mathbf{x}) d\mathbf{x}'.$$

Among the commonly used filters, we are particularly interested in those that are localized in physical space, such as the local volume average (Schumann 1975) and the Gaussian filters (Leonard 1974), since they describe local averaged effects. For reasons that will become clear later, we choose only these positive definite filters.

By applying a filter of size  $\Delta$ , which is generally the mesh size in LES, the Navier-Stokes equation can be written as

$$\frac{\partial \bar{u}_i}{\partial t} + \bar{u}_j \frac{\partial \bar{u}_i}{\partial x_j} = \nu \nabla^2 \bar{u}_i - \nabla \bar{p} - \frac{\partial \tau_{ij}}{\partial x_j}. \quad (1)$$

Here  $\tau_{ij} = \overline{u_i u_j} - \bar{u}_i \bar{u}_j$  is the SGS stress and is normally modeled by the eddy-viscosity model originally proposed by Smagorinsky (Smagorinsky 1963):

$$\tau_{ij} - \frac{1}{3} \tau_{kk} \delta_{ij} = -2C \Delta^2 |\bar{S}| \bar{S}_{ij}, \quad (2)$$

where  $S_{ij}$  is the strain rate tensor

$$S_{ij} = \frac{1}{2} \left( \frac{\partial \bar{u}_i}{\partial x_j} + \frac{\partial \bar{u}_j}{\partial x_i} \right)$$

and  $|\bar{S}| = \sqrt{2 \bar{S}_{ij} \bar{S}_{ij}}$ .

The same type of filter with larger size  $\tilde{\Delta} > \Delta$  can be applied to the same equation. The resulting SGS stress can be represented by

$$T_{ij} = \widehat{u_i u_j} - \tilde{u}_i \tilde{u}_j.$$

If the filters are well behaved ones such as the Gaussian filters, we will have the following convolution relation

$$G(\mathbf{x} - \mathbf{x}', l) = G(l_1) * G(l_2) = \int G(\mathbf{x} - \mathbf{x}_1, l_1) G(\mathbf{x}_1 - \mathbf{x}', l_2) d\mathbf{x}_1. \quad (3)$$

Take the Gaussian filter as an example; it can be shown that  $l^2 = l_1^2 + l_2^2$ . It is obvious from (3) that  $\tilde{A} = \hat{\hat{A}}$ , where “ $\hat{A}$ ” is the filtering performed by the “gap filter” between  $\tilde{\Delta}$  and  $\Delta$ . The Germano identity (Germano 1992)

$$T_{ij} - \hat{\tau}_{ij} = L_{ij} = \widehat{\bar{u}_i \bar{u}_j} - \hat{\tilde{u}}_i \hat{\tilde{u}}_j, \quad (4)$$

where the right hand side can be explicitly evaluated from the LES field, can then be used to calculate the local coefficient  $C$  for the Smagorinsky model (Germano *et al* 1991; Moin 1991; Lilly 1992).

A similar method can be applied to the turbulent scalar field  $\psi$ , which is governed by

$$\frac{\partial \psi}{\partial t} + u_j \frac{\partial \psi}{\partial x_j} = D \nabla^2 \psi + \omega(\psi(\mathbf{x}, t)). \quad (5)$$

Its large eddy counter-part can be written as

$$\frac{\partial \bar{\psi}}{\partial t} + \bar{u}_j \frac{\partial \bar{\psi}}{\partial x_j} = D \nabla^2 \bar{\psi} - \frac{\partial}{\partial x_j} (\overline{u_j \psi} - \bar{u}_j \bar{\psi}) + \bar{\omega}(\mathbf{x}, t). \quad (6)$$

Similar eddy-viscosity type models can be developed for the scalar field (Moin *et al* 1991), namely

$$\overline{u_j \psi} - \bar{u}_j \bar{\psi} = -D_s \frac{\partial \bar{\psi}}{\partial x_j}, \quad (7)$$

where  $D_s$  can again be obtained through the dynamic procedure described above.

The major problem is to find a suitable SGS model for the reaction source term  $\omega(\psi)$ . Noticing that

$$\bar{\omega}(\mathbf{x}, t) = \int_{-\infty}^{\infty} \omega(\psi(\mathbf{x}', t)) G(\mathbf{x}' - \mathbf{x}) d\mathbf{x}' = \int [d\phi \omega(\phi) \int_{-\infty}^{\infty} \rho(\phi; \mathbf{x}', t) G(\mathbf{x}' - \mathbf{x}) d\mathbf{x}'], \quad (8)$$

where

$$\rho(\phi; \mathbf{x}, t) = \delta(\phi - \psi(\mathbf{x}, t))$$

is the fine-grain function, it is clear that once

$$P_L(\phi; \mathbf{x}, t) = \int_{-\infty}^{\infty} \rho(\phi; \mathbf{x}', t) G(\mathbf{x}' - \mathbf{x}) d\mathbf{x}' \quad (9)$$

is known, the filtered equation for the scalar field  $\psi$  is closed. For positive-definite filters, it can be shown that  $P_L$  has all the properties a PDF should have. We define it as the large eddy PDF. It is a generalization of the existing PDF concept.

In fact, for a homogeneous field, where the ensemble average can be replaced by the space average, the traditional PDF (O'Brien 1980; Pope 1985) can be recovered from our definition if a volume average filter is applied to a large enough space volume. For more general cases,  $P_L$  can be regarded as a weighted average of all contributions from the neighboring field points, depending on how far they are from the observation point.

The governing equation for  $P_L$  can be derived following the standard procedure (O'Brien 1980; Pope 1985). It can be shown that

$$\frac{\partial \rho}{\partial t} + \mathbf{u} \cdot \nabla \rho = -\frac{\partial}{\partial \phi} [(D \nabla^2 \psi + \omega) \rho]. \quad (10)$$

Applying the filter on both hand sides of (10), we get

$$\frac{\partial P_L}{\partial t} + \bar{\mathbf{u}} \cdot \nabla P_L = -\frac{\partial}{\partial \phi} [D(\rho \nabla^2 \psi) + \omega(\phi) P_L] - \frac{\partial}{\partial x_j} (\bar{u_j \rho} - \bar{u_j} \bar{\rho}). \quad (11)$$

The last term on the RHS of (11) can again be modeled by the eddy viscosity assumption. Since  $\rho$  is controlled by the underlying process  $\psi$ , the  $D_s$  obtained for  $\psi$  is equally applicable for  $\rho$  (Jiang & O'Brien 1991). A brief proof follows.

Suppose the eddy-viscosity for  $P_L$  is  $D_p$ . Note that

$$\overline{f(\psi)} = \int \phi P_L(\phi) d\phi.$$

It can be shown, by multiplying  $\phi$  on both sides of equation (11) and integrating over the composition space after inserting

$$\bar{u_j \rho} - \bar{u_j} \bar{\rho} = -D_p \frac{\partial P_L}{\partial x_j}$$

that

$$\frac{\partial \bar{\psi}}{\partial t} + \bar{u_j} \frac{\partial \bar{\psi}}{\partial x_j} = D \nabla^2 \bar{\psi} + \frac{\partial}{\partial x_j} (D_p \frac{\partial \bar{\psi}}{\partial x_j}) + \bar{\omega}(\mathbf{x}, t).$$

Comparing this equation to equations (6) and (7), it is obvious that  $D_p = D_s$ .

It can be shown that

$$\overline{(\rho \nabla^2 \psi)} = E_L \{ \nabla^2 \psi | \phi \} P_L(\phi).$$

If  $A$  and  $B$  are composition space representation of the fields  $a(\mathbf{x})$  and  $b(\mathbf{x})$ , then  $E_L$  is defined by

$$E_L \{ A | B \} P_L(B) = \int A P_L(A, B) dA$$

and

$$P_L(A, B) = \int \delta(A - a(\mathbf{x}')) \delta(B - b(\mathbf{x}')) G(\mathbf{x}' - \mathbf{x}) d\mathbf{x}'.$$

$E_L \{ A | B \}$  can be interpreted as the average of  $A$ , weighted by  $G(\mathbf{x}' - \mathbf{x})$ , over the spots where  $b(\mathbf{x}') = B$ . The modeling of this term is generally difficult, as we have experienced in the traditional PDF approach. However, the fundamental physics expressed by this term remains the same – it represents the enhancement of diffusion by turbulent fluctuations. Therefore, models analogous to those used in the traditional PDF can be used to close this term. For example, if the LMSE model (O'Brien 1980) were used, we would have

$$E_L \{ \nabla^2 \psi | \phi \} \sim -\frac{1}{\tau_L} (\phi - \bar{\psi}) + D \nabla^2 \bar{\psi},$$

where  $1/\tau_L \propto (D + D_s)$ . After substituting this relation into (11), it can be shown that (11) recovers (6). Therefore, this relaxation model is adequate if one is only interested in the large eddy field.

Equation (11), supplemented by the above closure models, can be solved using the well established Monte-Carlo techniques for the scalar PDF (Pope 1981, 1985). A few advantages of this simulation scheme can be immediately identified. First, a general model for the chemical source term is developed based on the PDF. It, in principle, applies to all kinds of reactions and does not require any artificial pre-assumptions. Secondly, the interactions between chemical reaction and turbulent mixing are embedded in the current model – the effects of reaction on turbulent mixing are reflected in  $D_s$  through the dynamic procedure. Thirdly, the LES provides the flexibility of resolving a certain range of large scale structures while modeling the contributions from the rest of the scales. It can be applied to a wide range of problems with different degrees of resolution depending on the available resources. Moreover, it may be worth mentioning that the Monte-Carlo simulation for scalar PDF is a well established technique while LES has shown great potential with the introduction of the dynamic SGS model. The outlook for applying the proposed scheme seems to be promising. We intend to apply the scheme described above to reactive flow problems in a number of turbulent flows, such as in homogeneous flows, for which DNS results are available.

#### *A consistency condition for SGS model*

There are, however, certain problems that should be further investigated. Correctly modeling turbulent mixing in the PDF formulation has been a long-standing problem which surely deserves more attention (Gao 1993). The consistent determination of the eddy viscosity in the LES is another such problem.

Several different consistency conditions should be considered in calculating the eddy viscosity. First, the eddy viscosity is localized; namely, it is a function of both space and time. It can not be taken freely out of the space filter; therefore, it cannot be evaluated by simple algebraic procedures. A variational approach (Ghosal *et al* 1992), which leads to an integral equation for the coefficient  $C$ , and a differential equation approach, which will be described below, have been developed to overcome this problem. Another problem is that there is no reason to believe that the eddy viscosity should be the same on both the cut-off ( $\Delta$ ) and the test ( $\tilde{\Delta}$ ) filter levels. Since the equation for  $C$  constitutes an over-determined problem (six equations for two  $C$  in the case of velocity, if different model coefficients are assumed for different filter levels), the least mean square estimate technique can be used to evaluate these different model coefficients at different levels (Moin 1991; Lilly 1992). To use the variational approach, two integral equations will have to be solved. It could be numerically very intense to do so.

In fact, if  $\Delta$  and  $\tilde{\Delta}$  are in different scale ranges, there is no reason even to believe that  $T_{ij} \sim T_{ij}(\hat{S}_{ij})$  and  $\tau_{ij} \sim \tau_{ij}(\bar{S}_{ij})$  will have the same functional form. It is, therefore, helpful to imagine that the cut-off and the test levels are brought closer and closer to each other. In this limiting process, we can be assured that  $T_{ij}$  and  $\tau_{ij}$  will have the same functional form and that the coefficients  $C$  at different levels

will approach each other.

A formal procedure can be performed in this limiting case. For simplicity, we will omit the bar in  $\bar{u}$  in the following derivations.

We assume that the gap between the cut-off and the test filters are represented by  $\epsilon$ . As the gap between two filters narrows ( $\epsilon \rightarrow 0$ ),  $G(\mathbf{x}' - \mathbf{x}, \epsilon)$  becomes more "concentrated". In fact,

$$\lim_{\epsilon \rightarrow 0} G(\mathbf{x}' - \mathbf{x}, \epsilon) = \delta(\mathbf{x}' - \mathbf{x}).$$

Let

$$\theta = \int (\mathbf{x}_1 - \mathbf{x})^2 G(\mathbf{x}_1 - \mathbf{x}, \epsilon) d\mathbf{x}_1, \quad (12)$$

it is obvious that  $\lim_{\epsilon \rightarrow 0} \theta = 0$ .

For simplicity, we will only consider symmetric filters, i.e.  $G = G(|\mathbf{x}_1 - \mathbf{x}|)$ . However, this method is not restricted to symmetric filters.

Under symmetric conditions, we have

$$\hat{u}(\mathbf{x}) = \int u G(\mathbf{x}_1 - \mathbf{x}, \epsilon) d\mathbf{x}_1 = u(\mathbf{x}) + \frac{\theta}{2} \nabla^2 u + O(\theta^2). \quad (13)$$

Obviously,

$$L_{ij} = \theta \nabla u_i \cdot \nabla u_j + O(\theta^2). \quad (14)$$

Similarly, for the Smagorinsky type of SGS model, we have

$$\begin{aligned} T_{ij} - \hat{\tau}_{ij} = & \theta \left[ -2C\Delta^2 \left( \alpha \frac{|S|}{\Delta^2} S_{ij} + \frac{|S|}{2} \nabla^2 S_{ij} + \frac{S_{kl} \nabla^2 S_{kl}}{|S|} S_{ij} \right) \right. \\ & \left. + \Delta^2 \nabla^2 (C|S|S_{ij}) + \frac{1}{3} \delta_{ij} \frac{\partial u_k}{\partial x_l} \frac{\partial u_k}{\partial x_l} \right] + O(\theta^2), \end{aligned} \quad (15)$$

where we have used the relation  $\tilde{\Delta}^2 = \Delta^2 + \alpha\theta^2$ . For Gaussian filters,  $\alpha = 1$ .

Substituting both (14) and (15) into the Germano identity (4) and taking the limit  $\epsilon \rightarrow 0$ , we have

$$\begin{aligned} & -2C\Delta^2 \left( \alpha \frac{|S|}{\Delta^2} S_{ij} + \frac{|S|}{2} \nabla^2 S_{ij} + \frac{S_{kl} \nabla^2 S_{kl}}{|S|} S_{ij} \right) + \Delta^2 \nabla^2 (C|S|S_{ij}) \\ & = \nabla u_i \cdot \nabla u_j - \frac{1}{3} \delta_{ij} \frac{\partial u_k}{\partial x_l} \frac{\partial u_k}{\partial x_l}. \end{aligned} \quad (16)$$

This equation, when properly contracted, can be used to solve for the local model coefficient,  $C$ . Clearly, this procedure can be equally useful if different functional forms for  $S_{ij}$  and  $\tau_{ij}$  are chosen.



### Acknowledgments

This report is based on a paper co-authored by FG and Prof. E. E. O'Brien. FG has benefited from discussions with Prof. P. Moin and Drs. R. M. Moser and M. M. Rogers. I would also like to thank Dr. P. Durbin for revising this manuscript.

### REFERENCES

- GAO, F. 1993 PDF approach for turbulent scalar field: some recent developments, *Annual Research Briefs-1992*, Center for Turbulence Research, NASA Ames/Stanford University.
- GERMANO, M. 1992 Turbulence: the filtering approach. *J. Fluid Mech.* **238**, 325-336.
- GERMANO, M., PIOMELLI, U., MOIN, P. & CABOT, W. 1991 A dynamic subgrid-scale eddy-viscosity model. *Phys. Fluids A*. **3**, 1760-1765.
- GHOSAL, S., LUND, T.S. & MOIN, P. 1992 A dynamic localization model for large-eddy simulation of turbulent flows (submitted for publication).
- JIANG, T.L. & O'BRIEN, E.E. 1991 Simulation of scalar mixing by stationary isotropic turbulence. *Phys. Fluids A*. **3**, 1612-1624.
- KERSTEIN, A.R., ASHURST, W.T. & WILLIAMS, F.A. 1988 Field equation for interface propagation in an unsteady homogeneous flow field. *Phys. Rev. A*. **37**, 2728-2731.
- LEONARD, A. 1974 Energy cascade in large-eddy simulations of turbulent fluid flows. *Advances in Geophysics*. **18A**, 237-248.
- LILLY, D.K. 1992 A proposed modification of the Germano subgrid-scale closure method. *Phys. Fluids A*. **4**, 633-635.
- MOIN, P. 1993 A new approach for large eddy simulation of turbulence and scalar transport, in *New Approaches and Concepts in Turbulence*. Dracos and Tsinober, eds., Birkhauser.
- MOIN, P., SQUIRES, K., CABOT, W. & LEE, S. 1991 A dynamic subgrid-scale model for compressible turbulence and scalar transport. *Phys. Fluids A*. **3**, 2746-2757.
- O'BRIEN, E. E. 1980 The probability density function (pdf) approach to reacting turbulent flows. in *Turbulent Reacting Flows*. 185-218, Springer-Verlag.
- POPE, S.B. 1981 Monte Carlo method for the PDF equations of turbulent reactive flow. *Combust. Sci. Tech.* **25**, 159-174.
- POPE, S. B. 1985 PDF methods for turbulent reactive flows. *Prog. Energy Comb. Sci.* **11**, 119-192.
- POPE, S. B. 1990 Computations of turbulent combustion: progress and challenges. *Proc. Int. Symp. Combustion*, The Combustion Institute, Pittsburgh, 591.
- ROGALLO, R.S. & MOIN, P. 1984 Numerical simulation of turbulent flows. *Ann. Rev. Fluid Mech.* **16**, 99-137.

- REYNOLDS, W.C. 1990 The potential and limitations of direct and large eddy simulations, in *Whither Turbulence*, Springer-Verlag.
- SCHUMANN, U. 1975 Subgrid scale model for finite difference simulations of turbulent flows in plane channels and annuli. *J. Comp. Phys.* **18**, 376-404.
- SMAGORINSKY, J. 1963 General circulation experiments with the primitive equations. I. The basic experiment. *Mon. Weather Rev.* **91**, 99-165.
- TROUVÉ, A. & POINSOT, T. 1992 The evolution equation for the flame surface density in turbulent premixed combustion, in *Proc. 1992 Summer Program*, Center for Turbulence Research, NASA Ames/Stanford University.
- VALIÑO, L. & GAO, F. 1992 Monte Carlo implementation of a single-scalar mapping closure for diffusion in the presence of chemical reaction. *Phys. Fluid A*. **4**, 2062-2069.
- VERVISCH, L. 1993 Study and modeling of finite rate chemistry effects in turbulent non-premixed flames, *Annual Research Briefs-1992*, Center for Turbulence Research, NASA Ames/Stanford University.

77-25  
2014 87  
195  
N94-24150

## The combustion program at CTR

By T. J. Poinso<sup>1</sup>

### 1. Introduction

Understanding and modeling of turbulent combustion are key problems in the computation of numerous practical systems. Because of the lack of analytical theories in this field and of the difficulty of performing precise experiments, direct numerical simulation (DNS) appears to be one of the most attractive tools to use in addressing this problem. The general objective of DNS of reacting flows is to improve our knowledge of turbulent combustion but also to use this information for turbulent combustion models. For the foreseeable future, numerical simulation of the full three-dimensional governing partial differential equations with variable density and transport properties as well as complex chemistry will remain intractable; thus, various levels of simplification will remain necessary. On one hand, the requirement to simplify is not necessarily a handicap: numerical simulations allow the researcher a degree of control in isolating specific physical phenomena that is inaccessible in experiments.

CTR has pursued an intensive research program in the field of DNS for turbulent reacting flows since 1987. DNS of reacting flows is quite different from DNS of non-reacting flows: without reaction, the equations to solve are clearly the five conservation equations of the Navier Stokes system for compressible situations (four for incompressible cases), and the limitation of the approach is the Reynolds number (or in other words the number of points in the computation). For reacting flows, the choice of the equations, the species (each species will require one additional conservation equation), the chemical scheme, and the configuration itself is more complex:

- (1) The choice of the conservation equations to solve is open to discussion. Most DNS of non-reacting flows have been performed for incompressible constant-density flows. For reacting flows, incompressible (constant density, constant pressure), low-Mach number (variable density, constant pressure), or fully compressible formulations (variable density, variable pressure) may be used. Although incompressible formulations produce interesting information regarding certain mechanisms present in a turbulent flame, they are limited by the assumption of constant density and temperature ("cold" flames or zero heat release), which makes their results too different from real flames in many dynamical aspects. The following step for combustion is, therefore, to use a low-Mach number approximation where pressure is supposed to be constant but density may change because of heat release (Rutland 1989, Rutland and Trouve 1990, Mahalingam 1989). In

<sup>1</sup> C.N.R.S. and CERFACS, France

this formulation, acoustic waves are eliminated and the time step is not limited by the classical Courant condition on sound speed, making the formulation especially well-suited to slow flows (low-Mach number). Finally, performing a fully compressible computation is also possible and has the advantage of offering an easier treatment of boundary conditions.

- (2) The choice of the number of species to consider and of the chemical scheme is a source of controversy and speculation. Chemists argue that a realistic computation of most hydrocarbon fuels combustion requires at least thirty species while DNS specialists indicate that the numerical constraints of an unsteady computation in three dimensions make such a computation practically impossible today. In fact, the choice of the chemical scheme is essentially dependent on the question to address: studying the folding of premixed flames in low-intensity turbulence may be done without any chemistry at all (the knowledge of a flame speed is sufficient) while considering pollution problems with DNS will require a reasonably complete chemical scheme. The latter computation will be much more realistic (and expensive), but the former may also be quite valuable. Interesting results on turbulent combustion (Yeung *et al.* 1990, Cant and Rutland 1990) have been obtained with codes of the first type (where chemistry is absent).
- (3) The choice of the configuration and of the corresponding boundary conditions leads to additional difficulties. Most DNS of cold flows are performed in periodic domains. Periodicity is not achieved in most reacting flows, and, therefore, one must specify new boundary conditions which are compatible with the precision of DNS and are able to treat inlet and outlet flows, for example. Coupling phenomena between inlets and outlets are quite common in DNS because the numerical schemes which are used have very low artificial viscosity. Therefore, all waves (especially numerical or unphysical waves) may travel on the grid and propagate from the outlet to the inlet (Buell and Huerre 1988, Poinso and Lele 1992). For incompressible or low Mach number formulations (Rutland and Ferziger 1989, Lowery and Reynolds 1987), the specification of boundary conditions which prevent these phenomena requires a fine tuning to be compatible with the pressure solver used inside the domain. "Convective conditions" may be used near outlets to satisfy global mass conservation. Another solution is to sacrifice a certain part of the computational domain near the outlet and use it as a buffer zone where perturbations are damped by a high artificial viscosity before they reach the outlet (Rai and Moin 1991). There is a large body of literature on non-reflecting boundary conditions, and there is no doubt that it is one of the major problems in the development of DNS codes for reacting flows.
- (4) Because of cost considerations, the possibility of performing two-dimensional computations is often used, and the merits of this approach versus three-dimensional cases remain to be determined. The problem is similar to the choice of a chemical scheme: first-order arguments such as "Turbulence is always three-dimensional" do not always lead to sound numerical approaches. The situation here is different from non-reacting cases where the structure of turbulence is (indeed) intrinsically three-dimensional. For premixed flames, DNS (Ashurst 1991, Cant and Rutland

1990) shows that the probability of finding a cylindrical (2D) flame sheet is much higher than the probability of finding a really 3D spherical flame shape. Two-dimensional flame geometries appear to be the usual rule in real flames even though the flow field ahead of these flames is fully three-dimensional. When one considers the prohibitive cost of three-space dimensional computations for reacting flows, two-dimensional simulations remain an interesting and fruitful approach, and the rule at CTR has been to use them as often as possible.

- (5) To be complete, a DNS of reacting flows should also include a description of heat transfer (radiation and convection) because heat losses near flame fronts may be important when quenching phenomena are considered.
- (6) The choice of a numerical algorithm is strongly dependent on the assumptions used for the computation. In the case of constant density ("cold") flames, the codes used are the classical incompressible DNS codes for cold flows which are mostly based on spectral methods. The accuracy of these methods is well known as well as is their major drawback: the difficulty of using boundary conditions which are not periodic. Because of this difficulty, recent DNS work has used high-order finite difference schemes (Lele 1992) or mixed schemes which use spectral methods in two directions and a finite difference method along the non periodic direction (Lowery and Reynolds 1987).

## 2. Achievements

Research at CTR has focused on all aspects of the problem indicated above. Different approaches have been used and the main accomplishments are summarized below:

- from CTR experience in DNS of 'cold' flows, specific numerical schemes were developed for reacting flows. These schemes use either spectral methods (Rutland and Trounev 1990) or compact Pade schemes (Lele 1992) to estimate spatial derivatives. Finite difference schemes have been the most widely used and are usually fourth- or sixth-order accurate in space. Explicit time-advancement is used (Runge Kutta). In most practical situations they offer a performance which is comparable to spectral methods while being much more adapted to the treatment of complex boundary conditions.
- a new technique to implement boundary conditions in DNS codes for reacting flows was developed from an initial idea valid for inviscid flows (Thompson 1987) and validated in many different situations (acoustic waves and vortices leaving the computation box, Poiseuille flow, reacting and non reacting shear layers, sub- and supersonic flow) (Poinsot and Lele 1992). The same method has been used in all CTR DNS codes for combustion since 1990. It appears that compressible formulations lead to easier treatments of boundaries than incompressible formulations because waves are explicitly computed and available for boundary conditions. (Unfortunately, this is achieved at a higher cost).
- two-dimensional computations were performed and provided many new insights into the physics of quenching in premixed turbulent flames (Poinsot *et al.* 1991)

and the dynamics of these flames (Haworth and Poinso 1992). These works were based on flame-vortex interaction as well as on flame-turbulence interaction. Simple chemical models have been used (*Fresh*  $\rightarrow$  *Burnt*), but fully compressible approaches with variable density and large activation energies were utilized for these computations. Simple models for heat losses were used. These results have shown that some classical ideas in turbulent combustion theory were not justified: for example, small scales appear to be much less efficient than expected from classical analysis. These results have been confirmed later by experiments (Roberts and Driscoll 1991, Roberts *et al.* 1993). They have also shown the importance of thermodiffusive effects even in turbulent flames. The importance of this mechanism has been confirmed by other methods in separate works (Wu *et al.* 1991, Abdel-Gayed *et al.* 1984, Becker *et al.* 1990). Effects of flame curvature were studied and predicted by comparing a DNS with an experiment performed at Stanford and asymptotic analysis (Poinso *et al.* 1992).

- turbulent combustion models have been derived by combining multifractal analysis and flame vortex interaction results (Meneveau and Poinso 1991). These models have been implemented in aircraft and rocket engine computations (Candel *et al.* 1990(a), (b)) as well as in piston engine computations in collaboration with Institut Francais du Petrole (Boudier *et al.* 1992). In all cases, the integration of DNS-based sub-models leads to considerable improvement of the prediction capacities of these codes. In collaboration with Ecole Centrale Paris, a KPP (Kolmogorov, Petrovski, Piskunov) analysis (Hakberg and Gosman 1984, Fichot *et al.* 1993) was used to predict the turbulent flame speed of planar turbulent premixed flame. The performances of models derived from DNS were analyzed and compared with classical models (Duclos *et al.* 1993).
- ignition in turbulent premixed flames was also studied at CTR (Poinso 1991), and an ignition model based on this work was implemented and validated in KIVA (Boudier *et al.* 1992).
- three-dimensional computations were also developed, first in the constant density case (Rutland and Trouve 1993, Rutland 1989) and later with variable density and heat release (Trouve and Poinso 1993). These computations have confirmed many of the results obtained in two dimensions and brought a large number of intrinsically 3D results concerning, for example, flame shape statistics, orientation, and straining characteristics. More generally, they have been used in many turbulent combustion models (Bray 1990, Bray and Cant 1991, Kostiuik and Bray 1993). Different collaborations with combustion specialists (Prof. Cant, Dr. Ashurst, Dr. Hakberg) have taken place in the last three years to exploit these data bases. They were performed with simple chemical schemes (*Fresh*  $\rightarrow$  *Burnt*).
- two-dimensional computations of flame-wall interaction with simple chemistry have been performed, and models have been derived from DNS results and applied in piston engines models (Poinso *et al.* 1993).
- the feasibility of two-dimensional computations with complex chemistry and precise transport models was demonstrated in 1992 by coupling the CTR DNS code

with the SANDIA softwares CHEMKIN (for chemistry) and TRANSPORT (for viscosity and diffusion coefficients). This code, developed at Ecole Centrale Paris and CERFACS, was tested at CTR during the 1992 Summer Program. It allows the simulation of turbulent flames with complex chemistry and was applied to the prediction of turbulent H<sub>2</sub>-O<sub>2</sub> flames with a Warnatz scheme (9 species and 19 reactions) (Baum *et al.* 1993(a), (b), (c)).

- CTR has also investigated other ways to make progress in the field of turbulent combustion and developed a new experiment at Stanford University (Prof. Bowman) in the field of flame-vortex interaction. The capability of combining DNS and experiment offers CTR a powerful tool to deal with the problem. This project is presented by Dr. Mantel and Dr. Samaniego in the following reports.
- Although most of the CTR work has focused on premixed flames, diffusion flames have also been studied, both in the core program (Vervisch 1992) and during summer programs. Two- and three-dimensional simulations for turbulent diffusion flames have been performed and have allowed the structure analysis of these flames. The influence of the chemical scheme (one- versus two-step reactions) on quenching was studied in 1992 (Chen *et al.* 1992(a)) as well as the validity of flamelet assumptions (Chen *et al.* 1992(b), Mell 1990) and pdf models (Fox *et al.* 1992).
- CTR has also contributed to the development of DNS of reacting flows in other research centers by distributing its basic code (for simple chemistry). This code is now used at Univ. of Colorado (Boulder), Sandia, Univ. of Madison, Institut Francais du Petrole, Stanford Univ., Ecole Centrale Paris and CERFACS.

### 3. Future plans

Two main objectives will be pursued in 1994 at CTR in the field of combustion research:

- (1) Develop and improve CTR models for turbulent combustion
- (2) Improve data bases available at CTR to help outside researchers test their own models.

To reach these objectives, four parallel approaches will be used in 1994:

- (1) Flame - vortex interaction:

Flame vortex interaction studies will be pursued, both on the numerical and on the experimental side. Multiple goals may be reached through this study: to understand the basic features of flame-vorticity interaction, study flame generated turbulence, create artificial turbulent flames by sending periodic arrays of vortices into a flame front, check the validity of DNS by comparing them with experiments, and use joint experimental and numerical tools to explore larger ranges of parameters. The report of Dr. J. M. Samaniego describes this work in more detail.

- (2) Complete three-dimensional data bases:

The work of Dr. Trouvé on three-dimensional data bases for premixed turbulent flames with heat release has opened new perspectives in the field of turbulent combustion models. Many models have been compared to DNS data bases (Poinsot

*et al.* 1992, Cant and Rutland 1990, Trouve and Poinso 1993) and the ensemble of data bases and post processing techniques which has been developed has to be extended and made available to the outside community. Dr. T. Mantel is working on this problem and a description of his work is given in this report.

(3) Flame wall interaction studies:

The interaction between a cold wall and a flame has numerous practical implications but is poorly modeled at the present time: one needs to model the effect of the wall on the flame (possible quenching) but also the effect of the flame on the wall (increased heat transfer). Both aspects may be attacked using DNS. The first one was treated at CTR in 1992 (Poinso and Haworth 1992, Poinso *et al.* 1993) in collaboration with Institut Francais du Petrole (where a model was used for piston engine cases). In 1994, the study of this problem will be continued by using a full 3D channel flow simulation at CTR to study flame dynamics near a wall with stationary turbulence. This work will be done in collaboration with CERFACS where a model for heat transfer will be developed.

4) Stabilization of diffusion flames:

In addition to research dealing with premixed combustion, efforts at CTR also include investigations concerning nonpremixed combustion. The long term goal of this work is to provide an understanding of diffusion flame characteristics which can be used in developing models for large eddy simulations. These fundamental aspects of diffusion flames include the ignition and stabilization processes, which will be investigated in simple geometries using direct numerical simulations. The ignition and stability characteristics will be evaluated under a variety of configurations: a laminar flame where the triple-flame structure can be investigated; a shear layer where the effect of the splitter plate wake on the flame properties can be determined; and in analogy with the premixed studies, the effect of vortices on the above configurations will also be studied in order to examine possible quenching events. These areas are currently being investigated by Dr. G. Ruetsch using one-step chemical models. If need be, implementation of multiple-step chemistry (Chen *et al.* 1992(b)) can be included.

## REFERENCES

- ABDEL-GAYED, R. G., BRADLEY, D., HAMID, M. N. & LAWES, M. 1984 Lewis number effects on turbulent burning velocity. *20th Symposium (International) on Combustion*. The Combustion Institute, 505-512.
- ASHURST, W. T. 1991 SIAM Conference on Numerical Combustion
- BAUM, M., HAWORTH, D. & POINSOT, T. 1993(a) Direct Numerical Simulation of turbulent H<sub>2</sub>-O<sub>2</sub>-N<sub>2</sub> flames. *9th Turbulent Shear Flows*.
- BAUM, M., HAWORTH, D. & POINSOT, T. 1993(b) Direct Simulation of turbulent flames with complex chemistry. *J. Fluid Mech.* Submitted.
- BAUM, M., HAWORTH, D. & POINSOT, T. 1993(c) Using Direct Numerical Simulation to study H<sub>2</sub>/O<sub>2</sub>/N<sub>2</sub> flames with complex chemistry in turbulent flows. *Fifth Int. Conference on Numerical Combustion*.



- BECKER, H., MONKHOUSE, P., WOLFRUM, J., CANT, R., BRAY, K., MALY, R. & PFISTER, W. 1990 Investigation of extinction in unsteady flows in turbulent combustion by 2D LIF of OH radicals and flamelet analysis. *23rd Symp. (Int.) on Combustion*. The Combustion Institute, Pittsburgh.
- BOUDIER, P., HENRIOT, S., POINSOT, T. & BARITAUD, T. 1992 A model for turbulent flame ignition and propagation in piston engines.. *24th Symp. (Int.) on Combustion*. The Combustion Institute, Pittsburgh, 503-510.
- BRAY, K. N. C. 1990 Studies of the turbulent burning velocity. *Proc. R. Soc. Lond. A*. **431**, 315-335.
- BRAY, K. N. C. & CANT, R. S. 1991 Some applications of Kolmogorov's turbulence research in the field of combustion. *Proc. Roy. Soc. A London*. A. N. Kolmogorov Special Issue.
- BUELL, J. & HUERRE, P. 1988 Absolute instability of a shear layer. *Proceedings of the 1988 Summer Program*. Center for Turbulence Research, Stanford Univ./NASA-Ames, 19-27.
- CANDEL, S., VEYNANTE, D., LACAS, F., MAISTRET, E., DARABIHA, N. & POINSOT, T. 1990(a) Recent advances in combustion modeling. In *Series on advances in mathematics for applied sciences*. B. E. Larrouturnou, World Scientific, Singapore.
- CANDEL, S., VEYNANTE, D., LACAS, F., MAISTRET, E. & POINSOT, T. 1990(b) Flamelet concepts in turbulent combustion modeling. *9th International Heat Transfer Conference*.
- CANT, R. S. & RUTLAND, C. 1990 Statistics for laminar flamelet modeling. *Proceedings of the 1990 Summer Program*. Center for Turbulence Research, Stanford Univ./NASA-Ames, 271-279.
- CHEN, J. H., MAHALINGAM, S., PURI, I. & VERVISCH, L. 1992(a) Effect of finite rate chemistry and unequal Schmidt numbers on turbulent non-premixed flames models with single step chemistry. *Proceedings of the 1992 Summer Program*. Center for Turbulence Research, Stanford Univ./NASA-Ames, 367-388.
- CHEN, J. H., MAHALINGAM, S., PURI, I. & VERVISCH, L. 1992(b) Structure of turbulent non-premixed flames modeled with two-step chemistry. *Proceedings of the 1992 Summer Program*. Center for Turbulence Research, Stanford Univ./NASA-Ames, 389-402.
- DUCLOS, J. M., VEYNANTE, D. & POINSOT, T. 1993 A comparison of flamelet models for premixed turbulent combustion. *Combust. Flame*. **95**, 101-118.
- FICHOT, F., LACAS, F., VEYNANTE, D. & CANDEL, S. 1993 One-dimensional propagation of a premixed turbulent flame with the coherent flame model. *Combust. Sci. Tech.* **89**, 1-26.
- FOX, R., GAO, F., MOSER, R., ROGERS, M. & HILL, J. 1992 Stochastic modeling of turbulent reacting flows. *Proceedings of the 1992 Summer Program*. Center for Turbulence Research, Stanford Univ./NASA-Ames, 403-425.

- HAKBERG, B. & GOSMAN, A. D. 1984 Analytical determination of turbulent flame speed from combustion models. *20th Symposium (International) on Combustion*. The Combustion Institute, Pittsburgh, 225-232.
- HAWORTH, D. C. & POINSOT, T. J. 1992 Numerical simulations of Lewis number effects in turbulent premixed flames. *J. Fluid Mech.* **244**, 405-436.
- KOSTIUK, L. & BRAY, K. 1993 Mean effects of stretch on laminar flamelets in a premixed turbulent flame. *Combust. Flame*. Submitted.
- LELE, S. 1992 Compact finite difference schemes with spectral like resolution. *J. Comput. Phys.* **103**, 16-42.
- LOWERY, P. AND REYNOLDS, W. C. 1987 Passive scalar entrainment and mixing in a forced, spatially developing mixing layer. *25th AIAA Aerospace Sciences Meeting*.
- MAHALINGAM, S. 1989 "Non-premixed combustion: full numerical simulation of a coflowing axisymmetric jet, inviscid and viscous stability analysis". *PhD Thesis*, Stanford Univ.
- MELL, W. E., KOSALY, G., PLANCHE, O., POINSOT, T., & FERZIGER, J. H. 1990 Laminar Flamelet Modeling of Turbulent Diffusion Flames. *Proceedings of the Summer Program*. Center for Turbulence Research, Stanford Univ./NASA-Ames, 255.
- MENEVEAU, C. & POINSOT, T. 1991 Stretching and quenching of flamelets in premixed turbulent combustion. *Combust. Flame*. **86**, 311-332.
- POINSOT, T. 1991 DNS and modeling of ignition in turbulent flows. *Annual Research Briefs-1991*. Center for Turbulence Research, Stanford Univ./NASA-Ames.
- POINSOT, T., ECHEKKI, T. & MUNGAL, M. G. 1992 A study of the laminar flame tip and implications for premixed turbulent combustion. *Combust. Sci. Tech.* **81**, 45-73.
- POINSOT, T. & HAWORTH, D. 1992 DNS and modelling of the interaction between turbulent premixed flames and walls. *Proceedings of the Summer Program*. Center for Turbulence Research, Stanford Univ./NASA-Ames, 307-324.
- POINSOT, T., HAWORTH, D. & BRUNEAUX, G. 1993 DNS and modelling of flame-wall interaction. *Combust. Flame*. **95**, 118-133.
- POINSOT, T. & LELE, S. 1992 Boundary conditions for direct simulations of compressible viscous flows. *J. Comput. Phys.* **101**, 104-129.
- POINSOT, T., VEYNANTE, D. & CANDEL, S. 1991 Quenching processes and premixed turbulent combustion diagrams. *J. Fluid Mech.* **228**, 561-605.
- POINSOT, T., VEYNANTE, D., YIP, B., TROUVÉ, A., SAMANIEGO, J.-M. & CANDEL, S. 1992 Active control: an investigation method for combustion instabilities. *J. Phys. III*. **July**, 1331-1357.

- RAI, M. M. & MOIN, P. 1991 Direct numerical simulation of transition and turbulence in a spatially evolving boundary layer. *AIAA 10th Comp. Fluid Dynamics Conference*. AIAA Paper 91-1607.
- ROBERTS, W. L. & DRISCOLL, J. F. 1991 A laminar vortex interacting with a premixed flame: measured formation of pockets of reactants. *Combust. Flame*. **87**, 245-256.
- ROBERTS, W. L., DRISCOLL, J. F., DRAKE, M. C. & GOSS, L. P. 1993 Images of the quenching of a flame by a vortex: to quantify regimes of turbulent combustion. *Combust. Flame*. **94**, 58-70.
- RUTLAND, C. J. 1989 "Effect of strain, vorticity and turbulence on premixed flames". *Ph.D. Thesis*, Stanford Univ.
- RUTLAND, C. J. & FERZIGER, J. 1989 Interaction of a vortex and a premixed flame. *27th AIAA Aerospace Sciences Meeting*.
- RUTLAND, C. J. & TROUVE, A. 1990 Pre-mixed flame simulations for non-unity Lewis number. *Proceedings of the Summer Program*. Center for Turbulence Research, Stanford Univ./ NASA-Ames, 299-309.
- RUTLAND, C. J. & TROUVE, A. 1993 Pre-mixed flame simulations for non-unity Lewis number. *Combust. Flame*. **94**, 41-57.
- THOMPSON, K. W. 1987 *J. Comput. Phys.* **68**, 1-24.
- TROUVE, A. & POINSOT, T. 1993 The evolution equation for the flame surface density. *J. Fluid Mech.* Submitted.
- VERVISCH, L. 1993 Study and modelling of finite rate chemistry effects in turbulent non premixed flames. *Annual Research Briefs-1992*. **411-431**.
- WU, M. S., KWON, S., DRISCOLL, J. F. & FAETH, G. M. 1991 Preferential diffusion effects on the surface structure of turbulent premixed hydrogen/air flames. *Combust. Sci. Tech.* **78**, 69-96.
- YEUNG, P. K., GIRIMAJI, S. S. & POPE, S. B. 1990 Straining and scalar dissipation on material surfaces in turbulence: implications for flamelets. *Combust. Flame*. **79**, 340.



13-15  
20/6-08  
N94-24156

## Stretch-induced quenching in flame-vortex interactions

By J.-M. Samaniego

### 1. Motivation and objectives

The flame-vortex interaction problem is a natural configuration in which several issues relevant to turbulent combustion can be addressed: effect of strain-rate and curvature, effect of the Lewis number, effect of heat losses, effect of complex chemistry, and flame-generated turbulence (Jarosinski *et al.* 1988, Rutland and Ferziger 1991, Poinso *et al.* 1991, Roberts and Driscoll 1991, Roberts *et al.* 1993, Wu and Driscoll 1992, Lee *et al.* 1993, Lee and Santavicca 1993). In such an approach, the interaction of an isolated vortex with a laminar premixed flame is viewed as a unit process of a turbulent premixed flame in which the reaction zone keeps a laminar-like structure locally; this is precisely the case of the wrinkled flame or flamelet regime in turbulent combustion (Williams 1985, Borghi 1988).

Poinso *et al.* 1991 have carried out numerical simulations of a two-dimensional flow field where a vortex pair is convected through a laminar premixed flame. The authors identified three regimes of interaction depending on the ratios  $u_\theta/S_l$  and  $d/\delta_l$  (where  $u_\theta$  and  $d$  are the velocity perturbation and size of the vortex pair, and  $S_l$  and  $\delta_l$  are the flame speed and flame thickness): 1) for small values of  $u_\theta/S_l$  and  $d/\delta_l$ , the flame front is nearly unaffected; 2) for an intermediate range of these parameters, the flame front is wrinkled and pockets of unburnt mixture surrounded by burnt gases are formed; 3) for higher values, the flame front can be locally quenched in the presence of heat losses. These results were confirmed by experimental observations (Roberts and Driscoll 1991, Roberts *et al.* 1993).

The present work complements previous studies and involves the study of the interaction of a vortex pair and a laminar premixed flame in a planar two-dimensional geometry, together with numerical simulations. This geometry is quite unique since most studies have considered axisymmetric vortex rings. Such a geometry offers several advantages over previous studies:

- line-of-sight measurement techniques such as schlieren flow visualization,  $CH$  emission imaging, and infrared emission imaging can be used in order to obtain quantitative data: schlieren flow visualization can be used to determine the flame surface area; imaging of the light emission from electronically excited  $CH$  radicals in the reaction zone can be used to infer the reaction rate field (John and Summerfield 1957, Diederichsen and Gould 1965, Hurle *et al.* 1968, Poinso *et al.* 1987, Yip and Samaniego 1992, Samaniego *et al.* 1993); near-infrared emission from water vapor in the 700 – 1200 nm range can be used to obtain the temperature field in the burnt gases. In addition, laser-based diagnostics such as particle image velocimetry to measure the velocity field or Rayleigh scattering as an alternative way of measuring the temperature field can be applied.

- ensemble-averaging of several realizations can be performed in order to improve the signal-to-noise ratio.
- quantitative comparisons with a two-dimensional code described in Poinso *et al.* 1991 can be undertaken. This would allow to separately study the effects of non-unity Lewis numbers, heat losses, and complex chemistry. In particular, the validity and applicability of reduced chemical schemes for direct numerical simulation of turbulent premixed flames can be tested.
- in parallel to the single events where an isolated vortex pair interacts with a premixed flame, multiple vortex-flames interactions can be studied as an example of single-scale turbulence-flame interactions.

This paper presents initial experimental results of flame-vortex interactions. It is shown that, under certain circumstances, the flame undergoes a quenching-reignition process where quenching is associated to an excessive stretching of the flame front.

## 2. Accomplishments

### 2.1 Experimental facility

An experimental facility with a two-dimensional flow has been developed. The test section comprises a vertical duct with a square cross-section of  $63.5 \times 63.5 \text{ mm}$ , equipped with quartz windows for optical access (see Fig. 1). A mixture of propane or methane and air is fed into the test section through a contoured converging nozzle. Combustion is stabilized on an electrically-heated Nichrome wire of  $0.5 \text{ mm}$  diameter, resulting in a V-shaped flame. A vortex pair is generated by acoustic excitation through a  $3 \text{ mm}$  wide contoured slot located in the left wall. At time  $t = 0$ , a single pulse is sent to the speaker. The pulse is generated by filtering and amplifying a TTL pulse. The resulting signal is a ramp with a rise time of  $1 \text{ ms}$ . The slot has a rectangular shape and spans the entire lateral wall. In the present study, the aspect ratio of the slot was approximately  $21 : 1$ . Conceptually, the resulting vortex pair is two-dimensional, spans the entire test section, and is parallel to the Nichrome wire. As a consequence, the flow field during a flame-vortex interaction is expected to be two-dimensional.

Several parameters control the interaction of the vortex with the flame, including the type of fuel, the equivalence ratio ( $\phi$ ), the flow velocity of the fuel-air stream ( $V_0$ ), the flame thickness ( $\delta_l$ ) and flame speed ( $S_l$ ), the size of the vortex core ( $d_c$ ), and the maximum rotational velocity of the vortex ( $u_\theta$ ). Using methane or propane allows possible Lewis number ( $Le$ ) effects to be investigated.

In the absence of velocity measurements, it is difficult to give a definite value for the maximum velocity perturbation  $u_\theta$  induced by the vortex pair. However, based on smoke visualizations of the vortex pair in the absence of flame, a schematic diagram of the vortex pair has been developed (Fig. 2) (Samaniego 1993). In this case, the following relationship holds:  $u_\theta = 4V_d$ , where  $V_d$  is the self-induced velocity of the vortex pair.

Qualitative flow visualization showing both the position of the vortex pair and of the flame during the interaction has been performed with a schlieren arrangement.

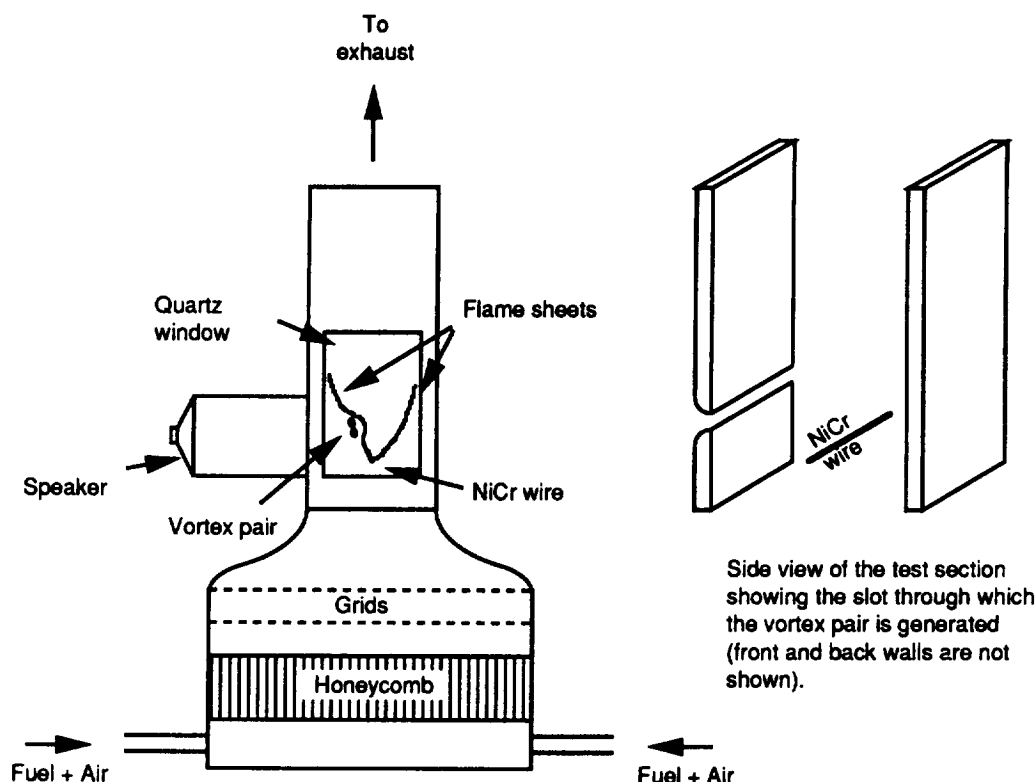


FIGURE 1. Schematic view of the test section.

The light source was a flashlamp delivering  $0.1\text{ ms}$  duration pulses. The schlieren image was recorded by a TM540 PULNIX video camera and VCR. The images were later digitized on a PC AT equipped with a DT-2851 digitizing board. A timing circuit allowed delaying the light pulse from the vortex generation so that images could be taken at different instants during the interaction.

Global emission measurements were done using a Hamamatsu 1P28A photomultiplier tube equipped with an interference filter isolating light emission from  $CH$  radicals from the  $^2\Delta \rightarrow ^2\Sigma$  transition at  $431.5\text{ nm}$ . A second PC AT equipped with a DT-2828 acquisition board was used to digitize the photomultiplier signal (typically, 1000 samples at a rate of  $10,000\text{ samples/s}$ ). Acquisition was synchronized with the vortex generation event.

## 2.2 Results and discussion

### 2.2.1 Schlieren flow visualization

Figure 3 shows a sequence of schlieren images of a flame-vortex interaction along with the overall reaction rate. This latter quantity was inferred from the  $CH$

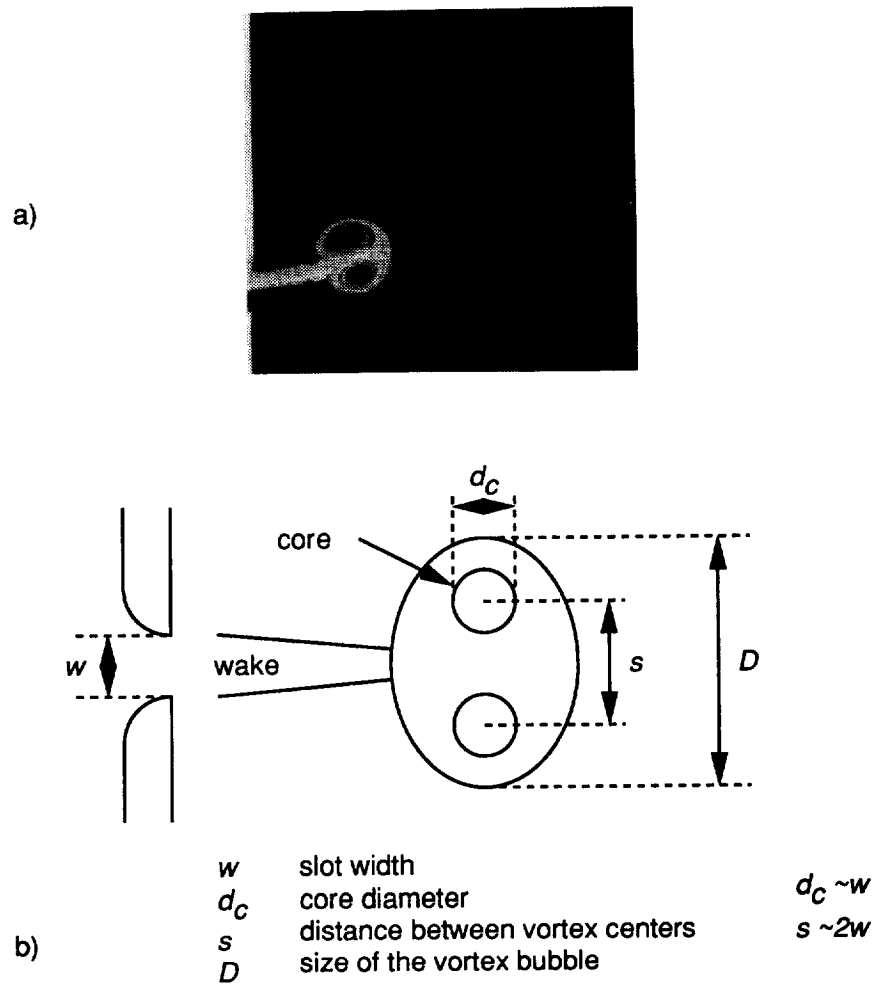


FIGURE 2. Vortex pair topology. a) light sheet illumination of a smoke pattern (from Samaniego 1993) - b) schematic diagram of the vortex pair.

emission from the entire flame. Fifty realizations were averaged and the standard deviation computed in order to check the repeatability of the interaction. In this case, the operating conditions are: fuel= $C_3H_8$ ,  $\phi = 0.55$ ,  $V_0 = 0.35 \text{ m/s}$ ,  $\delta_l = 1 \text{ mm}$ ,  $S_l = 0.12 \text{ m/s}$ ,  $d_c = 3 \text{ mm}$ ,  $u_\theta = 24 \text{ m/s}$ ,  $Le = 1.8$ , resulting in  $u_\theta/S_l = 200$ ,  $d/\delta_l = 3$ .

The first image shows the position of the unperturbed V-shaped flame. The flame is slightly curved towards the burnt gases due to confinement. The second image is taken  $4.8 \text{ ms}$  after acoustic excitation. A starting vortex pair is rolling-up. The flame already senses the presence of the vortical structure and starts straightening out. This can be attributed to mass-conservation and to a Biot-Savart effect induced



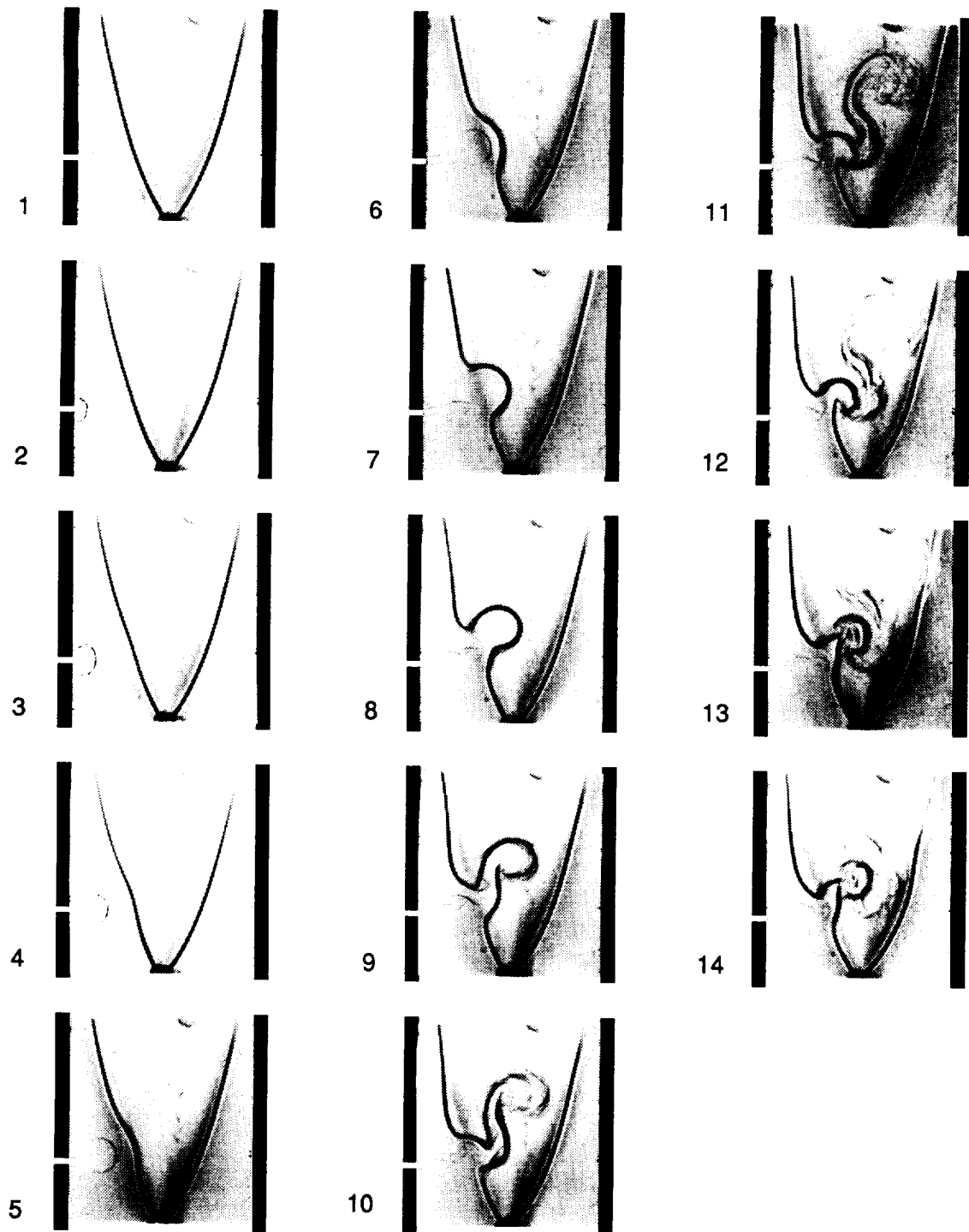


FIGURE 3a. Sequence of schlieren images. See caption on next page for more details.

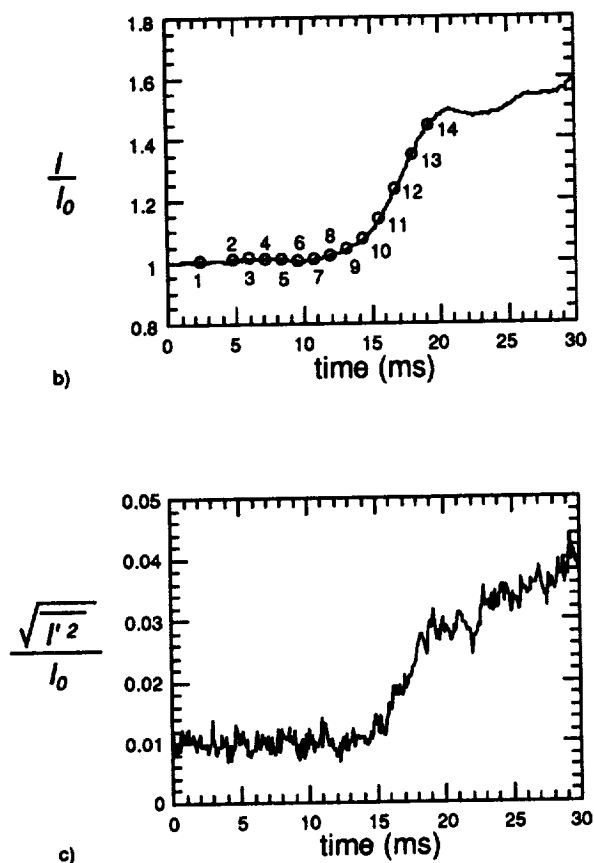


FIGURE 3. Flame-vortex interaction: fuel=  $C_3H_8$ ,  $\phi = 0.55$ ,  $V_0 = 0.35 \text{ m/s}$ ,  $\delta_l = 1 \text{ mm}$ ,  $S_l = 0.12 \text{ m/s}$ ,  $d_c = 3 \text{ mm}$ ,  $u_\theta = 24 \text{ m/s}$ ,  $Le = 1.8$  ( $u_\theta/S_l = 200$ ,  $d_c/\delta_l = 3$ ). a) Sequence of schlieren photographs showing the evolution of the reacting flow field (see previous page) - b) evolution of the corresponding  $I/I_0$ , where  $I$  is the mean global  $CH$  emission averaged over 50 realizations, and  $I_0$  is the initial value of  $I$ . The numbered circles correspond to the schlieren photographs - c) evolution of  $\sqrt{I'^2}/I_0$ , where  $\sqrt{I'^2}$  is the standard deviation of  $I$ , the global  $CH$  emission signal computed from 50 realizations, and  $I_0$  is the initial value of  $I$ .

by the vortex pair. The next 12 images are taken  $1.2 \text{ ms}$  apart and show the evolution of the flame-vortex interaction.

From both the schlieren pictures and the standard deviation of the photomultiplier signal, two phases of the flame-vortex interaction can be identified: 1) an initial phase lasting until approximately  $t = 13.2 \text{ ms}$ , where the flow field is two-dimensional and repeatable, and during which the flame surface area increases while the reaction rate remains constant; 2) a second phase in which the flow field starts becoming three-dimensional, is less repeatable, and during which the reaction rate increases significantly.

During the first phase, the vortex pair propagates toward the flame front and reaches it at  $t = 10.8 \text{ ms}$ . The flame front becomes more distorted as the vortex follows its path. The arc length of the flame contour increases steadily, while the reaction rate remains nearly constant. The vortex pair is followed by a wake featuring a Kelvin-Helmholtz instability.

The second phase starts at  $t = 13.2 \text{ ms}$ , when the schlieren image becomes blurred around the vortex pair. In the vortex wake is an elongated flame front which also becomes blurred at  $t = 15.6 \text{ ms}$ . This phase is characterized by a 40% increase of the overall reaction rate. The blurring of the schlieren pattern is due to combustion within the vortex pair.

The existence of two phases compares well with previous results obtained by Jarosinski *et al.* 1988, for the interaction of a vortex bubble with an upward propagating laminar flame. The authors associated each phase of the interaction with a physical mechanism and a time scale: first, a mixing time,  $\tau_m$ , during which entrainment of burnt material into the vortex core takes place, then a combustion time,  $\tau_c$ , after ignition of the vortex core. They found that  $\tau_c$  is weakly dependent on the mixture composition of the vortex and that  $\tau_c \simeq \tau_m$ . They concluded that the interaction is essentially controlled by fluid mechanical processes. Jarosinski *et al.* speculated that, during the first phase, the flame front is quenched by excessive stretching ahead of the vortex bubble. This assumption is checked and proved to be correct in the following section. However, the way combustion is initiated in the second phase and the structure of the reaction zone during this ignition process, whether it is flamelet-like or distributed over a volume, are still unknown.

### 2.2.2 Flame quenching and Lewis number effect

In order to address the issue of whether or not the flame front is locally quenched, the relationship between the flame surface area,  $\Sigma$ , and the overall reaction rate,  $W$ , is investigated. For this purpose,  $\Sigma$  was deduced from the arc length of the flame contour measured on the schlieren images. Only the images taken in the first phase, where the flow field is two-dimensional, have been considered.

It appears that  $W$  lags  $\Sigma$  by about 5 milliseconds (Fig. 4). Furthermore, while  $\Sigma$  increases by 40 %,  $W$  remains within 1% of its initial value. Since the reaction zone is flamelet-like during the first part of the interaction, as demonstrated by the schlieren pictures,  $W$  can be defined as follows:

$$W = \int_{\Sigma} \omega ds$$

where  $\omega$  is the local burning rate per unit surface. If we assume that  $\omega$  is constant then

$$W = \omega \Sigma$$

and  $W$  is proportional to  $\Sigma$  which is in contradiction with the observation. Consequently,  $\omega$  must decrease locally in order to balance the increase of  $\Sigma$ . This can be

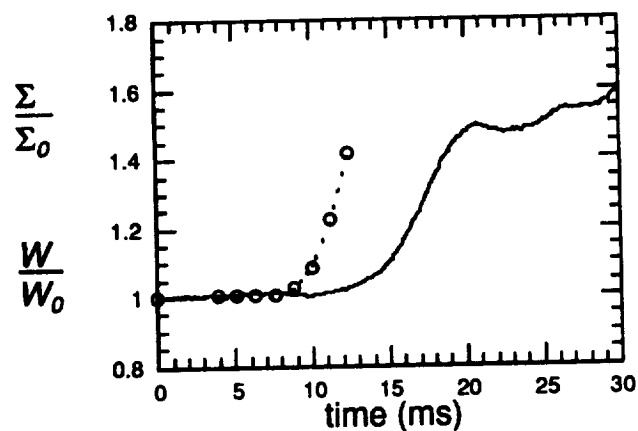


FIGURE 4. Evolution of  $W/W_0$  (—) and  $\Sigma/\Sigma_0$  (○), where  $W$  is the overall reaction rate,  $\Sigma$  is the total flame surface area, and the subscript 0 refers to the value at time  $t = 0$ . The operating conditions are the same as in Fig. 3.

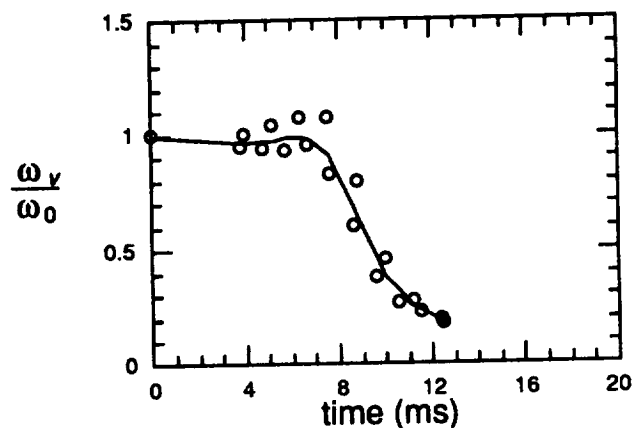


FIGURE 5. Evolution of  $\omega_v/\omega_0$ , where  $\omega_v$  is the mean reaction rate per unit surface along the distorted flame front, and  $\omega_0$  is the initial value of  $\omega_v$ . The operating conditions are the same as in Fig. 3.

quantified by defining  $\omega_v$  as the average value of  $\omega$  along the distorted part of the flame front. We obtain:

$$\frac{\omega_v}{\omega_0} = \frac{W_v}{\Sigma_v} \times \frac{\Sigma_0}{W_0}$$

with

$$W_v = W - W_0(1 - D/\Sigma_0) \quad \text{and} \quad \Sigma_v = \Sigma - \Sigma_0(1 - D/\Sigma_0)$$

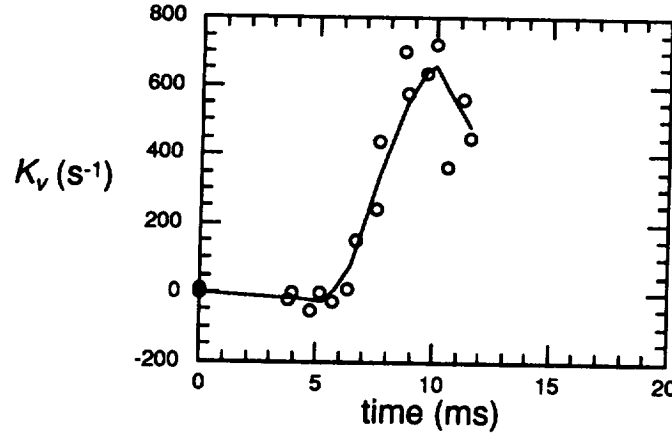


FIGURE 6. Evolution of mean stretch rate along the distorted flame front ( $K_v$ ). The operating conditions are the same as in Fig. 3.

where  $\omega_0$ ,  $W_0$ , and  $\Sigma_0$  are the initial values of the local reaction rate, of the global reaction rate, and of the flame surface area, respectively, and  $D$  is the size of the vortex pair = 12 mm, as measured on the schlieren images.  $W_v$  and  $\Sigma_v$  represent the reaction rate and flame surface area of the portion of the flame affected by the vortex. It appears that  $\omega_v$  decreases significantly to 20% of the initial value at the end of the first phase (Fig. 5). Similarly, an average value  $K_v$  for the stretch rate along the distorted front can be estimated by:

$$K_v = \frac{1}{\Sigma_v} \frac{d\Sigma_v}{dt}$$

Figure 6 shows that  $K_v$  reaches a maximum value of about  $700 \text{ s}^{-1}$  at  $t = 10 \text{ ms}$ . In comparison, the stretch rate leading to the extinction of a propane-air flame at  $\phi = 0.55$ , measured experimentally by Law *et al.* 1986 for a steady counterflow configuration, is an order of magnitude lower. Although unsteady effects, inherent of the present experiment, may play an important role and lead to different values of the extinction stretch rate, as indicated by Darabiha's work on the transient behavior of counterflow hydrogen-air diffusion flames (Darabiha 1992), the previous observation suggests that the flame front ahead of the vortex pair is quenched by excessive stretching. The same argument applies for various cases with the propane flame, where  $u_\theta/S_l$  was varied between 90 and 350 (the corresponding maximum stretch rates varied from  $400 \text{ s}^{-1}$  to  $1500 \text{ s}^{-1}$ ).

In order to study the effect of the Lewis number, experiments also have been performed on a methane-air flame. The operating conditions were: fuel =  $\text{CH}_4$ ,  $\phi = 0.55$ ,  $V_0 = 0.35 \text{ m/s}$ ,  $\delta_l = 2 \text{ mm}$ ,  $S_l = 0.07 \text{ m/s}$ ,  $d_c = 3 \text{ mm}$ ,  $u_\theta = 11$  and  $24 \text{ m/s}$ ,  $Le = 0.96$ .

In this case, the relationship between  $W$  and  $\Sigma$  changes when varying the ratio  $u_\theta/S_l$ . When  $u_\theta/S_l = 160$  ( $u_\theta = 11 \text{ m/s}$ ),  $W$  is approximately proportional to  $\Sigma$  during most of the first phase, and when  $u_\theta/S_l = 340$  ( $u_\theta = 24 \text{ m/s}$ ), there is a

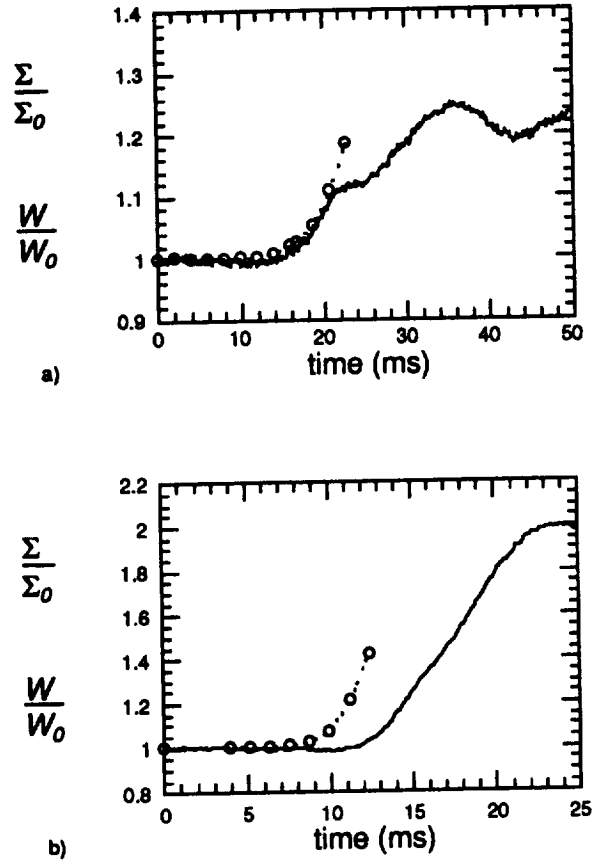


FIGURE 7. Methane-air flame. Evolution of  $W/W_0$  (—) and  $\Sigma/\Sigma_0$  (○), where  $W$  is the overall reaction rate,  $\Sigma$  is the total flame surface area, and the subscript 0 refers to the value at time  $t = 0$ . The conditions are: fuel =  $\text{CH}_4$ ,  $\phi = 0.55$ ,  $V_0 = 0.35 \text{ m/s}$ ,  $\delta_l = 2 \text{ mm}$ ,  $S_l = 0.07 \text{ m/s}$ ,  $d_c = 3 \text{ mm}$ ,  $Le = 0.96$ . a)  $u_\theta = 11 \text{ m/s}$  ( $u_\theta/S_l = 160$ ). b)  $u_\theta = 24 \text{ m/s}$  ( $u_\theta/S_l = 340$ )

time lag between  $W$  and  $\Sigma$ , as observed in the propane flame (Fig. 7 a and b). A transition in the response of the flame occurs when the vortex strength is increased. This difference in behavior can be seen in  $\omega_v$ , the average value of the reaction rate:  $\omega_v$  remains practically constant for the slower vortex pair, whereas it decreases significantly for the faster vortex pair (Fig. 8). The different behavior is due to a difference in stretch rates during the interaction. For  $u_\theta/S_l = 340$ ,  $K_v$  reaches values of  $800 \text{ s}^{-1}$ , whereas for  $u_\theta/S_l = 160$ ,  $K_v$  remains under  $200 \text{ s}^{-1}$ , and even under  $100 \text{ s}^{-1}$  during most of the first phase. Since the extinction stretch rate of a methane-air flame at  $\phi = 0.55$  is around  $100\text{--}200 \text{ s}^{-1}$ , it can be concluded that, in the case of the faster vortex, the flame is locally quenched by excess of stretch. In contrast, in the case of the slower vortex, the stretch rate experienced by the flame front is lower or of the order of the extinction stretch rate. The local reaction rate

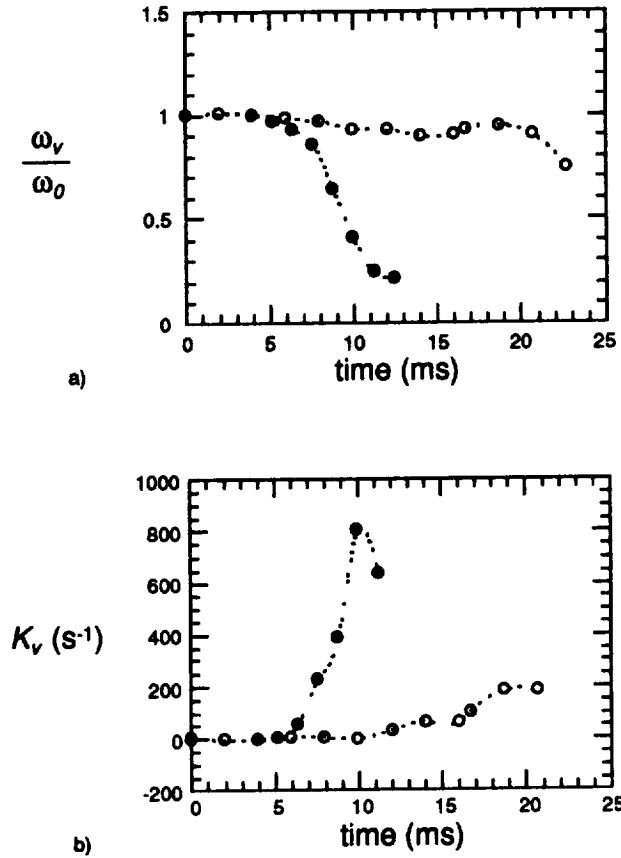


FIGURE 8. Methane-air flame for two values of  $u_\theta/S_l$ .  $\circ$  :  $u_\theta/S_l = 160$ ;  $\bullet$  :  $u_\theta/S_l = 340$ . a) Evolution of  $\omega_v/\omega_0$ , where  $\omega_v$  is the mean reaction rate per unit surface along the distorted flame front, and  $\omega_0$  is the initial value of  $\omega_v$  - b) Evolution of mean stretch rate along the distorted flame front ( $K_v$ ). The operating conditions are the same as in Fig. 7.

is weakly affected and  $W$  is approximately proportional to  $\Sigma$ .

The different response of the propane- and methane-air flames can be attributed to some extent to an effect of the Lewis number. During the interaction, both flames are positively stretched, and as suggested by the stretched flame theory, a positively stretched  $Le > 1$  flame should be quenched more easily than a  $Le < 1$  flame (Clavin 1985, Law 1988, Chung and Law 1988, Chung and Law 1989). Following Law, we obtain:

$$\omega_v/\omega_0 = 1 - \frac{\delta_l}{R_v} + \left(\frac{1}{Le} - 1\right) \frac{Ka}{(2T_{ad}/T_a)}$$

where  $\omega_0$  is the initial reaction rate,  $R_v$  is the average radius of curvature ( $R_v > 0$  when the flame front is convex towards the burnt gases, and  $R_v < 0$  when the

flame front is convex towards the cold gases),  $Ka$  is the Karlovitz number defined by  $Ka = \frac{K_u}{S_f \delta_f}$ ,  $T_{ad}$  is the adiabatic flame temperature, and  $T_a$  is the activation temperature. The influence of curvature is a consequence of flow divergence through a flame front having a finite thickness and does not involve the Lewis number. This term has probably the same influence on both the propane- and methane-air flames, hence its effect is not discussed here. In contrast, the influence of stretch on the flame response depends on the Lewis number. When  $Le > 1$ , the reaction rate is decreased by a positive stretch and quenching occurs by cooling of the flame. This is the case of the propane flame for which  $Le = 1.8$ . When  $Le < 1$  or close to 1 which is the case of the methane flame, the mechanism for quenching is not so well established. When positively stretched, the flame will experience an increase of its burning rate and of its temperature. Stretch-induced quenching may or may not be expected depending on whether the flame is considered restrained or unrestrained (Law 1988). If the flame is restrained, for example in a stagnation point flow, the flame is quenched by incomplete reaction (Darabiha *et al.* 1986, Law 1988). If the flame is unrestrained, which is the case in the experiment, incomplete reaction is prevented: quenching cannot result only from excessive stretching, but more likely from the combination of stretch with other phenomena such as heat loss and finite-rate kinetics. To summarize, it appears that the effect of the Lewis number explains why the propane flame is quenched more easily than the methane flame, but it does not provide a definite explanation for the quenching of the methane flame.

It is interesting to note that Poinso *et al.* 1991, in their numerical study of flame-vortex interactions, have found that radiative heat losses are the controlling mechanism for flame quenching irrespective of the value of the Lewis number. Following this analysis, Roberts *et al.* 1993 have characterized the effect of radiative heat losses from the burnt gases in their experiment, and although showing that Poinso *et al.* had overestimated the value of the heat losses in their simulations, concluded that they play an important role in flame quenching. The authors also reported an unexpected finding: they would observe quenching in the case of a lean methane-air, but not in the case of a lean propane-air flame. This is in contradiction with our own findings as well as with the stretched flame theory. They attributed this apparent anomaly to complex chemistry effects. It appears that the mechanisms leading to flame quenching are not yet well established, and that this problem needs further investigations.

### 3. Future plans

Further investigations of the mechanisms controlling the flame response are being conducted. In particular, the effects of the Lewis number and of heat losses will be studied. Future experiments will involve quantitative imaging of the reaction rate field using an intensified CCD camera equipped with a filter isolating the radiation of  $CH$  radicals. A particle image velocimetry system will provide the velocity field, and imaging of the near-infrared radiation of water vapor will be used for the measure of the temperature field in the burnt gases. Comparison with direct numerical simulations will be performed in order to study separately the effects of non-unity



Lewis number, heat losses, and complex chemistry. The validity and applicability of reduced chemical schemes for direct numerical simulation of turbulent premixed flames will also be tested.

### Acknowledgments

This work is conducted in collaboration with Prof. C. T. Bowman of the High Temperature Gasdynamics Laboratory. Helpful discussions with Prof. W. C. Reynolds and Prof. M. G. Mungal are also gratefully acknowledged. In addition, I wish to thank Dr. T. Poinot (C.E.R.F.A.C.S., Toulouse, France), Dr. A. Trouvé and Dr. T. Mantel, (Center for Turbulence Research), for their encouragement and for valuable discussions during the course of this project. I also want to express my gratitude to F. Levy for his invaluable help during the construction of the experimental facility.

### REFERENCES

- BORGHI, R. 1988 Turbulent Combustion Modelling. *Prog. Energy Combust. Sci.* **14**, 245-292.
- CHUNG, S. H. & LAW, C. K. 1988 An Integral Analysis of the Structure and Propagation of Stretched Premixed Flames. *Combust. Flame.* **72**, 325-336.
- CHUNG, S. H. & LAW, C. K. 1989 Analysis of Some Nonlinear Premixed Flame Phenomena. *Combust. Flame.* **75**, 309-323.
- CLAVIN, P. 1985 Dynamic behavior of premixed flame fronts in laminar and turbulent flows. *Prog. Energy Comb. Sci.* **11**, 1-59.
- DARABIHA, N. 1992 Transient Behavior of Laminar Counterflow Hydrogen-Air Diffusion Flames With Complex Chemistry. *Combust. Sci. Tech.* **86**, 163-181.
- DARABIHA, N., CANDEL, S. & MARBLE, F. E. 1986 The effect of strain rate on a premixed laminar flame. *Combust. Flame.* **64**, 203-217.
- DIEDERICHSEN, J. & GOULD, R. D. 1965 Combustion Instability: Radiation from Premixed Flames of Variable Burning Velocity. *Combust. Flame.* **9**, 25-31.
- HURLE, I. R., PRICE, R. B., SUGDEN, T. M., THOMAS, F. R. S. & THOMAS, A. 1968 Sound Emission From Open Turbulent Premixed Flames. *Proc. Roy. Soc. A.* **303**, 409-427.
- JAROSINSKI, J., LEE, J. & KNYSTAUTAS, R. 1988 Interaction of a Vortex Ring and a Laminar Flame. *Twenty-Second Symposium (International) on Combustion*, The Combustion Institute, 505-514.
- JOHN, R. & SUMMERFIELD, M. 1957 Effect of Turbulence on Radiation Intensity From Propane-Air Flames. *Jet Propul.* **27**, 169-178.
- LAW, C. K. 1988 Dynamics of Stretched Flames. *Twenty-Second Symposium (International) on Combustion*, The Combustion Institute, 1381-1402.

- LAW, C. K., ZHU, D. L. & YU, G. 1986 Propagation and Extinction of Stretched Premixed Flames. *Twenty-First Symposium (International) on Combustion*, The Combustion Institute, 1419-1426.
- LEE, T.-W., LEE, J. G., NYE, D. A. & SANTAVICCA, D. A. 1993 Local Response and Surface Properties of Premixed Flames During Interactions with Kármán Vortex Streets. *Combust. Flame*. **94**, 146-160.
- LEE, T.-W. & SANTAVICCA, D. A. 1993 Flame Front Geometry and Stretch During Interactions of Premixed Flames with Vortices. *Combust. Sci. Tech.* **90**, 211-230.
- POINSOT, T., TROUVÉ, A., VEYNANTE, D., CANDEL, S. & ESPOSITO, E. 1987 Vortex Driven Acoustically Coupled Combustion Instabilities. *J. Fluid Mech.* **177**, 265-292.
- POINSOT, T., VEYNANTE, D. & CANDEL, S. 1991 Quenching processes and premixed turbulent combustion diagrams. *J. Fluid Mech.* **228**, 561-605.
- ROBERTS, W. L. & DRISCOLL, J. F. 1991 A Laminar Vortex Interacting with a Premixed Flame : Measured Formation of Pockets of Reactants. *Combust. Flame*. **87**, 245-256.
- ROBERTS, W. L., DRISCOLL, J. F., DRAKE, M. C. & GOSS, L. P. 1993 Images of the Quenching of a Flame by a Vortex - To Quantify Regimes of Turbulent Combustion. *Combust. Flame*. **94**, 58-69.
- RUTLAND, C. J. & FERZIGER, J. H. 1991 Simulations of Flame-Vortex Interactions. *Combust. Flame*. **84**, 343-360.
- SAMANIEGO, J.-M. 1993 Generation of Two-Dimensional Vortices in a Cross-Flow. *CTR Annual Research Briefs - 1992*. Stanford Univ./NASA Ames.
- SAMANIEGO, J.-M., YIP, B., POINSOT, T. & CANDEL, S. 1993 Low-Frequency Combustion Instability Mechanisms in a Side-Dump Combustor. *Combust. Flame*. **94**, 363-380.
- WILLIAMS, F. A. 1985 *Combustion Theory*. The Benjamin/Cummings publishing Company, Inc.
- WU, M.-S. & DRISCOLL, J. F. 1992 A Numerical Simulation of a Vortex Convected Through a Laminar Premixed Flame. *Combust. Flame*. **91**, 310-322.
- YIP, B. & SAMANIEGO, J.-M. 1992 Direct  $C_2$  Radical Imaging in Combustion Instabilities. *Combust. Sci. Tech.* **84**, 81-90.

017-34  
201659  
N 94-24157  
**A transport equation for the scalar dissipation in reacting flows with variable density: first results**

By T. Mantel

**1. Motivation and objectives**

*1.1 Introduction*

Although the different regimes of premixed combustion are not well defined, most of the recent developments in turbulent combustion modeling are led in the so-called flamelet regime. The goal of these models is to give a realistic expression to the mean reaction rate  $\langle \dot{\omega} \rangle$ . Several methods can be used to estimate  $\langle \dot{\omega} \rangle$ . Bray and coworkers (Libby & Bray 1980, Bray 1985, Bray & Libby 1986) express the instantaneous reaction rate by means of a flamelet library and a frequency which describes the local interaction between the laminar flamelets and the turbulent flow field. In another way, the mean reaction rate can be directly connected to the flame surface density  $\langle \Sigma \rangle$ . This quantity can be given by the transport equation of the coherent flame model initially proposed by Marble & Broadwell 1977 and developed elsewhere (Pope 1988, Candel & Poinso 1990, Trouvé & Poinso 1992, Bidaux *et al.* 1993). The mean reaction rate,  $\langle \dot{\omega} \rangle$ , can also be estimated thanks to the evolution of an arbitrary scalar field  $G(\mathbf{x}, t) = G_0$  which represents the flame sheet.  $G(\mathbf{x}, t)$  is obtained from the  $G$ -equation proposed by Williams 1985, Kerstein *et al.* 1988 and Peters 1993. Another possibility proposed in a recent study by Mantel & Borghi 1991, where a transport equation for the mean dissipation rate  $\langle \epsilon_c \rangle$  of the progress variable  $c$  is used to determine  $\langle \dot{\omega} \rangle$ .

In their model, Mantel & Borghi 1991 considered a medium with constant density and constant diffusivity in the determination of the transport equation for  $\langle \epsilon_c \rangle$ . A comparison of different flamelet models made by Duclos *et al.* 1993 shows the realistic behavior of this model even in the case of constant density. Our objective in this present report is to present preliminary results on the study of this equation in the case of variable density and variable diffusivity. Assumptions of constant pressure and a Lewis number equal to unity allow us to significantly simplify the equation. A systematic order of magnitude analysis based on adequate scale relations is performed on each term of the equation. As in the case of constant density and constant diffusivity, the effects of stretching of the scalar field by the turbulent strain field, of local curvature, and of chemical reactions are predominant. In this preliminary work, we suggest closure models for certain terms, which will be validated after comparisons with DNS data.

*1.2 The role of scalar dissipation for premixed turbulent combustion*

For the prediction of chemical reactions in premixed media, the dissipation time scale of the concentration (or the temperature) fluctuations  $\tau_c$  and of the turbulent kinetic energy  $\tau_t$  are crucial quantities. Nevertheless, in most turbulent combustion

models (flamelets models, presumed pdf approach) where these scales are taken into account, proportionality between these quantities is very often assumed. Although, numerous experimental studies show that the ratio of these two scales is not a constant and varies for different flows (see Beguier *et al.* 1978).

One way of calculating the dissipation time scale of a scalar is to use a transport equation for the dissipation of the fluctuations of this scalar  $\langle \epsilon_c \rangle = \langle d \frac{\partial c'}{\partial x_i} \frac{\partial c'}{\partial x_i} \rangle$  (where  $d$  is the molecular diffusivity and  $c'$  the fluctuation of  $c$ ;  $c$  is defined to be equal to 1 in the burnt gases and to 0 in the fresh gases). Starting from the studies of Zeman & Lumley 1976, Borghi & Dutoya 1978 used this equation to investigate the case of a steady premixed flame. But the use of such an equation requires the modeling of many terms and very little knowledge exists to assess the adequacy of these models.

More recently, Mantel & Borghi 1991 have developed a transport equation for  $\langle \epsilon_c \rangle$  in the case of constant density and constant diffusivity. An order of magnitude analysis based on appropriate scale relations shows that the effects of stretching of the concentration field by the small scales of turbulence and the effects of local curvature are predominant. The authors present new closures for these terms in order to take into account the presence of laminar flamelet within the flow.

The applications of such an equation are significant and of fundamental interest:

- 1- In the particular case of high Damköhler number,  $Da = \tau_t / \tau_{ch}$  where  $\tau_{ch}$  is a chemical time scale, Bray & Moss 1977 and Borghi 1978 have demonstrated that  $\langle \dot{w} \rangle$  and  $\langle \epsilon_c \rangle$  are directly related:

$$\langle \dot{w} \rangle = \frac{\langle \epsilon_c \rangle}{\frac{1}{2} - b_0} \quad (1.1)$$

where,

$$b_0 = \frac{\int_0^1 c \dot{w}(c) dc}{\int_0^1 \dot{w}(c) dc}.$$

In accordance with Bray & Moss 1977, the equation for  $\langle \epsilon_c \rangle$  leads to a transport equation for the mean reaction rate and to a new formulation of the well known Eddy Break-Up model.

- 2- Moreover, in the flamelet regime,  $\langle \epsilon_c \rangle$  and  $\langle \Sigma \rangle$  can be directly connected by  $\langle \epsilon_c \rangle \propto S_L \langle \Sigma \rangle$  (see Borghi 1990), where  $S_L$  is the laminar flame velocity. Thus, a transport equation for  $\langle \Sigma \rangle$  is obtained in a different way from those proposed by other studies (Marble & Broadwell 1977, Candel & Poinot 1990, Trouvé & Poinot 1992, Bidaux *et al.* 1993).
- 3- Furthermore, the knowledge of the dissipation time scale for the scalar allows Mantel *et al.* 1993 to propose a new model for the equation for the correlation  $\langle u'_i c' \rangle$  which is another crucial problem in turbulent modeling that is often underestimated.

## 2. Accomplishments

We present in this section the different steps and assumptions leading to the equation for  $\langle \epsilon_c \rangle$ .

The methodology chosen here to calculate the transport equation for  $\langle E_c \rangle$  is to first establish the instantaneous equation for  $E_c = d \frac{\partial c}{\partial x_i} \frac{\partial c}{\partial x_i}$ . An averaging operation and an order of magnitude analysis of this equation will lead directly to the equation for  $\langle \epsilon_c \rangle$ .

### 2.1 Preliminaries

In order to determine the transport equation for  $E_c$ , some assumptions are made. A perfectly premixed medium is considered and a single chemical reaction occurs in the flow which can be described by:  $F_{\text{uel}} + O_{\text{xydizer}} \rightarrow P_{\text{roducts}}$ .

From the instantaneous transport equation for the progress variable  $c$ :

$$\frac{\partial c}{\partial t} + U_k \frac{\partial c}{\partial x_k} = \frac{1}{\rho} \frac{\partial}{\partial x_k} \left( \rho d \frac{\partial c}{\partial x_k} \right) + \dot{w} \quad (2.1)$$

The transport equation for  $E_c$  is obtained by differentiating Eq. (2.1) with respect to  $x_i$  and by multiplying the result by  $dc_{,i}$ , where  $c_{,i}$  represents  $\frac{\partial c}{\partial x_i}$ . After some algebra, the transport equation for  $E_c$  leads to:

$$\begin{aligned} \frac{\partial E_c}{\partial t} + U_k \frac{\partial E_c}{\partial x_k} = & c_{,i} c_{,i} d_{,t} + U_k d_{,k} c_{,i} c_{,i} - 2dc_{,i} c_{,k} \frac{\partial U_k}{\partial x_i} + \frac{1}{\rho} \frac{\partial}{\partial x_k} \left( \rho d \frac{\partial E_c}{\partial x_k} \right) \\ & + 2dc_{,i} c_{,k} \frac{\partial}{\partial x_i} \left( \frac{1}{\rho} (\rho d)_{,k} \right) - E_c \frac{\partial^2 d}{\partial x_k^2} - 2dd_{,k} \frac{\partial c_{,i} c_{,i}}{\partial x_k} - \frac{d}{\rho} \rho_{,k} d_{,k} c_{,i} c_{,i} \\ & - d_{,k} d_{,k} c_{,i} c_{,i} + 2dd_{,i} c_{,i} \frac{\partial^2 c}{\partial x_k^2} - 2d^2 \frac{\partial c_{,i}}{\partial x_k} \frac{\partial c_{,i}}{\partial x_k} + 2dc_{,i} \dot{w}_{,i} \end{aligned} \quad (2.2)$$

Obviously, Eq. (2.2) involves unclear correlations and cannot be used directly. New assumptions are needed in order to simplify Eq. (2.2) and to clarify the physical meaning of its terms. Let us consider setting the Lewis number equal to unity, no heat losses, and a constant pressure. Concerning this last assumption, even if a pressure drop occurs across a laminar flame, it is so weak that the density variations are essentially due to temperature variation across the flame front. This assumption could only be put into question in case of strong pressure waves spreading into the flame front (i.e. knock in I.C. engines).

In case of a Lewis number equal to unity and no heat losses, the temperature and the progress variable are directly related by:

$$T = T_0(1 + \theta c) \quad (2.3)$$

where  $\theta$  is the heat release parameter:  $\theta = \frac{T_{ad} - T_0}{T_0}$ ,  $T_{ad}$  and  $T_0$  represent respectively the adiabatic temperature and the temperature of the fresh gases.

Due to assumptions of constant pressure, unit Lewis number, and no heat losses, density and diffusivity derivatives can be related to the progress variable derivatives which allow to simplify Eq. (2.2).

The assumption of constant pressure and Eq. (2.3) imply:

$$\rho_{,k} = -\rho \frac{\theta}{1 + \theta c} c_{,k} \quad (2.4)$$

$$\frac{\partial \rho_{,i}}{\partial x_k} = 2\rho \frac{\theta^2}{(1 + \theta c)^2} c_{,i} c_{,k} - \rho \frac{\theta}{1 + \theta c} \frac{\partial c_{,i}}{\partial x_k} \quad (2.5)$$

and allow us to replace in Eq. (2.2) the density derivatives by the progress variable derivatives.

The diffusivity derivatives can be solved by considering that the dynamic viscosity  $\mu$  is only a function of the temperature, for example:

$$\mu = \mu_0 \left( \frac{T}{T_0} \right)^b \quad (2.6)$$

where  $b$  is a constant equal to 0.76. The dynamic viscosity at temperature  $T_0$  is denoted by  $\mu_0$ . Thus, the first and second derivatives for the molecular diffusivity can also be related to the first and second derivatives of the progress variable:

$$d_{,k} = (1 + b) d \frac{\theta}{1 + \theta c} c_{,k} \quad (2.7)$$

$$\frac{\partial^2 d}{\partial x_k^2} = b(b + 1) \frac{\theta^2}{(1 + \theta c)^2} d c_{,k} c_{,k} + (b + 1) \frac{\theta}{1 + \theta c} \frac{\partial^2 c}{\partial x_k^2} \quad (2.8)$$

$$\frac{\partial d_{,i}}{\partial x_k} = b(b + 1) \frac{\theta^2}{(1 + \theta c)^2} d c_{,i} c_{,k} + (b + 1) \frac{\theta}{1 + \theta c} \frac{\partial c_{,i}}{\partial x_k} \quad (2.9)$$

Substituting these new expressions for the derivatives of the density and molecular diffusivity, Eq. (2.2) becomes:

$$\begin{aligned} \rho \frac{\partial E_c}{\partial t} + \rho U_k \frac{\partial E_c}{\partial x_k} &= \frac{\partial}{\partial x_k} \left( \rho d \frac{\partial E_c}{\partial x_k} \right) - 2\rho d c_{,i} c_{,k} \frac{\partial U_k}{\partial x_i} + (1 + b) \rho E_c \frac{\partial U_k}{\partial x_k} \\ &\quad - 2b\rho \frac{\theta^2}{(1 + \theta c)^2} E_c^2 + (1 + b) \rho \frac{\theta}{1 + \theta c} d E_c \frac{\partial^2 c}{\partial x_k^2} \\ &\quad - 2(2 + b) \rho \frac{\theta}{1 + \theta c} d^2 c_{,i} c_{,k} \frac{\partial c_{,i}}{\partial x_k} - 2\rho d^2 \frac{\partial c_{,i}}{\partial x_k} \frac{\partial c_{,i}}{\partial x_k} + 2\rho d c_{,i} \dot{w}_{,i} \end{aligned} \quad (2.10)$$

In Eq. (2.10), derivatives of density and diffusivity disappear and a physical meaning of the terms of Eq. (2.10) can be seen more clearly. But before we give physical meanings to these terms and propose closures, averaging operations and an order of magnitude analysis are performed. We will see that the instantaneous gradients of  $c$  are predominant and allow us to derive an equation for  $\langle \epsilon_c \rangle$ .

## 2.2 Averaging and order of magnitude analysis

## 2.2.1 Preliminaries and scale relations

First, we decompose the velocity and the progress variable into a mean value and a fluctuating component (i.e. for  $c$ , we have  $c = \langle c \rangle + c'$  where  $\langle c \rangle = \frac{\bar{\rho}c}{\bar{\rho}}$  is the Favre averaging, and by definition  $\langle c' \rangle = 0$ ). The order of magnitude analysis needs appropriate scale relations which take into account the presence of chemical reactions in the fluid. For the gradient of the velocity, the approach of Tennekes & Lumley 1972 (pp 88-92) for the vorticity equation is retained. These scale relations are  $\frac{\partial \langle U_k \rangle}{\partial x_i} \propto \frac{u'}{l_t}$  and  $\frac{\partial u'_k}{\partial x_i} \propto \frac{u'}{\lambda}$  where  $l_t$  and  $\lambda$  are respectively the integral length scale and the Taylor microscale of the turbulence.

For the quantities related to the concentration flow field, the problem is more subtle. Because chemical reactions occur within the flow, we have to take into account the existence of flamelets in the turbulent flow field in order to estimate the scale relations, and we must also know the pdf (probability density function) of  $c$  for the averaging operation.

In the limit of very large  $Da$ , this pdf is essentially composed of two peaks corresponding to the fresh and burnt gases:

$$P(c) = \delta_0 \delta(c) + \gamma f(c) + \delta_1 \delta(1 - c) \quad (2.11)$$

The constant  $\gamma$  in Eq. (2.11) must to be proportional to  $Da^{-1}$  as demonstrated by Bray & Moss 1977. This can be easily justified by noting that in the case of very fast chemical reactions ( $\tau_c \rightarrow 0$ ), the instantaneous reaction rate tends to infinity ( $\tau_{ch}^{-1} = \int_0^1 \dot{w}(c)dc$ ) while the mean reaction rate, defined by:

$$\langle \dot{w} \rangle = \int_0^1 \dot{w}(c)P(c)dc \quad (2.12)$$

has to remain finite (since  $\dot{w}(0) = 0$ ,  $\dot{w}(1) = 0$ ). This point has a strong impact on the order of magnitude analysis on terms where concentration gradients appear.

We now go back to the gradients of the progress variable. Mantel and Borghi 1991 proposed to relate mean gradients to the integral length scale  $\frac{\partial \langle c \rangle}{\partial x_i} \propto \frac{\langle c'^2 \rangle^{1/2}}{l_t}$  and instantaneous gradients to the laminar flame thickness  $\delta_L$ :  $\frac{\partial c'}{\partial x_i} \propto \frac{\langle c'^2 \rangle^{1/2}}{\delta_L}$ .

The relations  $S_L \propto (d/\tau_{ch})^{1/2}$  and  $\delta_L \propto (d\tau_{ch})^{1/2}$  are also needed in this analysis. As an example, we can examine the case of  $\langle E_c \rangle$  itself. By definition, we have:

$$\langle E_c \rangle = \int_0^1 dc, i c, i P(c)dc \equiv d \frac{\langle c'^2 \rangle}{\delta_L^2} Da^{-1} \equiv \frac{\langle c'^2 \rangle}{\tau_t} Da^0 Re_t^0 \quad (2.13)$$

where,  $Re_t$  is the Reynolds number based on the integral length scale  $Re_t = u' l_t / \nu$ .

Decomposing  $c$  into a mean value and a fluctuating component,  $\langle E_c \rangle$  can be developed in different terms:

$$\langle E_c \rangle = \langle dc_{,i} c_{,i} \rangle = \underbrace{\langle d \rangle \langle c_{,i} \rangle \langle c_{,i} \rangle}_{Re_i^{-1} Da^0} + 2 \underbrace{\langle dc'_{,i} \rangle \langle c_{,i} \rangle}_{Re_i^{-1/2} Da^{-1/2}} + \underbrace{\langle dc'_{,i} c'_{,i} \rangle}_{Re_i^0 Da^0} \quad (2.14)$$

and we can conclude that in the case of large Reynolds and Damköhler numbers, only the last term of Eq. (2.14) has to be retained:

$$\langle E_c \rangle \equiv \langle dc'_{,i} c'_{,i} \rangle = \langle \epsilon_c \rangle \quad (2.15)$$

This explains why we can derive an equation for  $\langle \epsilon_c \rangle$  from the equation for  $\langle E_c \rangle$ .

### 2.2.2 The averaged equation

The separation of the velocity  $U_k$  and the progress variable  $c$  into a mean value and a fluctuation leads to a large number of correlations and new terms in the Eq. (2.10). However, the order of magnitude analysis permits an investigation concerning the relative importance of the terms of the equation and allows removal of these terms which are negligible.

After a systematic study of each term in Eq. (2.10), we obtain:

$$\begin{aligned} \frac{\partial}{\partial t} \bar{\rho} \langle \epsilon_c \rangle + \frac{\partial}{\partial x_k} (\bar{\rho} \langle U_k \rangle \langle \epsilon_c \rangle) &= \frac{\partial}{\partial x_k} \left( \bar{\rho} \langle d \frac{\partial \epsilon_c}{\partial x_k} \rangle \right) - \frac{\partial}{\partial x_k} \left( \bar{\rho} \langle u'_k \epsilon_c \rangle \right) + b \bar{\rho} \langle \epsilon_c \rangle \frac{\partial \langle U_k \rangle}{\partial x_k} \\ \text{(I)} \quad & \quad \text{(II)} \quad Re_i^0 Da^0 \quad \text{(III)} \quad Re_i^{-1/2} Da^{1/2} \quad \text{(IV)} \quad Re_i^0 Da^0 \quad \text{(V)} \quad Re_i^0 Da^0 \\ &+ b \bar{\rho} \langle \epsilon_c \frac{\partial u'_k}{\partial x_k} \rangle - \bar{\rho} \left( \langle dc_{,i} c_{,k} \rangle \frac{\partial \langle U_k \rangle}{\partial x_i} \right)_{i \neq k} - \bar{\rho} \left( \langle dc_{,i} c_{,k} \frac{\partial u'_k}{\partial x_i} \rangle \right)_{i \neq k} \\ \text{(VI)} \quad & Re_i^{1/2} Da^0 \quad \text{(VII)} \quad Re_i^0 Da^0 \quad \text{(VIII)} \quad Re_i^{1/2} Da^0 \\ &- 2b \bar{\rho} \left\langle \frac{\theta^2}{(1 + \theta c)^2} \epsilon_c^2 \right\rangle - 4b \bar{\rho} \langle c_{,i} \rangle \left\langle \frac{\theta^2}{(1 + \theta c)^2} dc_{,i} \epsilon_c \right\rangle \\ \text{(IX)} \quad & Re_i^0 Da^1 \quad \text{(X)} \quad Re_i^{-1/2} Da^{1/2} \\ &- 2(b + 3) \bar{\rho} \langle c_{,i} \rangle \left\langle \frac{\theta}{1 + \theta c} d^2 c'_{,i} \frac{\partial^2 c'}{\partial x_k^2} \right\rangle - (b + 3) \bar{\rho} \left\langle \frac{\theta}{1 + \theta c} d \epsilon_c \frac{\partial^2 c'}{\partial x_k^2} \right\rangle \\ \text{(XI)} \quad & Re_i^{-1/2} Da^{1/2} \quad \text{(XII)} \quad Re_i^0 Da^1 \\ &- 2 \bar{\rho} \left\langle d^2 \frac{\partial c_{,i}}{\partial x_k} \frac{\partial c_{,i}}{\partial x_k} \right\rangle + 2 \bar{\rho} \langle c_{,i} \rangle \langle d \dot{w}_{,i} \rangle + 2 \bar{\rho} \langle c'_{,i} d \dot{w}'_{,i} \rangle \\ \text{(XIII)} \quad & Re_i^0 Da^1 \quad \text{(XIV)} \quad Re_i^{-1/2} Da^{1/2} \quad \text{(XV)} \quad Re_i^0 Da^1 \end{aligned} \quad (2.16)$$

Some physical interpretations are proposed for the terms appearing in Eq. (2.16). From left to right, the following terms appear:

- (I) accumulation
- (II) convection



- (III) molecular diffusion
- (IV) turbulent diffusion
- (V) production (or destruction) due to expansion (or compression) of the mean velocity field
- (VI) production (or destruction) due to expansion (or compression) of the turbulent flow field
- (VII) production due to mean velocity gradient
- (VIII) production by stretching of the concentration field by the turbulent strain field
- (IX) destruction
- (X) production (or destruction) due to mean concentration gradients
- (XI) production (or destruction) due to local curvature effects
- (XII) destruction due to local curvature effects
- (XIII) destruction due to molecular dissipation
- (XIV) production (or destruction) due to chemical reactions
- (XV) production (or destruction) due to chemical reactions

### 2.3 First closure attempts

In this section, we present closures for some of the terms of Eq. (2.16). Because this study is in a preliminary phase, closure models do not exist for some terms but are currently under investigation.

- The turbulent diffusion term (IV) is closed by relating the correlation  $\langle u'_k \epsilon_c \rangle$  to a turbulent diffusion coefficient  $d_t$  and to the gradient of  $\langle \epsilon_c \rangle$ :

$$-\langle u'_k \epsilon_c \rangle = \frac{d_t}{\sigma_c} \frac{\partial \langle \epsilon_c \rangle}{\partial x_k} \quad (2.17)$$

where  $\sigma_c$  is a Schmidt number.

- The term due to expansion or compression (VI) can not be closed easily. The sign of this correlation depends on the local velocity field. This sign could be determined by analysis of DNS results.
- The production term due to mean velocity gradient (VII) can be modeled as in Zeman & Lumley 1976:

$$-\bar{\rho} \left( \langle dc_{,i} c_{,k} \rangle \frac{\partial \langle U_k \rangle}{\partial x_i} \right)_{i \neq k} = C_{P_U} \bar{\rho} \langle \epsilon_c \rangle \frac{\langle u'_i u'_k \rangle}{k} \frac{\partial \langle U_k \rangle}{\partial x_i} \quad (2.18)$$

where  $C_{P_U} = 1.0$  and  $k$  represents the turbulent kinetic energy.

- The production by stretching of the concentration field due to the turbulent strain field (VIII) can be modeled as in the case with constant density. Because the sign of this correlation seems to be negative (see the experimental results of Antonia & Browne 1983), this term represents a production of  $\langle \epsilon_c \rangle$ . Thus, the model proposed by Mantel & Borghi 1991 is still valid:

$$-\bar{\rho} \left( \langle dc_{,i} c_{,k} \rangle \frac{\partial u'_k}{\partial x_i} \right)_{i \neq k} = \alpha_0 \bar{\rho} Re_t^{1/2} \frac{\langle \epsilon_c \rangle}{\tau_t} \quad (2.19)$$

where  $\alpha_0$  is a constant ( $\alpha_0 = 0.9$ ).

- The term  $-2b\bar{\rho}\langle\frac{\theta^2}{(1+\theta c)^2}\epsilon_c^2\rangle$  is always negative and represents a destruction of  $\langle\epsilon_c\rangle$ . We propose as a first approximation:

$$2b\bar{\rho}\langle\frac{\theta^2}{(1+\theta c)^2}\epsilon_c^2\rangle = R_1\bar{\rho}\frac{\theta^2}{(1+\theta\langle c\rangle)^2}\langle\epsilon_c\rangle^2 \quad (2.20)$$

where  $R_1$  is a constant. Its value could be estimated from DNS results.

- The production (or destruction) due to mean concentration gradients  $4b\bar{\rho}\langle c,i\rangle\langle\frac{\theta^2}{(1+\theta c)^2}dc,i\epsilon_c\rangle$  can not be easily modeled. More information concerning the correlation  $c,i\epsilon_c$  has to be extracted from DNS or analytical study.
- The term  $-2(b+3)\bar{\rho}\langle c,i\rangle\langle\frac{\theta}{1+\theta c}d^2c',i\frac{\partial^2 c'}{\partial x_k^2}\rangle$  is a production (or a destruction) of  $\langle\epsilon_c\rangle$ . No clear closure can be proposed, and more investigation must be pursued.
- The term  $(b+3)\bar{\rho}\langle\frac{\theta}{1+\theta c}d\epsilon_c\frac{\partial^2 c'}{\partial x_k^2}\rangle$  is a production (or destruction) of  $\langle\epsilon_c\rangle$  due to local curvature effects. Following the closure proposed by Mantel & Borghi 1991 for the curvature, we propose:

$$(b+3)\bar{\rho}\langle\frac{\theta}{1+\theta c}d\epsilon_c\frac{\partial^2 c'}{\partial x_k^2}\rangle = R_2\bar{\rho}\frac{\theta}{1+\theta\langle c\rangle}\frac{\langle\epsilon_c\rangle^2}{\langle c'^2\rangle^{1/2}}Re_t^{1/4} \quad (2.21)$$

$R_2$  is a constant. Its sign depends of the sign of the correlation  $\epsilon_c\frac{\partial^2 c'}{\partial x_k^2}$  itself which could be obtained using DNS results.

- For the term of destruction due to molecular dissipation (XIII), the model proposed by Mantel & Borghi 1991 is still valid in the case of variable density. From these authors, we have:

$$2\bar{\rho}\langle d^2\frac{\partial c,i}{\partial x_k}\frac{\partial c,i}{\partial x_k}\rangle = \beta_0\bar{\rho}Re_t^{1/2}\frac{\langle\epsilon_c\rangle^2}{\langle c'^2\rangle} \quad (2.22)$$

$\beta_0$  is a constant ( $\beta_0 = 1.25$ ).

- concerning the production (or destruction) terms due to chemical reactions (XIV) and (XV), further investigations are in progress in order to propose new closures for these terms.

### 3. Conclusion and future plans

A transport equation for the dissipation of the fluctuation of a reactive scalar has been established in the case of variable density and variable diffusivity. The assumptions of constant pressure, no heat losses, and a Lewis number of unity significantly simplify the equation. As in the case with constant density (Mantel & Borghi 1991), an order of magnitude analysis using adequate scale relations shows

that the effects of stretching, molecular dissipation, local curvature, and chemical reactions are dominant. As a first approximation, some closure models are proposed, but further theoretical developments and comparison with DNS results must be done to confirm these models.

Analytical developments must be in the limit of large Damköhler and Reynolds numbers in order to study the relative importance of the unclosed terms.

DNS could also give essential information on the sign of some correlations and will allow the study the different terms of the equation separately. Existing DNS results of flame propagation in a decaying homogeneous turbulence for different Lewis number will be used. New computations will be performed over a large range of the ratio  $u'/S_L$  in order to assess the validity of the models and to complete the CTR DNS database.

### Acknowledgements

The author would like to thank Prof. Roland Borghi (University of Rouen - France) for his many helpful suggestions and comments and Dr. Thierry Poinsot (CERFACS - France) for his stimulating encouragements.

### REFERENCES

- ANTONIA, R. A. & BROWNE, L. W. R. 1983 The Destruction of Temperature Fluctuations in a Turbulent Plane Jet. *J. Fluid Mech.* **134**, 67-83.
- BEGUIER, C., DEKEYSER, J. & LAUNDER, B. E. 1978 Ratio of Scalar and Velocity Dissipation Time Scales in Shear Flow Turbulence. *Phys. Fluids*. **21-3**, 307-310.
- BIDAUX, E., VERVISCH, L. & BRAY, K. N. C. 1993 Study of the Transport Equation for a Surface Density Function and Some Implications for Turbulent Combustion Modelling. *Submitted for publication*.
- BORGHI, R. 1978 Réactions Chimiques en Milieu Turbulent. *Thèse de Doctorat d'Etat*, Université Pierre et Marie Curie Paris VI.
- BORGHI, R. 1990 Turbulent Premixed Combustion: Further Discussions on the Scales of Fluctuations. *Combustion and Flame*. **80**, 304-312.
- BORGHI, R. & DUTOYA, D. 1978 On the Scale of the Fluctuations in Turbulent Combustion. *Seventeenth Symp. (International) on Combust.* 235-244.
- BRAY, K. N. C. 1985 Laminar Flamelet Modelling of Turbulent Combustion. *Lecture Notes in Physics*, Springer Verlag. **241**, 3-19.
- BRAY, K. N. C. & LIBBY, P. A. 1986 Passage Times and Flamelet Crossing Frequencies in Premixed Turbulent Combustion. *Combustion, Science and Technology*. **47**, 253-274.
- BRAY, K. N. C. & MOSS, J. B. A Unified Statistical Model of the Premixed Turbulent Flame *Acta Astronautica* **4**, 291-319.
- CANDEL, S. M. & POINSOT, T. J. 1990 Flame Stretch and the Balance Equation for the Flame Area. *Combustion, Science and Technology*. **70**, 1-15.

- DUCLOS, J. M., VEYNANTE, D. & POINSOT, T. 1993 A Comparison of Flamelet Models for Premixed Turbulent Combustion. *Combustion and Flame*. **95**, 101-108.
- KERSTEIN, A. R., ASHURST, W. T. & WILLIAMS, F. A. 1988 Field Equation for Interface Propagation in an Unsteady Homogeneous Flow Field. *Physical Review*. **A-37-7**, 2728-2731.
- LIBBY, P. A. & BRAY, K. N. C. 1980 Implication of the Laminar Flamelets Model in Premixed Turbulent Combustion. *Combustion and Flame*. **39**, 33-41.
- MANTEL, T. & BORGHI, R. 1991 A New Model of Premixed Wrinkled Flame Propagation Based on a Scalar Dissipation Equation. *13th ICDERS*, Nagoya (Japan), (will appear in *Combustion and Flame*).
- MANTEL T., BORGHI R. & PICART A. 1993 Turbulent Premixed Flame Propagation Revisited Results with a New Model. *Ninth Symposium on Turbulent Shear Flows*, Kyoto (Japan).
- MARBLE, F. E. & BROADWELL, J. E. 1977 The Coherent Flame Model for Turbulent Chemical Reactions. *Technical Report TRW-9-TV*, Purdue University.
- PETERS, N. 1992 A Spectral Closure for Premixed Turbulent Combustion in the Flamelet Regime. *J. Fluid Mech.* **242**, 611-629.
- POPE, S. B. 1988 Evolution of Surfaces in Turbulence. *Int. Journal of Ing. Sciences*. **26**, 445-469.
- TENNEKES, H. & LUMLEY, J. L. 1972 A First Course in Turbulence. *The MIT Press*.
- TROUVÉ, A. & POINSOT, T. 1992 The Evolution Equation for the Flame Surface Density in Turbulent Premixed Combustion. *Proceedings of the 1992 Summer Program*. Center for Turbulence Research, Stanford Univ./NASA Ames, 325-343.
- WILLIAMS, F. A. 1985 In the Mathematics of Combustion. *SIAM Philadelphia*. 97-131.

## The production of premixed flame surface area in turbulent shear flow

By A. Trouvé

### 1. Motivation and objectives

In the flamelet theory, the modeling of the mean reaction rate is based primarily on a statistical description of the wrinkling of the flame surface due to the turbulent motions. The amount of wrinkling is quantified by the mean flame surface-to-volume ratio, also called the flame surface density. The flamelet theory produces an exact evolution equation for the flame surface density, called the  $\Sigma$ -equation, where basic physical mechanisms such as production by hydrodynamic straining and dissipation by propagation effects are described explicitly. In flamelet models, the flame surface density is obtained via a modeled formulation of this exact  $\Sigma$ -equation (Marble & Broadwell 1977; Darabiha *et al.* 1987; Pope & Cheng 1988; Maistret *et al.* 1989; Candel *et al.* 1990; Cant, Pope & Bray 1990; Borghi 1990; Mantel & Borghi 1991). Recent work at CTR, aimed at improving current models for the  $\Sigma$ -equation, focused primarily on the production and dissipation terms due to the turbulent flow field (Meneveau & Poinso 1991; Trouvé & Poinso 1993). In these studies, the turbulence upstream of the flame is considered isotropic and the mean flow velocity gradient tensor,  $[\partial \tilde{U}_i / \partial x_j]$ , features only one non-zero component that corresponds to the mean flow acceleration through the combustion zone. Flame configurations featuring more complex mean deformation patterns, as found in practical systems where the combustion occurs in shear layers, boundary layers, or stagnation point flows, have not been considered yet.

There is, in fact, little knowledge on the influence of mean velocity gradients on the dynamics of premixed flame surfaces. In current flamelet models, since the turbulent flame stretch in the equation for  $\Sigma$  depends on the turbulent kinetic energy,  $k$ , and its rate of dissipation,  $\epsilon$ , the effects of mean deformations are incorporated implicitly through their impact on  $k$  and  $\epsilon$ . An additional term that is linearly related to  $[\partial \tilde{U}_i / \partial x_j]$  is also sometimes introduced to account for possible direct effects (see Duclos, Poinso & Veynante 1993).

In the present work, we use three-dimensional Direct Numerical Simulation (DNS) of premixed flames in turbulent shear flow to characterize the effect of a mean shear motion on flame surface production. The shear is uniform in the unburnt gas, and simulations are performed for different values of the mean shear rate,  $S$ . The data base is then used to estimate and compare the different terms appearing in the  $\Sigma$ -equation as a function of  $S$ . The analysis gives in particular the relative weights of the turbulent flow and mean flow components,  $\widehat{a_T}$  and  $\widehat{A_T}$ , of the flame surface production term. This comparison indicates whether the dominant effects of a mean flow velocity gradient on flame surface area are implicit and scale with the modified turbulent flow parameters,  $k$  and  $\epsilon$ , or explicit and scale directly with the rate of deformation.

### 1.1 The evolution equation for the flame surface density

In the flamelet regime, it is convenient to describe the flame-flow interactions in terms of the following two basic ingredients: a flame speed that characterizes the mean combustion intensity, and a surface area that characterizes the flame wrinkling (Williams 1985; Peters 1986; Bray 1990; Pope 1990; Poinso, Veynante & Candel 1991). For instance, the mean reaction rate may be written as a mean integrated chemical rate times the flame surface density:

$$\langle \dot{\omega}_R \rangle = \langle \int \dot{\omega}_R dn \rangle_S \langle \Sigma' \rangle = \langle \int \dot{\omega}_R dn \rangle_S \Sigma, \quad (1)$$

where  $\dot{\omega}_R$  is the mass of fuel consumed per unit time and per unit volume;  $\int \dot{\omega}_R dn$  is the local integral of the reaction rate along the flame normal direction;  $\Sigma'$  is the flame surface area per unit volume;  $\Sigma$  is the flame surface density, defined as the expected value for  $\Sigma'$ ,  $\Sigma \equiv \langle \Sigma' \rangle$ . Note that in (1), all quantities are local and mean operators correspond to ensemble-averaging. While  $\langle \rangle$  denotes a standard, unweighted ensemble-average,  $\langle \rangle_S$  denotes a surface mean, defined as an area-weighted ensemble-average (Pope 1988),  $\langle Q \rangle_S \equiv \langle Q \Sigma' \rangle / \langle \Sigma' \rangle = \langle Q \Sigma' \rangle / \Sigma$ .

In (1), the integral of the reaction rate can be replaced by the local fuel consumption speed,  $S_C$ , defined as:

$$S_C \equiv \frac{1}{\rho_u Y_{R,u}} \int \dot{\omega}_R dn, \quad (2)$$

where  $\rho_u$  and  $Y_{R,u}$  are respectively the density and the fuel mass fraction in the unburnt gas. The mean reaction rate may then be expressed as the surface mean of  $S_C$ , called the flamelet speed, times the flame surface density:

$$\langle \dot{\omega}_R \rangle = (\rho_u Y_{R,u} \langle S_C \rangle_S) \Sigma. \quad (3)$$

(3) is the classical flamelet expression for the ensemble mean of the reaction rate. In this expression, the flamelet speed,  $\langle S_C \rangle_S$ , accounts for local variations of the reaction rate along the flame surface. Recent direct simulations suggest that for flame Lewis numbers close to unity, the departures of  $\langle S_C \rangle_S$  from the laminar consumption rate tend to average out when integrated across the whole turbulent flame (Ashurst, Peters & Smooke 1987; Haworth & Poinso 1992; Rutland & Trouvé 1993; Trouvé & Poinso 1993). In this situation, the flame surface density is to first order the single key quantity that determines the mean reaction rate. Note that Trouvé & Poinso (1993) also describe one flame with thermal-diffusive instability where the effect of the turbulence on the flame surface area is coupled with a significant increase in the mean flame intensity. In that case, both the flamelet speed and the flame surface density need to be modeled to determine the mean reaction rate.

In many situations, the principal effect of the turbulence is for the fluctuating velocity field to wrinkle the flame and greatly increase its surface area. This phenomenon is represented in (3) by the flame surface density,  $\Sigma$ . Following the pioneer

work of Marble & Broadwell (1997), an exact balance equation for the flame surface density was derived by Pope (1988) and Candel & Poinso (1990):

$$\frac{\partial \Sigma}{\partial t} + \nabla \cdot \langle \dot{\mathbf{X}} \rangle_S \Sigma = \langle \kappa \rangle_S \Sigma, \quad (4)$$

where  $\dot{\mathbf{X}}$  is the velocity of the flame surface, given by the sum of the fluid velocity and the flame propagation speed in the normal direction:  $\dot{\mathbf{X}} = \mathbf{u} + w\mathbf{n}$ ;  $\mathbf{n}$  is the unit vector normal to the flame surface; and  $\kappa$  is the flame stretch. A useful expression for  $\kappa$  is in terms of strain rate, flame curvature, and flame propagation speed (Candel & Poinso 1990):

$$\kappa = a_T + 2wk_m, \quad (5)$$

where  $a_T$  is the rate of strain acting in the flame tangent plane:  $a_T = \nabla \cdot \mathbf{u} - \mathbf{nn} : \nabla \mathbf{u}$  (we use here standard tensorial notations:  $\mathbf{nn} : \nabla \mathbf{u} = n_i n_j \partial u_i / \partial x_j$ ); and  $k_m$  is the flame surface curvature, as given by the divergence of the flame normal direction:  $2k_m = \nabla \cdot \mathbf{n}$ . In (5), positive curvature is chosen convex towards the reactants.

Equation (4) can be cast in various forms. For modeling purposes, it is useful to split the velocity vector into a mean component and a turbulent fluctuation:  $\mathbf{u} = \tilde{\mathbf{U}} + \mathbf{u}''$ , where the tilde superscript denotes a Favre-averaged quantity:  $\tilde{\mathbf{U}} = \langle \rho \mathbf{U} \rangle / \langle \rho \rangle$ . We can then re-write (4) as follows:

$$\frac{\partial \Sigma}{\partial t} + \nabla \cdot \tilde{\mathbf{U}} \Sigma + \nabla \cdot \langle \mathbf{u}'' \rangle_S \Sigma + \nabla \cdot \langle w\mathbf{n} \rangle_S \Sigma = \langle A_T \rangle_S \Sigma + \langle a_T \rangle_S \Sigma + 2\langle wk_m \rangle_S \Sigma, \quad (6)$$

where we use the following notations:

$$\langle A_T \rangle_S = \nabla \tilde{\mathbf{U}} - \langle \mathbf{nn} \rangle_S : \nabla \tilde{\mathbf{U}}, \quad (7)$$

$$\langle a_T \rangle_S = \langle \nabla \cdot \mathbf{u}'' - \mathbf{nn} : \nabla \mathbf{u}'' \rangle_S. \quad (8)$$

The three convective terms on the left-hand side of (6) are transport terms that correspond respectively to convection by the mean flow, turbulent diffusion, and flame propagation. The terms on the right-hand side of the equation are the source and sink terms for the flame surface density:  $\langle A_T \rangle_S$  is the tangential strain rate due to the mean flow field;  $\langle a_T \rangle_S$  is the strain rate due to the turbulent flow field; and  $2\langle wk_m \rangle_S$  is a term that accounts for the combined effects of flame curvature and flame propagation.

We are particularly interested in this study in the effect of mean flow deformations on the dynamics of flame surface densities. As seen in the equation for  $\Sigma$ , in the presence of mean flow velocity gradients,  $\partial \tilde{U}_i / \partial x_j$ , the flame surface is modified in two different ways: first by a rapid distortion that accounts for the direct straining of the flame surface by the mean velocity gradients (this effect is represented in (6) by  $\langle A_T \rangle_S$ ) and second by a slower modification resulting from the adjustment of the turbulence to the applied deformations and from the corresponding variations in the turbulent flame stretch (this effect is represented mainly by  $\langle a_T \rangle_S$  and  $2\langle wk_m \rangle_S$ ).

### 1.2 Direct numerical simulation of turbulent premixed flames

We use DNS to analyze the different terms in the equation for the flame surface density. The simulations are performed using a three-dimensional, compressible Navier-Stokes solver that fully resolves the turbulent flow field. The solver uses a high-order finite difference scheme: spatial derivatives are computed with a modified Padé scheme that is sixth-order accurate (Lele 1992); solutions are advanced in time with a third-order Runge-Kutta method (Wray 1990); boundary conditions are specified with the NSCBC method (Poinsot & Lele 1992). We refer the reader to Lele (1992) and Poinsot & Lele (1992) for further details concerning the system of equations solved and the numerical methods.

Because of the otherwise prohibitive computational cost, simulations are limited to simple but finite-rate reaction schemes. In this work, the chemistry model is a single step, irreversible chemical reaction where the reaction rate depends exponentially on temperature (Arrhenius kinetics):

$$\dot{\omega}_R = B\rho Y_R \exp\left(-\frac{T_a}{T}\right), \quad (9)$$

where  $T_a$  is the activation temperature and  $B$  is a constant that is determined according to the selected laminar flame speed. This formulation corresponds to a binary reaction in which one of the reactants,  $Y_R$ , is strongly deficient, for example, in fuel-lean combustion. Also, it is worth emphasizing that the simulations do not use the constant density assumption; the reaction is exothermic and heat release effects are fully accounted for.

Following Williams (1985), we re-write the reaction rate as:

$$\dot{\omega}_R = \Lambda\rho Y_R \exp\left(\frac{-\beta(1-\Theta)}{1-\alpha(1-\Theta)}\right), \quad (10)$$

where  $\Theta$  is the reduced temperature,  $\Theta = (T - T_u)/(T_b - T_u)$ ;  $T_u$  is the temperature of the fresh reactants;  $T_b$  is the adiabatic flame temperature; and the coefficients  $\Lambda$ ,  $\alpha$ , and  $\beta$  are, respectively, the reduced pre-exponential factor, the heat release factor, and the reduced activation energy:

$$\Lambda = B \exp(-\beta/\alpha), \quad \alpha = (T_b - T_u)/T_b, \quad \text{and} \quad \beta = \alpha T_a/T_b. \quad (11)$$

The values of the flame parameters are reported in Table 1.

Another important feature of the simulations is that the transport coefficients are temperature dependent. These coefficients satisfy the following relations:

$$\mu = \mu_u (T/T_u)^b, \quad Le = \lambda_{th}/\rho D c_p = \text{constant}, \quad Pr = \mu c_p/\lambda_{th} = \text{constant}, \quad (12)$$

where  $\mu$ ,  $\lambda_{th}$ , and  $D$  are the molecular diffusivities of, respectively, momentum, internal energy, and species mass;  $c_p$  is the specific heat at constant pressure;  $b$  is a constant; and  $Le$  and  $Pr$  are respectively the Lewis number and the Prandtl number. The simulations were performed for a non-unity Lewis number,  $Le = 0.8$ .



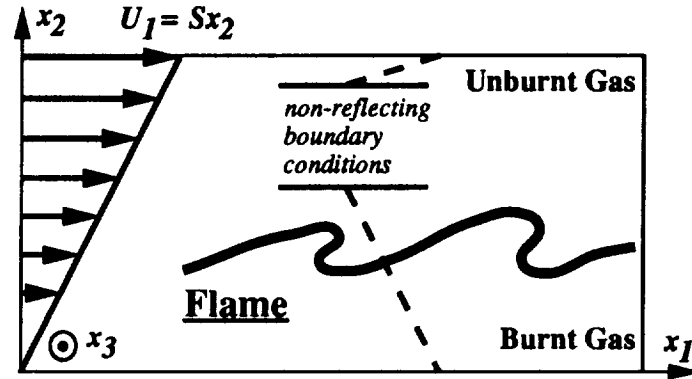


FIGURE 1. Numerical configuration.

$Le$	$\alpha$	$\beta$	$\Lambda^+$	$b$	$Pr$
0.8	0.75	8.0	456	0.76	0.75

TABLE 1. Dimensionless flame parameters,  $\Lambda$  is made non-dimensional by the laminar flame time,  $\Lambda^+ = \Lambda (\lambda_{th}/\rho c_p)u/sL^2$ .

The computational configuration corresponds to a premixed flame embedded in a three-dimensional, turbulent shear flow (see figure 1). The calculations are initialized with fresh reactants on the top side of the domain ( $x_2 > 0$ ) and burnt products on the bottom ( $x_2 < 0$ ); the two are separated by a plane laminar flame. The turbulence is initially isotropic, its velocity field being specified according to a model energy spectrum:

$$E(k) = C \left(\frac{k}{k_i}\right)^4 \exp\left\{-2\left(\frac{k}{k_i}\right)^2\right\}, \quad (13)$$

where  $k$  is the wavenumber and  $C$  and  $k_i$  are model parameters that are specified according to, respectively, the initial turbulent rms velocity,  $u''$ , and integral length scale,  $l$ .

At  $t = 0$ , a simple shearing motion,  $\partial\tilde{U}_1/\partial x_2 = S$ , is applied on the flow system. Note that due to the flow acceleration through the flame, the shear rate does not remain uniform in the cross-stream  $x_2$  direction; in the flame zone, the velocity gradient  $\partial\tilde{U}_1/\partial x_2$  is a function of both time and cross-stream position. Outside the flame zone, however, the turbulence remains homogeneous in all three directions. In the burnt gas, the mean velocity gradient changes with time; it remains constant and equal to  $S$  in the unburnt gas.

The top and bottom walls of the computational domain are inflow and outflow boundaries while periodic boundary conditions are applied in the  $x_1$  and  $x_3$  directions. Non-periodic boundary conditions are needed along  $x_2$  for the following two

reasons: to be able to maintain numerically a constant shear; to account for the density change from unburnt to burnt gases. Note, however, that no turbulence is generated at the inflow boundary, and the simulations are time-evolving rather than space-evolving.

Values of the run parameters are reported in Table 2. At time  $t = 0$ , the turbulence is characterized by flow length scales that are a few times larger than the laminar flame thickness,  $l/l_F \approx 4 - 5$  with  $l_F = (\lambda_{th}/\rho c_p)_u/s_L$ , and turbulence intensities that are higher than the laminar flame speed,  $u''/s_L > 5$ . The initial influence of the mean shear on the overall turbulence dynamics is measured by a time scale ratio,  $S\tau_0$ , where  $\tau_0$  designates the initial, turbulent eddy turn-over time,  $\tau_0 = l/u''$ . All simulated cases correspond to similar values of the initial Reynolds number. The initial turbulent Reynolds number based on the Taylor microscale,  $\lambda$ , is approximately  $Re_\lambda \approx 25$ . The initial turbulent Reynolds number based on the integral length scale is  $Re_l \approx 35$ . In Table 2, a Damköhler number is also introduced using the Kolmogorov time scale and the laminar flame time:  $Da = (\lambda/u'')/(l_F/s_L) = \sqrt{15}(\eta_k/v_k)/(l_F/s_L)$ , where  $\eta_k$  and  $v_k$  are respectively the Kolmogorov length and velocity scales. While the simulated flames correspond to relatively low Damköhler numbers,  $Da < 1$ , the reaction zone can still be described as a surface and the simulated flames occur in the flamelet regime.

Since in the presence of mean shear the turbulent structures are elongated in the streamwise direction, we use a computational domain that is twice as long in the streamwise direction compared to the cross-stream and spanwise directions. The grid spacing is uniform in all three directions; the grid resolution is  $129 \times 129 \times 65$  and is, therefore, twice better in the direction of mean flame propagation,  $x_2$ . Also, given the growth of the turbulent length scales in the streamwise direction, the numerical simulations are all limited to relatively low total shears,  $St < 15$ , after which the eddies have sizes that are comparable to the computational domain and the numerical simulations suffer from insufficient resolution.

Run designation	$S\tau_0$	$Re_l$	$Re_\lambda$	$Sl_F/s_L$	$u''/s_L$	$l/l_F$	$Da$	$Le$
Case 1 (lew08tSR)	10.5	35.	25.	10.	5.0	5.3	0.8	0.8
Case 2 (lew08SR)	7.0	35.	25.	6.7	5.0	5.3	0.8	0.8
Case 3 (lew08sSR)	3.5	35.	25.	3.3	5.0	5.3	0.8	0.8
Case 4 (lew08wSR)	3.3	38.	28.	6.7	7.5	3.8	0.4	0.8
Case 5 (lew08uSR)	1.7	38.	28.	3.3	7.5	3.8	0.4	0.8
Case 6 (lew08vSR)	0.7	38.	28.	1.3	7.5	3.8	0.4	0.8

TABLE 2. Dimensionless parameters for the reacting flow simulations.

All parameters correspond to the initial condition,  $t = 0$ .

All terms in (6) can be obtained from the simulations. We refer the reader to Trouvé (1993) and Trouvé & Poinot (1993) for further details concerning the diagnostics that were developed to extract the relevant information from the DNS

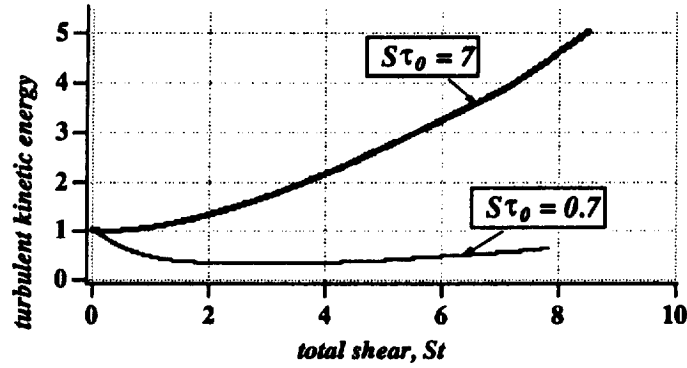


FIGURE 2. The effect of the turbulence-to-mean shear time scale ratio,  $S\tau_0$ , on the relative increase of total turbulent kinetic energy. A comparison between cases 2 and 6.

database. We simply briefly recall here that flame-based quantities are defined by making the assumption that the resolved finite-thickness reaction zone can be viewed as a constant progress variable surface,  $c = c_f = 0.8$  where  $c \equiv 1 - (Y_R/Y_{R,u})$ . Ensemble-averaging is conveniently performed in the homogeneous  $x_1 - x_3$  planes. For completion, we recall the expressions used to calculate the flame propagation speed, the flame surface density, and the surface means:

$$w = \dot{\mathbf{X}} \cdot \mathbf{n} - \mathbf{u} \cdot \mathbf{n} = \frac{1}{|\nabla c|} \frac{Dc}{Dt} = \frac{1}{\rho |\nabla Y_R|} (\dot{\omega}_R - \nabla \cdot (\rho D \nabla Y_R)), \quad (14)$$

$$\Sigma = \frac{1}{L_{x_1} L_{x_3}} \int_{c=c_f} \frac{|\nabla c|}{\sqrt{(\frac{\partial c}{\partial x_1})^2 + (\frac{\partial c}{\partial x_3})^2}} dl, \quad (15)$$

where  $L_{x_1}$  and  $L_{x_3}$  are the  $x_1$  and  $x_3$  dimensions of the computational domain.

$$\langle Q \rangle_S \equiv \frac{\langle Q \Sigma' \rangle}{\langle \Sigma' \rangle} = \frac{\int_{c=c_f} (Q |\nabla c| dl / \sqrt{(\frac{\partial c}{\partial x_1})^2 + (\frac{\partial c}{\partial x_3})^2})}{\int_{c=c_f} (|\nabla c| dl / \sqrt{(\frac{\partial c}{\partial x_1})^2 + (\frac{\partial c}{\partial x_3})^2})}. \quad (16)$$

## 2. Accomplishments

The simulations describe the wrinkling of the flame zone by the flow as well as the transition of the flow field from isotropic decaying to anisotropic sheared turbulence. The mean shear rate,  $S$ , is used as a control parameter to modify the coupling between the mean flow, the turbulence, and the flame. Since the wrinkling of the flame is mainly driven by the turbulent motions in the unburnt gas, we first describe in §2.1 the mean shear-turbulence interactions that modify the turbulence upstream of the flame. We then turn in §2.2 to the impact of these modifications on the evolution of flame surface densities with emphasis on the effect of  $S$  on the flame surface production term.

### 2.1 The effect of mean shear in homogeneous turbulent shear flow

Turbulent shear flows present several additional levels of complication compared to isotropic turbulence because of the anisotropy of the flow, the production of turbulent kinetic energy by the mean strain, the possible amplification of hydrodynamic (Kelvin-Helmholtz) instabilities, and the resulting presence of large scale coherent structures. The general complexity of sheared turbulence is significantly reduced in the case of homogeneous shear flows, where the mean shear is uniform throughout the flow. For instance, such basic flow configurations are free of large scale hydrodynamic instabilities. In addition, homogeneous turbulent flows allow much simplified and more powerful statistical descriptions. Due to this increase in simplicity, homogeneous shear flows have been extensively studied in the literature, experimentally (Tavoularis & Corrsin 1981; Rohr *et al.* 1988; Tavoularis & Karnik 1989), as well as numerically (Rogallo 1981; Rogers & Moin 1987; Lee, Kim & Moin 1990; Holt, Koseff & Ferziger 1992).

We are particularly interested in this work in the effect of changing the mean shear rate,  $S$ , on the energy levels and the structure of the turbulence. To characterize the effect of  $S$ , we performed a preliminary series of six simulations without flame. The run parameters are identical to the ones given in Table 2, except for the absence of chemical reaction. The grid resolution is  $129 \times 65 \times 65$ . The results are used in the subsequent simulations with flame to describe the dynamics of the turbulence in the unburnt gas. We present in this section the main results from these non-reacting flow simulations.

The evolution of initially isotropic turbulence in a mean flow of uniform simple shearing motion,  $S = d\bar{U}_1/dx_2 = \text{constant}$ , can be described in terms of the following three dimensionless parameters: the total shear,  $St$ , that gives a non-dimensional time; the time scale ratio  $S\tau_0$ ; and a turbulent Reynolds number,  $Re_t = u''l/\nu$ , taken at  $t = 0$ .  $S\tau_0$  is a measure of the initial importance of the applied shear.  $Re_t$  determines the impact of viscous effects. Both parameters serve to describe the effect of initial conditions, and their influence will be negligible at large times.

The present simulations, however, are limited to total shears of approximately 10. At time  $St = 10$ , the turbulent eddies remains in non-equilibrium. For instance, the quantity  $Sk/\epsilon$  is still evolving. It is generally believed that uniformly sheared turbulence will ultimately achieve a self-preserving state in which the turbulence changes at a rate independent of the initial conditions. In the simulations, the turbulence is clearly still far from this equilibrium state.

For small values of the total shear  $St$ , the simulations reveal a range of flow regimes ranging from viscous decay for small values of  $S\tau_0$ , to rapid distortion for  $S\tau_0 > 5$ . This diversity in the turbulent flow response to the mean shear is shown in figure 2. While for  $S\tau_0 = 0.7$  the flow goes through an initial phase characteristic of decaying grid turbulence and energy growth is only observed at later times,  $S\tau_0 > 3$ , for  $S\tau_0 = 7$ , the flow is dominated by the mean shear-turbulence interactions and the energy growth starts immediately at  $t = 0$ .

Figures 3 and 4 describe the partition of turbulent kinetic energy between the

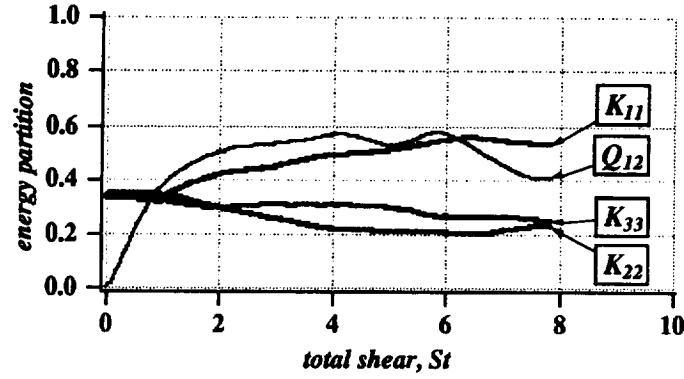


FIGURE 3(A). Partition of the turbulent kinetic energy,  $k$ ;  $K_{ij} \equiv \widetilde{u_i'' u_j''} / 2k$ ;  $Q_{12} \equiv K_{12} / \sqrt{K_{11} K_{22}}$ . Case 6,  $S\tau_0 = 0.7$ .

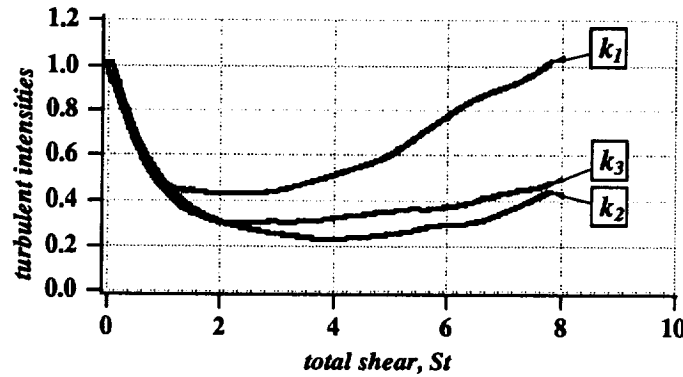


FIGURE 3(B). Partition of the turbulent kinetic energy,  $k$ ;  $k_i \equiv \widetilde{u_i'' u_i''} / 2 = K_{ii} \times k$ . Case 6,  $S\tau_0 = 0.7$ .

streamwise, cross-stream, and spanwise velocity fluctuations. As seen in figures 3(a) and 4(a), the simulations feature an initial transient phase,  $0 \leq St \leq 6$ , where the anisotropy levels,  $K_{ij} \equiv \widetilde{u_i'' u_j''} / 2k$ , change rapidly, followed by a phase of slower adjustment where the flow approaches structural equilibrium with  $K_{ij}$  asymptoting to constant values. Note that the flow remains more isotropic in case 6 compared to case 2. This result is consistent with the findings by Lee, Kim & Moin (1990), who show that the structure of shear-driven homogeneous turbulence changes drastically when the mean shear rate,  $S$ , is increased and that the degree of anisotropy of the flow increases with  $S$ .

Figures 3(b) and 4(b) compare the magnitudes of the different turbulent kinetic energy components,  $k_i \equiv \widetilde{u_i'' u_i''} / 2 = K_{ii} \times k$ . The initial decay phase is very pronounced in case 6: in figure 3(b), the different turbulent intensities remain lower than their initial value up to  $St = 8$ . The situation is drastically different at high

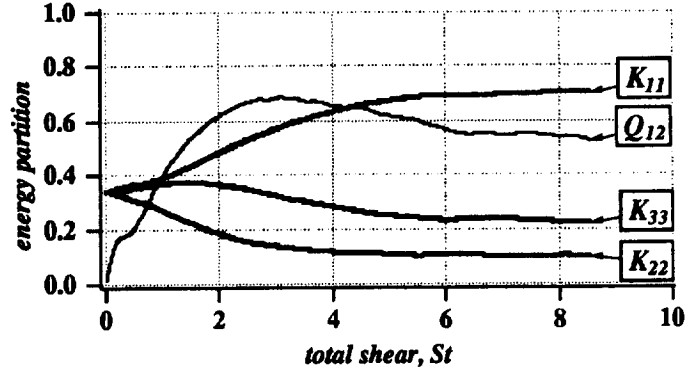


FIGURE 4(A). Partition of the turbulent kinetic energy,  $k$ ;  $K_{ij} \equiv \widetilde{u_i'' u_j''}/2k$ ;  $Q_{12} \equiv K_{12}/\sqrt{K_{11}K_{22}}$ . Case 2,  $S\tau_0 = 7$ .

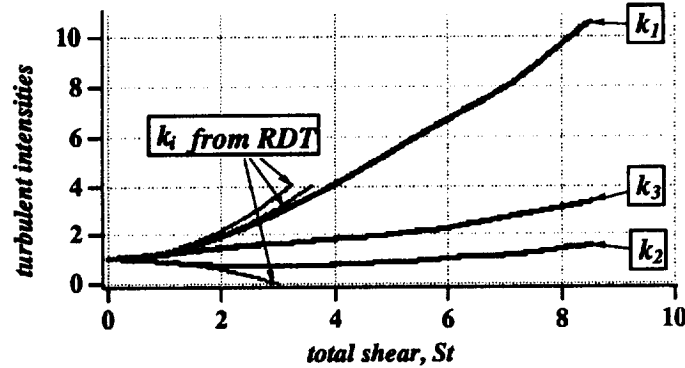


FIGURE 4(B). Partition of the turbulent kinetic energy,  $k$ ;  $k_i \equiv \widetilde{u_i'' u_i''}/2 = K_{ii} \times k$ . Case 2,  $S\tau_0 = 7$ .

shear rates: in figure 4(b), at  $St = 8$ , the streamwise component  $k_1$  is already an order of magnitude larger than its initial value. Furthermore, the simulations feature the following classical arrangement:  $k_1 > k_3 > k_2$ . The first inequality reflects the fact that the streamwise component receives energy directly from the mean shear, while the other components are maintained by redistribution of energy through the pressure-strain correlation.

We also present in figure 4(b) a comparison between the DNS data and the predictions from Rapid Distortion Theory (RDT) (see for example Townsend 1976; Maxey 1982). RDT is a linear theory that applies to situations in which the mean shear-turbulence interactions dominate the nonlinear turbulence-turbulence interactions. Its domain of validity corresponds to  $S\tau_0 \gg 1$ . RDT sheds light on the mechanisms of energy exchange between the different turbulent velocity components. For instance, RDT shows that while most of the energy is concentrated in the streamwise component,  $k_1$ , energy is also transferred from both  $k_1$  and  $k_2$  to  $k_3$

by the pressure-strain correlation, which accounts for the net reduction (increase) in  $k_2$  ( $k_3$ ) by the shear distortion seen in figure 4(b).

Hence, while the initial time evolutions of  $k_1$  and  $k_3$  depend strongly on the parameter  $S\tau_0$ , the cross-stream turbulent velocities are less sensitive to its value: for  $S\tau_0 < 1$ ,  $k_2$  decreases at small times because of viscous decay; for  $S\tau_0 \gg 1$ ,  $k_2$  also decreases because of a net energy loss to  $k_3$ .

## 2.2 The evolution of flame surface area in sheared turbulence

It is well known that in the presence of mean shear, the turbulent rates of mixing and chemical reaction tend to be increased. One reason for this increase is the development of large scale coherent structures that are amplified by the Kelvin-Helmholtz hydrodynamic instability. This pseudo-laminar mechanism has been extensively studied in the last twenty years, including in premixed and nonpremixed combustion systems. In homogeneous turbulent shear layers, the hydrodynamic instability does not occur, and the enhancement of mixing and chemical reaction results from increased straining and increased turbulent transport due to shear-production of turbulent kinetic energy. This turbulent mechanism has been studied in a number of recent numerical studies in the context of mixing problems (Rogers, Mansour & Reynolds 1989; Holt, Koseff & Ferziger 1992) and nonpremixed chemical reactions (Leonard & Hill 1992; Nomura & Elghobashi 1992). Nomura & Elghobashi assume in their study an infinitely fast reaction, while Leonard & Hill consider a finite-rate reaction both with temperature-independent and temperature-dependent kinetics. Both studies are limited by the constant density assumption. In these studies, the enhancement of chemical reaction due to the mean shear is explained by the increased turbulent strain rates and increased reactant concentration gradients found along the flame surface. Since in the absence of quenching, higher concentration gradients are equivalent to higher reaction rates, it is suggested that one basic effect of mean shear is to increase the mean flame intensity. This effect is related in (3) to modifications of the flamelet speed,  $\langle S_C \rangle_S$ , not to modifications of the flame surface density,  $\Sigma$ .

In premixed flames, however, the departures of  $\langle S_C \rangle_S$  from the laminar consumption rate tend to average out when integrated across the whole turbulent flame, and in many situations the mean combustion intensity is only weakly sensitive to the turbulence. Therefore, the argument that relates the increased combustion efficiency observed in nonpremixed flames with shear to a change in the flame structure is not expected to apply to premixed configurations. In that case, the effect of mean shear must be related to a modification of the total flame surface area. In the following, we use DNS to get basic information on the dynamics of flame surface densities as a function of the mean shear rate,  $S$ . The mean shear rate,  $S$ , is varied in the proportion of 1 to 10, as seen in Table 2. Large values of the shear rate (as in cases 1, 2, and 4) are relevant to a flame propagating in the near-wall region of a turbulent channel flow. Lower values (as in case 6) can be found in flames stabilized in subsonic shear layers.

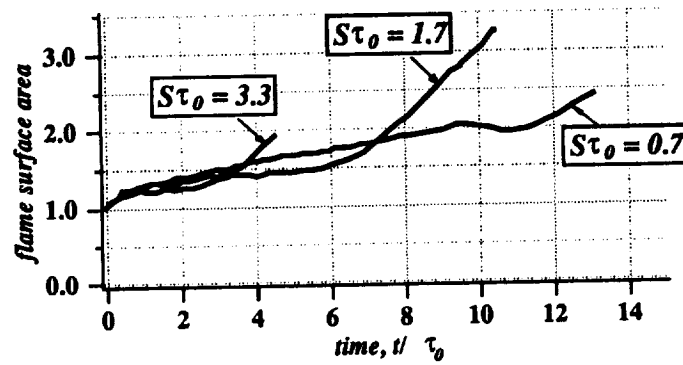


FIGURE 5(A). The effect of the turbulence-to-mean shear time scale ratio,  $St_0$ , on the relative increase of total flame surface area,  $\langle S_V \rangle / L_{x_1} L_{x_3}$ . A comparison between cases 4, 5, and 6. Time is made non-dimensional by the initial, turbulent eddy turn-over time,  $\tau_0$ .

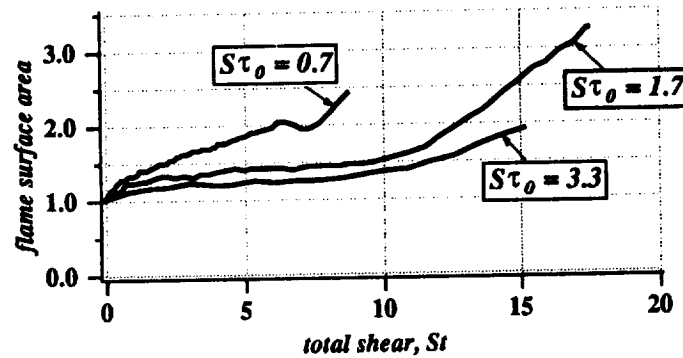


FIGURE 5(B). The effect of the turbulence-to-mean shear time scale ratio,  $St_0$ , on the relative increase of total flame surface area,  $\langle S_V \rangle / L_{x_1} L_{x_3}$ . A comparison between cases 4, 5, and 6. Time is made non-dimensional by the mean shear rate,  $S$ .

### 2.2.1 The total flame surface area

As described in §1.2, six different cases have been simulated that correspond to turbulent flames characterized by the same laminar flame thickness,  $l_F$ , the same laminar flame speed,  $s_L$ , embedded in two different initial turbulent flow fields (in this respect cases 4, 5, and 6 differ from cases 1, 2, and 3), and with different values of the mean shear rate,  $S$ .

The effect of changing the shear rate on the production of flame surface area,  $\langle S_V \rangle$ , is shown in figure 5 for cases 4, 5, and 6. In figure 5(a),  $\langle S_V \rangle$  is plotted versus time, with time made non dimensional by  $\tau_0$ . Cases 4 and 5 feature an initial phase of slow growth followed by a phase of more rapid growth. In case 6, the transition to this second phase is not observed. These two successive phases are



more clearly seen when  $\langle S_V \rangle$  is plotted as a function of total shear,  $St$  (figure 5(b)). For  $0 \leq St \leq 10$ , the production of flame surface area is slow and the differences between all simulated cases remain moderate. In contrast, for  $St > 10$ , the flame surface is rapidly growing at a rate that does not seem to depend on  $S$ . In case 6, the simulation is stopped at  $St \approx 8.5$ , before the transition to the second phase is completed.

One important result in figure 5(b) is that the flame response to the applied shear scales like the turbulent flow field (§2.1) with the total shear,  $St$ .

### 2.2.2 The production and dissipation of flame surface area

Using the diagnostics presented in §1.2, we now turn to the analysis of the source and sink terms of flame surface area as they appear on the right-hand-side of equation (6). These terms can be resolved spatially across the turbulent flame (Trouné 1993; Trouné & Poinso 1993). In the following, they are space-averaged in the cross-stream direction, and we limit our discussion to time variations of global flame properties. We estimate the global value of any quantity  $Q$  using the following  $\Sigma$ -weighted space-averaging scheme:

$$\hat{Q}(t) \equiv \left( \int \langle Q \rangle_S(x_2, t) \Sigma(x_2, t) dx_2 \right) / \left( \int \Sigma(x_2, t) dx_2 \right). \quad (17)$$

Using (17), we define the total production of flame surface by hydrodynamic staining,  $\hat{P}$ , the total dissipation by flame propagation effects,  $\hat{D}$ , and the resulting net total flame stretch,  $\hat{\kappa}$  as follows:

$$\hat{P}(t) \equiv \widehat{A_T} + \widehat{a_T}, \quad (18)$$

$$\hat{D}(t) \equiv 2\widehat{wk_m}, \quad (19)$$

$$\hat{\kappa}(t) \equiv \hat{P} + \hat{D}. \quad (20)$$

Also, the total flame surface area,  $\langle S_V \rangle$ , is equal to the volume-integral of the flame surface density:

$$\frac{\langle S_V \rangle(t)}{L_{x_1} L_{x_3}} = \int \Sigma(x_2, t) dx_2, \quad (21)$$

and, using (4),  $\hat{\kappa}$  can be directly related to the instantaneous rate of change of the total flame surface area in the computational domain:

$$\hat{\kappa}(t) = \frac{d\langle S_V \rangle}{dt} / \langle S_V \rangle. \quad (22)$$

Figure 6 shows  $\hat{P}$ ,  $\hat{D}$ , and  $\hat{\kappa}$  as a function of total shear for cases 4, 5, and 6. It is seen that while the simulated cases exhibit large differences in the time history of the production term,  $\hat{P}$ , these differences tend to be balanced by corresponding variations in the dissipation term,  $\hat{D}$ , and the net total flame stretch,  $\hat{\kappa}$ , follows approximately the same time evolution for all cases. In other words, the total

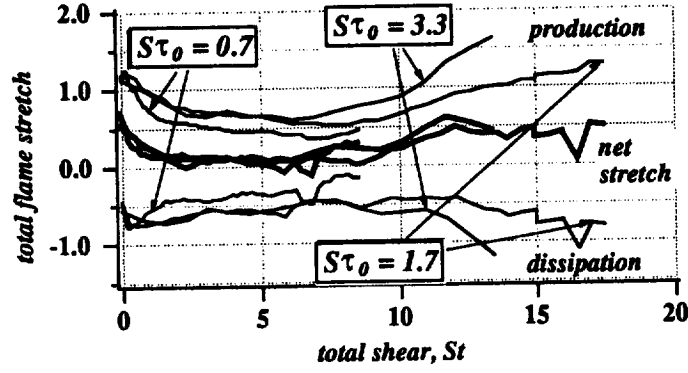


FIGURE 6. Time evolution of flame surface production,  $\hat{P}$ , flame surface dissipation,  $\hat{D}$ , and total flame stretch,  $\hat{\kappa}$ . A comparison between cases 4, 5, and 6.  $\hat{P}$ ,  $\hat{D}$ ,  $\hat{\kappa}$  are made non-dimensional by the laminar flame time,  $(\lambda_{th}/\rho c_p)u/s_L^2$ .

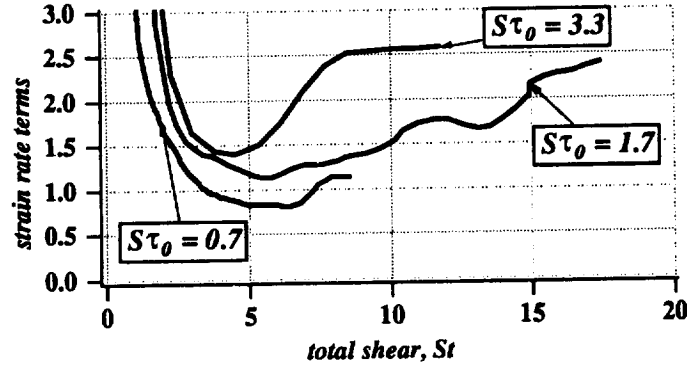


FIGURE 7.  $\hat{a}_T/\hat{A}_T$  vs  $St$ . Relative weights of  $\hat{a}_T$  and  $\hat{A}_T$  in their contributions to flame surface production,  $\hat{P}$ . A comparison between cases 4, 5, and 6.

flame stretch scales with the total shear,  $St$ , but does not depend on the parameter  $S\tau_0$ . It is worth emphasizing that this result is somewhat unexpected given the large impact of  $S\tau_0$  on the turbulence dynamics as described in §2.1. One quantity, however, that remains approximately the same from one simulation to the other is the cross-stream turbulent rms velocity, as measured by  $k_2$ . It is believed that the insensitivity of the total flame stretch to changes in  $S\tau_0$  is a strong indication that  $\hat{\kappa}$  scales with  $k_2$  rather than  $k$ .

Furthermore, since  $\hat{\kappa}$  appears to be a function of  $St$  and not of  $S\tau_0$ , (22) can be re-written as:

$$\langle S_V \rangle(St) = \langle S_V \rangle(t=0) \exp \left( \frac{1}{S} \int_0^{St} \hat{\kappa}(T) dT \right). \quad (23)$$

(23) shows that at constant total shear,  $St = \text{constant}$ , the flame surface area is a

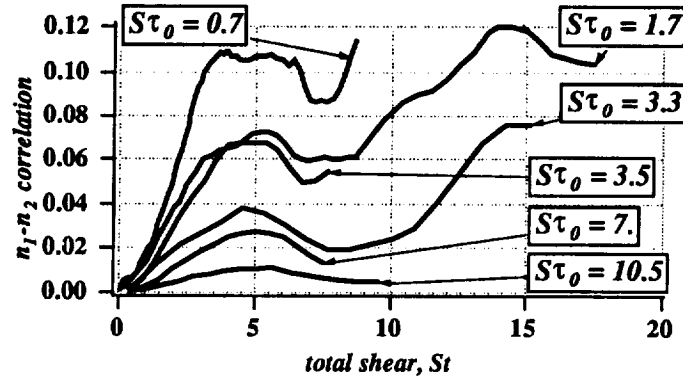


FIGURE 8(A). The effect of  $S$  on the magnitude of  $-\widehat{n_1 n_2}$ . A comparison between cases 1 to 6.

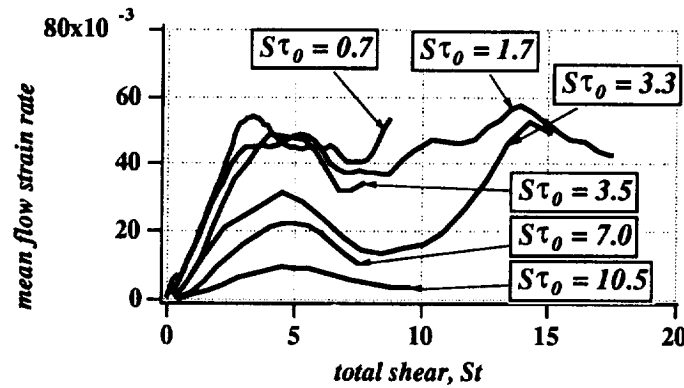


FIGURE 8(B). The effect of  $S$  on the magnitude of  $\widehat{A_{T_{12}}}$ . A comparison between cases 1 to 6.  $\widehat{A_{T_{12}}}$  is made non-dimensional by the mean shear rate  $S$ .

decreasing function of  $S$ , as was found in figure 5(b).

As seen in (18), the mean tangential strain rate at the flame can be decomposed into two components:  $\widehat{A_T}$  represents the contribution of the mean rate of deformation; and  $\widehat{a_T}$  represents the effects of the turbulent flow velocity gradients. Figure 7 presents the ratio  $\widehat{a_T}/\widehat{A_T}$  versus non-dimensional time for cases 4, 5, and 6. At  $t = 0$ , the flame is plane and there is no strain rate due to the mean flow field,  $\widehat{A_T} = 0$ . As the flame gets wrinkled, the effect of the mean flow field gets more pronounced and  $\widehat{A_T}$  and  $\widehat{a_T}$  take comparable values. For  $St > 5$ , however, both the absolute value of  $\widehat{a_T}$  and its relative weight in the expression for  $\widehat{P}$  are increasing. These results indicate that a transition to a fully turbulent regime is occurring: for  $St > 5$ , the turbulence levels,  $k_1$ ,  $k_3$ , and also  $k_2$  are all increasing; the hydrodynamic straining at the flame, as measured by  $\widehat{P}$ , takes higher values; in the expression for  $\widehat{P}$ ,  $\widehat{a_T}$  is increasing faster than  $\widehat{A_T}$  and the turbulent flow component of flame production is becoming dominant.

We now take a closer look at the strain rate due to the mean flow field.  $\langle A_T \rangle_S$  is a production term that depends on the mean cross-stream velocity gradient and the flamelets orientation:

$$\langle A_T \rangle_S = (1 - \langle n_2^2 \rangle_S) \frac{\partial \tilde{U}_2}{\partial x_2} - \langle n_1 n_2 \rangle_S \frac{\partial \tilde{U}_1}{\partial x_2}, \quad (24)$$

where  $n_i$  is the  $x_i$ -component of the flame normal vector. The first term in (24) accounts for the flow acceleration through the flame; the second term describes the rapid distortion of the flame surface due to the applied shear. Both terms remain positive across the turbulent flame. Note that since in (24) the velocity gradients are multiplied by quantities that are direct measures of the turbulent flame wrinkling, the magnitude and relative weights of the two components of  $\langle A_T \rangle_S$  are difficult to assess *a priori*. In the simulations, the statistics describing the flamelet's orientation do not vary significantly across the turbulent brush;  $\langle n_2^2 \rangle_S$  and  $\langle n_1 n_2 \rangle_S$  are functions of time but nearly independent of  $x_2$  position. Therefore, space-averaging across the turbulent flame yields the following approximation:

$$\widehat{A_T} \equiv \widehat{A_{T_{22}}} + \widehat{A_{T_{12}}} \approx \alpha \frac{\partial \widehat{\tilde{U}_2}}{\partial x_2} + \beta \frac{\partial \widehat{\tilde{U}_1}}{\partial x_2}, \quad (25)$$

where  $\alpha$  and  $\beta$  are constant coefficients.

Figure 8(a) presents the time variations of  $-\widehat{n_1 n_2}$  which can be considered as an estimate of  $\beta$ . All simulated cases follow the same time evolution when scaled in terms of  $St$ : growth from the initial zero value; saturation at  $St \approx 5$ ; short period of decrease; and rapid growth for  $St > 8$ . The magnitude of  $-\widehat{n_1 n_2}$  is a strong decreasing function of  $S$ . This result may be explained as follows.  $-\widehat{n_1 n_2}$  is determined by two simultaneous effects, a mean deformation effect and a turbulent diffusion effect. Let us consider, for instance, a sinusoidal flame surface of constant amplitude subjected at  $t = 0$  to a simple shearing motion:  $-\widehat{n_1 n_2}$  first increases, saturates at a time that scales with  $St$ , and then decreases as the flame elements are turned away from the direction of maximum positive strain rate (inclined at 45 degrees from the mean flow direction) by the rotation component of the applied shear. In the simulations, this mean deformation effect is coupled with an increase of the turbulent flame thickness due to turbulent diffusion that is constantly counteracting the flattening of the flame due to the mean rotation. The characteristic time scale of the mean deformation effect is  $1/S$ . The characteristic time scale of the turbulent diffusion effect is a turbulent time scale that is likely to scale with  $1/\sqrt{k_2}$ . The largest magnitude for  $-\widehat{n_1 n_2}$  is obtained for cases where the turbulence dominates the mean deformation, that is for small values of  $S$ .

Hence, in (25) the increase of  $\partial \widehat{\tilde{U}_1} / \partial x_2$  with  $S$  is cancelled by a corresponding decrease of the coefficient  $\beta$ . Figure 8(b) illustrates this result and shows that the resulting strain rate is more than one order of magnitude smaller than  $S$ . Also, in all cases,  $\alpha$  is always 5 to 10 times larger than  $\beta$  and both terms in (25) have comparable contributions to  $\widehat{A_T}$ .

### 3. Conclusion

Direct simulations of premixed flames in turbulent shear flow are used in this study to examine the effect of a mean shear motion on the flame surface dynamics. The shear is uniform in the unburnt gas, and simulations are performed for different values of the mean shear rate,  $S$ . A detailed analysis of the rate of change of flame surface densities is performed, based on the exact  $\Sigma$ -equation. In particular, the time evolution of the total flame stretch,  $\hat{\kappa}$ , is compared for different values of  $S$ . In the expression for the total flame stretch, the production term by hydrodynamic straining is decomposed into two components: a component,  $\hat{A}_T$ , that depends explicitly on the mean rate of deformation; and a component,  $\hat{a}_T$ , that is determined by the turbulent flow field.

The data show that while  $\hat{\kappa}$  scales with the total shear,  $St$ , it does not depend on the turbulence-to-mean shear time scale ratio,  $S\tau_0$ . This is a surprising result since the turbulence is strongly influenced by this parameter. This result implies that the principal effect of changing the mean shear rate,  $S$ , is to re-scale the time evolution of flame stretch. For instance, the results show that for  $0 \leq St \leq 10$ , the rate of change of flame surface area is small; in contrast, for  $St > 10$ , a transition to a phase of rapid growth is observed. The main effect of  $S$  is then to make that transition occur faster. Note also that, while flame stretch scales with  $St$ , since the total flame surface area,  $\langle S_V \rangle$ , is related to the time integral of stretch,  $\langle S_V \rangle$  is found to scale both with  $St$  and  $S$ .

The relative insensitivity of  $\hat{\kappa}$  to changes in  $S\tau_0$  was further studied by examining the direct contribution of the applied shear to  $\hat{A}_T$ . This contribution is always small in the simulations. It is shown to scale with the product of the magnitude of the mean velocity gradient and a coefficient that depends on the flame wrinkling. The magnitude of that coefficient is determined by competing effects: a positive turbulent effect and an initially positive and subsequently negative effect controlled by the mean rotation component of the applied shear. It is argued that this coefficient scales with the inverse of a characteristic turbulent time divided by  $S$  so that at high shear rates, the increased mean velocity gradient is multiplied by a decreased coefficient and there is no net variation of  $\hat{A}_T$ .

Finally, the question of which term in the  $\Sigma$ -equation is responsible for the transition to rapid growth of flame surface area, at  $St > 10$ , is studied by comparing  $\hat{a}_T$  and  $\hat{A}_T$ . Results show that  $\hat{a}_T$  is increasingly dominant in the expression for flame stretch; the main effect of the applied shear is to increase the turbulent straining motions, and  $\hat{A}_T$  may be neglected in the models.

### REFERENCES

- ASHURST, W. T., PETERS, N. & SMOOKE, M. D. 1987 Numerical simulation of turbulent flame structure with non-unity Lewis number. *Combust. Sci. Tech.* **53**, 339-375.
- BORGHI, R. 1990 Turbulent premixed combustion: further discussion on the scales of the fluctuations. *Combust. Flame.* **80**, 304-312.

- BRAY, K. N. C. 1990 Studies of the turbulent burning velocity. *Proc. R. Soc. Lond. A* **431**, 315-335.
- CANDEL, S. M. & POINSOT, T. 1990 Flame stretch and the balance equation for the flame surface area. *Combust. Sci. Tech.* **70**, 1-15.
- CANDEL, S. M., VEYNANTE, D., LACAS, F., MAISTRET, E., DARABIHA, N. & POINSOT, T. 1990 Coherent flame model: applications and recent extensions. in *Series on Advances in Mathematics for Applied Sciences*. World Scientific.
- CANT, R. S., POPE, S. B. & BRAY, K. N. C. 1990 Modelling of flamelet surface-to-volume ratio in turbulent premixed combustion. *Twenty-Third Symp. (International) on Combust.* 809-815. The Combustion Institute.
- DARABIHA, N., GIOVANGIGLI, V., TROUVÉ, A., CANDEL, S. M. & ESPOSITO, E. 1987 Coherent flame description of turbulent premixed ducted flames. in *Proc. of the France-USA Joint Workshop on Turbulent Combustion*. Springer Verlag.
- DUCLOS, J. M., POINSOT, T. & VEYNANTE, D. 1993 A comparison of flamelet models for premixed turbulent combustion. *Combust. Flame*. **95**, 101-117.
- HAWORTH, D. C. & POINSOT, T. 1992 Numerical simulations of Lewis number effects in turbulent premixed flames. *J. Fluid Mech.* **244**, 405-436.
- HOLT, S. E., KOSEFF, J. R. & FERZIGER, J. H. 1992 A numerical study of the evolution and structure of homogeneous stably stratified sheared turbulence. *J. Fluid Mech.* **237**, 499-539.
- LEE, M. J., KIM, J. & MOIN, P. 1990 Structure of turbulence at high shear rate. *J. Fluid Mech.* **216**, 561-583.
- LELE, S. K. 1992 Compact finite difference schemes with spectral-like resolution. *J. Comp. Phys.* **103**, 16-42.
- LEONARD, M. J. & HILL, J. C. 1992 Mixing and chemical reaction in sheared and nonsheared homogeneous turbulence. *Fluid Dynamics Res.* **10**, 273-297.
- MAISTRET, E., DARABIHA, N., POINSOT, T., VEYNANTE, D., LACAS, F., CANDEL, S. M. & ESPOSITO, E. 1989 Recent developments in the coherent flamelet description of turbulent combustion. in *Proc. 3rd Int. SIAM Conf. on Numerical Combustion*.
- MANTEL, T. & BORGHI, R. 1991 A new model of premixed wrinkled flame propagation based on a scalar dissipation equation. in *Proc. 13th ICDERS*.
- MARBLE, F. E. & BROADWELL, J. E. 1977 The coherent flame model for turbulent chemical reactions. *Project Squid Technical Report*. TRW-9-PU.
- MAXEY, M. R. 1982 Distortion of turbulence in flows with parallel streamlines. *J. Fluid Mech.* **124**, 261-282.
- MENEVEAU, C. & POINSOT, T. 1991 Stretching and quenching of flamelets in premixed turbulent combustion. *Combust. Flame*. **86**, 311-332.

- NOMURA, K. K. & ELGHOBASHI, S. E. 1992 Mixing characteristics of an inhomogeneous scalar in isotropic and homogeneous sheared turbulence. *Phys. Fluids A*, **4**, 606-625.
- PETERS, N. 1986 Laminar flamelet concepts in turbulent combustion. *Twenty-First Symp. (International) on Combust.* 1231-1250. The Combustion Institute.
- POINSOT, T., VEYNANTE, D. & CANDEL, S. M. 1991 Quenching processes and premixed turbulent combustion diagrams. *J. Fluid Mech.* **228**, 561-605.
- POINSOT, T. & LELE, S.K. 1992 Boundary conditions for direct simulations of compressible viscous flows. *J. Comp. Phys.* **101**, 104-129.
- POPE, S. B. 1988 Evolution of surfaces in turbulence. *International J. Engng. Sci.* **26**, 445-469.
- POPE, S. B. 1990 Computations of turbulent combustion: progress and challenges. *Twenty-Third Symp. (International) on Combust.* 591-612. The Combustion Institute.
- POPE, S. B. & CHENG, W. K. 1988 The stochastic flamelet model of turbulent premixed combustion. *Twenty-Second Symp. (International) on Combust.* 781-789. The Combustion Institute.
- ROGALLO, R. S. 1981 Numerical experiments in homogeneous turbulence. *NASA Technical Memorandum*. 81315.
- ROGERS, M. M. & MOIN, P. 1987 The structure of the vorticity field in homogeneous turbulent flows. *J. Fluid Mech.* **176**, 33-66.
- ROGERS, M. M., MANSOUR, N. N. & REYNOLDS, W. C. 1989 An algebraic model for the turbulent flux of a passive scalar. *J. Fluid Mech.* **203**, 77-101.
- ROHR, J. J., ITSWEIRE, E. C., HELLAND, K. N. & VAN ATTA, C. W. 1988 An investigation of the growth of turbulence in a uniform-mean-shear flow. *J. Fluid Mech.* **187**, 1-33.
- RUTLAND, C. J. & TROUVÉ, A. 1993 Direct simulations of premixed turbulent flames with non-unity Lewis numbers. *Combust. Flame*. **94**, 41-57.
- TAVOULARIS, S. & CORRSIN, S. 1981 Experiments in nearly homogeneous turbulent shear flow with a uniform mean temperature gradient. Part 1. *J. Fluid Mech.* **104**, 311-347.
- TAVOULARIS, S. & KARNIK, U. 1989 Further experiments on the evolution of turbulent stresses and scales in uniformly sheared turbulence. *J. Fluid Mech.* **204**, 457-478.
- TOWNSEND, A. A. 1976 *The structure of turbulent shear flow*. 2nd ed., Cambridge University Press.
- TROUVÉ, A. 1993 The evolution equation for the flame surface density in turbulent premixed combustion. in *CTR Annual Research Briefs - 1992*, Center for Turbulence Research, Stanford Univ./NASA-Ames.

- TROUVÉ, A. & POINSOT, T. 1993 The evolution equation for the flame surface density in turbulent premixed combustion. *J. Fluid Mech.* (submitted for publication).
- WILLIAMS, F. A. 1985 *Combustion theory*. 2nd ed., Benjamin Cummings.
- WRAY, A. A. 1990 Minimal storage time-advancement schemes for spectral methods. *J. Comp. Phys.* (submitted for publication).



## On streak spacing in wall-bounded turbulent flows

By J. M. Hamilton and J. Kim

### 1. Motivation and objectives

In the 1992 CTR Annual Research Briefs, Hamilton, Kim & Waleffe (1993a) presented the results of a study of the regeneration mechanisms of near-wall turbulence structures. One of the primary motivations of this study was the observation that the low- and high-speed streaks in the near-wall region have a characteristic spanwise "wavelength" of about  $100 \nu/u_\tau$  ( $u_\tau = \sqrt{\tau_w/\rho}$  is the friction velocity and  $\tau_w$  is the shear stress at the wall). This value of 100 wall units has been reported by numerous investigators in a wide range of flows, but many attempts to develop a theory of streak spacing have been unsuccessful.

Waleffe, Kim & Hamilton (1993) examined direct resonance (Jang, Benney & Gran, 1986) and selective amplification, two of the linear mechanisms that have been proposed to explain the characteristic streak spacing, and found that these theories fail in several respects. Jiménez and Moin (1991) addressed the issue of streak spacing with a series of direct numerical simulations of a plane Poiseuille flow at moderate Reynolds number, but of very limited streamwise and spanwise extent. They found that turbulence was not sustained in computational domains narrower than about  $100 \nu/u_\tau$ . In light of this result and the failings of linear theory, Waleffe *et al.* conjectured that the streak spacing depends on the *entire* process of regeneration of near-wall structures.

The present study is a continuation of the examination by Hamilton *et al.* (1993a) of the regeneration mechanisms of near-wall turbulence and an attempt to investigate the conjecture of Waleffe *et al.* The basis of this study is an extension of the "minimal channel" approach of Jiménez and Moin that emphasizes the near-wall region and reduces the complexity of the turbulent flow by considering a plane Couette flow of near minimum Reynolds number and streamwise and spanwise extent. Reduction of the flow Reynolds number to the minimum value which will allow turbulence to be sustained has the effect of reducing the ratio of the largest scales to the smallest scales or, equivalently, of causing the near-wall region to fill more of the area between the channel walls. A plane Couette flow was chosen for study since this type of flow has a mean shear of a single sign, and at low Reynolds numbers, the two wall regions are found to share a single set of structures.

Hamilton *et al.* (1993a,b) found that the near-wall structures are regenerated quasi-cyclically and that this regeneration process can be broken down into three stages: streak formation, through a simple process of advection by streamwise vortices; streak breakdown as a result of an instability mechanism; and vortex regeneration, the result of nonlinear interactions among the modes produced by streak breakdown. This last step is necessary to complete the cycle since the streamwise vortices would otherwise decay through viscous diffusion.

To examine the conjecture by Waleffe *et al.* (1993) that it is the entire regeneration process that determines the spanwise spacing of streaks, the methods developed to study the regeneration cycle can be applied to flows in which the spanwise dimension of the computational domain has been reduced below the value required to sustain turbulence. The results of this approach are discussed in the remainder of this report.

## 2. Accomplishments

### 2.1 Numerical method and flow geometry

The direct numerical simulation results presented here were obtained using the pseudo-spectral channel flow code of Kim, Moin & Moser (1987) modified to simulate plane Couette flow and using a third-order Runge-Kutta time advancement for the convective terms rather than the original Adams-Bashforth. Dealiased Fourier expansions are used in the streamwise ( $x$ ) and spanwise ( $z$ ) directions, and Chebyshev polynomials are used in the wall-normal ( $y$ ) direction. Boundary conditions are periodic in  $x$  and  $z$ , and the no-slip condition is imposed at the walls. The mean streamwise pressure gradient is zero, and the flow is driven by the motion of the walls. The flow velocities in the  $x$ ,  $y$ , and  $z$  directions are  $u$ ,  $v$ , and  $w$ , respectively. The Fourier transforms of the velocities are “hatted” and are functions of the streamwise wavenumber,  $k_x$ , the spanwise wavenumber,  $k_z$ , and the untransformed  $y$ -coordinate, *e.g.*  $\hat{u}(k_x, y, k_z)$ . The fundamental streamwise and spanwise wavenumbers are  $\alpha \equiv 2\pi/L_x$  and  $\beta \equiv 2\pi/L_z$ . Quantities are nondimensionalized by outer variables: half the wall separation,  $h$ , and the wall velocity,  $U_w$ . In some cases, a plus superscript is used to denote quantities nondimensionalized by wall variables: kinematic viscosity,  $\nu$ , and friction velocity,  $u_\tau = \sqrt{\tau_w/\rho}$ . The flow Reynolds number is based on outer variables:  $Re = U_w h/\nu$ . The computational grid is  $16 \times 33 \times 16$  in  $x$ ,  $y$ , and  $z$ . The resolution in wall units for all cases presented here is better than  $\Delta x^+ = 13.1$ ,  $\Delta z^+ = 9.0$ , and  $\Delta y^+ = .19$  near the wall, and 3.8 at the center of the channel.

### 2.2 Dynamics of regeneration cycle

Since periodic solutions are obtained in these simulations, Fourier decomposition is a natural tool with which to examine the details of the flow. The size of the computational domain is such that the low- and high-speed streaks extend the full length of the flow in the streamwise ( $x$ -) direction, and a single pair of streaks fill the domain in the spanwise ( $z$ -) direction. In Fourier space, this means that the dominant mode for the streaks is the ( $k_x = 0, k_z = \beta$ ) (or  $k_z = -\beta$ ) mode. The modal RMS velocity (the square root of the “kinetic energy”) is given by

$$M(m\alpha, n\beta) \equiv \left\{ \int_{-1}^1 [\hat{u}^2(m\alpha, y, n\beta) + \hat{v}^2(m\alpha, y, n\beta) + \hat{w}^2(m\alpha, y, n\beta)] dy \right\}^{\frac{1}{2}}, \quad (1)$$

and  $M(0, \beta)$  is a useful quantity for studying the time evolution of the streaks.

For the first flow considered here,  $L_x = 1.75\pi$ ,  $L_z = 1.2\pi$  ( $L_z^+ = 116.9$ – $143.6$ ), and  $Re=400$ . The upper curve in Figure 1 is a plot of  $M(0, \beta)$  for this flow. The

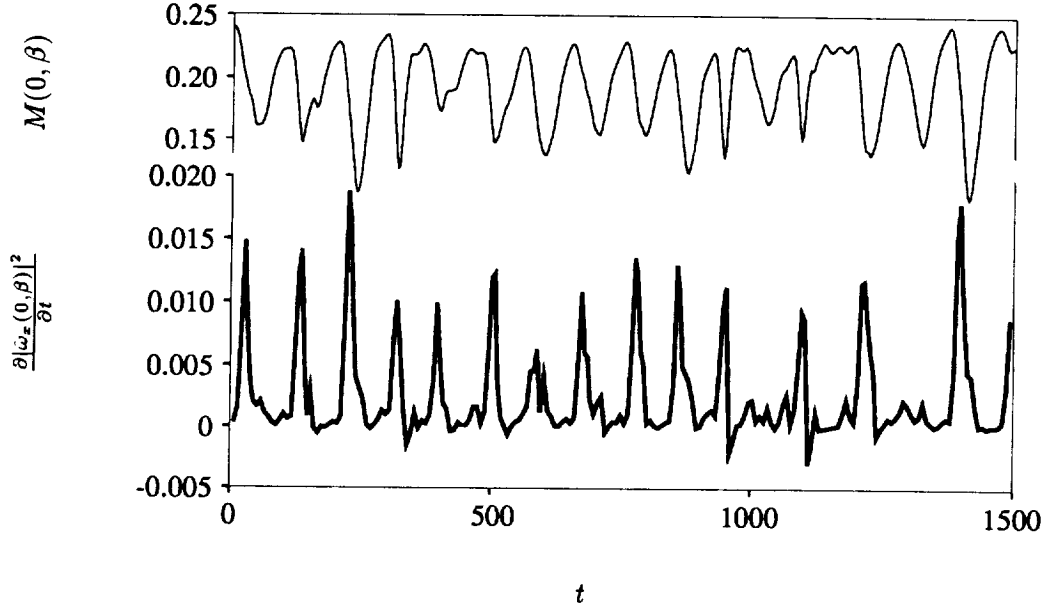


FIGURE 1. Regeneration process over many cycles. —,  $M(0, \beta)$ ; —,  $\partial|\hat{\omega}_x(0, y, \beta)|^2/\partial t$ , due to nonlinear terms only, integrated in  $y$ .

quasi-cyclic nature of the turbulence in this domain is evident in this figure, and the maxima in  $M(0, \beta)$  correspond to well-defined, nearly  $x$ -independent streaks, while the minima correspond to “wavy”, poorly-defined,  $x$ -dependent streaks. The cycle can be broken down into two parts: streak formation where  $dM(0, \beta)/dt > 0$ , and streak breakdown, where  $dM(0, \beta)/dt < 0$ .

Streak formation has been found to be the result of a simple process of advection of streamwise momentum by the  $x$ -independent vortices, and streak breakdown is the result of an instability of the streaks (Hamilton *et al.* 1993a,b). It can be shown that the  $x$ -independent vortices responsible for streak formation will decay in the absence of any interactions among the  $x$ -dependent modes; it i.e.  $x$ -independent vortices cannot extract energy directly from the mean flow,  $\hat{u}(0, y, 0)$ . Therefore, some form of vortex regeneration mechanism must function in order for turbulence to be sustained.

This regeneration mechanism is found to be a rather complicated set of non-linear interactions of the  $k_x = \alpha$  modes (Hamilton *et al.* 1993a,b) that produce  $x$ -independent streamwise vorticity,  $\hat{\omega}_x(0, y, n\beta)$ . The time evolution of vortex regeneration is most easily seen by considering the quantity

$$\frac{\partial|\hat{\omega}_x|^2}{\partial t} = \hat{\omega}_x^\dagger \frac{\partial\hat{\omega}_x}{\partial t} + \hat{\omega}_x \frac{\partial\hat{\omega}_x^\dagger}{\partial t} \quad (2)$$

(where the  $^\dagger$  superscript represents the complex conjugate), since this quantity is positive at  $y$ -locations where the existing streamwise vorticity is being augmented

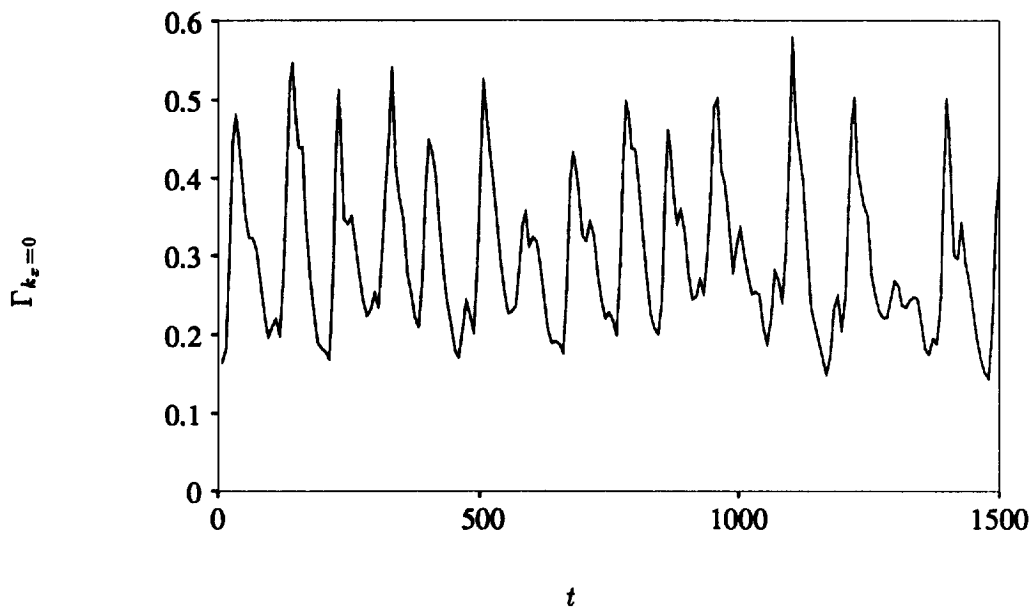


FIGURE 2. Circulation of  $k_x = 0$  modes over many regeneration cycles. Circulation plotted is based on contour that gives the maximum circulation from among all rectangular contours on computational grid points in  $y$ - $z$  plane.

and negative where the vorticity is being reduced. Only the contribution of the nonlinear terms to  $\partial|\hat{\omega}_x|^2/\partial t$  is included; the effects of viscosity are ignored since viscosity acts only to diffuse  $k_x = 0$  mode vorticity.

The lower curve in Figure 1 is a plot of  $\partial|\hat{\omega}_x(0, y, \beta)|^2/\partial t$ , integrated in  $y$ . Vortex regeneration occurs during streak breakdown, with peak amplitudes ranging from about 0.008 to nearly 0.02, except during the cycles at  $t \approx 1000$  and  $t \approx 1300$ . These cycles produce almost no regeneration of the streamwise vortices. One measure of the strength of the streamwise vortices is the circulation of the  $k_x = 0$  modes

$$\Gamma_{k_x=0} \equiv \int (\omega_x)_{k_x=0} dA, \quad (2)$$

and this quantity is plotted in Figure 2. Circulation was calculated for all possible rectangular contours of integration conforming to the computational grid, and the maximum values at each time,  $t$ , are plotted. Experiments by Hamilton & Abernathy (1993) showed that, in a laminar flow, streamwise vortices must have a circulation above some threshold in order to cause transition to turbulence. Analogously, near-wall streamwise vortices in a turbulent flow would be expected to require a threshold value of circulation in order to produce unstable streaks. If this is the case, regeneration of the vortices need not occur every cycle as long as vortex circulation does not decay below the threshold before subsequent cycles.

$\Gamma_{k_x=0}$  typically reaches a maximum value during streak breakdown and decays as the streak forms, reaching a minimum value at about the same time that  $M(0, \beta)$

peaks. Thus, the form of the streaks at the peak in  $M(0, \beta)$  is most closely tied to the minimum value of  $\Gamma_{k_x=0}$  each cycle; the maximum value is relatively unimportant. Hamilton & Abernathy (1993) found that the threshold value of the circulation, using the present nondimensionalization, is about 0.15 in a steady flow. This is consistent with Figure 2 since the minimum circulations never fall much below that value, even during the two cycles which have no regeneration of the vortices.

### 2.3 Spanwise spacing of structures

Some of the dynamics of the regeneration process have been discussed in the previous section, and this section will focus on the question of the spanwise spacing of the streaks. To do this, the width of the computational domain is reduced so that turbulence is not sustained. It can then be established whether a single step in the regeneration process is disrupted by the constraint of the reduced spanwise dimension, or whether, as Waleffe, *et al.* (1993) conjectured, the entire process is affected. Two flows with unsustained turbulence are considered.

The modal decomposition of the first flow is plotted in the upper half of Figure 3. It is not evident in this figure, but  $M(0, \beta)$  decays monotonically after  $t = 1000$ , and the flow eventually becomes laminar. The spanwise dimension of the flow is  $L_z = 1.1\pi$ , or  $L_z^+ = 109.2$  to  $126.1$  (where  $L_z^+$  is based on  $u_\tau$  during the early part of the simulation before the turbulence begins to decay). The streamwise dimension is  $L_x = 1.6\pi$ , and the same Reynolds number, 400, is used. This flow was obtained by first reducing the spanwise dimension of a sustainable turbulent flow, and then reducing the streamwise dimension so as to get a well defined regeneration cycle before the turbulence decays. The simulation begins at  $t = 0$ , but only the last few cycles are shown.

The quasi-cyclic behavior of the streaks in the unsustained turbulent flow of Figure 3 appears similar to that of the sustained flow (Figure 1) until the final peak in  $M(0, \beta)$ . There is no breakdown of the flow after this peak, and without breakdown, the regeneration cycle is broken. It is found that breakdown does not occur because the streaks are too stable; *i.e.* the growth rates of small disturbances are very small or negative near the peak in  $M(0, \beta)$  (cf. Hamilton *et al.* 1993a). In sustained turbulent flow, the streaks are the result of advection of momentum by streamwise vortices. Whatever changes occur in the streaks to increase their stability in the unsustained turbulent flow are likely then to be traceable to changes in the streamwise vortices. The regeneration of the streamwise vortices for the last few cycles of the unsustained turbulent flow is shown by the plot of  $\partial|\bar{\omega}_x(0, \beta)|^2/\partial t$  integrated in  $y$  in the lower half of Figure 3 (heavy solid line). Note that the first two vortex regeneration events in the plot peak during streak breakdown, while the final event does not peak until the new streaks have already begun to form. Thus, even though the peak amplitude of the vortex regeneration process is nearly constant for each of the three regeneration events plotted, the final regeneration occurs late relative to the beginning of streak formation. The circulation of the vortices is plotted in Figure 4, and it can be seen that the streamwise vortices continue to decay during this delay, with the circulation falling to about 0.11 before regeneration begins. This value is lower than any observed during the sustained cycle of Figure 2.

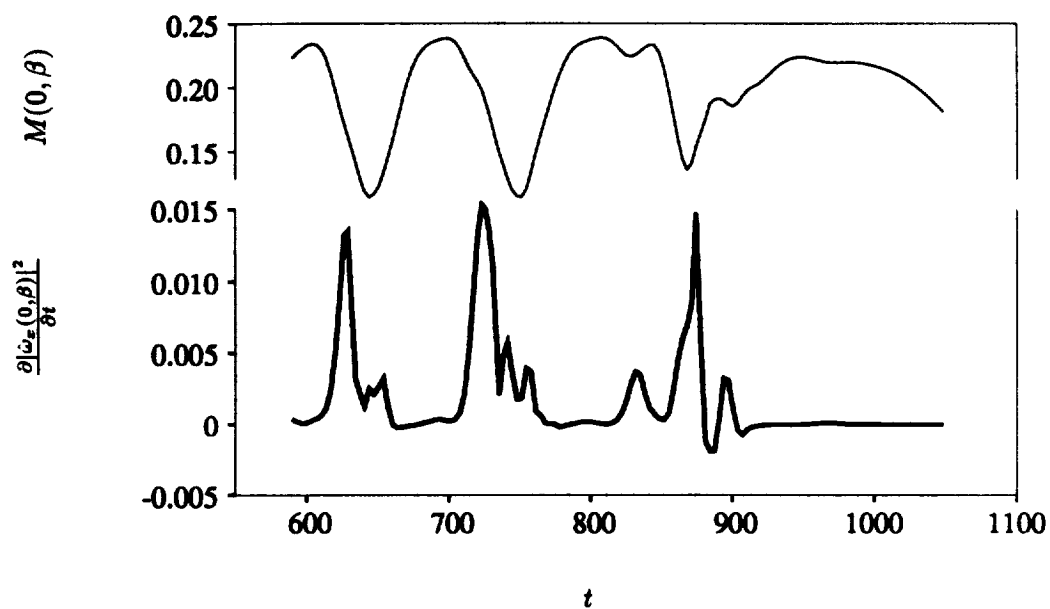


FIGURE 3. Regeneration process over last few cycles of unsustained flow. —,  $M(0, \beta)$ ; —,  $\partial |\hat{\omega}_x(0, y, \beta)|^2 / \partial t$ , due to nonlinear terms only, integrated in  $y$ .

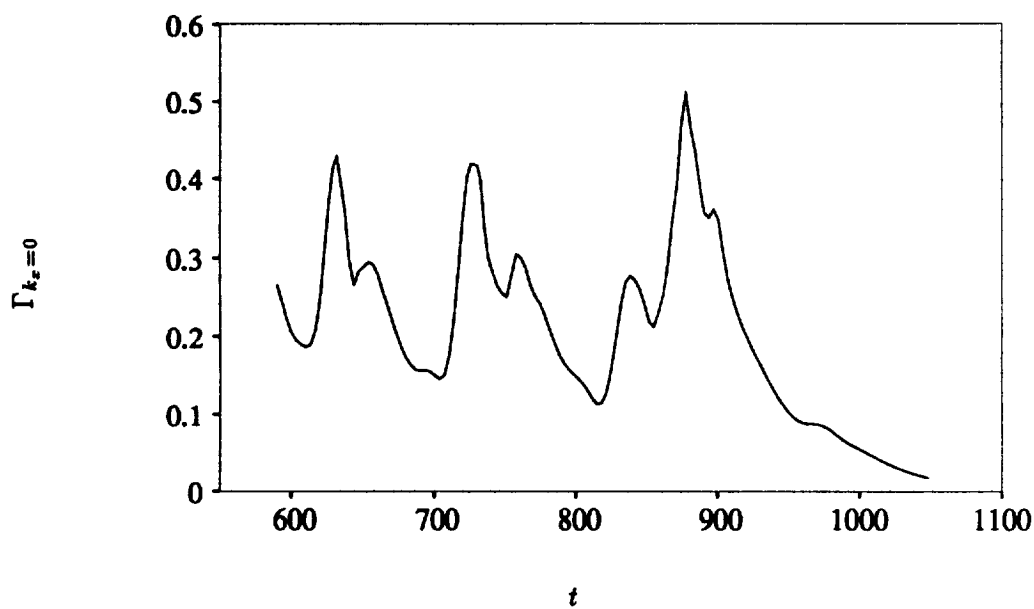


FIGURE 4. Circulation of  $k_x = 0$  modes over last few cycles of flow of Figure 3.

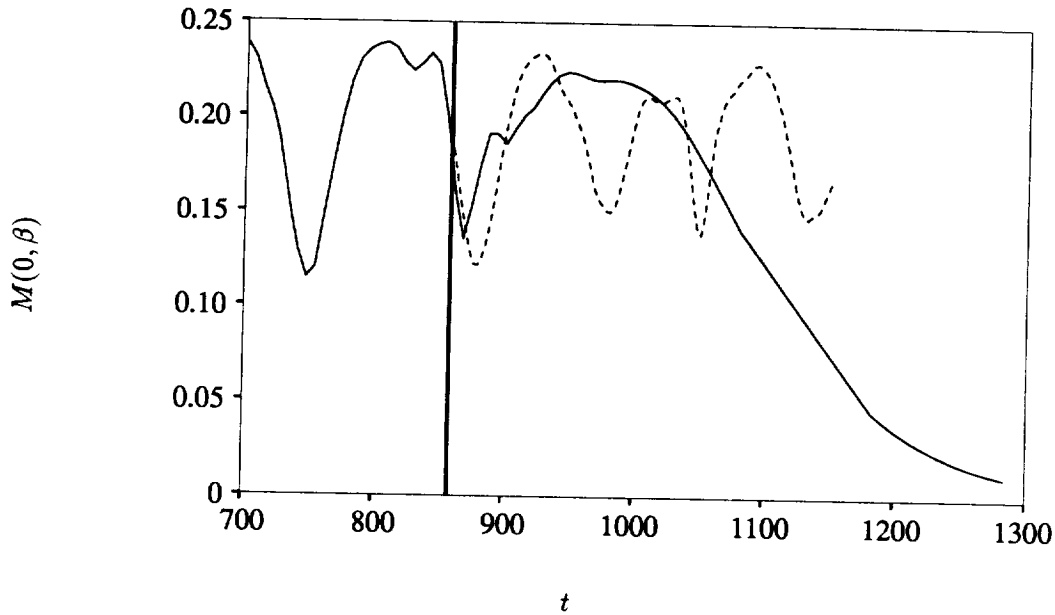


FIGURE 5.  $M(0, \beta)$  for: —, unsustained turbulent flow of Figure 3; ----, same flow with  $\hat{v}, \hat{w}(0, y, n\beta)$  ( $n \neq 0$ ) modes multiplied by 2.0 at  $t = 858.5$  (denoted by heavy vertical line).

After regeneration finally takes place, the circulation drops to about 0.09 at the final maximum in  $M(0, \beta)$ , and there is no subsequent breakdown. To verify that the relative delay in vortex regeneration does indeed cause the turbulence to decay, the strength of the streamwise vortices was artificially boosted at  $t = 858.5$ , a time corresponding to mid-breakdown in the final full regeneration cycle of Figure 3. The result is plotted in Figure 5. The strength of the vortices was increased by multiplying the  $\hat{v}(0, y, n\beta)$  and  $\hat{w}(0, y, n\beta)$  ( $n \neq 0$ ) modes by a factor of 2.0, and all other modes were left unmodified. The effect of increasing the vortex strength is immediate, and the flow returns to the normal regeneration cycle. Note that the turbulence does not subsequently decay; the domain size is such that turbulence is marginally sustainable and can go through a large number of cycles before decaying.

A second case of unsustained turbulence ( $L_z^+ = 97.0-86.5$ ) is presented in Figure 6. The solid line in the upper half of the plot is  $M(0, \beta)$ , and the associated vortex regeneration,  $\partial|\hat{\omega}_x(0, \beta)|/\partial t$ , is shown in the lower half. In this flow, vortex regeneration takes place at about the same point in the cycle as in the sustained cases, and the circulation, plotted in Figure 7, is increased appropriately. Thus, there is no delay in regeneration as in the previous flow. Indeed, the opposite is true, and vortex regeneration takes place too early; at the time of the final peak in  $M(0, \beta)$  in Figure 6,  $\Gamma_{k_x=0}$  has dropped to about 0.1. To verify this assertion,  $\Gamma_{k_x=0}$  was increased by a factor of 1.5 at  $t = 130.0$  (the peak in circulation in Figure 7), and  $M(0, \beta)$  of the resulting flow is plotted as a dashed line in Figure 6.

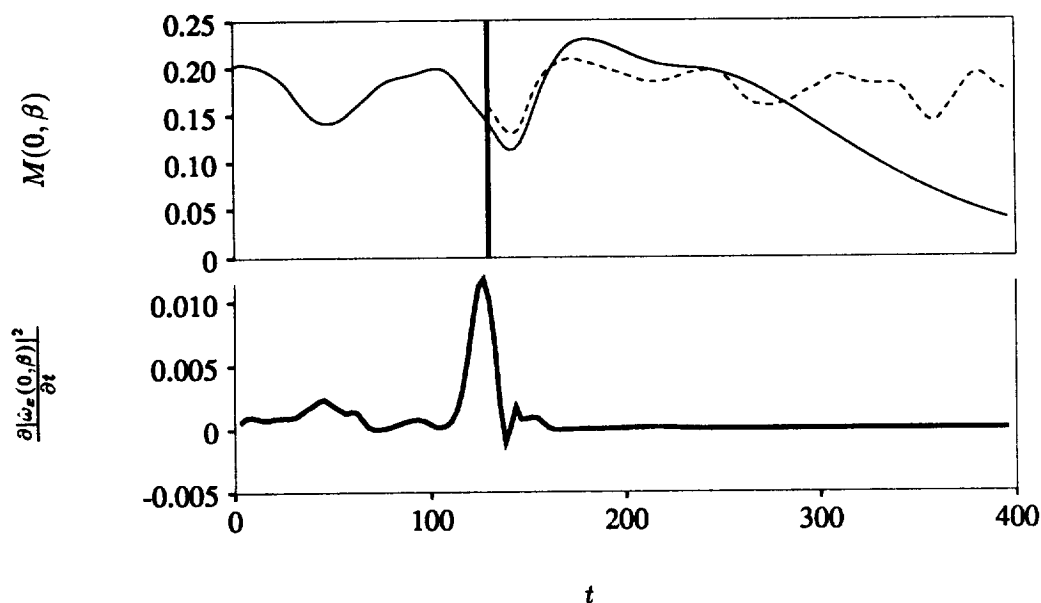


FIGURE 6. Regeneration process of unsustained flow, and modified flow. —,  $M(0, \beta)$ ; ---, same flow with  $\hat{v}$ ,  $\hat{w}(0, y, n\beta)$  ( $n \neq 0$ ) modes multiplied by 1.5 at  $t = 130.0$  (denoted by heavy vertical line); —,  $\partial |\hat{\omega}_x(0, y, \beta)|^2 / \partial t$ , due to nonlinear terms only, integrated in  $y$  for unmodified flow.

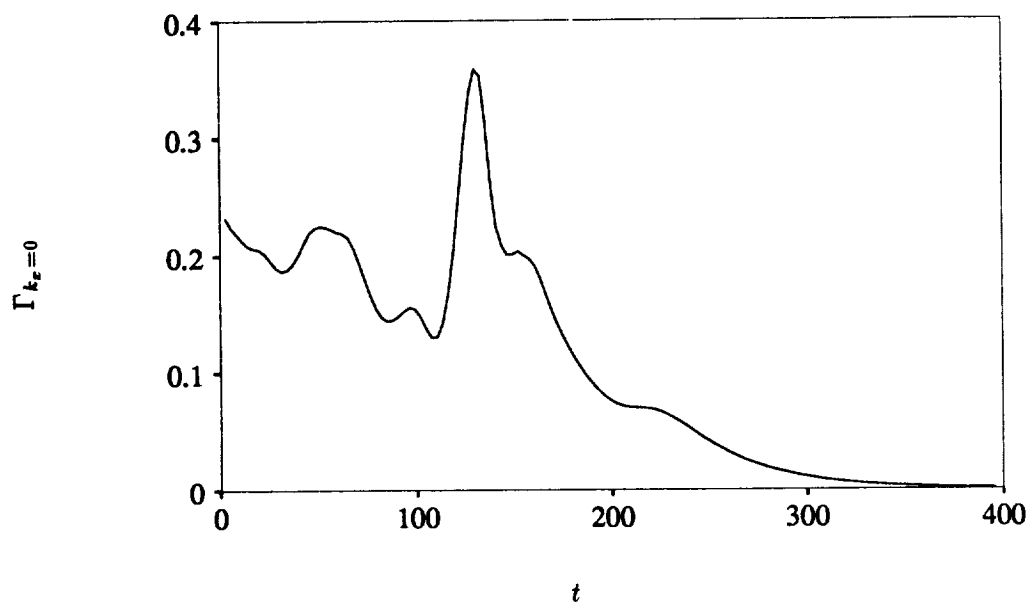


FIGURE 7. Circulation of  $k_x = 0$  modes of unsustained (unmodified) turbulent flow of Figure 6.



The increase in circulation produces unstable streaks followed by breakdown and a return to a (rather chaotic) regeneration cycle. Since streak formation takes place during the decay of the vortex, the increase in circulation at the peak in  $\Gamma_{k_z=0}$  increases circulation by a like amount at subsequent times and simulates a delay in regeneration. There are several ways to think about the effects of reducing the computational domain size below that required for sustained turbulence, but these results suggest that the most useful may be to think of the small domain as causing the flow to develop a very critical dependence on the timing of each process in the regeneration cycle. As the domain becomes smaller, the flow becomes unable to accommodate the variations in the intervals between events that naturally accompany turbulent flow. In the two cases of unsustained turbulence presented here, the regeneration of streamwise vortices occurred with full vigor, but at the wrong times. Turbulence can be sustained only when streak formation, streak breakdown, and vortex regeneration occur at the appropriate intervals.

The results of this section support the conjecture by Waleffe *et al.* (1993) that the minimum spanwise wavelength is set by the entire regeneration process, rather than any individual element of regeneration. When the computational domain is too narrow, turbulence decays because breakdown does not occur. Breakdown, in turn, depends on the creation of unstable streaks by sufficiently strong streamwise vortices. The strength of the streamwise vortices depends on vortex regeneration, and this, of course, returns us to the starting point, since regeneration depends on streak breakdown during the previous cycle.

#### REFERENCES

- HAMILTON, J. M. & ABERNATHY, F. H. 1993 Streamwise vortices and transition to turbulence. Accepted for publication in *J. Fluid Mech.*
- HAMILTON, J. M., KIM, J. & WALEFFE, F. 1993a Regeneration of near-wall turbulence structures. *Annual Research Briefs-1992*, Center for Turbulence Research, Stanford Univ./NASA Ames.
- HAMILTON, J. M., KIM, J. & WALEFFE, F. 1993b Regeneration of near-wall turbulence structures. *Proceedings of the Ninth Symposium on Turbulent Shear Flows*, Kyoto, Japan, Aug. 16-18.
- JANG, P. S., BENNEY, D. J., & GRAN, R. L. 1986 On the origin of streamwise vortices in a turbulent boundary layer. *J. Fluid Mech.* **169**, 109-123.
- JIMÉNEZ, J. & MOIN, P. 1991 The minimum flow unit in near-wall turbulence. *J. Fluid Mech.* **225**, 213-240.
- KIM, J., MOIN, P. & MOSER, R. 1987 Turbulence statistics in fully developed channel flow at low Reynolds number. *J. Fluid Mech.* **177**, 133-166.
- WALEFFE, F., KIM, J. & HAMILTON, J. M. 1993 On the origin of streaks in turbulent boundary layers. *Turbulent Shear Flows 8*, F. Durst, R. Friedrich, B. E. Launder, F. W. Schmidt, U. Schumann, J. H. Whitelaw (eds.), Springer-Verlag, Berlin.



201002 259

N94-24160

## Numerical simulation of non-Newtonian free shear flows

By G. M. Homsy<sup>1</sup> AND J. Azaiez<sup>1</sup>

### 1. Motivation and objectives

Free shear flows, like those of mixing layers, are encountered in aerodynamics, in the atmosphere, and in the ocean as well as in many industrial applications such as flow reactors or combustion chambers. It is, therefore, crucial to understand the mechanisms governing the process of transition to turbulence in order to predict and control the evolution of the flow. Delaying transition to turbulence as far downstream as possible allows a gain in energy expenditure while accelerating the transition can be of interest in processes where high mixing is desired. Various methods, including the use of polymer additives, can be effective in controlling fluid flows.

The drag reduction obtained by the addition of small amounts of high polymers has been an active area of research for the last three decades. It is now widely believed that polymer additives can affect the stability of a large variety of flows and that dilute solutions of these polymers have been shown to produce drag reductions of over 80% in internal flows and over 60% in external flows under a wide range of conditions. (Berman 1978, Sellin 1985 and Sellin & Moses 1989)

The major thrust of this work is to study the effects of polymer additives on the stability of the incompressible mixing layer through large scale numerical simulations. In particular, we focus on the two-dimensional flow and examine how the presence of viscoelasticity may affect the typical structures of the flow, namely roll-up and pairing of vortices.

### 2. Accomplishments

#### 2.1 Problem definition

The flow is examined in a reference frame moving with the average velocity. In such frame, the flow is characterized by the upper free-stream velocity  $u_o$  and the momentum thickness of the mixing layer  $\delta$ . We used a vorticity-streamfunction formulation for Cauchy's momentum equation,

$$\rho \frac{D\vec{v}}{Dt} = -\nabla p + \nabla \cdot \tau \quad (1)$$

This equation is closed through evolution equations relating the stress tensor to the shear rate tensor. In all the subsequent analysis, the stress tensor is written as the sum of two terms (Larson (1988) and Bird *et al.* (1987)):

$$\tau = \tau^s + \tau^p = \eta_s \dot{\gamma} + \eta_p \mathbf{a} = \eta [\kappa \dot{\gamma} + (1 - \kappa) \mathbf{a}] \quad (2)$$

<sup>1</sup> Stanford University

The first term corresponds to the contribution of the Newtonian solvent and is proportional to the shear rate tensor with  $\eta_s$  the solvent viscosity. The second term represents the polymeric contribution to the stress, and is proportional to the tensor  $\mathbf{a}$  with  $\eta_p$  the polymeric contribution to the shear viscosity. The parameter  $\kappa = \frac{\eta_s}{\eta_s + \eta_p} = \frac{\eta_s}{\eta}$  may vary between 0 and 1. When  $\kappa = 1$ , the field equations and the constitutive equations can be decoupled, and the problem reduces to that of purely Newtonian flow.

The tensor  $\mathbf{a}$  satisfies the appropriate rheological equation that can be of differential or integral form (Bird 1967). In the present study, we used two rheological models, the Oldroyd-B model and the FENE-P model.

## 2.2 Rheological models

In the Oldroyd-B model, the polymer stress  $\mathbf{a}$  satisfies the upper convected Maxwell equation:

$$\lambda \frac{\delta \mathbf{a}}{\delta t} + \mathbf{a} = \dot{\gamma} \quad (3)$$

where:

$$\frac{\delta \mathbf{a}}{\delta t} = \frac{\partial \mathbf{a}}{\partial t} + \vec{v} \cdot \nabla \mathbf{a} - \nabla \vec{v}^\perp \cdot \mathbf{a} - \mathbf{a} \cdot \nabla \vec{v} \quad (4)$$

is the upper-convected derivative of  $\mathbf{a}$ , and  $\lambda$  is the relaxation time of the polymer. This model gives a reasonably good qualitative description of dilute polymer solutions, but unfortunately, it gives rise to a steady state elongational viscosity that diverges at a finite elongational rate. This unlikely behavior results from the infinite extensibility of the linear Hookean spring used to model the polymer. In order to avoid this problem, a nonlinear spring based on Warner law can be used to describe the finite extensibility of the polymer, leading to the FENE-P model.

This model is best formulated in terms of the tensor  $\mathbf{B} = \frac{H \langle \mathbf{RR} \rangle}{kT}$  where  $\langle \mathbf{RR} \rangle$  is the configuration tensor,  $H$  the spring constant,  $k$  the Boltzmann constant, and  $T$  the absolute temperature. The tensor  $\mathbf{B}$  satisfies the following equation:

$$Z\mathbf{B} + \lambda \frac{\delta \mathbf{B}}{\delta t} = \mathbf{I} \quad (5)$$

In Eq. (5),  $\mathbf{I}$  is the unit tensor and  $Z = (1 - \langle \frac{R^2}{R_o^2} \rangle)^{-1} = (1 - \frac{tr \mathbf{B}}{b})^{-1}$ . The parameter

$b = \frac{H R_o^2}{kT}$ , where  $R_o$  represents the maximal possible extension of the polymer, is a measure of the extensibility of the polymer chain. An equivalent formulation of Eq. (5) in terms of the tensor  $\mathbf{a}$  can be obtained using the transformation:

$$\mathbf{a} = \frac{Z\mathbf{B} - \mathbf{I}}{\lambda} \quad (6)$$

### 2.3 Scaling and parameters

Using  $u_o$  and  $\delta$  as the reference velocity and the reference length, respectively, the flow is characterized by the Reynolds number,  $Re = \frac{\rho \delta u_o}{\eta} = \frac{\delta u_o}{\nu}$ , where  $\nu$  is the kinematic viscosity of the fluid, and the Weissenberg number,  $We = \frac{\lambda u_o}{\delta}$ , is a dimensionless measure of the relaxation time of the polymer. The elasticity number  $E = \frac{We}{Re} = \frac{\lambda \nu}{\delta^2}$  is often used to characterize the elasticity of the fluid. In addition to  $Re$  and  $We$ ,  $\kappa$  and, in the case of the FENE-P model,  $b$  are the other model parameters.

### 2.4 Numerical method

The simulations reported in this study were performed by solving the vorticity equation:

$$\left[ \frac{\partial}{\partial t} - \frac{\kappa}{Re} \nabla^2 \right] \omega = - \left[ u \frac{\partial}{\partial x} + v \frac{\partial}{\partial y} \right] \omega + \frac{(1-\kappa)}{Re} \left[ \left( \frac{\partial^2}{\partial x^2} - \frac{\partial^2}{\partial y^2} \right) a_{12} - \frac{\partial^2}{\partial x \partial y} (a_{22} - a_{11}) \right] \quad (7)$$

coupled with the appropriate stress equations. In the present study, we are interested in the forced, temporally growing mixing layer. The initial flow is composed of the viscously spreading *tanh* vorticity profile and the corresponding base-state polymer stress, seeded with the wave that, according to linear stability analysis (Azaiez & Homsy 1993), has the largest growth rate.

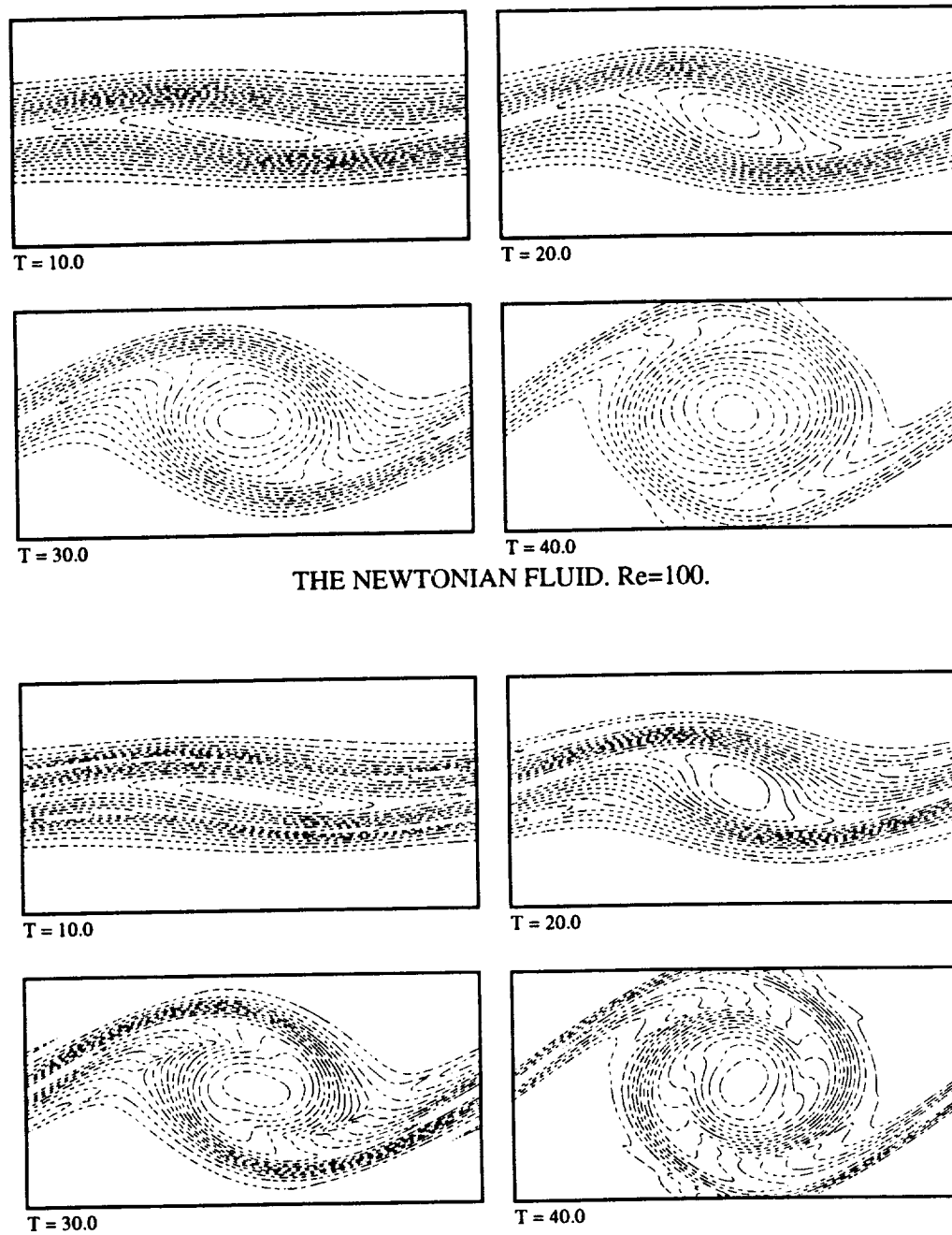
The dynamical equations are solved using a pseudo-spectral method in which the flow variables are expanded in a modified Hartley series (Zimmerman & Homsy (1991)). The resulting set of ordinary differential equations is advanced in time using an operator splitting algorithm (see *e.g.* Tan & Homsy (1987)). In addition to those with the spectral code, a few simulations have been conducted using a finite difference scheme second order accurate in space and in time. A description of the scheme can be found in the paper by Orlandi *et al.* (1992). The results obtained from these two codes were always in total concordance. The codes were validated by comparing with the linear stability results (Azaiez & Homsy (1993)) and by checking that they reproduced the same results as the Newtonian code when we set  $\kappa = 1$ .

A typical run for the roll-up of the non-Newtonian fluid required 128x128 spectral modes and a time step  $\Delta t = 0.04$ . This resolution gives satisfactory results at moderate values of the Weissenberg number and was refined for large values of  $We$ . Throughout this study, the value of the parameter  $\kappa$  is fixed to 0.5.

## 3. Results

### 3.1 The Oldroyd-B model

The vorticity and stress equations for the Oldroyd-B model have been solved numerically for various values of  $We$ , and for  $Re = 100$ . For small values of  $We$  ( $We \sim 1$ ), the flow does not show any noticeable changes from the Newtonian case. Numerical simulations at moderately high  $We$  ( $We \sim 10$ ) developed an instability that

FIGURE 1. Vorticity contours for  $Re=100$ .

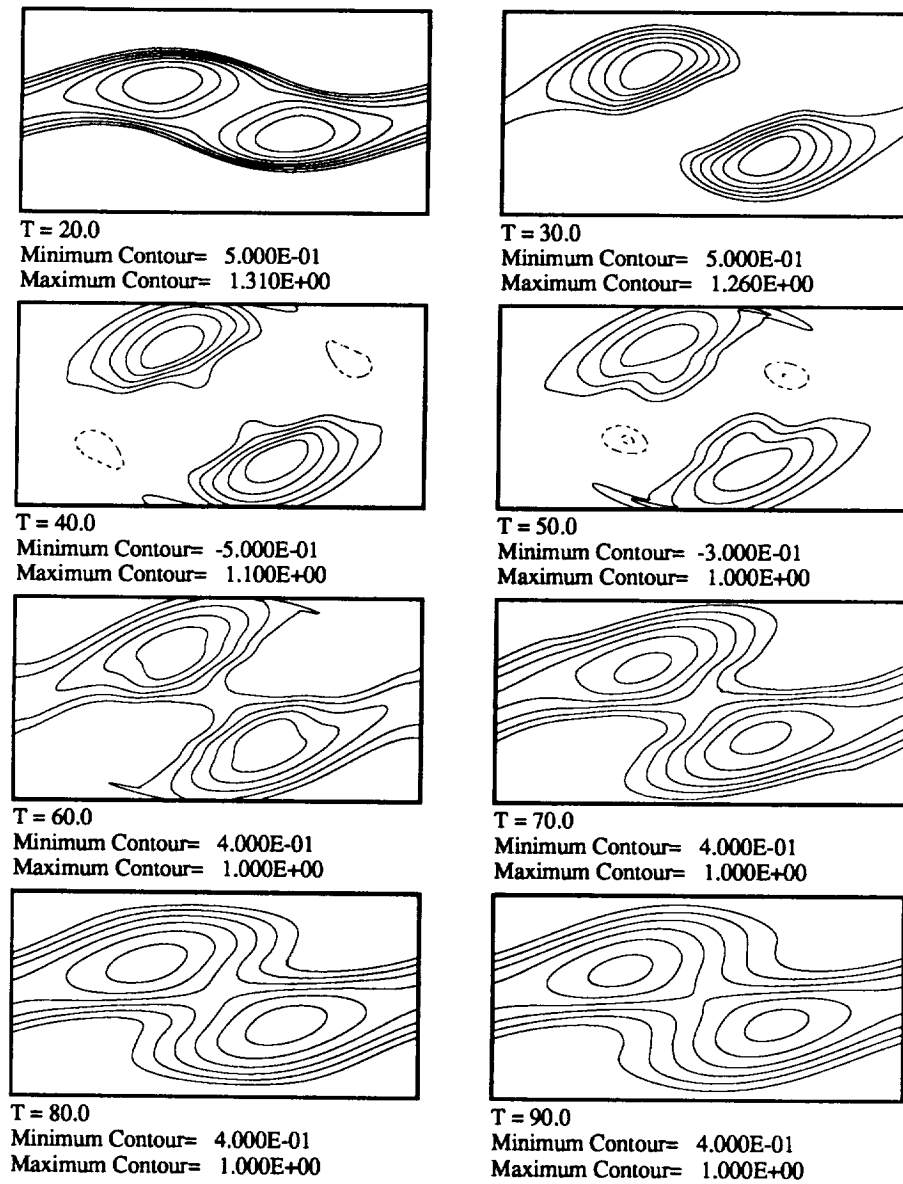


FIGURE 2.  $(B_{11} - B_{22})$  contours for FENE-P model.  $Re=50$ ,  $E=0.5$ , and  $b=5$ .

lead to the divergence of the code. We examined the origin of this instability by looking at the evolution of the different terms in the polymer stress equations. The analysis of these terms showed that the instability is associated with a deficiency of the Oldroyd-B model that allows stresses to grow indefinitely. The instability starts to develop first in the braid regions where the product of the Weissenberg number and the dimensionless local extensional rate exceeds unity. In these regions, and due to high extensional rates, the chain is stretched rapidly, and because of its large relaxation time associated with the high  $We$ , it is prevented from coiling up as quickly as its stretching. As a consequence, the chain gets extended indefinitely and the stresses grow exponentially. The intense build-up of the stresses ultimately leads to the divergence of the numerical code.

### 3.2 The FENE-P model

Unlike the Oldroyd-B model, the FENE-P model does not allow infinite extension of the spring used to model the polymer, and as we have seen, the maximal extension of the spring is characterized by the parameter  $b$ . The viscoelastic mixing layer has been successfully simulated for various values of the three parameters,  $Re$ ,  $E$ , and  $b$ . In what follows, we describe results for the two mechanisms of instability of the two-dimensional mixing layer, namely the roll-up and the pairing of the flow.

#### 3.2.1 Roll-up

We explored values of the Reynolds number between 50 and 400, varied the Weissenberg number between 20 and 200, and examined values of  $b$  between 1 and 20. Figure 1 shows a time sequence of the roll-up of the flow for the Newtonian case and for the FENE-P model. As it has been experimentally documented (Riediger 1988), we observed a trend for smaller values of the minimal (negative) vorticity in the case of the viscoelastic flow, as well as a tendency for the vortex structures to be more compact and to have longer life times than in the Newtonian fluid. The global structure of the flow as well as the roll-up time are basically the same for both fluids. However, the local distribution of the vorticity is affected by the presence of the viscoelasticity in the flow with high gradients tending to appear in some parts of the flow, namely in the braids. The evolution of the absolute value of the minimal vorticity at various streamwise locations confirms the conclusion of the tendency to have *more spanwise vorticity remaining in the braid region*.

The examination of contours of the first normal polymer stress ( $B_{11} - B_{22}$ ) showed that there is a spatial correlation between the regions of intensification of the vorticity gradients and those where there is a build-up of the first normal polymer stress.

In order to understand the reasons why the global structure of the roll-up remains unchanged, we examined the evolution of the polymer stresses in connection with that of the vorticity (Figure 2). This study revealed that the first normal stresses reach a quasi-steady state characterized by the absence of any extensional forces and a balance between shearing forces and the polymer relaxation stresses, and it is interesting to note the spatial relationships between vorticity and normal stresses that characterize this quasi-steady state. After the first stage of roll-up, most of the



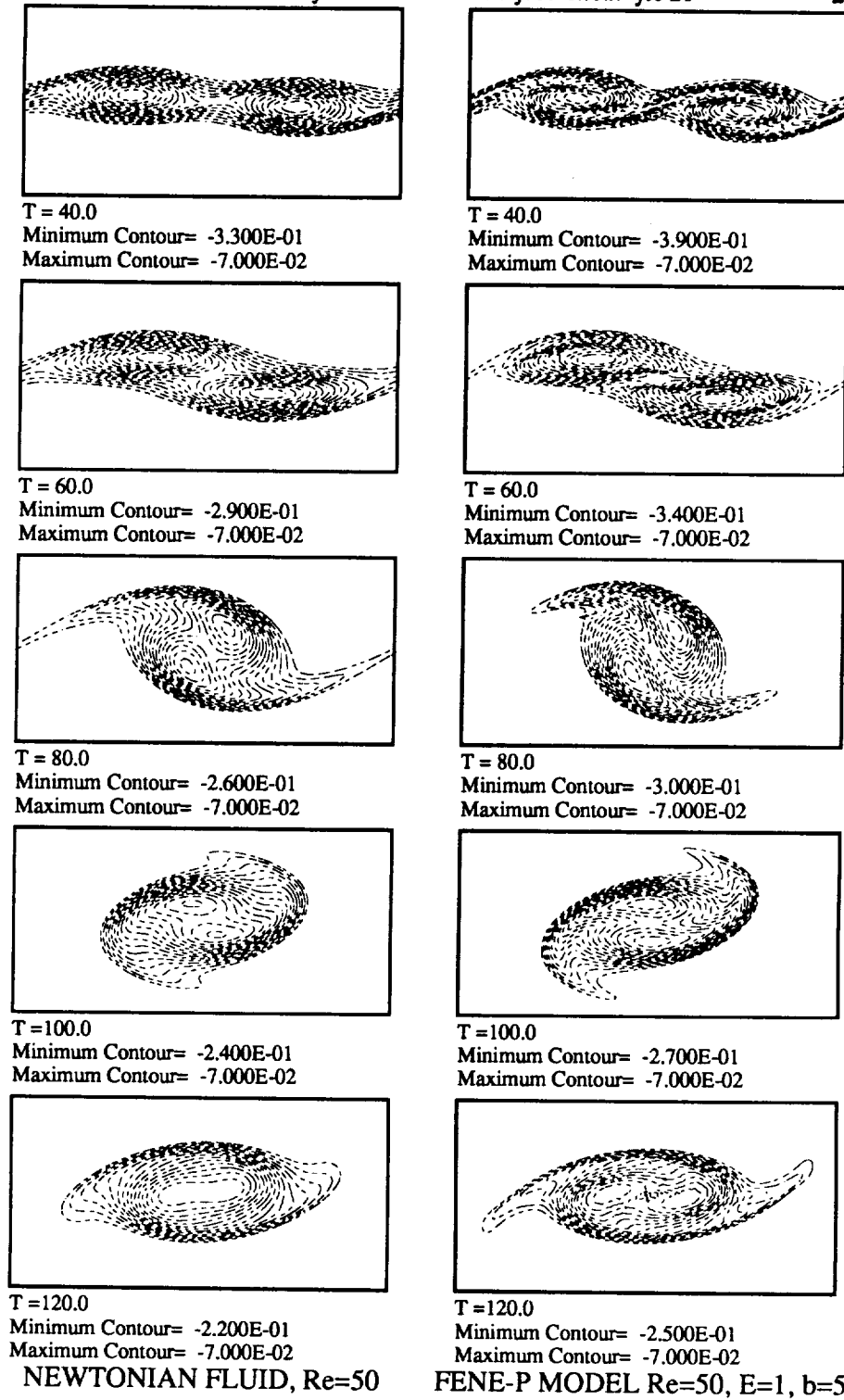


FIGURE 3. Vorticity contours for FENE-P model.  $Re=50$ ,  $E=1$ , and  $b=2$ .

vorticity is entrained into the vortex core with only little remaining in the braids, while the stress fields are highest in regions of highest shear, which tend to lie in nearly irrotational regions surrounding the vortex core. This feature may be key to explaining why the global flow structure is unaffected by viscoelasticity.

Simulations at various values of the parameters  $E$  and  $b$  show that the establishment of the steady state for  $(B_{11} - B_{22})$  is, at least for the range of  $E$  and  $b$  examined, a common trend of the evolution of the polymer stresses in free shear flows and is insensitive to the value of  $E$  or  $b$ . A detailed discussion of this steady state is found in the article by Azaiez & Homsy (1994)

### 3.2.2 Pairing

We examined the pairing of the flow for  $Re = 50$  and various values of  $E$  and  $b$ . In the bulk of the simulations, we used 256 grid points in the streamwise direction and 128 grid points in the transverse direction and a time step  $\Delta t = 0.02$ . Simulations at large  $E$  ( $E \sim 2$ ) required a finer resolution and we used  $256 \times 256$  spectral modes and a time step  $\Delta t = 0.01$ . Figure 3 shows a time sequence of the vorticity contours for the Newtonian fluid with  $Re=50$  and the non-Newtonian fluid with  $Re = 50$ ,  $E = 1$  and  $b = 5$ . In the early stage, the flow shows the same trends for intensification of the vorticity that we have encountered in the case of the single roll-up. Later the two vortices start their orbital motion, with the tendency for a slightly faster rotational motion in the case of the viscoelastic fluid. Note that during roll-up as well as pairing, the vortices are more diffuse in the case of the Newtonian fluid and that the maximal absolute value of the vorticity over the whole flow is larger for the viscoelastic fluid. We attribute the faster rotation of the two parent vortices around each to the vorticity gradients that develop in the braids during the roll-up of the flow. These gradients lead to a stronger outer field between the two parent vortices that enhances the mutually induced rotational motion of the two vortices (Azaiez & Homsy (1994))

## 4. Conclusion

In the present study, we examined the instability of the plane, incompressible, non-Newtonian mixing layer, focusing on simulations with high  $Re$  and  $We$ . Numerical simulations using the Oldroyd-B model developed an instability for moderate  $We$ . We examined the origin of this instability by looking at the evolution of the different terms in the stress equations, which showed that the instability is associated with a deficiency of the Oldroyd-B model that allows stresses to grow indefinitely. The instability starts to develop first in the braid regions where the product of the Weissenberg number and the local extensional rate is larger than one is larger than one. The unbounded growth and intense build-up of the stresses ultimately leads to the divergence of the numerical code. Most of the numerical simulations have been performed with the FENE-P equations which revealed to be the most appropriate model for the simulation of free shear flows at high elasticity. These simulations showed that, for the range of parameters examined, the global structure of the flow as well as the roll-up and pairing times are unchanged from the Newtonian case. However, local vorticity intensifications associated with the build-up

of normal stresses have been observed in the braids as well as in the vortex core. As it has been experimentally documented (Riediger 1988), we observed a trend for smaller values of the minimal (negative) vorticity in the case of the viscoelastic flow as well as the tendency for the vortex structures to be more compact and to have longer life times than in the Newtonian fluid.

The examination of the evolution of the first normal stresses revealed a very interesting steady state characterized by the absence of any extensional forces and a balance between shearing forces and the polymer relaxation stresses.

### Acknowledgements

The authors would like to acknowledge useful discussions with Professor E. J. Hinch from Cambridge University and Professor P. Orlandi from the University di Roma. They also thank Professor E. S. G. Shaqfeh for his helpful comments and suggestions.

### REFERENCES

- AZAIEZ, J., & HOMSY, G. M. 1993 Linear stability of free shear flows of viscoelastic liquids. Submitted to *J. Fluid Mech.*
- AZAIEZ, J., & HOMSY, G. M. 1994 Numerical simulation of non-Newtonian free shear flows at high Reynolds numbers. Submitted to *J. Non-Newtonian Fluid Mech.*
- BERMAN, N. 1978 Drag Reduction by Polymers. *Ann. Rev. Fluid Mech.* **10**, 47-64.
- BIRD, R. B. 1976 Useful non-Newtonian Models. *Ann. Rev. Fluid Mech.* **8**, 13-34.
- BIRD, R. B., CURTISS, C. F., ARMSTRONG, R. C. & HASSAGER, O. 1987 *Dynamics Polymeric Liquids*, vol. 2, 2nd edn. Wiley-Intersciences.
- LARSON, R. G. 1988 *Constitutive Equations for Polymer Melts and Solutions*, Butterworths Series in Chemical Engineering.
- ORLANDI, P., HOMSY G. M., & AZAIEZ, J. 1992 Direct simulation of polymer drag reduction in free shear flows and vortex dipoles. *Proceedings of the 1992 Summer Program*. Center for Turbulence Research, NASA Ames-Stanford University.
- RIEDIGER, S. 1989 *Drag Reduction in Fluid Flows*, Ellis Horwood Limited, 303-310.
- SELLIN, R. H. J. 1985 Industrial Applications for Drag Reducing Polymer Additives: A review *Proceedings of the third International conference on drag reduction*. Bristol.
- SELLIN, R. H. J. & MOSES, R. T. 1989 *Drag Reduction in Fluid Flows*. Ellis Horwood-Publishers.

- TAN, C. T. & HOMSY G. M. 1987 Simulation of nonlinear viscous fingering in miscible displacement. *Phys. Fluids*. **31**, 1330-1338.
- ZIMMERMAN, W. B. & HOMSY, G. M. 1991 Nonlinear viscous fingering in miscible displacement with anisotropic dispersion. *Phys. Fluids A*. **3** 8, 1859-1872.

## Transition to turbulence in an elliptic vortex

By T. S. Lundgren<sup>1</sup> AND N. N. Mansour

### 1. Motivation and objectives

We study the three dimensional instability and nonlinear growth of the two-dimensional flow described by the streamfunction

$$\Psi = \frac{A \sin b_1 x \sin b_2 y}{b_1^2 + b_2^2} \quad (1)$$

where  $b_1 = \pi/L_1$ ,  $b_2 = \pi/L_2$ . This is a swirling flow in a box which is bounded by  $0 \leq x \leq L_1$ ,  $0 \leq y \leq L_2$  and is infinite in the  $z$  direction. This flow is a solution of the Navier-Stokes equation with  $A = \exp(-\nu(b_1^2 + b_2^2)t)$  which slowly decays. We seek a viscous solution which starts near this one and slips along but does not penetrate the bounding walls. The vorticity of the basic flow is  $\omega_z = A \sin b_1 x \sin b_2 y$  which has maximum value  $A$  at the center of the box and drops to zero at the boundaries. We can think of the resulting flow as that of a captive vortex.

Denote  $E = L_1/L_2$ . What is interesting about this flow is that when  $E \neq 1$ , it is unstable to three-dimensional disturbances. Periodic waves grow along the  $z$  direction, causing the captive vortex to distort into a snake-like configuration. Components of vorticity perpendicular to the  $z$  axis grow. As the instability grows, we find that the vorticity becomes increasingly sheet-like. Ultimately, the sheets break up into a turbulent mixture of intense vortex tubes. When  $E = 1$ , the flow is completely stable.

The streamline pattern of the basic flow is elliptical in the central part of the box, with aspect ratio  $E$ , becoming more rectangular as the boundaries are approached. Figure 1 shows the streamline pattern when  $E = 2$ . Bayly (1989) has shown analytically and numerically that the flow is unstable to high wavenumber disturbances when the Reynolds number is large. At high wavenumber, the instability in this bounded geometry is similar to the broad band instability in an unbounded flow with elliptical streamlines and uniform vorticity studied by Pierrehumbert (1986), Bayly (1986), Waleffe (1989, 1990), and Landman and Saffman (1987). The mechanism for the instability is a resonance between inertial oscillations, which can exist when the streamlines are circular, and the periodicity introduced by the ellipticity.

The work which motivated these studies was that of Orszag and Patera (1983). They numerically found a three-dimensional instability on a flow which is a superposition of a Tollmein-Schlichting wave and the Blasius boundary layer flow. This flow contains an elongated elliptically shaped swirling region. It is believed that the

<sup>1</sup> University of Minnesota

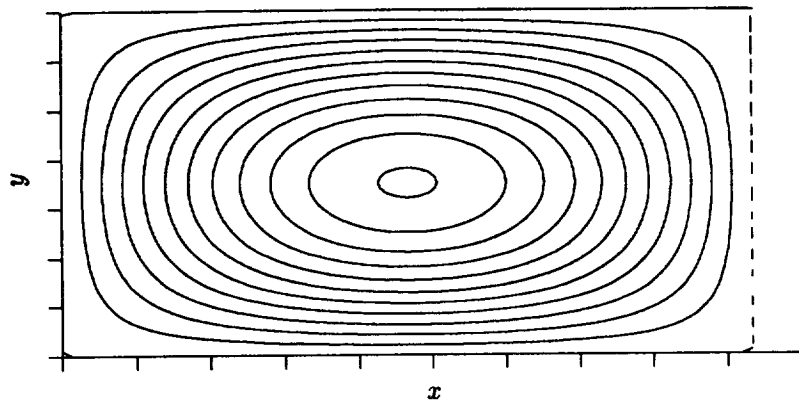


FIGURE 1. Streamline pattern and vorticity contours for  $E = 2$ . The tick marks are at .6 intervals in the  $x$ -direction and .4 intervals in the  $y$ -direction.

wavy instability which develops explains the generation of streamwise vorticity in boundary layer transition.

An even earlier work of Gledzer *et al.* (1974, 1975) showed instability in a swirling flow within an elliptic cylinder. The experiment consisted of rotating a water-filled elliptic cylinder until solid body rotation was achieved. Upon stopping the rotation, the water continues to rotate with approximately elliptical streamlines. It was observed that the flow rapidly developed swirls perpendicular to the rotation axis, with one or more cells depending on the length of the cylinder. Malkus (1989) did clever experiments with a water-filled flexible cylinder which was made elliptical by rotating it between stationary rollers. In this flow, the unstable wave rapidly flashes into small scale turbulence.

There is another class of flows which is closely related to the present work. This is the bending instability of a sharp-edged vortex with uniform vorticity exposed to a transverse straining flow treated by Widnall, Bliss and Tsai (1974), Moore and Saffman (1975), and Robinson and Saffman (1984). In this flow, wavy disturbances, comparable in length to the dimensions of the vortex, grow on the vortex. In the absence of the straining flow, non-rotating planar waves exist. The strain causes such a wave to align with and grow along the plane of maximum strain rate. In our flow, the vorticity distribution rises smoothly to a maximum at the center instead of being sharp-edged, and there are finite boundaries; nevertheless, some of the stability results are very similar.

In the present work, we show numerically that the basic flow described by Eq. (1) is unstable at modest axial wavenumbers when the Reynolds number is greater than a critical value. In section 2, we present stability diagrams which superficially resemble those for two-dimensional parallel flows. In section 3, we present the results of a nonlinear computation which clearly shows transition to turbulent flow.

## 2. Stability

For the stability problem, we set  $A = 1$ , neglecting the slow decay. This is similar

to the traditional method of studying the stability of a growing boundary layer by treating it as a parallel flow. In the usual way, we decompose the velocity field into the velocity field  $\mathbf{U}$  of the basic flow plus a small perturbation  $\mathbf{u}'$ . The linearized equations for  $\mathbf{u}'$  are

$$\nabla \cdot \mathbf{u}' = 0 \quad (2)$$

$$\frac{\partial \mathbf{u}'}{\partial t} + \nabla \cdot (\mathbf{U} \mathbf{u}' + \mathbf{u}' \mathbf{U}) = -\nabla p' + \nu \nabla^2 \mathbf{u}'. \quad (3)$$

We separate variables in the form

$$u' = \exp i k_z z \frac{1}{b_1} \sum_{m,n=-\infty}^{\infty} \tilde{u}(m,n) \exp i(m b_1 x + n b_2 y) \quad (4)$$

$$v' = \exp i k_z z \frac{1}{b_2} \sum_{m,n=-\infty}^{\infty} \tilde{v}(m,n) \exp i(m b_1 x + n b_2 y) \quad (5)$$

$$w' = \exp i k_z z \sum_{m,n=-\infty}^{\infty} \tilde{w}(m,n) \exp i(m b_1 x + n b_2 y) \quad (6)$$

with a similarly defined pressure variable. (Note that we have suppressed the time dependence in  $\tilde{u}, \tilde{v}$  and  $\tilde{w}$ .) Upon equating coefficients of  $\exp i(k_z z + m b_1 x + n b_2 y)$  and using the continuity equation to eliminate the pressure, we get the following equations:

$$\frac{\partial \tilde{u}(m,n)}{\partial t} = \frac{b_1 b_2 R_x(m,n)}{b_1^2 + b_2^2} - \nu(m^2 b_1^2 + n^2 b_2^2 + k_z^2) \tilde{u}(m,n) \quad (7)$$

$$\frac{\partial \tilde{v}(m,n)}{\partial t} = \frac{b_1 b_2 R_y(m,n)}{b_1^2 + b_2^2} - \nu(m^2 b_1^2 + n^2 b_2^2 + k_z^2) \tilde{v}(m,n) \quad (8)$$

where

$$R_x(m,n) = F(m,n) - \frac{m b_1^2 (m F + n G + k_z H)}{m^2 b_1^2 + n^2 b_2^2 + k_z^2} \quad (9)$$

$$R_y(m,n) = G(m,n) - \frac{n b_2^2 (m F + n G + k_z H)}{m^2 b_1^2 + n^2 b_2^2 + k_z^2} \quad (10)$$

and

$$\begin{aligned} F(m,n) = & -\frac{m}{2} [\tilde{u}(m-1, n-1) + \tilde{u}(m-1, n+1) - \tilde{u}(m+1, n-1) - \tilde{u}(m+1, n+1)] \\ & + \frac{n}{4} [\tilde{u}(m-1, n-1) - \tilde{u}(m-1, n+1) + \tilde{u}(m+1, n-1) - \tilde{u}(m+1, n+1)] \\ & - \frac{n}{4} [\tilde{v}(m-1, n-1) + \tilde{v}(m-1, n+1) - \tilde{v}(m+1, n-1) - \tilde{v}(m+1, n+1)] \end{aligned}$$

$$-\frac{k_z}{4} [\tilde{w}(m-1, n-1) + \tilde{w}(m-1, n+1) - \tilde{w}(m+1, n-1) - \tilde{w}(m+1, n+1)] \quad (11)$$

$$\begin{aligned} G(m, n) = & -\frac{m}{4} [\tilde{v}(m-1, n-1) + \tilde{v}(m-1, n+1) - \tilde{v}(m+1, n-1) - \tilde{v}(m+1, n+1)] \\ & + \frac{n}{2} [\tilde{v}(m-1, n-1) - \tilde{v}(m-1, n+1) + \tilde{v}(m+1, n-1) - \tilde{v}(m+1, n+1)] \\ & + \frac{m}{4} [\tilde{u}(m-1, n-1) - \tilde{u}(m-1, n+1) + \tilde{u}(m+1, n-1) - \tilde{u}(m+1, n+1)] \\ & + \frac{k_z}{4} [\tilde{w}(m-1, n-1) - \tilde{w}(m-1, n+1) + \tilde{w}(m+1, n-1) - \tilde{w}(m+1, n+1)] \quad (12) \end{aligned}$$

$$\begin{aligned} H(m, n) = & -\frac{m}{4} [\tilde{w}(m-1, n-1) + \tilde{w}(m-1, n+1) - \tilde{w}(m+1, n-1) - \tilde{w}(m+1, n+1)] \\ & + \frac{n}{4} [\tilde{w}(m-1, n-1) - \tilde{w}(m-1, n+1) + \tilde{w}(m+1, n-1) - \tilde{w}(m+1, n+1)] \quad (13) \end{aligned}$$

and, everywhere,  $\tilde{w}(m, n)$  is given by

$$\tilde{w}(m, n) = -\frac{m \tilde{u}(m, n) + n \tilde{v}(m, n)}{k_z}. \quad (14)$$

Since  $\tilde{w}$  can be eliminated from  $R_x$  and  $R_y$  by means of the last equation, Eqs. (7) and (8) are a system of linear equations for  $\tilde{u}(m, n)$  and  $\tilde{v}(m, n)$  for  $-\infty < m, n < \infty$ .

The conditions that the bounding box be impenetrable requires that  $u'$  be zero for  $x = 0$  and  $L_1$  for all  $y$  and  $z$ , and  $v'$  be zero for  $y = 0$  and  $L_2$  for all  $x$  and  $z$ . A consistent set of symmetry conditions which ensure these constraints are the following, for all integer values of  $m, n$ ,

$$\tilde{u}(-m, n) = -\tilde{u}(m, n) \quad (15)$$

$$\tilde{v}(-m, n) = \tilde{v}(m, n) \quad (16)$$

$$\tilde{w}(-m, n) = \tilde{w}(m, n) \quad (17)$$

$$\tilde{u}(m, -n) = \tilde{u}(m, n) \quad (18)$$

$$\tilde{v}(m, -n) = -\tilde{v}(m, n) \quad (18)$$

$$\tilde{w}(m, -n) = \tilde{w}(m, n). \quad (19)$$

It follows from these that  $\tilde{u}(0, n) = \tilde{v}(m, 0) = 0$  and that  $\tilde{u}(0, 0) = \tilde{v}(0, 0) = 0$ . It can be shown that these conditions persist if they are satisfied by the initial conditions. These conditions mean that Eqs. (7) and (8) only have to be solved on the first quadrant of the  $m, n$  plane, i.e.,  $m = 0, 1, 2, \dots, N$ ,  $n = 0, 1, 2, \dots, N$ ,



where  $N$  is a large integer where we truncate the system. For instance, if we write Eq. (7) with  $m = 0$  and some  $n$ , this would require  $F(0, n)$ , and from Eq. (11) we see that we would need  $\tilde{u}(-1, n - 1)$ . From Eq. (15), this is equal to  $-\tilde{u}(1, n - 1)$ , which is within the solution set. In general, the column  $m = -1$  and the row  $n = -1$  are shifted into the solution set.

From the structure of the equations, one can see that an equation for mode  $(m, n)$  is only coupled to four neighboring modes  $(m - 1, n - 1)$ ,  $(m - 1, n + 1)$ ,  $(m + 1, n - 1)$ , and  $(m + 1, n + 1)$ . These are the nearest four on diagonal lines through  $(m, n)$ , and these four are each coupled to the nearest four on its diagonals, and so on. This means that the modes can be decomposed into two independent "checkerboard" subsets, the "even" modes where  $m + n$  is an even integer and the "odd" modes where  $m + n$  is an odd integer. This was pointed out by Bayly (1989).

In the numerical work, we have taken  $E = 2$  and set the length and time scales by taking the maximum vorticity of the basic flow to be unity ( $A = 1$ ) and  $L_1 = 5.6$ ,  $L_2 = 2.8$ . The Reynolds number is  $\nu^{-1}$  in this dimensionless scheme. One could, of course, rescale the box so that one of the sides has unit length and rescale the Reynolds number and wavenumbers accordingly. The reason for our particular choice was determined by the requirements of the nonlinear code which will be described in the next section.

Equations (7) and (8) were solved by a second order Runge-Kutta method over a range of values of the parameters  $R_e$  and  $k_z$ . Even or odd modes were excited by taking initial conditions in which all the mode amplitudes were zero except  $\tilde{u}(2, 0) = 1$  to generate even modes or  $\tilde{u}(1, 0) = 1$  for odd modes. Energy growth rates  $\beta$  were computed from

$$\beta = \lim_{t \rightarrow \infty} \frac{\ln(\text{energy})}{t} \quad (20)$$

where "energy" is the sum of the squares of all the mode amplitudes. It was necessary to integrate for a long time to approach an asymptote in this formula. Over the range computed, we have found that the cutoff  $N = 40$  was adequate. The results are presented in two figures. Figure 2 shows the neutral curve ( $\beta = 0$ ) for both even and odd modes up to Reynolds numbers of 2000. The band of unstable wavenumbers rapidly expands with increasing Reynolds number. Figure 3 shows the growth rate  $\beta$  versus wavenumber  $k_z$  at Reynolds number 2000. Computations at Reynolds numbers 200, 500, and 1000 are similar, with a pronounced notch in the odd mode curve. The growth rate curves computed by Robinson and Saffman (1984) for the strained vortex have a similar shape made up of the union of separate growth rate curves for modes with differing internal structure, which look like inverted parabolas. The growth rate at their second peak (multiplying their result by 2 to get energy growth rate) is about .3 for  $E = 2$ , which is comparable to our value of about .24.

A result for unstable plane waves in the unbounded flow with elliptical streamlines may be obtained from Landman and Saffman (1987). The result is

$$\frac{\beta}{\omega_0} = 2 \left( \frac{\sigma_0}{\omega_0} - \nu K^2 \right) \quad (21)$$

C-4

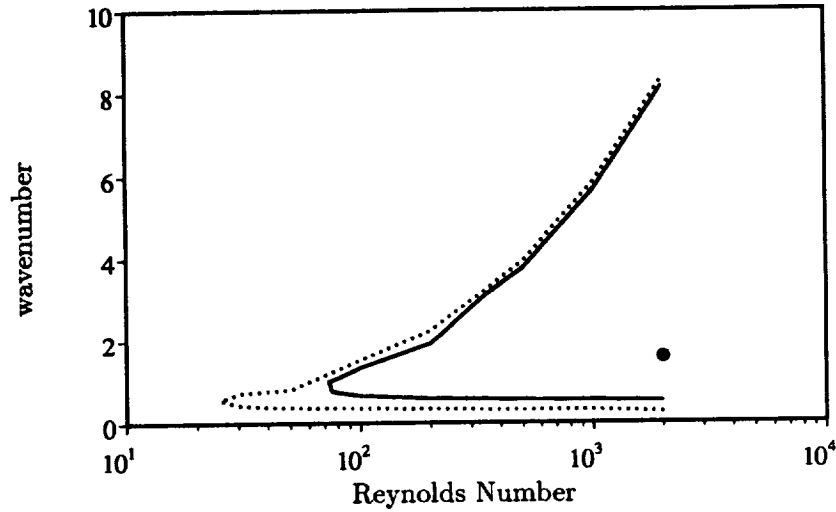


FIGURE 2. Neutral stability curves,  $E = 2$ : — even modes; ..... odd modes. Heavy dot is at  $R_e$  number and lowest wave number used in the computation.

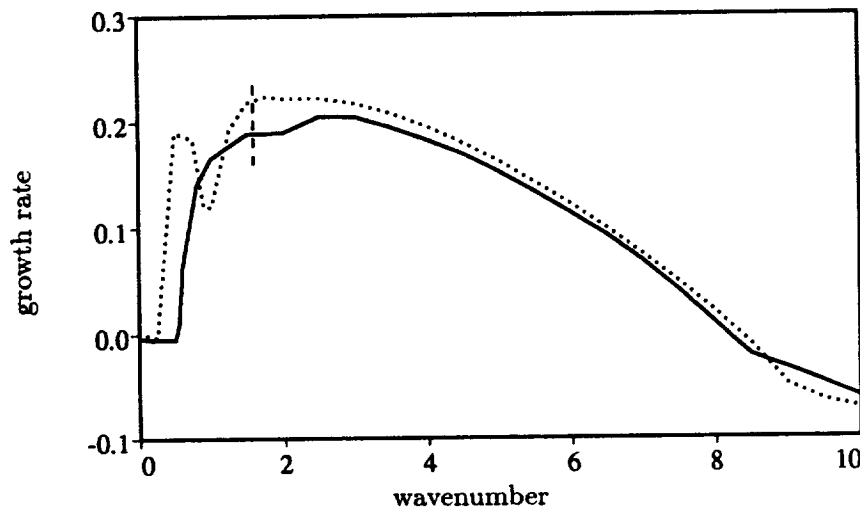


FIGURE 3. Growth rate versus axial wavenumber at  $R_e = 2000$ ,  $E = 2$ : — even modes; ..... odd modes. Vertical dash is at the lowest wave number used in the computation.

where  $\omega_0$  is the uniform vorticity,  $\sigma_0$  is the inviscid amplitude growth rate, and  $K^2 = k_x^2 + k_y^2 + k_z^2$ . The factor two is inserted to convert to energy growth rate. Now  $\sigma_0/\omega_0$  is a function of  $\epsilon/\gamma/[= (E^2 - 1)/(E^2 + 1)]$  where  $\epsilon$  is strain rate and  $\gamma$  is  $\omega_0/2$ . For  $\epsilon/\gamma < .7$  ( $E < 2.4$ ), it is approximately

$$\frac{\sigma_0}{\omega_0} = \frac{1}{2} \left( \frac{9}{16} \left( \frac{\epsilon}{\gamma} \right) - .1 \left( \frac{\epsilon}{\gamma} \right)^2 \right). \quad (22)$$

For an unstable wave with maximum growth rate, the wavevector makes an angle of  $60^\circ$  with the rotation axis; therefore,  $k_x^2 + k_y^2 = 3k_z^2$ . Using this and  $\nu = 1/R_e$  gives

$$\frac{\beta}{\omega_0} = 2\left(\frac{\sigma_0}{\omega_0} - \frac{4k_z^2}{R_e}\right). \quad (23)$$

For our case with  $E = 2$  and  $\omega_0 = 1$ , we get

$$\beta = .3 - \frac{8k_z^2}{R_e}. \quad (24)$$

For fixed  $R_e$ , this gives a curve similar in shape to figure 2 with a maximum of .3 at  $k_z = 0$ . A neutral curve may be derived from Eq. (24), namely

$$k_z = .19R_e^{1/2}. \quad (25)$$

We can check a few values. At  $R_e = 2000, 1000, 500$ , and  $200$  the formula gives 8.50, 6.01, 4.25, and 2.68, which compare with the computed values 8.32, 5.81, 3.92, and 2.25. The agreement is quite good at the larger Reynolds numbers. Equations (24) and (25) should allow a reasonable extrapolation to Reynolds numbers larger than those for which we have computed.

We conclude that the stability results are similar to those for bending waves on a concentrated vortex at small wavenumbers and similar to results for an unbounded flow with elliptical streamlines at large wavenumber, with comparable growth rates.

### 3. Transition to turbulence

Nonlinear computations have been performed on the Intel Hypercube (i860) using a version of Rogallo's (1981) box code (the "pencil" code) written by Rogallo for this parallel processing machine. This code was designed to solve the Navier-Stokes equations in a box with periodic boundary conditions. The box is not required to have equal sides, but must have volume  $(2\pi)^3$ . We will take the sides to be  $2L_1 \times 2L_2 \times L_3$  with the  $x$  and  $y$  dimensions double the size of the impenetrable box. By using proper symmetry in the initial conditions, we can insure that there is no flow across the surfaces  $x = 0, L_1$  and  $y = 0, L_2$ . The finite dimension in the  $z$  direction means that  $L_3$  is the longest axial wavelength allowed. Defining  $b_1 = \pi/L_1, b_2 = \pi/L_2$  as before and  $b_3 = 2\pi/L_3$ , the volume constraint makes  $b_1 b_2 b_3 = 1$ . The parameter  $b_3$  is the smallest non-zero axial wavenumber. Allowed values are  $k_z = b_3 k$ , where  $k$  is an integer. Solutions in this periodic system are thus of the form

$$u(x, y, z, t) = \sum_{m,n,k=-N}^N \tilde{u}(m, n, k) \exp i(mb_1 x + nb_2 y + kb_3 z) \quad (26)$$

$$v(x, y, z, t) = \sum_{m,n,k=-N}^N \tilde{v}(m, n, k) \exp i(mb_1 x + nb_2 y + kb_3 z) \quad (27)$$

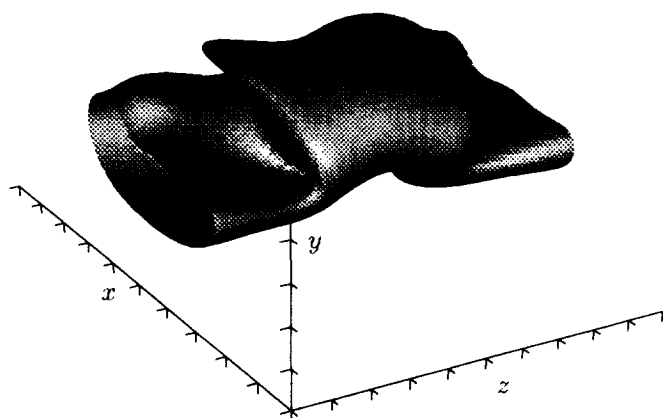


FIGURE 4. Surface of  $3/8$  max vorticity at  $T = 55.66$ . Max vorticity is 2.01. The tick marks are at .6 intervals in the  $x$ -direction and .4 intervals in the  $y$ - and  $z$ -direction.

$$w(x, y, z, t) = \sum_{m, n, k=-N}^N \tilde{w}(m, n, k) \exp i(mb_1 x + nb_2 y + kb_3 z) \quad (28)$$

Conjugate symmetry ( $\tilde{u}(-m, -n, -k) = \tilde{u}(m, n, k)^*$ , etc.) is imposed to ensure that the velocity components are real. Symmetries in the initial conditions like those in Eqs. (15)–(19) for each  $k$  ensure impenetrability of the side walls. For instance, the velocity field of the basic flow,  $U = b_2 \sin b_1 x \cos b_2 y / (b_1^2 + b_2^2)$ ,  $V = -b_1 \cos b_1 x \sin b_2 y / (b_1^2 + b_2^2)$  is generated by the four modes

$$\begin{aligned} \tilde{u}(1, 1, 0) &= \tilde{u}(1, -1, 0) = -\tilde{u}(-1, 1, 0) = -\tilde{u}(-1, -1, 0) = -\frac{b_2 i}{4(b_1^2 + b_2^2)} \\ \tilde{v}(1, 1, 0) &= -\tilde{v}(1, -1, 0) = -\tilde{v}(-1, 1, 0) = \tilde{v}(-1, -1, 0) = -\frac{b_2 i}{4(b_1^2 + b_2^2)} \end{aligned} \quad (29)$$

which have all these symmetries. Perturbations from this can be generated in many different ways and will generate different flows. For instance, we could use random small initial perturbations. For the flow computed here, we excited both even and odd modes by

$$u' = .001 \sin b_1 x \cos b_3 k z + .001 \sin 2b_1 x \cos b_3 k z \quad (30)$$

with  $v' = 0$  and the corresponding  $w'$  determined from continuity, that is,

$$\tilde{u}(1, 0, k) = -\tilde{u}(-1, 0, k) = \tilde{u}(1, 0, -k) = -\tilde{u}(-1, 0, -k) = -.001i/4$$

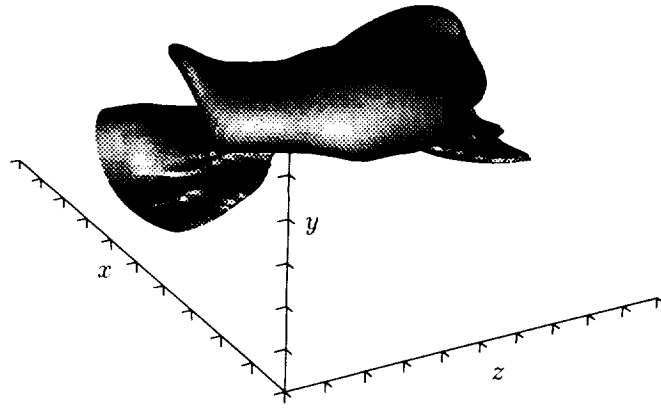


FIGURE 5. Surface of  $3/8$  max vorticity at  $T = 61.71$ . Max vorticity is 2.78. See Figure 4 for the value of the intervals on the axes.

$$\tilde{u}(2, 0, k) = -\tilde{u}(-2, 0, k) = \tilde{u}(2, 0, -k) = -\tilde{u}(-2, 0, -k) = -.001i/4 \quad (31)$$

for all integer  $k$ . With the cosine dependence in the  $z$  direction, the endwalls and the midplane  $z = L_3/2$  will also be impenetrable.

Finally, we chose to do the computation with  $E = 2 = L_1/L_2$  and  $L_3 = \sqrt{L_1 L_2}$ . The volume constraint then makes  $L_1 = 5.60$ ,  $L_2 = 2.8$ ,  $L_3 = 3.96$ , and then  $b_1 = .56$ ,  $b_2 = 1.12$ , and  $b_3 = 1.59$ . We have computed with  $R_e = 2000$  and  $N = 128$ . The lowest wave number in the initial conditions,  $k_z = 1.59$ , is shown in the stability diagrams as a circle in figure 2 and as a vertical dashed line in figure 3. It is near the position of maximum growth rate and was chosen for this reason.

The major results of the computations are presented in figures 4–9, where surfaces of constant magnitude of the vorticity are shown at 6 different times during the evolution of this flow. In each figure, the surface is of the vorticity value which is  $3/8$  of the maximum vorticity at this time. Both the time and the value of the maximum vorticity are given in the figure legends. The coordinate axes shown have  $x$  to the left,  $y$  vertical, and  $z$  off to the right. The viewpoint and illumination are from the origin. At the initial time (not shown), the surface is approximately an elliptic cylinder. The instability causes distortion into a wave oriented roughly along a  $45^\circ$  plane with the vortex moving downward and toward positive  $x$  at the ends of the box and upward and toward negative  $x$  in the middle. The secondary flow which causes this motion also causes the vortex to be greatly distorted into sheet-like structures which resemble the “cups” found by Rogers and Moser (1992) in their study of the development of three-dimensional structure in a mixing layer after the primary rollup into spanwise rollers. In figures 10a and 10b, we look

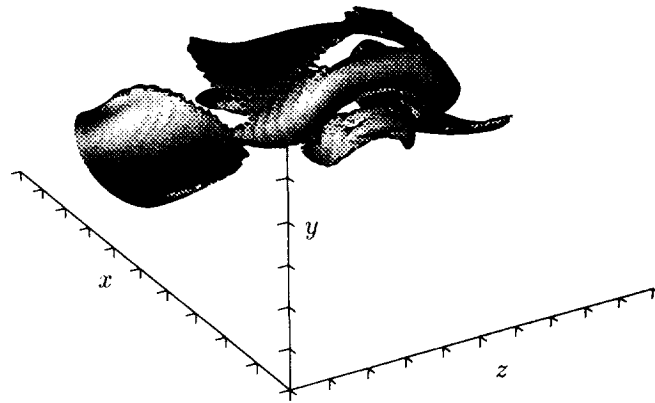


FIGURE 6. Surface of  $3/8$  max vorticity at  $T = 70.43$ . Max vorticity is 5.50. See Figure 4 for the value of the intervals on the axes.

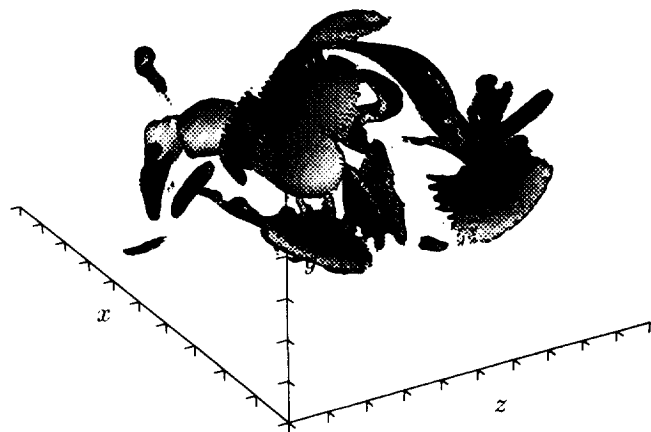


FIGURE 7. Surface of  $3/8$  max vorticity at  $T = 79.09$ . Max vorticity is 9.61. See Figure 4 for the value of the intervals on the axes.

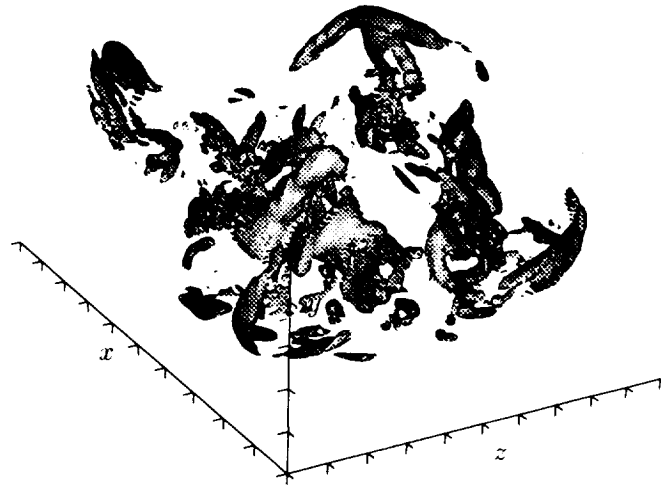


FIGURE 8. Surface of  $3/8$  max vorticity at  $T = 83.94$ . Max vorticity is 13.19. See Figure 4 for the value of the intervals on the axes.

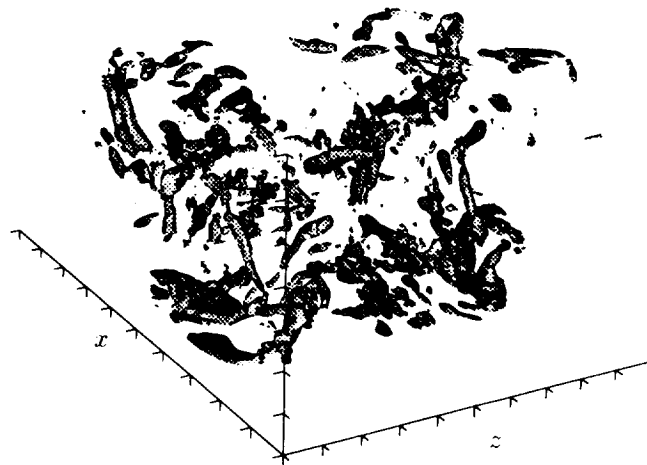


FIGURE 9. Surface of  $3/8$  max vorticity at  $T = 87.95$ . Max vorticity is 15.70. See Figure 4 for the value of the intervals on the axes.

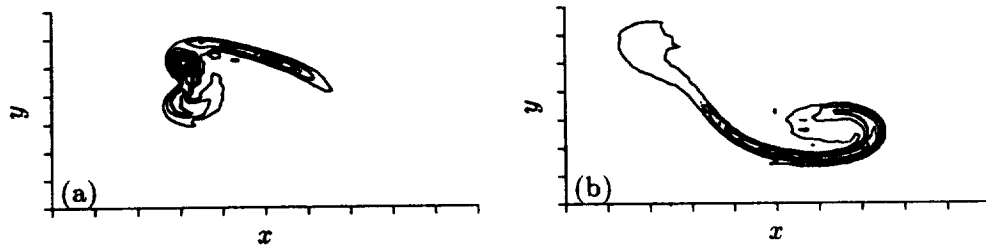


FIGURE 10. Vorticity contours at the time corresponding to figure 6; a) on the plane  $z = L_3/2$ ; b) on the planes  $z = 0$  and  $z = L_3$ . See Figure 1 for the value of the intervals on the axes.

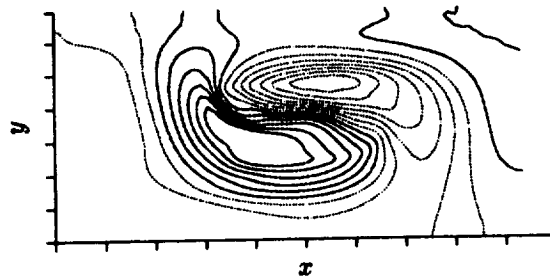


FIGURE 11. Contours of axial velocity on the plane  $z = L_3/4$  at the time corresponding to figure 6. Solid contours are positive velocity, dotted contours are negative velocity. Maximum velocities are  $\pm 3.5$ . See Figure 1 for the value of the intervals on the axes.

at vorticity contours on cuts through the structure shown in figure 6 in order to elucidate its structure. In figure 10a, we have taken the cut through the middle of the structure along the plane  $z = L_3/2$ . By symmetry only, the  $z$  component of vorticity is nonzero on this plane. The maximum vorticity in the box, 5.5, occurs at the center of the rather strong round vortex which is apparent here. In the three-dimensional rendering this vortex is seen from in front and appears to be like a horseshoe vortex. The heavier contour line in figure 10a is at the same vorticity level as the surface in the three-dimensional view. In figure 10b, the cut is at the ends of the box at planes  $z = 0$  and  $z = L_3$ , where again only  $\omega_z$  is non-zero. The maximum vorticity in the strong sheet-like structure is 3.5.

In figure 11, we show contours of the axial velocity  $w$  in the plane  $z = L_3/4$  through the same structure shown in figure 6. This is more regular than we expected and shows characteristics of the 1,1 mode in Robinson and Saffman (1984). The first 1 refers to the angular wave number and the second to the number of nodes in the axial velocity. Here, despite the already complicated vorticity, the underlying secondary flow of the instability is still evident, much amplified, with maximum velocities  $\pm 3.5$ . Since  $w$  is zero at both ends of the box and in the middle, and  $w$  on the plane  $z = 3L_3/4$  is just the reverse of that shown in figure 11, we can picture the secondary flow as two eddies, one in each half of the box, with the velocity toward



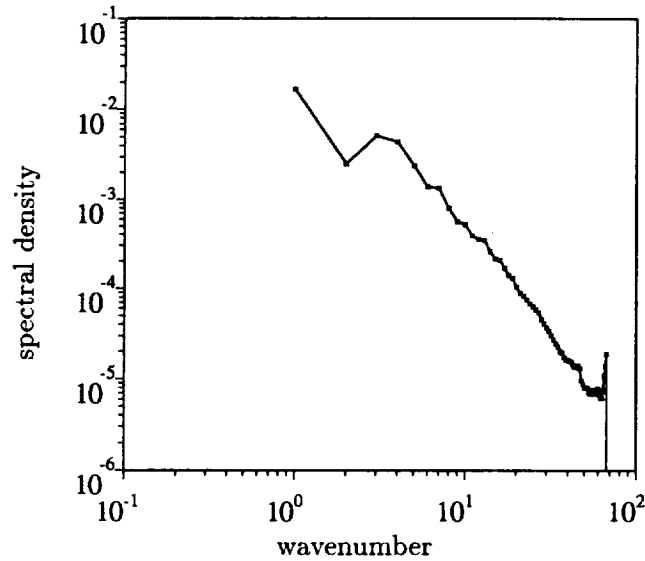


FIGURE 12. Energy spectrum at  $T = 87.95$ .

the center of the box in the lower part and away from the center above. Completion of this circulation is such as to smash the vorticity downwards and toward positive  $x$  at the ends while stretching it, and upward and toward negative  $x$  in the middle, stretching it here also. What is remarkable is that this secondary motion is evident throughout the entire sequence of views, even at the time of figure 9 where it is quite irregular but with the main trends described above.

As we proceed from figure 6 to figure 7, the strong vortex which was evident in figure 6 has disappeared. The central part has apparently been carried downward into the compressive part of the circulation which decreased its vorticity below the plotting level. The remnants of its sides have been stretched into the shield-shaped vortex sheets on each side of the center. In the next view, figure 8, there is no vorticity at the level plotted across the plane  $z = L_3/2$ . This is not clear from the figure, but when we rotated it we had an open view down the middle. The structures we see are mostly tubelike now, and this is even more evident in figure 9, which is the time at which the maximum vorticity in the box is largest. At later times, this begins to decrease, but the tubelike nature of the vorticity is evident still at the time of 103.8 when we ended the computation.

Figure 12 shows the three dimensional energy spectrum at the time of figure 9. While this is quite broad, indicating turbulence, we do not see a  $-5/3$  range at this Reynolds number.

#### 4. Discussion

Our overall impression of this flow is of two large counter-rotating turbulent eddies, each carrying many intense interacting vortex tubes. One can see the development of this pretty clearly in figures 7 and 8, less clearly in figure 9. This motion was already present as the growing secondary flow of the instability and

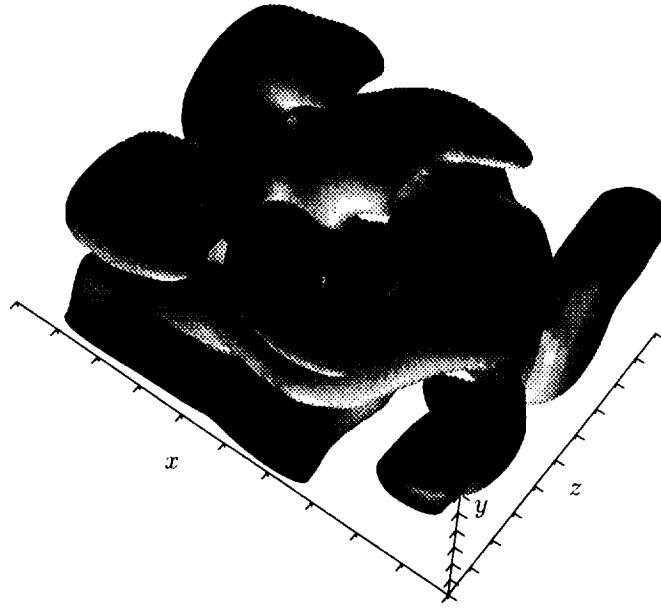


FIGURE 13. Surface of  $3/8$  max filtered vorticity at  $T = 87.95$ . Max filtered vorticity is 1.19. See Figure 4 for the value of the intervals on the axes.

was the controlling factor in the development of the vortex sheets. To understand the large scale swirling motion without the masking effect of the small vortices, we have filtered out the high wavenumber part of the velocity with a Gaussian filter with width .2. We have computed the magnitude of the vorticity in this filtered flow at the same time as in figure 9. The result is presented in figure 13 as a surface of  $3/8$  of the maximum vorticity, which is 1.19 in this filtered flow. This looks like a horseshoe vortex with two vortices wrapping around each of its counterrotating legs. The head of the vortex, which is lifted up, contains the point of maximum vorticity. The sense of motion is upward between the legs of the vortex and forward over the top of the nose, which is the sense of rotation of the original swirling flow.

The evolution of the sheets into tubes appears to be through the Kelvin-Helmholtz instability, or by the Lin-Corcors (1984) version which includes vortex stretching, but nothing very dramatic occurs. Local thick spots gradually become thicker and develop into tubes. In some preliminary computations at higher Reynolds number, the cup-shaped vortex sheet developed into three clearly defined parallel vortex tubes.

In the future, we plan to compute this flow at higher Reynolds number and greater resolution with the objective of looking more carefully at the development of small scale structure. As a generator of small scale turbulence, this flow is similar to the Taylor-Green flow (Brachet *et al.*, 1983). The present flow has some advantages for the study of turbulence because of its development from a typical instability and the fact that the turbulent region tends to avoid close contact with the impenetrable boundaries.

### Acknowledgement

The authors would like to acknowledge several very useful discussions with Dr. Karim Shariff of NASA-Ames. We are especially grateful to Dr. Robert Rogallo for allowing us to use his computer program and to Dr. Michael Rogers for generously providing us with his data reduction code. The direct numerical simulations were performed on the iPSC/860 at the Numerical Aerodynamic Simulation facility, NASA Ames Research Center.

### REFERENCES

- BAYLY, B. J. 1986 Three-Dimensional Instability of Elliptical Flow. *Phys. Rev. Lett.* **57**, 2160-2163.
- BAYLY, B. J. 1989 Computations of Broad-Band Instabilities in a Class of Closed-Streamline Flows. In *Mathematical Aspects of Vortex Dynamics*, (ed. R. E. Caflisch.) SIAM, Philadelphia, PA, 50-58.
- BRACHET, M. E., MEIRON, D. I., ORSZAG, S. A., NICKEL, B. G., MORF, R. H. & FRISCH, U. Small-scale structure of the Taylor-Green vortex. *J. Fluid Mech.* **190**, 411-452.
- LIN, S. J. & CORCOS, G. M. 1984 The mixing layer: deterministic models of a turbulent flow. Part 3. The effect of plane strain on the dynamics of streamwise vortices. *J. Fluid Mech.* **141**, 139-178.
- GLEDZER, YE. B., NOVIKOV, YU. V., OBUKHOV, A. M. & CHUSOV, A. M. 1974 An investigation of the stability of liquid flows in a three-axis ellipsoid. *Izv., Atmospheric and Oceanic Physics*. **10**, 115-118.
- GLEDZER, YE. B., DOLZHANSKIY, F. V., OBUKHOV, A. M. & PONOMAREV, V. M. 1975 An experimental and theoretical study of the stability of motion of a liquid in an elliptic cylinder. *Izv., Atmospheric and Oceanic Physics*. **11**, 981-992.
- LANDMAN, M. J. & SAFFMAN, P. G. 1987 The three-dimensional instability of strained vortices in a viscous fluid. *Phys. Fluids*. **30**, 2339-2342.
- MALKUS, W. V. R. 1989 An Experimental Study of Global Instabilities Due to the Tidal (Elliptical) Distortion of a Rotating Elastic Cylinder. *Geophys. Astrophys. Fluid Dyn.* **48**, 123-134.
- ORSZAG, S. A. & PATERA, A. T. 1983 Secondary instability of wall-bounded shear flows. *J. Fluid Mech.* **128**, 347-385.
- PIERREHUMBERT, R. T. 1986 Universal Short-Wave Instability of Two Dimensional Eddies in an Inviscid fluid. *Phys. Rev. Lett.* **57**, 2157-2159.
- ROGALLO, R. S. 1981 Numerical Experiments in Homogeneous Turbulence. *NASA Technical Memorandum* 81315.
- ROGERS, M. M. & MOSER, R. D. 1992 The three-dimensional evolution of a plane mixing layer: the Kelvin-Helmholtz rollup. *J. Fluid Mech.* **243**, 183-226.

- WALEFFE, F. 1989 The 3D Instability of a Strained Vortex and its Relation to Turbulence. *Ph.D Thesis*, Massachusetts Institute of Technology.
- WALEFFE, F. 1990 On the three-dimensional instability of strained vortices. *Phys. Fluids A*, **2**, 76–80.

## Vortical structure in a forced plane mixing layer

By R. L. LeBoeuf

The objective of this phase of an ongoing study is to obtain detailed three-dimensional phase-averaged measurements of forced mixing layer vorticity development and evolution. Acoustic forcing is being used to phase-lock the initial development and subsequent pairing of the spanwise vortical structures. Phase-averaged measurements of the three velocity components will permit the study of three-dimensional vorticity distributions without invoking Taylor's hypothesis which is known to introduce uncertainty. Currently two sine waves, one at the fundamental roll-up frequency and the second, its subharmonic, are being used to force the initial roll-up and first pairing of the spanwise rollers. The two-dimensional measurements described in this report were obtained in order to determine the best operating conditions for the detailed three-dimensional study of the mixing layer undergoing pairing via various pairing mechanisms.

### 1. Motivation and objectives

Being one of the fundamental transitional flows as well as a technologically significant flow, the mixing layer has been scrutinized for many decades. Among the experimental investigations, many, especially the earlier studies, involved one- and two-dimensional measurements of time-averaged turbulence quantities. The results of these studies have been useful for corroborating turbulence theories and tuning turbulence models. In the late sixties and early seventies, the advent of the search for coherent structures and their dynamics lead to more detailed studies of mixing layer structure. For example, Winant & Browand (1974) showed that spanwise vortex pairing is a controlling factor for mixing layer growth. Coherent structure eduction, aided by artificial excitation of the mixing layer roll-up and pairing, has continued through to the present.

In addition to the two-dimensional coherent structures discussed above, signs of spatially coherent streamwise structures in plane mixing layers were identified in flow visualization studies at Caltech during the early eighties (eg. Breidenthal 1981 and Bernal & Roshko 1986). Models of the three-dimensional mixing layer structure (eg. Bernal 1981) and attempts to quantify the observations quickly followed. These earlier studies were limited to three-dimensional time-averaged measurements (Bell & Mehta 1992), measurements of partial vorticity (Huang & Ho 1990 and Nygaard & Glezer 1991) and/or the extension of temporal measurements to three-dimensional grids using Taylor's hypothesis (Nygaard & Glezer 1991 and Tung 1992). The appearance of mean streamwise vorticity in time-averaged measurements confirmed the existence of coherent spatially-stationary secondary vorticity in mixing layers (Bell & Mehta 1992). However, the details and interactions of the secondary structure are lost through the averaging process. Furthermore, Taylor's hypothesis was

shown by Zaman & Hussein (1981) to be inadequate for transforming temporal measurements to a spatial grid for a circular jet – especially in regions of vortex interactions. Included in this report is an extensive comparison of data generated using Taylor's hypothesis to their true counterparts which indicates that the same deficiencies also apply to a two-stream plane mixing layer.

In addition to the large set of mixing layer measurements, there have been several computations of the mixing layer development. In one study related to the results detailed in this report, a spatial simulation employing a two-dimensional vortex method was used by Inoue (1992) to investigate the effect of double-frequency forcing on the initial spanwise vortex development and subsequent pairing. The dependence of the pairing mechanism on the relative forcing signal phase, demonstrated earlier using two-dimensional temporal simulations (eg. Riley & Metcalfe 1980), was confirmed. Three-dimensional spatial simulations of the mixing layer performed in the late eighties (Buell 1991) clearly showed the presence and development of the primary and secondary vorticity. Spatial simulations soon gave way to the more economical temporal simulations (eg. Rogers & Moser 1992, Moser & Rogers 1993). The sequence of temporal simulations which have since been conducted have been used to clarify many of the details of the three-dimensional evolution of plane mixing layers. However, limits imposed by the expense associated with computational grid size and computation time make it difficult to evaluate the relationship between the time-averages and the true structure using simulations, especially in the mid- to far-field regions of mixing layer development.

The objective of this study is to investigate the development of three-dimensionality and transition to turbulence in a forced plane two-stream mixing layer. Acoustic forcing is being used to generate specific pairing mechanisms which would otherwise occur randomly in an unforced mixing layer. Phase-averaged measurements are being used to then quantify the resulting vorticity development and interaction. These measurements, coupled with the previous direct numerical simulation results, should shed new light on the development of spatially evolving mixing layers. In particular, the relationship between time-averaged measurements and the three-dimensional structure will be clarified.

## 2. Accomplishments

### 2.1 *The experiment*

The experiments were conducted in a mixing layer wind tunnel specifically designed for free-shear flow experiments (Bell & Mehta 1989). The wind tunnel consists of two separate legs which are driven independently by centrifugal blowers connected to variable speed motors. The two streams merge at the sharp trailing edge of a slowly tapering splitter plate; the included angle at the splitter plate edge, which extends 15 cm into the test section, is about  $1^\circ$ . The test section is 36 cm in the cross-stream direction, 91 cm in the spanwise direction, and 366 cm in length. An adjustable side-wall is used to zero the streamwise pressure gradient. To facilitate 3-D traversing, a slotted 3/32 inch thick aluminum plate was mounted on the traverse which moves the probe in the streamwise ( $X$ ) direction. The plate,

which slides against the inside surface of the one side-wall, was large enough to allow traversing in the streamwise direction of approximately 30 cm for a fixed traversing table location.

In the present experiments, the two sides of the mixing layer were set to 12 m/s and 7.2 m/s for a velocity ratio equal to that used by Bell & Mehta (1992) in the same facility,  $r = U_2/U_1 = 0.6$  [ $\lambda = (U_1 - U_2)/(U_1 + U_2) = 0.25$ ]. These operating conditions resulted in the lowest initial wake unsteadiness levels and free-stream streamwise turbulence levels ( $u'/U_e$ ) of approximately 0.2% and the transverse levels ( $v'/U_e$  and  $w'/U_e$ ) of approximately 0.05%. The mean core-flow was found to be uniform to within 0.5% and cross-flow angles were less than  $0.25^\circ$ . The boundary layers on the splitter plate were laminar at these operating conditions.

Velocity measurements were made using a single cross-wire probe which is rotated in order to measure flow in two-coordinate planes. The *Dantec* cross-wire probe (Model 55P51) consisted of 5  $\mu\text{m}$  platinum-plated tungsten sensing elements approximately 1 mm long with approximately 1 mm spacing. The probes were calibrated statically in the potential core of the flow assuming a 'cosine-law' response to yaw, with the effective angle determined by calibration. The analog signals generated by *DISA* (Model 55M01) anemometers were sampled using a *Tustin* (Model 110-9C) 15 bit simultaneous sample-and-hold A/D converter with a multiplexed connection to the computer.

Conversion of the hot-wire data to effective normal velocities is achieved on-line through the use of look-up tables. The linear decoding afforded by using the cosine-law allows post-experimental calculation of velocity statistics from effective velocity statistics written to disk. This scheme, used for both time averages and phase averages, substantially decreased (by approximately 60%) the experimental run-time calculations required relative to calculating velocities for each time step and subsequently averaging. Similarly, for velocity spectra measurements, the effective velocity spectra were calculated on-line using a Fast Fourier Transform (FFT) routine, output to disk, and later decoded. The increased experimental run-time calculations of this approach are more than offset by the savings in disk read/writes required by saving entire time-series for post-processing of spectra. Additional time savings were gleaned by using double-buffering, a scheme whereby a block of data is acquired via the A/D converter and a previously acquired block of data is processed *simultaneously*. In the future, a multi-tasking scheme may be employed in order to perform the calculations during both the data acquisition *and* traversing times.

Due to the large quantities of data required by this study, many aspects of this experiment were automated. The data acquisition and control systems are shown diagrammatically in Fig. 1. A *DEC MicroVax II* computer using the VMS operating system is the platform. While taking data for a single run, typically over the course of *many days*, the MicroVax is able to coordinate the traversing, A/D control, blower speed control, and relative phase of forcing signals without human intervention. To insure measurement accuracy, a number of conditions including blower drift, hot-wire calibration drift, forcing signal variation, and traverse malfunction are tested periodically during every data acquisition run.

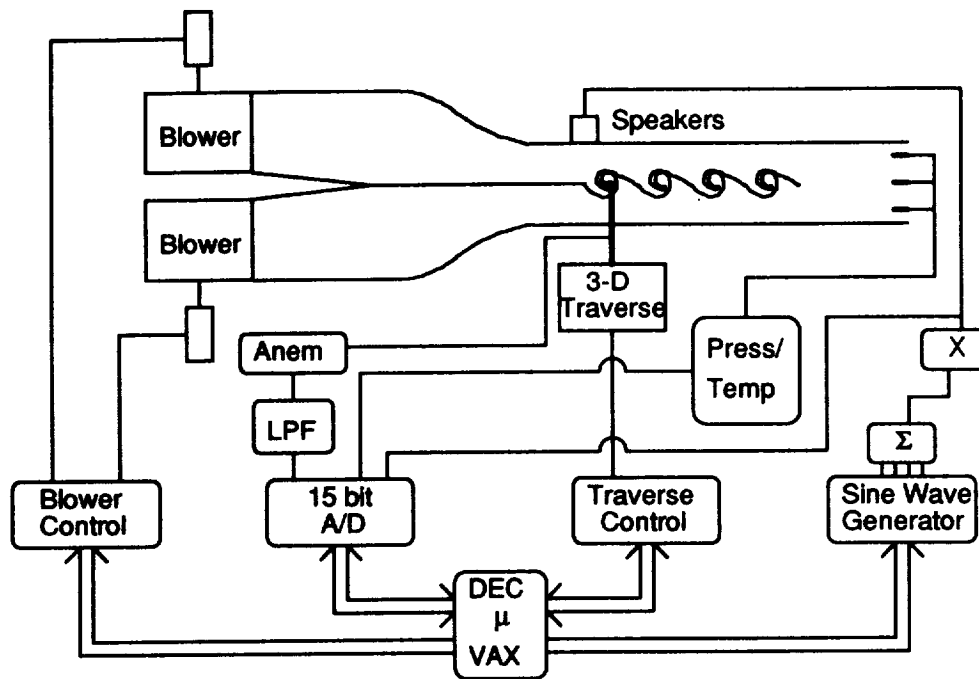


FIGURE 1. Forced mixing layer data acquisition and control system.

Since the temperature in the laboratory may change by 10-15°C over the course of a day, the test-section velocity and hot-wire calibration drift-checks are performed approximately every ten minutes. If, during a drift-check, the cross-wire measurements differ from the reference (measured using a pitot-static tube) by more than 1.5%, then a new constant angle calibration is performed and new effective velocity look-up tables are calculated. Note, since the yaw calibration is not automated, the effective wire angles obtained from a yaw calibration at the beginning of each run are maintained for an entire run. This is not expected to introduce significant error into the measurements since the wire angles would not be expected to change rapidly. If either the hot-wire drift or the test-section velocity drift exceeds 2%, the data acquired between the previous drift-check and the current one is re-acquired.

Since the traverse employs stepper motors operated in open-loop, the integrity of the traverse locations is also tested. The threshold levels of roller actuated switches are used to determine the calibration/drift-check location during each drift-check. If the traverse is found to deviate more than 5% of the grid spacing (i.e. typically 0.5% of the spanwise structure size), then the previous data is re-acquired. After each drift-check, the test-section velocities are adjusted to the set-points (12 and 7.2 m/s) to within 0.3%. The forcing signals are measured before and after each plane to verify their integrity as well. Note, the true relative forcing signal phase was determined by correlating the sine-wave generator outputs and phase-average microphone measurements of the speaker output.



A digital sine-wave generator capable of outputting up to four signals simultaneously was designed (by Dr. J. H. Watmuff) and built for this project. The amplitudes and frequencies are tunable from the front panel of the device while the relative phase of the sine-waves can be adjusted using front panel BCD switches or digital input. The digital control of the relative phase by the MicroVax was used during sequential runs for which the only parameter varied from one run to the next was the relative phase. The forcing signals used to obtain the results shown in this report consisted of the sum of a sine-wave at the fundamental roll-up frequency (obtained from centerline spectra) and its subharmonic:

$$s(t) = A_1 \sin 2\pi f_1 t + A_2 \sin(2\pi f_2 t + \beta_2)$$

where  $f_1 = 500$  Hz and  $f_2 = 250$  Hz. The amplitude ratio ( $a = A_2/A_1$ ), which largely dictates the pairing location for multiple-frequency forcing (Inouye 1992), was set equal to 2.0 for all of the measurements described in this report. However, measurements of the speaker output indicated that the amplitude ratio was in approximately 40. This forced the first pairing to occur at about 15 cm from the splitter plate trailing edge.

The individual sine-waves were combined using a simple summing circuit and output by an audio amplifier to a spanwise array of three four inch speakers. The frequency response of the amplifier (*Realistic* SA-155) and speakers were rated at 20 Hz to 25 kHz and 55 Hz to 5 kHz, respectively. The speakers were mounted in a rectangular wood box which, with the exception of a vertical slot, was lined with foam to decrease the occurrence of acoustic reflections. The speakers were placed directly across from the splitter plate trailing edge (see Fig. 1) at a side-wall slot location. Measurements along the slot of the speaker box with a microphone showed that the pressure induced by the speakers was uniform within 3% along the span of the test-section. The sine-wave generator also output digital start sample pulses and a clock signal with  $2^n$  pulses per cycle, where  $n$  can be any integer from 3 to 8. These signals were used to synchronize the A/D sampling with the forcing signals. For the phase-averages shown in the next section, 768 ensembles of 16 samples per phase were measured. The internal A/D clock set to 2500 Hz was used for the spectra measurements described in the next section. Low-pass filters (Krohn-Hite Model 3343, LPF in Fig. 1) set to 1200 Hz were used to avoid aliasing the hot-wire spectra measurements. Five hundred blocks were found to adequately converge the 256 sample spectral estimates.

## 2.2 Results and discussion

### 2.2.1 Spanwise structure coherence

Recognizing the importance of the structure-to-structure repeatability gained by forcing the mixing layer, the first set of measurements were used to identify the relative phase of forcing signals resulting in optimal coherence of the pairing spanwise structures. Given the triple decomposition representation of the flow component  $u_i(\mathbf{x}, t)$ :

$$u_i(\mathbf{x}, t) = \bar{u}_i(\mathbf{x}) + \tilde{u}_i(\mathbf{x}, t) + u_i''(\mathbf{x}, t)$$

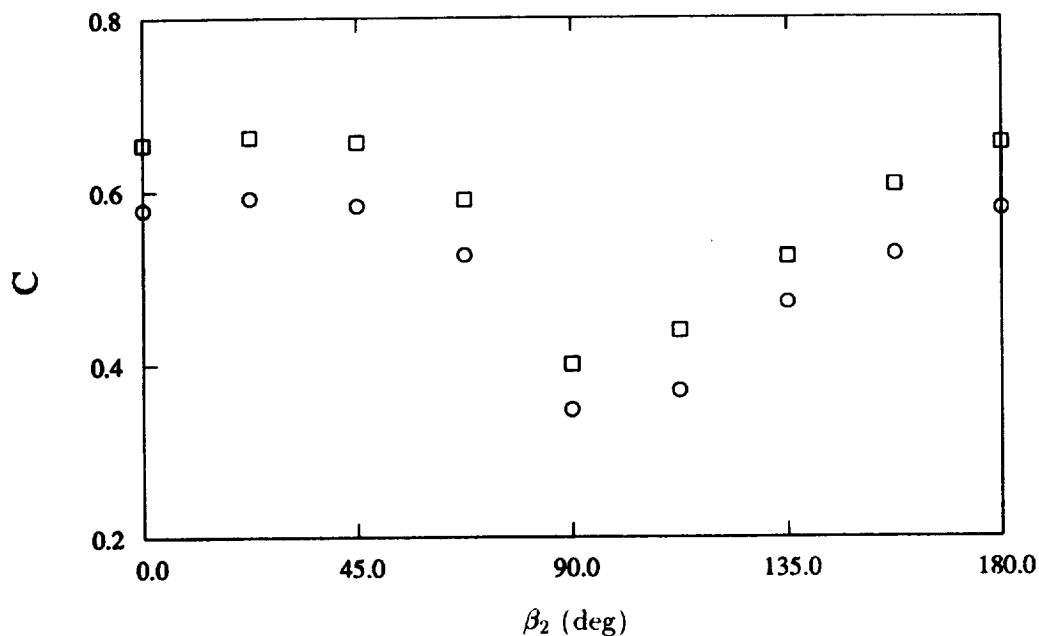


FIGURE 2. Centerplane average coherence,  $u$   $\circ$  ;  $v$   $\square$  .

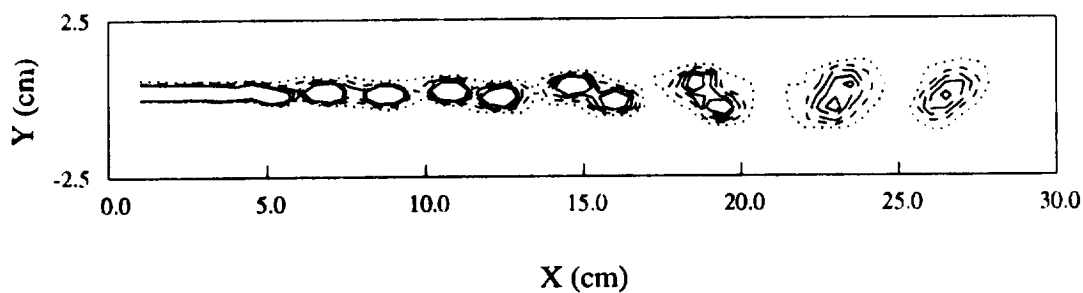


FIGURE 3. Centerplane spanwise vorticity normalized by  $U_1 - U_2$  at  $T = 0$  for  $\beta_2 = 22.5^\circ$ , 0.125 ..... ; 0.25 ---- ; 0.375 --- ; 0.5 — — ; 0.625 ——— ( $s^{-1}$ ).

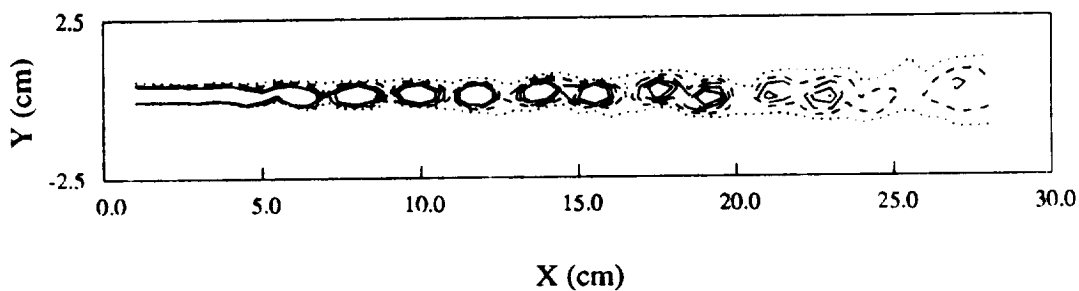


FIGURE 4. Centerplane spanwise vorticity normalized by  $U_1 - U_2$  at  $T = 0$  for  $\beta_2 = 90^\circ$ , 0.125 ..... ; 0.25 ---- ; 0.375 --- ; 0.5 — — ; 0.625 ——— ( $s^{-1}$ ).

where  $\bar{u}_i(\mathbf{x}) = \overline{u_i(\mathbf{x}, t)}$  is the local time-average,  $\tilde{u}_i(\mathbf{x}, t) = \langle u_i(\mathbf{x}, t) \rangle$  is the periodic unsteadiness, and  $u_i''(\mathbf{x}, t)$  is the random component of  $u_i(\mathbf{x}, t)$ . Note, the overbar denotes time-averaging while the brackets ( $\langle \rangle$ ) denote a phase-locked ensemble average over one fundamental period. The measure of coherence used to characterize the relative success of forcing was the ratio of the periodic contribution to the normal Reynolds stress to the total normal Reynolds stress:

$$C_i = \frac{\langle u_i(\mathbf{x}, t) \rangle^2}{(\langle u_i(\mathbf{x}, t) \rangle + u_i''(\mathbf{x}, t))^2}.$$

This quantity was averaged over a centerplane oriented normal to the mixing layer ( $X - Y$  plane) for nine different relative phases ( $\beta_2$ ) ranging from 0 to 180°. Note, the phase is defined such that the forcing signal repeats for every 180° shift of the subharmonic relative to the fundamental. The measurement grid consisted of 55 uniformly spaced  $X$  locations in the range 1 to 28 cm and 13 uniformly spaced  $Y$  locations distributed over a linearly increasing range of -1 to 1 cm at  $X = 1$  cm to the range -2.5 to 2.5 cm at  $X = 28$  cm. The resulting distribution of the coherence versus relative forcing signal phase is shown in Fig. 2. Clearly, the coherence displays a broad peak between approximately 0° and 45°, while the minimum is much sharper at a phase of 90°. The resulting centerplane phase-averaged spanwise vorticity contours for the two extreme cases each at dimensionless time  $T = 0$  are shown in Figs. 3 ( $\beta_2 = 22.5^\circ$ ) and 4 ( $\beta_2 = 90^\circ$ ). Clearly, Fig. 3 illustrates the traditional pairing mechanism for which two adjacent vortices begin to corotate and finally merge into a single larger vortex. This results in a higher coherence than the shredding mechanism illustrated in Fig. 4. Double-frequency forcing with relative phase ( $\beta_2$ ) set equal to 22.5° was therefore chosen for measurements of the usual pairing mechanism. These results confirm that double-frequency forcing with a relative phase of 90° results in shredding/tearing as shown by Riley & Metcalfe (1980) using a 2-D temporal simulation.

To help clarify this observed variation of the mean coherence parameter, the spatial distributions of the coherence parameter for the phases corresponding to the peak mean coherence ( $\beta_2 = 22.5^\circ$  and 4  $\beta_2 = 90^\circ$ ) are included in Figs. 5 and 6, respectively. The relatively higher average  $u$  component phase coherence for the optimum forcing signal phase setting results from the recovery of the coherence near the onset of pairing ( $X = 15$  cm) and the minor recovery at the edges of the mixing layer after pairing [see Figs. 5 (a) and 6 (a)]. Figures 5 (b) and 6 (b) show that at the optimum phase, the  $v$  component coherence recovers to its peak value immediately after pairing. This recovery does not occur for the shredding interaction. It remains to be shown whether the loss of coherence in either of these cases is due to large-scale jitter or small-scale motions. One possible scheme for isolating the contributions of the small-scale motions and large-scale jitter is to simultaneously phase-average the raw hot-wire signals and their low-pass filtered counterparts. For appropriate low-pass filter settings, the ratio of the random contribution of the filtered signals to the Reynolds stress to the total random contribution to the Reynolds stress would be indicative of the large scale jitter contribution to the total randomness.

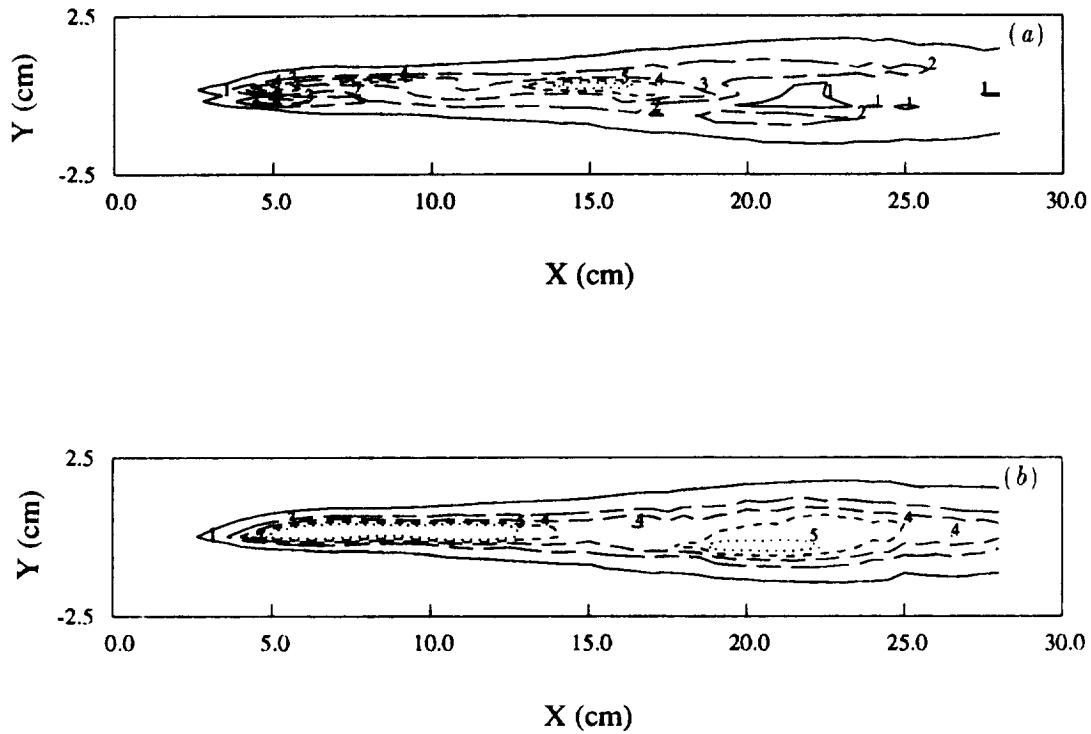


FIGURE 5. Centerplane coherence distribution for  $\beta_2 = 22.5^\circ$ . (a)  $u$  (b)  $v$ ; 0.05 — ; 0.275 — — ; 0.5 — — — ; 0.725 — — — — ; 0.95 ..... .

### 2.2.2 Centerline spectra

With the exception of a relative phase shift, the coherence versus relative phase relationship shown in Fig. 2 resembles the subharmonic amplification rate measured in the near field of a double-frequency forced water tunnel mixing layer by Zhang, Ho & Monkewitz (1985). The phase shift, as mentioned above, is in part due to the audio amplifier and may be augmented by the additional transfer function associated with the speakers. Nevertheless, to investigate this possible relationship further, centerline spectra of the forced mixing layer were measured for relative phases ranging from  $0^\circ$  to  $180^\circ$  in increments of  $22.5^\circ$ . For each phase,  $u$  and  $v$  spectra were measured for  $X$  ranging from 1 to 28 cm in 1 cm increments. Contours of the streamwise  $[S_{uu}(f_1, X)]$  and transverse  $[S_{vv}(f_1, X)]$  spectra at the fundamental forcing frequency ( $f_1$ ) are shown in Fig. 7 (a) and (b). Similarly, the measured spectra at the subharmonic frequency ( $f_2$ ) are shown in Figs. 8 (a) and (b). For the phase range between  $90^\circ$  and  $135^\circ$ , the subharmonic spectra of Figs. 8 (a) and (b) begin to rise during the onset of the initial roll-up (at approximately  $X = 5$  cm) and maintain a plateau until pairing is complete. For that same range of forcing signal phases, Figs. 7 (a) and (b) show a rapid amplification of the energy at the fundamental which begins to decay as pairing progresses. For the forcing phase leading to shredding ( $\beta_2 = 90^\circ$ ), the subharmonic energy grows less rapidly and does not

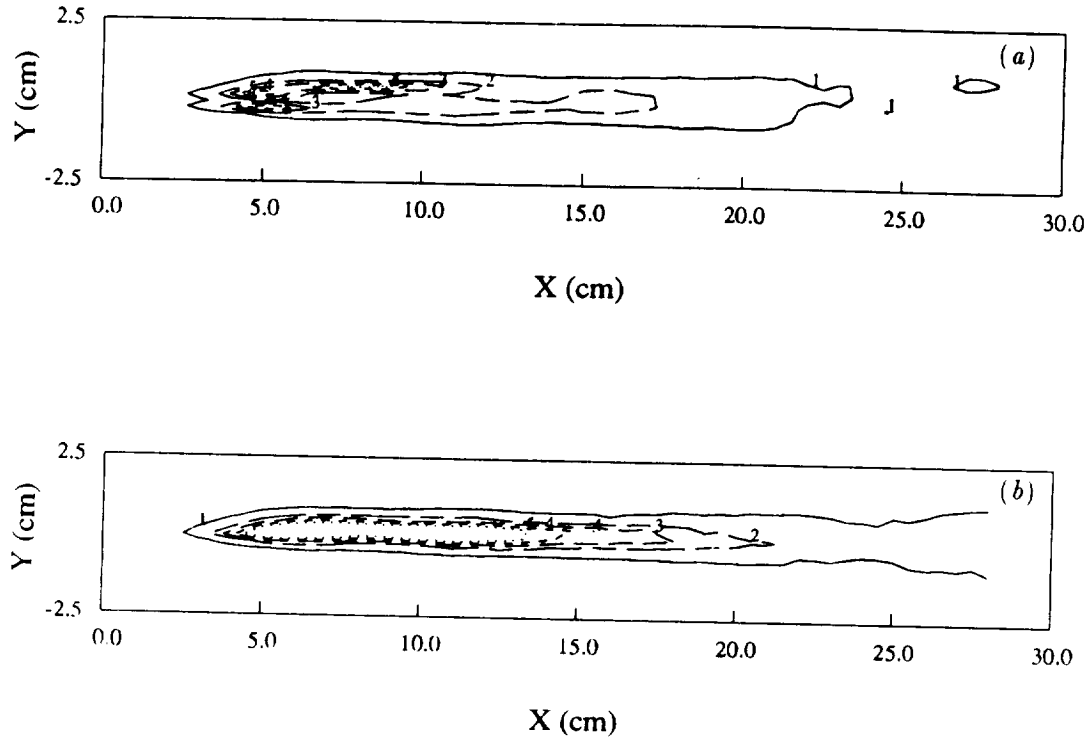


FIGURE 6. Centerplane coherence distribution for  $\beta_2 = 90^\circ$ . (a)  $u$  (b)  $v$ ; 0.05 — ; 0.275 — — ; 0.5 — — — ; 0.725 — — — — ; 0.95 ..... .

reach as high an amplitude as that for the high coherence phase range. Figure 7 (b) illustrates the weak dependence of the initial growth of the energy at the fundamental forcing frequency on the relative forcing phase; a result demonstrated by Zhang, Ho and Monkewitz (1985). Furthermore, the spectra at the fundamental frequency decays more quickly for forcing signal phase leading to shredding. The combination of lower sustained subharmonic energy growth and more rapid fundamental energy decay are apparently responsible, or at least symptomatic, of a decrease in the coherence of the spanwise structure.

### 2.2.3 Taylor's hypothesis error

The sequence of centerplane phase-averaged  $u - v$  data obtained with forcing relative phase set to  $112.5^\circ$  were also used to demonstrate the limitation of Taylor's hypothesis (herein denoted TH) for the plane mixing layer. For each streamwise location between  $X = 10$  cm and  $X = 28$  cm, TH was used to generate spatial distributions of streamwise ( $u$ ) and transverse ( $v$ ) velocity components at upstream locations using phase averaged data at different non-dimensional times. Note, a single convection velocity ( $U_c = 9.6$  m/s) equal to the average of the streamwise velocities on the two sides of the layer (suggested by Zaman & Hussein 1981 based on jet mixing layer comparisons) was transformed to  $\tilde{X} = X - U_c t$ . The resulting

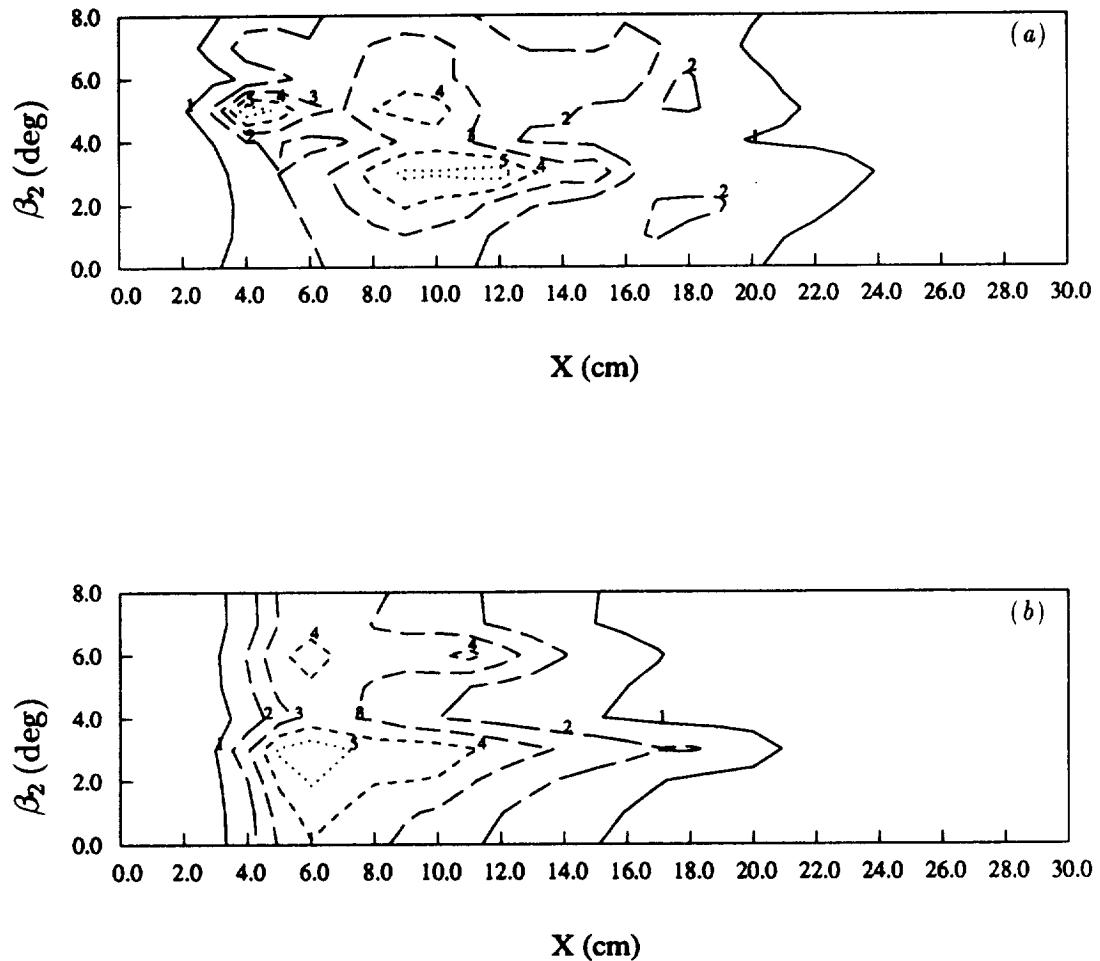


FIGURE 7. Streamwise development of fundamental centerline spectra. (a)  $u$ , levels are 0.001 —; 0.004 — —; 0.007 — — —; 0.010 — — — —; 0.013 ·····, (b)  $v$ , levels are 0.005 —; 0.017 — —; 0.029 — — —; 0.041 — — — —; 0.053 ·····,  $m^2$ .

streamwise TH grid spacing for the sampling rate used was then  $\Delta\tilde{X} = 0.24$  cm (i.e. less than half the true grid spacing). A central difference scheme was used to calculate the spanwise vorticity which was then interpolated onto the true measurement grid. The spanwise vorticity generated using TH was then directly compared to that calculated from measured velocity components using a central difference scheme. Using the field shown in Fig. 3 as the reference (i.e.  $t = 0$ ), the results of TH for locations before pairing ( $X = 13$  cm), during pairing ( $X = 20$  cm) and after pairing ( $X = 25$  cm) are shown in Fig. 9. The TH vorticity contours appear similar to their measured counterparts although a close examination reveals that they differ in shape and orientation.

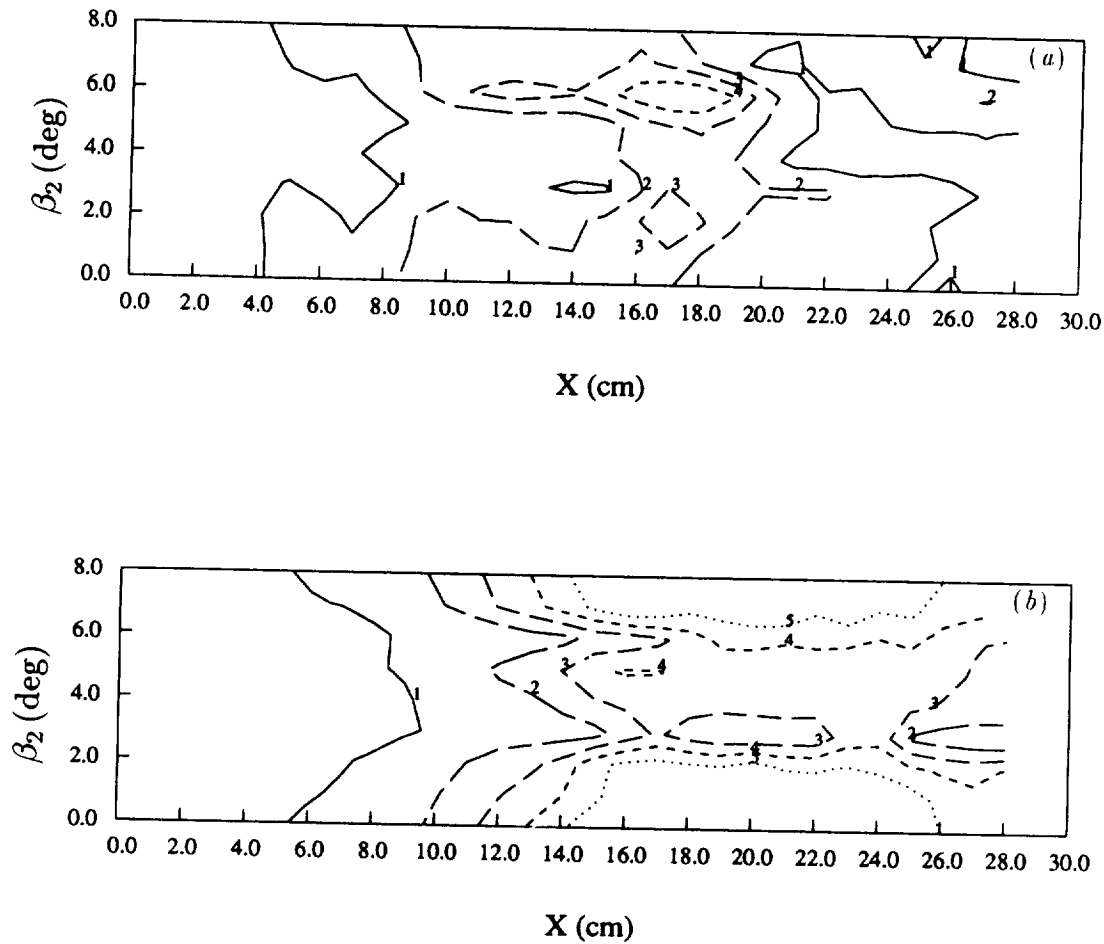


FIGURE 8. Streamwise development of subharmonic centerline spectra. (a)  $u$ , levels are 0.003 —; 0.008 — —; 0.013 — — —; 0.018 — — — —; 0.023 ·····,  $m^2$ . (b)  $v$ , levels are 0.003 —; 0.010 — —; 0.017 — — —; 0.024 — — — —; 0.031 ·····,  $m^2$ .

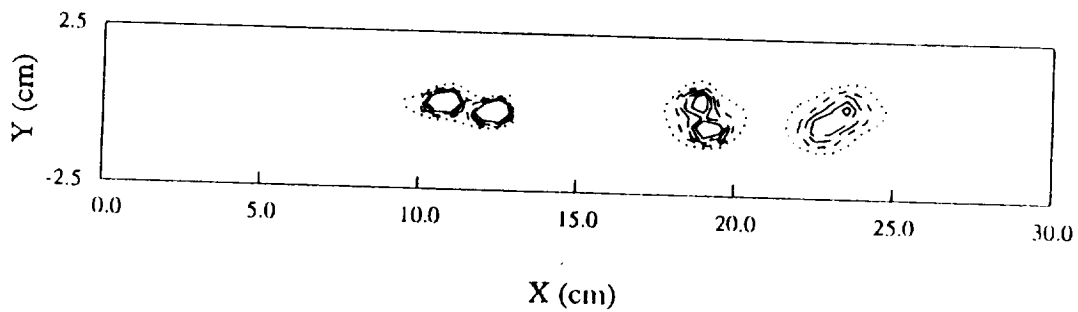


FIGURE 9. Centerplane spanwise vorticity calculated using Taylor's hypothesis at  $X = 13$  cm,  $X = 20.5$  cm and  $X = 25$  cm normalized by  $U_1 - U_2$  for  $\beta_2 = 22.5^\circ$ , 0.125 ·····; 0.25 — — —; 0.375 — — — —; 0.5 — — — —; 0.625 — — — — ( $s^{-1}$ ).

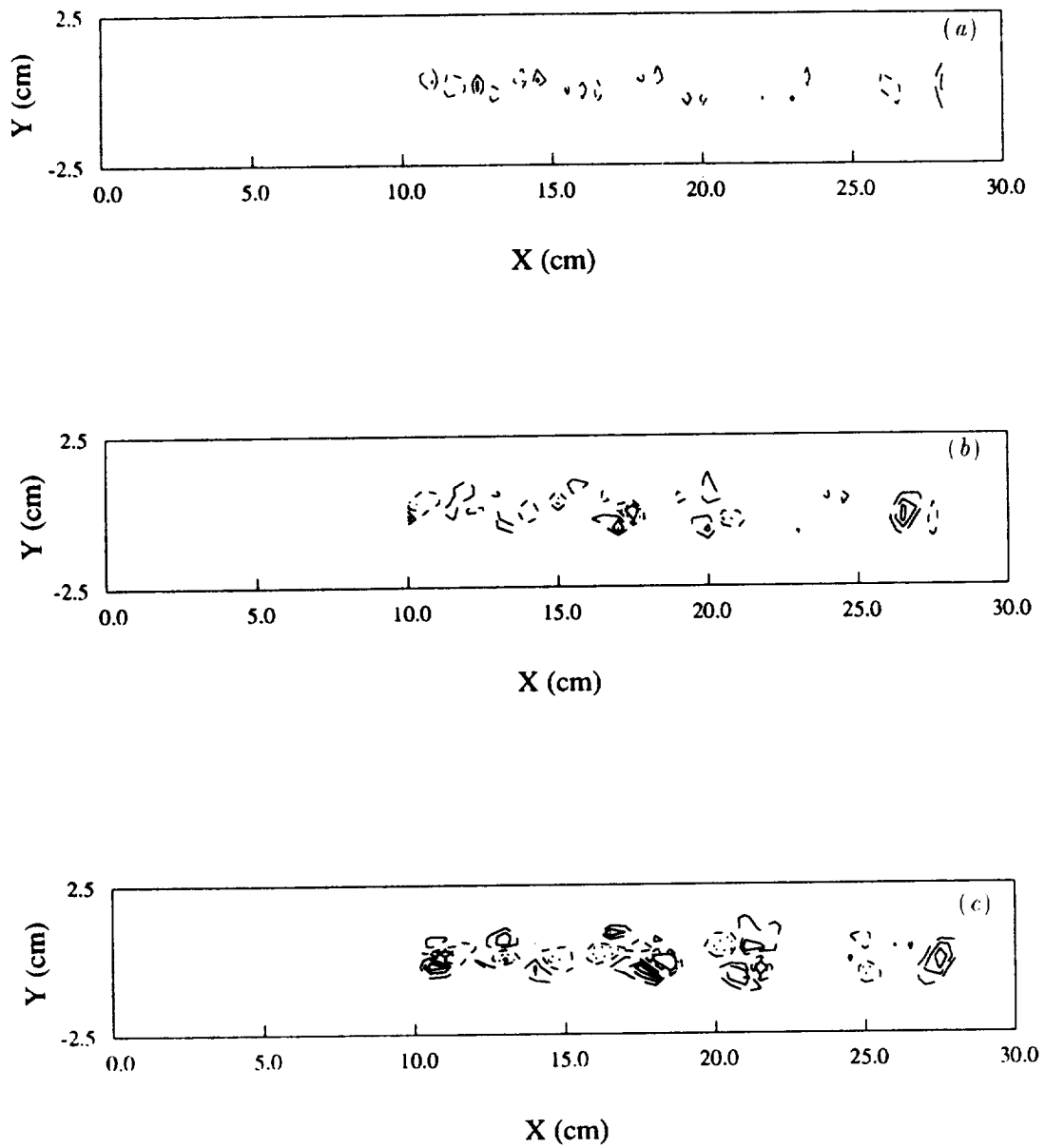


FIGURE 10. Centerplane spanwise vorticity error from using Taylor's hypothesis normalized by the peak spanwise vorticity. (a)  $\Delta X = 0$  cm, (b)  $\Delta X = 0$  cm, (c)  $\Delta X = 0$  cm. -0.15 — (not in (a)); -0.10 — — ; -0.05 — — — ; 0.05 — — — — ; 0.10 ..... ; 0.15 — · — (not in (a)).



To quantify the error resulting from this approximation, the difference between true vorticity and the TH result, normalized by the peak true vorticity, is shown in Fig. 10. Each of these plots shows the error at a given distance from the measurement location ( $\Delta X$ ). The error for  $\Delta X = 0$  is shown in Fig. 10 (a). The error would be expected to be zero since the measurement location and the approximation location coincide; however, the vorticity is calculated using differences of TH results offset from the true location. Of course, the errors resulting from using TH get progressively worse as the distance from the measurement location increases as shown in Figs. 10 (b) ( $\Delta X = 1.0$  cm) and (c) ( $\Delta X = 2.0$  cm). The failure of Taylor's hypothesis in this flow is especially prominent in the core of the spanwise vortices before, during, and after pairing. Since the peak vorticity is typically orders of magnitude greater than the vorticity of most of the field, the corresponding percent error of the approximated vorticity is in general several hundred percent for  $\Delta X$  as low as 0.5 cm. These results confirm the observations of Zaman & Hussein (1981) that Taylor's Hypothesis should be avoided if the details of the mixing layer flow structure are of interest.

### 3. Future plans

During the remainder of the program, vortex interaction and transition to turbulence will be studied using benchmark three-dimensional phase-locked measurements of a plane mixing layer. In addition to the two pairing mechanisms observed in the two-dimensional data sets shown in this report (normal pairing and shredding), other combinations of forcing signals will be used to attempt to excite interactions such as tripling, the second pairing, and possibly the third pairing. In this manner, the pairing mechanisms which would normally occur randomly in time and space can be isolated and studied in a real flow. This systematic study of the mixing layer should not only increase the current level of understanding of mixing layer structure interactions, but also provide a valuable data base for computation validation.

### Acknowledgements

This work is being performed in the Fluid Mechanics Laboratory, NASA Ames Research Center in collaboration with Dr. R. D. Mehta. We would like to thank Dr. J. H. Watmuff for many invaluable suggestions and helpful discussions of this work.

### REFERENCES

- BELL, J. H. & MEHTA, R. D. 1989 Design and Calibration of the Mixing Layer Wind Tunnel. *JIAA Report TR-84*. Dept. of Aeronautics and Astronautics, Stanford University.
- BELL, J. H. AND MEHTA, R. D. 1992 Measurements of the Streamwise Vortical Structures in a Plane Mixing Layer. *J. Fluid Mech.* **239**, 213.
- BERNAL, L. P. 1981 The Coherent Structure of Turbulent Mixing Layers I. Similarity of the Primary Vortex Structure. II. Secondary Streamwise Structure. *PhD thesis*. Calif. Inst. Tech.

- BERNAL, L. P. & ROSHKO, A. 1986 Streamwise Vortex Structure in Plane Mixing Layers. *J. Fluid Mech.* **170**, 499-525.
- BREIDENTHAL, R. 1981 Structure in Turbulent Mixing Layers and Wakes Using a Chemical Reaction. *J. Fluid Mech.* **109**, 1-24.
- BUELL, J. C. 1991 A Hybrid Numerical Method for Three-Dimensional Spatially-Developing Free-Shear Flows. *J. Comp. Phys.* **95**, 313-338.
- HUANG, L. S. & HO, C. M. 1990 Small-Scale Transition in a Plane Mixing Layer. *J. Fluid Mech.* **210**, 475-500.
- INOUE, O. 1992 Double-Frequency Forcing on Spatially Growing Mixing Layers. *J. Fluid Mech.* **234**, 553-581.
- MOSER, R. D. & ROGERS, M. M. 1993 The Three-Dimensional Evolution of a Plane Mixing Layer: Pairing and Transition to Turbulence. *J. Fluid Mech.* **247**, 275-320.
- NYGAARD, K. J. & GLEZER, A. 1991 Evolution of Streamwise Vortices and Generation of Small-Scale Motion in a Plane Mixing Layer. *J. Fluid Mech.* **231**, 257-301.
- RILEY, J. J. & METCALFE, R. W. 1980 Direct Numerical Simulation of a Perturbed Turbulent Mixing Layer. *AIAA Paper No. 80-0274*.
- ROGERS, M. M. & MOSER, R. D. 1992 The Three-Dimensional Evolution of a Plane Mixing Layer: The Kelvin-Helmholtz Rollup. *J. Fluid Mech.* **243**, 183-226.
- TUNG, C. H. 1992 Initial Streamwise Vorticity Formation in a Two-Stream Mixing Layer. *PhD Dissertation*, University of Houston.
- WINANT, C. D. & BROWAND, F. K. 1974 Vortex Pairing: The Mechanism of Turbulent Mixing-Layer Growth at Moderate Reynolds Number. *J. Fluid Mech.* **63**, 237-255.
- ZAMAN, K. B. M. Q. & HUSSEIN, A. K. M. F. 1981 Taylor Hypothesis and Large-Scale Coherent Structures. *J. Fluid Mech.* **112**, 379-396.
- ZHANG, Y. Q. & HO, C. M. 1985 The Mixing Layer Forced by Fundamental and Subharmonic. In *IUTAM Symp. on Laminar-Turbulent Transition*. Novosibirsk (ed V. Kozlov), Springer, 385-395.

## Sound radiation due to boundary layer transition

By Meng Wang

### 1. Motivation and objectives

This report describes progress made to date towards calculations of noise produced by the laminar-turbulence transition process in a low Mach number boundary layer formed on a rigid wall. The primary objectives of the study are to elucidate the physical mechanisms by which acoustic waves are generated, to clarify the roles of the fluctuating Reynolds stress and the viscous stress in the presence of a solid surface, and to determine the relative efficiency as a noise source of the various transition stages. In particular, we will examine the acoustic characteristics and directivity associated with three-dimensional instability waves, the detached high-shear layer, and turbulent spots following a laminar breakdown. Additionally, attention will be paid to the unsteady surface pressures during the transition, which provide a source of flow noise as well as a forcing function for wall vibration in both aeronautical and marine applications.

Interest in flow transition as a potential noise source stems from the transient nature of the transition process (Farabee *et al.* 1989). A clear understanding of the phenomena has so far been elusive due to fundamental difficulties associated with the strong nonlinear effects in the Navier-Stokes equation system. For this reason, rigorous analytical studies are mostly concerned with the early, linear stages of transition. For instance, Tam & Morris (1980) and Akylas & Toplosky (1986) examined the sound emitted by linear instability wave packets in a plane shear layer and a laminar boundary layer, respectively, by using multiple-scale perturbation techniques. The analysis of Haj-Hariri & Akylas (1986), although weakly nonlinear, is limited to slightly supercritical Reynolds numbers so that the unstable disturbance is only weakly amplified. Because of the small amplification rate for linear Tollmien-Schlichting (T-S) waves in a boundary layer, the associated sound field is typically of very small magnitude.

An alternate approach for studying flow induced sound is the theory due to Lighthill (1952), which provides a formal expression for the linear acoustic field driven by equivalent source terms representing the nonlinear turbulent fluctuations in a spatially concentrated region. The theory, also known as acoustic analogy, is essentially a rearrangement of the exact equations for mass and momentum conservation into a wave equation form. The driving terms on the right hand side are assumed known *a priori* rather than treated as part of the solution, thus simplifying the problem tremendously. For compact flows at low Mach number, this assumption can be viewed as a leading order approximation to the fully coupled acoustic-fluid dynamic system. By using the method of matched asymptotic expansions based on small Mach number, Crow (1970) shows that Lighthill's solution is adequate for sound emission from compact eddy regions. More recently, Mitchell

*et al.* (1993) tested Lighthill's theory and its extensions against solutions computed directly from the compressible Navier-Stokes equations, for the case of the merger of two co-rotating vortices. Excellent agreement has been obtained.

To predict the emitted sound using acoustic analogy theories, one requires knowledge of the source region, or the unsteady flow field. Traditionally, the source terms are approximated by empirical correlations based on experimental measurements. The rapid development in CFD applications in recent years has made it possible to compute the transitional and turbulent flow quantities directly by solving the full Navier-Stokes equations, thus allowing a more detailed assessment of the acoustic source. With the currently available supercomputers, direct numerical simulations (DNS) for controlled boundary layer transition can be carried out up to the laminar breakdown stage (see, for example, Zang and Hussaini 1990; Kleiser & Zang 1991; Fasel 1990). This has motivated us to undertake the present work, focusing on acoustic processes during boundary layer transition. By combining a DNS approach for the source region with modeling efforts based on Lighthill's theory, we attempt to reveal the sound production features during the transition process, in parameter ranges not accessible previously.

## 2. Accomplishments

### 2.1 Formulation

The continuity and momentum equations for a compressible flow above a flat surface can be combined to generate, in dimensionless form,

$$\left[ \left( \frac{\partial}{\partial t} + M \frac{\partial}{\partial X_1} \right)^2 - \frac{\partial^2}{\partial X_j \partial X_j} \right] \rho = \frac{\partial^2 \rho}{\partial x_1^2} - 2 \frac{\partial^2 (\rho u_j)}{\partial x_1 \partial x_j} + \frac{\partial^2 T_{ij}}{\partial x_i \partial x_j}, \quad (1)$$

where

$$T_{ij} = \rho u_i u_j + \frac{\delta_{ij}}{M^2} \left( \frac{p}{\gamma} - \rho \right) - \tau_{ij} \quad (2)$$

is called Lighthill's stress tensor. It contains the Reynolds stress (the term is used in a generalized sense since  $\rho u_i u_j$  contains both mean and fluctuating velocities), deviation from isentropy (the second term), and the viscous part of the Stokes stress tensor

$$\tau_{ij} = \frac{1}{Re} \left( \frac{\partial u_i}{\partial x_j} + \frac{\partial u_j}{\partial x_i} - \frac{2}{3} \delta_{ij} \frac{\partial u_k}{\partial x_k} \right). \quad (3)$$

In (1)–(3), the velocity components and the thermodynamic variables are nondimensionalized with respect to the undisturbed free-stream values  $U'_\infty$ ,  $p'_\infty$ ,  $\rho'_\infty$ , and  $T'_\infty$ , respectively. The spatial variables are defined by  $x_i = x'_i/L'_f$ , where  $L'_f$  is a characteristic length scale of the flow field such as the boundary layer displacement thickness and  $X_i = M x_i$ . The latter, resembling the outer scale in matched asymptotic expansions, is introduced here to facilitate the description of far field acoustic propagation. We will be using  $x_i$  and  $X_i$  simultaneously to represent the near-field source region and the far-field observation points, respectively, bearing in mind that

they are not independent of one another. The nondimensional time,  $t = t'U'_\infty/L'_f$ , is the same for both acoustic and fluid dynamic disturbances. The Mach number is defined in terms of the equilibrium sound speed in the free stream,  $M = U'_\infty/c'_\infty$ ;  $c'_\infty = (\gamma p'_\infty/\rho'_\infty)^{1/2}$ , and the Reynolds number is defined as  $Re = U'_\infty L'_f/\nu'$ .

Eqn. (1) is equivalent to a convective wave equation for a medium moving uniformly along the  $X_1$  axis, if the right hand side is viewed as distributed source terms. In the spirit of Lighthill's theory, we treat the right hand side as pure fluid dynamic quantities confined within the thin boundary layer and decoupled from acoustic disturbances, on the basis that the latter are much smaller in magnitude. Thus, the flow noise issue is reduced to a problem of finding the solution to (1) under the appropriate boundary conditions once the flow field is known.

For a low Mach number flow, the proper scales for the thermodynamic variables in the boundary layer are

$$p = 1 + M^2 \tilde{p}, \quad \rho = 1 + M^2 \tilde{\rho}, \quad T = 1 + M^2 \tilde{T}. \quad (4)$$

It can be easily shown that the governing equations for an ideal gas have the following form:

$$\frac{\partial u_j}{\partial x_j} = O(M^2), \quad (5)$$

$$\frac{\partial u_i}{\partial t} + u_j \frac{\partial u_i}{\partial x_j} = -\frac{1}{\gamma} \frac{\partial \tilde{p}}{\partial x_i} + \frac{1}{Re} \frac{\partial^2 u_i}{\partial x_j \partial x_j} + O(M^2), \quad (6)$$

$$\begin{aligned} \frac{\partial \tilde{s}}{\partial t} + u_j \frac{\partial \tilde{s}}{\partial x_j} &= \frac{1}{Pr Re} \frac{\partial^2 \tilde{s}}{\partial x_j \partial x_j} + \frac{1}{Pr Re} \left( \frac{\gamma - 1}{\gamma} \right) \frac{\partial^2 \tilde{p}}{\partial x_j \partial x_j} \\ &+ \frac{\gamma - 1}{Re} \Phi + O(M^2), \end{aligned} \quad (7)$$

where the entropy  $\tilde{s} = \tilde{p}/\gamma - \tilde{\rho}$  is exactly the second term in Lighthill's stress tensor. Eqns. (5)–(7) suggest that for low Mach number flows, one only needs to solve the incompressible version of the governing equations in order to evaluate the acoustic source terms with reasonable accuracy. In fact, the first two terms in the forcing function in (1) can be ignored because they are of  $O(M^2)$  (cf. (4) and (5)). The density in the Reynolds stress terms in (2) can be replaced by 1. The viscous stress terms in  $T_{ij}$ , on the other hand, must be retained at the moment even though they appear to be  $O(M^2)$ . As will become clear later, viscous stress tends to form dipoles on the solid wall that are efficient acoustic radiators.

The effect of entropy change on sound production deserves special comments. Although it is customary to ignore it entirely in the application of Lighthill's theory, there is no clear justification for doing so in a transitional boundary layer, based upon the above analysis. Eqn. (7) implies that the entropy production can be quantified by solving a passive-scalar type of equation together with the incompressible Navier-Stokes equations, rather than resorting to a fully compressible code. It would be of interest to pursue this issue in a future endeavor. In the present work, however, we will focus on the Reynolds stress and viscous stress contributions to sound production, assuming that the entropy effect is relatively small.

If the  $O(M)$  effect of bulk flow convection is ignored, (1) becomes the Lighthill equation in a uniform acoustic medium at rest. Its solution in the upper half space  $X_2 \geq 0$  can be written as (Crighton *et al.* 1992)

$$\begin{aligned} 4\pi[\rho(\vec{X}, t) - 1] = & M^5 \frac{\partial^2}{\partial X_i \partial X_j} \int_{V_0} \frac{T_{ij}(\vec{y}, t - |\vec{X} - M\vec{y}|)}{|\vec{X} - M\vec{y}|} dV(\vec{y}) \\ & + M^5 \frac{\partial^2}{\partial X_i^* \partial X_j^*} \int_{V_0} \frac{T_{ij}(\vec{y}, t - |\vec{X}^* - M\vec{y}|)}{|\vec{X}^* - M\vec{y}|} dV(\vec{y}) \\ & - 2M^4 \frac{\partial}{\partial X_\alpha} \int_{S_0} \frac{\tau_{\alpha 2}(\vec{y}, t - |\vec{X} - M\vec{y}|)}{|\vec{X} - M\vec{y}|} dS(\vec{y}), \end{aligned} \quad (8)$$

where  $\vec{X}^* = (X_1, -X_2, X_3)$  is the image of the position  $\vec{X}$  in the rigid surface  $X_2 = 0$ , and unlike indices  $i$  and  $j$ ,  $\alpha$  takes the values of 1 and 3 only. The volume integrations are to be carried out throughout the entire source region, and the surface integral should be evaluated on the wall. The three terms on the right hand side of (8) represent, respectively, a volume distribution of acoustic quadrupoles, reflection on the rigid surface, and a surface distribution of viscous dipoles. It should be noted that the dipole term has a coefficient  $O(M^{-1})$  times larger than that for the quadrupole terms, and hence it is not necessarily negligible despite the apparent smallness of  $\tau_{ij}$ .

Under the assumption that the unsteady flow region is small in comparison to the emitted acoustic wavelengths (compact source), (8) can be approximated by

$$\begin{aligned} 4\pi[\rho(\vec{X}, t) - 1] = & M^5 \frac{X_i X_j + X_i^* X_j^*}{|\vec{X}|^3} \left[ \frac{\partial^2}{\partial t^2} Q_{ij}(t - |\vec{X}|) \right. \\ & \left. + \frac{3}{|\vec{X}|} \left( 1 + \frac{\partial}{\partial t} \right) Q_{ij}(t - |\vec{X}|) \right] \\ & + 2M^4 \frac{X_\alpha}{|\vec{X}|^2} \left[ \frac{\partial}{\partial t} R_\alpha(t - |\vec{X}|) + \frac{1}{|\vec{X}|} R_\alpha(t - |\vec{X}|) \right] \end{aligned} \quad (9)$$

The quadrupole and dipole sources are

$$Q_{ij}(t) = \int_{V_0} T_{ij}(\vec{y}, t) dV(\vec{y}), \quad R_\alpha(t) = \int_{S_0} \tau_{\alpha 2}(\vec{y}, t) dS(\vec{y}). \quad (10)$$

They do not contain the retarded potential as in (8) and are, therefore, straightforward to evaluate. In the far field,  $|\vec{X}| \gg 1$ , only the first term in the two square brackets in (9) are of importance.

It is sometimes of interest to calculate the sound field caused by a two-dimensional boundary layer. A two-dimensional version of (8)–(10) has been derived by the method of descent, *i.e.*, by integrating (8) along the  $Y_3$  axis from  $-\infty$  to  $+\infty$ ,

noting that the source properties are independent of  $Y_3$ . For brevity, only the far field solution for a compact source is presented here:

$$\begin{aligned} \pi[\rho(\vec{X}, t) - 1] = & M^4 \frac{X_1^2}{|\vec{X}|^2} \int_0^\infty \frac{1}{\cosh^2(\xi)} \frac{\partial^2}{\partial t^2} Q_{11} \left( t - |\vec{X}| \cosh(\xi) \right) d\xi \\ & + M^4 \frac{X_2^2}{|\vec{X}|^2} \int_0^\infty \frac{1}{\cosh^2(\xi)} \frac{\partial^2}{\partial t^2} Q_{22} \left( t - |\vec{X}| \cosh(\xi) \right) d\xi \\ & + M^3 \frac{X_1}{|\vec{X}|} \int_0^\infty \frac{1}{\cosh(\xi)} \frac{\partial}{\partial t} R_1 \left( t - |\vec{X}| \cosh(\xi) \right) d\xi. \end{aligned} \quad (11)$$

The quantities  $Q_{11}$ ,  $Q_{22}$ , and  $R_1$  are surface and line integrals defined as

$$Q_{ij}(t) = \int_{S_0} T_{ij}(\vec{y}, t) dS(\vec{y}), \quad R_1(t) = \int_{C_0} \tau_{12}(\vec{y}, t) dC(\vec{y}). \quad (12)$$

A similar solution without the solid boundary effect has been obtained by Mitchell *et al.* (1993), using a Green's function approach.

## 2.2 Numerical method and boundary conditions

In order to evaluate the acoustic source terms associated with boundary layer transition, (5) and (6) are solved using an incompressible Navier-Stokes solver developed by Le and Moin (1991). The equations are discretized using finite difference on a staggered grid, with uniform grid spacing in the streamwise ( $x_1$ ) and spanwise ( $x_3$ ) directions. In the wall-normal direction ( $x_2$ ), non-uniform mesh is employed to allow grid refinement near the plate. Time advancement is of predictor-corrector type combined with a fractional step method. Each time step treats the convective terms explicitly and the viscous terms implicitly. The pressure is calculated by solving the Poisson equation. The numerical scheme is second order accurate in both space and time.

The domain of integration consists of a rectangular box that covers 5–10 streamwise Tollmien-Schlichting wavelengths in  $x_1$  and one spanwise wavelength in  $x_3$ . The distance from the wall to the free-stream boundary is equal to 20 times the inflow displacement thickness. A no-slip boundary condition is applied at the solid wall. At the free-stream boundary, a normal velocity distribution based on the Blasius solution is imposed; in addition, the vorticity is assumed to be negligible there. In the  $x_3$  direction, periodicity is assumed of all dependent variables.

The inflow boundary conditions for the simulations are of the form

$$\begin{aligned} u_i(x_1 = 0) = \text{Real} \Big\{ & u_i^B(x_2) + \epsilon^{2D} u_i^{2D}(x_2) e^{i\theta} e^{-i\beta t} \\ & + \frac{1}{2} \epsilon^{3D} u_i^{3D+}(x_2) e^{i[(\alpha \sin \phi) x_3 - \beta t]} \\ & + \frac{1}{2} \epsilon^{3D} u_i^{3D-}(x_2) e^{i[-(\alpha \sin \phi) x_3 - \beta t]} \Big\} \end{aligned} \quad (13)$$

where  $u_i^B(x_2)$  represents the Blasius solution for a 2-D boundary layer.  $u_i^{2D}(x_2)$  and  $u_i^{3D\pm}(x_2)$  are the least stable linear modes of the Orr-Sommerfeld (Squire) equation for given frequency  $\beta$  and oblique angle  $\phi$ . The eigenfunctions are normalized such that the maximum streamwise velocity has a magnitude of 1. Since we are primarily interested in laminar breakdown of the fundamental type, the same excitation frequency is applied to both the 2-D and 3-D disturbances. For 2-D calculations, one simply ignores the 3-D terms in (13).

At the outflow boundary, an ideal boundary condition must allow smooth passage of disturbance structures while maintaining the correct mean velocity profile. The convective boundary condition

$$\frac{\partial u_i}{\partial t} + U \frac{\partial u_i}{\partial x_1} = 0 \quad (14)$$

is frequently used for this purpose (see Pauley *et al.* (1988) for an extensive discussion), where  $U$  is the mean exit velocity. When tested for the case of 2-D T-S waves, however, the normal velocity  $u_2$  exhibits point-to-point oscillations in both mean and disturbance quantities (Fig. 1a). In addition, the mean velocity deviates significantly from the true value (the top curve in Fig. 1b) near the exit boundary  $x_1 = 50$ . Errors for the streamwise velocity  $u_1$  have the same absolute magnitude as for  $u_2$ , but are less prominent in relative terms. These errors occur because of unphysical boundary layers formed along the exit plane, which are not resolved properly on the given grid (Johansson 1993).

An improvement has been made by replacing (14) with

$$\frac{\partial u_i}{\partial t} + U_j \frac{\partial u_i}{\partial x_j} = U_j \frac{\partial u_i^B}{\partial x_j} \quad (15)$$

where  $u_i^B$  is the Blasius solution and  $U_j$  denotes the characteristic velocity at the exit plane.  $U_j = (1, 0, 0)$  for calculations presented in the present work. Eqn. (15) ensures that the steady solution converges to the laminar velocity profile while disturbances are allowed to be convected out of the domain. For turbulence simulations,  $u_i^B$  should be replaced by the appropriate mean profiles, perhaps through an iterative procedure.

One way to remove the wiggles in the disturbance velocities is by grid refinement near the outflow boundary so that the unphysical boundary layer can be resolved. This is, however, expensive and often impractical. The method adopted in this study is to employ a small buffer zone consisting of 5 to 10 grid points next to the exit boundary. In this zone, the velocity field is filtered at each integration step using an explicit, three-point low pass filter. As can be observed in Fig. 1b, this expedient approach removes the wiggles quite effectively. Since the buffer zone is very small and located in the downstream direction, its impact on the overall computational solution is expected to be negligible.

The time-dependent code is shown to be capable of producing and maintaining steady state solutions that are in excellent agreement with the Blasius solution. It



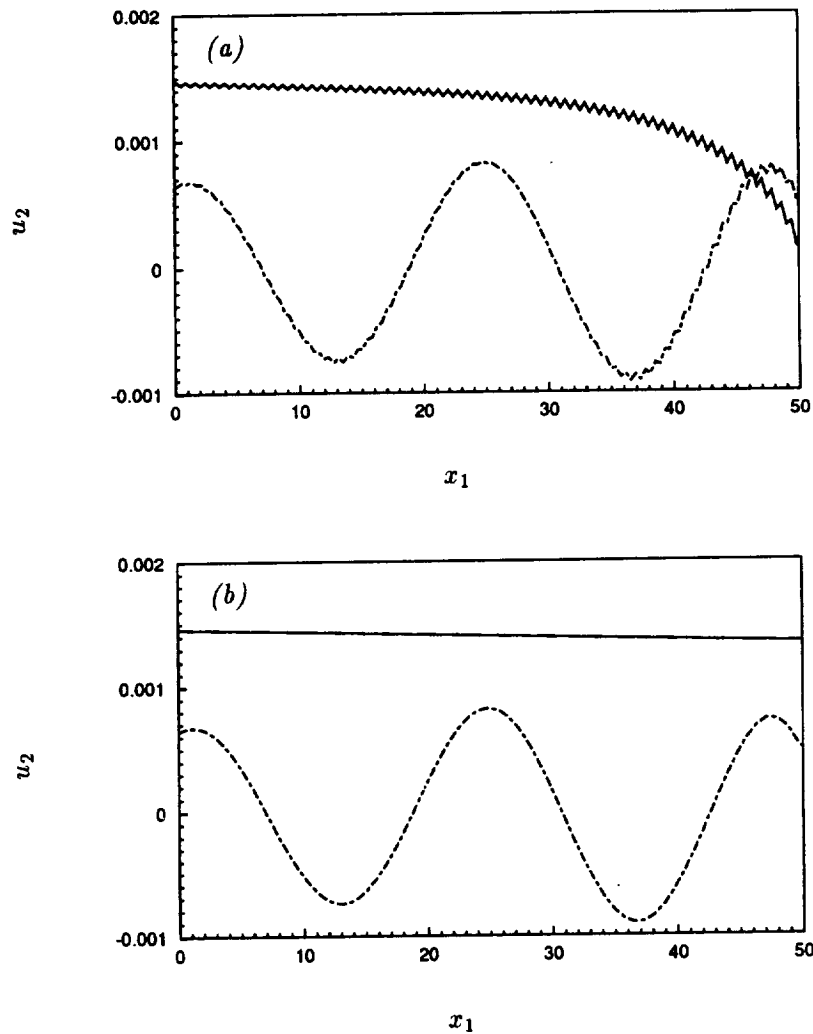


FIGURE 1. Streamwise distribution of mean (—) and disturbance (---) normal velocities at  $x_2 = 3.1$ , caused by T-S waves in a Blasius boundary layer. (a) is obtained using outflow condition (14), and (b) is obtained using (15) with a small buffer zone. The inlet Reynolds number  $Re_0^* = 1000$ .

has also been subjected to critical tests for linearly growing, small, two-dimensional disturbances. The computational results agree well with linear stability theory results in terms of both the eigenmode shape and the spatial amplification rate.

### 2.3 Preliminary results

#### 2.3.1 2-D Tollmien-Schlichting waves

The first numerical experiment conducted deals with the sound field produced by

spatially amplifying, two-dimensional Tollmien-Schlichting waves. A 2-D version of (5) and (6) is solved using  $514 \times 66$  grid points in a domain ( $0 \leq x_1 \leq 200$ ,  $0 \leq x_2 \leq 20$ ), where the spatial coordinates are nondimensionalized relative to the displacement thickness at the inflow boundary. The inflow Reynolds number based on the displacement thickness is  $Re_0^* = 1000$ .

After a steady flow field has been established, inflow velocities are disturbed at the least stable frequency corresponding to the 2-D eigenmodes described in (13). The T-S wave train so created exhibits linear or nonlinear characteristics, depending on the amplitude of boundary excitation, as demonstrated in Fig. 2. One notices that, in both cases, there is no appreciable distortion in the T-S waveform near the inflow/outflow boundary.

An attempt has been made to deduce the far-field sound emitted by the amplification and/or nonlinearization of T-S waves in the boundary layer. If the flow Mach number is very small (say, 0.01, as in marine applications), the computational domain can be considered as a compact source, and (11) is valid. Numerical integrations of (11) and (12) show basically harmonic density variations at the T-S wave frequency at a given far-field point  $\vec{X}$ . However, it is discovered that the amplitude of the sound signal alters dramatically when the front of the T-S wave train crosses the outflow boundary. Further numerical tests verify the existence of a strong, artificial boundary effect on the calculated sound level, which masks the true sound of flow instability. This arises not because of the numerical boundary condition treatment for the flow region, but rather due to the fact that the entire T-S wave train is not included in the finite computational domain. Based on (11), the calculated sound signal is determined by the time derivatives of the total Reynolds stress and surface viscous stress in the source region. In the present case since the source region has artificially defined open boundaries, the time variations of  $Q_{ij}$  and  $R_1$  (cf. (12)) are caused primarily by T-S waves crossing the boundaries, rather than by their slow amplification within the region.

The situation is best illustrated by considering an isolated 2-D wave packet, instead of the entire wave series, as it traverses the source region. The wave packet is generated by multiplying the 2-D mode in (13) by  $\exp[-((t - 210)/70)^2]$ . The time history of the longitudinal quadrupole  $\ddot{Q}_{11}$  (the double dots denote second time-derivative) computed from (12) is depicted in Fig. 3, which shows two distinct regimes of oscillations, one as the packet enters from the upstream boundary and the other as it exits at downstream. The effect of wave amplification and spreading is represented by the relatively quiet regime in-between. Similar behavior has been observed for  $\ddot{Q}_{22}$  and  $\dot{R}_1$ . The unphysical boundary effect on sound calculation is probably exacerbated because of the compact source assumption. Non-compact sources (larger  $M$ ) are acoustically more efficient, and the boundary effect is expected to become less predominant. Nonetheless, an accurate assessment of T-S wave generated sound is still impossible unless those artificial boundary effects are eliminated or adequately accounted for.

In view of the small effect of T-S waves on sound radiation, we decide to concentrate on a practically more important issue – the sound generated by a local

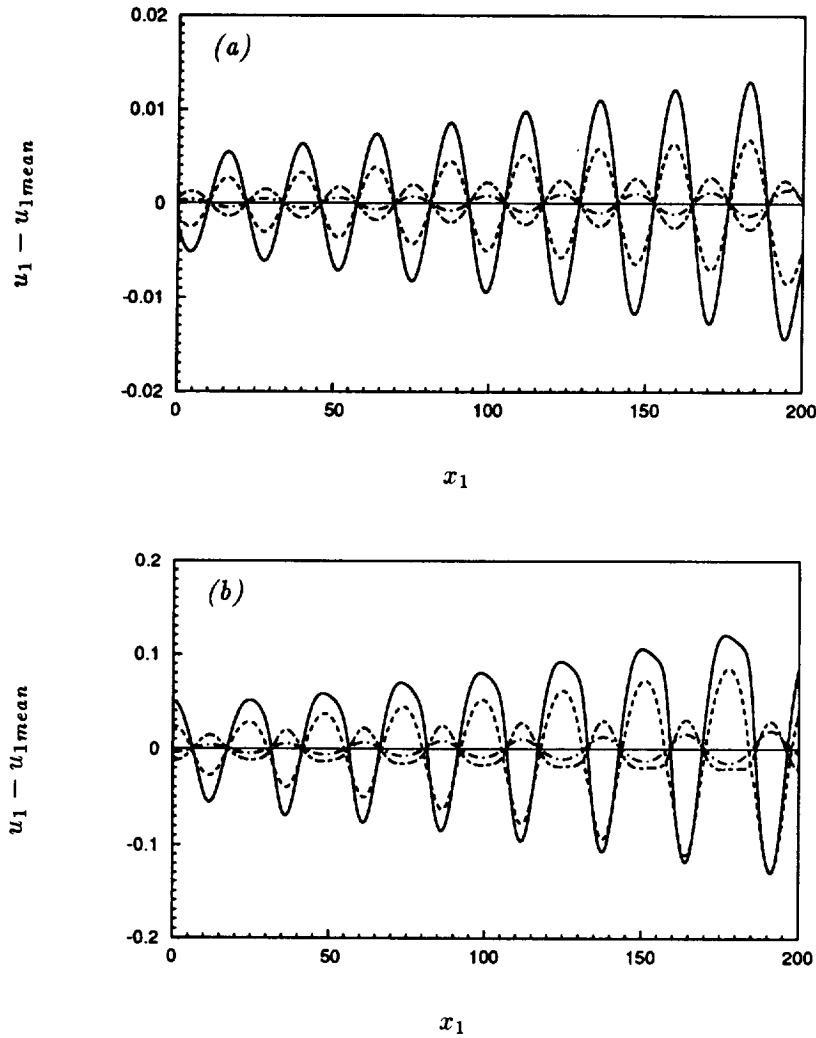


FIGURE 2. Streamwise disturbance velocity ( $u_1 - u_{1mean}$ ) as a function of  $x_1$  at four  $x_2$ -locations (—  $x_2 = 0.44$ , ----  $x_2 = 1.35$ , -.-  $x_2 = 3.02$ , —·—  $x_2 = 7.87$ ) in a Blasius boundary layer. The T-S waves are caused by a 2-D upstream excitation given in (13). (a)  $\epsilon^{2D} = 0.005$ , and (b)  $\epsilon^{2D} = 0.05$ .

breakdown of the laminar boundary layer.

### 2.3.2 3-D laminar breakdown

Simulations are under way for the three-dimensional development of boundary layer instability that leads to laminar breakdown of the fundamental type. In order to enhance grid resolution as well as to isolate the true acoustic source from boundary-induced artifacts, the eigenmode excitation described in (13) is multiplied by  $\exp[-((t-80)/40)^4]$ . This creates a perturbed flow region of limited streamwise

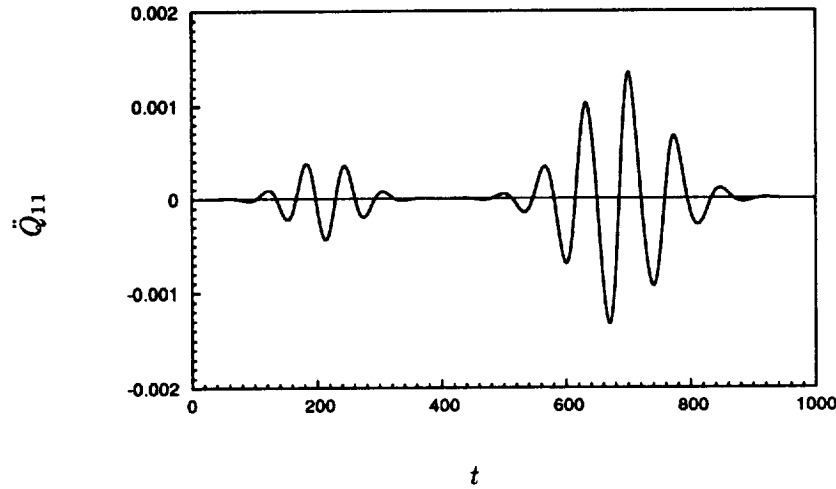


FIGURE 3. Longitudinal quadrupole  $\ddot{Q}_{11}$  calculated using (12) for the case of a 2-D wave packet crossing the source region. The wave packet is created by disturbing the upstream boundary for a short time duration.  $\epsilon^{2D} = 0.01$  and  $\epsilon^{3D} = 0$ .

extent, completely enclosed within the computational domain. Numerical experiments show that the isolated wave packet evolves in a way similar to that for regular T-S wave series in forced transition, at least up to the multiple spike stage.

The following parameters are employed in the simulation:  $Re_0^* = 1000$ ,  $\epsilon^{2D} = 0.025$ ,  $\epsilon^{3D} = 0.01$ ,  $\theta = 0$ ,  $\phi = \pi/4$ , and  $\beta = 0.094$ . The latter corresponds to the least stable frequency for 2-D T-S waves at inflow. Computations start out on a  $514 \times 98 \times 66$  grid covering a physical domain defined in  $0 \leq x_1 \leq 180$ ,  $0 \leq x_2 \leq 20$  and  $0 \leq x_3 \leq \lambda_z$ , where  $\lambda_z \approx 25.95$  is the spanwise wavelength. As a detached high shear layer appears in the peak  $x_1$ - $x_2$  plane (cf. Fig. 4a), the spatial resolution demand becomes increasingly severe for the unstable region as the secondary instability intensifies and higher instabilities develop. Meanwhile, the flow field for  $x_1 < 50$  has become basically steady after the passage of the disturbance structure. Consequently, the inflow boundary is moved from  $x_1 = 0$  to 50, and the solution is interpolated onto a refined grid of  $1026 \times 98 \times 130$ .

Results of the ensuing computation are exemplified in Figs. 4b-4d, which, like Fig. 4a, plot the spanwise vorticity contours in the peak plane. The spatial resolution requires further improvement. Nonetheless, these plots capture the essential features of the shear layer roll-up and the formation of one, two, and multiple spikes as time progresses.

Figs. 5 depicts time-variations of the quadrupole acoustic source terms  $\ddot{Q}_{ij}$  calculated from (10), again under the compact source assumption. In the calculation, Lighthill's stress tensor is approximated by the Reynolds stress only; the viscous stress contribution, computed separately, is found to be a factor of  $10^{-3}$  smaller. The time instants corresponding to the four snapshots depicted in Fig. 4 are marked

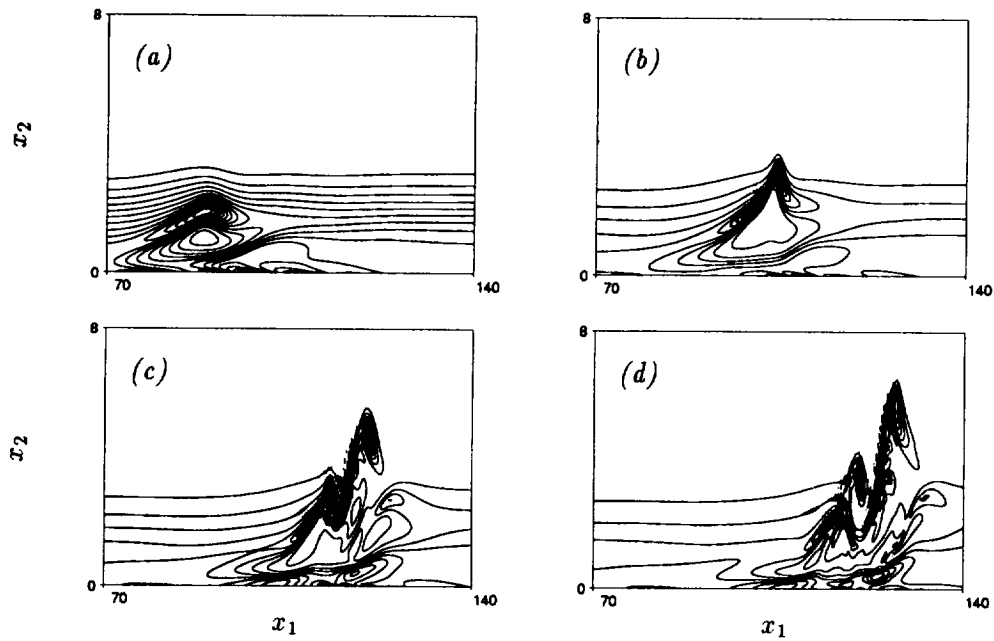


FIGURE 4. Instantaneous spanwise vorticity contours in the peak  $x_1$ - $x_2$  plane during breakdown of high-shear layer. (a)  $t = 279$ ; (b)  $t = 305$ ; (c)  $t = 326$ ; and (d)  $t = 335$ .

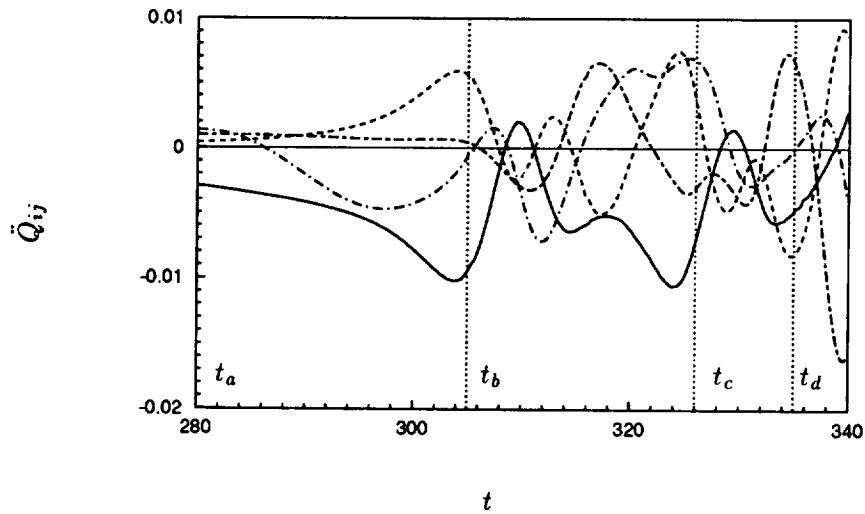


FIGURE 5. Quadrupole acoustic source terms (—  $\ddot{Q}_{11}$ , ----  $\ddot{Q}_{22}$ , -.-  $\ddot{Q}_{33}$ , — —  $\ddot{Q}_{12}$ ) calculated using (10) during high-shear layer breakdown. The time marks  $t_a$ ,  $t_b$ ,  $t_c$  and  $t_d$  correspond to the four snapshots in Fig. 4.

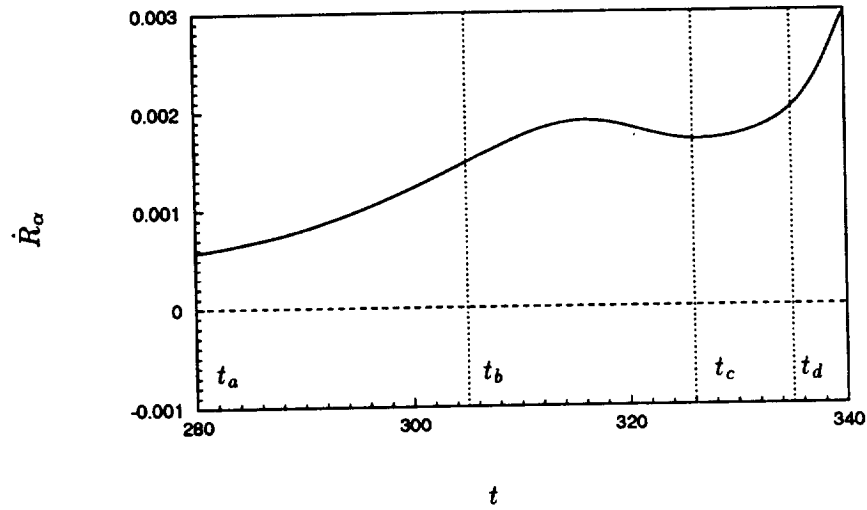


FIGURE 6. Surface dipole source (—  $\dot{R}_1$ , ----  $\dot{R}_3$ ) calculated using (10) during high-shear layer breakdown. The time marks  $t_a$ ,  $t_b$ ,  $t_c$  and  $t_d$  correspond to the four snapshots in Fig. 4.

as  $t_a$ ,  $t_b$ ,  $t_c$ , and  $t_d$  in Fig. 5 for clear comparison. Due to symmetry with respect to the peak plane,  $\dot{Q}_{13}$  and  $\dot{Q}_{23}$  vanish. The other four source terms are seen to develop oscillations with higher frequency components relative to the basic T-S wave frequency (the T-S wave period  $\approx 66.8$ ). Apparently, these higher harmonics are associated with the roll-up of the detached high-shear layer. During the same time period, the surface dipole  $\dot{R}_1$  calculated from (10) is still dominated by low frequency behavior, as demonstrated in Fig. 6. However, it is expected to rise in both frequency and amplitude as the shear layer near the wall intensifies. The other dipole,  $\dot{R}_3$ , is identically zero again due to symmetry.

Because of insufficient data and relatively poor resolution for the source flow simulation at the present stage, a more quantitative analysis of acoustic implications is deferred to future work.

### 3. Future plans

The first priority is to improve the accuracy of the source field computation by grid refinement and optimization so that reliable results for more advanced transition stages can be obtained. A nonuniform mesh in the streamwise direction should allow much better resolution in the region of intense shear without increasing the total number of grid points in that direction. As pointed out by Zang *et al.* (1989), resolution requirements for numerical simulations of transition are extremely severe, and inadequate resolution may result in less intense detached shear layers and premature roll-up.

Once an accurate source field is obtained, attention will be focused upon the radiated acoustic waves. We will analyze the sound characteristics and directivity

associated with specific source mechanisms during boundary layer transition, and we will identify the dominant contributors to the radiated sound field. The analysis will not be restricted to compact sources; a more general formulation based on (8) should be used to investigate the effect of non-compact source distributions.

In the long run, it would be of interest to study the sound of turbulent spots and to compare the results with those due to laminar breakdown. A more difficult extension of this work would be to include the coupling between the fluid motion and the vibration of an elastic plate. Such flow-structure interactions are often the dominant source of sound production and are, therefore, of great practical importance.

### Acknowledgements

This work was produced in collaboration with Prof. S. Lele and Prof. P. Moin. We would like to thank Y. Na for assistance with the Navier-Stokes code, and S. Collis for providing the Orr-Sommerfeld eigensolver. Throughout this work, we have benefited from discussions with T. Colonius and B. Mitchell of the aeroacoustics group at Stanford.

### REFERENCES

- AKYLAS, T. R. & TOPLOSKY, N. 1986 The sound field of a Tollmien-Schlichting wave. *Phys. Fluids*. **29**, 685–689.
- CRIGHTON, D. G., DOWLING, A. P., FLOWCS WILLIAMS, J. E., HECKL, M., & LEPPINGTON, F. G. 1992 *Modern Methods in Analytical Acoustics*, Chapt. 16. Springer-Verlag.
- CROW, S. C. 1970 Aerodynamic sound emission as a singular perturbation problem. *Stud. Appl. Math.* **49**, 21–44.
- FARABEE, T. M., HANSEN, R. J., & KELTIE, R. F. (eds.) 1989 *Flow-induced Noise due to Laminar-Turbulence Transition Process*, Symposium for ASME Winter Annual Meeting, San Francisco, 1989.
- FASEL, H. F. 1990 Numerical simulation of instability and transition in boundary layer flows. In *Laminar-Turbulent Transition*. IUTAM Symposium, Toulouse, France, 1989 (Arnal, D. & Michel, R. Eds.), Springer-Verlag.
- HAI-HARIRI, H. & AKYLAS, T. R. 1986 Sound radiation by instability wavepackets in a boundary layer. *Stud. Appl. Math.* **75**, 57–76.
- JOHANSSON, B. C. V. 1993 Boundary conditions for open boundaries for the incompressible Navier-Stokes equation. *J. Comp. Phys.* **105**, 233–251.
- KLEISER, L. & ZANG, T. A. 1991 Numerical simulations of transition in wall-bounded shear flows. *Ann. Rev. Fluid Mech.* **23**, 495–537.
- LE, H. & MOIN, P. 1991 An improvement of fractional step methods for the incompressible Navier-Stokes equations. *J. Comp. Phys.* **92**, 369–379.
- LIGHTHILL, M. J. 1952 On sound generated aerodynamically; I. General theory. *Proc. Roy. Soc. London Ser. A*. **211**, 564–587.

- MITCHELL, B. E., LELE, S. K., & MOIN, P. 1993 Direct computation of the sound from a compressible co-rotating vortex pair. *J. Fluid Mech.* Accepted for publication.
- PAULEY, L. L., MOIN, P., & REYNOLDS, W. C. 1988 *A Numerical Study of Unsteady Laminar Boundary Layer Separation*, Report No. TF-34, Dept. of Mech. Engr., Stanford University.
- TAM, C. K. W. & MORRIS, P. J. 1980 The radiation of sound by the instability waves of a compressible plane turbulent shear layer. *J. Fluid Mech.* **98**, 349–381.
- ZANG, T. A. & HUSSAINI, M. Y. 1990 Multiple paths to subharmonic laminar breakdown in a boundary layer. *Phys. Rev. Lett.* **64**, 641–644.
- ZANG, T. A., KRIST, S. E. & HUSSAINI, M. Y. 1989 Resolution requirements for numerical simulations of transition. *J. Sci. Comp.* **4**, 197–217.



201666  
16  
N94-26164

## Direct simulation of isothermal-wall supersonic channel flow

By Gary N. Coleman

### 1. Motivation, objectives, and approach

The motivation for this work is the fact that in turbulent flows where compressibility effects are important, they are often poorly understood. A few examples of such flows are those associated with astrophysical phenomena and those found in combustion chambers, supersonic diffusers and nozzles, and over high-speed airfoils. For this project, we are primarily interested in compressibility effects near solid surfaces. Our main objective is an improved understanding of the fundamentals of compressible wall-bounded turbulence, which can in turn be used to cast light upon modeling concepts such as the Morkovin hypothesis and the Van Driest transformation (Bradshaw 1977).

To this end, we have performed a direct numerical simulation (DNS) study of supersonic turbulent flow in a plane channel with constant-temperature walls. All of the relevant spatial and temporal scales are resolved so that no subgrid scale or turbulence model is necessary. The channel geometry was chosen so that finite Mach number effects can be isolated by comparing the present results to well-established incompressible channel data (Kim, Moin & Moser 1987). Here the fluid is assumed to be an ideal gas with constant specific heats, constant Prandtl number, and power-law temperature-dependent viscosity. Isothermal-wall boundary conditions are imposed so that a statistically stationary state may be obtained. The flow is driven by a uniform (in space) body force (rather than a mean pressure gradient) to preserve streamwise homogeneity, with the body force defined so that the total mass flux is constant.

The variables are nondimensionalized by the wall temperature, the channel half-width, the bulk-averaged ("mixed-mean") density, and the bulk velocity, such that  $\frac{1}{2} \int_{-1}^{+1} \bar{\rho} dy = 1$  and  $\frac{1}{2} \int_{-1}^{+1} \bar{\rho} u dy = 1$ , where the channel walls are at  $y = \pm 1$ . All variables are henceforth assumed to be dimensionless, with  $\rho$  representing the density,  $u = u_1$  the streamwise velocity,  $(x, y, z) = (x_1, x_2, x_3)$  respectively the streamwise, wall-normal, and spanwise coordinates, and an overbar defines an average over time and streamwise and spanwise directions. The nondimensional governing equations are:

$$\frac{\partial \rho}{\partial t} + u_j \frac{\partial \rho}{\partial x_j} = -\rho \frac{\partial u_j}{\partial x_j}, \quad (1)$$

$$\frac{\partial u_i}{\partial t} + u_j \frac{\partial u_i}{\partial x_j} = -\frac{1}{\gamma M^2} \frac{\partial T}{\partial x_i} - \frac{T}{\gamma M^2 \rho} \frac{\partial \rho}{\partial x_i} + \frac{1}{Re} \frac{\partial \tau_{ij}}{\partial x_j} + \Phi_i, \quad (2)$$

$$\frac{\partial T}{\partial t} + u_j \frac{\partial T}{\partial x_j} = -(\gamma - 1)T \frac{\partial u_j}{\partial x_j} + \frac{\gamma(\gamma - 1)M^2}{Re} \frac{\tau_{ij}}{\rho} \frac{\partial u_i}{\partial x_j} - \frac{\gamma}{Re Pr} \frac{\partial q_j}{\partial x_j} + S, \quad (3)$$

where

$$\tau_{ij} = \mu \left( \frac{\partial u_i}{\partial x_j} + \frac{\partial u_j}{\partial x_i} - \frac{2}{3} \delta_{ij} \frac{\partial u_l}{\partial x_l} \right) \quad \text{and} \quad q_j = -\mu \frac{\partial T}{\partial x_j}.$$

The pressure is normalized by the bulk density and bulk velocity, so the ideal gas law is  $p = \rho T / \gamma M^2$ . The body force term  $\Phi_i$  is nonzero only for  $i = 1$ . The purpose of  $S$ , the source/sink term in (3), is explained below. Equations (1) – (3) are to be solved numerically subject to the isothermal, no-slip boundary conditions,

$$T = 1 \quad \text{and} \quad \mathbf{u} = 0 \quad \text{at} \quad y = \pm 1. \quad (4)$$

We therefore have as relevant nondimensional parameters (i) a Mach number,  $M$ , based on the bulk velocity and wall sound speed; (ii) a Reynolds number,  $Re$ , based on the bulk density, bulk velocity, channel halfwidth, and wall viscosity; (iii) the Prandtl number,  $Pr$ ; (iv) the ratio of specific heats,  $\gamma$ ; and (v) the viscosity exponent,  $n$ , where the dynamic viscosity  $\mu \propto T^n$ . These 5 parameters are used to define the various DNS runs. But besides choosing appropriate values for the “physical” parameters, we will also artificially introduce another – to allow us to differentiate between mean and fluctuation compressibility effects.

The Mach number appears in the energy equation (3) in the term that represents the irreversible loss of kinetic energy into heat. Following Buell (1991), we interpret (in our simulations) the actual Mach number  $M$  in (2) and the “dissipation Mach number”  $M_d$  in (3) as separate parameters. By setting  $M_d$  to values different from  $M$  in the DNS, we produce an effective heat source/sink  $S$  in (3) which is given by

$$S = (M_d^2 - M^2) \frac{\gamma(\gamma - 1)}{Re} \frac{\tau_{ij}}{\rho} \frac{\partial u_i}{\partial x_j}. \quad (5)$$

Consequently, we can consider cases with different mean temperature profiles (and thus different mean property variations) at the same  $M$ . Results from these “unphysical”  $M \neq M_d$  DNS runs can, therefore, be used to determine the relative importance of turbulent-fluctuation and variable-property influences at a given Mach number.

Three DNS cases will be discussed, with the Mach number ranging from  $M = 1.5$  to 3. All the runs share the same Prandtl number, specific heat ratio, and viscosity exponent ( $Pr = 0.7$ ,  $\gamma = 1.4$  and  $n = 0.7$ ), while the Reynolds number (for reasons given below) is either 3000 or 4880. A summary of the parameters is listed in table 1. Cases denoted by a single letter (A and B) in table 1 represent “physical” simulations for which  $M_d = M$ . For the  $M_d \neq M$  run, Case AX,  $M = 1.5$  and  $M_d = 0$ . Since the temperature fields in both the physical and unphysical runs depend almost exclusively on  $M_d$  (Coleman *et al.* 1993), this parameter combination will produce the behavior of the “extra” source/sink  $S$ , eq. (5), that is necessary to isolate mean and fluctuation effects. With  $M_d = 0$ ,  $S$  is such that the mean temperature and density are constant across the channel, as we shall see below.

The DNS results were generated using the code developed by Buell to study compressible Couette flow. During the computations, the body force  $\Phi_i$  is adjusted

Table 1. DNS physical parameters.

Case	$M$	$M_d$	$Re$	$Pr$	$\gamma$	$\mu$
A	1.5	1.5	3000	0.7	1.4	$T^{0.7}$
B	3	3	4880	0.7	1.4	$T^{0.7}$
AX	1.5	0	3000	0.7	1.4	$T^{0.7}$

Table 2. DNS numerical parameters.

$nx$	$ny$	$nz$	$nxc$	$nyc$	$nzc$	$L_x$	$L_z$
110	90	60	144	119	80	$4\pi$	$4\pi/3$

so that the total mass flux through the channel remains constant. (Once the flow reaches a statistically stationary state the variations of  $\Phi_i$  with time are small). The code utilizes a Fourier-Legendre spectral discretization along with a hybrid implicit-explicit third-order time-advance algorithm designed to maximize the range of Mach numbers that may be considered (Buell 1991). The numerical parameters used by all three runs are given in table 2, where  $L_x$  and  $L_z$  are the streamwise and spanwise domain sizes, and  $(nx, ny, nz)$  and  $(nxc, nyc, nzc)$  are respectively the number of expansion coefficients and collocation (quadrature) points in the streamwise, wall-normal, and spanwise directions. The runs were made on the CCF and NAS Cray YMP and C-90 computers at NASA Ames Research Center.

## 2. Results

An indication of the numerical fidelity of the DNS is provided by the streamwise and spanwise one-dimensional spectra from the channel centerline and near the walls, shown in figure 1. They are typical of those found from all three DNS runs in their rapid fall-off at high wavenumber, which implies that the  $x$ - and  $z$ -resolution is adequate. The "Legendre spectra" (not shown) also verify that the wall-normal resolution is sufficient. The high wavenumber streamwise and spanwise spectra of the velocity at both the channel centerline (figure 1(a,b)) and near the wall (figure 1(c,d)) are similar to those found in the incompressible channel (see figure 3 of Kim *et al.* 1987). In the present simulations, we find that the density and temperature spectra are closely related to each other and that their magnitudes are much larger near the walls than they are at the centerline. The streamwise and spanwise correlations in figure 2 are also roughly equivalent to the incompressible results (cf. figure 2 of Kim *et al.* 1987) except for two characteristics: the large spanwise coherence of the density and temperature at the centerline (figure 2b), and the greater streamwise coherence of the  $\rho$ ,  $u$ , and  $T$  fields near the wall (figure 2c).

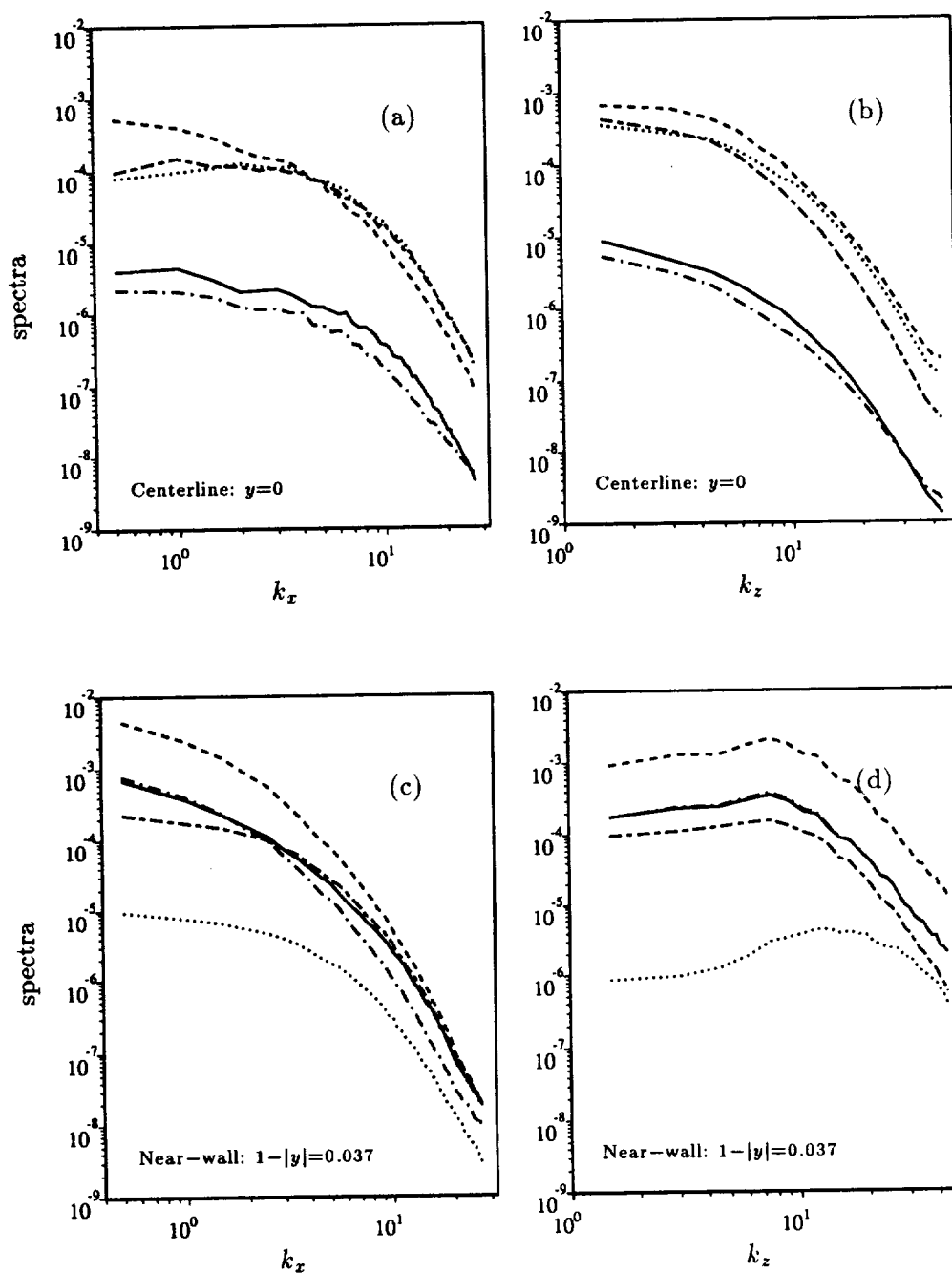


FIGURE 1. One-dimensional spectra for Case A: —,  $\rho$ ; ---,  $u$ ; ..... ,  $v$ ; — · —,  $w$ ; — — —,  $T$ . (a) & (c) Streamwise; (b) & (d) spanwise.

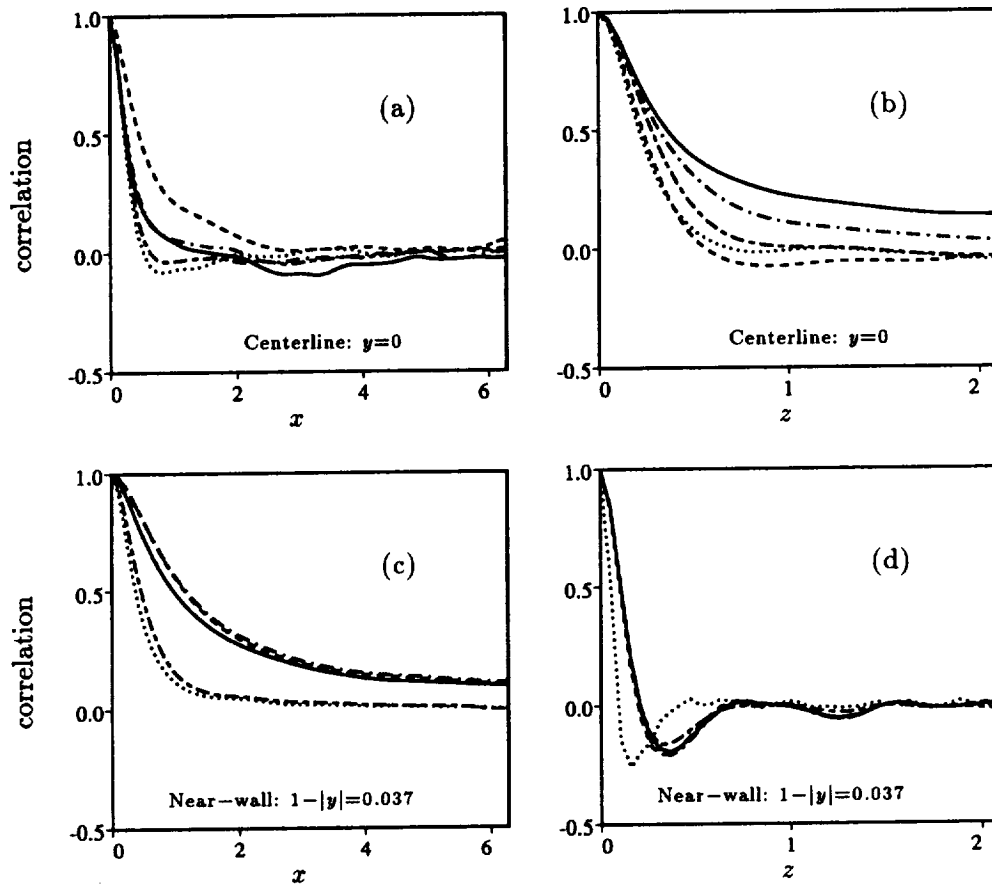


FIGURE 2. Two-point correlations for Case A: symbols as in figure 1. (a) & (c) Streamwise; (b) & (d) spanwise.

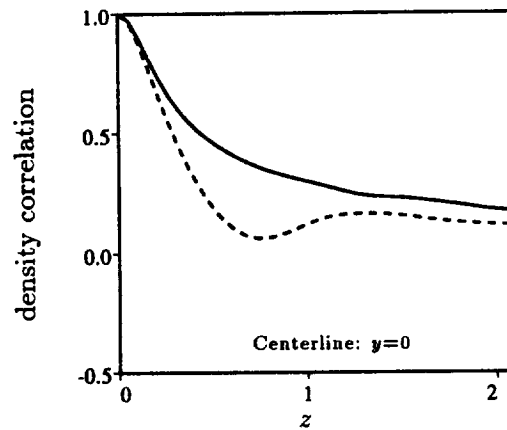


FIGURE 3. Two-point density correlations for Case A at channel centerline: —, full field; ----, with acoustic eigenfunctions removed.

We first discuss the spanwise coherence at the centerline, which is thought to be due to acoustic resonance. Evidence for this is provided first by the fact that the coherence is not present in the velocity, and most significantly by the results in figure 3, which contrast the spanwise density correlation from an instantaneous field (one which contributed to the figure 2b curve) with that obtained by eliminating the contribution from several "acoustic eigenfunctions." This is done by projecting the DNS fields on eigenfunctions of the linear inviscid isentropic problem for a given base flow. The acoustic density and velocity fluctuations are respectively assumed to satisfy  $\rho^a(\mathbf{x}, t) = \sum_{\mathbf{k}} \hat{\rho}(\mathbf{k}, y) e^{i(\mathbf{k} \cdot \mathbf{x} - \omega t)}$  and  $u_i^a(\mathbf{x}, t) = \sum_{\mathbf{k}} \hat{u}_i(\mathbf{k}, y) e^{i(\mathbf{k} \cdot \mathbf{x} - \omega t)}$ . At a given wavenumber  $\mathbf{k} = (k_x, k_z)$ , the linearized, isentropic Euler equations in Fourier space in terms of the "acoustic eigenfunctions"  $\mathbf{q}_\ell(\mathbf{k}, y) = (\hat{\rho}(\mathbf{k}, y), \hat{u}(\mathbf{k}, y), \hat{v}(\mathbf{k}, y), \hat{w}(\mathbf{k}, y))^T$  can then be written as  $\mathcal{L}(\mathbf{q}) = \omega \mathbf{q}$ , where

$$\mathcal{L}(\mathbf{q}) = \begin{pmatrix} k_x \bar{u} \hat{\rho} + k_z \bar{\rho} \hat{u} - i(\bar{\rho} \hat{v})_y + k_z \bar{\rho} \hat{w} \\ k_x \bar{u} \hat{u} - i(d\bar{u}/dy) \hat{v} + k_x \frac{a^2}{\bar{\rho}} \hat{\rho} \\ k_x \bar{u} \hat{v} - i a^2 (\hat{\rho}/\bar{\rho})_y \\ k_x \bar{u} \hat{w} + k_z \frac{a^2}{\bar{\rho}} \hat{\rho} \end{pmatrix}, \quad (6)$$

with  $a$  equal to the sound speed and  $\hat{v} = 0$  at  $y = \pm 1$ .

The projection of the full DNS field onto the acoustic subspace is performed by computing the inner product  $\int_{-1}^{+1} \mathbf{q}_{\text{DNS}} \cdot \mathbf{q}_m^* dy$  of the DNS field with eigenfunctions  $\mathbf{q}_m^*$  of the adjoint problem to (6),  $\mathcal{L}^*(\mathbf{q}^*) = \omega \mathbf{q}^*$ , such that  $\int_{-1}^{+1} \mathcal{L}(\mathbf{q}) \cdot \mathbf{q}^* dy \equiv \int_{-1}^{+1} \mathbf{q} \cdot \mathcal{L}^*(\mathbf{q}^*) dy$ . The adjoint operator is

$$\mathcal{L}^*(\mathbf{q}^*) = \begin{pmatrix} k_x \bar{u} \hat{\rho}_* + k_x \frac{a^2}{\bar{\rho}} \hat{u}_* + \frac{i}{\bar{\rho}} (a^2 \hat{v}_*)_y + k_z \frac{a^2}{\bar{\rho}} \hat{w}_* \\ k_x \bar{u} \hat{u}_* + k_x \bar{\rho} \hat{\rho}_* \\ k_x \bar{u} \hat{v}_* + i \bar{\rho} (\hat{\rho}_*)_y - i(d\bar{u}/dy) \hat{u}_* \\ k_x \bar{u} \hat{w}_* + k_z \bar{\rho} \hat{\rho}_* \end{pmatrix}, \quad (7)$$

where  $\hat{v}_* = 0$  at  $y = \pm 1$ .

When the base flow is uniform (no  $y$  variation), the eigenfunctions from (6) are irrotational, and the eigenvalues  $\omega$  from (6) and (7) give phase speeds  $c_x = \text{Real}(\omega)/k_x$  that satisfy

$$\bar{u} - c_x = \pm a [(\ell \pi / 2 k_x)^2 + 1]^{1/2}, \quad (8)$$

where  $\ell$  is the wall-normal wave number (equivalent to the number of times  $|\hat{\rho}|$  and  $|\hat{u}|$  change sign between  $-1 \leq y \leq +1$ ). Here we use the Case A mean profiles shown in figure 4 as the base flow and numerically compute solutions to (6) and (7), which leads to "acoustic" (isentropic) eigenfunctions that do not satisfy the above phase relation and, in fact, have nonzero vorticity near the walls. Near the channel centerline, however, the eigenfunctions have a more typically acoustic behavior in that their ratio of dilation to enstrophy is very large and in that a given  $\ell$  mode (now

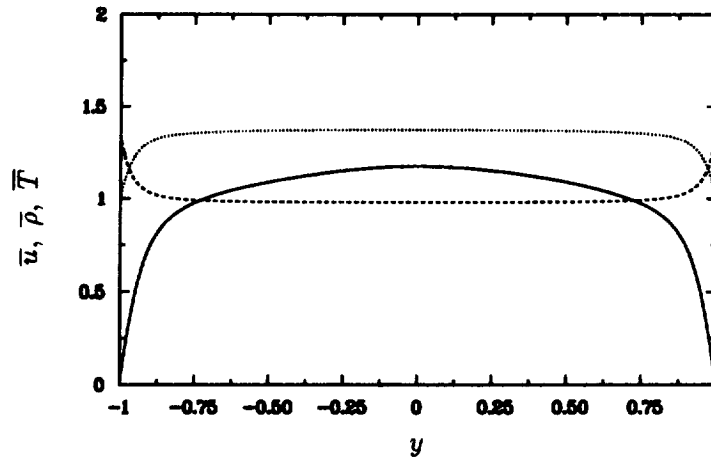
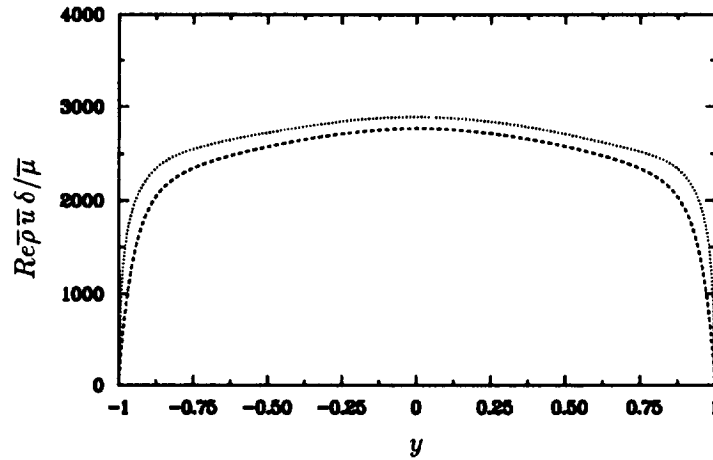
FIGURE 4. Mean profiles for Case A: —,  $\bar{u}$ ; ----,  $\bar{\rho}$ ; ·····,  $\bar{T}$ .

FIGURE 5. Local Reynolds number profiles: ----, Case A; ·····, Case B.

defined as the number of  $|\hat{\rho}|$  sign changes) consists of an upstream- and downstream-propagating pair<sup>†</sup> with positive and negative phase speeds relative to the centerline velocity,  $\bar{u}_c - c_x$ . The dashed curve in figure 3 represents the density field after the isentropic modes  $\mathbf{q}_\ell$  that are recognized as acoustic in the range  $\ell = [0, \dots, 4]$  have been projected and removed, for  $k_x L_x / 2\pi = [0, \dots, +4]$  (using conjugate symmetry to account for  $k_x < 0$ ) and  $k_z L_z / 2\pi = [-4, \dots, +4]$ . Only the eigenfunctions with (a) very large dilation-to-entropy ratio near the centerline, (b) an equal number of sign changes for  $|\hat{\rho}|$  and for  $|\hat{u}|$ , and (c) no more than two modes at each  $\ell$  – one with positive and one with negative relative phase speed – were chosen from the full inviscid isentropic function space to be included in the projection. The second criterion is overly conservative: it is useful when automating the selection

<sup>†</sup> Although some  $\ell$  modes appear to have only a single downstream-propagating component.

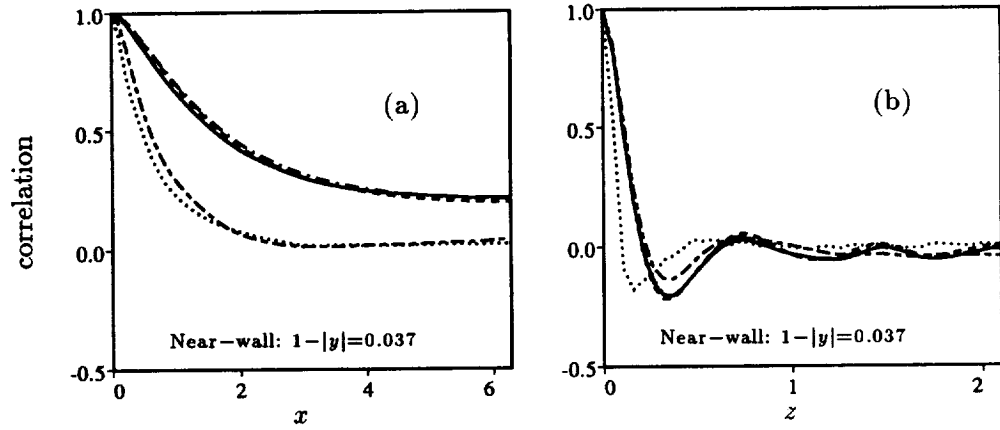


FIGURE 6. Near-wall two-point correlations for Case B: symbols as in figure 1. (a) Streamwise; (b) spanwise.

process, but excludes a few modes (because of low amplitude “wiggles” in  $|\hat{u}|$ ) that are thought to be acoustic rather than vortical. For this reason, and perhaps also because of physical differences between the uniform and variable mean cases that produce at certain  $\ell$  no non-vortical modes moving upstream with respect to the centerline velocity, the projection at some  $k$  did not include two modes for every  $\ell$  in the 0 to 4 range. Nevertheless, the magnitude of the reduction in figure 3 suggests that there are significant acoustic disturbances within the simulation results. The correlation at  $z \approx 2$  would presumably be reduced still further if more  $k_z = 0$  modes were used in the projection. Note that because the computations assume that the channel walls are perfectly rigid (and use periodic boundary conditions), any acoustic signals present in the DNS are not necessarily expected to be identical to those found in a laboratory wind tunnel since in the simulations there is no mechanism for the acoustic energy to radiate away.

The other difference, mentioned above, between the two-point correlations for the present and incompressible DNS is in the larger near-wall streamwise correlations found in figure 2c; this indicates that the near-wall streaks, which are characteristic of wall-bounded turbulent flows (Robinson 1991), are more coherent in Case A than in the incompressible channel results. At first glance, it might appear that the streak modification is a low Reynolds number effect (so that the effective streamwise domain size in wall units is smaller) since the Reynolds number based on mean centerline velocity is higher in the incompressible DNS than that found here. The variation of the local Reynolds number across the channel is shown by the dashed curve in figure 5, and the centerline value (2770) is seen to be slightly less than the 3300 quoted for the incompressible channel data (Kim *et al.* 1987). But because the isothermal boundary conditions lead to a flow with a maximum mean temperature near the centerline and maximum density at the walls (figure 4), the mean kinematic viscosity  $\bar{\mu}/\bar{\rho}$  (where  $\bar{\mu} = \bar{T}^n$ ) is maximum at  $y = 0$ . Therefore, the local Reynolds



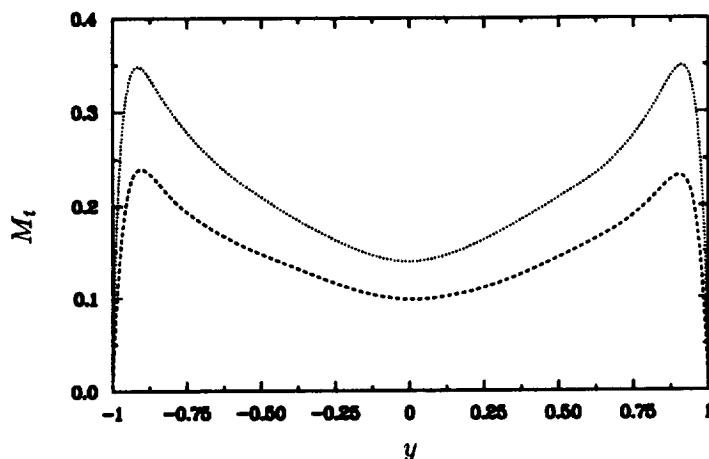


FIGURE 7. Turbulent Mach number,  $M_t = M\sqrt{u'_i u'_i}/\sqrt{T}$ : ----, Case A; ·····, Case B.

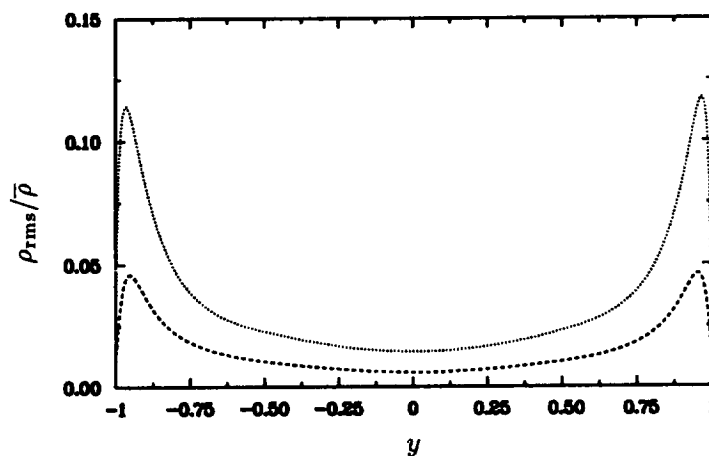


FIGURE 8. Root mean square density fluctuations: ----, Case A; ·····, Case B.

number in the present DNS is apt to be larger near the walls than for when  $\nu = \text{constant}$ . This suggests that the enhanced near-wall coherence in figure 2c is solely a compressibility effect, a fact that is reinforced by the Case B results. In order to obtain a local Reynolds number profile  $Re\bar{\rho}\bar{u}\delta/\bar{\mu}$  (where  $\delta = 1$ ) at  $M = 3$  (Case B) that remains comparable to that for Case A, the bulk Reynolds number was increased from 3000 to 4880. As the Case B profile (dotted curve) in figure 5 shows, the Reynolds number is in fact at any  $y$  slightly larger than that for Case A (dashed), which implies that the further increase shown in figure 6a (over that seen in figure 2c) of the near-wall streamwise correlation for Case B is not a viscous effect.

It therefore appears that the extra coherence is due to compressibility, although its precise source is at this point uncertain. One possibility is near-wall viscosity

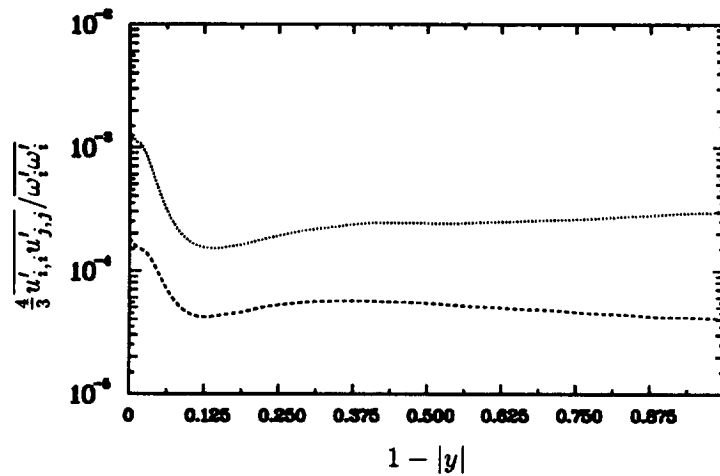


FIGURE 9. Dilatation-to-entropy ratio: ----, Case A; ·····, Case B.

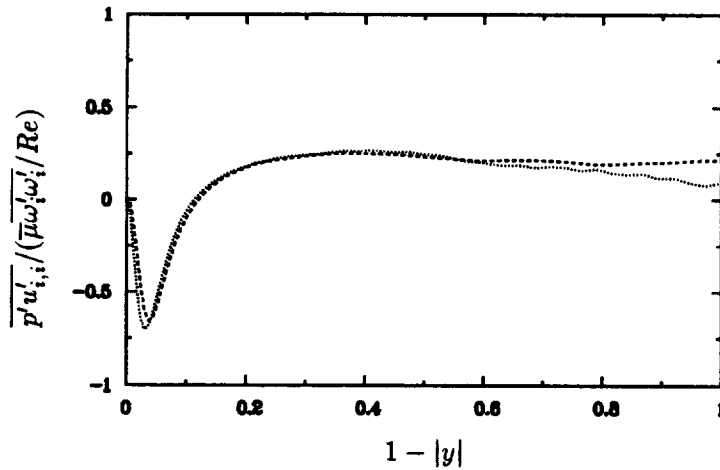


FIGURE 10. Pressure-dilatation correlation: ----, Case A; ·····, Case B.

fluctuations (Tritton 1961; Bradshaw & Ferriss 1971); another is small-scale acoustic fluctuations that are “channeled” along the cold, low-speed streaks, which act as an acoustic “wave-guide.” Fairly large turbulent Mach numbers and r.m.s. density fluctuations are found in both flows, especially near the walls (figures 7 & 8), which might be evidence of significant dilational effects. However, the dilational field associated with the near-wall fluctuations is not so important as to directly increase the turbulent kinetic energy dissipation rate to any great degree. This can be seen from figure 9, which gives the ratio of the mean-square dilatation fluctuations to those of the mean-square vorticity: the ratio of dilatational-to-solenoidal homogeneous kinetic energy dissipation (Zeman 1990; Blaisdell, Mansour & Reynolds 1993;

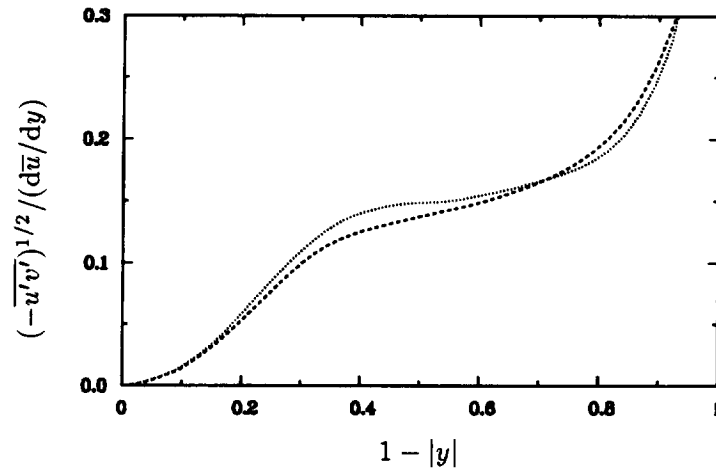


FIGURE 11. Mixing length: ----, Case A; ·····, Case B.

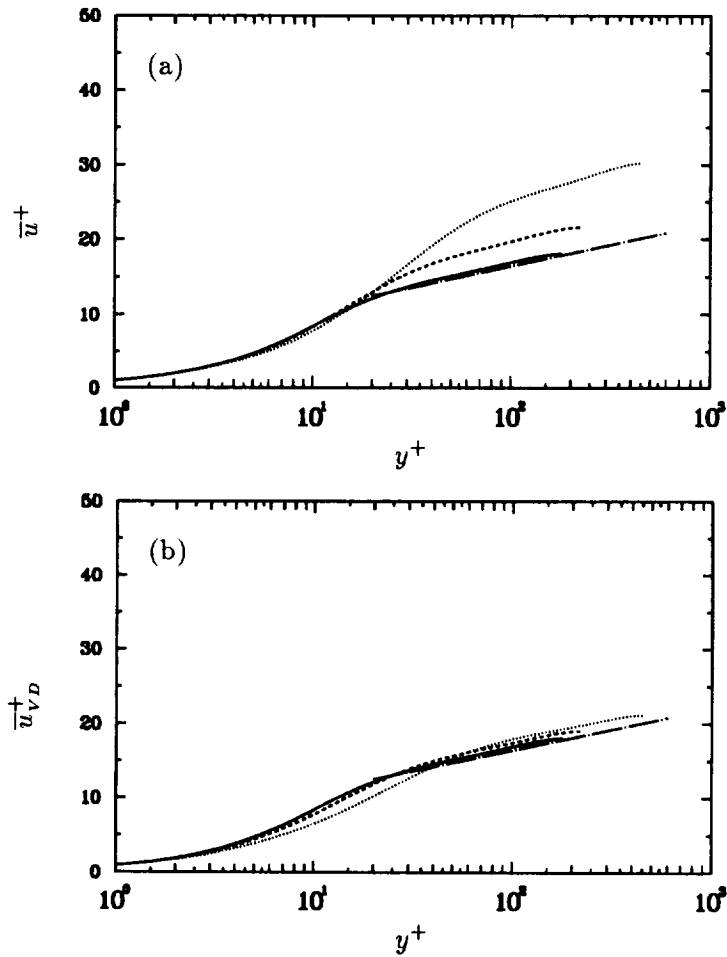


FIGURE 12. Mean velocity: (a), in wall units; (b), with Van Driest transformation; —,  $M = 0$  (Kim *et al.* 1987); ----, Case A; ·····, Case B; — · —,  $2.44 \ln y^+ + 5.2$ .

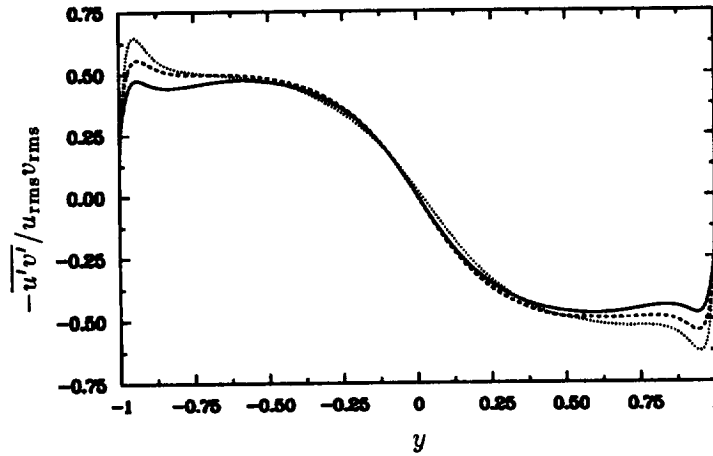


FIGURE 13. Reynolds-stress correlation coefficient: —,  $M = 0$  (Kim *et al.* 1987); ----, Case A; ·····, Case B.

Speziale & Sarkar 1991; Lele 1994). While the ratio increases by an order of magnitude as  $M$  increases from 1.5 to 3, it never becomes significantly larger than  $10^{-3}$ . On the other hand, the pressure-dilation correlation is found to be larger than 50% of the solenoidal dissipation for *both* Mach numbers. Figure 10 shows that near the walls the dilatational field creates a strong sink of turbulent kinetic energy as kinetic energy is transferred to the pressure fluctuations (Blaisdell *et al.* 1993; Lele 1994), while toward the centerline, the pressure-dilatation acts as a smaller – but still important – *source* of kinetic energy. In the future, we hope to understand the link between the large negative  $\overline{p'u'_{i,i}}$  and the observed wall-streak modification.

With such large dilational effects present, one might surmise that this flow is not governed by Morkovin's hypothesis (Favre 1992), which states that relationships between statistical properties of turbulence are unaffected by compressibility if the r.m.s. density fluctuations are small (of order 1/10) compared to the absolute density (Bradshaw & Ferriss 1971; Bradshaw 1977; Spina *et al.* 1994). But the density fluctuations for both Mach numbers are within the allowed range of  $\mathcal{O}(1/10)$  (Figure 8), and for at least one important statistical ratio, the mixing length  $(-\overline{u'v'})^{1/2}/(d\bar{u}/dy)$ , Morkovin's hypothesis is found to work fairly well. Figure 11 demonstrates that this quantity is reasonably independent of Mach number.

With the invariance of the mixing length established, the so-called Van Driest transformation for the mean velocity immediately follows. That is, the density-weighted mean velocity

$$\bar{u}_{vD}^+ = \int_0^{\bar{u}^+} \left( \frac{\bar{\rho}}{\bar{\rho}_w} \right)^{1/2} d\bar{u}^+ \quad (9)$$

(where  $\bar{\rho}_w$  is the mean density at the wall and the + superscript denotes wall units),

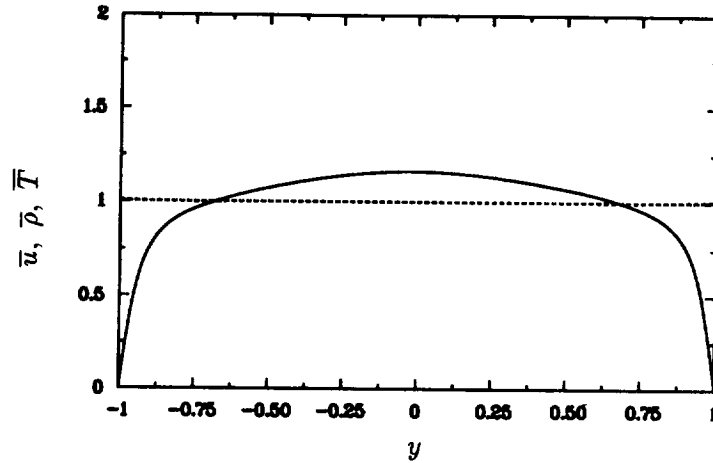


FIGURE 14. Mean profiles for Case AX: —,  $\bar{u}$ ; ----,  $\bar{\rho}$ ; ..... ,  $\bar{T}$ .

is expected to satisfy the incompressible log law,

$$\bar{u}_{VD}^+ = \frac{1}{\kappa} \ln y^+ + C, \quad (10)$$

with  $\kappa$  and  $C$  similar to their incompressible values,  $\kappa \approx 0.4$ , and  $C \approx 5.2$  (Bradshaw 1977; Huang, Bradshaw & Coakley 1993; Huang & Coleman 1993). The mean velocity in both wall units and the Van Driest form is plotted in figure 12 (using for the latter a mixing length formulation for the mean temperature to write  $\bar{u}_{VD}^+$  as a function of  $\bar{u}^+$ , the surface heat flux and the mean surface temperature (Bradshaw 1977)). The agreement of the curves in figure 12b, especially their slopes, tends to reinforce the validity of the Van Driest transformation (cf. Huang & Coleman 1993) and, by extension, the Morkovin hypothesis.

Not *all* statistical ratios are found to be independent of Mach number, however, as the Reynolds-stress correlation coefficients in figure 13 show. The near-wall maximum of  $|u'v'|/u_{rms}v_{rms}$  increases from less than 0.5 for the incompressible channel to over 0.6 for  $M = 3$ . (Note that for  $M = 0$ , this correlation coefficient does not vary appreciably with Reynolds number (Kim *et al.* 1987), which points to compressibility and not viscous effects as the source of the differences in figure 13.)

It thus appears that the isothermal-wall channel contains some “non-Morkovin” phenomena. However, it would not at this point be appropriate to firmly state that the results in figure 13 represent a formal contradiction to the Morkovin hypothesis since the hypothesis does not (regardless of the density fluctuation level) claim to account for the influence of spatial gradients of the mean properties (Bradshaw 1977), which are apt to be important for this flow. Evidence of just how important can be found in the results from Case AX, for which  $M_d = 0$  so that the mean density and temperature are constant (figure 14). The near-wall streamwise correlations for Case AX are given in figure 15. No indication of the enhanced streak coherence found for Cases A and B is observed (cf. figures 2(c) & 6(a)). Therefore, wall-normal gradients of the mean properties are required for the streak modification to

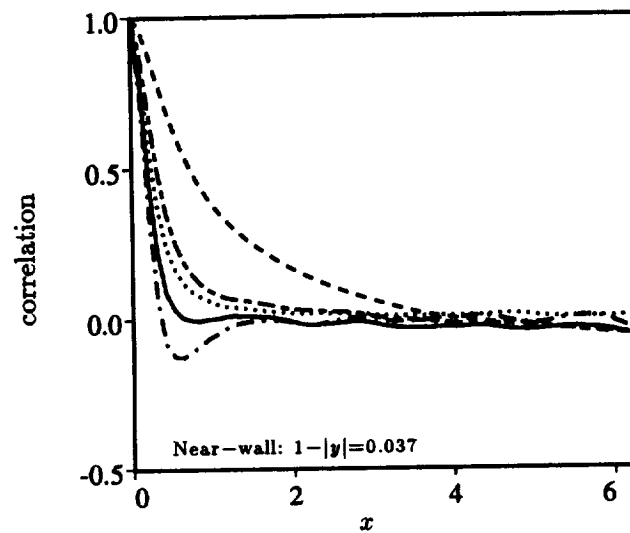


FIGURE 15. Near-wall two-point streamwise correlations for Case AX: symbols as in figure 1.

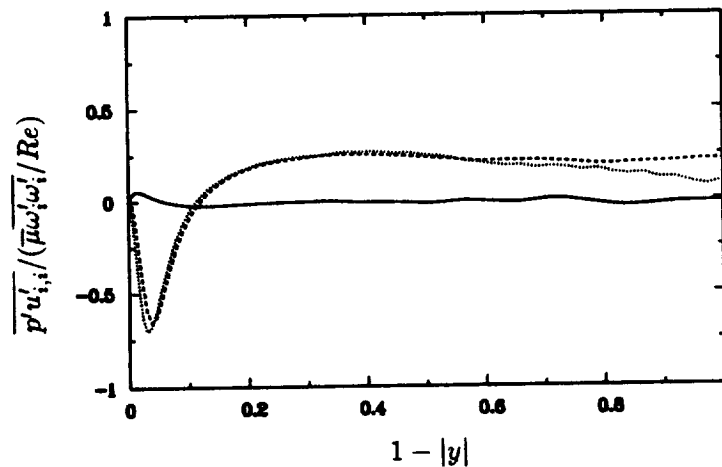


FIGURE 16. Pressure-dilatation correlation: ----, Case A; ·····, Case B; —, Case AX.

occur. The mean gradients are also necessary for the near-wall fluctuation effects (which are presumably related to the streak coherence) to be present, as is shown by the Case AX pressure-dilatation profile in figure 16 (solid curve). Compared to the  $M_d = 1.5$  and 3 results, when the mean properties are uniform,  $p'u'_{i,i}$  is much less important and represents a near-wall source rather than sink of kinetic energy.

### 3. Future plans

An immediate task is to attempt to resolve the open questions regarding the extra streak coherence induced by the compressibility. Namely:

- A) How do the dilatation fluctuations inferred by the large pressure-dilatation correlations influence the vortical field and hence the streak structure?
- B) In what sense is the enhanced streak coherence related to the increased  $\overline{u'v'}$  correlation coefficient?
- C) How do the variable-mean properties couple with near-wall dilatational fluctuations?

Recommended long-term efforts include comparing the present results to those computed for the adiabatic-wall channel (which to develop a statistical equilibrium will require either one wall to be isothermal or for the flow to contain a distributed heat sink). It should also be of interest to compare channel results to compressible boundary layer turbulence and thus ascertain the importance of the acoustic disturbances that are trapped between the channel walls but free to radiate away in a boundary layer. New numerical schemes, possibly using a fully implicit time-advance algorithm, should be developed to allow study of turbulent compressible flows in the hypersonic regime.

### Acknowledgements

This work was done in collaboration with J. Buell, J. Kim and R. Moser. The author is also grateful to P. Bradshaw, G. Huang, S. Lele, N. Mansour, K. Shariff, A. Wray and O. Zeman for their helpful contributions. Computations were performed on the CCF and NAS computers at NASA Ames Research Center.

### REFERENCES

- BLAISDELL, G. A., MANSOUR, N. N., & REYNOLDS, W. C. 1993 Compressibility effects on the growth and structure of homogeneous turbulent shear flow. To appear in *J. Fluid Mech.*
- BRADSHAW, P. 1977 Compressible turbulent shear layers. *Ann. Rev. Fluid Mech.* **9**, 33–54.
- BRADSHAW, P. & FERRISS, D. H. 1971 Calculation of boundary layer development using the energy equation: compressible flow on adiabatic walls. *J. Fluid Mech.* **46**, 83–110.
- BUELL, J. C. 1991 Direct simulations of compressible wall-bounded turbulence. In *Annual Research Briefs - 1990*. Center for Turbulence Research, Stanford Univ./NASA-Ames.
- COLEMAN, G. N., BUELL, J. C., KIM, J. & MOSER, R. D. 1993 Direct simulation of compressible wall-bounded turbulence. *Ninth Symposium on Turbulent Shear Flows*, Kyoto, Japan, August 16–18, 1993.
- FAVRE, A.-J. 1992 Formulation of the statistical equations of turbulent flows with variable density. *Studies in Turbulence* (T.B. Gatski *et al.*, eds.) Springer.

- HUANG, P. G., BRADSHAW, P. & COAKLEY, T. J. 1993 A skin friction and velocity profile family for compressible turbulent boundary layers. *AIAA J.* **31**, 1600–1604.
- HUANG, P. G. & COLEMAN, G. N. 1993 On the Van Driest transformation and compressible wall-bounded flows. Submitted to *AIAA J.*
- KIM, J., MOIN, P. & MOSER, R. 1987 Turbulence statistics in fully developed channel flow at low Reynolds number. *J. Fluid Mech.* **177**, 133–166.
- LELE, S. K. 1994 Compressibility effects on turbulence. To appear in *Ann. Rev. Fluid Mech.* **26**.
- ROBINSON, S.K. 1991 Coherent motions in the turbulent boundary layer. *Ann. Rev. Fluid Mech.* **23**, 601–639.
- SPEZIALE, C. G. & SARKAR, S. 1991 Second-order closure models for supersonic turbulent flows. *AIAA Paper No. 91-0212*.
- SPINA, E.F., SMITS A.J. & ROBINSON, S.K. 1994 The physics of supersonic turbulent boundary layers. To appear in *Ann. Rev. Fluid Mech.* **26**.
- TRITTON, D.J. 1961 Notes on approximations for turbulent flows with large temperature differences. *J. Fluid Mech.* **11**, 440–446.
- ZEMAN, O. 1990 Dilatation dissipation: The concept and modeling in modeling compressible mixing layers. *Phys. Fluids. A.* **2**, 178–188



## Effects of shock strength on shock turbulence interaction

N94-24165

By Sangsan Lee

Direct numerical simulation (DNS) and linear analysis (LIA) of isotropic turbulence interacting with a shock wave are performed for several upstream shock normal Mach numbers ( $M_1$ ). Turbulence kinetic energy (TKE) is amplified across the shock wave, but this amplification tends to saturate beyond  $M_1 = 3.0$ . TKE amplification and Reynolds stress anisotropy obtained in DNS are consistent with LIA predictions. Rapid evolution of TKE immediate downstream of the shock wave persists for all shock strengths and is attributed to the transfer between kinetic and potential modes of turbulence energy through acoustic fluctuations. Changes in energy spectra and various length scales across the shock wave are predicted by LIA, which is consistent with DNS results. Most turbulence length scales decrease across the shock. Dissipation length scale ( $\bar{\rho}q^3/\epsilon$ ), however, increases slightly for shock waves with  $M_1 < 1.65$ . Fluctuations in thermodynamic variables behind the shock wave stay nearly isentropic for  $M_1 < 1.2$  and deviate significantly from isentropy for the stronger shock waves due to large entropy fluctuation generated through the interaction.

### 1. Motivation and objective

The presence of shock waves is an important feature that distinguishes high-speed supersonic flows. Understanding the mechanisms of turbulence interacting with a shock wave is not only of generic interest, but also of fundamental importance in predicting the interactions of turbulent boundary layers with the shock waves which occur in many engineering applications. Since the 1950's, linear analyses (LIA) on the modification of elementary disturbance waves, such as vortical, acoustic, and entropic waves, by the shock wave have been performed with an emphasis on the acoustic wave generation behind the shock wave (Ribner 1953, 1954, 1968, Moore 1953, Kerrebrock 1956, Chang 1957, McKenzie and Westphal 1968). Recently, the applicability of homogeneous Rapid Distortion Theory (RDT) on shock/turbulence interaction was investigated by Jacquin *et al.* (1993).

There has been a significant accumulation of experimental data on the shock turbulence interaction during the last decade. Interaction of turbulent boundary layers with a shock wave over a corner was investigated by many research groups, among them are Dolling and Or (1985), Andreopoulos and Muck (1987), Smits and Muck (1987). A general finding from these experiments is that Reynolds shear stress and turbulence intensities are amplified across the shock wave. The studies of oblique shock wave/turbulent boundary layer interaction included several additional phenomena which complicated the flow behavior (Honkan and Andreopoulos 1992). To isolate the effects of a shock wave on turbulence, several experiments (Debieve and

Lacharme 1986, Keller and Merzkirch 1990, Jacquin *et al.* 1991, Honkan *et al.* 1992) on the interaction between the shock wave and grid-generated turbulence have been performed. They found that turbulence is amplified and turbulence length scales increase across the shock wave. But the length scale increase contradicts the intuitive expectation that mean flow compression should decrease the relevant turbulence length scales. The issue of length scale change will be thoroughly discussed in the present paper (Sec. 2.2).

Numerical simulations of the shock turbulence interaction are just beginning to emerge. Using a shock capturing numerical technique, Rotman (1991) calculated the change in a two dimensional turbulent flow caused by the passage of the traveling shock wave. He found that the shock causes an increase in the turbulent kinetic energy and that the length scale of the turbulent field is reduced upon passage of the shock. Lee *et al.* (1991a, 1992) conducted direct numerical simulations of two and three dimensional turbulence interacting with a shock wave. They found that vorticity amplification compared well with the linear analysis predictions, and turbulent kinetic energy undergoes rapid increase behind the shock wave. The spectrum was found to be enhanced more at large wave numbers, leading to an overall length scale decrease.

In the present report, interaction of isotropic turbulence with a strong shock wave is studied to investigate the effects of shock strength on turbulence modification. A numerical technique to simulate turbulence interacting with a strong shock wave without resolving its structure was developed, and it validated this technique against the shock-resolving simulations (Lee 1993). The simulation results are compared with the results from a linear analysis, and they are contrasted against the results from the weak shock case to show the shock strength effects.

## 2. Accomplishments

The parameters of the simulation are the mean Mach number ( $M_1$ ), the fluctuation Mach number ( $M_t$ ), and the turbulence Reynolds number based on the Taylor microscale ( $Re_\lambda$ ) upstream of the shock wave. In the simulation, all of the turbulence scales are fully resolved, while the effect of the shock wave on turbulence is captured (rather than fully resolved). Two new simulations are conducted for the interaction with strong shock waves ( $M_1 = 2.0, 3.0$ ), and the results from shock-resolving simulations (Lee *et al.* 1993) for the interaction with a weak shock wave ( $M_1 = 1.05, 1.1, 1.2$ ) are quoted to investigate the effects of the shock normal Mach number. Table 1 lists the simulation parameters, where the values of  $M_t$  and  $Re_\lambda$  are taken at the location immediately upstream of the shock.

Table 1. Parameters for the simulations of shock turbulence interaction

Case	$M_1$	$M_t$	$Re_\lambda$	$k_o$
A	2.0	0.108	19.0	4.0
B	3.0	0.110	19.7	4.0

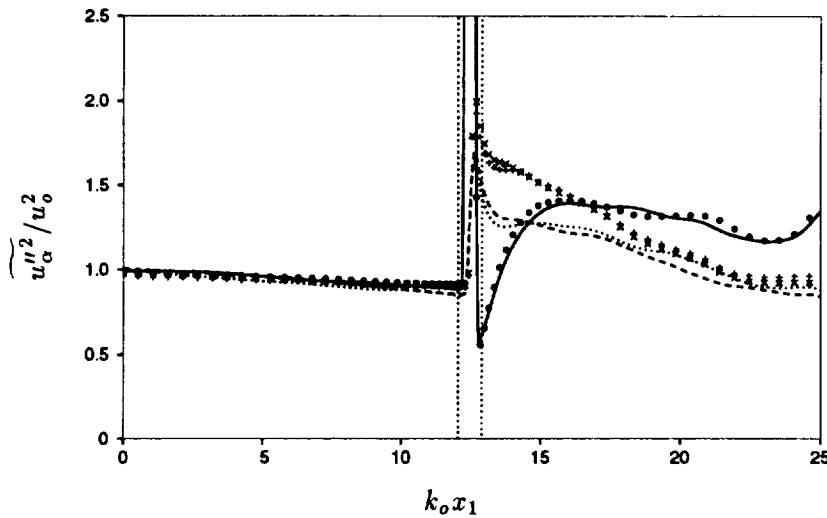


FIGURE 1(A). Evolution of the normal components of the Reynolds stress: lines for  $M_1 = 2.0$ , and symbols for  $M_1 = 3.0$ . —, • :  $R_{11}$ , ----, × :  $R_{22}$ , ·····, + :  $R_{33}$ . Vertical lines denote the boundaries of shock intermittency.

### 2.1 Turbulence velocity fluctuation

Interaction of turbulence with a shock wave generates acoustic waves downstream of the shock, part of which undergo rapid decay (Ribner 1953). LIA predicts that turbulent kinetic energy is amplified across the shock wave and the decaying acoustic waves contribute significantly to the streamwise fluctuations just behind the shock wave.

Figure 1(A) shows the evolution of the diagonal components of the Reynolds stress tensor,  $R_{ij} = \widetilde{u''_i u''_j}$ . The off-diagonal components stay close to zero over the entire flow field since turbulence is isotropic upstream and axisymmetric downstream of the shock. The streamwise component in the shock region contains the intermittency effects due to the oscillations of the shock. For more details of the intermittency effects on turbulence statistics, see Lee *et al.* (1992). The boundaries of the shock oscillations are defined as the locations where mean dilatation  $d\bar{u}_1/dx_1 = 0$ ;  $d\bar{u}_1/dx_1$  is negative inside the shock wave and slightly positive away from the shock due to viscous heating. All the velocity fluctuations are enhanced during the interaction. The velocity fluctuations are axisymmetric behind the shock, and their return to isotropy is negligible compared to the decay. Away from the shock wave, all the velocity fluctuations decay monotonically due to the viscous dissipation.

Mach number dependence of the far-field velocity fluctuation amplification predicted by LIA is shown in Figure 1(B). All components of the velocity fluctuation are amplified across the shock wave, and the amplification of TKE tends to saturate beyond  $M_1 = 3.0$ . The shock normal component is amplified more for shock waves with  $M_1 < 2.0$  while the opposite is true for  $M_1 > 2.0$ . In DNS, however, the streamwise velocity fluctuation away from the shock is larger than the transverse velocity fluctuations, which apparently contradicts with the LIA prediction. Viscous

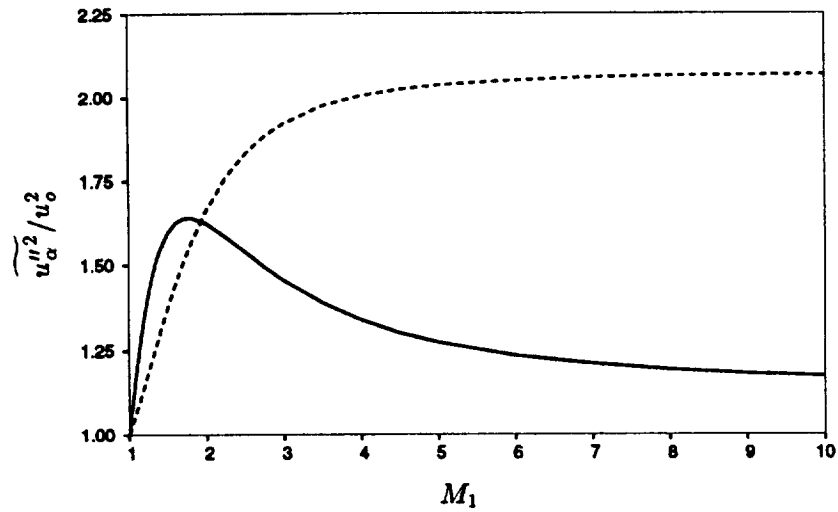


FIGURE 1(B). Amplification of velocity fluctuation variances across the shock wave predicted by LIA at far away from the shock. —  $\widetilde{u_1''^2}$ , ----  $\widetilde{u_2''^2}$  &  $\widetilde{u_3''^2}$ .

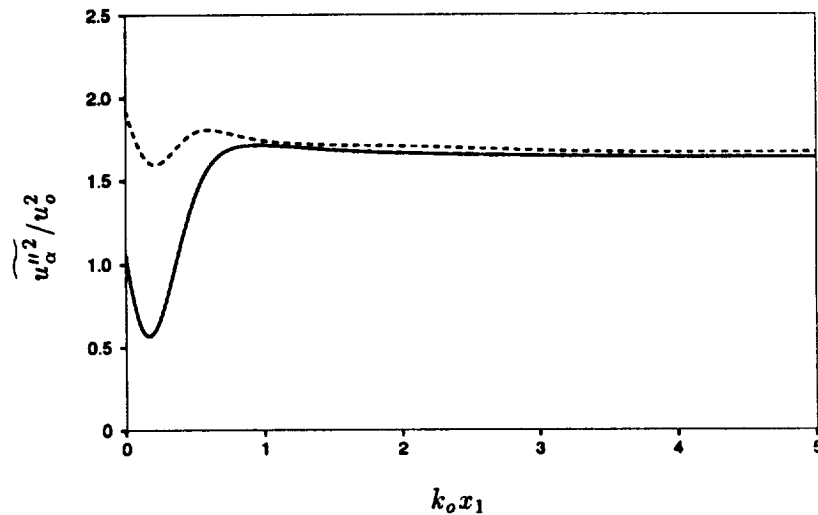


FIGURE 1(C). Evolution of velocity fluctuation variances behind the shock wave predicted by LIA ( $M_1 = 2.0$ ). —  $\widetilde{u_1''^2}$ , ----  $\widetilde{u_2''^2}$  &  $\widetilde{u_3''^2}$ .

TKE dissipation rate behind the shock for the transverse components are found to be significantly higher than the streamwise component. Therefore, comparing low Reynolds number DNS results directly with the inviscid linear analysis is not fair. After the viscous decay is compensated for by extrapolating the curves to the shock location, the trend of amplification from the DNS is found to be consistent with the LIA prediction.

The rapid evolution of velocity fluctuations which was observed for weak shock turbulence interaction (Lee *et al.* 1993) persists in the present simulations of strong shock turbulence interaction. In order to understand the downstream evolution of the velocity fluctuations, the budget of the Reynolds stress transport equation downstream of the shock wave is investigated. All terms in the transport equation can be accurately evaluated, since all the flow variables are fully resolved both in time and space outside the shock wave. As for weak shock case, the pressure transport term  $(-\overline{p'u''_1})_{,1}$  in the inhomogeneous (or the shock normal) direction is mainly responsible for the rapid evolution of the streamwise velocity fluctuation. The evolution of the velocity fluctuations downstream of the shock wave predicted by LIA is shown in Figure 1(C), which reproduces the main feature of the rapid evolution from the DNS. Hence, the rapid TKE evolution behind the shock wave can be explained mainly as a linear process. This rapid evolution in the streamwise velocity fluctuation is due to a correlation between the vortical and decaying acoustic fluctuations behind the shock wave. The acoustic velocity fluctuations and vortical velocity fluctuations are anti-correlated just behind the shock, and the correlation between the two fluctuations decreases rapidly as the amplitude of the acoustic wave decays exponentially away from the shock wave. In previous studies (Lee *et al.* 1991a, 1992, 1993), the correlations between vortical and acoustic waves were not properly accounted for, and the prediction capability of the linear analysis was not fully appreciated.

Another facet of the rapid evolution of velocity fluctuations is revealed by an equation for linear acoustic energy balance (Thompson 1985). The continuity and momentum equations for the linearized fluctuating components can be written as

$$\begin{aligned}\frac{\partial \rho'}{\partial t} + \tilde{u}_k \frac{\partial \rho'}{\partial x_k} + \bar{\rho} \frac{\partial u''_k}{\partial x_k} &= 0, \\ \frac{\partial u''_i}{\partial t} + \tilde{u}_k \frac{\partial u''_i}{\partial x_k} + \frac{1}{\bar{\rho}} \frac{\partial p'}{\partial x_i} - \frac{\partial \sigma''_{ik}}{\partial x_k} &= 0\end{aligned}$$

by assuming that there exist no mean flow gradients, where  $\bar{\rho}\sigma''_{ij}(=\tau''_{ij})$  denotes the viscous stress. For an ideal gas, an infinitesimal density fluctuation can be related to the pressure and entropy ( $s$ ) fluctuations by

$$\frac{\rho'}{\bar{\rho}} = \frac{1}{\gamma} \frac{p'}{\bar{p}} - \frac{s'}{c_p},$$

where  $c_p$  is the specific heat at constant pressure. Multiplying the continuity equation by  $\rho'$ , contracting the momentum equations by  $u''_i$ , and cancelling density-dilatation correlation by using above thermodynamic relation with neglecting entropy fluctuation effect  $(-s'u''_{i,i}/c_p\bar{c})$ , the following equation (in the averaged form) follows.

$$\frac{\partial}{\partial x_k} \left[ \frac{\tilde{u}_k}{\bar{c}} \left( \frac{\overline{u''_i u''_i}}{2\bar{c}^2} + \frac{\overline{\rho'^2}}{2\bar{\rho}^2} \right) + \frac{1}{\gamma} \frac{\overline{p' u''_k}}{\bar{p} \bar{c}} \right] - \frac{\overline{u''_i}}{\bar{c}^3} \frac{\partial \sigma''_{ik}}{\partial x_k} = 0.$$

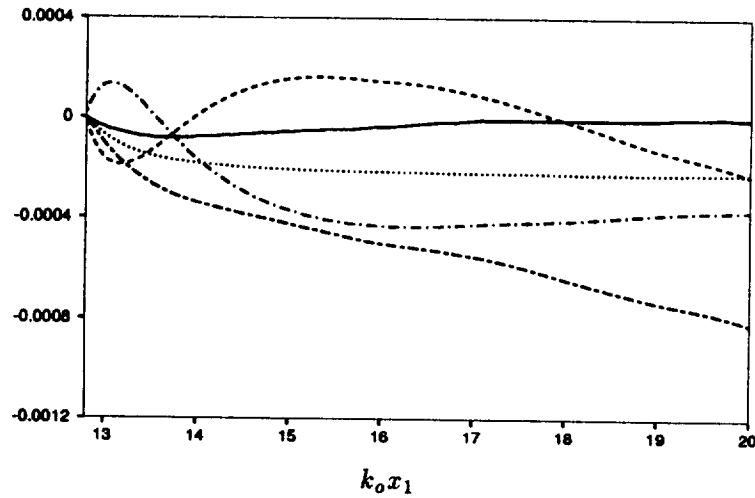


FIGURE 2(A). Evolution of the integrated quantities from the acoustic energy balance for  $M_1 = 2.0$ : ----  $A$ , .....  $B$ , -.-  $C$ , ---  $A+B+C$ , —  $A+B+C+D$ .

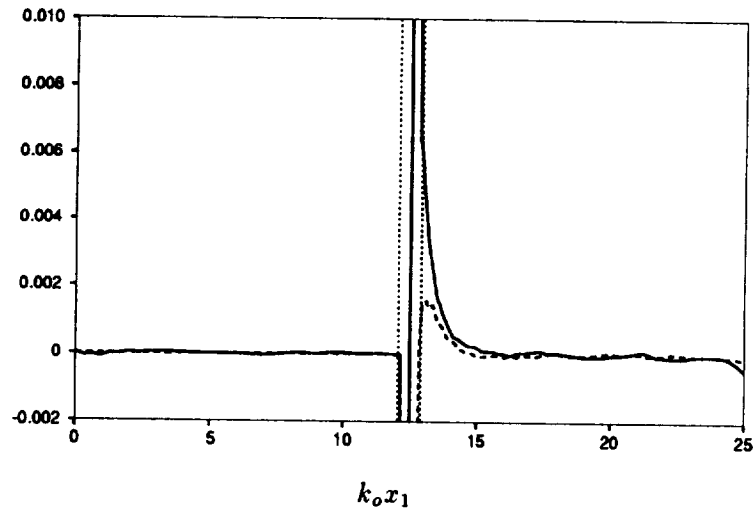


FIGURE 2(B). Evolutions of pressure-dilatation correlation and entropy-dilatation correlation for  $M_1 = 2.0$ : —  $\overline{p'u''_{k,k}}/\gamma\bar{p}u_o k_o$ , ----  $-\overline{s'u''_{k,k}}/c_p u_o k_o$ . Vertical lines denote the boundaries of shock intermittency.

If this relation is satisfied the phenomenon can be explained in terms of linear acoustic energy balance.

The acoustic balance equation is integrated in the streamwise direction from the downstream side of the shock ( $x_s$ ) to give

$$\underbrace{\left\| \frac{\tilde{u}_1}{\bar{c}} \frac{\overline{u_i'' u_i''}}{2\bar{c}^2} \right\|_{x_s}^{x_1}}_A + \underbrace{\left\| \frac{\tilde{u}_1}{\bar{c}} \frac{\overline{\rho'^2}}{2\bar{\rho}^2} \right\|_{x_s}^{x_1}}_B + \underbrace{\left\| \frac{1}{\gamma} \frac{\overline{p' u_1''}}{\bar{p} \bar{c}} \right\|_{x_s}^{x_1}}_C - \underbrace{\int_{x_s}^{x_1} \frac{\overline{u_i''}}{\bar{c}^3} \frac{\partial \sigma_{ik}''}{\partial x_k} dx_1}_D = 0,$$

where  $\|f\|_a^b = f(b) - f(a)$ . The integrated results are shown in Figure 2(A). In all the cases we investigated (with different shock strengths and upstream turbulence intensities) the acoustic energy balance is satisfied with little deviation. The rapidly evolving acoustic energy — sum of scaled density and velocity fluctuations — is found to be mainly balanced by the pressure transport once the decay due to viscous dissipation is compensated. Therefore, the rapid evolution of velocity fluctuations can be attributed to the acoustic energy balance: energy transfer from the acoustic potential energy in the form of density (or pressure) fluctuations to turbulence kinetic energy. This is consistent with the fact that the pressure-transport term is scaled best by flow variables associated with acoustic wave propagation (Lee *et al.* 1993). Note that density fluctuation is replaced by the pressure fluctuation using the isentropic relation in deriving the acoustic energy balance equation, even though entropy fluctuation behind the shock wave contributes significantly to the density fluctuation (as is shown in Sec. 2.3). This is justified because as shown in Figure 2(B) the neglected entropy-dilatation correlation is found to be less than 30% of the pressure-dilatation correlation in the zone of interest, and 5% of the pressure transport term. Even though thermodynamic fluctuations are far from isentropic, the contribution of entropy fluctuations to the acoustic energy balance can be neglected. The entropy-dilatation correlation vanishes in the linear limit and the acoustic energy balance derived above holds exactly in the linear analysis, which ignores viscous dissipation.

Variance of vorticity fluctuation is a main contributor to the TKE dissipation rate. Figure 3(A) shows the evolution of vorticity components. The transverse components are amplified across the shock, while the streamwise component is hardly affected. Mach number dependence of transverse vorticity variance amplification predicted by LIA is shown in Figure 3(B). LIA predicts no amplification of the streamwise component. The amplification trend and its amplification ratio obtained from DNS are found to be consistent with the LIA prediction.

## 2.2 Turbulence length scales

Experimental studies (Debieve *et al.* 1986, Keller *et al.* 1990, Honkan *et al.* 1992) have reported that large scale turbulent motions are enhanced more than small scale motions as turbulence passes through a shock wave, leading to the overall increase of turbulence length scales, especially of microscales. LIA predicts that Taylor microscales decrease across the shock wave for all shock strengths, which was confirmed by DNS for weak shock waves (Lee *et al.* 1991a, 1993). For weak shock waves, changes in some turbulence length scales were too small to draw definite conclusions on the issue.

To investigate the scale-dependent amplification of turbulence, the modification of power spectra across the shock wave ( $M_1 = 2.0$ ) is computed through LIA for

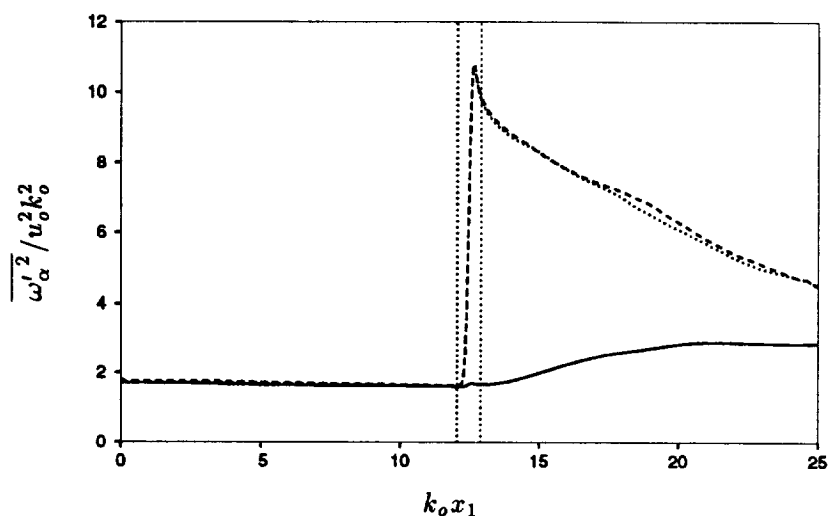


FIGURE 3(A). Evolution of the vorticity fluctuation variances with  $M_1 = 2.0$ :  
 —  $\overline{\omega_1'^2}$ , ---  $\overline{\omega_2'^2}$ , .....  $\overline{\omega_3'^2}$ .

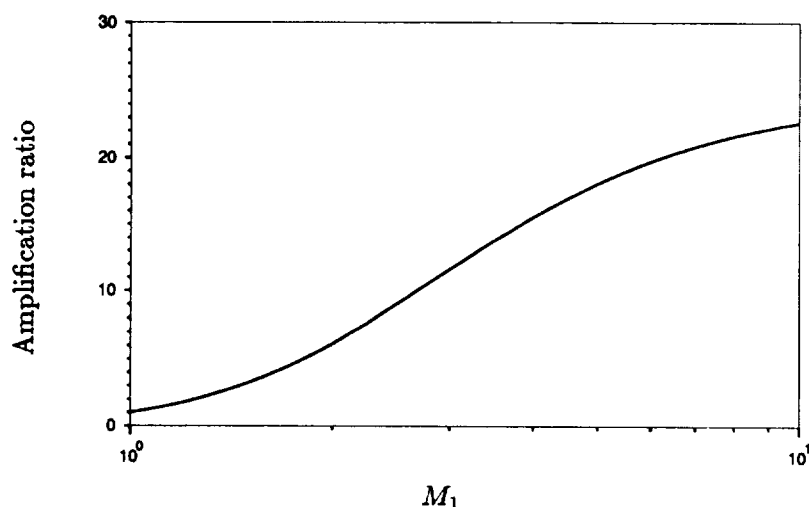


FIGURE 3(B). Amplification of transverse vorticity fluctuation variances predicted by LIA.

the one dimensional spectrum in the shock-normal (longitudinal) and transverse direction which is shown in Figure 4(A) and (B), respectively. In the longitudinal spectrum, significant scale-dependent amplification is observed: more amplification at small scales than at large scales. Large scale part of  $E_2(k_1)$  is even suppressed through the interaction. In the transverse spectrum, more amplification at small scales is found for  $E_1(k_2)$  and  $E_2(k_2)$ , while more amplification at large scale is found for  $E_3(k_2)$ . The energy spectrum used in the analysis is the von Karman



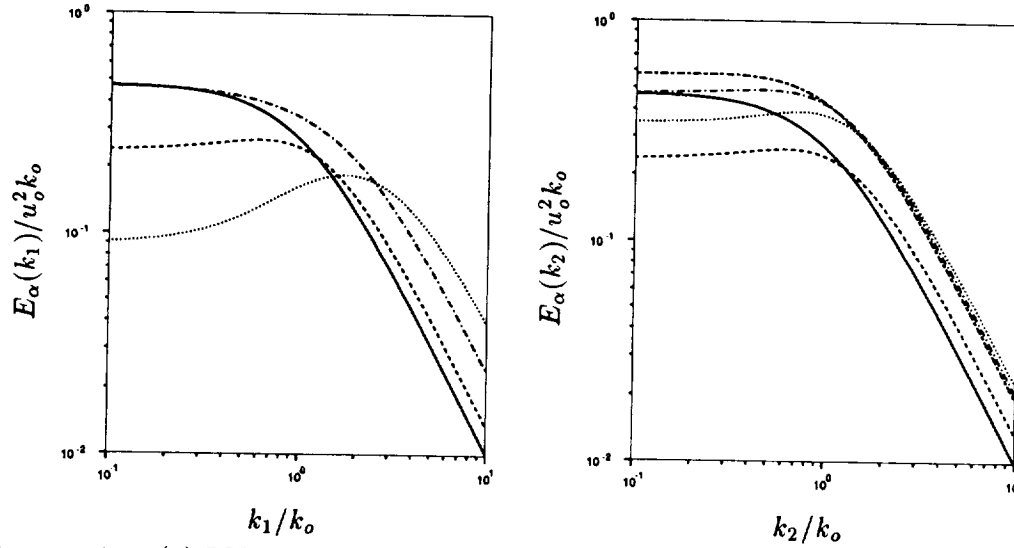


FIGURE 4. (a) LIA prediction of the shock-normal direction (vs.  $k_1$ ) one dimensional energy spectra change across the shock wave for  $M_1 = 2.0$ :  $E_1$ : — upstream, — downstream,  $E_2$  &  $E_3$ : ---- upstream, ..... downstream. (b) LIA prediction of the transverse direction (vs.  $k_2$ ) one dimensional energy spectra change across the shock wave for  $M_1 = 2.0$ :  $E_2$ : — upstream, — downstream,  $E_1$ : ---- upstream, ..... downstream,  $E_3$ : ---- upstream, — downstream.

spectrum (Hinze 1975), but the results obtained in the analysis are insensitive to choice of the spectrum. Since the spectrum amplification pattern is different for different spectrum (e.g.  $E_1(k_2)$  or  $E_3(k_2)$ ), the issue of the length scale change should be addressed for the specific length scale only. In the following, changes in various turbulence length scales are discussed.

To directly check the scale-dependent turbulence amplification, transverse power spectra of velocity fluctuations in a numerically simulated field from case A are shown for upstream and downstream of the shock wave in Figure 5. Amplification is more pronounced at the large wave numbers, which is consistent with the prediction by the linear analysis in Figure 4(B).

Keller *et al.* (1990) reported that both the density microscale and the integral length scale in the shock normal direction increase for shock waves with  $M_1 < 1.24$ . In the present simulation, the spectrum changes of density and temperature fluctuations across the shock are found to be similar to those of velocity fluctuations: Spectrum is amplified more at small scales than at large scales. The difference between the present study and the experiment may be due to the assumptions made in the experimental data analysis, such as turbulence isotropy/homogeneity, and negligible pressure fluctuations, which may be too crude in light of the simulation. Velocity fluctuation variances are axisymmetric as shown in Sec. 2.1, and thermodynamic property fluctuations are not isobaric and decay rapidly behind the shock wave as shown in Sec. 3.3. The effects of these imperfect assumptions on the data

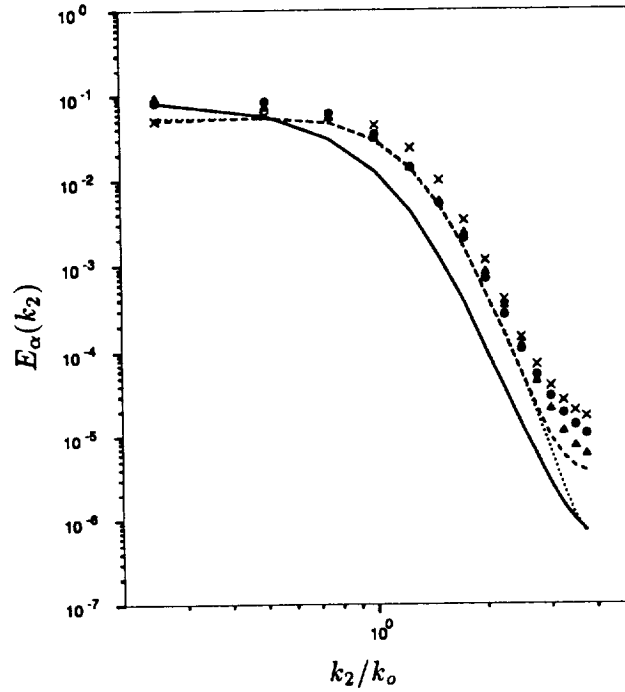


FIGURE 5. Changes in one dimensional spectra across the shock wave which is at  $k_0 x_s = 12.29$ : lines for upstream spectra at  $k_0 x_1 = 10.59$ , and symbols for downstream spectra at  $k_0 x_1 = 13.68$ . —, • :  $E_2(k_2)$ , ----, × :  $E_1(k_2)$ , ·····, △ :  $E_3(k_2)$ .

analysis are not clearly documented in Keller *et al.* (1990).

Figure 6(A) shows the evolutions of Taylor microscales ( $\lambda_\alpha$ ) and the transverse density microscale ( $\lambda_\rho$ ), which are defined as

$$\lambda_\alpha = \frac{\sqrt{u_\alpha'^2}}{\sqrt{u_{\alpha,\alpha}'^2}} \quad \text{and} \quad \lambda_\rho = \frac{\sqrt{\rho'^2}}{\sqrt{\rho_{',2}'^2}},$$

respectively. All the microscales decrease significantly across the shock wave: the streamwise Taylor microscale by about 50%, the transverse Taylor microscales by about 20%, and the density microscale by about 30%. Mach number dependence of Taylor microscale change predicted by LIA is shown in Figure 6(B). The higher the Mach number, the Taylor microscales are reduced further through the shock wave. The reduction is more pronounced in the shock-normal direction. The reduction observed in the simulation agrees well with the LIA prediction. The Taylor microscale which was reported to increase (Debieve *et al.* 1986) was the time scale, not the length scale (Debieve 1992, private communication). If the mean velocity decrease across the shock is properly accounted for, their experimental result is consistent with the present simulation and analysis.

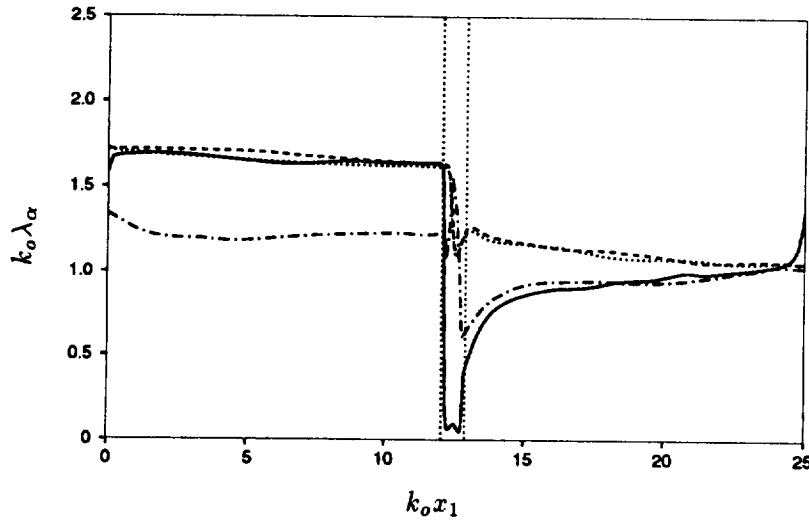


FIGURE 6(A). Evolution of microscales throughout the computational domain for  $M_1 = 2.0$ : —  $\lambda_1$ , ----  $\lambda_2$ , .....  $\lambda_3$ , —·—  $\lambda_\rho$ . Vertical lines denote the boundaries of shock intermittency.

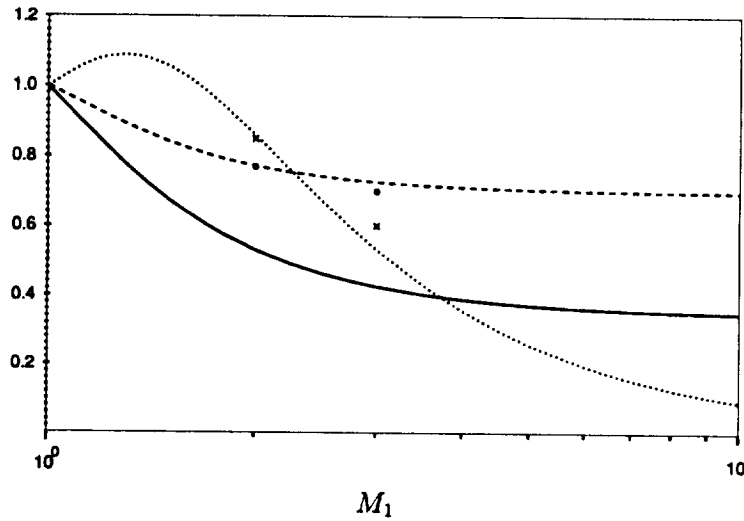


FIGURE 6(B). Change of Taylor microscales and dissipation length scale across the shock wave predicted by LIA. —  $\lambda_1$ , ----  $\lambda_2$  &  $\lambda_3$ , .....  $l_\epsilon$ . Symbols for DNS: •  $\lambda_2$ , ×  $l_\epsilon$ .

Integral scale ( $\Lambda_f$ ) of turbulent fluctuation  $f'$  in the  $x_2$ -direction is defined from its two-point correlation,  $C_f(r; x_1)$ , defined as

$$C_f(r; x_1) = \frac{\overline{f'(x_1, x_2, x_3, t) f'(x_1, x_2 + r, x_3, t)}}{\overline{f'(x_1, x_2, x_3, t) f'(x_1, x_2, x_3, t)}},$$

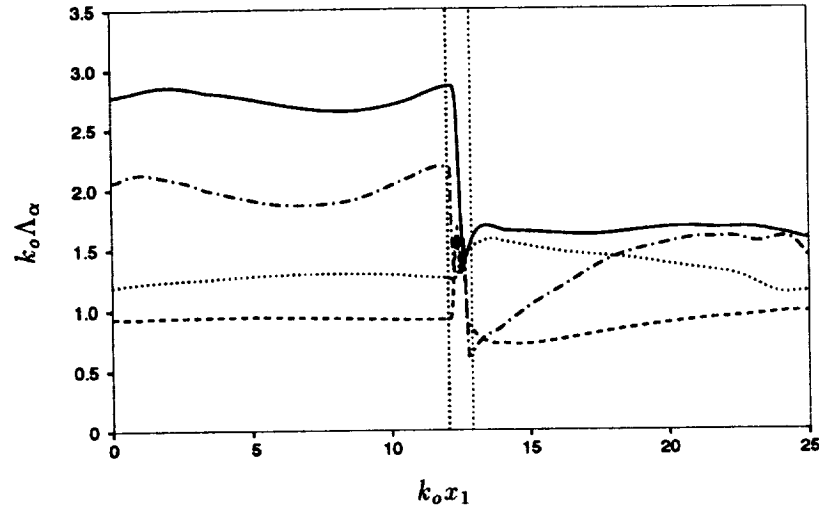


FIGURE 7. Evolution of integral scales throughout the computational domain for  $M_1 = 2.0$ : —  $\Lambda_{u_2}$ , ----  $\Lambda_{u_1}$ , .....  $\Lambda_{u_3}$ , —·—  $\Lambda_\rho$ . Vertical lines denote the boundaries of shock intermittency.

where the average is taken over time and homogeneous directions ( $x_2$ - and  $x_3$ -directions). The integral scale ( $\Lambda_f$ ) is, then, defined as

$$\Lambda_f(x_1) = \int_0^\infty C_f(r; x_1) dr,$$

where the upper limit of the integration is replaced by  $L/2$  when dealing with numerically simulated field with  $L$  being the computational box size in the  $x_2$ -direction, where the periodic boundary condition is enforced. Figure 7 shows the evolutions of four integral scales throughout the flow field. Three integral scales ( $\Lambda_{u_1}$ ,  $\Lambda_{u_2}$ , and  $\Lambda_\rho$ ) undergo reductions across the shock wave, most significantly in  $\Lambda_{u_2}$  by about 45%, while  $\Lambda_{u_3}$  increases by about 30%. Mach number dependence of the integral length scale change can be predicted by LIA. For the shock wave with  $M_1 = 2.0$ , the ratio of the downstream to the upstream integral length scale (with the von Karman upstream spectrum) is 0.91, 0.60, 1.46 for  $\Lambda_{u_1}$ ,  $\Lambda_{u_2}$ , and  $\Lambda_{u_3}$ , respectively. The simulation results agree well with the LIA predictions considering the difference in the upstream energy spectrum shape (see Fig. 4).

Most widely used length scale in turbulence modelling is the dissipation length scale ( $l_\epsilon$ ), defined as

$$l_\epsilon = \bar{\rho} q^3 / \epsilon,$$

where  $\epsilon$  is the dissipation rate of turbulence kinetic energy, which includes contributions from both solenoidal and dilatational motions. Figure 8 shows the evolution of the length scale  $l_\epsilon$ . The dissipation length scale also decreases across the shock wave. Just behind the shock wave, the length scale undergoes rapid increase as was the case with the streamwise Taylor microscale (Figure 6(A)), due to the rapid

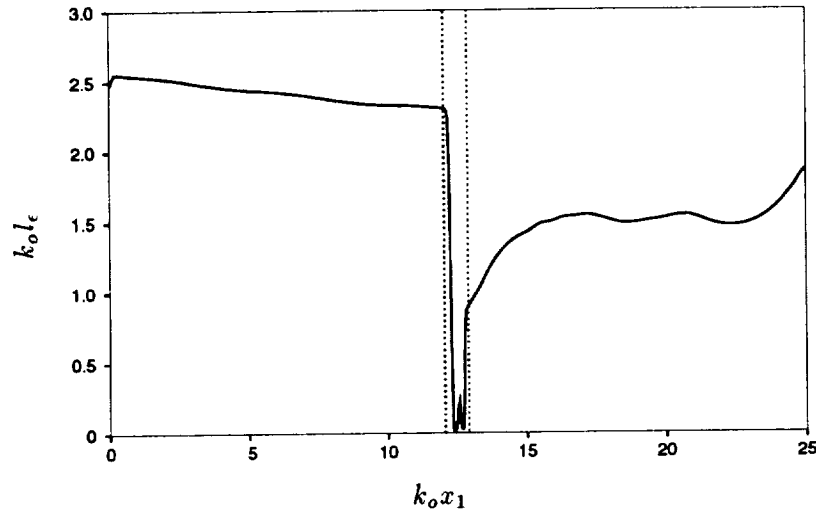


FIGURE 8. Evolution of the dissipation length scale throughout the computational domain for  $M_1 = 3.0$ . Vertical lines denote the boundaries of shock intermittency.

decay of the acoustic waves (or, the dilatational motions). The Mach number dependence of the dissipation length scale change predicted by LIA is presented in Figure 6(B). The length scale is reduced for strong shock waves, while it shows a mild increase for shock waves with  $M_1 < 1.65$ . For weak shock waves, TKE and its dissipation rate is comparably amplified to give slight increase in  $l_\epsilon$  across the shock wave, while TKE amplification saturate much faster than vorticity variance amplification to give the reduction in the length scale (Lee *et al.* 1993). The length scale increase observed by Honkan *et al.* (1992) at  $M_1 = 1.24$  (the equivalent shock normal Mach number in their experiment is 1.24 not 1.62) might be explained as the phenomenon occurring for weak shock waves, but the analyzed experimental results are not in quantitative agreement with the simulation and the analysis: LIA predicts less than 10% increase, while the analyzed experimental data shows more than 600% increase. This difference seems to suggest that the assumptions used in the experimental data analysis may be too crude, such as negligence of pressure fluctuations and applicability of Taylor's hypothesis in high intensity turbulence, and should be examined carefully.

### 2.3 Thermodynamic quantities

Thermodynamic fields which are obtained from the freely decaying turbulence (Lee *et al.* 1991b) and prescribed at the inflow are nearly isentropic. As the flow passes through the shock wave, all the fluctuations are amplified, followed by a decay. A general assumption on the relation between thermodynamic fluctuations is polytropic (with a polytropic exponent  $n$ ), where

$$\frac{p'}{\bar{p}} = n \frac{\rho'}{\bar{\rho}} = \frac{n}{n-1} \frac{T''}{\bar{T}}.$$

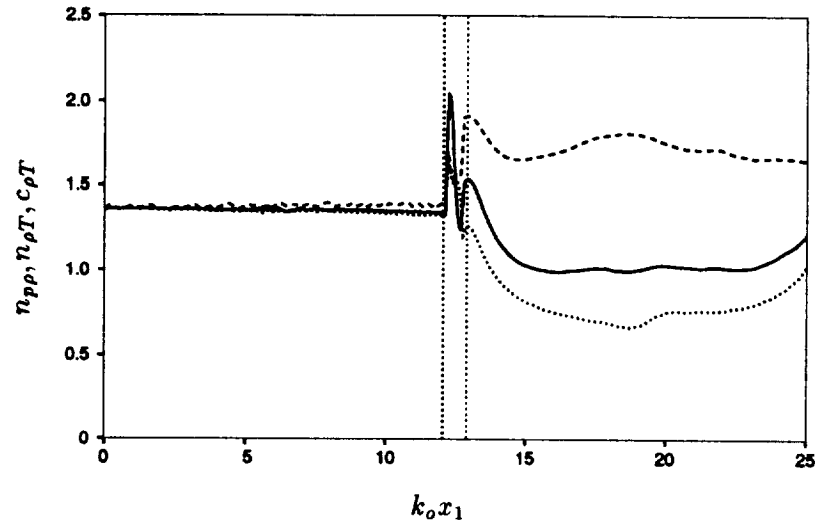


FIGURE 9. Evolution of exponents for the fluctuations in thermodynamic variables for  $M_1 = 2.0$ : —  $n_{p\rho}$ , ----  $n_{\rho T}$ , .....  $c_{\rho T}$ . Vertical lines denote the boundaries of shock intermittency.

For polytropic fluctuations, specification of one property fluctuation and the polytropic exponent is enough to describe the thermodynamic fluctuations. Based on the above relations, different polytropic exponents can be defined using normalized rms fluctuations ( $n_{p\rho}, n_{\rho T}$ ) and the correlations between instantaneous fluctuations ( $c_{\rho T}$ ) as

$$n_{p\rho} = \frac{\sqrt{p'^2/\bar{p}}}{\sqrt{\rho'^2/\bar{\rho}}}, \quad n_{\rho T} = 1 + \frac{\sqrt{T'^2/\bar{T}}}{\sqrt{\rho'^2/\bar{\rho}}},$$

and

$$c_{\rho T} = 1 + \frac{\bar{\rho}}{\bar{T}} \frac{\overline{\rho' T''}}{\rho'^2}.$$

For weak shock waves with  $M_1 \leq 1.20$ , relations between thermodynamic property fluctuations are close to isentropic ( $n = \gamma$ ) throughout the flow field (Lee *et al.* 1993).

In order to check the polytropy for the strong shock case, the polytropic exponents,  $n_{p\rho}, n_{\rho T}$ , defined above are investigated. If the fluctuations are indeed polytropic, the two exponents should be the same, which is defined as the polytropic exponent. The evolutions of the two exponents are shown in Figure 10. The exponents are the same upstream of the shock wave with  $n_{p\rho} = n_{\rho T} \simeq \gamma$ . Downstream of the shock wave, however, they differ significantly with  $n_{p\rho}$  decreasing and  $n_{\rho T}$  increasing. Their return to polytropy is very slow. To further investigate the relation between instantaneous fluctuations, the correlation between the fluctuations of density and temperature ( $\overline{\rho' T''}$ ) is studied.

The evolution of the exponent is also shown in Figure 9. Upstream of the shock wave, the exponent is quite close to the  $\gamma (= 1.40)$ . It drops significantly across the shock wave, and its further evolution is rather slow. The change in the exponents across the shock wave is found to be consistent with the LIA prediction (shown in Figure 10). Upstream thermodynamic fluctuations are polytropic (close to isentropic), and downstream fluctuations are not isentropic due to significant entropy fluctuations produced by the shock turbulence interaction. To properly describe the thermodynamic fluctuations in strong shock turbulence interaction, specification of at least one thermodynamic fluctuation along with two exponents (*i. e.*,  $n_{p\rho}$  and  $n_{\rho T}$ ) are required.

The shock strength effects on thermodynamic fluctuations for wider range of shock normal Mach numbers can easily be investigated through the linear analysis. In the following, polytropic exponents downstream of the shock in the interaction of solenoidal velocity fluctuations with a shock wave is studied. The effects of the shock strength on downstream polytropic exponents are shown in Figure 10. For isentropic or acoustic fluctuations, all the exponents are same and equal to the specific heat ratio. For entropic or isobaric fluctuations,  $n_{p\rho}$  and  $c_{\rho T}$  become 0 and  $n_{\rho T}$  becomes 2. For weak shock waves with  $M_1 < 1.2$ , thermodynamic fluctuations behind the shock can be regarded as isentropic. As the shock becomes stronger beyond this limit, the entropy fluctuation behind the shock cannot be neglected, and its importance becomes more dominant for the stronger shock waves. The results of the polytropic exponents from DNS are consistent with LIA predictions with the values from DNS systematically deviating from the LIA predictions toward the isentropic value of 1.4. This may be due to (incompressible) pressure fluctuations associated with dilatation-free velocity fluctuations (Sarkar *et al.* 1991), which accompany mainly isentropic thermodynamic fluctuations.

In order to quantify the importance of entropy fluctuations behind the shock wave, the contributions of acoustic and entropic fluctuations to the density fluctuation are quantified by the linear analysis and also shown in Figure 10. Since the acoustic fluctuations and entropic fluctuations are completely decorrelated in the linear limit, the relative importance of entropy fluctuations can be expressed as  $\frac{\overline{s'^2}/c_p^2}{\rho'^2/\bar{\rho}^2}$ . For weak shock waves with  $M_1 < 1.2$ , entropy fluctuations contribute less than 2% to the density fluctuations. However, entropy fluctuations become more important than acoustic fluctuations beyond  $M_1 = 1.65$ .

In summary, thermodynamic fluctuations downstream of the shock wave are found to be isentropic for weak shock waves ( $M_1 < 1.2$ ) and become non-polytropic for strong shock waves, where the importance of entropy fluctuations are comparable to the acoustic fluctuations. The thermodynamic fluctuations cannot be modelled using polytropic exponents in this regime. Therefore, modelling effort should be made separately for the acoustic fluctuations and entropic fluctuations. Zeman (1993) stressed the need for such a separation for the mean thermodynamic quantities.

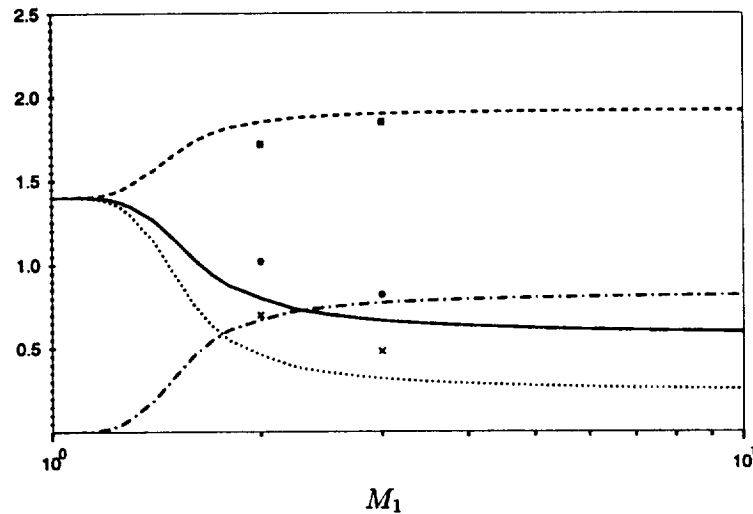


FIGURE 10. Downstream polytropic exponents and entropy fluctuation contribution predicted by LIA. —  $n_{p\rho}$ , ---  $n_{\rho T}$ , .....  $c_{\rho T}$ , — Entropy fluctuation contribution. Symbols for DNS: •  $n_{p\rho}$ , □  $n_{\rho T}$ , ×  $c_{\rho T}$ .

### 3. Future plans

The varied evolution of thermodynamic variables in Large-eddy Simulation (LES) using different formulations (where no explicit removal of aliasing errors is performed) has not yet been understood. In order to have a reference case where aliasing errors are removed exactly, a specific volume formulation in solving compressible Navier-Stokes equations is being pursued. Large eddy simulation of isotropic turbulence with a shock wave will be performed once the cause for the difference in the evolution of thermodynamic quantities is better understood.

Numerical simulation will be extended for a more practical situation where the turbulent boundary layer is subjected to externally imposed strains: a boundary layer under rapid expansion and over a compression ramp.

This work was produced in collaboration with Prof. S. Lele and Prof. P. Moin.

### REFERENCES

- ANDREOPOULOS, J. & MUCK, K.-C. 1987 Some New Aspects of the Shock-Wave Boundary Layer Interaction in Compression Ramp Corner. *J. Fluid Mech.* **180**, 405-428.
- CHANG, C.-T. 1957 Interaction of a Plane Shock Wave and Oblique Plane Disturbances with Special Reference to Entropy Waves. *J. Aero. Sci.* **24**, 675-682.
- DOLLING, D. S. & OR, C. T. 1985 Unsteadiness of the Shock Wave Structure in Attached and Separated Compression Ramp Flows. *Exp. Fluids*. **3**, 24-32.
- DEBIEVE, J. F. & LACHARME, J. P. 1986 A Shock-Wave/ Free Turbulence Interaction. *Turbulent Shear Layer/ Shock Wave Interactions*, J. Détery (ed.), Springer, Berlin.



- FAVRE, A. 1965 Équations des gaz turbulents compressibles I. *Journal Mécanique*. **4**, 361-390.
- GILES, M. B. 1990 Nonreflecting Boundary Conditions for Euler Equation Calculations. *AIAA Journal*. **28**, 2050-2058.
- HINZE, J. O. 1975 *Turbulence*, McGraw-Hill, p. 247.
- HONKAN, A. & ANDREPOULOS, J. 1992 Rapid Compression of Grid-Generated Turbulence by a Moving Shock Wave. *Phys. Fluids A*. **4**, 2562-2572.
- JACQUIN, L., BLIN, E., & GEFFROY, P. 1991 Experiments on Free Turbulence/Shock Wave Interaction. *Eighth Symposium on Turbulent Shear Flows, Munich*.
- JACQUIN, L., CAMBON, C., & BLIN, E. 1993 Turbulence Amplification by a Shock Wave and Rapid Distortion Theory. *Phys. Fluids A*. **5**, 2539-2550.
- KELLER, J. & MERZKIRCH, W. 1990 Interaction of a Normal Shock Wave with a Compressible Turbulent Flow. *Exp. Fluids*. **8**, 241-248.
- KERREBROCK, J. L. 1956 The Interaction of Flow Discontinuities with Small Disturbances in a Compressible Fluid. *Ph.D. Thesis*. California Institute of Technology.
- LEE, S. 1993 Large Eddy Simulation of Shock Turbulence Interaction. *Annual Research Briefs-1992*, Center for Turbulence Research, Stanford Univ./NASA Ames.
- LEE, S., LELE, S. K., & MOIN, P. 1991a Direct Numerical Simulation and Analysis of Shock Turbulence Interaction. *AIAA Paper No. 91-0523*, Reno, Nevada.
- LEE, S., LELE, S. K., & MOIN, P. 1991b Eddy Shocklets in Decaying Compressible Turbulence. *Phys. Fluids A*. **3**, 657-664.
- LEE, S., MOIN, P., & LELE, S. K. 1992 Interaction of Isotropic Turbulence with a Shock Wave. *Report TF-52*, Department of Mechanical Engineering, Stanford University.
- LEE, S., LELE, S. K., & MOIN, P. 1993 Direct Numerical Simulation of Isotropic Turbulence Interacting with a Weak Shock Wave. *J. Fluid Mech.* **251**, 533-562.
- LELE, S. K. 1992 Compact Finite Difference Schemes with Spectral-Like Resolution. *J. Comp. Phys.* **103**, 16-42.
- MCKENZIE, J. F. & WESTPHAL, K. O. 1968 Interaction of Linear Waves with Oblique Shock Waves. *Phys. Fluids*. **11**, 2350-2362.
- MEADOWS, K. R., CAUGHEY, D. A., & CASPER, J. 1993 Computing Unsteady Shock Waves for Aeroacoustic Applications. *AIAA Paper No. 93-4329*, Long Beach, CA.
- MOORE, F. K. 1953 Unsteady Oblique Interaction of a Shock Wave with a Plane Disturbances. *NACA TN-2879*.
- RIBNER, H. S. 1953 Convection of a Pattern of Vorticity through a Shock Wave. *NACA TN-2864*.



7-17  
N94-24166

## Local isotropy in distorted turbulent boundary layers at high Reynolds number

By Seyed G. Saddoughi

### 1. Motivation and background

This is a report on the continuation of our experimental investigations (Saddoughi 1993; Saddoughi & Veeravalli 1993) of the hypothesis of local isotropy in shear flows. This hypothesis, which states that at sufficiently high Reynolds numbers the small-scale structures of turbulent motions are independent of large-scale structures and mean deformations (Kolmogorov 1941), has been used in theoretical studies of turbulence and computational methods such as large-eddy simulation. Since Kolmogorov proposed his theory, there have been many experiments, conducted in wakes, jets, mixing layers, a tidal channel, and atmospheric and laboratory boundary layers, in which attempts have been made to verify – or refute – the local-isotropy hypothesis. However, a review of the literature over the last five decades indicated that, despite all these experiments in shear flows, there was no consensus in the scientific community regarding this hypothesis, and, therefore, it seemed worthwhile to undertake a fresh experimental investigation into this question.

#### 1.1 Plane boundary layer

In our previous reports, we presented hot-wire measurements of the velocity fluctuations in the test-section-ceiling boundary layer of the 80- by 120-foot Full-Scale Aerodynamics Facility at NASA Ames Research Center, the world's largest wind tunnel. At our measurement location, the boundary-layer thickness,  $\delta$ , was about 1.1 m, and the maximum Reynolds numbers based on momentum thickness,  $R_\theta$ , and on Taylor microscale,  $R_\lambda$ , were approximately 370,000 and 1,450 respectively. These were the largest ever attained in laboratory boundary-layer flows. The boundary layer developed over a rough surface, but the Reynolds-stress profiles agreed with canonical data sufficiently well for our purposes. Spectral and structure-function relations for isotropic turbulence were used to test the local-isotropy hypothesis, and our results established the condition under which local isotropy can be expected.

Here we use a Cartesian co-ordinate system  $x_i = (x, y, z)$  with  $x$ -axis along the flow direction,  $y$ -axis normal to the solid surface, and  $z$ -axis in the spanwise direction. The respective mean-velocity components in these directions are  $U_i = (U, V, W)$ , and the fluctuating components are  $u_i = (u, v, w)$ . Overbars denote time averages.

Our plane boundary-layer data showed that, to within the accuracy of measurement, the shear-stress co-spectral density  $E_{12}(k_1)$ , which is the most sensitive indicator of local isotropy, fell to zero at a wavenumber about a decade *larger* than that

at which the energy spectra first followed  $-5/3$  power laws. At the highest Reynolds number,  $E_{12}(k_1)$  vanished about one decade *before* the start of the dissipation range, and it remained zero in the dissipation range.

We found that the lower-wavenumber limit of locally-isotropic behavior of the shear-stress co-spectra is given by  $k_1 \sqrt{\epsilon/S^3} \approx 10$  where  $S$  is the mean shear,  $\partial U/\partial y$ , and  $\epsilon$  is the average turbulent energy dissipation rate per unit mass. Our investigation also indicated that for energy spectra this limit could be relaxed to  $k_1 \sqrt{\epsilon/S^3} \approx 3$ ; this is Corrsin's (1958) criterion, with the numerical value obtained from our data. The existence of an isotropic inertial range requires that this wavenumber be much less than the wavenumber at the onset of viscous effects,  $k_1 \eta \ll 1$  ( $\eta$  is the Kolmogorov length scale), so that the combined condition (Corrsin 1958 and Uberoi 1957) is  $S\sqrt{\nu/\epsilon} \ll 1$ .

Among other detailed results, it was observed that in the dissipation range, the energy spectra had a simple exponential decay (Kraichnan 1959) with an exponent prefactor close to the value  $\beta = 5.2$  obtained in direct numerical simulations at low Reynolds number. Plots of compensated spectra,  $k^{5/3} E(k_1)$ , proved to be a very sensitive test in the inertial subrange. The Kolmogorov constants obtained from the one-dimensional data at high Reynolds numbers satisfied the isotropic relations for the spectra and the second-order structure functions, and the constant for the three-dimensional spectrum,  $C$ , was estimated to be  $1.5 \pm 0.1$  (Monin & Yaglom 1975). Spectral "bumps" between the  $-5/3$  inertial range and the dissipative range were observed on all the compensated energy spectra. The shear-stress co-spectra rolled-off with a  $-7/3$  power law and scaled linearly with  $S$  (Lumley 1967).

In summary, our results confirmed the local-isotropy hypothesis for "simple" shear layers, and it was shown that one decade of inertial subrange with truly negligible shear-stress co-spectral density requires  $S\sqrt{\nu/\epsilon}$  not more than about 0.01 (for a shear layer with turbulent kinetic energy production  $\approx$  dissipation, this implies a microscale Reynolds number of about 1500).

### 1.2 Distorted boundary layer

The effects of extra mean strain rates on the large-scale structure of shear flows (Bradshaw 1973) have been investigated extensively. The unanswered question for us was "*will our criteria for the existence of local isotropy hold for complex non-equilibrium flows*". Therefore, experiments to address this question were designed for the 80- by 120-foot wind tunnel. One possible experiment was to study the plane-of-symmetry flow in front of an obstacle placed vertically in a fully-developed two-dimensional turbulent boundary layer, e.g. a circular cylinder placed with its axis perpendicular to the plate. There have been a number of experimental investigations dealing with the large-scale structural changes that occur in this kind of flow (Johnston 1960; Hornung & Joubert 1963; Belik 1973; Mehta 1984; Agui & Andreopoulos 1990; Devenport & Simpson 1990; to name a few). In this type of boundary layer, the pressure rises strongly as the obstacle is approached and in the plane of symmetry of the flow the boundary layer is also influenced by the effects of lateral divergence (Saddoughi & Joubert 1991). Hence, in addition to the basic shear,  $\partial U/\partial y$ , the extra strain rates involved in the flow are  $\partial U/\partial x$ ,  $\partial V/\partial y$  and

$\partial W/\partial z$ . To obtain the desired effects, the size of the cylinder should be at least of the order of the thickness of the boundary layer. To conduct such an experiment in the 80' by 120' wind tunnel, a very large cylinder had to be fixed to the ceiling of the tunnel. This presented considerable construction difficulties. Here some of the results taken in front of this cylinder at the highest speed of the tunnel will be discussed.

## 2. Accomplishments

### 2.1 Apparatus and measurement techniques

The only possible way for attaching an obstacle to the ceiling of the 80- by 120-foot wind tunnel was to use one of the existing light ports for this purpose. Since the diameter of our test cylinder had to be larger than the clear opening of a typical light port, we had to use two concentric cylinders. As shown in Plate 1(a), the main cylinder is a ready-made light-weight polyethylene tank (wall thickness =  $\frac{1}{4}$ " , diameter  $D = 4'$  and height  $L = 6'$ ) and the inner (second) cylinder is a  $\frac{1}{2}$ " thick, 8" diameter aluminum (6061-T651) tube, which extends for about 6' into the attic through the light port. Steel rods are bolted to the aluminum cylinder. A  $\frac{1}{4}$ " thick high-density polyethylene plate and a  $\frac{1}{8}$ " thick aluminum plate are respectively bolted to the inside and outside of the bottom of the polyethylene tank. The effective wall thickness at the bottom of the tank is  $\frac{5}{8}$ ". Another  $\frac{1}{4}$ " thick high-density polyethylene plate is bolted to the top of the tank, and the space between the aluminum cylinder and the tank is filled with high-density Polyurethane foam. This provided us with a fairly light-weight (500 lb) and solid cylinder.

From the attic above the test-section ceiling, this whole unit was pulled up through the light port and was attached to the attic structure. Plate 1(b) shows the test cylinder in place as viewed from inside the test section. The NASA safety requirements were satisfied, and the cylinder and its attachments were designed for maximum possible aerodynamic load and dynamic loading due to seismic activity with an overall factor of safety of 5 on yield strength.

Another light port upstream of the cylinder was used for traversing the probe through the boundary layer. Therefore, our measurement location was fixed at  $x/D \approx 0.85$  with respect to the front of the cylinder. The measurement strategy, instrumentation, and procedure were all similar to those explained by Saddoughi (1993) and Saddoughi & Veeravalli (1993), and details will not be repeated here.

### 2.2 Results and discussion

The measurements to be discussed here correspond to the maximum reference velocity of the tunnel,  $U_{ref} = 51.25$  m/s. The normalized profiles of the longitudinal mean velocity,  $U/U_{ref}$ , for the present distorted boundary layer are compared with the profiles obtained for both the high-speed and low-speed cases of the plane boundary layer in figure 1, where  $y$  is the distance from the wall. Also shown in this figure are the least-squares polynomial fit to each of the data sets (solid lines), which have been used to obtain the mean-flow integral parameters for each experiment. The shape of the velocity profile for the distorted boundary layer is typical

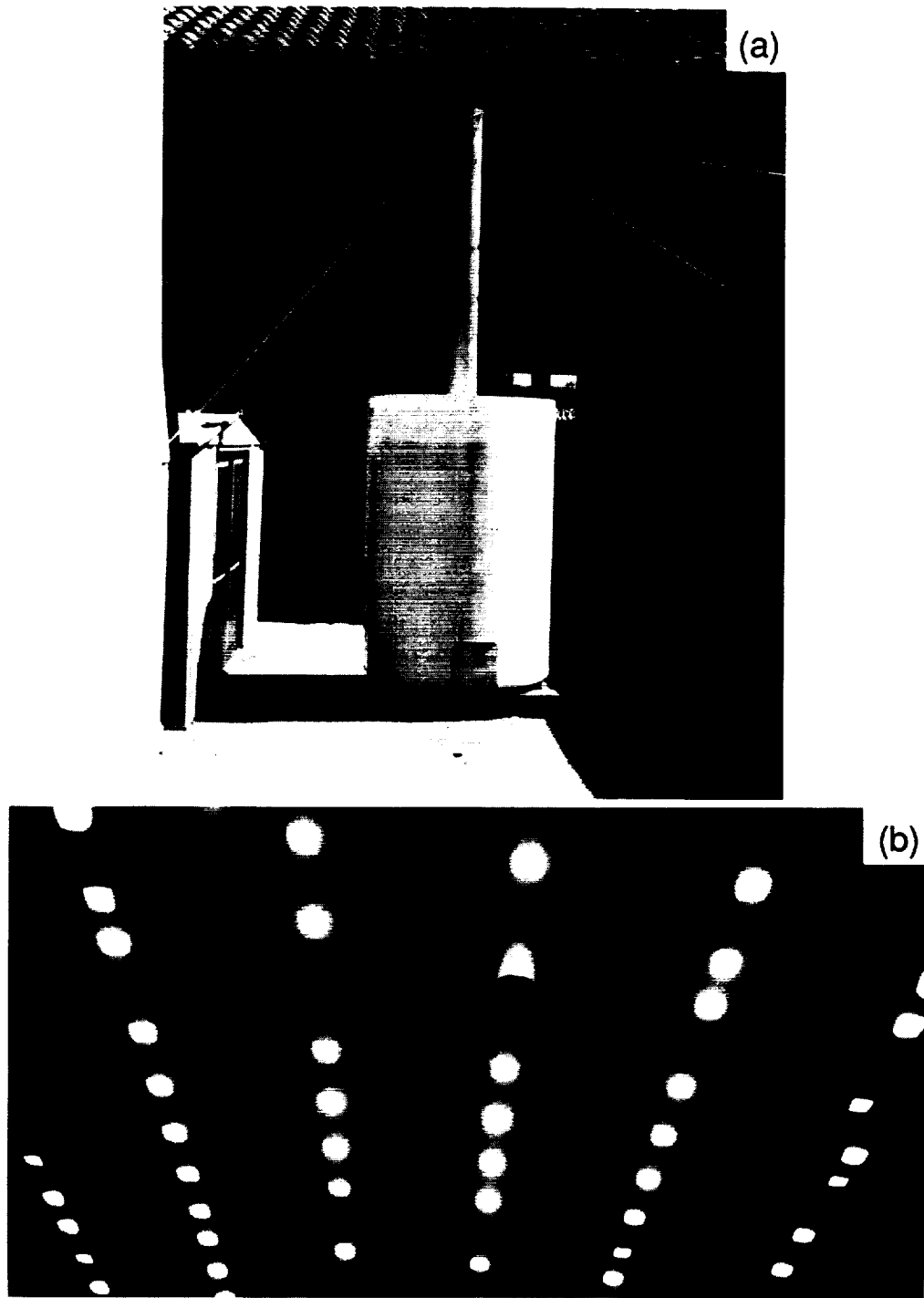


Plate 1. Test cylinder. (a) Outer (main) cylinder (polyethylene tank: wall thickness =  $\frac{1}{4}$ " , diameter  $D = 4'$ , and height  $L = 6'$ ) and the inner (support) cylinder (aluminum 6061-T651 tube:  $\frac{1}{2}$ " thick, 8" diameter and 12' height). (b) Test cylinder attached to the ceiling of the 80' X 120' wind tunnel, as viewed from inside the test section.

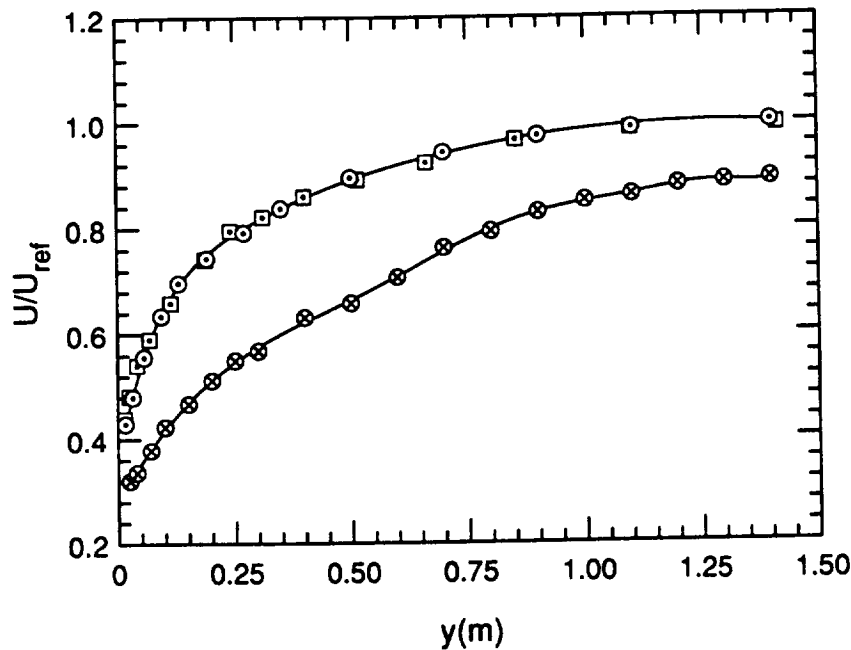


FIGURE 1. Normalized longitudinal mean-velocity profiles measured in plane and distorted boundary layers.  $\circ$ ,  $U_{ref} \approx 50$  m/s and  $\square$ ,  $U_{ref} \approx 10$  m/s plane boundary layer;  $\otimes$ ,  $U_{ref} \approx 51$  m/s distorted boundary layer. The solid lines are the least-square polynomial fit to each data set.

of the adverse-pressure-gradient flows: reduction in  $\partial U/\partial y$ . The boundary-layer thickness,  $\delta$  (the point where  $U/U_e = 0.995$ ) has increased to approximately 1250 mm in the distorted boundary layer. Here the shape factor  $H \approx 1.85$ , and in the freestream the pressure coefficient  $C_p \approx 0.23$ .

Figure 2 shows the normalized profiles of the normal velocity component,  $V/U_{ref}$ , and the spanwise component,  $W/U_{ref}$ , which were measured by the X-wires in UV- and UW-mode respectively. It can be seen that, as expected, in the plane of symmetry of the flow the crossflow,  $W$ , is approximately equal to zero. A least-squares polynomial fit to the  $V$  profile was used to obtain the values of  $\partial V/\partial y$ .

The magnitudes of the extra strain rate due to the streamline divergence,  $\partial W/\partial z$ , influencing the plane of symmetry of the flow can be obtained from  $(\partial W/\partial z) = U(\partial\beta/\partial z)$  (see e.g. Saddoughi & Joubert 1991), where  $\beta$  is the flow yaw angle measured at different spanwise locations  $z$ . The profiles of  $\beta$  measured by a yaw-meter probe for three spanwise locations ( $z/D = -0.21, 0, 0.21$ ) through the boundary layer are shown in figure 3. The profiles are typical of three-dimensional boundary layers: larger flow yaw angles near the wall than the freestream. Finally, the continuity equation was used to obtain the  $\partial U/\partial x$  values.

The profiles of the Reynolds normal stresses ( $\overline{u_1^2}/U_{ref}^2, \overline{u_2^2}/U_{ref}^2, \overline{u_3^2}/U_{ref}^2$ ), and

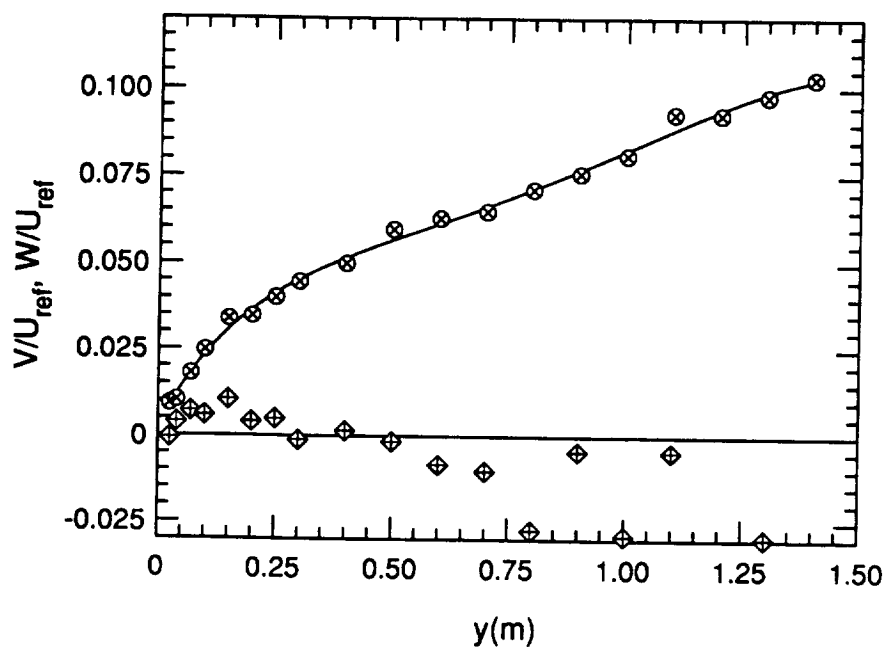


FIGURE 2. Normalized vertical and spanwise mean-velocity profiles measured in the plane of symmetry of the distorted boundary layer.  $\otimes$ ,  $V/U_{ref}$ ;  $\diamond$ ,  $W/U_{ref}$ .

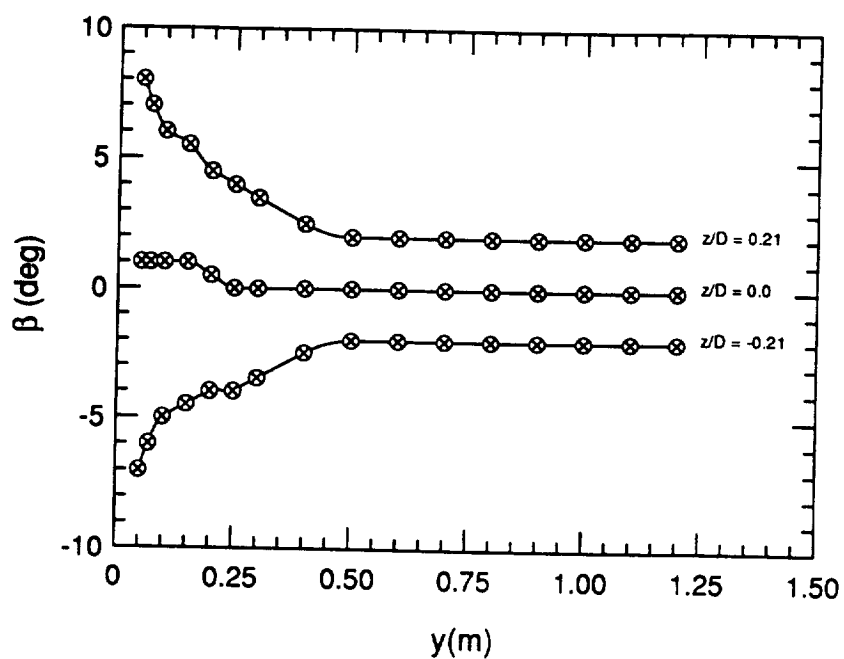


FIGURE 3. Flow yaw-angle profiles measured in the distorted boundary layer at different spanwise locations.



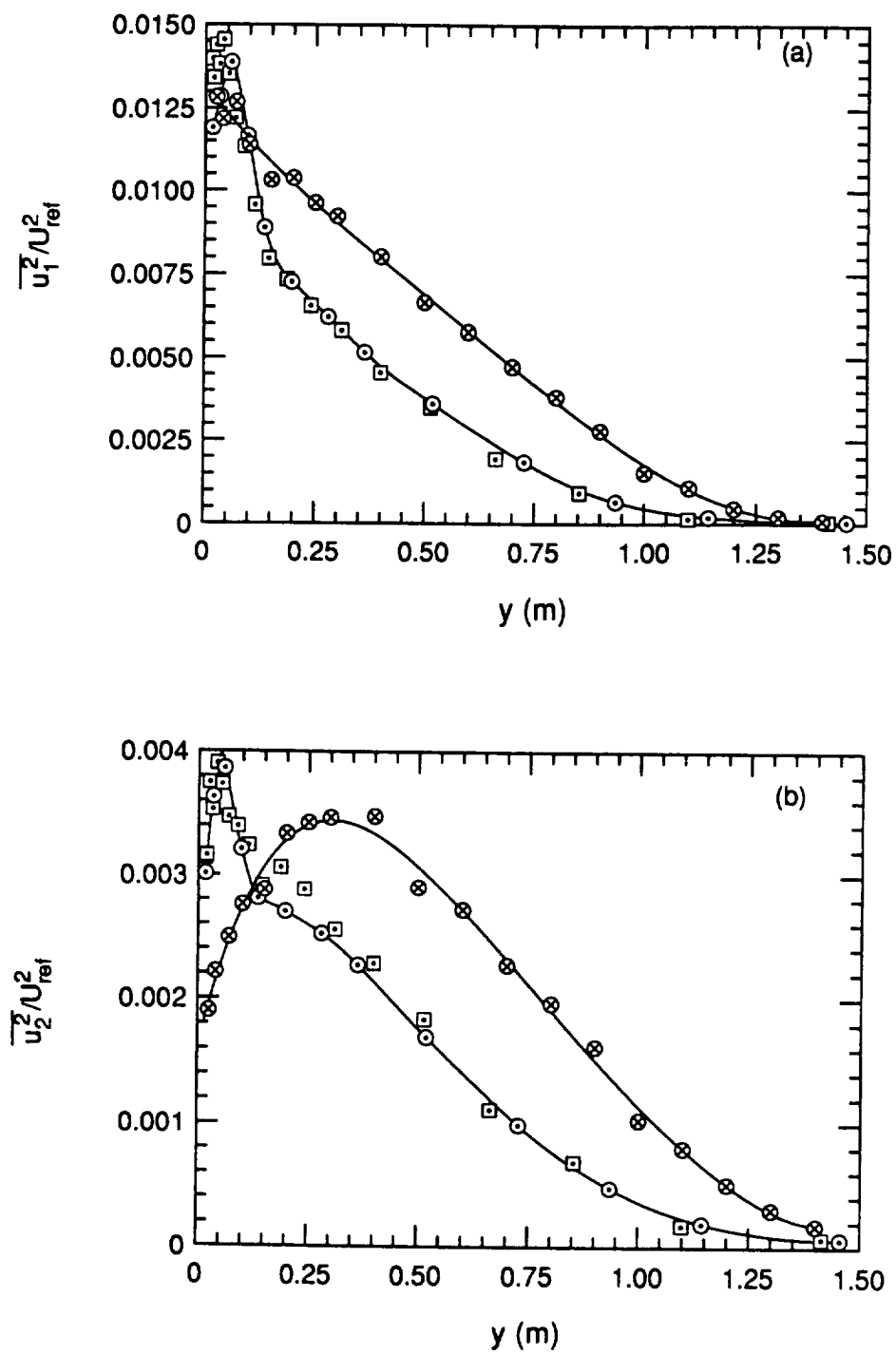


FIGURE 4(A,B). For caption see next page.

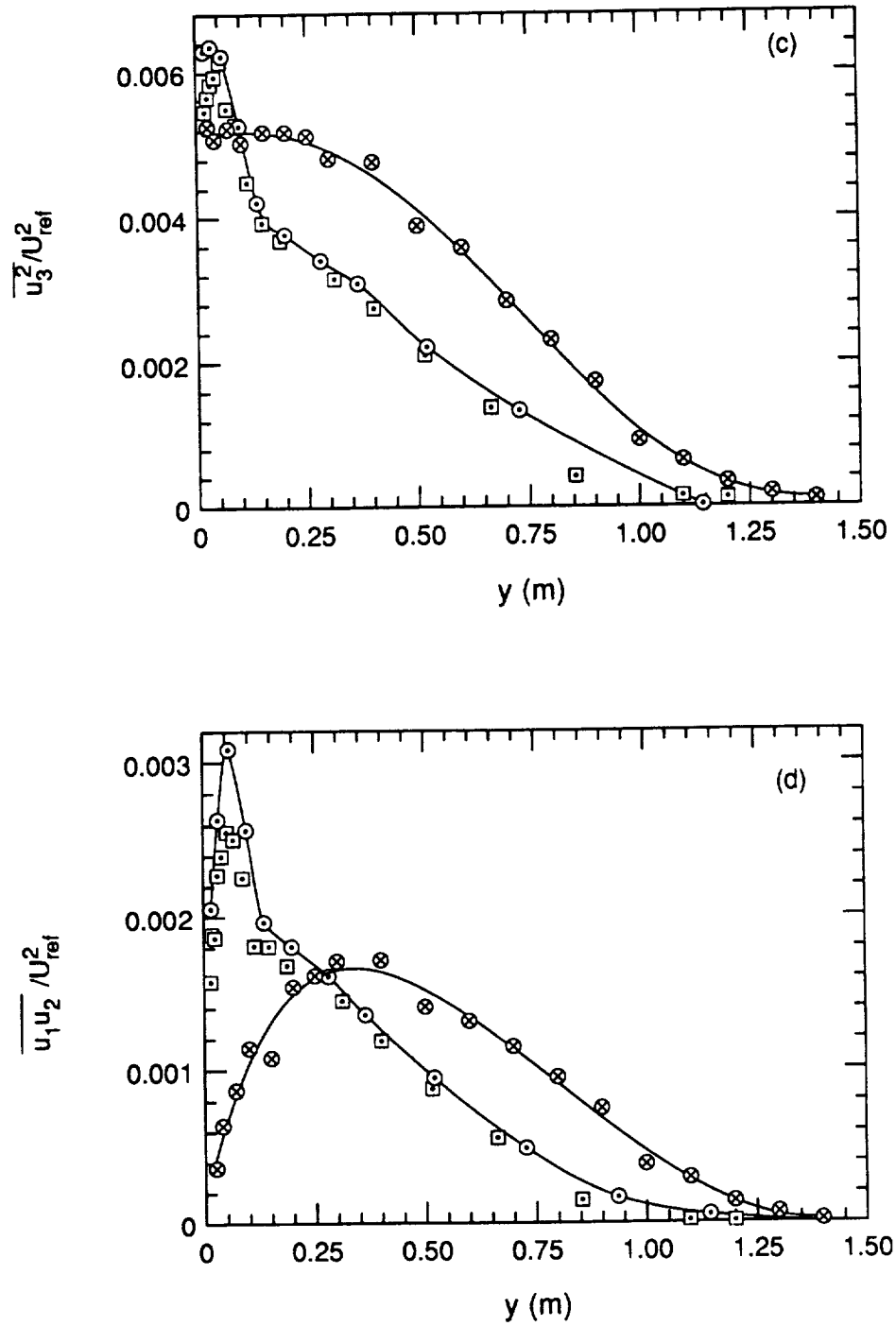


FIGURE 4. Profiles of Reynolds stresses measured in plane and distorted boundary layers: (a)  $\overline{u_1^2}/U_{ref}^2$ , (b)  $\overline{u_2^2}/U_{ref}^2$ , (c)  $\overline{u_3^2}/U_{ref}^2$ , (d)  $\overline{u_1 u_2}/U_{ref}^2$ . For key to symbols see figure 1.

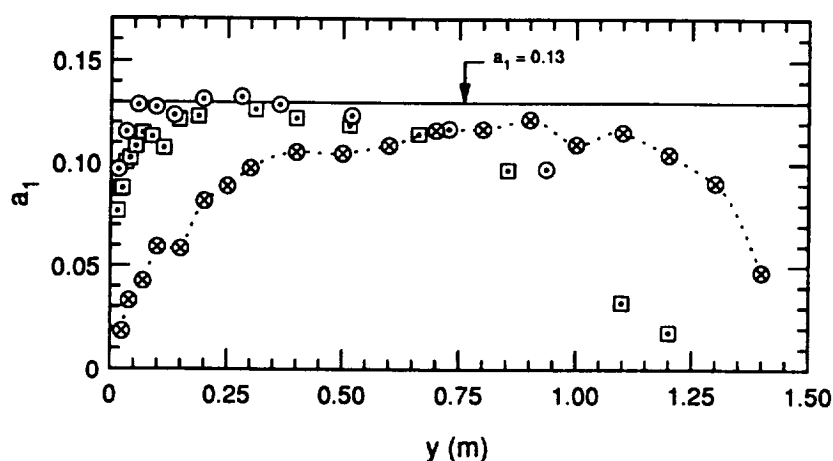


FIGURE 5. The structure parameter,  $a_1 \equiv -\overline{u_1 u_2}/q^2$ . The solid line is the canonical smooth-wall value (Townsend 1976). For key to symbols see figure 1.

the shear stress,  $-\overline{u_1 u_2}/U_{ref}^2$ , for the distorted and plane boundary layers are compared in figure 4. The profiles for the distorted boundary layer appear to be quite different from the plane flow case. The peaks of  $\overline{u_2^2}$  and the shear stress,  $-\overline{u_1 u_2}$ , profiles have moved away from the wall to  $y \approx 300$  mm, and in the outer part of the layer the values of all the Reynolds stresses have increased. The changes in the large-scale structure of turbulence can be seen in figure 5, which shows the profiles of Townsend's structure parameter,  $a_1 \equiv (-\overline{u_1 u_2}/q^2)$ , where  $q^2 (\equiv \overline{u_i u_i})$  is twice the turbulent kinetic energy per unit mass. The large drop in the values of this parameter in the inner part of the boundary layer, and their recovery to the canonical values in the outer part of the layer are apparently due to the effects of adverse pressure gradients (see Bradshaw 1967).

The spectral measurements of the three components of the velocity made at  $y = 100$  mm, 300 mm, and 500 mm are analyzed here. The location  $y = 300$  mm was chosen because, as shown earlier, the peak of the Reynolds stresses occurred at this position in the layer. For these three locations, the values of the extra-mean-strain rates,  $(\partial U/\partial x)/(\partial U/\partial y)$ ,  $(\partial V/\partial y)/(\partial U/\partial y)$ , and  $(\partial W/\partial z)/(\partial U/\partial y)$  are all larger than 0.1, which according to Bradshaw (1973) should produce large non-linear effects on the large-scale structures of the boundary layer.

In figure 6, we examine the  $II (\equiv -\frac{1}{2} b_{ij} b_{ji})$  and  $III (\equiv \frac{1}{3} b_{ij} b_{jk} b_{ki})$  invariants map of the Reynolds stress anisotropy tensor (Lumley & Newman 1977; Lee & Reynolds 1985),  $b_{ij} \equiv (\overline{u_i u_j}/q^2) - \delta_{ij}/3$ , where  $\delta_{ij} = 1$  or 0 for  $i = j$  or  $i \neq j$  respectively. The data points shown in this figure correspond to those positions in both the boundary layers where spectral measurements were taken. It appears that for both the plane and distorted layers, the values are close to the axisymmetric expansion limit. However, note that there is a fairly large increase for the distorted boundary layer, particularly at  $y = 100$  mm, which is represented by the highest point in each

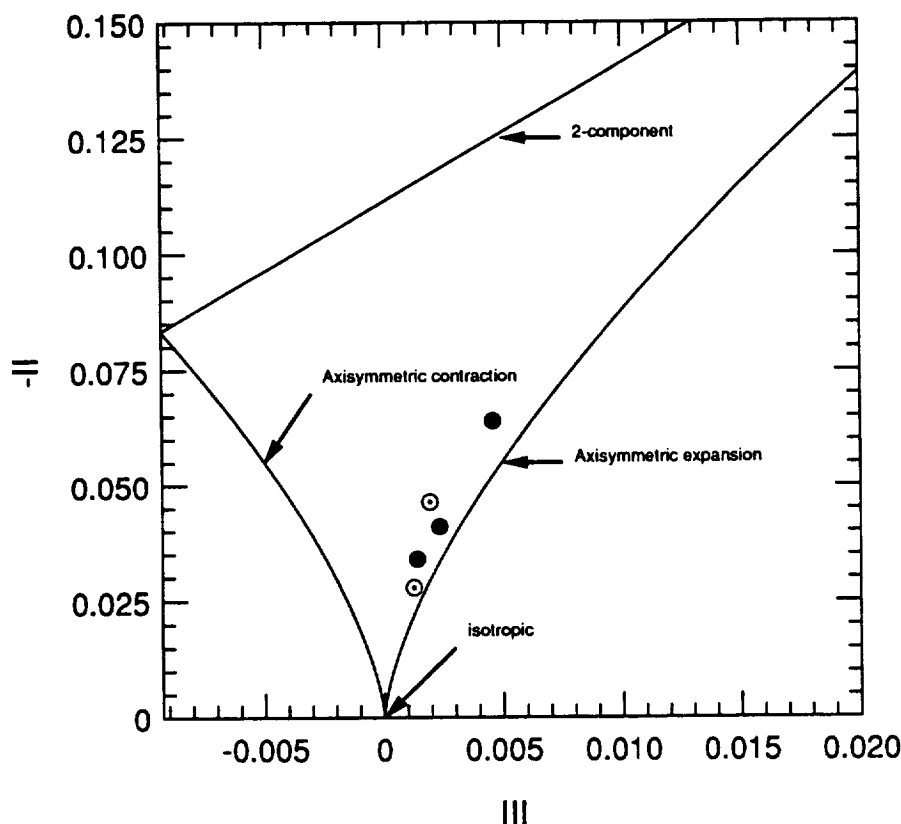


FIGURE 6. Anisotropy invariant map of Reynolds stress. Open and solid symbols are for the plane and distorted boundary layers respectively. The maximum value in each case corresponds to measurements at  $y = 100$  mm.

data set.

As an example of the spectral measurements, figure 7 shows Kolmogorov's universal scaling of the one-dimensional longitudinal power spectra at the inner-layer position of the distorted boundary layer and the mid-layer position of the plane boundary layer, compared with a compilation of previous experimental work taken from Chapman (1979) with later additions. The Reynolds numbers for the present distorted boundary layer have increased substantially, and a maximum  $R_\lambda \approx 1960$  has been obtained for the inner-layer position.

The intensity (or rapidity) of a mean strain rate can be measured in terms of  $s = \sqrt{s_{ij}s_{ij}/2}$ , (Lee & Reynolds 1985). To be consistent with our earlier definition, we shall use  $S = 2s$  as the equivalent mean strain rate. To test the local-isotropy hypothesis in the distorted layer, log-linear plots of the correlation-coefficient spectra,  $R_{12}(k_1) \equiv -E_{12}(k_1)/\sqrt{E_{11}(k_1)E_{22}(k_1)}$ , are plotted versus the non-dimensional wavenumber  $k_1\sqrt{\varepsilon/S^3}$  in figure 8. In isotropic flow the shear-stress co-spectrum,  $E_{12}(k_1)$ , which satisfies  $\int_0^\infty E_{12}(k_1)dk_1 = -\overline{u_1u_2}$ , is equal to zero. This indicates

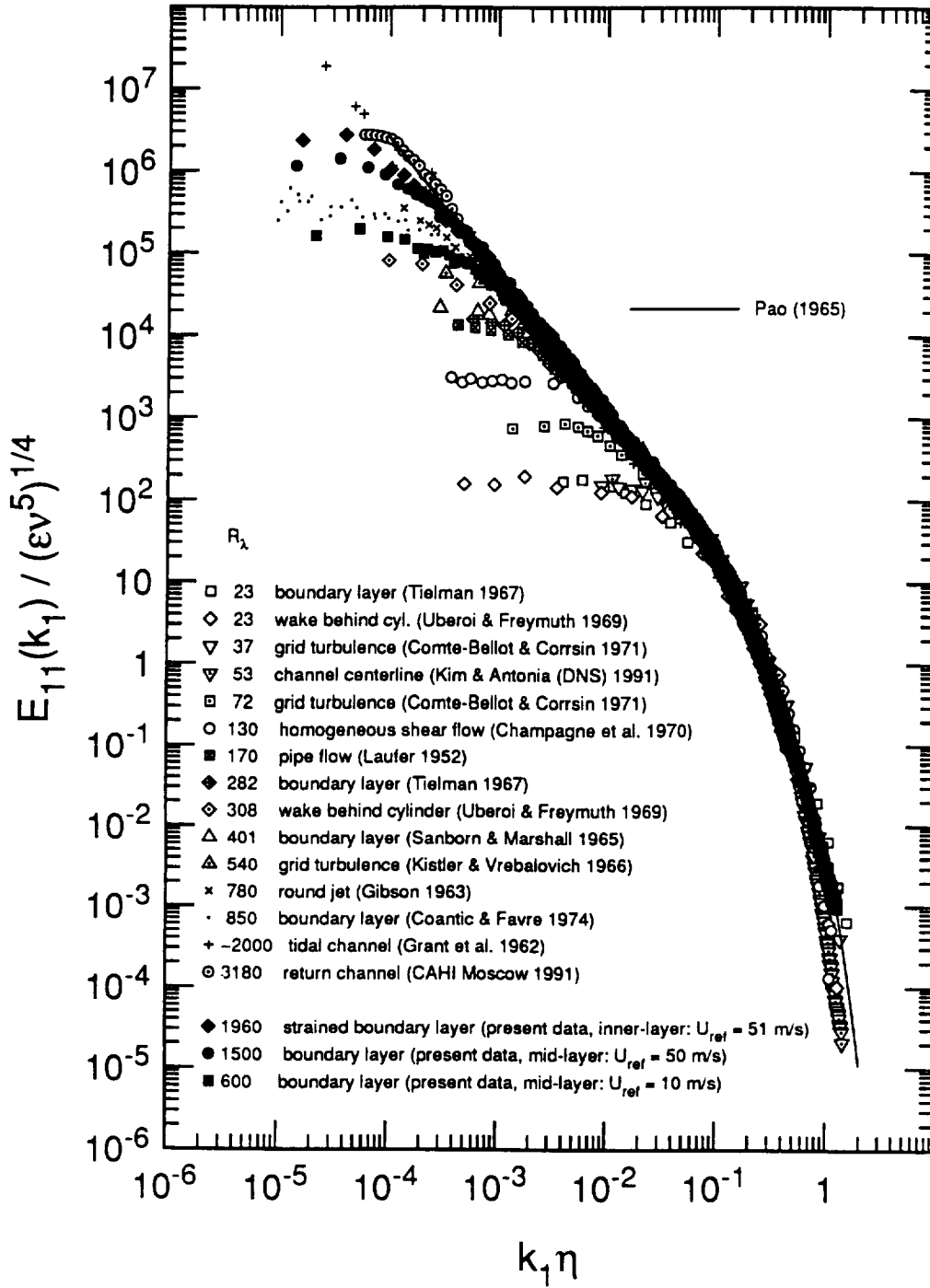


FIGURE 7. Kolmogorov's universal scaling for one-dimensional longitudinal power spectra. The present mid-layer and inner-layer spectra for the respective plane and distorted boundary layers are compared with data from other experiments. This compilation is from Chapman (1979), with later additions.

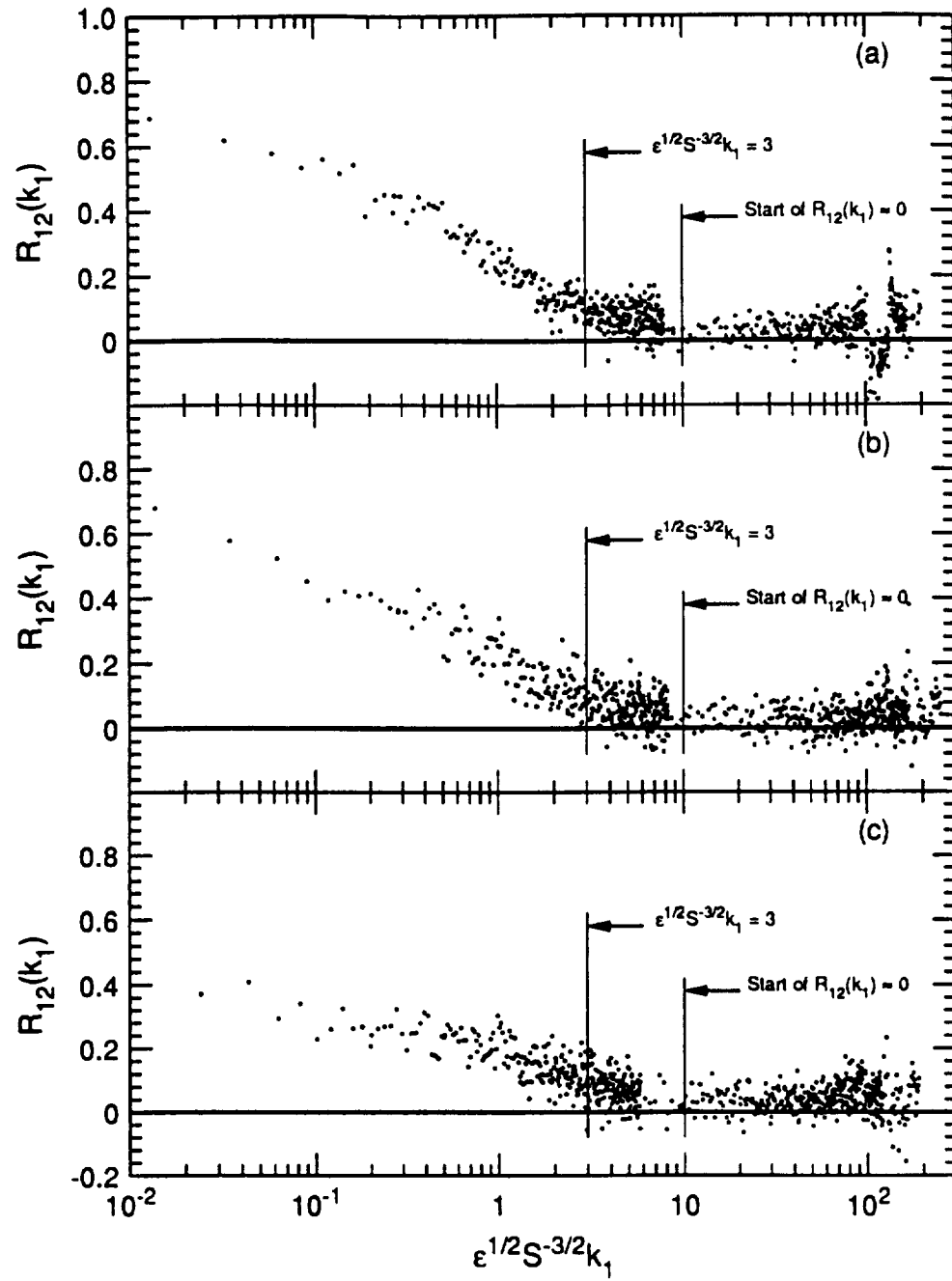


FIGURE 8. Correlation-coefficient spectra obtained at different locations in the distorted boundary layer for  $U_{ref} = 51$  m/s: wavenumber scaled with  $\sqrt{\epsilon/S^3}$ . (a)  $y = 500$  mm,  $R_\lambda \approx 1960$ ; (b)  $y = 300$  mm,  $R_\lambda \approx 1950$ ; (c)  $y = 100$  mm,  $R_\lambda \approx 1750$ .

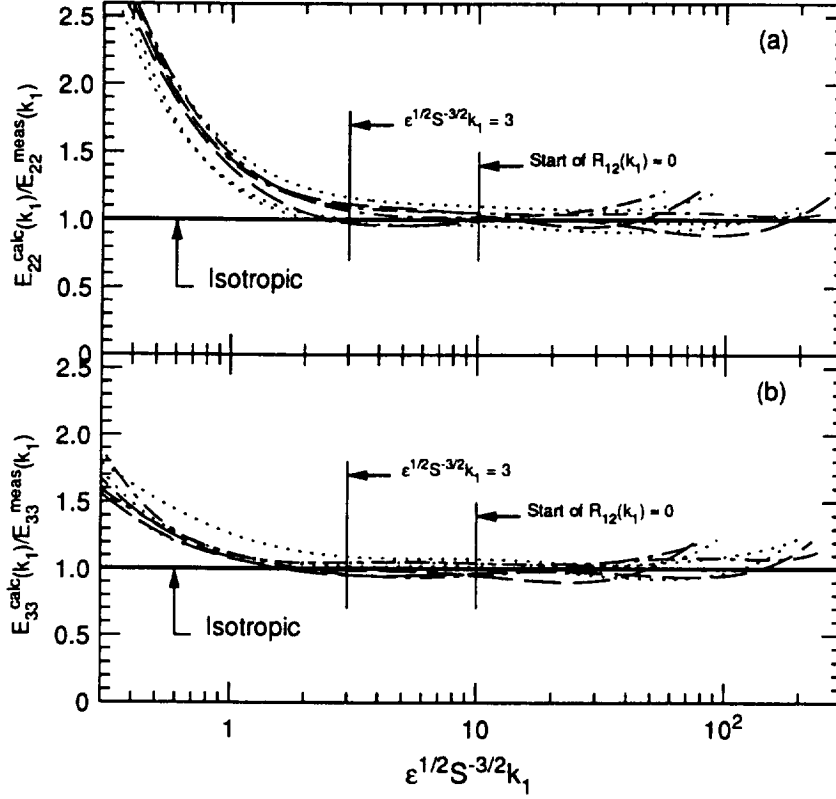


FIGURE 9. Ratios of calculated to measured transverse spectra at different locations and freestream velocities in the plane (----) and distorted (.....) boundary layers: wavenumber scaled with  $\sqrt{\epsilon}/S^3$ .

that for local isotropy the correlation-coefficient spectrum should fall to zero at high wavenumbers. For all the three measurement positions in the boundary, the Corrsin-Ubroi condition  $S_c^* \equiv S\sqrt{\nu/\epsilon} \ll 1$  was satisfied. It can be seen from figure 8 that at all the measurement locations  $R_{12}(k_1)$  reaches the isotropic value of zero at  $k_1\sqrt{\epsilon}/S^3 \approx 10$ , which is the same limit found for the plane boundary layer for the onset of local isotropy.

If the motion is isotropic, the transverse spectra  $E_{22}(k_1)$  and  $E_{33}(k_1)$  are uniquely determined by the longitudinal spectrum  $E_{11}(k_1)$  (e.g. Batchelor 1953):  $E_{22}(k_1) = E_{33}(k_1) = \frac{1}{2}(1 - k_1 \frac{\partial}{\partial k_1})E_{11}(k_1)$ . The transverse spectra,  $E_{22}^{calc}(k_1)$  and  $E_{33}^{calc}(k_1)$ , can be calculated from the measured longitudinal spectrum,  $E_{11}^{meas}(k_1)$ , using the above equation. An anisotropy measure may be defined as  $E_{\alpha\alpha}^{calc}(k_1)/E_{\alpha\alpha}^{meas}(k_1)$ , where  $\alpha = 2$  or  $3$  corresponds to  $u_2$  or  $u_3$  respectively. These anisotropy measures should be equal to 1.0 in an isotropic flow. We have used 9<sup>th</sup>-order, least-squares polynomial log-log fits to the data to calculate these measures, which are shown in figure 9 scaled using the length scale  $\sqrt{\epsilon}/S^3$ . The data for the plane boundary layer are also shown in this figure. It is obvious that the uncertainty in estimating the  $S$  values for the distorted boundary layer is larger than the plane case.

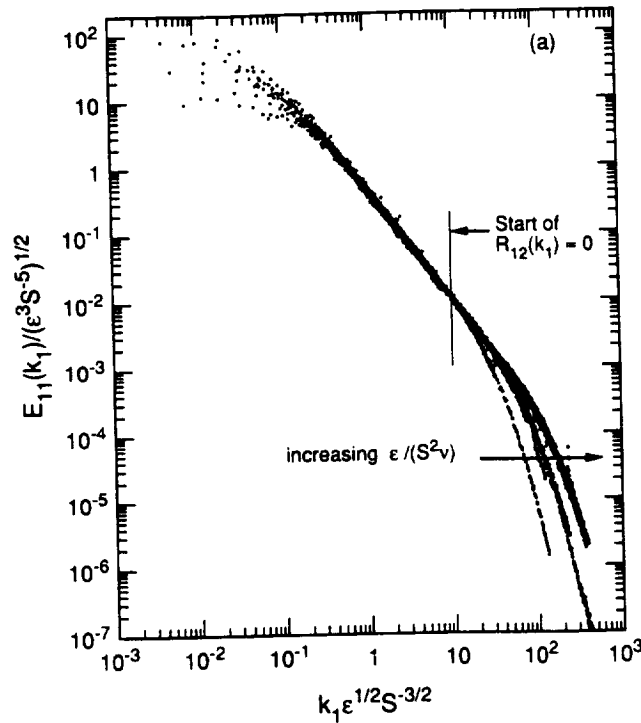


FIGURE 10(a). For caption see next page.

However, it appears that a reasonably good collapse is obtained and local isotropy of energy spectra is achieved ( $\pm 10\%$ ) in the inertial subrange for non-dimensional wavenumbers  $k_1 \sqrt{\epsilon/S^3} > 3$ .

For both plane and distorted boundary layers, the collapse of the longitudinal and transverse spectra achieved using  $\sqrt{\epsilon/S^3}$  and  $\sqrt{\epsilon/S}$  as length and velocity scales, respectively, is shown in figure 10. As to be expected, these scales will not collapse the low and high-wavenumber ranges of the spectra. Also marked on this figure is the wavenumber corresponding to the start of  $R_{12}(k_1) \approx 0$ , which is about one decade higher than the start of the  $-5/3$  law on the energy spectra. This plot clearly demonstrates the fact that a  $-5/3$  law does not necessarily imply local isotropy. We also note that in the *high-wavenumber* range the extent of the  $-5/3$  law does not increase with  $R_\lambda$ , but it is a function of  $(\epsilon/S^2\nu)$ , which is the Reynolds number based on the above length and velocity scales. However, the accuracy of this observation will be examined further after completing the upcoming low-speed measurements.

### Acknowledgements

We wish to thank Dr. Fredric Schmitz, Chief of the Full-Scale Aerodynamics Research Division at NASA Ames for permitting us to use their facility and to



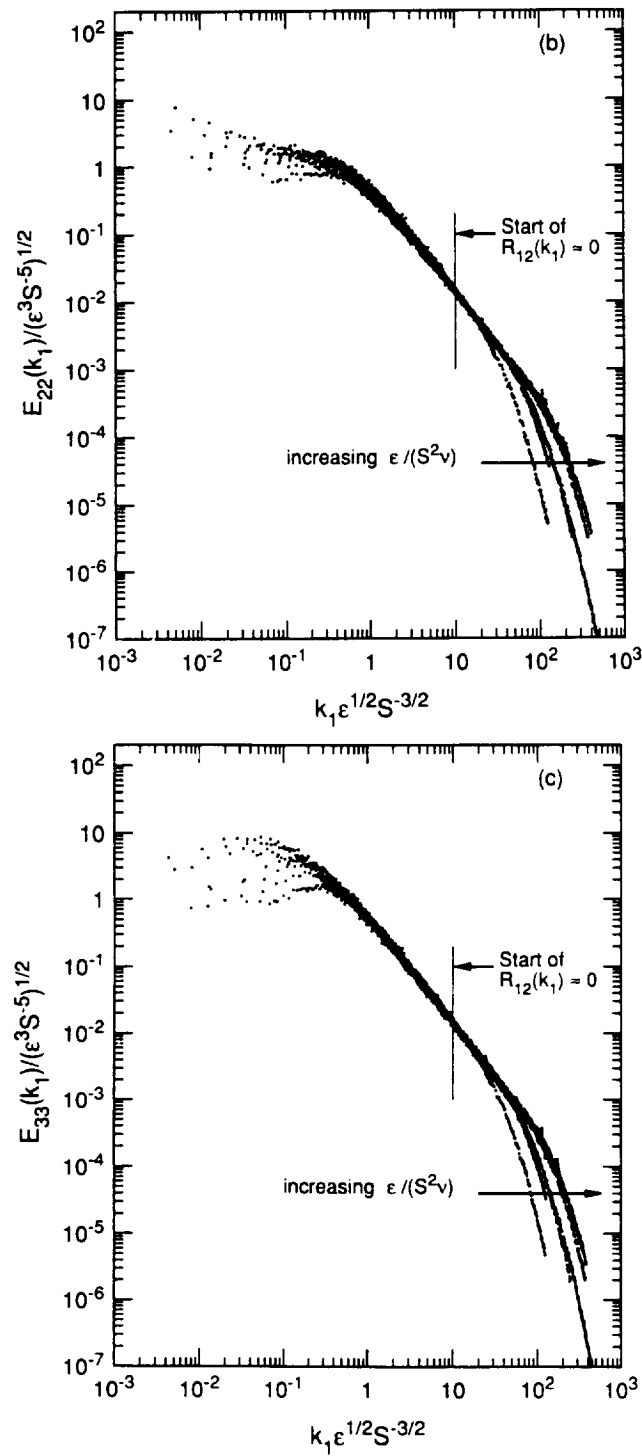


FIGURE 10. Spectra measured at different locations and freestream velocities in the plane and distorted boundary layers non-dimensionalized using  $\sqrt{\epsilon/S^3}$  and  $\sqrt{\epsilon/S}$  as length and velocity scales respectively. (a)  $E_{11}(k_1)$ ; (b)  $E_{22}(k_1)$ ; (c)  $E_{33}(k_1)$ .

thank Dr. James Ross, Group Leader-Basic Experiments, who has been and will be in charge of coordinating our tests in the 80' by 120' wind tunnel. We also wish to thank Ms. Wendy Lanser, Mr. Gavin Botha, Mr. Ken Kono and Mr. Bill Dotty. Our experiments would have not been possible without their help and efforts.

During the design and construction of the cylinder and its accessories, we received extensive advice from Prof. Bill Reynolds and Mr. Robin Birch of Stanford University and Dr. Joseph Huang of CALSPAN Corp. We gratefully thank them for all their suggestions. We wish to thank Prof. Bill Reynolds, Prof. Parviz Moin, Prof. Peter Bradshaw, and Dr. Bob Rogallo for many valuable discussions of our results. We have benefited from the expert advice of Prof. Roger Simpson. I am grateful to my wife, Elizabeth, and Mr. Eric Buice, who helped me with the measurements during all those "graveyard" shifts.

## REFERENCES

- AGUI, J. & ANDREOPOULOS, J. 1990 Experimental investigation of a three-dimensional boundary layer flow in the vicinity of an upright wall mounted cylinder. *AIAA 90-1545*.
- BATCHELOR, G. K. 1953 *The Theory of Homogeneous Turbulence*. Cambridge University Press.
- BELIK, L. 1973 The secondary flow about circular cylinders mounted normal to a flat plate. *Aero Q.* **24**, 47-54.
- BRADSHAW, P. 1973 Effects of streamline curvature on turbulent flow. *AGARDograph*. **169**.
- BRADSHAW, P. 1967 The turbulence structure of equilibrium boundary layers. *J. Fluid Mech.* **29**, 625-645.
- CHAPMAN, D. 1979 Computational aerodynamics development and outlook. *AIAA J.* **17**, 1293.
- CORRSIN, S. 1958 On local isotropy in turbulent shear flow. *Report NACA R & M 58B11*.
- DEVENPORT, W. J. & SIMPSON, R. L. 1990 Time-dependent and time-averaged turbulence structure near the nose of a wing-body junction. *J. Fluid Mech.* **210**, 23-55.
- HORNUNG, H. G. & JOUBERT, P. N. 1963 The mean velocity profile in three-dimensional turbulent boundary layers. *J. Fluid Mech.* **15**, 368-384.
- JOHNSTON, J. P. 1960 The turbulent boundary layer at a plane of symmetry in a three-dimensional flow. *Trans. A.S.M.E. Series D.* **82**, 622-628.
- KOLMOGOROV, A. N. 1941 The local structure of turbulence in incompressible viscous fluid for very large Reynolds numbers. *C. R. Acad. Sci. U.R.S.S.* **30**, 301.
- KRAICHNAN, R. H. 1959 The structure of isotropic turbulence at very high Reynolds numbers. *J. Fluid Mech.* **5**, 497.

- LEE, M. J. & REYNOLDS, W. C. 1985 Numerical experiments on the structure of homogeneous turbulence. *Technical Report TF-24*. Department of Mechanical Engineering, Stanford University.
- LUMLEY, J. L. 1967 Similarity and the turbulent energy spectrum. *Phys. Fluids*. **10**, 855-858.
- LUMLEY, J. L. & NEWMAN, G. R. 1977 The return to isotropy of homogeneous turbulence. *J. Fluid Mech.* **82**, 161-178.
- MEHTA, R. D. 1984 Effect of wing nose shape on the flow in a wing/body junction. *Aeronaut. J.* **88**, 456-460.
- MONIN, A. S. & YAGLOM, A. M. 1975 *Statistical Fluid Mechanics*, vol. 2. M.I.T. Press.
- SADDOUGHI, S. G. 1993 Local isotropy in high Reynolds number turbulent shear flows. *Annual Research Briefs-1992*, Center for Turbulence Research, Stanford University/NASA Ames. 237-262.
- SADDOUGHI, S. G. & JOUBERT, P. N. 1991 Lateral straining of turbulent boundary layers. Part 1. Streamline divergence. *J. Fluid Mech.* **229**, 173-204.
- SADDOUGHI, S. G. & VEERAVALLI, S. V. 1993 Local isotropy in turbulent boundary layers at high Reynolds number. *J. Fluid Mech.* To be published.
- TOWNSEND, A. A. 1976 *The Structure of Turbulent Shear Flow*, 2nd edn. Cambridge University Press.
- UBEROI, M. S. 1957 Equipartition of energy and local isotropy in turbulent flows. *J. Appl. Phys.* **28**, 1165-1170.



NO 4-24 167

## Computation of large-scale statistics in decaying isotropic turbulence

By Jeffrey R. Chasnov

### 1. Motivation and objectives

The most basic result in a study of decaying isotropic turbulence is the evolution of the kinetic energy as a function of time. By postulating a self-similar decay of the energy spectrum based on an exact invariant  $B_0$  of the flow, Saffman (1967a,b) determined the high Reynolds number decay law

$$\langle u^2 \rangle \propto B_0^{\frac{2}{3}} t^{-\frac{2}{3}} \quad (1)$$

where  $B_0$  is the leading coefficient of the energy spectrum near  $k = 0$

$$E(k) \sim 2\pi B_0 k^2 \quad k \rightarrow 0. \quad (2)$$

Saffman's determination of the high Reynolds number decay exponent was based on earlier work by Kolmogorov (1941) in which it was assumed that a self-similar decay of the spectrum could be based on the invariance of the Loitsianski integral  $B_2$  (Loitsianski, 1939), yielding the decay law

$$\langle u^2 \rangle \propto B_2^{\frac{2}{7}} t^{-\frac{10}{7}} \quad (3)$$

where now

$$E(k) \sim 2\pi B_2 k^4 \quad k \rightarrow 0. \quad (4)$$

However, it was later shown (Proudman & Reid, 1954; Batchelor & Proudman, 1956) that  $B_2$  was in fact not invariant and depended on time during the turbulence decay.

However, one may still postulate an exact self-similar decay of the energy spectrum at large-scales (Lesieur, 1990). If it is assumed that

$$B_2(t) = \beta t^\gamma, \quad (5)$$

then (3) still holds but with  $B_2(t)$  given by (5). When  $\gamma$  is positive, as is indicated by numerical simulations and quasi-normal closure models, this results in a less rapid decay of the energy as  $t^{-10/7+2\gamma/7}$ .

We have performed large-eddy simulations of decaying isotropic turbulence (Chasnov, 1994) to test the prediction of self-similar decay of the energy spectrum and to compute the decay exponents of the kinetic energy. In general, good agreement between the simulation results and the assumption of self-similarity were obtained. However, the statistics of the simulations were insufficient to compute the value of  $\gamma$  which corrects the decay exponent when the spectrum follows a  $k^4$  wavenumber behavior near  $k = 0$ . To obtain good statistics, it was found necessary to average over a large ensemble of turbulent flows. We report on this work here as well as in a recent *Physics of Fluids A* letter (Chasnov, 1993).

PRECEDING PAGE BLANK NOT FILMED

364

## 2. Computation of the Loitsianski integral

The coefficient  $B_2$  above, the so-called Loitsianski integral, can be written as an integral over the infinite flow volume as

$$B_2 = -\frac{1}{48\pi^3} \lim_{V \rightarrow \infty} \int_V \langle u_i(\mathbf{x}) u_i(\mathbf{x} + \mathbf{r}) \rangle r^2 d\mathbf{r}. \quad (6)$$

To compute  $B_2$  by numerical simulation, we assume that the velocity field is periodic in three directions with periodicity length  $L = 2\pi$ . The velocity field may then be expanded in a Fourier series as

$$\mathbf{u}(\mathbf{x}) = \sum_{\mathbf{k}} \hat{\mathbf{u}}(\mathbf{k}) \exp(i\mathbf{k} \cdot \mathbf{x}), \quad (7)$$

where the components of  $\mathbf{k}$  in the sum span the set of integers. A good approximation to homogeneous turbulence is thus obtained when the integral scale of the turbulence is much less than  $\pi$ . Treating the average in (6) as a volume average, and substituting the Fourier expansion (7) into (6), we obtain after one integration over the volume

$$B_2 = -\frac{1}{48\pi^3} \sum_{\mathbf{k}} \hat{u}_i(\mathbf{k}) \hat{u}_i(-\mathbf{k}) \int_V \exp(i\mathbf{k} \cdot \mathbf{r}) r^2 d\mathbf{r}. \quad (8)$$

The remaining volume integral in (8) may be evaluated analytically, and making use of  $\hat{u}_i(-\mathbf{k}) = \hat{u}_i(\mathbf{k})^*$ , where  $*$  denotes the complex conjugate, and  $\hat{u}_i(0, 0, 0) = 0$  we obtain

$$B_2 = -\frac{2}{3} \sum_{k=1}^{\infty} \frac{(-1)^k}{k^2} [|\hat{\mathbf{u}}(k, 0, 0)|^2 + |\hat{\mathbf{u}}(0, k, 0)|^2 + |\hat{\mathbf{u}}(0, 0, k)|^2]. \quad (9)$$

There are two main difficulties in the direct use of (9) to compute  $B_2$  in a numerical simulation. Firstly, the correlation  $\langle u_i(\mathbf{x}) u_i(\mathbf{x} + \mathbf{r}) \rangle$  in (6) decreases in general as  $O(r^{-5})$  in homogeneous turbulence (Batchelor & Proudman, 1956) – although it decreases faster as  $o(r^{-6})$  in an isotropic turbulence – so that the integral scale of the turbulence must be small enough for the integral in (6) to converge within the computational domain. Secondly, as the value of  $r$  in (6) becomes comparable to  $\pi$ , the replacement of the ensemble average in (6) by a volume average becomes inaccurate because of a lack of sample of the largest computed scales. Explicit computation has shown that direct use of (9) to compute  $B_2$  in a single realization of a turbulent flow is highly inaccurate. We are thus led to average  $B_2$  over an ensemble of such flows. This is equivalent to treating the original average in (6) as a combination of a volume and ensemble average.

In this research brief, we report on a computation of  $B_2(t)$  accomplished by performing 1024 independent simulations of resolution  $64^3$ . The size of this ensemble is sufficient to compute  $B_2(t)$  to a statistical accuracy better than 5% over the entire time-evolution considered. The computations are performed on an Intel

iPSC/860 hypercube parallel machine containing 128 processors. The machine had eight megabytes RAM per processor which allowed 64 realizations to be performed in parallel with each independent realization computed on 2 processors. Communication between processors computing different realizations is minimal so that the simulation of an ensemble of turbulent flows makes very efficient use of parallel computer architectures. Sixteen independent runs — each of 800 total time-steps — were performed. With each time-step taking approximately 10.6 seconds of cpu time, a total of 38 hours of dedicated machine use was required.

Our main goal in computing  $B_2(t)$  is to determine its long time, high Reynolds number behavior. Under the constraints imposed by  $64^3$  resolution simulations, this necessitates the use of a large-eddy simulation with the initial peak of the energy spectrum placed at as large a value of  $k$  magnitude as possible (Chasnov, 1994). Here, the initial energy spectrum is taken to be

$$E(k, 0) = 2\pi B_2(0)k^4 \exp \left[ -2(k/k_p)^2 \right], \quad (7)$$

with  $k_p = 25$  and  $B_2(0) = 6.934 \times 10^{-8}$ , so that  $\langle \mathbf{u}^2 \rangle = 1$ . As we have done previously, an eddy-viscosity subgrid scale model (Kraichnan, 1976; Chollet & Lesieur, 1981) is used to model the unresolved small-scale turbulence. Although the inclusion of a stochastic backscatter term in the subgrid model (Chasnov, 1991) can directly affect the time-variation of  $B_2$ , this effect is negligible at the later times of the turbulence evolution of interest to us here.

The finite resolution of the simulation results in a spherical truncation of the Fourier series in (7) at  $k_m$ , the maximum wavenumber of the simulation, so that the sum to  $\infty$  in (9) is replaced by a sum to  $k_m/\sqrt{3}$ . At small times when the peak of the energy spectrum is near  $k_m$ , this sharp cutoff results in errors in the computed value of  $B_2$ . We have shown that these errors can be easily removed by applying an additional Gaussian filter of the form  $\exp[-(k/k_f)^2]$  with  $k_f = 12$  to  $\hat{\mathbf{u}}(\mathbf{k})$  before computing (9). At the later evolution times of interest to us here, the effect of this additional filter is negligible.

The results obtained from the simulations are shown in figures 1-3. In figure 1, we plot the time-evolution of the ensemble-averaged energy spectrum obtained from the large-eddy simulations by summing the contributions of  $|\hat{\mathbf{u}}(\mathbf{k})|^2$  into wavenumber shells of thickness  $\Delta k = 1$  in the usual way, *i.e.*,

$$E(k, t) = \frac{2\pi k^2}{S_k} \sum_{k-\frac{1}{2} \leq |\mathbf{q}| < k+\frac{1}{2}} \hat{u}_i(\mathbf{q}, t) \hat{u}_i(-\mathbf{q}, t),$$

where  $S_k$  is the number of Fourier modes in each wavenumber shell and  $k = 1.5, 2.5, 3.5, \dots, 29.5$ . A good approximation to the homogeneous turbulence energy spectrum is thus obtained at high wavenumbers, while the approximation is less accurate at low wavenumbers. Nevertheless, the increase in time of the low wavenumber  $k^4$  coefficient is clearly evident from the plot.

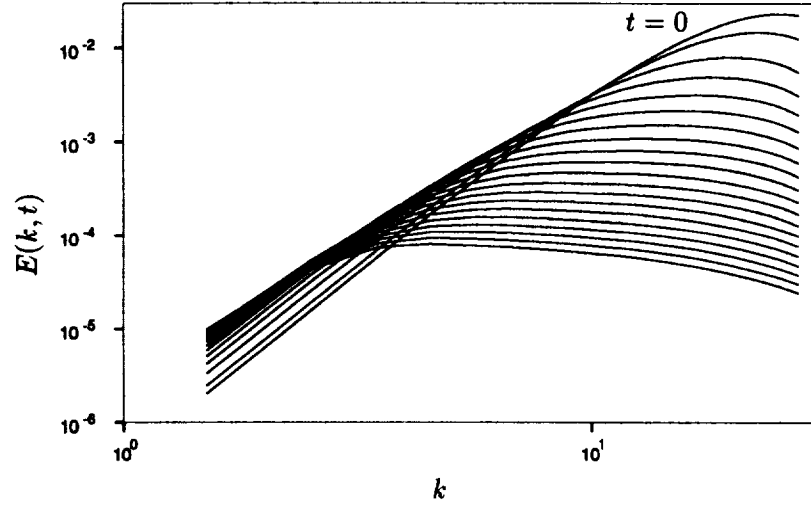


FIGURE 1. Time-evolution of the energy spectrum.

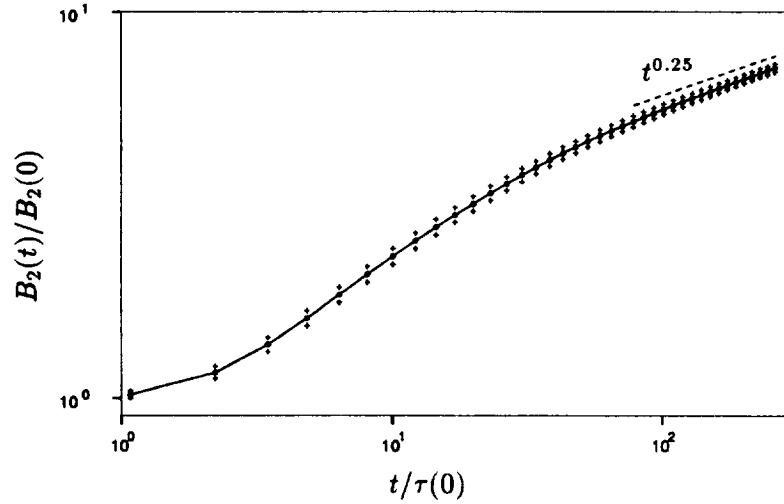


FIGURE 2. Time-evolution of the Loitsianski integral.

The coefficient  $B_2(t)/B_2(0)$  versus time, in units of the initial large-eddy turnover time  $\tau(0)$  where  $\tau(0) = 1.38/(k_p^7 B_2(0))^{1/2}$ , is plotted in figure 2. The points represent the statistical mean of the ensemble while the pluses represent one standard deviation from the mean. The standard deviation of the distribution of  $B_2$  itself, which we have shown from the simulation data to be approximately Gaussian, varies somewhat over the course of the simulation but at the latest time plotted is 80% of the mean. With 1024 realizations, the statistical uncertainty of the mean at the latest time is 2.5%.



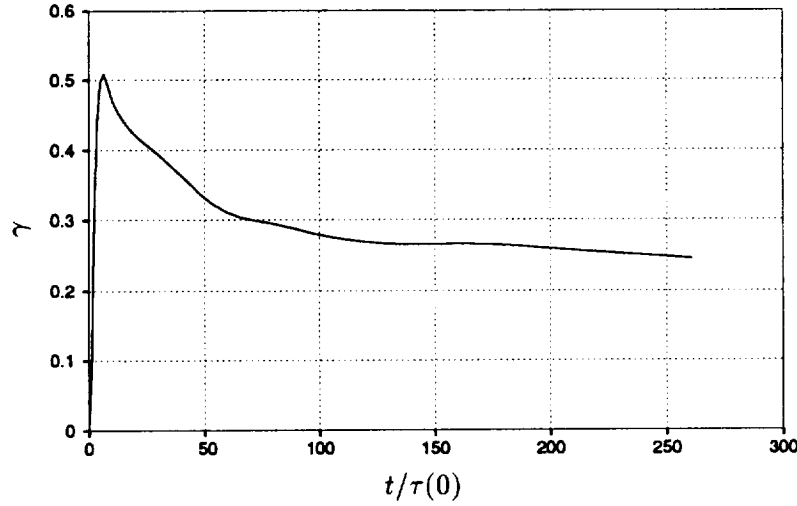


FIGURE 3. Time-evolution of the logarithmic derivative of the Loitsianski integral.

In figure 3, we plot the logarithmic derivative of  $B_2$  with respect to time in order to determine the validity of (5) and to compute a value of  $\gamma$  from the simulation. In agreement with the EDQNM model, we find that  $B_2(t)$  follows an approximate power-law at large times. From figure 3, we estimate the power law exponent to be  $\gamma \approx 0.25$ , with a statistical uncertainty of 6% at the latest time. The straight line drawn on the log-log plot of figure 2 represents this result. The value of  $\gamma$  we obtain from the simulation is about 50% larger than that estimated previously (Lesieur & Schertzer, 1978; Lesieur, 1990). Using our computed value for  $\gamma$ , the Kolmogorov decay exponent becomes  $-1.36$  instead of  $-1.43$ , a difference of 5%.

The statistical uncertainty of our asymptotic result for  $\gamma$  can be reduced further by computing additional realizations. However, there may be other errors in our result associated with the deviation of “periodic turbulence” from homogeneous turbulence at the latest times of evolution, as well as the expected slow approach of the turbulence to asymptotics (Chasnov, 1994). The evident trend of figure 3 is towards a somewhat smaller asymptotic value for  $\gamma$  than we have estimated. It would be of interest to repeat the present computation at higher resolution with a larger ensemble after parallel machines have become substantially more powerful.

We also note here another approach to the current computation. Rather than simulate  $1024 \ 64^3$  turbulent fields, we could have simulated  $16 \ 256^3$  fields with slightly more computer time due to the need for inter-processor communication. To obtain similar statistics between these two simulations, we would have to increase the initial peak of the energy spectrum  $k_p$  by a factor of four and truncate the volume integration in (8) to  $1/64$  the volume of the entire periodic domain. It is unclear which simulation would result in a more accurate computation of  $B_2(t)$ , but we chose the former mainly to illustrate the efficiency of performing realization averages of turbulent flows on parallel machines.

### 3. Conclusions

This work has demonstrated the capability of numerical simulations to compute large-scale statistics of turbulent flows by means of an ensemble average over a large number of independent realizations of the flow. Such a technique is "embarrassingly parallel" and is ideally suited for the new parallel computer architectures. This technique may also be applicable to turbulence simulation on virtual parallel machines in which many powerful workstations are connected together over a local network. If the memory of each workstation is sufficiently large so that each realization can be performed independently on each workstation, then the only communication required between workstations is to perform the ensemble average.

### Acknowledgments

Extensive discussions with Dr. Robert Rogallo on this work are gratefully acknowledged. The parallel code was written by Drs. A. Wray and R. S. Rogallo.

### REFERENCES

- BATCHELOR, G. K. 1948 *The Theory of Homogeneous Turbulence*, (Cambridge University Press, Cambridge, 1953).
- BATCHELOR, G. K. & PROUDMAN, I 1956 The large-scale structure of homogeneous turbulence. *Phil. Trans. Roy. Soc.* **248**, 369.
- CHASNOV, J. R. 1991 Simulation of the Kolmogorov inertial subrange using an improved subgrid model. *Phys. Fluids A*. **3**, 188.
- CHASNOV, J. R. 1993 Computation of the Loitsianski integral in decaying isotropic turbulence. *Phys. Fluids A*. **5**, 1-3.
- CHASNOV, J. R. 1994 Similarity states of passive scalar transport in isotropic turbulence. To appear in *Phys. Fluids A*.
- CHOLLET, J. P. & LESIEUR, M. 1981 Parameterization of small scales of three-dimensional isotropic turbulence utilizing spectral closures. *J. Atmos. Sci.* **38**, 2747.
- KOLMOGOROV, A. N. 1941 On degeneration of isotropic turbulence in an incompressible viscous liquid. *Dokl. Akad. Nauk. SSSR*. **31**, 538.
- KRAICHNAN, R. H. 1976 Eddy viscosity in two and three dimensions. *J. Atmos. Sci.* **33**, 1521.
- LESIEUR, M. 1990 *Turbulence in Fluids*, (Kluwer Academic Publishers, Dordrecht, 1990).
- LESIEUR, M. AND SCHERTZER, D. 1978 Amortissement auto similaire d'une turbulence a grand nombre de Reynolds. *J. de Mecanique*. **17**, 609.
- LIN, C. C. 1947 Remarks on the spectrum of turbulence. *Proc. 1st Symp. Appl. Math.* **81**.
- LOITSIANSKI, L. G. 1939 Some basic laws for isotropic turbulent flow. *Trudy Tsentr. Aero.-Gidrodin. Inst.* **440**, 31.

- PROUDMAN, I. AND REID, W. H. 1954 On the decay of a normally distributed and homogeneous turbulent velocity field. *Phil. Trans. A.* **247**, 163.
- SAFFMAN, P.G. 1967a The large-scale structure of homogeneous turbulence. *J. Fluid Mech.* **27**, 581.
- SAFFMAN, P.G. 1967b Note on decay of homogeneous turbulence. *Phys. Fluids.* **10**, 1349.



## On the dynamics of approximating schemes for dissipative nonlinear equations

By Don A. Jones

### 1. Motivation and objectives

Since one can rarely write down the analytical solutions to nonlinear dissipative partial differential equations (PDEs), it is important to understand whether, and in what sense, the behavior of approximating schemes to these equations reflects the true dynamics of the original equations. Further, because standard error estimates between approximations of the true solutions coming from spectral methods—finite difference or finite element schemes, for example—and the exact solutions grow exponentially in time, this analysis provides little value in understanding the infinite time behavior of a given approximating scheme.

The notion of the *global attractor* has been useful in quantifying the infinite time behavior of dissipative PDEs, such as the Navier-Stokes equations. Loosely speaking, the global attractor is all that remains of a sufficiently large bounded set in phase space mapped infinitely forward in time under the evolution of the PDE. Though the attractor has been shown to have some nice properties—it is compact, connected, and finite dimensional, for example—it is in general quite complicated.

Nevertheless, the global attractor gives a way to understand how the (infinite time) behavior of approximating schemes such as the ones coming from a finite difference, finite element, or spectral method relates to that of the original PDE. Indeed, one can often show that such approximations also have a global attractor. We therefore only need to understand how the structure of the attractor for the PDE behaves under approximation. This is by no means a trivial task. Several interesting results have been obtained in this direction. However, we will not go into the details. We mention here that approximations generally lose information about the system no matter how accurate they are. There are examples that show certain parts of the attractor may be lost by arbitrary small perturbations of the original equations (see Humphries, Jones, Stuart, 1993, and the references therein for a description of some of the results).

Under certain hypothesis on the approximation, one can be guaranteed some structures of the attractor survive the approximation. For example, consider the ordinary differential equation (ODE)

$$\frac{dx}{dt} = X(x), \quad (1)$$

where we suppose that  $x \in \mathbb{R}^n$  and that  $X$  is a  $C^1$  function. Further, we suppose that the system (1) is dissipative and hence has a global attractor. Now suppose that (1) is approximated by

$$\frac{dy}{dt} = X(y) + Y(y), \quad (2)$$

where  $y \in \mathbb{R}^n$  and  $Y$  is a  $C^1$  function. Suppose further that

$$\|Y\|_{C^1} \leq \epsilon$$

for some suitable  $\epsilon > 0$ . That is, (1) and (2) may be viewed as small  $C^1$  perturbations of one another. This seems to be a natural condition to require of a perturbation in order to say something about how the global attractor of (2) relates to that of (1). Indeed, such systems have been studied by several authors and increasingly stronger results have been obtained (see *e.g.* Pliss & Sell, 1992, and the references therein). It is known, for example, that normally hyperbolic, invariant manifolds persist under such perturbations.

In order to apply these results to PDEs, one must first construct finite systems of ODEs that have the same global attractor as the infinite-dimensional PDE. This has been done for several dissipative PDEs including, for example, the Kuramoto-Sivashinsky equation, Cahn-Hilliard equation, Ginzburg-Landau, certain reaction-diffusion equations, and the Navier-Stokes equations, Kwak, 1991. Such systems are called *inertial forms*.

To be more specific, each of these PDEs can be viewed as an ordinary differential equation on a suitably chosen Hilbert space,  $H$ . We denote by  $(\cdot, \cdot)$  the inner product and  $|\cdot|$  the norm on  $H$ . Then these equations take the form

$$\frac{du}{dt} + Au + R(u) = f \quad (3)$$

$$u(0) = u_0.$$

Typically, the operator  $Au$  is  $-\nabla^2$  with Dirichlet or periodic boundary conditions. For the Navier-Stokes equations, for example, the term  $R(u)$  is the divergence free part of  $(u \cdot \nabla)u$  (see Temam 1988).

In all cases but the Navier-Stokes equations, the existence of inertial forms (IF) has been proven by showing the existence of an Inertial Manifold. To date, inertial manifolds have been constructed as a graph in phase space of a Lipschitz function  $\Phi$  (see Foias, Sell, Temam, 1988). An inertial manifold (IM) for a dissipative evolution partial differential equation is a smooth finite-dimensional manifold in phase space, which is positively invariant under the solution operator and which uniformly attracts every bounded subset of phase space at an exponential rate. It is clear that if the IM exists, then it must contain the global attractor. Moreover, the reduction of the partial differential equation to the IM yields the inertial form.

We denote by  $P$  the orthogonal projection of the space  $H$  onto the span of the first  $M$  eigenfunctions of  $A$ , and  $Q = I - P$ . We set  $p = Pu, q = Qu$ . Then the evolution equation (3) is equivalent to the system

$$\frac{dp}{dt} + Ap + PR(p + q) = Pf,$$

$$\frac{dq}{dt} + Aq + QR(p + q) = Qf.$$

If the IM is given as a graph of a Lipschitz function  $\Phi : PH \mapsto QD(A)$  for  $M$  sufficiently large, then on this manifold the solutions of (3) are of the form  $u(t) = p(t) + \Phi(p(t))$ . Moreover, in this case, the inertial form is given by

$$\frac{dp}{dt} + Ap + PR(p + \Phi(p)) = Pf \quad p \in PH. \quad (4)$$

Equation (4) does not have the same solutions as Equation (3) (only on  $M$ ). Rather, it has the same infinite time behavior as original PDE. Most importantly, it is an ODE. In view of the work of Pliss & Sell (1992) mentioned above, there is an advantage in approximating (4) in the  $C^1$  sense. A candidate for such a system is

$$\frac{dp}{dt} + Ap + PR(p + \Phi_{app}(p)) = Pf \quad p \in PH, \quad (5)$$

with

$$\sup_{p \in PH} (|A(\Phi_{app}(p) - \Phi(p))| + \|A(D\Phi_{app}(p) - D\Phi(p))\|_{\mathcal{L}(PH, QH)}) \leq \epsilon,$$

and where  $D\Phi$  denotes the Fréchet derivative of the function  $\Phi$ . In this case, under reasonable assumptions on  $R$ , the vector field in the approximate inertial form (5) may be viewed as a small  $C^1$  perturbation of the vector field in the inertial form (4).

## 2. Accomplishments

The main goal of this method of reduction is to implement the reduced ordinary differential system (5) in long-time simulations of solutions to the PDE, (3). Even in the case that the IM or a smooth function  $\Phi$  does not exist, the theory suggests looking for a global function  $\Phi_{app}$  whose graph in phase space approximates the attractor. Indeed, many  $\Phi_{app}$  have been constructed. These approximations have been implemented in numerical schemes for a variety of equations and settings (see Jones, Margolin, Titi, 1993, and the references therein). We will discuss the effectiveness of these schemes below.

Perhaps the most important role the IF, Equation (4), can play, as mentioned above, is to understand how the dynamics of approximating schemes relates to that of the original PDE. The first attempt at approximating  $\Phi$  in the  $C^1$  sense was in Jones, Titi, 1993. There,  $\Phi$  was viewed as the asymptotically stable stationary solution of a certain PDE. One can then approximate  $\Phi$  by integrating this PDE forward for a short time.

However, the situation may be much simpler than this. Consider the spectral approximation of (3) based on the eigenfunction of the linear operator  $A$ . One obtains the approximation

$$\frac{du_N}{dt} + Au_N + P_N R(u_N) = P_N f \quad (6)$$

with initial data  $u_N(0) = u_{0,N}$ . As shown in Foias, Sell, Temam, 1988, and Foias, Sell, Titi, 1988, if  $N$  is chosen sufficiently large, there exists a global function  $\Phi_N$  such that  $M_N = \text{Graph}(\Phi_N)$  is an inertial manifold for (6). On this manifold, solutions are of the form  $u_N(t) = p_N(t) + \Phi_N(p_N(t))$  with  $p_N(t) = Pu_N(t)$ . Further, on this manifold, (6) reduces to

$$\frac{dp_N}{dt} + Ap_N + PR(p_N + \Phi_N(p_N(t))) = Pf, \quad (7)$$

where  $P$  is defined above. Notice also that Equation (7) remains of dimension  $M$ , the same dimension as (4), as  $N \rightarrow \infty$ . Again, it is not that (7) has the same solutions as (6) (only on  $M_N$ ), but rather it has the same global attractor as (6) (since the IM contains the attractor).

Now Equation (7) will play the role of the approximate inertial form, Equation (4). That is, we take  $\Phi_{app} = \Phi_N$ . Moreover, it was shown in these two papers that

$$\sup_{p \in PH} |A(\Phi(p) - \Phi_N(p))| \leq \frac{C}{\lambda_N^{1-\beta}}$$

for some  $0 \leq \beta \leq 1/2$  which depends on the nonlinear term  $R$ . However, more is true.

**Theorem** Suppose that  $M$  is so large (determined by the spectral properties of  $A$ ) that  $\Phi, \Phi_N$  as described above exist. Then for all  $\epsilon > 0$  there exists a  $N(\epsilon)$  such that

$$\sup_{p \in PH} [|A(\Phi(p) - \Phi_N(p))| + \|A(D\Phi(p) - D\Phi_N(p))\|_{\mathcal{L}(PH, PH)}] \leq \epsilon$$

for all  $N \geq N(\epsilon)$ .

Proof. See Jones, Titi (1993).

The IF, Equation (4), has the same dynamics as the original PDE. Moreover, the above shows that the spectral method based on the eigenfunctions of  $A$  is a small  $C^1$  perturbation of the IF for  $N$  sufficiently large, since Equation (6) and (7) have the same attractor. Thus, this spectral method preserves certain structures of the attractor of the PDE, for example, the ones studied in Pliss, Sell, 1991, for  $N$  sufficiently large.

A similar type of analysis may be possible for finite element methods. To do this properly, we should turn to a specific PDE. However, we will attempt to keep the exposition as general as possible. We denote by  $\{V^h\}_{h>0}$  a finite dimensional subspace of differentiable functions (most typically piecewise linear functions), where one can think of  $h$  as being the maximum partition size. Then one attempts to approximate solutions  $u(t)$  of (3) by functions  $u^h(t)$  in  $V^h$ . The functions  $u^h$  solve

$$(u_t^h, \chi) + (A^{1/2}u^h, A^{1/2}\chi) + (R(u^h), \chi) = (f, \chi) \quad (8)$$

$$u^h(0) = u_0^h \in V^h,$$



where one can think of  $A^{1/2}$  as  $d/dx$  in the 1D case.

The operator  $A^h$  can be defined from the equation  $(A^h\psi, \chi) = (A^{1/2}\psi, A^{1/2}\chi)$ . Further, projecting  $R$  and  $f$  onto the space  $V^h$ , Equation (8) takes the form

$$\frac{du^h}{dt} + A^h u^h + R^h(u^h) = f^h. \quad (9)$$

Since  $A$  is assumed to be self-adjoint,  $A^h$  is also. Moreover, the spectrum of  $A^h$  can be shown to approximate that of  $A$ . Thus, the space  $V^h$  may be decomposed  $V^h = P^h V^h \oplus Q^h V^h$ . In the same manner that the  $\Phi_N$  was constructed in Foias, Sell, Titi, 1988, a global function  $\Phi^h$  may be constructed for Equation (9) (see Jones, Stuart, 1993, for the details) such that  $M^h = \text{Graph}(\Phi^h)$  is an inertial manifold for (9). On this manifold, solutions are of the form  $u^h(t) = p^h(t) + \Phi^h(p^h(t))$ , where  $p^h = P^h u^h$ . On the IM, (9) reduces to

$$\frac{dp^h}{dt} + A^h p^h + P^h R^h(p^h + \Phi^h(p^h)) = P^h f \quad (10)$$

for  $h$  sufficiently small. As in the case of the spectral method, the dynamics of (10) are the same as that of (9). Moreover, the dimension of (10) remains fixed (roughly on the order of  $M$ ) as  $h \rightarrow 0$ . One would like to show  $C^1$  closeness of (10) and (4). However, at this point all we have is the following

**Theorem** For  $h$  sufficiently small there exists a function  $\Phi^h$  such that (10) holds. Moreover,

(i) for any  $p \in PH$  there exists  $C(p) > 0$  such that

$$\|(p + \Phi(p)) - (P^h p + \Phi^h(P^h p))\| \leq C(p)h;$$

(ii) for any  $p^h \in P^h H$  there exists  $C(p^h) > 0$  such that

$$\|(Pp^h + \Phi(Pp^h)) - (p^h + \Phi^h(p^h))\| \leq C(p^h)h.$$

Proof. See Jones, Stuart (1993).

### On the Practical Side

The above theory suggests that there may be an advantage in enslaving the high Fourier modes (in the case of the spectral method based on the eigenfunctions of  $A$ ) in terms of the lower modes through the function  $\Phi_{app}$ . Shortly after the discovery of the IF, Equation (4), many  $\Phi_{app}$  were constructed and studied for various equations (see Jones, Margolin, Titi, 1993, and the references therein), including the Navier-Stokes equations (see for example Jolly, 1993). Schemes based on enslaving  $q \approx \Phi_{app}(p)$  are generally referred to as *nonlinear Galerkin methods* since  $\Phi_{app} = 0$  gives the standard Galerkin scheme.

In Jones, Margolin, Titi, 1993, we evaluate the effectiveness of the nonlinear Galerkin method in the context of spectral method (such schemes have now been constructed for finite element and finite difference schemes; see the references in Jones et al. 1993). The goal of this work is to understand under what conditions the nonlinear Galerkin methods lead to a significant improvement in accuracy over the standard Galerkin method from a purely numerical analysis point of view.

Recall that in general, if one approximates a smooth function  $u$  with respect to some basis, the rate of convergence is limited by the smoothness of the basis functions. If the basis elements are  $C^\infty$  functions as in the case of the eigenfunctions of the linear operator  $A$ , the rate of convergence is only limited by the smoothness of  $u$  and compatibility of the function  $u$  with the basis elements of the expansion at the boundary (the presence of Gibb's phenomenon, for example).

Thus, if the solutions  $u(t)$  of equation (3) are very regular and compatible with the eigenfunctions  $\{\varphi_j\}$  of  $A$  at the boundary, then the Fourier coefficients of the solution may decay very rapidly in wave number. Indeed, Foias, Temam, 1989, showed that, under such circumstances, solutions of the Navier-Stokes equation may decay exponentially in Fourier space. Similar results hold for the other equations mentioned above. Thus, the business of trying to approximate the  $q$  part of solutions via the function  $\Phi_{app}$  may not be effective when the  $q = Qu$  part of the solutions is exponentially small. That is, the approximation  $\Phi_{app} = 0$ , which leads to the standard Galerkin scheme, may already be good enough. It turns out that what controls the regularity and compatibility of solutions coming from the NSE and related equations is the compatibility with the basis functions and regularity of the forcing term  $f$ .

We demonstrate this for the Kuramoto-Sivashinsky equation (KS). A similar analysis holds for the NSE. This equation is given by

$$\frac{\partial u}{\partial t} + \frac{\partial^4 u}{\partial x^4} + \frac{\partial^2 u}{\partial x^2} + u \frac{\partial u}{\partial x} = f(x)$$

$$u(0, x) = u_0(x)$$

$$u(t, x) = u(t, x + L) \quad L > 0, \quad t \geq 0.$$

The KS equation appears in physics literature with  $f = 0$ . Here we have added an additional feature to the KS equation, namely, a forcing term  $f$ . We will use this forcing term to control the level of regularity of the solutions to the KS equation. It is clear that whenever  $f(x)$  is an odd function then the space of odd functions is invariant under the solution operator for the KS equation. For simplicity, we will restrict ourselves to the odd case. Hence, under these assumptions, one can easily show that the KS equation is equivalent to the evolution equation

$$\frac{du}{dt} + Au - A^{1/2}u + B(u, u) = f,$$

$$u(0) = u_0$$

on the Hilbert space  $H = \{u \in L^2((0, L)) | u(x) = u(x + L), u(x) = -u(L - x), x \in \mathbb{R}\}$ . Here  $A = \frac{\partial^4}{\partial x^4}$ ; the eigenvalues of  $A$  are  $\lambda_m = (2\pi m/L)^4$  corresponding to the eigenfunctions  $\varphi_m = \sin(2\pi m x/L)$ , for  $m = 1, 2, \dots$

In either case, one can define the operators  $A^\alpha$  for  $\alpha \geq 0$ . One defines  $D(A^\alpha) = \{u \in H | u = \sum_{j=1}^{\infty} u_j \varphi_j, \sum_{j=1}^{\infty} \lambda_j^{2\alpha} |u_j|^2 < \infty\}$ . Consequently, functions in  $D(A^\alpha)$  are more regular, and more compatible (whenever it applies) with the eigenfunctions of  $A$  at the boundary, for larger  $\alpha$ .

We may then approximate solutions of the KS equation with either the standard Galerkin scheme

$$\frac{dy_n}{dt} + Ay_n + A^{1/2}y_n + P_n B(y_n, y_n) = P_n f \quad (11)$$

or by the nonlinear Galerkin method

$$\frac{dz_n}{dt} + Az_n + A^{1/2}z_n + P_n B(z_n + \Phi_{app}(z_n), z_n + \Phi_{app}(z_n)) = P_n f \quad (12)$$

for some clever choice for  $\Phi_{app}$ .

As mentioned, the rate of convergence of the two schemes is tied to the smoothness of the solutions and compatibility of the solutions with the basis functions. (Since we are considering the KS equation with periodic boundary conditions, compatibility of the solutions is not an issue here. However, such cases are studied in Jones, Margolin, Titi, 1993.) This is, in turn, tied to the smoothness and compatibility of the forcing term  $f$ . The rates of convergence of the two schemes is given by the following two theorems which is based on the work of Devulder, Marion, Titi, 1993, and whose proofs can be found in Jones, Margolin, Titi, 1993.

**Theorem** Let  $u(t) = p(t) + q(t)$  be a solution of the KS equation with  $u_0$  on the attractor and  $f \in D(A^\alpha)$ . Suppose  $y_n$  solves (11) with  $y_n(0) = P_n u(0)$ . Then

$$\|u(t) - y_n(t)\|_{L^2} \leq \frac{C_1(t)}{\lambda_{n+1}^{1+\alpha}}.$$

In general, requiring  $f \in D(A^\alpha)$  for some  $\alpha > 0$  requires not only that  $f$  be smooth, but also that  $f$  and its derivatives up to order  $4\alpha$  must satisfy the boundary conditions. Now we suppose that  $\Phi_{app}$  satisfies certain conditions described in Jones, Margolin, Titi, 1993—such  $\Phi_{app}$  abound. For the nonlinear Galerkin method, we have

**Theorem** Let  $u(t)$  be as in the previous theorem. Suppose  $z_n$  solves (12) with  $z_n(0) = P_n u(0)$ . Then

$$\|u(t) - (z_n(t) + \Phi_{app}(z_n(t)))\|_{L^2} \leq \frac{C_1(t)}{\lambda_{n+1}^{\beta+\alpha}},$$

for some  $\beta > 1$ .

For most  $\Phi_{app}$ ,  $\beta$  is not larger than two. Now one can see the issue here. As  $f$  becomes more smooth, larger  $\alpha$ , the difference in the theoretical rates of convergence of the two schemes decreases.

Let us push the smoothness of the solutions to an extreme. Consider the forced KS equation and suppose that for some  $\sigma > 0$ ,  $f \in D(e^{\sigma A^{1/4}})$ ; that is,  $f$  is in a Gevrey class (real analytic). Notice that

$$\|e^{\sigma A^{1/4}} f\|_{L^2}^2 = \sum_{j=1}^{\infty} e^{2\sigma \lambda_j^{1/4}} |f_j|^2 < \infty,$$

where  $f = \sum_{j=1}^{\infty} f_j \varphi_j$ . Under these assumptions for the forced KS equation, we have (Proposition 3.6 of Jones, Margolin, Titi, 1993) that the Fourier expansion of the solution converges exponentially fast. This means that the solutions are infinitely compatible with the basis functions at the boundary and analytic inside the domain. Hence, the high Fourier modes of the solutions have exponentially small norms, and there may be little advantage in approximating them. Indeed, in this case, we have

$$\|u(t) - y_m(t)\|_{L^2} \leq C_1(t) \frac{e^{-\sigma_1 \lambda_{m+1}^{1/4}}}{\lambda_{m+1}},$$

where  $y_m$  solves the Galerkin scheme (11)

As in the above theorem, we have

$$\|u(t) - (z_m(t) + \Phi_{app}(z_m(t)))\|_{L^2} \leq C_2(t) \frac{e^{-\sigma_1 \lambda_{m+1}^{1/4}}}{\lambda_{m+1}^\beta},$$

where  $z_m$  is the solution of the nonlinear Galerkin scheme (12).

Thus, in the case that the solutions have Gevrey class regularity (spatially real analytic), the nonlinear Galerkin method only leads to algebraic improvements in the upper bounds of the rates of convergence over the standard Galerkin scheme. This little improvement might not be significant in computations. Of course, the overall improvement depends on how small the constant  $\sigma_1$  is.

We demonstrate this numerically. We choose  $\Phi_{app}$  to be

$$\Phi_1(p) = A^{-1} Q_m(f - B(p, p)),$$

which we first studied for the NSE in Foias, Manley, Temam, 1988. For this choice,  $\beta = 7/4$ . For our first example, we force the KS equation with

$$f = \sum_{j=1}^{\infty} \frac{1}{j} \sin(jx).$$

Notice that for this choice  $f \in D(A^\alpha)$  for  $\alpha < 1/8$ .

We have found a stable periodic orbit with this forcing. Such trajectories are on the attractor. To obtain the “exact” periodic solution, we run a Galerkin scheme using 100 modes; when we reach .5 time units, we start recording the data every .002 time units up to a time of .7 time units (Figure 1). If the initial data is taken near the periodic orbit, it will take some .4 time units to converge to the periodic solution. Since the periodic solution is on the attractor, we expect that the rate of convergence in this case to be of the form

$$E_{gal} = \max_{.5 \leq t \leq .7} \|u(t) - y_m(t)\|_{L^2} \leq \frac{c_1}{\lambda_{m+1}^{\alpha_1}},$$

of course, here we are ignoring errors due to the discretization of time. Also

$$E_1 = \max_{.5 \leq t \leq .7} \|u(t) - (z_m(t) + R_n \Phi_1(z_m(t)))\|_{L^2} \leq \frac{c_2}{\lambda_{m+1}^{\alpha_2}}.$$

Since in this case  $\lambda_m = m^4$ , we have

$$\log E_{gal} = c_1 - 4\alpha_1 \log(m+1),$$

and

$$\log E_1 = c_2 - 4\alpha_2 \log(m+1).$$

Thus, a log-log plot of the error in terms of the wave number will easily determine the rate of convergence. In Figure 2, we have plotted the rate of change of the graph of the log-log plot of the error in terms of wave number. The theory suggests that the rate of convergence for the Galerkin method  $\alpha_1$  is less than or almost equal to  $9/8$  and for the nonlinear Galerkin method  $\alpha_2$  is less than or almost equal to  $15/8$ . The results plotted in Figure 2 show that the Galerkin calculation asymptotes at a value of 1.1, whereas the nonlinear Galerkin asymptotes at a value of 1.92, which is in a good agreement with the theory.

Now we turn to the case when the force is in the Gevrey class (real analytic). We consider the KS equation with zero forcing. With the help of the software package AUTO, we start the calculation with initial data on the unstable manifold of a periodic orbit, which again is on the attractor. The solution converges to a steady state as time goes to infinity. Thus, this trajectory is contained in the global attractor, and the theory presented in Section 3 holds for this trajectory. We first compute this trajectory using 100 Fourier modes, which we will consider as our “exact” solution. The  $L^2$  norm of this solution vs. time is shown in Figure 3. We integrate this trajectory out to 1.3 time units and record the solution every .01 time units.

We expect from the theory outlined in Section 3 that

$$E_{gal} := \max_{0 \leq t \leq 1.3} \|u(t) - y_m(t)\|_{L^2} \leq \frac{c_1 e^{-\sigma_1 \lambda_{m+1}^{1/4}}}{\lambda_{m+1}},$$

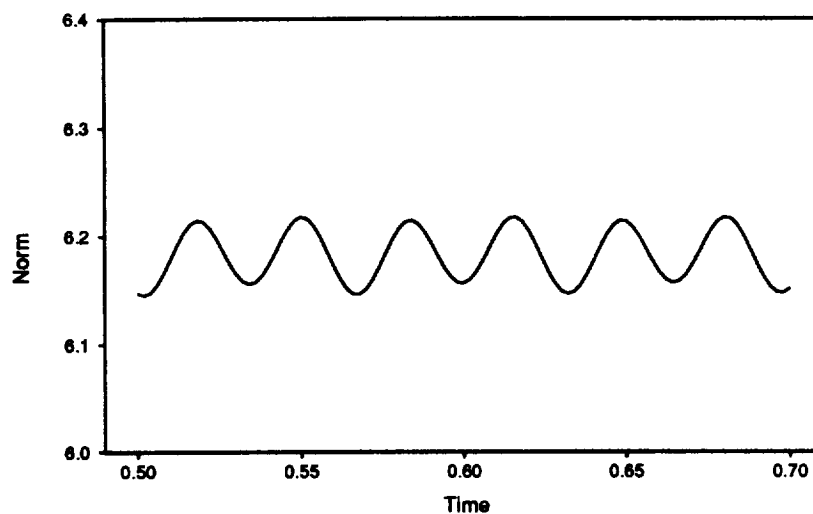


FIGURE 1.  $L^2$  norm of the solution vs. time for the KS eq. of a Galerkin scheme with 100 modes forced with  $f = \sum_{j=1}^{\infty} 1/j \sin(jx)$ .

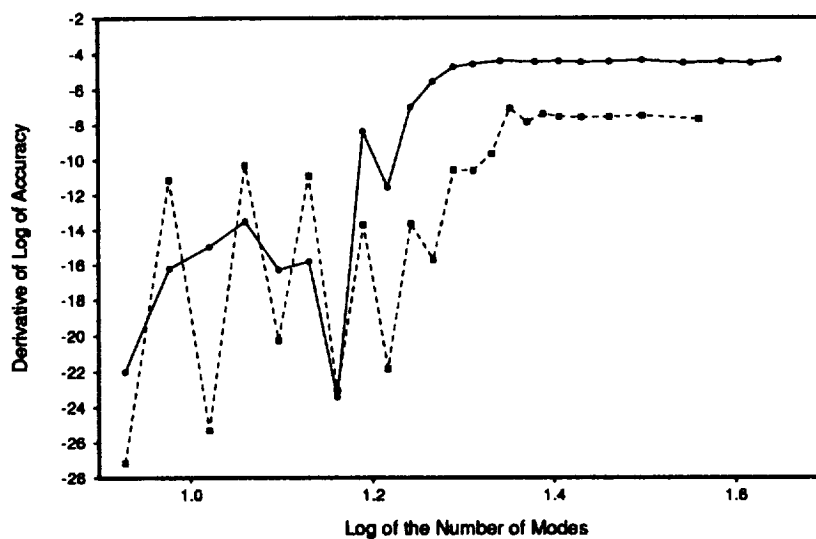


FIGURE 2. Rate of change of the log of the accuracy  $\times 10^{11}$  vs. log of the number of modes. The Galerkin asymptotes at 4.4 and the nonlinear Galerkin at 7.7. The theory suggests that the Galerkin should asymptote near 4.5 and the nonlinear Galerkin near 7.5.  $\bullet$ , Galerkin;  $\blacksquare$ , FMT.

$$E_1 := \max_{0 \leq t \leq 1.3} \|u(t) - (z_m(t) + R_n \Phi_1(z_m(t)))\|_{L^2} \leq \frac{c_2 e^{-\sigma_1 \lambda_{m+1}^{1/4}}}{\lambda_{m+1}^{7/4}},$$

for some  $\sigma_1 > 0$ . Since  $\lambda_{m+1} = (m+1)^4$ , we have

$$\log E_{gal} = -\sigma_1(m+1) + \log(c_1 \lambda_{m+1}^{-1})$$

and

$$\log E_1 = -\sigma_1(m+1) + \log(c_2 \lambda_{m+1}^{-7/4}).$$

Thus, a log-linear plot of the error versus the number of modes should be nearly linear. This is confirmed in Figure 4. In fact, the two lines are parallel. That is, they have the same exponential rate of convergence (same  $\sigma_1$ ). In addition, notice that the nonlinear Galerkin method still exhibits an algebraic improvement over the standard Galerkin. This is manifested by the fact that the graph for the nonlinear Galerkin is below the graph for the Galerkin.

Similar considerations apply where the compatibility of the solutions with the basis functions is an issue. Let us recall how this can come about. Consider Burgers' equation forced on the boundary

$$\frac{\partial u}{\partial t} - \frac{\partial^2 u}{\partial x^2} + u \frac{\partial u}{\partial x} = 0, \quad (13)$$

$$u(0, t) = 1 \quad u(1, t) = 0.$$

To formulate this problem in the same setting as Equation (3), one can set  $v = u - (1 - x)$  to obtain

$$\frac{\partial v}{\partial t} - \frac{\partial^2 v}{\partial x^2} + v \frac{\partial v}{\partial x} + (1 - x) \frac{\partial v}{\partial x} - v = 1 - x,$$

$$v(0, t) = 0 \quad v(1, t) = 0.$$

To apply the nonlinear Galerkin method, we must first expand the forcing term, here  $f = 1 - x$ , in terms of the eigenfunctions of the linear dissipative operator  $\varphi_j(x) = \sin(j\pi x)$ . We find

$$f = 1 - x = \sum_{j=1}^{\infty} \frac{4}{\pi j} \sin(j\pi x).$$

It is easily seen that, in terms of the spectral method based on the eigenfunctions of the Laplacian, the forcing term is only  $L^2((0, 1))$ , ( $\alpha = 0$ ). We therefore expect the nonlinear Galerkin method to be significantly more accurate in this case.

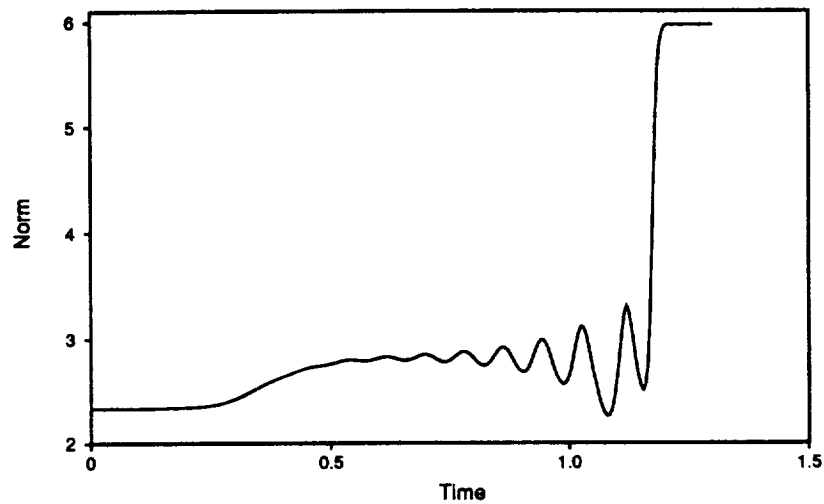


FIGURE 3.  $L^2$  norm of "exact" solution vs. time for the KS equation with zero forcing with initial data on an unstable manifold.

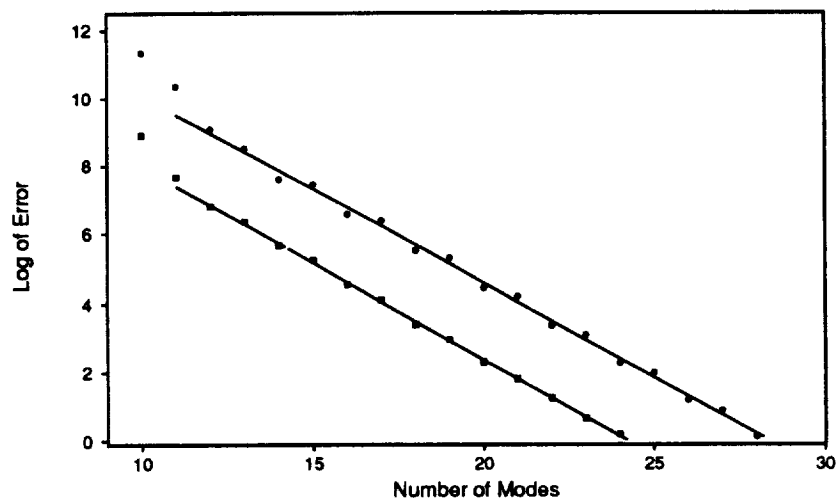


FIGURE 4. Log of the error  $\times 10^{13}$  vs. the number of modes for the KS equation with zero forcing. Notice that the rate of convergence of both schemes is exponential.  
 • , Gelerkin; ■ , FMT



### 3. Future plans

The goal remains to understand what aspects of the long time behavior of infinite-dimensional PDEs are retained by their finite-dimensional approximations. Perhaps the ultimate test of an approximation will remain how well it predicts nature. However, there are a growing number of applications where one does not know *a priori* nor is there a way to test experimentally the behavior of some systems. Therefore, assuming the dynamics of the PDEs accurately reflects the physical phenomenon it is meant to depict, we hope understanding the behavior of approximating schemes of these PDEs will prove valuable in the future.

### Acknowledgments

The author would sincerely like to thank the Center for Turbulence Research for a most productive and enjoyable year. We also have a special thanks to Joseph Keller and Andrew Stuart for the many stimulating discussions throughout the course of the year.

### REFERENCES

- DEVULDER, C. MARION, M. & TITI, E. S. 1991 On the rate of convergence of the nonlinear Galerkin methods. *Math. Comp.* To appear.
- FOIAS, C. SELL, G. & TEMAM, R. 1988 Inertial manifolds for nonlinear evolutionary equations. *J. Diff. Eq.* **73**, 309-353.
- FOIAS, C. SELL, G. & TITI, E.S. 1988 Exponential tracking and approximations of inertial manifolds for dissipative nonlinear equations. *J. Dynam. Diff. Eq.* **1**, 199-244.
- HUMPHRIES, A.R. JONES, D.A. & STUART, A.M. 1993 Approximations of dissipative partial differential equations over long time intervals. *Proceedings of the 14<sup>th</sup> Biannual Numerical Analysis Conference, Dundee*. Edited by D.F. Griffiths & G.A. Watson. Pitman. London, 1994.
- JOLLY, M.S. 1993 Bifurcation computations on an approximate inertial manifold for the 2D Navier-Stokes equations. *Physica*. **D63**, 8-20.
- JONES, D.A. MARGOLIN, L.G. & TITI, E.S. 1993 On the effectiveness of the approximate inertial manifold-a computational study. Submitted, also a CTR preprint.
- JONES, D.A. & STUART, A.M. 1993 Attractive invariant manifolds under approximation. Preprint.
- JONES, D.A. & TITI, E.S. 1993  $C^1$  approximations of inertial manifolds for dissipative nonlinear equations. Submitted.
- KWAK, M. 1992 Finite dimensional inertial form for the 2D Navier-Stokes equations. *Indiana Univ. Math. J.* **41**, 927-982.
- PLISS, V. A. & SELL, G. S. 1991 Perturbations of attractors of differential equations. *J. Differential Eq.* **92**, 100-124.

TEMAM, R. 1988 *Infinite Dimensional Dynamical Systems in Mechanics and Physics*, Springer Verlag, New York.

1-61  
71  
N94-28169

## Tensoral for post-processing users and simulation authors

By Eliot Dresselhaus

The CTR post-processing effort aims to make turbulence simulations and data more readily and usefully available to the research and industrial communities. The *Tensoral* language — which provides the foundation for this effort — is introduced here in the form of a user's guide. The *Tensoral* user's guide is presented in two main sections. Section 1 acts as a general introduction and guides database users who wish to post-process simulation databases. Section 2 gives a brief description of how database authors and other advanced users can make simulation codes and/or the databases they generate available to the user community via *Tensoral* database backends.

The two-part structure of this document conforms to the two-level design structure of the *Tensoral* language. *Tensoral* has been designed to be a general computer language for performing tensor calculus and statistics on numerical data. *Tensoral*'s generality allows it to be used for stand-alone native coding of high-level post-processing tasks (as described in section 1 of this guide). At the same time, *Tensoral*'s specialization to a minute task (namely, to numerical tensor calculus and statistics) allows it to be easily embedded into applications written partly in *Tensoral* and partly in other computer languages (here, C and *Vectoral*). Embedded *Tensoral* — aimed at advanced users for more general coding (e.g. of efficient simulations, for interfacing with pre-existing software, for visualization, etc.) — is described in section 2 of this guide.

### 1. *Tensoral* user's guide

#### Overview

The post-processing problem entails computing quantities derived from given base quantities such as a velocity vector field  $\vec{u}(\vec{x}, t)$ , a scalar field  $\phi(\vec{x}, t)$ , or a vorticity field  $\vec{\omega}(\vec{x}, t)$ . (Which base quantities are present will vary from database to database.) Derived quantities are typically those commonly arising in theories of fluid mechanics, turbulence, and in practical problems; all of these quantities involve performing calculus and statistics on numerically represented tensor quantities.

A *Tensoral* post-processor canonically starts with one or more given fields (e.g.  $\vec{u}(\vec{x}, t)$ ) and computes one or more derived quantities and outputs the results of these computations in some form. For example, given a velocity field one may wish to calculate pressure, strain, vorticity, strain times vorticity, mean and mean square velocity, skin friction, etc.

*Tensoral* presents users with two main abstractions: *tensors* and *operators*, which we presently introduce. All quantities in *Tensoral* (whether base or derived) are

represented as *tensors*. *Tensoral* tensors correspond loosely to mathematical tensor fields. This correspondence is loose in that *Tensoral* tensors are not defined by how they transform under coordinate change. Instead, *Tensoral* tensors are “computational” tensors: that is, they are indexed numerical arrays (for example,  $a_{ij}(x,y,z)$ ) — with one set of tensor indices ( $ij$ ) and one set of coordinate indices ( $xyz$ ). *Tensoral* tensors have *rank* and *dimension* which respectively define the number and range of tensor indices;  $a_{ij}$  is a rank 2 tensor and indices  $i$  and  $j$  take integral values from 1 to  $d$ , the dimension of  $a$ . Coordinate indices describe which coordinates (if any) a tensor depends on. Normally, coordinate indices are transparent to post-processing users — operations on tensors always apply to the entire array. Adding two tensors, for example, adds array values at corresponding spatial points and for corresponding tensor indices. Explicit coordinate values are also available via projection (introduced below).

*Tensoral* tensors are modified and combined with *operators*. Standard *Tensoral* operators include tensor assignment ( $=$ ), algebraic operations (addition, subtraction, multiplication, division, exponentiation), differentiation, integration, averaging, and projection. Such operators are built into *Tensoral* syntax and are hence “standard.” Tensor rank and coordinate dependencies are appropriately updated when variables are assigned, algebraically combined, differentiated, averaged, or indices contracted (dot product). Thus, performing a derivative increases rank by one, averaging removes coordinate dependencies, etc.

User defined operators can be provided at will by database authors. Useful examples of such operators include reading and writing databases, output of tensors for visualization or graphing, etc. *Tensoral* provides an extremely flexible mechanism for such operators to be added by database authors. However, available user defined operators must be documented by a database author for users to be able to effectively use them.

It should be mentioned here that *Tensoral* tensors and operators are abstract notions. How an abstract tensor is represented numerically (e.g. as an array in memory, across processors in a multi-computer, split between memory and disk, etc.) and how operators operate (e.g. derivatives as finite differences or as multiplication in wave space, etc.) is completely determined by a database *backend*. Such backends (described in section 2 of this guide) are provided by simulation authors and give all of the information necessary to convert *Tensoral* post-processors into an executable computer program to perform the intended computation and output the result.

### *Mathematical syntax*

Mathematical notation in *Tensoral* is a super-set of *Vectoral* notation and as with *Vectoral* aims to present a syntax as close as possible to standard mathematical notation. Thus, given tensors  $a$  and  $b$ ,  $a+b$ ,  $a-b$ ,  $a*b$ ,  $a.b$ ,  $a/b$ ,  $a^b$  and  $|a|$  represent point-wise addition, subtraction, cross product, dot product, division, exponentiation and absolute value (for scalars), respectively. Juxtaposition  $a\ b$  can also be used for outer (tensor) product (but only if  $a$  and  $b$  are within parenthesis or are not within parentheses but are on the same input line). Floating point constants

(which are tensors of rank 0 with no coordinate dependencies) are entered as in *Vectoral*: as sequences of base ten digits and optional decimal point, followed with an optional *e* or *E* for exponent and optional *i* or *I* for the imaginary unit ( $\sqrt{-1}$ ). Any balanced parenthesis (*()*, *{}* or *[]*) may be used for grouping mathematical expressions.

### Tensor notation

In addition *Tensoral* supports tensor notation as follows. Tensor indices are introduced by the underscore character *\_* and followed by arbitrary mixtures of single digits or single letter coordinate directions (for indices with explicit values – e.g. *a\_12*  $\equiv$  *a\_xy*), or single letters which are not coordinates (for dummy indices – e.g. *a\_ij*). No spaces are allowed before or after indices or the leading *\_*. Indices whether explicit or dummy must be single letters or digits. One should think of *Tensoral* indexed expressions as atomic variable references which — as in most other computer languages — contain no white space.

Any tensor index which is not a number or a coordinate direction (as defined in a particular simulation backend) is assumed to be a dummy index. Dummy indices label how tensor indices are to be combined in an expression — for example, distinguishing the statements *a\_ij* = *b\_j c\_i* and *a\_ij* = *b\_i c\_j*. Dummy indices are also often used in conjunction with the summation convention: namely, that repeated dummy indices in a product are summed over. Use of the summation convention in indexed products is controlled by whether *\** or *.* or juxtaposition is used for multiplication. Products involving pure juxtaposition imply the summation convention; otherwise, summation is not implied. *Tensoral* provides the standard symbols  $\delta_{ij}$  (totally symmetric) and  $\epsilon_{ijk}$  (totally anti-symmetric) as *delta* and *epsilon*. Here are some illustrative examples of tensor index notation:

<i>c_k</i> = <i>epsilon_ij k a_i b_j</i>	cross product of rank 1 <i>a</i> , <i>b</i> .
<i>c</i> = <i>a_i b_i</i>	dot product of rank 1 <i>a</i> , <i>b</i> .
<i>c_ik</i> = <i>a_ij b_jk</i>	matrix multiplication of rank 2 <i>a</i> , <i>b</i> .

Tensor expressions need not have explicit indices. If indices are missing *Tensoral* deduces the tensor rank (either from the tensor assigned to the given expression or zero if there is no such tensor) and inserts dummy indices in missing slots from left to right. Summation over repeated dummy indices is implied for index-free expressions, independent of which form of multiplication is used. Also, for index-free expressions the multiplication operators *\** and *.* generate dummy indices for cross and dot products, respectively. Using index free notation, the above examples are coded as follows:

<i>c</i> = <i>a</i> * <i>b</i>	cross product.
<i>c</i> = <i>a</i> . <i>b</i>	dot product.
<i>c</i> = <i>a</i> <i>b</i>	matrix multiplication.

### Coordinate indexing: projection

Indexing (also referred to as *projection*) is also supported for spatial coordinates, but with a different notation than for tensor indexing. A tensor *u* depending on

coordinates **xyz** can be evaluated at particular **x**, **y** or **z** values for  $x = 17$  planes as **u(17,y,z)**, for  $x = 17$ ,  $z = 19$  pencils as **u(17,y,19)**, or at a single point  $x = y = z = 0$  as **u(0,0,0)**. All coordinate names in *Tensoral* are single characters, whose definition, semantics, and values are determined by database backends.

*Tensoral* coordinates are not required to be the native coordinates of a simulation. A database author can provide various coordinate systems for a single simulation as appropriate and physically meaningful. Typical coordinates for Rogallo's wave space isotropic turbulence simulation would include, for example:

<b>x y z</b>	standard Cartesian coordinates,
<b>X Y Z</b>	Cartesian wave space,
<b>r</b>	the radial coordinate $r^2 = x^2 + y^2 + z^2$ ,
<b>k</b>	the wave vector magnitude $k^2 = X^2 + Y^2 + Z^2$ .

### *Tensoral operators*

Mathematical functions (e.g. sine, cosine, log, exponential), differentiation, laplace and curl operator inversion, among others) all appear in *Tensoral* as operators. Operators in *Tensoral* act from the left and apply to a given number of tensors or tensor expressions on the right. Operator arguments are flanked by parentheses (one of **()**, **{}** or **[]**) and separated by commas as in standard mathematical notation. (Additional operator notation is provided at statement level and will be discussed below.) If an operator takes a single operand (for example, square root), these parenthesis may be omitted so long as the argument is a tensor. Thus, **sqrt z** is permissible in place of **sqrt(z)**.

Operators are either built into *Tensoral* or are defined by database authors' backends. Since they must be specially defined by backends or are built into *Tensoral*, operators can be recognized as syntactically differentiated from tensors, making it possible to differentiate tensor projection (e.g. **a(0,0,0)** for tensor **a**) from operator notation (e.g. **f(0,0,0)** for operator **f**).

The standard mathematical functions in *Tensoral* are as in *Vectoral* and are listed in the following table:

<b>conj z</b>	Complex conjugate
<b>exp x, log x, log10 x</b>	Exponential, log, log base 10.
<b>sqrt x</b>	Square root
<b>sin x, cos x, tan x</b>	Trigonometric functions.
<b>arcsin x, arccos x</b>	
<b>arctan x</b>	Trigonometric inverse functions.

Like tensors, operators can also have rank and be indexed (like any other tensor). In particular, differentiation (**diff** or **grad**), integration (**int**), averaging (**ave**), minimum (**min**), and maximum (**max**) are all indexed operators in *Tensoral*.

Differentiation has rank one and can be explicitly indexed (e.g. **diff.y u\_x** for  $\partial_y u_x$ ) or can be index free:

<b>w = grad * u</b>	encodes the curl of <b>u</b> ;
<b>divu = grad . u</b>	encodes its divergence.

In addition, a special indexed shorthand is available for derivatives: any dummy indices following a comma are taken as derivatives. Thus,  $u_{,i,j}$  is shorthand for  $\text{diff\_j } u_{,i}$ , and  $v_{,ii}$  generates a Laplacian  $\nabla^2 v$ .

The remainder of the indexed operators listed above are special in that they do not have fixed rank. Consider **ave** as a typical example. **ave\_x** performs an average over the  $x$  coordinate direction (as defined by the database backend); **ave\_xy** performs averaging over both  $x$  and  $y$  coordinate directions. The remainder of the average-like operators (**int**, **min**, **max**) behave in a similar fashion: operator indices determine which coordinates are to be integrated and minimized or maximized over.

### Tensoral statements

There are only two forms of statement in *Tensoral*: assignments and statement-level operator expressions. Assignments can use multiple left-hand sides as long as they are tensors and multiple assignments may be performed in parallel as in *Vectoral* with the **&** character joining the multiple assignments. In parallel assignment, right hand sides of all **&**-linked assignments are evaluated *before* any assignments are performed, so that the statement **a = b & b = a**, for example, swaps tensors **a** and **b**.

Statement-level operator expressions may optionally use a special operator syntax, different from standard functional notation (e.g.  $f(a,b,c)$ ). At statement-level operator expressions may be written without parenthesis. If all arguments are tensors (either indexed or index-free) an operator expression may be written without commas. In either case, the final argument is terminated by a newline, which replaces the closing parenthesis of functional notation. The following are valid examples of statement-level operators **f** and **g**: **g a+b**, **a-b** and **f a b**. (Of course, both of these examples must be terminated with a new line.)

### Example and usage

Here we illustrate what has just been presented and give a complete example of how *Tensoral* can be used to perform a simple post-processing task. Suppose — for the sake of example — one wants to study vorticity generation in an evolving incompressible boundary layer (evolving along the  $x$  direction). A simple question to ask would be “what does the plane-averaged vortex stretching term look like as a function of  $x$ ?” Suppose further that one desires to measure this stretching in an exponential sense, i.e. to calculate  $d/dt \log(\bar{\omega}^2) = \bar{\omega} \cdot \mathbf{S} \bar{\omega} / \bar{\omega}^2$ , and average it along  $yz$  directions. One would code the following *Tensoral* program into a file **test** on the computer disk:

```
S_ij = 1/2 (u_{,i,j} + u_{,j,i})
w_k = 1/2 epsilon_ijk (u_{,i,j} - u_{,j,i})
print ave_yz (w . S w / w . w)
```

To execute the *Tensoral* program **test** on simulation restart file **run1**, one would execute a command (for example, to a Unix shell program) **t1 test run1** and the entire  $x$  direction of mean exponential vorticity production should be output on the computer console. (Details, of course have been omitted here: in particular, **run1** must be associated with some author-contributed *Tensoral* database backend.)

## 2. Tensoral author's guide

This author's guide seeks to introduce simulation and database authors to how the *Tensoral* compiler operates and to how database backends interact with and control this operation. Thus, we give here a general introduction to the inner workings of the *Tensoral* compiler and follow it with a brief description of the tools with which backends are coded.

### Overview

The *Tensoral* system compiles high-level tensor expressions and statements — either in the form of a native post-processor (as described in the above user's guide) or as embedded within a lower-level host computer language — into host language code which numerically realizes these tensor operations. The lower-level language program output by a *Tensoral* compilation is itself compiled by another (e.g. *C* or *Vectoral*) compiler into an executable computer program. *Tensoral* has been designed to be easily adapted to generate any sufficiently powerful host language. Thus, the prototype system currently under development has separate versions for *C* and *Vectoral* as host languages.

By compiling tensor operations into a host language, *Tensoral* can be simultaneously general and efficient. Also, this design allows for *Tensoral* to be flexibly embedded within non-tensor specific host language code. In this way *Tensoral* specializes in numerical tensor computations and leaves other language features (input/output, file handling, graphics calls, etc.) to the host language.

The process of converting *Tensoral* into host code is mediated by the *Tensoral* compiler and is controlled by database backends. The *Tensoral* compiler presents backends with several constructs for describing exactly how abstract *Tensoral* tensors and the operators which combine them are realized in host code. In particular, the compiler presents database authors with mechanisms for host-coding both tensor and coordinate indices, for host-coding operators and how they combine tensors in mathematically meaningful ways, and for host-coding loops to iterate over tensors' coordinates.

The backend constructs for looping, operators, and tensor indexing are given using a parenthesized Lisp-like notation: *Tensoral* employs the *Scheme* dialect of Lisp for both its internal coding and as an extension language. Host code is specified within *Scheme* in the form of a simple *template* language. Templates are fragments of host code which can refer to other templates or arbitrary *Scheme* code, can have other templates substituted in them, and can be split and subsequently inserted onto the loops which iterate over tensor's dependent coordinates. The details and syntax for templates, as well as for the backend looping, indexing, and operator constructs just mentioned, will be touched upon in the following and detailed elsewhere.

### How *Tensoral* works

How then is a *Tensoral* program compiled into host language code? Tensors in *Tensoral* must somehow correspond to numeric arrays. Hence, operations involving tensors must correspond to host code which iterates numerical operations over the



elements of these arrays. The first step in generating host code must then involve specifying how *Tensoral* tensors and expressions are to be iterated over.

The *Tensoral* compiler represents this iteration with a scaffolding of nested host language loops — for loops in *C* or *Vectoral*; do loops in *Fortran*. Looping constructs are defined by simulation authors' backends with the `loop` function and are meant to be flexible and general so as to support various data management strategies such as splitting data into one dimensional pencils, two dimensional planes, groups of planes, or splitting data across processors of a multi-computer (such as the Intel Hypercube or Paragon systems).

The ordering and nesting of these loops is dynamic and under the control of either the database backend or the *Tensoral* program (or both). Loop nests are determined and changed either implicitly through the *Tensoral* operators present in an expression (the typical case for native *Tensoral* post-processors) or explicitly in *Tensoral* code (the typical case for embedded *Tensoral*).

Once the loop scaffolding has been erected, host code templates for tensor operations and expressions can be built around and inside it. *Tensoral* statements are first parsed by the compiler into *Scheme* code. Parsing involves mapping *Tensoral* operator notation (for example,  $f(a,b,c)$  and  $a = b*c$ ) to corresponding *Scheme* function calls (`(f a b c)` and `(= a (* b c))`) for appropriately defined or re-defined *Scheme* functions (`f`, `=`, and `*`). This *Scheme* code, which only involves function calls and tensor references, is then recursively evaluated by the *Scheme* interpreter. The results of evaluating *Tensoral* operators at each recursion level are a template representing the operator applied to its operands in host code and a representation of which coordinates this expression depends on. Both of these evaluation results come in the form of *Scheme* strings.

When tensors are encountered while evaluating *Tensoral* expressions, special templates are used to generate host code for them. These special templates are given by backends and completely implement how tensor and coordinate indexing behaves. Coordinate dependency information, built into to how tensors are internally represented by the *Tensoral* compiler, determines how this indexing is to be performed. Tensor indexing templates are generally the most complex in a database backend since they almost completely implement how tensors are represented numerically. Template and coordinate dependency information are returned as results of this evaluation.

The evaluation of *Tensoral* operator expressions also involves generating both a template and corresponding coordinate dependency information. Operator evaluation begins by recursively evaluating the operator's operands giving the operands templates and coordinate dependencies. All *Tensoral* operators have templates associated with them. These templates are either built into *Tensoral* or are given by database backends via the `operator` command. In either case, these operator templates specify where and how operand templates are to be placed within them. In this way, expression templates are formed. All *Tensoral* operators also have coordinate dependency information which specify how they combine the coordinate dependencies of their operands. Thus, evaluation results in a template and

coordinate dependencies.

After expression and tensor operands have been substituted, host code is generated from templates by “cut and paste.” Substituted templates — whether evaluated from statement level or nested within an expression — are split (the “cut” operation) at points specified in the template and the pieces of the split template (“sub-templates”) are inserted (the “paste” operation) onto the loop nest according to the nesting levels specified along with these split points. The sub-template after the final split point of a template (or the entire template if no split point is present) is taken as the *value* of the template. Template values represent host code for the value of a template. For nested expressions, template values are inserted into the expression which recursively contains them (e.g. the  $*$  template value in  $(= a (* b c))$ ); template values at the statement-level (e.g.  $=$  value in  $(= a (* b c))$ ) are inserted into the loop nest according to the statement-level coordinate dependency information generated in the evaluation process.

Once all tensor expressions have been evaluated and all templates generated and split, the loop nest contains only host language strings and *Scheme* code. Any *Scheme* code on the loop nest needs to be further evaluated and will, presumably, generate more templates and/or *Scheme* code. The evaluation process just outlined is repeated until no more *Scheme* code remains on the loop nest and the entire loop nest may be output as host code. Initially host and *Scheme* code exist on a single loop nest; however, as further *Scheme* code is evaluated, further structure may be added under the direction of this the *Scheme* code. One of the most important uses of *Scheme* code within templates is to structure loop nests as appropriate to a given computation.

### 3. Current status and future direction

At present a prototype of a pre-*Tensoral* language — a lower-level language than *Tensoral* as described here — has been completed and is operational. This language generates *Vectoral* post-processors given pre-*Tensoral* code and includes many of the backend concepts described here. However, this pre-*Tensoral* language is missing many of the features and even some of the general concepts described in this document. The full *Tensoral* language described here is currently under development and will hopefully be completed in a matter of months.

As for the future, I hope to have a prototype *Tensoral* system functional for the next CTR summer program. Use of *Tensoral* in a summer program should provide significant experience towards how to use *Tensoral* effectively and how to refine its design to increase its utility. For the near future, my goal is to have Rogallo’s isotropic turbulence simulation and database post-processing coded purely in *Tensoral*.

## Appendix

### NAME/TERM

### AREA OF RESEARCH

#### POSTDOCTORAL FELLOWS

CHASNOV, Dr. Jeffrey 9/91-8/93	(Ph.D. Physics, 1990, Columbia University)	Turbulence theory and simulation
COLEMAN, Dr. Gary 5/92-11/93	(Ph.D. Mechanical Engineering, 1990, Stanford University)	Compressible turbulence
GAO, Dr. Feng 9/90-3/93	(Ph.D. Mechanical Engineering, 1990, SUNY at Stony Brook)	PDF approach and related closures for turbulent scalar fields
GHOSAL, Sandip 2/92-present	(Ph.D. Physics, 1992, Columbia University)	Subgrid scale modeling
HAMILTON, Dr. James M. 6/91-8/93	(Ph.D. Engineering Science, 1991, Harvard University)	Structure of turbulent boundary layers
JANSEN, Dr. Kenneth 9/93-present	(Ph.D., Mechanical Engineering, 1993, Stanford)	Large eddy simulation of complex flows
JONES, Dr. Donald A. 9/92-8/93	(Ph.D. Mathematics, 1992, UC-Irvine)	Mathematical theory of the Navier-Stokes equations
KALTENBACH, Dr. H.-J. 9/92-present	(Ph.D. Atmospheric Physics, 1992, DLR )	Large eddy simulation
KO, Dr. Sung Ho 7/91-6/93	(Ph.D. Mechanical Engineering, 1991, Texas A&M University)	Application of turbulence models
LEBOEUF, Dr. Richard L. 9/91-present	(Ph.D. Mechanical Engineering, 1991, SUNY at Buffalo)	Experimental study of turbulent mixing layer

MANTEL, Dr. Thierry 7/93-present	(Ph.D. Physics, 1993, U. Rouen)	Turbulent combustion
RUETSCH, Dr. Gregory 9/93-present	(Ph.D. Applied Mathematics, 1991, Brown University)	Turbulent combustion
SADDOUGHI, Dr. Seyed G. 6/91-present	(Ph.D. Mechanical Engineering, 1989, The University of Melbourne)	Experimental investigation of local isotropy in high- Reynolds-number turbulence
SAMANIEGO, Dr. J.-M. 4/92-present	(Ph.D. Combustion, 1992, Ecole Centrale Paris)	Reacting flows
TROUVE, Dr. Arnaud 4/90-5/93	(Ph.D. Mechanical Engineering, 1989, Ecole Centrale de Paris)	Turbulent combustion
VERVISCH, Dr. Luc 1/92-12/92	(Ph.D. Physics, 1991, Univ. Rouen, France)	Turbulent combustion
WANG, Dr. Meng 9/92-present	(Ph.D. Mechanical Engineering, 1989, Univ. of Colorado)	Aerodynamic noise

#### RESEARCH ASSOCIATES

CABOT, Dr. William H. 3/88-present	(Ph.D. Physics, 1983, University of Rochester)	Large eddy simulation and convection
DRESSELHAUS, Dr. Eliot 9/91-present	(Ph.D. Applied Mathematics, 1991, Columbia University)	Postprocessing and computer languages
LEE, Dr. Sangsan 4/92-present	(Ph.D. Mechanical Engineering, 1992, Stanford University)	Shock waves
LUND, Dr. Thomas S. 11/90-present	(Ph.D. Aero-Astro, 1987, Stanford)	Large eddy simulation

**SENIOR VISITING FELLOWS**

LUNDGREN, Prof. Thomas Summer 1993	Professor, University of Minnesota	Transition to turbulence
POINSOT, Dr. Thierry 8/93	Director of CFD CERFACS, Toulouse	Turbulent combustion
SPEZIALE, Prof. Charles 8/93	Professor, Boston University	Turbulence modeling
SQUIRES, Kyle D. Summer 1993	Assistant Professor, University of Vermont	Large eddy simulation and rotating turbulence
TEMAM, Prof. Roger 8/93	Professor, Univ. of Paris - SUD and Univ. of Indiana	Flow control
TOKUNAGA, Prof. Hiroshi 4/92-4/93	Professor, Kyoto Institute of Technology	Computational algorithms

**SR. RESEARCH FELLOWS**

DURBIN, Dr. Paul 1/90-present	DAMTP, Cambridge University	Turbulence modeling
HILL, Dr. D. Christopher 5/92-present	Cambridge University	Flow control
JIMENEZ, Prof. Javier 7/93-11/93	Professor of Fluid Mech., School of Aeronautics, University of Madrid	Energy cascade and subgrid scale parameterization
ZEMAN, Dr. Otto 3/1/89-present	Pennsylvania State University	Turbulence modeling

**GRADUATE STUDENTS**

AIAIEZ, Jalel 10/91-9/92	Viscoelastic mixing layers
LE, Hung 4/88-8/93	Simulation of turbulent flow over a backward-facing step
PEROT, Blair 10/92-present	Physics and modeling of shear- free turbulent boundary layers

## 1993 ADVISORY COMMITTEE

Prof. Ronald J. Adrian  
University of Illinois

Prof. George K. Batchelor  
DAMTP, Univ. of Cambridge

Prof. Garry Brown  
Princeton University

Dr. Dennis M. Bushnell  
NASA Langley Research Center

Dr. Coleman Donaldson  
Gloucester, VA

Dr. Marvin E. Goldstein (Chairman)  
NASA Lewis Research Center

Dr. Spiro Lekoudis  
Office of Naval Research

Dr. James M. McMichael  
Air Force Office of Scientific Research

Dr. Robert Melnik  
Grumman Corporation

Prof. Richard A. Seebass  
Univ. Colorado at Boulder

Prof. Stephen B. Pope  
Cornell University

Dr. A. D. (Bert) Welliver  
Boeing Airplane Company

Dr. Ron Bailey (Ex-officio)  
NASA Ames Research Center

Dr. Kristen Hessenius (Ex-officio)  
NASA Headquarters

## 1993 STEERING COMMITTEE

Prof. Dean R. Chapman  
Dept. of Aeronautics & Astronautics  
and Mechanical Engineering, Stanford

Dr. Terry L. Holst  
Chief, Applied Computational Fluids Branch,  
NASA Ames Research Center

Prof. Javier Jimenez  
Senior Visiting Fellow, Center for Turbulence  
Research, 7/93-11/93  
Professor, Fluid Mechanics, University of  
Madrid

Dr. John J. Kim  
Ames Coordinator, Center for Turbulence  
Research  
Head, Turbulence Physics Section, NASA  
Ames Research Center

Dr. N. N. Mansour  
Turbulence Physics Section, NASA Ames  
Research Center

Mr. Joseph G. Marvin  
Chief, Experimental Fluid Dynamics Branch,  
NASA Ames Research Center

Prof. Parviz Moin  
Director, Center for Turbulence Research  
Professor, Mechanical Engineering, Stanford  
Sr. Staff Scientist, NASA Ames Research  
Center

Prof. William C. Reynolds  
Program Coordinator, Center for Turbulence  
Research  
Professor and Chairman, Mechanical  
Engineering, Stanford  
Sr. Staff Scientist, NASA Ames Research  
Center

Prof. Roger Temam  
Senior Visiting Fellow, Center for Turbulence  
Research, July 1993  
Professor, Univ. Paris, SUD & Univ. Indiana